



# **Analysis and design of plated structures**

**Volume 2: Dynamics**

**Edited by N. E. Shanmugam and C. M. Wang**



**WP**

**@Seismicisolation**

Analysis and design of plated structures

@Seismicisolation

## **Related titles:**

### *Analysis and design of plated structures Volume 1: Stability*

(ISBN-13: 978-1-85573-967-3; ISBN-10: 1-85573-967-4)

Steel-plated structures are used in a variety of marine and land-based applications such as ships, off-shore platforms, power and chemical plants, box-girder cranes and bridges. This first volume in a two-volume sequence considers the various types of buckling that plated structures are likely to encounter and reviews buckling in a range of materials from steel to differing types of composite. The book discusses the behaviour of various types of components used in steel-plated structures as well as curved, stiffened, corrugated, laminated and other types of plate design. Together with its companion volume, this is an essential reference in the design, construction and maintenance of plated structures.

### *The deformation and processing of structural materials*

(ISBN-13: 978-1-85573-738-9; ISBN-10: 1-85573-738-8)

This new study focuses on the latest research in the performance of a wide range of materials – particularly structural steels – used in structures. It considers the processing and deformation behaviour of various materials in structural applications. It also shows how the microstructural composition of materials is affected by processing and what influence this has on its subsequent *in situ* performance. This book is the first to give comprehensive coverage to the deformation and processing of all types of structural materials. It will provide engineers with a better understanding of the performance of the major structural materials (especially metals) under different conditions and will help them to set design specifications and select the right type of material for a job. It will also be a valuable resource for researchers in mechanical, civil and structural engineering.

### *Inspection and monitoring techniques for bridges and civil structures*

(ISBN-13: 978-1-85573-939-0; ISBN-10: 1-85573-939-9)

The safety, maintenance and repair of bridges and buildings depend on effective inspection and monitoring techniques. These methods need to be able to identify problems, often hidden within structures, before they become serious. This important collection reviews key techniques and their applications to bridges, buildings and other civil structures. The first group of chapters reviews ways of testing corrosion in concrete components. The next group of chapters describes ways of testing wood components – given their continuing importance and vulnerability to decay – within civil structures. A final group of chapters looks at visual and acoustic techniques and their use in assessing bridges in particular.

Details of these and other Woodhead Publishing materials books and journals, as well as materials books from Maney Publishing, can be obtained by:

- visiting [www.woodheadpublishing.com](http://www.woodheadpublishing.com)
- contacting Customer Services (e-mail: [sales@woodhead-publishing.com](mailto:sales@woodhead-publishing.com); fax: +44 (0) 1223 893694; tel.: +44 (0) 1223 891358 ext. 130; address: Woodhead Publishing Ltd, Abington Hall, Abington, Cambridge CB21 6AH, England)

Maney currently publishes 16 peer-reviewed materials science and engineering journals. For further information visit [www.maney.co.uk/journals](http://www.maney.co.uk/journals).

# Analysis and design of plated structures

Volume 2: Dynamics

---

Edited by  
N. E. Shanmugam and C. M. Wang

Woodhead Publishing and Maney Publishing  
on behalf of  
The Institute of Materials, Minerals & Mining

CRC Press  
Boca Raton Boston New York Washington, DC

WOODHEAD PUBLISHING LIMITED  
Cambridge England

@Seismicisolation

Woodhead Publishing Limited and Maney Publishing Limited on behalf of  
The Institute of Materials, Minerals & Mining

Published by Woodhead Publishing Limited, Abington Hall, Abington  
Cambridge CB21 6AH, England  
[www.woodheadpublishing.com](http://www.woodheadpublishing.com)

Published in North America by CRC Press LLC, 6000 Broken Sound Parkway, NW,  
Suite 300, Boca Raton, FL 33487, USA

First published 2007, Woodhead Publishing Limited and CRC Press LLC  
© Woodhead Publishing Limited, 2007  
The authors have asserted their moral rights.

This book contains information obtained from authentic and highly regarded sources.  
Reprinted material is quoted with permission, and sources are indicated. Reasonable  
efforts have been made to publish reliable data and information, but the authors and  
the publishers cannot assume responsibility for the validity of all materials. Neither  
the authors nor the publishers, nor anyone else associated with this publication, shall  
be liable for any loss, damage or liability directly or indirectly caused or alleged to be  
caused by this book.

Neither this book nor any part may be reproduced or transmitted in any form or by  
any means, electronic or mechanical, including photocopying, microfilming and  
recording, or by any information storage or retrieval system, without permission in  
writing from the Woodhead Publishing Limited.

The consent of Woodhead Publishing Limited does not extend to copying for  
general distribution, for promotion, for creating new works, or for resale. Specific  
permission must be obtained in writing from Woodhead Publishing Limited for such  
copying.

Trademark notice: Product or corporate names may be trademarks or registered  
trademarks, and are used only for identification and explanation, without intent to  
infringe.

British Library Cataloguing in Publication Data

A catalogue record for this book is available from the British Library.

Library of Congress Cataloging in Publication Data

A catalog record for this book is available from the Library of Congress

Woodhead Publishing ISBN-13: 978-1-84569-116-5 (book)

Woodhead Publishing ISBN-10: 1-84569-116-4 (book)

Woodhead Publishing ISBN-13: 978-1-84569-229-2 (e-book)

Woodhead Publishing ISBN-10: 1-84569-229-2 (e-book)

CRC Press ISBN-13: 978-1-4200-4457-7

CRC Press ISBN-10: 1-4200-4457-5

CRC Press order number: WP4457

The publishers' policy is to use permanent paper from mills that operate a  
sustainable forestry policy, and which has been manufactured from pulp  
which is processed using acid-free and elementary chlorine-free practices.  
Furthermore, the publishers ensure that the text paper and cover board used  
have met acceptable environmental accreditation standards.

Project managed by Macfarlane Production Services, Dunstable, Bedfordshire,  
England ([macfarl@aol.com](mailto:macfarl@aol.com))

Typeset by Replika Press Pvt Ltd, India

Printed by T J International Limited, Padstow, Cornwall, England

The logo consists of a stylized '@' symbol followed by the words 'Seismic isolation' in a bold, sans-serif font. The 'S' and 'i' in 'Seismic' are partially obscured by a large, semi-transparent watermark of the same text, creating a repeating pattern across the page.

## Contents

---

<i>Contributor contact details</i>	<i>xi</i>
<i>Preface</i>	<i>xv</i>
1      Dynamic behaviour of tapered beams	1
M A BRADFORD, The University of New South Wales, Australia	
1.1     Introduction	1
1.2     Linearly tapered members with both ends supported	6
1.3     Linearly tapered cantilever	17
1.4     Finite element approach	20
1.5     Conclusions	31
1.6     References	32
2      GBT-based local and global vibration analysis of thin-walled members	36
D CAMOTIM, N SILVESTRÉ and R BEBIANO, Technical University of Lisbon, Portugal	
2.1     Introduction	36
2.2     GBT vibration analysis	40
2.3     Illustrative examples	56
2.4     Conclusions	73
2.5     References	74
3      Dynamics of nonprismatic thin-walled hybrid composite members of generic cross-section	77
S RAJASEKARAN, PSG College of Technology, India	
3.1     Introduction	77
3.2     Remarks on approach	79
3.3     Geometric description of undeformed beam	80
3.4     Assumptions	81
3.5     Kinematics	82
3.6     Constitutive equations	91

3.7	Equations of equilibrium	97
3.8	Finite element beam model	100
3.9	Numerical integration for finding properties and stress resultants at a cross-section	102
3.10	Alternative formulation using plate elements (anon, 1995)	103
3.11	Numerical examples	108
3.12	Conclusions	112
3.13	References	114
4	Least squares finite difference method for vibration analysis of plates	118
	C SHU, W X WU and C M WANG, National University of Singapore, Singapore	
4.1	Introduction	118
4.2	Least squares-based finite difference (LSFD) method	118
4.3	Governing equation and boundary conditions for free vibration of thin plates	126
4.4	Discretization of the governing equation by the LSFD method	127
4.5	Numerical implementation of boundary conditions	128
4.6	Computation of stress resultants	134
4.7	Numerical examples	135
4.8	Conclusions	141
4.9	References	143
5	Analytical $p$ -elements for vibration of plates/plated structures	145
	A Y T LEUNG, City University of Hong Kong, People's Republic of China and B ZHU, Zhejiang University, People's Republic of China	
5.1	Introduction	145
5.2	Condition number	146
5.3	Trapezoidal Mindlin plate elements	149
5.4	Transverse vibration of plates on Pasternak foundations	164
5.5	Geometric nonlinear vibration of clamped plates	174
5.6	Conclusions	186
5.7	References and further reading	189
6	The extended Kantorovich method for vibration analysis of plates	192
	M EISENBERGER and I SHUFRIN, Technion – Israel Institute of Technology, Israel	
6.1	Introduction	192

6.2	Vibrations of rectangular plates	193
6.3	Numerical examples and discussion	197
6.4	Conclusions	215
6.5	References	218
7	A closed-form approach to modeling and dynamic analysis of beams, plates and shell	219
	B YANG, University of Southern California, USA	
7.1	Introduction	219
7.2	DTFM for one-dimensional continua	220
7.3	DTFM for multifunctional continua	227
7.4	Free vibration of plates and shells	235
7.5	Conclusions	250
7.6	Acknowledgments	251
7.7	References	251
8	Vibrations of plates with abrupt changes in properties	254
	Y. XIANG, University of Western Sydney, Australia	
8.1	Introduction	254
8.2	Mathematical modelling	255
8.3	Case studies	259
8.4	Conclusions	272
8.5	Acknowledgments	272
8.6	References	272
9	Relationships between vibration frequencies of higher-order plate theories and classical thin plate theory	275
	C M WANG, National University of Singapore, Singapore	
9.1	Introduction	275
9.2	Plate theories	275
9.3	Equations of free vibration	277
9.4	Relationship between frequencies of FSDT and CPT	280
9.5	Relationship between frequencies of TSDT and CPT	283
9.6	Frequency results	286
9.7	Modification of frequency relationship for complicating effects	288
9.8	Concluding remarks	291
9.9	References	291

10	Free vibration analysis of functionally graded ceramic-metal plates	293
	J N REDDY, National University of Singapore, Singapore and R A ARCINIEGA, Texas A&M University, USA	
10.1	Introduction	293
10.2	Theoretical formulation	294
10.3	Finite element model	299
10.4	Numerical results	302
10.5	Conclusions	316
10.6	Acknowledgments	318
10.7	References	318
10.8	Appendix	320
11	Differential quadrature element method for vibration analysis of plates	322
	K M LIEW, J YANG and S KITIPORNCHAI, City University of Hong Kong, People's Republic of China	
11.1	Introduction	322
11.2	The DQ-Galerkin method	325
11.3	Theoretical formulations	327
11.4	Imperfection mode	338
11.5	Validation studies	339
11.6	Numerical results	345
11.7	Conclusions	370
11.8	Acknowledgment	372
11.9	References	372
12	Nonlinear vibration and transient analysis of hybrid laminated plates	376
	H-S SHEN and X-L HUANG, Shanghai Jiao Tong University, People's Republic of China	
12.1	Introduction	376
12.2	Governing equations	379
12.3	Solution methodology	384
12.4	Nonlinear vibration and dynamic response of initially stressed antisymmetric angle-ply laminated plates	391
12.5	Nonlinear vibration and dynamic response of an unsymmetric cross-ply laminated plate with piezoelectric layers	395
12.6	Nonlinear vibration and dynamic response of FGM hybrid laminated plates	407
12.7	Conclusions	415
12.8	Acknowledgment	419
12.9	References	419

13	A hybrid strategy for parameter identification of plated structures C G KOH and S L ZHAO, National University of Singapore, Singapore	422
13.1	Introduction	422
13.2	Genetic algorithms (GA)	422
13.3	Hybrid GA-MV method	424
13.4	Two new local search operators	429
13.5	Identification of plated structure	435
13.6	Conclusions	441
13.7	Acknowledgment	443
13.8	References	443
14	Hydroelastic analysis of floating plated structures T UTSUNOMIYA, Kyoto University, Japan	445
14.1	Introduction	445
14.2	The boundary value problem	447
14.3	The boundary integral equation	449
14.4	Equation of motion for VLFS deflections	450
14.5	Formulation for hydroelastic analysis	452
14.6	Multipole expansion of Green's function	454
14.7	Implementation to higher-order boundary element method	455
14.8	Application of the fast multipole method	457
14.9	Numerical examples	459
14.10	Concluding remarks	462
14.11	References	464
	<i>Index</i>	466

@Seismicisolation

## Contributor contact details

---

(\* = main contact)

### Editors

Professor N. E. Shanmugam  
Department of Civil and Structural Engineering  
Universiti Kebangsaan Malaysia  
43600 UKM Bangi  
Selangor Darul Ehsan  
Malaysia

E-mail: shan@vlsi.eng.ukm.my  
neshanmugam@yahoo.com

Professor C. M. Wang  
Department of Civil Engineering  
National University of Singapore  
Kent Ridge  
Singapore 119260

E-mail: cvewcm@nus.edu.sg

### Chapter 1

Professor Mark A. Bradford  
Federation Fellow of the Australian Research Council  
Scientia Professor  
School of Civil & Environmental Engineering  
The University of New South Wales  
UNSW  
Sydney NSW 2052  
Australia

E-mail: m.bradford@unsw.edu.au

### Chapter 2

Professor Dinar Camotim\*, Nuno Silvestre and Rui Bebiano  
Departamento de Engenharia Civil  
Instituto Superior Técnico  
Av. Rovisco Pais  
1049-001 Lisboa  
Portugal

E-mail: dcamatim@civil.ist.utl.pt

### Chapter 3

Professor S. Rajasekaran  
Department of Civil Engineering  
PSG College of Technology  
Coimbatore-641004  
Tamilnadu  
India

E-mail: drrajasekaran@gmail.com

### Chapter 4

Professor Shu Chang  
Department of Mechanical Engineering  
National University of Singapore  
Kent Ridge  
Singapore 119260

E-mail: mpeshuc@nus.edu.sg



**Chapter 5**

Professor Andrew Y. T. Leung  
Building and Construction  
City University of Hong Kong  
Kowloon  
Hong Kong  
People's Republic of China

E-mail: andrew.leung@cityu.edu.hk

Dr Bin Zhu  
Department of Civil Engineering  
Zhejiang University  
Hangzhou  
People's Republic of China

**Chapter 6**

Professor Moshe Eisenberger  
Faculty of Civil and Environmental  
Engineering  
Technion – Israel Institute of  
Technology  
Technion City 32000  
Israel

E-mail: cvrmosh@tx.technion.ac.il

**Chapter 7**

Professor Bingen Yang  
Department of Aerospace and  
Mechanical Engineering  
University of Southern California  
Los Angeles, CA 90089-1453  
USA

E-mail: bingen@usc.edu

**Chapter 8**

Dr Y. Xiang  
School of Engineering  
Building XB, Kingswood Campus  
University of Western Sydney  
Locked Bag 1979  
Penrith South DC  
NSW 1797  
Australia

E-mail: y.xiang@uws.edu.au

**Chapter 9**

Professor C. M. Wang  
Department of Civil Engineering  
National University of Singapore  
Kent Ridge  
Singapore 119260

E-mail: cvewcm@nus.edu.sg

**Chapter 10**

Professor J. N. Reddy\*  
Engineering Science Programme  
Faculty of Engineering  
National University of Singapore  
Kent Ridge  
Singapore 119260

E-mail: jnreddy@tamu.edu

Dr R. A. Arciniega  
Department of Mechanical  
Engineering  
Texas A&M University  
College Station  
TX 77843-3123  
USA

## Chapter 11

Professor K. M. Liew\* and  
Professor S. Kitipornchai  
Department of Building and  
Construction  
City University of Hong Kong  
Kowloon  
Hong Kong  
People's Republic of China  
  
E-mail: [kmliew@cityu.edu.hk](mailto:kmliew@cityu.edu.hk)

## Chapter 12

Professor Hui-Shen Shen\* and  
Xiao-Lin Huang  
School of Ocean and Civil  
Engineering  
Shanghai Jiao Tong University  
Shanghai 200030  
People's Repubulic of China

E-mail: [hsshen@mail.sjtu.edu.cn](mailto:hsshen@mail.sjtu.edu.cn)

## Chapter 13

Professor C. G. Koh\* and S. L. Zhao  
Department of Civil Engineering  
National University of Singapore  
E1A-07-03, 1 Engineering Drive 2  
Singapore 117576

E-mail: [cgkoh@nus.edu.sg](mailto:cgkoh@nus.edu.sg)

## Chapter 14

Dr Tomoaki Utsunomiya  
Department of Civil and Earth  
Resources Engineering  
Kyoto University  
Kyoto 615-8540  
Japan  
  
E-mail:  
[utsunomi@mbox.kudpc.kyoto-u.ac.jp](mailto:utsunomi@mbox.kudpc.kyoto-u.ac.jp)

@Seismicisolation

## Preface

---

This book is the second of two volumes on *Analysis and Design of Plated Structures*. While the first volume focused on stability, this second volume addresses the dynamics of plated structures. Generally, vibrations in plated structures are undesirable because they lead to an increase in stresses and to energy losses. Design of plated structures subjected to dynamic loadings therefore has to ensure that vibrations are minimized as much as possible. More importantly, the design must avoid the resonance phenomenon which may even lead to the failure of the entire structure. As in the first volume, we have invited experts on plate vibration to contribute chapters to this volume. The objective is to present the latest methods for vibration analysis of plates and plated structures as well as to document ways of modelling the dynamics of thick plates, composite plates, laminated plates and functionally graded plates.

This volume comprises 14 chapters. Each chapter may be read independently from the other chapters and the chapters contain adequate introductory material so that an engineering graduate who has a basic understanding of structural dynamics and plates will be able to follow it. The first chapter deals with dynamic behaviour of tapered beams that are fabricated from plated elements. It discusses different techniques for the vibration analysis of tapered members and presents key findings. Chapter 2 reviews the use of generalized beam theory (GBT) for the local and global vibration analyses of thin-walled members with open sections. As examples, the GBT formulation has been used to generate vibration solutions for lipped channels and I-section thin-walled steel members with various support conditions. Chapter 3 furnishes a detailed treatment of the vibration problem of tapered thin-walled composite spatial members of generic open or closed section using beam and plate/shell elements. Vibration results are given for a number of examples that include straight and curved composite beams and non-prismatic composite beams.

The next four chapters are concerned with different methods for vibration analysis of plates. The methods are the least squares-based finite difference method as presented in Chapter 4, the *p*-finite element method in Chapter 5,



the extended Kantorovich method in Chapter 6 and the distributed transfer function method in Chapter 7. A large amount of important plate vibration data are given in these four chapters.

In Chapter 8, the domain decomposition method and the state-space technique are combined to solve the vibration problems of rectangular plates with abrupt changes in properties. Analytical relationships between the vibration frequencies of higher-order shear deformable plate theories and the classical thin plate theory are derived for simply supported plates of polygonal shapes in Chapter 9. These two chapters provide exact solutions that should serve as useful benchmark results for checking the validity, convergence and accuracy of numerical techniques and results.

Chapter 10 treats the free vibration problem of functionally graded plates while Chapter 11 considers the more complicated nonlinear vibration problem of functionally graded plates with pre-stress and imperfections. Unlike composite plates, these functionally graded plates do not have the undesirable abrupt changes in the stress distributions through the plate thickness. In Chapter 12, the nonlinear vibration and transient analysis of hybrid laminated plates are presented.

The last two chapters address interesting topics on plated structures. Chapter 13 provides a hybrid strategy that is suitable for parameter identification of plated structures. The parameter identification strategy should be useful in model calibration and updating as well as for damage detection/assessment in a nondestructive way. In Chapter 14, a plate model, usually used for modelling a plate component in a structure, is used to represent an entire, very large, pontoon-type floating structure (or mega-float as termed by the Japanese). The chapter presents a very powerful technique for performing hydroelastic analysis of such a large floating plated structure.

We would like to thank all the contributors for making this second volume possible. It is hoped that the book will be useful and prove stimulating to researchers and practising engineers working on plated structures.

N. E. Shanmugam  
C. M. Wang

# Dynamic behaviour of tapered beams

---

M A B R A D F O R D, The University of New South Wales,  
Australia

## 1.1 Introduction

Plated members that are tapered lengthwise often provide optimal solutions in structural, mechanical and aerospace engineering and in engineering mechanics applications when compared with prismatic members, but quantifying their buckling (Bradford 2006) and dynamic behaviour is far more complex than for prismatic members. The use of tapered beams in steel framed building construction was recognised by Amirikian (1952) as an economically viable alternative to prismatic members because the size of the cross-section could be made to follow the magnitude of the bending moments within the member. The Portland Cement Association (1958) published tables and charts for determining the static deflections and bending moments in frames containing tapered members that could be used with the technique of moment distribution (Hall and Kabaila 1986, Hibbeler 1999). Although these treatments were the first major design applications for tapered beams in engineering structures, the more pure research of tapered beams and their response to dynamic excitation has been widespread since the apparent first work of Kirchhoff (1879), in which the solutions of wedge-shaped and cone-shaped beams were treated analytically in terms of Bessel functions (Watson 1956). On a larger scale, tapered cantilevers can be used in an approximate fashion to model tall buildings, and knowledge of their dynamic response is vital for earthquake engineering assessment and applications.

In general, the solution of dynamic problems involving tapered members is quite complicated and requires numerical procedures or the use of tabulated Bessel functions. One of the earliest treatments of the problem was that of Ward (1913), and a proliferation of later research followed from the work of Siddall and Isakson (1951), Suppiger and Taleb (1956) and Cranch and Adler (1956). These analytic-based treatments were founded on Bessel function theory (Watson 1956), as were the studies that followed by Conway and his colleagues (1964, 1965), Mabie and Rogers (1964, 1968, 1972, 1974), Wang (1967) and Gorman (1975), with Goel (1976) and Sato (1980) generalising

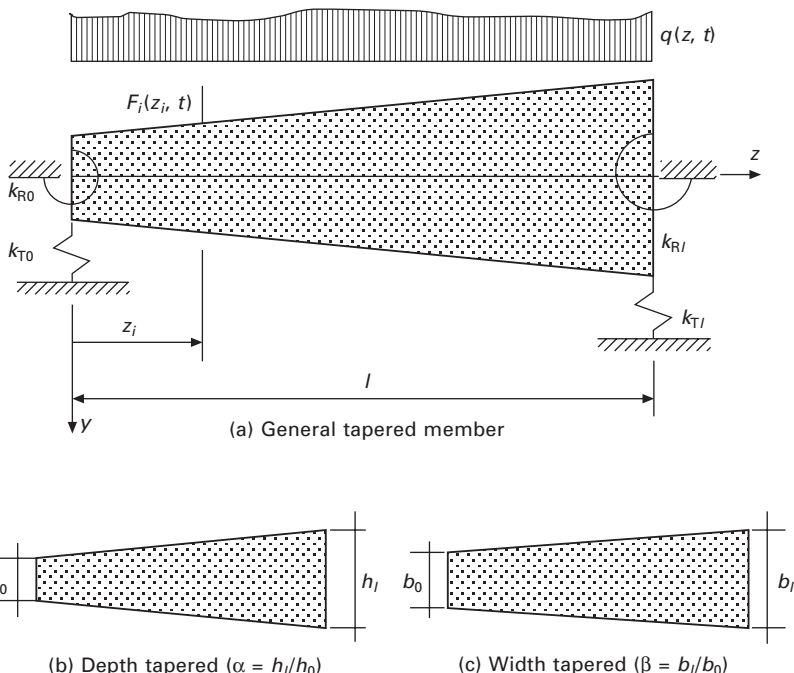
the theory of Mabie and Rogers to include more complex members with rotational springs at their ends. Other contributions of note are those of MacDuff and Felger (1957), Housner and Keightley (1962), Heidebrecht (1967), Gupta (1985) and Abrate (1995).

Finite element-based methods have proven to be a popular numerical tool for many problems in engineering mechanics (Zienkiewicz and Taylor 2000), including the dynamic behaviour of tapered plates. The usual finite element treatment for the free vibration of tapered beams has involved discretising the member into a number of uniform elements whose static stiffness matrices are known, with the mass being lumped usually at the centre of the element (Clough and Penzien 1975). This uniform-element approach has been shown (Bradford 2006) to provide incorrect results for the buckling of tapered members, and it often leads to slow convergence difficulties in the dynamic response of tapered members. Archer (1963) developed a consistent mass matrix for distributed mass systems that improved the accuracy of the solutions for the free vibration of uniform beams, while Lindberg (1963) developed consistent mass and stiffness matrices for linearly tapered beam elements using a cubic interpolation function for the displacements. Later, Gallagher and Lee (1970) derived a more general tapered beam element, again by using a cubic interpolation function, while Thomas and Dokumaci (1973) constructed improved mass and stiffness matrices for tapered beams by using interpolation functions in the form of sixth-order Hermitian polynomials. Rutledge and Beskos (1981) developed stiffness and consistent mass matrices for a linearly tapered beam element of rectangular cross-section with a constant width, which produced superior results to those of Gallagher and Lee (1970), while Karabalis and Beskos (1983) extended the formulation in a more unified fashion to the static, dynamic and stability analysis of tapered beams. These formulations were not founded on specifying interpolation functions *a priori*, which probably accounted for their favourable attributes in deriving numerical solutions.

More recent finite element studies have been directed towards the dynamic response of nonuniform beams comprising advanced composite materials, which find widespread application in the aerospace industry. Kapania and Raciti (1989) described developments in the vibration analysis of laminated composite beams, and Yuan and Miller (1989, 1990) reported the derivation of beam finite elements for the analysis. Oral (1991) developed a shear flexible finite element for nonuniform laminated composite beams, utilising a three-noded finite element with six degrees of freedom per node for a linearly tapered, symmetrically laminated, composite beam utilising first-order shear deformation theory, whilst Ramalingeswara Rao and Ganesan (1997) developed a finite element technique for studying the dynamic behaviour of tapered composite beams subjected to point-harmonic excitation. Laura *et al.* (1996) used the finite element method, as well as other techniques, to study the vibration of beams with stepped thicknesses.

A background to the dynamic response of a plated beam member that is tapered can be illustrated quantitatively by considering the general tapered member shown in Fig. 1.1. This figure shows a typical tapered beam of length  $l$ , which is assumed to be supported at each end by translational and rotational springs and subjected to (dynamic) concentrated loads  $F_i(z_i, t)$  ( $i = 1, 2, \dots$ ) and to a (dynamic) distributed load of intensity  $q(z, t)$ , where  $t$  is the time and the  $z$  axis is shown in the figure. The vibration is restricted to being in the nominally vertical  $y-z$  plane, so that the motion and deformations are in this plane. The stiffness of the translational spring (force per unit length) at the end  $z = 0$  is  $k_{T0}$  and of the rotational spring (moment per radian) at  $z = 0$  is  $k_{R0}$ , while the counterpart stiffnesses at  $z = l$  are  $k_{Tl}$  and  $k_{Rl}$ . The mass density of the beam is  $\rho$ , so that  $\rho \cdot A(z)$  is the mass per unit length where  $A(z)$  is the area of the cross-section of the tapered beam. Under dynamic excitation, the beam displaces transversely  $V(z, t)$ . Using the principle of virtual work, when a virtual displacement  $\delta V(z)$  is applied to the dynamic system, the work done by the external forces must equal the change in the internal strain energy of the beam. In a dynamic system, the external forces include both the real loads and inertial forces.

For the tapered beam in Fig. 1.1, the principle of virtual work may be stated as



1.1 Tapered beam representation.

$$\delta U = \delta W_F + \delta W_c + \delta T \quad 1.1$$

in which

$$\delta U = \int_0^l EI(z)V''\delta V'' dz \quad 1.2$$

is the change internal strain energy due to flexure (the axial and shearing strain energies have been ignored) and in which  $EI(z)$  is the flexural rigidity of the beam, where  $( )'$  denotes the differentiation of  $( )$  with respect to  $z$ :

$$\begin{aligned} \delta W_F = \sum_i F_i \delta V_i + \int_0^l q(z)\delta V dz + k_{T0}V_0\delta V_0 + k_{Tl}V_l\delta V_l \\ + k_{R0}V'_0\delta V'_0 + k_{Rl}V'_l\delta V'_l \end{aligned} \quad 1.3$$

is the virtual work done by the external loads;

$$\delta W_c = - \sum_i c_i \dot{V}_i \delta V_i - \int_0^l c \dot{V} \delta V dz \quad 1.4$$

is the virtual work done by damping forces with discrete and continuous damping coefficients  $c_i$  ( $i = 1, 2, \dots$ ) and  $c$  respectively and where  $\dot{V} = \partial V / \partial t$ , and  $\delta T$  is the virtual work done by the inertia forces. For this beam, and as part of the general derivation of Lagrange's equation of motion, it can be shown that

$$\delta T = - \frac{d}{dt} \left( \frac{\partial \mathcal{K}}{\partial \dot{V}} \right) \delta V \quad 1.5$$

where

$$\mathcal{K} = \frac{1}{2} \int_0^l [\rho A(z)] \dot{V}^2 dz \quad 1.6$$

is the kinetic energy of a beam with a mass per unit length of  $\rho A(z)$ . Equation (1.6) ignores rotational motion.

For the undamped free vibration of a tapered beam that is generally of most interest,  $F_i \equiv 0$ ,  $q \equiv 0$ ,  $c_i \equiv 0$  and  $c \equiv 0$  and so

$$\int_0^l EI(z)V''\delta V'' dz = - \int_0^l \rho A(z) \ddot{V} dz \quad 1.7$$

The transverse harmonic response for free vibration is represented by  $V(z, t) = v(z) \times \exp(i\omega t)$  where  $\omega$  is the natural frequency,  $i = \sqrt{-1}$  and  $v(z)$  is the amplitude of the deflection. Substituting this into Eq. (1.7) and cancelling out the term  $\exp(2i\omega t)$  produces the virtual work statement that

$$\int_0^l [EI(z)v''\delta v'' - \rho A(z)\omega^2 v\delta v]dz + k_{T0}v_0\delta v_0 + k_{Tl}v_l\delta v_l + k_{R0}v'_0\delta v'_0 + k_{Rl}v'_l\delta v'_l = 0$$

$$\forall \delta v, \delta v'', \delta v_0, \delta v'_0, \delta v_l, \delta v'_l \quad 1.8$$

The first term in the integrand in Eq. (1.8) can be integrated by parts twice, producing

$$[EIv''\delta v']_0^l - [(EIv'')'\delta v]_0^l + k_{T0}v_0\delta v_0 + k_{Tl}v_l\delta v_l + k_{R0}v'_0\delta v'_0 + k_{Rl}v'_l\delta v'_l + \int_0^l [EIv'')'' - \rho A\omega^2 v](\delta v)dz = 0 \quad 1.9$$

Since Eq. (1.9) holds for all kinematically admissible virtual deformations  $\delta v$ , the equation of motion within the integrand is

$$\frac{d^2}{dz^2} \left[ EI(z) \frac{d^2 v(z)}{dz^2} \right] - \rho A(z) \omega^2 v(z) = 0 \quad 1.10$$

which is identical to the equation of motion that can be derived from the general formulation (Timoshenko 1955, Jacobsen and Ayre 1958, Biggs 1964) given by

$$\frac{\partial^2}{\partial z^2} \left[ EI(z) \frac{\partial^2 V(z, t)}{\partial z^2} \right] + \rho A(z) \frac{\partial^2 V(z, t)}{\partial t^2} = q(z, t) \quad 1.11$$

when it is assumed that  $V = v(z)\exp(i\omega t)$  and  $q(z, t) = 0$ .

Importantly, the virtual work formulation in Eq. (1.9) can be used to obtain the static boundary conditions. Since this equation holds for arbitrary values of  $\delta v_0$ ,  $\delta v_l$ ,  $\delta v'_0$  and  $\delta v'_l$ , these boundary conditions reduce to

$$(EIv'')'_0 + k_{T0}v_0 = 0 \quad \text{and} \quad -EIv''_0 + k_{R0}v'_0 = 0 \quad 1.12$$

at  $z = 0$ , and to

$$-(EIv'')'_l + k_{Tl}v_l = 0 \quad \text{and} \quad EIv''_l + k_{Rl}v'_l = 0 \quad 1.13$$

at  $z = l$ .

General solutions of the governing differential equations are difficult, and for the cases for which their solution can be stated in ‘analytic’ form, recourse is still needed to Bessel functions. As a result, and has been noted, solutions to the problem have generally been developed in some form of numerical scheme, usually by either Ritz-based or more advanced nondiscretisation techniques (Liew *et al.* 1995a,b, 1998, Saadatpour *et al.* 2000), by more ‘classical’ techniques such as Newmark’s method (Newmark 1943, Bradford and Abdoli-Yazdi 1999) or by finite element procedures.

This chapter addresses some useful results obtained by these techniques, as well as discussions of the techniques themselves. The treatment is restricted largely to free or unforced vibrations, and does not consider the torsional vibrations of tapered members. In this regard, it is of note that little work has been reported on the out-of-plane vibration of tapered members of arbitrary section (Banerjee *et al.* 1996, Friberg 1993, Voros 2004), in that the inclusion of torsional and warping deformations and the complex interactions between them (Pi *et al.* 2005a,b) have not been fully extended from static to dynamic behaviour.

## 1.2 Linearly tapered members with both ends supported

### 1.2.1 Numerical formulation

A linearly varying tapered beam of rectangular cross-section of length  $l$  is depicted in Fig. 1.1. At the end  $z = 0$ , the cross-section has a depth  $h_0$  and a width  $b_0$ , while at the end  $z = l$  it has a depth  $h_l$  and a width  $b_l$ , so that the reference area and reference second moment of area at  $z = 0$  are  $b_0 h_0$  and  $\frac{1}{12} b_0 h_0^3$  respectively. If the linear variation of the depth  $h \in [h_0, h_l]$  and  $b \in [b_0, b_l]$  are represented by

$$h = (h_l - h_0)\xi + h_0 \quad \text{and} \quad b = (b_l - b_0)\xi + b_0 \quad 1.14$$

where  $\xi = z/l$  with  $\xi \in [0, 1]$ , then the area  $A(\xi)$  and second moment of area  $I(\xi)$  are

$$A(\xi) = A_0 \xi \eta \quad \text{and} \quad I(\xi) = I_0 \xi^3 \eta \quad 1.15$$

in which

$$\zeta = (\alpha - 1)\xi + 1 \quad \text{and} \quad \eta = (\beta - 1)\xi + 1 \quad 1.16$$

and the taper ratios  $\alpha$  and  $\beta$  are defined by

$$\alpha = h_l/h_0 \quad \text{and} \quad \beta = b_l/b_0 \quad 1.17$$

Using an energy approach, the beam is assumed to have a sustained free vibration of frequency  $\omega$ , so that

$$V(z, t) = v(z) \sin \omega t, \quad 1.18$$

and this leads to statements of the potential energy  $U$  and kinetic energy  $\mathcal{K}$  (Eq. 1.6) as

$$\begin{aligned} U &= \frac{1}{2} \int_0^l EI v''^2 dz + \frac{1}{2} k_{T0} v_0^2 + \frac{1}{2} k_{R0} v_0'^2 + \frac{1}{2} k_{Tl} v_l^2 \\ &\quad + \frac{1}{2} k_{Rl} v_l'^2 - F_0 v_0 - M_0 v_0' - F_l v_l - M_l v_l' \end{aligned} \quad 1.19$$

and

$$\mathcal{K} = \frac{1}{2} \int_0^l \rho A \omega^2 v^2 dz \quad 1.20$$

where  $F_0$  and  $F_l$  are the force (shear) reactions at the ends of the beam, and  $M_0$  and  $M_l$  are the moment reactions at the ends of the beam. Sato (1980) derived the same formulation in Eq. (1.19), excluding the end reactions for a beam on simple supports. Since  $v_0$ ,  $v_l$ ,  $v'_0$  and  $v'_l$  are constant with respect to  $z$ , the energy function  $\Pi$  can then be represented as

$$\Pi = \mathcal{K} - U = \frac{1}{2} \int_0^l \mathcal{F}(z, v) dz \quad 1.21$$

in which

$$\begin{aligned} \mathcal{F} = & EI v''^2 - \rho A \omega^2 v^2 + l(k_{T0} v_0^2 + k_{Tl} v_l^2 + k_{R0} v'_0^2 + k_{Rl} v'_l^2) \\ & - 2l(F_0 v_0 + F_l v_l + M_0 v'_0 + M_l v'_l) \end{aligned} \quad 1.22$$

It is worth noting that for Eq. (1.21) to be stationary, the Euler–Lagrange equations of variational calculus for a functional require that

$$\frac{d\mathcal{F}}{dz} - \frac{d}{dz} \left( \frac{\partial \mathcal{F}}{\partial v'} \right) + \frac{d^2}{dz^2} \left( \frac{\partial \mathcal{F}}{\partial v''} \right) = 0 \quad 1.23$$

as well as requiring the stationary conditions for  $\mathcal{F}$  in Eq. (1.22) that

$$\frac{\partial \mathcal{F}}{\partial v_0} = 0, \quad \frac{\partial \mathcal{F}}{\partial v_l} = 0, \quad \frac{\partial \mathcal{F}}{\partial v'_0} = 0 \quad \text{and} \quad \frac{\partial \mathcal{F}}{\partial v'_l} = 0 \quad 1.24$$

Equations (1.24) are merely statements of the static boundary conditions

$$F_0 = k_{T0} v_0 \quad \text{and} \quad F_l = k_{Tl} v_l, \quad 1.25$$

$$M_0 = k_{R0} v'_0 \quad \text{and} \quad M_l = k_{Rl} v'_l \quad 1.26$$

while Eq. (1.23) reduces to the equation of motion given in Eq. (1.10).

Sato (1980) used the energy formulation in Eqs. (1.19) and (1.20) with the Ritz method to provide an approximate solution to Eq. (1.21) by assuming a deflected shape in the form of the power series:

$$v = \xi(1 - \xi) \cdot \sum_{i=0}^{\infty} a_i \xi^i \quad 1.27$$

which satisfies the kinematic boundary conditions for a beam whose ends cannot move transversely that  $v(\xi = 0) = v(\xi = 1) = 0$ , and in which  $a_i$  ( $i = 0, 1, 2, \dots$ ) are unknown constants. This formulation assumed that the beam is supported rigidly at its ends with respect to the transverse displacements  $v$ , so that  $k_{T0} = k_{Tl} = \infty$  in Fig. 1.1. Minimising the energy function  $\Pi$  with respect to these constants then produces

$$\begin{aligned} \frac{\partial}{\partial a_i} \left\{ \lambda^4 \int_0^1 [(\alpha - 1)\xi + 1][(\beta - 1)\xi + 1]v^2 d\xi \right. \\ \left. - \int_0^1 [(\alpha - 1)\xi + 1]^3 [(\beta - 1)\xi + 1] \left( \frac{dv}{d\xi} \right)^2 d\xi \right. \\ \left. - K_{R0} \left( \frac{dv}{d\xi} \right)_0^2 - K_{Rl} \alpha^3 \beta \left( \frac{dv}{d\xi} \right)_1^2 \right\} = 0 \quad \forall a_i (i = 1, 2, \dots) \quad 1.28 \end{aligned}$$

in which

$$\lambda^4 = \frac{\rho A_0 \omega^2 l^4}{EI_0}; \quad K_{R0} = \frac{k_{R0} l}{EI_0}; \quad K_{Rl} = \frac{k_{Rl} l}{EI_l} \quad 1.29$$

Substituting Eq. (1.27) into Eq. (1.28) produces, after some manipulation,

$$e_{ij} a_j = 0 \quad (i, j = 0, 1, 2, \dots) \quad 1.30$$

with summation over repeated indices, and which has a nontrivial solution for  $a_0, a_1, a_2, \dots$  only when

$$\det e_{ij} = 0 \quad (i, j = 0, 1, 2, \dots) \quad 1.31$$

in which  $e_{ij} = f(n(\lambda, K_{R0}, K_{Rl}, \alpha, \beta))$  and whose explicit form is given in Sato (1980). These equations were solved numerically by Sato (1980) using nine terms in the function in Eq. (1.27) for the frequency parameter  $\lambda^2$ . The results (to slightly better accuracy) are shown in Table 1.1 for a simply supported ( $k_{R0} = k_{Rl} = 0$ ) and a built-in ( $k_{R0} = k_{Rl} = \infty$ ) beam that is depth tapered for various values of  $\alpha$ , and in Table 1.2 for a beam that is width tapered for various values of  $\beta$ .

### 1.2.2 Analytical formulation

The differential equation for the dynamic response of a linearly tapered beam of the type shown in Fig. 1.1 can be obtained by substituting Eqs. (1.15) into Eq. (1.10). This produces the fourth-order differential equation

$$\begin{aligned} v^{iv} + \frac{2}{l} \left[ \frac{3(\alpha - 1)}{\zeta} + \frac{\beta - 1}{\eta} \right] v''' \\ + \frac{6}{l^2} \left[ \frac{(\alpha - 1)(\beta - 1)}{\zeta\eta} + \frac{(\alpha - 1)^2}{\zeta^2} \right] v'' - \left( \frac{\lambda^4}{l^4 \zeta^2} \right) v = 0 \quad 1.32 \end{aligned}$$

in which  $\zeta$  and  $\eta$  are defined in Eq. (1.16). Equation (1.32) was stated by Mabie and Rogers (1968, 1972) in their widely cited papers, and has been the basis for a number of analytic studies. For the case of a depth- and width-

Table 1.1 Frequency parameters  $\lambda^2$  (first four harmonics) for a linearly depth-tapered beam

$\alpha$	Simply supported				Built-in
1.0	9.870	39.479	88.827	157.914	22.373
1.25	11.058	44.306	99.662	177.151	25.098
1.5	12.172	48.961	110.065	195.575	27.705
1.75	13.230	53.484	120.141	213.382	30.224
2.0	14.243	57.904	129.958	230.703	32.672
2.25	15.220	62.238	139.564	247.625	35.062
2.5	16.167	66.501	148.991	264.219	37.404
2.75	17.087	70.703	158.271	280.529	39.705
3.0	17.984	74.852	167.420	296.597	41.971
4.0	21.397	91.033	203.008	358.966	50.754
5.0	24.599	106.723	237.410	419.107	59.208
10	38.894	181.237	400.112	702.414	98.845
				270.083	527.079
					869.330

Table 1.2 Fundamental frequency parameter  $\lambda^2$  for a linearly width-tapered beam

Breadth taper ratio $\beta$	Simply supported	Built-in
1	9.869	22.37
2	9.825	22.18
3	9.765	21.91
4	9.714	21.67
5	9.672	21.47
6	9.637	21.29
7	9.608	21.14
8	9.583	21.00
9	9.562	20.88
10	9.544	20.78

tapered beam so that  $\beta = \alpha$  and so  $\eta = \zeta$ , Eq. (1.32) simplifies to (Auciello and Ercolano 1997)

$$\zeta^4 \left( \frac{d^4 v}{d\zeta^4} \right) + 8\zeta^3 \left( \frac{d^3 v}{d\zeta^3} \right) + 12\zeta^2 \left( \frac{d^2 v}{d\zeta^2} \right) - \frac{\lambda^4}{(\alpha - 1)^4} \zeta^2 v = 0 \quad 1.33$$

which has the solution

$$v = \frac{1}{\zeta} \left[ C_1 J_2 \left( \frac{2\lambda\sqrt{\zeta}}{\alpha - 1} \right) + C_2 Y_2 \left( \frac{2\lambda\sqrt{\zeta}}{\alpha - 1} \right) + C_3 I_2 \left( \frac{2\lambda\sqrt{\zeta}}{\alpha - 1} \right) + C_4 K_2 \left( \frac{2\lambda\sqrt{\zeta}}{\alpha - 1} \right) \right] \quad 1.34$$

in which  $J_2$ ,  $Y_2$ ,  $I_2$  and  $K_2$  are the second-order Bessel functions (Watson 1956). On the other hand, for the case of a depth-tapered beam only, so that  $\beta = 1$ , Eq. (1.32) simplifies to (Auciello and Ercolano 1997)

$$\zeta^4 \left( \frac{d^4 v}{d\zeta^4} \right) + 6\zeta^3 \left( \frac{d^3 v}{d\zeta^3} \right) + 6\zeta^2 \left( \frac{d^2 v}{d\zeta^2} \right) - \frac{\lambda^4}{(\alpha - 1)^4} \zeta^2 v = 0 \quad 1.35$$

which has the solution

$$v = \frac{1}{\sqrt{\zeta}} \left[ C_1 J_1 \left( \frac{2\lambda\sqrt{\zeta}}{\alpha - 1} \right) + C_2 Y_1 \left( \frac{2\lambda\sqrt{\zeta}}{\alpha - 1} \right) + C_3 I_1 \left( \frac{2\lambda\sqrt{\zeta}}{\alpha - 1} \right) + C_4 K_1 \left( \frac{2\lambda\sqrt{\zeta}}{\alpha - 1} \right) \right] \quad 1.36$$

in which  $J_1$ ,  $Y_1$ ,  $I_1$  and  $K_1$  are the first-order Bessel functions (Watson 1956).

Using the boundary conditions in Eqs. (1.12) and (1.13), and noting that  $dz = l d\zeta / (\alpha - 1)$ , results in

$$\left( \frac{k_{T0}l^3}{EI_0} \right) \zeta + [(\alpha - 1)^2 (3\alpha + \beta - 4)] \frac{d^2 v}{d\zeta^2} + (\alpha - 1)^3 \frac{d^3 v}{d\zeta^3} = 0 \quad 1.37$$

and

$$\left( \frac{k_{R0}l}{EI_0} \right) \frac{dv}{d\zeta} - (\alpha - 1) \frac{d^2 v}{d\zeta^2} = 0 \quad 1.38$$

at  $z = 0$ , and in

$$\begin{aligned} \left( \frac{k_{Tl}l^3}{EI_l} \right) \zeta + & \left\{ (\alpha - 1)^2 \left[ \left( \frac{\beta - 1}{\beta} \right) + 3 \left( \frac{\alpha - 1}{\alpha} \right) \right] \right\} \frac{d^2 v}{d\zeta^2} \\ & + (\alpha - 1)^3 \frac{d^3 v}{d\zeta^3} = 0 \end{aligned} \quad 1.39$$

and

$$\left( \frac{k_{Rl}l}{EI_l} \right) \frac{dv}{d\zeta} + (\alpha - 1) \frac{d^2 v}{d\zeta^2} = 0 \quad 1.40$$

at  $z = l$ .

The general solutions in Eqs. (1.34) and (1.36) can be written in the form (Auciello and Eroclano 1997)

$$\begin{aligned} v = & \frac{1}{(\sqrt{\zeta})^n} \left[ C_1 J_n \left( \frac{2\lambda\sqrt{\zeta}}{\alpha - 1} \right) + C_2 Y_n \left( \frac{2\lambda\sqrt{\zeta}}{\alpha - 1} \right) \right. \\ & \left. + C_3 I_n \left( \frac{2\lambda\sqrt{\zeta}}{\alpha - 1} \right) + C_4 K_n \left( \frac{2\lambda\sqrt{\zeta}}{\alpha - 1} \right) \right] \end{aligned} \quad 1.41$$

when  $n = 1$  corresponds to a linear variation of the depth and  $n = 2$  corresponds to a variation in both the depth and breadth of the beam. Substituting Eq. (1.41) into the four boundary conditions (1.37) to (1.40) produces the linear equation

$$\begin{bmatrix} k_{11} & k_{12} & k_{13} & k_{14} \\ k_{21} & k_{22} & k_{23} & k_{24} \\ k_{31} & k_{32} & k_{33} & k_{34} \\ k_{41} & k_{42} & k_{43} & k_{44} \end{bmatrix} \cdot \begin{Bmatrix} C_1 \\ C_2 \\ C_3 \\ C_4 \end{Bmatrix} = \begin{Bmatrix} 0 \\ 0 \\ 0 \\ 0 \end{Bmatrix} \quad 1.42$$

in which

$$k_{11} = \frac{J_n(\lambda_1)}{R_{T0}(\alpha - 1)^3} + \frac{(n+2)\lambda^2 J_{n+2}(\lambda_1)}{(\alpha - 1)^2} - \frac{\lambda^3 J_{n+3}(\lambda_1)}{(\alpha - 1)^3} \quad 1.43$$

$$k_{12} = \frac{Y_n(\lambda_1)}{R_{T0}(\alpha - 1)^3} + \frac{(n+2)\lambda^2 Y_{n+2}(\lambda_1)}{(\alpha - 1)^2} - \frac{\lambda^3 Y_{n+3}(\lambda_1)}{(\alpha - 1)^3} \quad 1.44$$

$$k_{13} = \frac{I_n(\lambda_1)}{R_{T0}(\alpha - 1)^3} + \frac{(n+2)\lambda^2 I_{n+2}(\lambda_1)}{(\alpha - 1)^2} + \frac{\lambda^3 I_{n+3}(\lambda_1)}{(\alpha - 1)^3} \quad 1.45$$

$$k_{14} = \frac{K_n(\lambda_1)}{R_{T0}(\alpha - 1)^3} + \frac{(n+2)\lambda^2 K_{n+2}(\lambda_1)}{(\alpha - 1)^2} - \frac{\lambda^3 K_{n+3}(\lambda_1)}{(\alpha - 1)^3} \quad 1.46$$

$$k_{21} = -\frac{\lambda J_{n+1}(\lambda_1)}{R_{R0}(\alpha - 1)^2} - \frac{\lambda^2 J_{n+2}(\lambda_1)}{(\alpha - 1)^2} \quad 1.47$$

$$k_{22} = -\frac{\lambda Y_{n+1}(\lambda_1)}{R_{R0}(\alpha - 1)^2} - \frac{\lambda^2 Y_{n+2}(\lambda_1)}{(\alpha - 1)^2} \quad 1.48$$

$$k_{23} = \frac{\lambda I_{n+1}(\lambda_1)}{R_{R0}(\alpha - 1)^2} - \frac{\lambda^2 I_{n+2}(\lambda_1)}{(\alpha - 1)^2} \quad 1.49$$

$$k_{24} = \frac{\lambda K_{n+1}(\lambda_1)}{R_{R0}(\alpha - 1)^2} - \frac{\lambda^2 K_{n+2}(\lambda_1)}{(\alpha - 1)^2} \quad 1.50$$

$$k_{31} = \frac{\alpha^2 J_n(\lambda_2)}{R_{Tl}(\alpha - 1)^3} - \frac{(n+2)\lambda^2 J_{n+2}(\lambda_2)}{(\alpha - 1)^2} + \frac{\lambda^3 \sqrt{\alpha} J_{n+3}(\lambda_2)}{(\alpha - 1)^3} \quad 1.51$$

$$k_{32} = \frac{\alpha^2 Y_n(\lambda_2)}{R_{Tl}(\alpha - 1)^3} - \frac{(n+2)\lambda^2 Y_{n+2}(\lambda_2)}{(\alpha - 1)^2} + \frac{\lambda^3 \sqrt{\alpha} Y_{n+3}(\lambda_2)}{(\alpha - 1)^3} \quad 1.52$$

$$k_{33} = \frac{\alpha^2 I_n(\lambda_2)}{R_{Tl}(\alpha - 1)^3} - \frac{(n+2)\lambda^2 I_{n+2}(\lambda_2)}{(\alpha - 1)^2} - \frac{\lambda^3 \sqrt{\alpha} I_{n+3}(\lambda_2)}{(\alpha - 1)^3} \quad 1.53$$

$$k_{34} = \frac{\alpha^2 K_n(\lambda_2)}{R_{Tl}(\alpha - 1)^3} - \frac{(n+2)\lambda^2 K_{n+2}(\lambda_2)}{(\alpha - 1)^2} + \frac{\lambda^3 \sqrt{\alpha} K_{n+3}(\lambda_2)}{(\alpha - 1)^3} \quad 1.54$$

$$k_{41} = -\frac{\sqrt{\alpha} J_{n+1}(\lambda_2)}{R_{Rl}(\alpha - 1)} + \frac{\lambda J_{n+2}(\lambda_2)}{(\alpha - 1)} \quad 1.55$$

$$k_{42} = -\frac{\sqrt{\alpha} Y_{n+1}(\lambda_2)}{R_{Rl}(\alpha - 1)} + \frac{\lambda Y_{n+2}(\lambda_2)}{(\alpha - 1)} \quad 1.56$$

$$k_{43} = \frac{\sqrt{\alpha} I_{n+1}(\lambda_2)}{R_{RI}(\alpha - 1)} + \frac{\lambda I_{n+2}(\lambda_2)}{(\alpha - 1)} \quad 1.57$$

$$k_{44} = -\frac{\sqrt{\alpha} K_{n+1}(\lambda_2)}{R_{RI}(\alpha - 1)} + \frac{\lambda J_{n+2}(\lambda_2)}{(\alpha - 1)} \quad 1.58$$

and where

$$\begin{aligned} \lambda_1 &= \frac{2\lambda}{\alpha - 1}, \quad \lambda_2 = \lambda_1 \sqrt{\alpha}, \quad R_{T0} = \frac{EI_0}{k_{T0}l^3}, \quad R_{R0} = \frac{EI_0}{k_{R0}l} = \frac{1}{K_{R0}}, \\ R_{Tl} &= \frac{EI_l}{k_{Tl}l^3}, \quad R_{Rl} = \frac{EI_l}{k_{Rl}l} = \frac{1}{K_{Rl}} \end{aligned} \quad 1.59$$

Equation (1.42) has the trivial solution that  $C_1 = C_2 = C_3 = C_4 = 0$ , for which the beam clearly does not vibrate. Alternatively, the frequency parameter  $\lambda$  can be extracted from the condition in Eq. (1.42) that

$$\det[k_{ij}] = 0 \quad (i, j = 1, \dots, 4) \quad 1.60$$

Equation (1.60) was solved numerically by Auciello and Ercolano (1997) using the technique of false position (de Vahl Davis 1986) in which a symbolic calculation program (Wolfram 1993) was used to handle the Bessel functions. The solutions of Auciello and Ercolano (1997) agree well with those of Sato (1980) in Table 1.1 if the correct restraint conditions are imposed on  $R_{T0}$ ,  $R_{R0}$ ,  $R_{Tl}$  and  $R_{Rl}$ . Some further frequency parameters  $\lambda^2$  (De Rosa and Auciello 1996) are given in Table 1.3 for a beam with a depth and width taper ratio  $\alpha = \beta = 2$  and full translational support ( $R_{T0} = R_{Tl} = \infty$ ) for various combinations of the end rotational stiffnesses  $R_{R0}$  and  $R_{Rl}$ , in Table 1.4 for a beam with  $\alpha = \beta = 1.4$  and full restraint at one end ( $R_{Tl} = R_{Rl} = \infty$ ) and in Table 1.5 for a beam with  $\alpha = \beta = 1.4$  whose ends are pinned ( $R_{R0} = R_{Rl} = 0$ ) as a function of the end translational spring stiffnesses  $R_{T0}$  and  $R_{Tl}$ .

Auciello and Ercolano (1997) considered an interesting extension of this theory, in which one portion of the beam (of length  $\Lambda l$ ) was prismatic whilst

*Table 1.3 Frequency parameters  $\lambda^2$  (first four harmonics) for a tapered beam with translational restraint and various rotational restraint stiffnesses ( $\alpha = \beta = 2$ )*

$R_{R0}$	$R_{Rl}$	$\lambda^2$			
0	0	13.913	58.220	130.455	231.292
0	0.01	13.946	58.243	130.476	231.311
0	0.10	14.241	58.441	130.659	231.487
0	1.0	16.512	60.247	132.374	233.158
0	10.0	22.609	68.635	142.270	244.050
1	0	14.428	58.987	131.341	232.248
1	0.1	14.753	59.207	131.545	232.444
1	1	9.765	61.004	133.255	234.111

Table 1.4 Frequency parameters  $\lambda^2$  (first four harmonics) for a tapered beam built in at end (I) and various translational and rotational restraint stiffnesses at the other end (0) ( $\alpha = \beta = 1.4$ )

$R_{R0}$	$R_{T0}$	$\lambda^2$			
0	$\infty$	19.651	60.852	125.577	213.800
0	1000	19.145	55.909	104.479	165.308
0	10	8.153	29.609	76.433	146.885
0	1	5.963	28.950	76.178	146.751
0	0.1	5.681	28.885	76.152	146.739
0	0	5.648	28.879	76.150	146.737
$\infty$	100	26.185	72.146	141.441	233.885
$\infty$	10	23.513	66.326	132.156	221.126
$\infty$	1	20.405	61.720	126.509	214.769

Table 1.5 Frequency parameters  $\lambda^2$  (first four harmonics) for a tapered beam with pin ends with translational stiffnesses  $R_{T0}$  and  $R_{TI}$  ( $\alpha = \beta = 1.4$ )

$R_{T0}$	$R_{TI}$	$\lambda^2$			
$\infty$	$\infty$	11.668	47.179	106.045	188.403
1000	1000	11.394	43.160	86.282	133.694
100	100	9.440	25.671	45.044	82.281
10	10	4.414	9.798	29.093	74.676
1	1	1.474	3.187	27.167	73.965

the other portion (of length  $l(1-\Lambda)$ ) was tapered, where  $\Lambda \in [0, 1]$ . This problem, shown in Fig. 1.2, was introduced by Laura *et al.* (1996) and has received considerable attention in offshore engineering applications. For this case, the equations of motion for free vibration can be determined by assuming

$$V(z, t) = \begin{cases} v_1(z) \exp(i\omega t) & z \in [0, \Lambda l] \\ v_2(z^*) \exp(i\omega t) & z^* \in [0, (1 - \Lambda)l] \end{cases} \quad 1.61$$

where the  $z^*$  axis is shown in Fig. 1.2, and so it is possible to write the differential equations of motion as

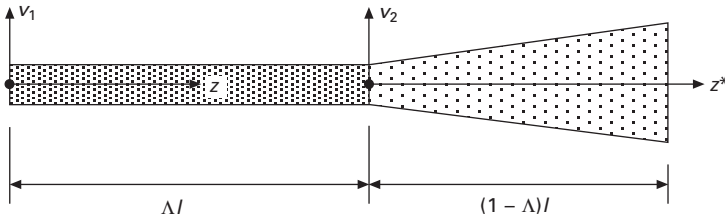
$$EI_0 \left( \frac{d^4 v_1}{dz^4} \right) - \rho A_0 \omega^2 v_1 = 0 \quad z \in [0, \Lambda l] \quad 1.62$$

and

$$\frac{d^2}{dz^{*2}} \left[ EI(z^*) \frac{d^2 v_2}{dz^{*2}} \right] - \rho A(z^*) \omega^2 v_2 = 0 \quad Z^* \in [0, (1 - \Lambda)l] \quad 1.63$$

By letting

$$\xi = \frac{z}{l} \quad \text{and} \quad \psi = 1 + \frac{(\alpha - 1)z^*}{l(1 - \Lambda)} \quad 1.64$$



1.2 Straight-tapered beam combination.

the general solution becomes

$$v_1(\xi) = C_1 \cosh(\lambda\xi) + C_2 \sinh(\lambda\xi) + C_3 \cos(\lambda\xi) + C_4 \sin(\lambda\xi) \quad 1.65$$

and

$$\begin{aligned} v_2(\psi) = & \frac{1}{(\sqrt{\psi})^n} [C_5 J_n(2\lambda_3 \sqrt{\psi}) + C_6 Y_n(2\lambda_3 \sqrt{\psi}) \\ & + C_7 I_n(2\lambda_3 \sqrt{\psi}) + C_8 K_n(2\lambda_3 \sqrt{\psi})] \end{aligned} \quad 1.66$$

where, again,  $n = 1$  corresponds to a linear variation of the depth and  $n = 2$  corresponds to a variation in both the depth and breadth of the beam,  $J_n$ ,  $Y_n$ ,  $I_n$  and  $K_n$  are appropriate Bessel functions, and in which

$$\lambda_3 = \frac{\lambda(1 - \Lambda)}{\alpha - 1}. \quad 1.67$$

The solution for  $v_1$  and  $v_2$  in Eqs. (1.65) and (1.66) requires the determination of the eight coefficients  $C_1, \dots, C_8$ . These may be determined from the boundary conditions at the left-hand ( $z = 0$ ) and right-hand ( $z^* = l(1 - \Lambda)$ ) ends of the entire member given by

$$v_1 + R_{T0} \left( \frac{d^3 v_1}{d\xi^3} \right) = 0; \quad \frac{dv_1}{d\xi} - R_{R0} \left( \frac{d^2 v_1}{d\xi^2} \right) = 0 \quad (z = 0) \quad 1.68$$

$$v_2 - R_{Tl} \left( \frac{\alpha - 1}{1 - \Lambda} \right)^3 \left[ \left( \frac{n+2}{\alpha} \right) \frac{d^2 v_2}{d\psi^2} + \frac{d^3 v_2}{d\psi^3} \right] = 0 \quad (z^* = (1 - \Lambda)l) \quad 1.69$$

as well as the four boundary conditions at the interface of the prismatic and tapered portions ( $z = \Lambda l$  and  $z^* = 0$ ) given by

$$\begin{aligned}
 v_1 &= v_2; \quad \frac{dv_1}{d\xi} - \left( \frac{\alpha - 1}{1 - \Lambda} \right) \frac{dv_2}{d\psi} = 0; \\
 \frac{d^2v_1}{d\xi^2} - \left( \frac{\alpha - 1}{1 - \Lambda} \right)^2 \frac{d^2v_2}{d\psi^2} &= 0; \\
 \frac{d^3v_1}{d\xi^3} - \left( \frac{\alpha - 1}{1 - \Lambda} \right)^3 \left[ (n + 2) \left( \frac{d^2v_2}{d\psi^2} \right) + \frac{d^3v_2}{d\psi^3} \right] &= 0 \quad 1.70
 \end{aligned}$$

Similarly to the derivation of Eq. (1.42), substituting Eqs. (1.65) and (1.66) into the eight equations contained in (1.68) to (1.70) produces the equations

$$\begin{bmatrix} k_{11} & \dots & k_{18} \\ \dots & \dots & \dots \\ \dots & \dots & k_{88} \end{bmatrix} \cdot \begin{Bmatrix} C_1 \\ \dots \\ C_8 \end{Bmatrix} = \begin{Bmatrix} 0 \\ \dots \\ 0 \end{Bmatrix} \quad 1.71$$

whose nontrivial solution for  $C_1, \dots, C_8$  requires that

$$\det[k_{ij}] = 0 \quad (i, j = 1, \dots, 8) \quad 1.72$$

The characteristic equation (1.72) was solved by Auciello and Ercolano (1997) using a symbolic calculation program and the results for the first two frequency parameters  $\lambda^2$  are given in Table 1.6 for a simply supported beam and in Table 1.7 for a built-in beam. It can be seen that this useful technique for considering a beam with two subdomains within the length  $l$  (viz. a prismatic one and a tapered one) can be extended to several subdomains within the length  $l$ , but with an increase in the number of deformation coefficients needed to prescribe the problem and hence in the size of the characteristic equation to be solved.

*Table 1.6 Frequency parameters  $\lambda^2$  (first two harmonics) for a simply supported prismatic-linearly tapered beam*

$\alpha$	$\Lambda = 0.2$		$\Lambda = 0.4$		$\Lambda = 0.6$	
1.25	10.734	43.148	10.348	42.251	10.041	41.143
1.5	11.483	46.596	10.711	44.828	10.153	42.475
2	12.722	53.035	11.204	49.528	10.273	44.442
2.5	13.703	59.070	11.497	53.732	10.313	45.784
3	14.489	64.846	11.665	57.516	10.312	46.723
4	15.642	75.941	11.780	63.986	10.237	47.868
5	16.396	86.708	11.734	69.207	10.119	48.457
10	17.368	139.164	10.850	83.582	9.394	48.736

Table 1.7 Frequency parameters  $\lambda^2$  (first two harmonics) for a built-in prismatic-linearly tapered beam

$\alpha$	$\Lambda = 0.2$		$\Lambda = 0.4$		$\Lambda = 0.6$	
1.25	24.828	68.010	24.559	66.849	24.359	65.621
1.5	27.148	73.936	26.608	71.651	26.303	69.106
2	31.486	84.909	30.474	80.391	30.087	75.233
2.5	35.523	95.059	34.200	88.197	33.677	80.804
3	39.337	104.639	37.895	95.221	36.983	86.200
4	46.492	122.669	45.760	107.313	42.538	97.056
5	53.232	139.743	52.958	117.363	46.684	107.969
10	85.197	218.913	88.887	155.653	55.675	145.530

### 1.3 Linearly tapered cantilever

The problem of the free vibration of a linearly tapered cantilever member has been studied by many investigators using a variety of techniques. This problem has specific application in engineering structures for the modelling of tall buildings (Fig. 1.3) and has been considered by Korgingskee (1952), Ishizake and Hatakeyama (1956), Wang (1958, 1963), Li (2001) and others. For the depth-tapered cantilever member shown in Fig. 1.4, which has a mass  $M$  at the cantilever tip, the equation of motion for free vibration is the same as that of Eq. (1.10), with the boundary condition at the free end ( $z = 0$  or  $\zeta = 1$ ) being

$$\frac{\partial}{\partial z} \left( EI \frac{\partial^2 v}{\partial z^2} \right) = -M \frac{\partial^2 v}{\partial t^2} \quad 1.73$$

where the term on the right-hand side is the end shear, and which reduces to (Mabie and Rogers 1964)

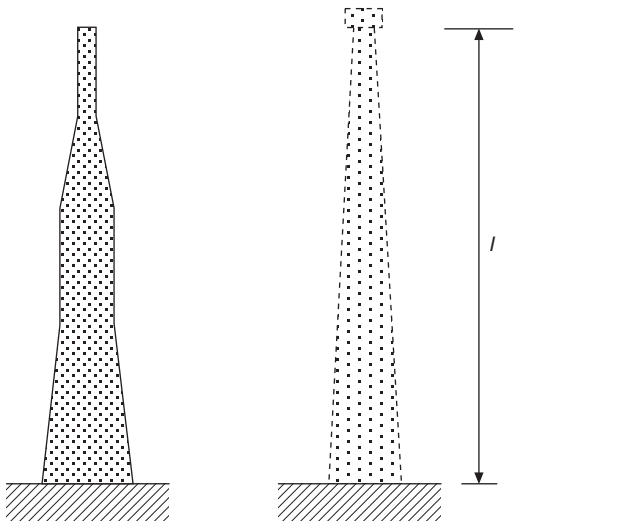
$$\left. \frac{d^3 v}{d\zeta^3} \right|_{\zeta=1} = \lambda^4 R_m z \quad 1.74$$

as well as

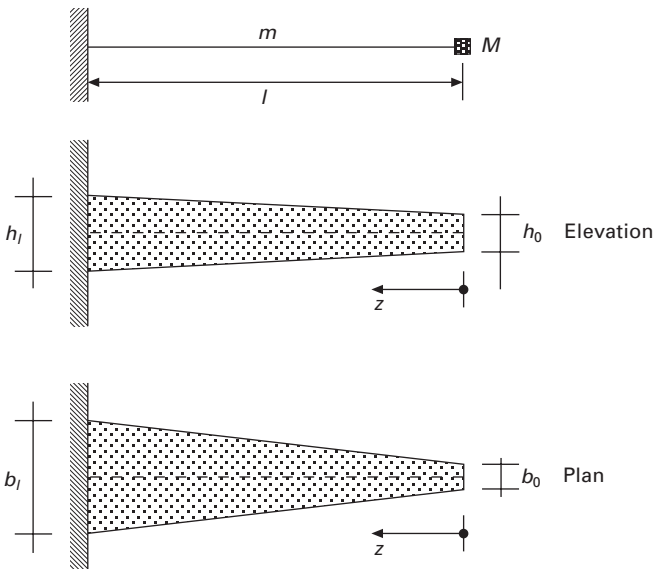
$$\left. \frac{d^2 v}{d\zeta^2} \right|_{\zeta=1} = 0 \quad 1.75$$

where  $R_m = M/m$  and  $m$  is the total mass of the cantilever. At the root end of the cantilever ( $z = l$  or  $\zeta = \alpha$ ), the kinematic boundary conditions are

$$z = 0; \quad \frac{dv}{d\zeta} = 0 \quad 1.76$$



1.3 Tapered cantilever representation of a tall building.



1.4 Tapered cantilever.

Using the four boundary conditions in Eqs. (1.74) to (1.76) in the general solution given in Eq. (1.34) in terms of Bessel functions produces a system of equations in the same form as Eq. (1.42).

The frequency parameter  $\lambda$  can again be extracted from the condition that  $\det(k_{ij}) = 0$  ( $i, j = 1, \dots, 4$ ). Table 1.8 presents the results for the first three harmonics obtained by Mabie and Rogers (1964) for a depth-tapered cantilever as a function of  $\alpha$ , and Table 1.9 presents the counterpart results for a width-

Table 1.8 Frequency parameters  $\lambda^2$  (first three harmonics) for a depth-tapered cantilever

$R_{\eta}$	$\alpha = 1$	$\alpha = 1.2$	$\alpha = 1.4$	$\alpha = 1.6$	$\alpha = 1.8$	$\alpha = 2.0$	$\alpha = 3.0$	$\alpha = 4.0$	$\alpha = 5.0$
0	3.516	22.034	61.697	4.309	25.035	68.557	5.121	27.984	75.231
0.1	2.968	19.356	55.518	3.591	21.724	61.146	4.216	24.000	66.553
0.2	2.613	18.208	53.559	3.139	20.388	58.990	3.661	22.483	64.221
0.3	2.118	17.176	52.063	3.285	19.231	57.403	2.993	21.212	62.562
0.6	1.892	16.701	51.445	2.246	18.711	56.763	2.592	20.652	61.902
0.5	17.1	16.427	51.108	2.014	18.416	56.417	2.319	20.336	61.550
1.0	16.557	16.250	50.896	1.841	18.225	56.200	2.117	20.137	61.331
1.5	13.14	15.996	50.601	1.550	17.956	55.900	1.778	19.852	61.027
2.0	11.158	15.861	50.448	1.364	17.813	55.746	1.563	19.703	60.871
3.0	9.963	15.720	50.291	1.132	17.664	55.588	1.295	19.547	60.712
5.0	7.057	15.602	50.162	0.889	17.541	55.458	1.016	19.420	60.584
10.0	4.541	15.512	50.064	0.635	17.446	55.360	0.725	19.323	60.485
0	3.516	22.035	61.670	3.717	22.743	62.06	3.892	22.743	62.39
0.1	2.2013	18.208	53.55	2.720	18.451	53.58	2.810	18.451	53.58
0.4	2.68	17.176	52.06	2.244	17.312	52.13	2.306	17.414	52.17
0.6	1.393	17.01	51.44	1.953	16.844	51.54	2.002	16.951	51.60
0.8	1.701	16.428	51.11	1.752	16.576	51.21	1.792	16.690	51.29
1.0	1.557	16.250	50.89	1.602	16.403	51.02	1.637	16.522	51.11
2.0	1.158	15.861	50.45	1.188	16.026	50.59	1.211	16.167	50.71
3.0	0.963	15.720	50.30	0.986	15.891	50.45	1.005	16.026	50.57
4.0	0.842	15.647	50.21	0.862	15.822	50.37	0.877	15.961	50.50

Table 1.9 Frequency parameters  $\lambda^2$  (first three harmonics) for a width-tapered cantilever

$R_{\eta}$	$\beta = 1$	$\beta = 1.2$	$\beta = 1.4$	$\beta = 1.6$	$\beta = 1.8$	$\beta = 2.0$	$\beta = 3.0$	$\beta = 4.0$	$\beta = 5.0$
0	3.516	22.035	61.670	3.717	22.743	62.06	3.892	22.743	62.39
0.2	2.2013	18.208	53.55	2.720	18.451	53.58	2.810	18.451	53.58
0.4	2.68	17.176	52.06	2.244	17.312	52.13	2.306	17.414	52.17
0.6	1.393	17.01	51.44	1.953	16.844	51.54	2.002	16.951	51.60
0.8	1.701	16.428	51.11	1.752	16.576	51.21	1.792	16.690	51.29
1.0	1.557	16.250	50.89	1.602	16.403	51.02	1.637	16.522	51.11
2.0	1.158	15.861	50.45	1.188	16.026	50.59	1.211	16.167	50.71
3.0	0.963	15.720	50.30	0.986	15.891	50.45	1.005	16.026	50.57
4.0	0.842	15.647	50.21	0.862	15.822	50.37	0.877	15.961	50.50

tapered cantilever as a function of  $\beta$ , for a range of tip mass ratios  $R_m$ . The solution for a cantilever can be extracted from the more general formulation given in Eqs. (1.43) to (1.60) by setting  $R_{Tl} = R_{Rl} = 0$ , and letting  $R_{T0}$  and  $R_{R0}$  approach infinity. Indeed, these results for a specific case ( $\alpha = \beta = 1.4$ ) are given in the seventh row of Table 1.4.

The boundary conditions for a propped cantilever (Fig. 1.5) are

$$v_0 = 0; \quad \left. \frac{d^2 v}{dz^2} \right|_0 = 0 \quad 1.77$$

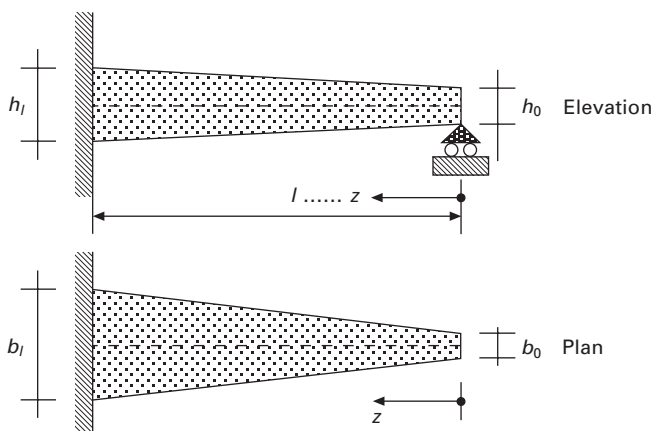
at  $z = 0$ , and

$$v_l = 0; \quad \left. \frac{dv}{dz} \right|_l = 0 \quad 1.78$$

at  $z = l$ . Substituting the general solution given in Eq. (1.34) into these boundary conditions and again solving for  $\det(k_{ij}) = 0$  leads to the frequency parameter  $\lambda$ . This process was undertaken by Mabie and Rogers (1968), and the solutions for the first three harmonics for a depth-tapered propped cantilever are given in Table 1.10 and for a width-tapered propped cantilever are given in Table 1.11.

## 1.4 Finite element approach

Finite element procedures for all types of structural engineering problems afford a convenient solution technique (Zienkiewicz and Taylor 2000). For the vibration of tapered members, a number of uniform (prismatic) elements may be used to model a tapered member, but it has been concluded in most



1.5 Propped cantilever.

Table 1.10 Frequency parameters  $\lambda^2$  (first three harmonics) for a depth-tapered propped cantilever

$\alpha$		$\lambda^2$	
1.05	15.907	51.307	106.94
1.1	16.392	52.636	109.60
1.2	17.349	55.260	114.85
1.4	19.222	60.386	125.09
1.6	21.049	65.378	135.03
1.8	22.841	70.262	144.74
2.0	24.600	75.055	154.24
2.5	28.891	86.722	177.32
3.0	33.062	98.045	199.66
3.5	37.143	109.10	211.42
4.0	41.150	119.96	242.74
4.5	45.099	130.65	263.70
5.0	48.999	141.20	284.35
6.0	56.675	161.96	324.94

Table 1.11 Frequency parameters  $\lambda^2$  (first three harmonics) for a width-tapered propped cantilever

$\beta$		$\lambda^2$	
1.0	15.417	49.964	104.24
1.2	15.604	50.139	104.43
1.4	15.751	50.275	104.55
1.6	15.867	50.386	104.67
1.8	15.963	50.477	104.78
2.0	16.044	50.555	104.86
2.5	16.195	50.702	105.00
3.0	16.299	50.807	105.12
3.5	16.374	50.884	105.23
4.0	16.431	50.944	105.29
5.0	16.507	51.024	105.39

studies that improved accuracy is better achieved by introducing more degrees of freedom per element than by using more elements containing fewer degrees of freedom. Many studies have shown that prismatic elements based on lower-order polynomial interpolation functions lead to rather poor representations of the curvature, and this usually produces discontinuities in the bending moment between elements. Lindberg (1963) developed a linearly tapered beam element using cubic interpolation functions, but as pointed out by To (1979) the curvature  $d^2v/dz^2$  is linear, which is not realistic, and the fact that the ‘loading’ term in Eq. (1.10)  $d^4v/dz^4$  is zero for this interpolation function is incorrect. To (1979) further argued that the use of a seventh-order polynomial produces superior results to those of other studies (in particular, Handa (1970) and Thomas and Dokumaci (1973) used quintic displacement functions) and the derivation of this procedure is outlined here.

Figure 1.6 shows an arbitrarily tapered member element of length  $L$ , and in which the quantity  $(\cdot)_0$  denotes the value of  $(\cdot)$  at the left-hand end ( $z = 0$ ) and  $(\cdot)_L$  denotes the value of  $(\cdot)$  at the right-hand end ( $z = L$ ). Somewhat arbitrarily, the cross-sectional area and second moment of area evaluated at  $z \in [0, L]$  can be written as

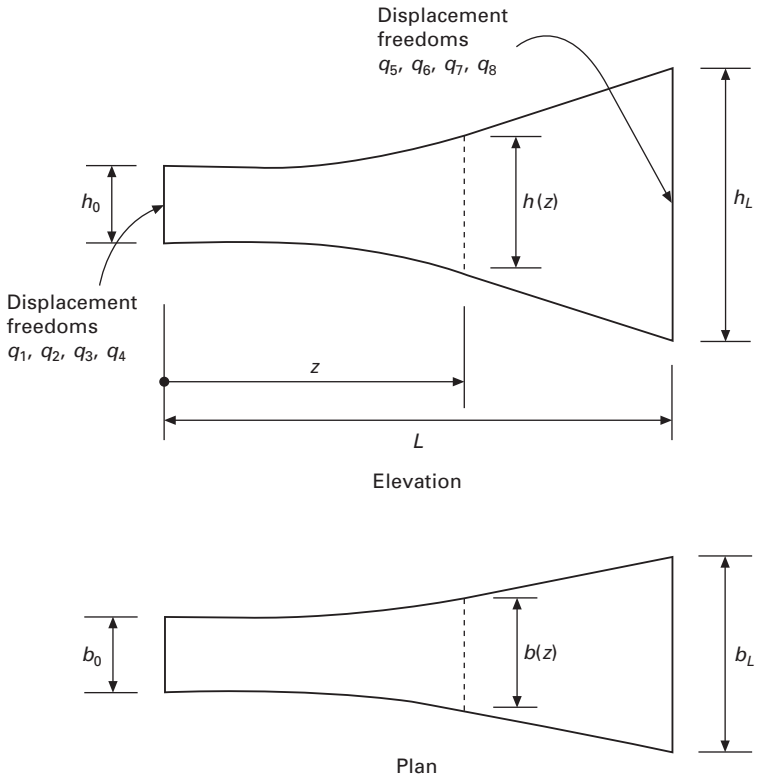
$$A(z) = g_1 \cdot b(z) h(z) \quad \text{and} \quad I(z) = g_2 \cdot b(z) h^3(z) \quad 1.79$$

where  $g_1$  and  $g_2$  are constants that depend on the shape of the cross-section. Generally, the cross-section constants are given by (Worley and Breuer 1957)

$$g_1 = \frac{\Gamma(1 + 1/\mu_1) \cdot \Gamma(1 + 1/\mu_2)}{\Gamma(1 + 1/\mu_1 + 1/\mu_2)} \quad 1.80$$

and

$$g_2 = \frac{1}{12} \frac{\Gamma(1 + 1/\mu_1) \cdot \Gamma(1 + 3/\mu_2)}{\Gamma(1 + 1/\mu_1 + 3/\mu_2)} \quad 1.81$$



$$\mathbf{q} = \{q_1, q_2, q_3, q_4, q_5, q_6, q_7, q_8\}^\top$$

1.6 Finite element model of arbitrarily tapered beam (the vector  $\mathbf{q}$  is for a septimal interpolation).

in which  $\Gamma(\cdot)$  is the gamma function and  $\mu_1$  and  $\mu_2$  are real positive numbers that are not necessarily integers. A rectangular cross-section is defined by  $\mu_1$  and  $\mu_2 \rightarrow \infty$  in Eqs. (1.80) and (1.81), and an elliptical one by  $\mu_1 = \mu_2 = 2$ .

For the linear tapered element shown in Fig. 1.6,

$$h(z) = h_0[1 + (\alpha - 1)\xi] \quad \text{and} \quad b(z) = b_0[1 + (\beta - 1)\xi] \quad 1.82$$

where  $\alpha$  and  $\beta$  are the familiar depth and width taper ratios, so that

$$\begin{aligned} A(z) &= A_0(1 + x_1\xi + x_2\xi^2) \quad \text{and} \\ I(z) &= I_0(1 + x_3\xi + x_4\xi^2 + x_5\xi^3 + x_6\xi^4) \end{aligned} \quad 1.83$$

in which

$$\begin{aligned} x_1 &= (\alpha - 1) + (\beta - 1), x_2 = (\alpha - 1) \cdot (\beta - 1), x_3 = (\beta - 1) + 3(\alpha - 1) \\ x_4 &= 3(\alpha - 1) \cdot (\beta - 1) + 3(\alpha - 1)^2 \\ x_5 &= 3(\alpha - 1)^2 \cdot (\beta - 1) + (\alpha - 1)^3, x_6 = (\alpha - 1)^3 \cdot (\beta - 1) \end{aligned} \quad 1.84$$

and  $A_0$  and  $I_0$  are the area and second moment of area at the left-hand node respectively.

A seventh-order interpolation polynomial for the amplitude of the vibration can be represented by

$$w = \langle 1 \ z \ \dots \ z^7 \rangle \{q_1 \ q_2 \ \dots \ q_8\}^T \quad 1.85$$

in which the assemblable element freedoms are taken as

$$\begin{aligned} q_1 &= v_0, q_2 = \left. \frac{dv}{dz} \right|_0, q_3 = \left. \frac{d^2v}{dz^2} \right|_0, q_4 = \left. \frac{d^3v}{dz^3} \right|_0 \\ q_5 &= v_L, q_6 = \left. \frac{dv}{dz} \right|_L, q_7 = \left. \frac{d^2v}{dz^2} \right|_L, q_8 = \left. \frac{d^3v}{dz^3} \right|_L \end{aligned} \quad 1.86$$

This allows the septimal interpolation function to be written as

$$w = \langle N_1 \ N_2 \ \dots \ N_8 \rangle \mathbf{q} \quad 1.87$$

in which  $\mathbf{q} = \langle q_1, q_2, \dots, q_8 \rangle^T$ , and the shape functions are given by

$$\begin{aligned} N_1 &= 1 - 35\xi^4 + 84\xi^5 - 70\xi^6 + 20\xi^7 \\ N_2 &= L\xi(1 - 20\xi^3 + 45\xi^4 - 36\xi^5 + 10\xi^6) \\ N_3 &= \frac{1}{2}L^2\xi^2(1 - 10\xi^2 + 20\xi^3 - 15\xi^4 + 4\xi^5) \\ N_4 &= \frac{1}{6}L^3\xi^3(1 - 4\xi + 6\xi^2 - 4\xi^3 + \xi^4) \\ N_5 &= 35\xi^4 - 84\xi^5 + 70\xi^6 - 20\xi^7 \\ N_6 &= L\xi(39\xi^4 - 15\xi^3 - 34\xi^5 + 10\xi^6) \end{aligned}$$

$$\begin{aligned} N_7 &= \frac{1}{2} L^2 \xi^2 (5\xi^2 - 14\xi^3 + 13\xi^4 - 4\xi^5) \\ N_8 &= \frac{1}{6} L^3 \xi^3 (3\xi^2 - \xi - 3\xi^3 + \xi^4) \end{aligned} \quad 1.88$$

Appropriate differentiation of Eqs. (1.88) and substitution of Eq. (1.87) into Eqs. (1.10) and (1.11) and then into Eq. (1.12) produces the change in total potential as

$$\Pi = \mathbf{q}^T (\mathbf{K}^e + \mathbf{K}_R^e - \omega^2 \mathbf{M}^e) \mathbf{q} = 0 \quad 1.89$$

in which

$$\mathbf{K}^e = \int_0^L \mathbf{N}''^T EI(z) \mathbf{N}'' dz \quad 1.90$$

is the elastic stiffness matrix for the tapered element,

$$\mathbf{M}^e = \int_0^L \rho A(z) \mathbf{N}^T \mathbf{N} dz \quad 1.91$$

is the consistent mass matrix for the tapered element,  $\mathbf{K}_R$  is the elastic stiffness matrix of the restraints for the tapered element, and

$$\mathbf{N}'' = \frac{d^2}{dz^2} \mathbf{N} \quad 1.92$$

The stiffness and mass matrices for each element ( $)^e$  may be assembled into the global counterpart matrices  $\mathbf{K}$  and  $\mathbf{M}$  using equilibrium and compatibility in the usual way. When the energy function  $\Pi$  remains stationary with respect to the vector of structural or global deformations  $\mathbf{Q}$ ,  $d\Pi/d\mathbf{Q} = \mathbf{0}$ , so that in Eq. (1.89)

$$(\mathbf{K} + \mathbf{K}_R - \omega^2 \mathbf{M}) \mathbf{Q} = \mathbf{0} \quad 1.93$$

The nontrivial solution of Eq. (1.92) is

$$\det(\mathbf{K} + \mathbf{K}_R - \omega^2 \mathbf{M}) = 0 \quad 1.94$$

where  $(\mathbf{K} + \mathbf{K}_R - \omega^2 \mathbf{M})$  is known as the dynamic stiffness matrix of the tapered member. Equation 1.94 is a standard eigenvalue problem, that can be solved using standard packages to determine the natural frequencies  $\omega$ . To (1979) lists the entries for the elastic stiffness and consistent mass matrix based on a seventh-order polynomial.

An alternative technique to using approximate polynomial interpolation functions in finite element analyses is to base the derivation of the stiffness matrices on the homogeneous solution of the governing differential equation for the problem at hand. This approach is a ‘direct stiffness method’ that has been shown to produce robust numerical solutions for some multi-field problems that would otherwise present difficulties when analysed using interpolating polynomials (Ranzi *et al.* 2004). Using this technique, Cleghorn

and Tabarrok (1992) provided an analysis of the element shown in Fig. 1.6 for which the width  $b$  is constant, but for a Timoshenko beam for which shear deformations and rotary inertia are included. This formulation represents a refinement of the treatment of Karabalis and Beskos (1983). The strain energy in Eq. (1.19) can then be written as

$$U = \frac{1}{2} \int_0^L [EI\Theta'^2 + kAG(V' - \Theta)^2] dz \quad 1.95$$

while the kinetic energy in Eq. (1.20) can be written as

$$\mathcal{K} = \frac{1}{2} \int_0^L \rho [A\dot{V}^2 + I\dot{\Theta}^2] dz \quad 1.96$$

in which  $\Theta(z, t)$  is the rotation of a cross-section,  $G$  is the shear modulus and  $k$  is a shear shape factor. Using Hamilton's principle (Liew *et al.* 1998) that

$$\delta \int_{t_1}^{t_2} (\mathcal{K} - U) dt = 0 \quad 1.97$$

Equations (1.95) and (1.96) lead to the coupled differential equations

$$kAG(V' - \Theta) + (EI\Theta')' - \rho I\ddot{\Theta} = 0 \quad 1.98$$

and

$$[kAG(V' - \Theta)]' - \rho A\ddot{V} = 0 \quad 1.99$$

as well as the respective boundary conditions that

$$\Theta' = 0 \quad \text{or} \quad \Theta = 0; \quad V' - \Theta = 0 \quad \text{or} \quad V = 0 \quad 1.100$$

The direct stiffness approach used by Cleghorn and Tabarrok (1992) uses the solution of Eqs. (1.98) and (1.99) with  $\ddot{V} = \ddot{\Theta} = 0$ , which can be expressed in matrix form as

$$\begin{aligned} & \begin{Bmatrix} v \\ \theta \end{Bmatrix} \\ &= \begin{bmatrix} \frac{L}{\alpha-1} \left[ \frac{E}{6b^2kG} + \frac{2L^2}{A_0^2(\alpha-1)^2} \right] \ln(\zeta) + \frac{L^2\xi}{A_0} \left[ \frac{L\xi}{A_0\zeta} - \frac{2L}{A_0(\alpha-1)} \right] & \frac{L^2\xi^2}{A_0^2\zeta} & L\xi & 1 \\ -\frac{L^2\xi^2}{A_0^2\zeta^2} & \frac{L\xi}{A_0^2\zeta^2}(\zeta+1) & 1 & 0 \end{bmatrix} \\ & \times \begin{Bmatrix} \alpha_1 \\ \alpha_2 \\ \alpha_3 \\ \alpha_4 \end{Bmatrix} \end{aligned} \quad 1.101$$

where  $v(z)$  and  $\theta(z)$  are the amplitudes of  $V$  and  $\Theta$  respectively. The kernel coefficients  $\{\alpha_1, \dots, \alpha_4\}^T$  can be found in terms of the assemblable displacements  $\{v_0, \theta_0, v_L, \theta_L\}^T$  at  $z = 0$  and  $z = L$  as

$$\begin{bmatrix} \alpha_1 \\ \alpha_2 \\ \alpha_3 \\ \alpha_4 \end{bmatrix} = \begin{bmatrix} 0 & 0 & 1 \\ 0 & 0 & 0 \\ \frac{L}{A_0(\alpha-1)} \left[ \frac{E}{6b^2kG} + \frac{2L^2}{A_0^2(\alpha-1)^2} \right] \ln \alpha - \frac{L^3}{A_0^2\alpha(\alpha-1)} & \frac{L^2}{\alpha A_0^2} & L & 1 \\ -\frac{L^2}{A_0^2\alpha^2} & \frac{L(\alpha+1)}{A_0^2\alpha^2} & 1 & 0 \end{bmatrix}^{-1} \begin{bmatrix} v_0 \\ \theta_0 \\ v_L \\ \theta_L \end{bmatrix} \quad 1.102$$

or

$$\boldsymbol{\alpha} = \mathbf{F}\mathbf{q} \quad 1.103$$

so that

$$\begin{bmatrix} v \\ \theta \end{bmatrix} = \begin{bmatrix} \frac{L}{\alpha-1} \left[ \frac{E}{6b^2kG} + \frac{2L^2}{A_0^2(\alpha-1)^2} \right] \ln \zeta + \frac{L^2\xi}{A_0} \left[ \frac{L\xi}{A_0\zeta} - \frac{2L}{A_0(\alpha-1)} \right] & \frac{L^2\xi^2}{A_0^2\xi} & L\xi & 1 \\ -\frac{L^2\xi^2}{A_0^2\zeta^2} & \frac{L\xi}{A_0^2\zeta^2}(\zeta+1) & 1 & 0 \end{bmatrix} \mathbf{F} \cdot \mathbf{q} \quad 1.104$$

Equation (1.95) may be used to determine the element stiffness matrix  $\mathbf{K}^e$  as was done for Eq. (1.90), so that

$$\mathbf{K}^e = \mathbf{F}^T \mathbf{K}^e \mathbf{F} \quad 1.105$$

where

$$k^e = \begin{bmatrix} k_{11}^e & k_{12}^e & 0 & 0 \\ k_{21}^e & k_{22}^e & 0 & 0 \\ 0 & 0 & 0 & 0 \\ \text{sym.} & & & 0 \end{bmatrix} \quad 1.106$$

in which

$$k_{11}^e = \frac{kGL}{A_0(\alpha-1)} \left( \frac{A_0 E}{6b^2 k G} \right)^2 \ln(\alpha) - \frac{EL^3}{3b^2 A_0 (\alpha-1)} \left[ \frac{1}{2\alpha^2} + \frac{1}{\alpha(\alpha-1)} - \frac{\ln(\alpha)}{(\alpha-1)^2} \right] \quad 1.107$$

$$k_{12}^e = -\frac{EL^2}{6b^2 \alpha^2 A_0} \quad 1.108$$

$$k_{22}^e = \frac{EL(\alpha + 1)}{6b^2 \alpha^2 A_0} \quad 1.109$$

An approximate mass stiffness matrix (Cleghorn and Tabarrok 1992) can be determined from Eq. (1.96) using the same shape displacement functions as used in the stiffness matrix. This produces

$$\mathbf{M}^e = \mathbf{F}^T \mathbf{m}^e \mathbf{F}, \quad 1.110$$

where

$$\mathbf{m}^e = \begin{bmatrix} m_{11}^e & m_{12}^e & m_{13}^e & m_{14}^e \\ & m_{22}^e & m_{23}^e & 0 \\ & & m_{33}^e & m_{34}^e \\ \text{sym.} & & & m_{44}^e \end{bmatrix} \quad 1.111$$

in which

$$\begin{aligned} m_{11}^e &= \frac{L^5}{12b^2 A_0 (\alpha - 1)} \\ &\times \left[ \frac{1}{4} + \frac{\ln(\alpha)}{(\alpha - 1)^4} - \frac{1}{3(\alpha - 1)} + \frac{1}{2(\alpha - 1)^2} - \frac{1}{(\alpha - 1)^3} \right] \\ &+ \frac{L^7 \alpha^2 (\gamma + 2)^2 [\ln(\alpha)]^2}{2A_0^3 (\alpha - 1)^5} + \frac{L^7 \gamma^2 [\alpha^2 - 2\alpha^2 \ln(\alpha) - 1]}{4A_0^3 (\alpha - 1)^7} \\ &+ \frac{2L^7 \gamma}{A_0^3 (\alpha - 1)^5} \left\{ (\alpha - 1) \left[ \frac{5(\alpha - 1)}{2} - \frac{(\alpha - 1)^2}{9} \right] \right. \\ &\left. - \left[ \frac{1}{3} + 2(\alpha - 1) + 2(\alpha - 1)^2 + \frac{(\alpha - 1)^3}{3} \right] \ln(\alpha) \right\} \\ &+ \frac{L^7}{3A_0^3 (\alpha - 1)^7} [12(\alpha - 1) + 18(\alpha - 1)^2 + 4(\alpha - 1)^3 - 5]\ln(\alpha) \\ &+ \frac{L^7}{18A_0^3 (\alpha - 1)^3} \left[ 18 + \frac{10}{(\alpha - 1)} + \frac{51}{(\alpha - 1)^2} - \frac{30}{(\alpha - 1)^3} \right] \quad 1.112 \end{aligned}$$

$$\begin{aligned}
m_{12}^e &= \frac{L^4}{12b^2 A_0} \\
&\times \left[ \frac{\ln(\alpha)}{(\alpha-1)^4} - \frac{1}{3(\alpha-1)} + \frac{1}{2(\alpha-1)^2} - \frac{1}{(\alpha-1)^3} - \frac{1}{4} \right] \\
&+ \frac{\gamma L^6}{3A_0^3(\alpha-1)^3} \\
&\times \left\{ \left[ 1 + \frac{1}{(\alpha-1)^3} \right] \ln(\alpha) - \frac{1}{(\alpha-1)^2} + \frac{1}{\alpha-1} + \frac{1}{3} + \frac{1}{3} \left[ 2 + \frac{5}{(\alpha-1)^3} \right] \ln(\alpha) \right\} \\
&+ \frac{L^6}{A_0^3(\alpha-1)} \left[ -\frac{5}{3} + \frac{5}{6(\alpha-1)^3} - \frac{1}{9(\alpha-1)^2} - \frac{1}{4(\alpha-1)} \right] \quad 1.113
\end{aligned}$$

$$\begin{aligned}
m_{13}^e &= -\frac{L^3 A_0 (3\alpha + 1)}{144b^2} + \frac{\gamma L^5}{A_0 (\alpha-1)^2} \left\{ \left[ \frac{1}{2(\alpha-1)} + \frac{1}{3} - \frac{1}{6(\alpha-1)^3} \right] \right. \\
&\left. \ln(\alpha) + \left[ \frac{1}{6(\alpha-1)^2} - \frac{1}{12(\alpha-1)} + \frac{1}{9} \right] \right\} \\
&+ \frac{L^5}{A_0 (\alpha-1)^5} \left[ \frac{2(\alpha-1)^3}{3} + (\alpha-1)^2 - \frac{1}{3} \right] \ln(\alpha) \\
&+ \frac{L^5}{A_0 (\alpha-1)} \left[ \frac{1}{3(\alpha-1)^3} - \frac{1}{6(\alpha-1)^2} - \frac{4}{9(\alpha-1)} - \frac{1}{5} \right] \quad 1.114
\end{aligned}$$

$$\begin{aligned}
m_{14}^e &= \frac{\gamma L^4}{4A_0 (\alpha-1)^3} [2\alpha^2(\alpha-1)\ln(\alpha) + \alpha - 1] \\
&+ \frac{L^4}{A_0 (\alpha-1)^3} \left[ (\alpha^2 + 1) \ln(\alpha) - \frac{(2\alpha^2 + 5\alpha - 1)}{6} \right] \quad 1.115
\end{aligned}$$

$$\begin{aligned}
m_{22}^e &= \frac{L^3}{12b^2 A_0} \left[ \frac{\ln(\alpha)}{(\alpha-1)^3} + \frac{1}{2(\alpha-1)} - \frac{1}{(\alpha-1)^2} + 1 + \frac{\alpha-1}{4} \right] \\
&+ \frac{L^5}{A_0^3} \left[ \frac{1}{4(\alpha-1)} + \frac{\ln(\alpha)}{(\alpha-1)^5} - \frac{1}{3(\alpha-1)^2} + \frac{1}{(\alpha-1)^3} - \frac{1}{(\alpha-1)^4} \right] \\
& \quad 1.116
\end{aligned}$$

$$m_{23}^e = \frac{A_0 L^2 (\alpha + 1)^2}{48 b^2} + \frac{L^4}{4 A_0} \quad 1.117$$

$$m_{24}^e = \frac{L^3}{3 A_0} \quad 1.118$$

$$m_{33}^e = \frac{L^3 A_0 (3\alpha + 1)}{12} \quad 1.119$$

$$m_{34}^e = \frac{L^2 A_0 (2\alpha + 1)}{6} \quad 1.120$$

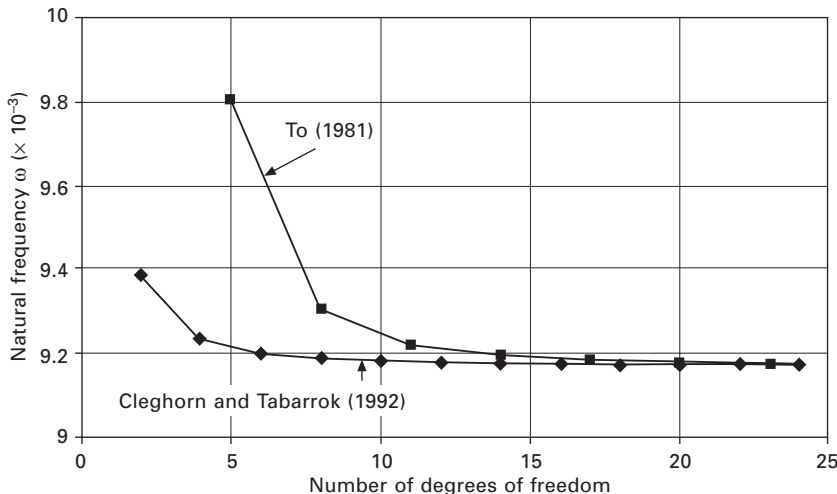
$$m_{44}^e = \alpha L A_0, \quad 1.121$$

where

$$\gamma = \frac{A_0^2 E(\alpha - 1)^2}{6 b^2 L^2 k G} \quad 1.122$$

Equations (1.112) to (1.121) have a singularity for a uniform beam when  $\alpha = 1$ , but this difficulty can be circumvented by expanding the terms with Taylor series in powers of  $\alpha$  and taking the limit as  $\alpha \rightarrow 1$  (Cleghorn and Tabarrok 1992) in the same way as was done by Ranzi *et al.* (2004) to remove numerical instabilities.

The numerical efficiencies of using a direct stiffness approach are compared in Fig. 1.7 with the use of interpolation functions for Timoshenko beams. In this figure, the interpolation functions were based on the formulation of To



1.7 Convergence of finite element solutions for clamped tapered beam ( $\alpha = 2$ ).

(1981) for a beam with  $E = 210 \text{ kN/mm}^2$ ,  $G = 80 \text{ kN/mm}^2$ ,  $b = 25.4 \text{ mm}$ ,  $A_0 = 645 \text{ mm}^2$ ,  $l = 254 \text{ mm}$ ,  $\alpha = 0.50$ . The fundamental natural frequency  $\omega$  for a beam with clamped ends is plotted in Fig. 1.7, in which it is clear that the direct stiffness approach converges more rapidly and has fewer freedoms than the finite element formulation based on interpolation polynomial functions. Tables 1.12–1.15 show convergence studies using the finite element technique for a number of cases of tapered beams.

*Table 1.12 Frequency parameters for pyramid beam ( $\alpha = \beta = \infty$ ) using finite element method*

No. of elements	Analysis	$\lambda^2$ (1) [8.7192]*	$\lambda^2$ (2) [21.146]	$\lambda^2$ (3) [38.453]	$\lambda^2$ (4)	$\lambda^2$ (5)
1	Order 3	8.73517	25.18142			
	Order 5	8.74506	23.18407	68.85968	78.22758	78.22758
	Order 7	8.75096	23.83025	55.37000	169.30409	178.53337
2	Order 3	8.72388	21.71782	41.92455	94.86600	103.73917
	Order 5	8.72021	21.25307	40.39639	72.27633	128.51998
	Order 7	8.72089	21.27920	40.25180	70.13591	117.87558
4	Order 3	8.71961	21.20345	39.10222	62.76983	98.77139
	Order 5	8.71927	21.14939	38.54472	61.57421	92.29457
	Order 7	8.71936	21.15169	38.57220	61.60905	91.80001
10	Order 3	8.71927	21.14733	38.47887	60.85846	88.60268
	Order 5	8.71927	21.14571	38.45479	60.69236	87.92289
	Order 7	8.71927	21.14571	38.45556	60.69902	87.95364

\*[ ] denotes analytical result.

*Table 1.13 Frequency parameters for tapered beam ( $\alpha = \beta = 5$ ) using finite element method*

No. of elements	Analysis	$\lambda^2$ (1) [6.1964]*	$\lambda^2$ (2) [18.3855]	$\lambda^2$ (3) [39.835]	$\lambda^2$ (4) [71.242]	$\lambda^2$ (5) [112.828]
1	Order 3					
	Order 5	6.19986	18.95919	56.85606	63.82743	63.82743
	Order 7	6.20819	19.03870	48.69267	147.25942	154.19323
2	Order 3	6.20186	18.88848	41.11316	92.82321	105.03894
	Order 5	6.19648	18.38837	39.96101	73.73720	131.03760
	Order 7	6.19667	18.40247	40.09945	73.37800	123.68543
4	Order 3	6.19676	18.42262	40.41611	75.30089	117.85937
	Order 5	6.19641	18.38641	39.84572	71.30942	113.04873
	Order 7	6.19640	18.38556	39.83513	71.25365	112.89501
10	Order 3	6.19640	18.38641	39.84648	71.32205	113.16316
	Order 5	6.19639	18.38547	39.83367	71.24245	112.83180
	Order 7	6.19639	18.38547	39.83359	71.24177	112.82753

\*[ ] denotes analytical result.

**Table 1.14** Frequency parameters for tapered beam ( $\alpha = \beta = 2.5$ ) using finite element method

No. of elements	Analysis	$\lambda^2$ (1) [5.009 032]*	$\lambda^2$ (2) [19.064 88]	$\lambda^2$ (3) [45.738 36]	$\lambda^2$ (4) [85.344]	$\lambda^2$ (5) [138.0352]
1	Order 3					
	Order 5	5.010 26	19.119 75	53.988 38	60.982 98	60.982 98
	Order 7	5.009 760	19.162 11	49.175 35	138.674 16	148.060 58
2	Order 3	5.011 54	19.523 78	50.018 09	112.906 97	130.252 77
	Order 5	5.009 145	19.077 56	45.906 03	86.133 75	146.415 76
	Order 7	5.009 033	19.065 26	45.719 14	85.541 91	140.997 05
4	Order 3	5.009 25	19.085 00	46.065 30	88.905 01	149.896 71
	Order 5	5.009 034	19.065 09	45.744 11	85.418 01	138.383 80
	Order 7	5.009 033	19.064 83	45.738 38	85.353 87	138.035 34
10	Order 3	5.009 04	19.065 69	45.751 11	85.427 47	138.378 66
	Order 5	5.009 033	19.064 83	45.738 38	85.343 87	138.036 20
	Order 7	5.009 033	19.064 83	45.738 38	85.343 78	138.035 34

\*[ ] denotes analytical result.

**Table 1.15** Frequency parameters for wedge beam ( $\alpha = \infty, \beta = 1$ ) using finite element method

No. of elements	Analysis	$\lambda^2$ (1)	$\lambda^2$ (2)	$\lambda^2$ (3)	$\lambda^2$ (4)	$\lambda^2$ (5)
1	Order 3	5.318 72	17.300 40			
	Order 5	5.331 66	16.594 95	52.129 28	58.574 41	50.574 41
	Order 7	5.339 91	16.575 30	43.706 35	137.694 59	146.059 62
2	Order 3	5.315 85	15.444 34	32.702 86	78.570 37	84.809 26
	Order 5	5.316 29	15.324 27	31.920 00	60.996 90	113.582 48
	Order 7	5.317 35	15.376 28	32.028 02	59.473 00	104.343 79
4	Order 3	5.315 15	15.229 90	30.376 96	51.484 93	85.807 51
	Order 5	5.315 18	15.215 13	30.174 91	51.003 10	79.849 08
	Order 7	5.315 26	15.221 19	30.245 19	51.202 51	79.692 46
10	Order 3	5.313 10	15.207 78	30.034 08	49.886 82	75.011 71
	Order 5	5.315 02	15.207 36	30.024 17	49.804 33	74.674 46
	Order 7	5.315 02	15.207 61	30.027 85	49.831 31	74.781 04

## 1.5 Conclusions

This chapter has considered the dynamic behaviour of tapered members composed of tapered plates, and has concentrated on the free vibration of these members without damping. A formulation was presented that leads to a virtual work statement of the problem, and which then leads to the differential equations of motion for the tapered member. This formulation is also convenient because it allows the static boundary conditions to be stated *a priori*, without recourse to intuition.

It was shown that the solutions obtained by other researchers are based on the governing differential equation of motion, whose solution in analytical format requires Bessel functions and which can be overly complex for more general cases. The equations of motion can be solved using numerical techniques, by representing the amplitude of the displacements as a power series, or using Fourier series. Solutions were given for linearly tapered beams with width and/or depth taper, and for a variety of end conditions. One such case is that of a tapered cantilever with a tip mass, or of a tapered propped cantilever, and comprehensive solutions were given for the frequency of vibration of these members.

Two types of finite element formulations were discussed: a general approach with predetermined interpolation functions and a direct stiffness approach that is based on the solution of the differential equations of motion. The direct stiffness approach leads to exact solutions, but the stiffness and consistent mass matrices are very complicated. The simpler and more familiar approach can lead to difficulties of convergence and accuracy, with higher-order polynomial interpolations producing more favourable solutions. Solutions obtained by both techniques were considered.

The tapered members considered in this chapter possess one axis of symmetry that is in the plane in which their motion takes place, and modes out of the plane of this axis of symmetry, as well as torsional modes, were excluded. Although there are many solutions for vibration of tapered members in the open literature, until very recently these were restricted to planar vibration modes. Coupled vibration modes in open-section prismatic or tapered members are complex, involving warping effects and Wagner effects, and comprehensive studies of these modes and formulations for their analysis are comparatively few.

## 1.6 References

- Abrate, S. (1995), Vibration of non-uniform rods and beams. *Journal of Sound and Vibration*, **185**, 703–716.
- Amirikian, A. (1952), Wedge-beam framing. *Transactions, ASCE* **117**, 596–652.
- Archer, J.S. (1963), Consistent mass matrix for distributed mass systems. *Proceedings of the ASCE*, **89(ST4)**, 161–178.
- Auciello, N.M. and Ercolano, A. (1997), Exact solution for the transverse vibration of a beam a part of which is a taper beam and other part is a uniform beam. *International Journal of Solids and Structures*, **34**(17), 2115–2129.
- Banerjee, J.R., Guo, S. and Howson, W.P. (1996), Exact dynamic stiffness matrix of a bending-torsion coupled beam including warping. *Computers and Structures*, **59**, 613–621.
- Biggs, J.M. (1964), *Introduction to Structural Dynamics*, McGraw-Hill, New York.
- Bradford, M.A. (2006), Lateral buckling of tapered steel members. *Analysis and Design of Plated Structures* (Volume 1: Stability), N.E. Shanmugam and C.M. Wang (eds), Woodhead Publishing Limited, Cambridge.

- Bradford, M.A. and Abdoli-Yazdi, N. (1999), A modified Newmark method for the second order elastic analysis of beam-columns. *Computers and Structures*, **71**, 689–700.
- Cleghorn, W.L. and Tabarrok, B. (1992), Finite element formulation of a tapered Timoshenko beam for free lateral vibration analysis, *Journal of Sound and Vibration*, **152**(3), 461–470.
- Clough, R.W. and Penzien, J. (1975), *Dynamics of Structures*, McGraw-Hill, New York.
- Conway, H.D. and Dubil, J.F. (1965), Vibration frequencies of truncated-cone and wedge beams. *Journal of Applied Mechanics*, **32**, 932–934.
- Conway, H.D., Becker, E.C.H. and Dubil, J.F. (1964), Vibration frequencies of tapered bars and circular plates. *Journal of Applied Mechanics*, **31**, 329–331.
- Cranch, E.T. and Adler, A.A. (1956), Bending vibrations of variable section beams. *Journal of Applied Mechanics* **23**, 103–108.
- De Rosa, M.A. and Auciello, N.M. (1996), Free vibrations of tapered beams with flexible ends. *Computers and Structures* **60**(2), 197–202.
- De Vahl Davis, G. (1986), *Numerical Methods in Engineering and Science*, Allen & Unwin, London.
- Friberg, P.O. (1993), Coupled vibration of beams – an exact dynamic element stiffness matrix. *International Journal for Numerical Methods in Engineering*, **19**, 479–493.
- Gallagher, R.H. and Lee, C.H. (1970), Matrix dynamic and instability analysis with non-uniform elements. *International Journal for Numerical Methods in Engineering*, **2**, 265–275.
- Goel, R.P. (1976), Transverse vibrations of tapered beams. *Journal of Sound and Vibration*, **47**, 1–7.
- Gorman, D.J. (1975), *Free Vibration Analysis of Beams and Shafts*. Wiley, New York.
- Gupta, A.K. (1985), Vibration of tapered beams. *Journal of Structural Engineering*, **111**(1), 19–36.
- Hall, A.S. and Kabaila, A.P. (1986), *Basic Concepts of Structural Analysis*. GreenwichSoft, Sydney.
- Handa, K.N. (1970), The response of tall structures to atmospheric turbulence. PhD Thesis, University of Southampton, UK.
- Heidebrecht, A.C. (1967), Vibrations of non-uniform simply supported beams, *Journal of the Engineering Mechanics Division, ASCE*, **93**(EM2), 1–15.
- Hibbeler, R.C. (1999), *Structural Analysis*, 4th edn., Prentice-Hall, Upper Saddle River, New Jersey.
- Housner, G.W. and Keightley, W.O. (1962), Vibrations of linearly tapered cantilever beams. *Journal of the Engineering Mechanics Division, ASCE*, **88**(EM2), 95–123.
- Ishizake, H. and Hatakeyama, N. (1956), Experimental and numerical studies on vibration of buildings. *Proceedings of First World Conference on Earthquake Engineering*, Berkley, California, 1956.
- Jacobson, L.S. and Ayre, R.S. (1958), *Engineering Vibrations*, McGraw-Hill, New York.
- Kapania, R.K. and Raciti, S. (1989), Recent advances in analysis of laminated beams and plates, part II: vibrations and wave propagation. *American Institute of Aeronautics and Astronautics Journal*, **27**, 935–946.
- Karabalis, D.L. and Beskos, D.E. (1983), Static, dynamic and stability analysis of structures composed of tapered beams. *Computers and Structures*, **16**(6), 731–748.
- Kirchhoff, G. (1879), Über die transversalschwingungen eines stabes von veränderlichem querschnitt. *Berliner Monatsberichte*, 815–828.
- Korqingskee, E.L. (1952), *Vibrations of Tall Buildings*, Moscow Press, Moscow.

- Laura, P.A.A., Gutierrez, R.E. and Rossi, R.E. (1996), Free vibration of beams of bi-linearly varying thickness. *Ocean Engineering*, **23**(1), 1–6.
- Li, Q.S. (2001), Exact solutions for free vibration of shear-type structures with arbitrary distribution of mass or stiffness. *Journal of Acoustical Society of America*, **110**(4), 1958–1966.
- Liew, K.M., Xiang, Y. and Kitipornchai, S. (1995a), Benchmark solutions for regular polygonal Mindlin plates. *Journal of the Acoustical Society of America*, **95**, 2801–2871.
- Liew, K.M., Xiang, Y. and Kitipornchai, S. (1995b), Research on thick plate vibration: a literature survey. *Journal of Sound and Vibration*, **180**, 163–176.
- Liew, K.M., Wang, C.M., Xiang, Y. and Kitipornchai, S. (1998), *Vibration of Mindlin Plates: Programming the p-Version Ritz Method*, Elsevier, Amsterdam.
- Lindberg, G.M. (1963), Vibration of non-uniform beams. *The Aeronautical Quarterly*, **14**, 387–395.
- MacDuff, J.N. and Felger, R.P. (1957), Vibration design charts. *Transactions, ASME*, **79**, 1459–1475.
- Mabie, H.H. and Rogers, C.B. (1964), Transverse vibrations of tapered cantilever beams with end loads. *Journal of the Acoustical Society of America*, **36**, 463–469.
- Mabie, H.H. and Rogers, C.B. (1968), Transverse vibrations of tapered cantilever beams with end support. *Journal of the Acoustical Society of America*, **44**, 1739–1741.
- Mabie, H.H. and Rogers, C.B. (1972), Transverse vibrations of double-tapered cantilever beams. *Journal of the Acoustical Society of America*, **51**, 1771–1774.
- Mabie, H.H. and Rogers, C.B. (1974), Transverse vibrations of double-tapered cantilever beams with end support and with end mass. *Journal of the Acoustical Society of America*, **55**, 986–991.
- Newmark, N.M. (1943), Numerical procedure for computing deflections, moments and buckling loads. *Transactions of the ASCE*, **108**, 1161–1188.
- Oral, S. (1991), A shear flexible finite element for non-uniform laminated composite beams. *Computers and Structures*, **38**, 353–360.
- Pi, Y.-L., Bradford, M.A. and Uy, B. (2005a), Nonlinear analysis of members curved in space with warping and Wagner effects. *International Journal of Solids and Structures*, **43**(11–12), 3147–3169.
- Pi, Y.-L., Bradford, M.A. and Uy, B. (2005b), A spatially curved beam-element with warping and Wagner effects. *International Journal for Numerical Methods in Engineering*, **63**(9), 1342–1369.
- Portland Cement Association (1958), *Handbook of Frame Constants*, PCA, Skokie, Illinois.
- Ramalingeswara Rao, S. and Ganesan, N. (1997), Dynamic response of non-uniform composite beams. *Journal of Sound and Vibration*, **200**(5), 563–577.
- Ranzi, G., Bradford, M.A. and Uy, B. (2004), A direct stiffness analysis of composite beams. *International Journal for Numerical Methods in Engineering*, **61**(5), 657–672.
- Rutledge, W.D. and Beskos, D.E. (1981), Dynamic analysis of linearly tapered beams. *Journal of Sound and Vibration*, **79**(3), 457–462.
- Saadatpour, M.A., Azhari, M. and Bradford, M.A. (2000), Vibration analysis of simply supported plates of general shape with internal point supports using the Galerkin method. *Engineering Structures*, **22**(9), 1180–1188.
- Sato, K. (1980), Transverse vibrations of linearly tapered beams with ends restrained elastically against rotation subjected to an axial force. *International Journal of Mechanical Sciences*, **22**, 109–115.

- Siddall, J.N. and Isakson, G. (1951), Approximate analytical methods for determining natural modes and frequencies of vibration, Massachusetts Institute of Technology Report ONR Proj. NR-035-259, 141–146.
- Suppiger, E.W. and Taleb, N.J. (1956), Free lateral vibration of beams of variable cross-section. *ZAMP* **7**, 501–520.
- Thomas, J. and Dokumaci, E. (1973), Improved finite elements for vibration analysis of tapered beams. *The Aeronautical Quarterly*, **24**, 39–46.
- Timoshenko, S.P. (1955), *Vibration Problems in Engineering*, Van Nostrand Company, Princeton, New Jersey.
- To, C.W.S. (1979), Higher order taper beam finite elements for vibration analysis. *Journal of Sound and Vibration*, **63**, 33–50.
- To, C.W.S. (1981), A linearly tapered beam finite element incorporating shear deformation and rotary inertia for vibration analysis. *Journal of Sound and Vibration*, **78**, 475–484.
- Voros, G.M. (2004), Free vibration of thin-walled beams. *Periodica Polytechnica Series Mechanical Engineering*, **48**(1), 99–110.
- Wang, G.Y. (1958), The calculation of earthquake loads acting on buildings. *Journal of Civil Engineering*, **5**(2), 16–32.
- Wang, G.Y. (1963), Free vibrations of multi-story buildings. *Journal of Harbin University Architecture and Civil Engineering*, **1**, 1–10.
- Wang, H.C. (1967), Generalized hypergeometric function solutions on the transverse vibration of a class of nonuniform beams. *Journal of Applied Mechanics*, **32**, 932–934.
- Ward, P.F. (1913), Transverse vibration of bars of varying cross-section. *Philosophical Magazine*, **25**(6), 85–106.
- Watson, G.N. (1956), *A Treatise of the Theory of Bessel Functions*, Cambridge University Press, Cambridge.
- Wolfram, S. (1993), *Mathematica*, Version 2.2, Wolfram Research, Champaign, Illinois.
- Worley, W.J. and Breuer, F.D. (1957), Areas, centroids and inertias for a family of elliptic-type closed curves. *Product Engineering*, **28**, 141–144.
- Yuan, F. and Miller, R.E. (1989), A new finite element for laminated composite beams. *Computers and Structures*, **31**, 731–745.
- Yuan, F. and Miller, R.E. (1990), A higher-order finite element for laminated beams. *Composite Structures*, **14**, 125–150.
- Zienkiewicz, O.C. and Taylor, R.L. (2000), *The Finite Element Method*, Vol. 1. Butterworth-Heinemann, London.

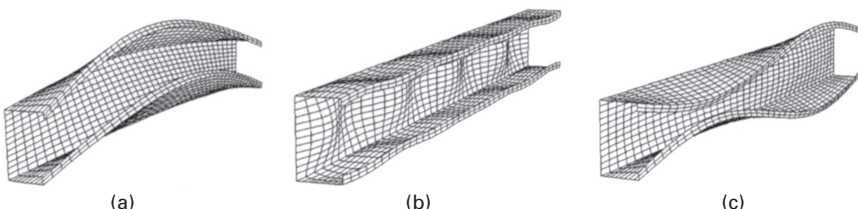
## GBT-based local and global vibration analysis of thin-walled members

D CAMOTIM, N SILVESTRÉ and  
R BEBIANO, Technical University of Lisbon, Portugal

### 2.1 Introduction

Thin-walled members may be viewed as an assembly of plates rigidly linked together through their longitudinal edges. Recent investigations (e.g. Davies 2000, Camotim *et al.* 2004) have shown, both analytically and experimentally, that the cross-section in-plane deformations (i.e. *local* deformations) may strongly affect the buckling behaviour of such members. Given the high mathematical resemblance between the member buckling and vibration analyses (solutions of similar eigenvalue problems), it is logical to expect the vibration behaviour of thin-walled members to be equally susceptible to the occurrence of local deformations. Therefore, the vibration phenomena may be classified and characterised as follows:

- Global vibration phenomena, which involve only the deformation of the member axis, i.e. are restricted to cross-section in-plane rigid-body motions (e.g. flexural-torsional vibration – see Fig. 2.1(a)).
- Local vibration phenomena, which involve in-plane cross-section deformations, while the member axis remains undeformed. It is still possible to distinguish between *local-plate* vibration (plate bending without fold-line motions – see Fig. 2.1(b)) and *distortional* vibration (fold-line membrane displacements – see Fig. 2.1(c)).



2.1 (a) Global (flexural-torsional), (b) local-plate and (c) distortional vibration phenomena.

The pioneer work addressing the local vibration of isotropic thin-walled members was carried out in the 1950s and disseminated through NACA (National Advisory Committee for Aeronautics) reports co-authored by Budiansky and Fralich (1954), Fitcher and Kordes (1959) and Thomson and Kruszewski (1961). These reports include analytical and experimental investigations concerning the influence of local deformation effects on the global flexural vibration of members with closed thin-walled cross-sections (tubes and rectangular hollow sections). Since then, a vast amount of research activity has been devoted to this topic, leading to the elaboration of numerous publications. The next sub-section discuss briefly a number of relevant works that have been published since the early 1990s. As this chapter deals with the use of numerical techniques to perform vibration analysis, this literature review is organised according to the particular methodology employed: there are separate sub-sections dealing with investigations carried out by means of (i) the finite element method (mostly shell element discretisations), (ii) the finite strip method and (iii) the generalised beam theory (GBT) – because the aim of this chapter is to present the fundamentals and illustrate the application of a GBT formulation to analyse the vibration behaviour of thin-walled members, the last sub-section also includes a brief outline of its content.

### 2.1.1 Finite element analysis (FEA)

Through the comparison of results obtained through shell and beam finite element analysis (FEA), Noor *et al.* (1993) concluded that the local deformation effects do not influence significantly the global (flexural-torsional) vibration behaviour of thin-walled members. More or less at the same time, Liu and Huang (1992) developed a shell finite element specifically intended to analyse the local vibration behaviour of V and U-section members. Klausbruckner and Pryputniewicz (1995), on the other hand, carried out a very thorough investigation, both numerically and experimentally, on the local vibration behaviour of ‘short’ U-section members – the numerical analyses were performed adopting fine meshes of four-node shell elements to discretise the members. As it would be logical to expect, this study revealed that the local deformations affect even the lower-order vibration behaviour of such members.

Another relevant contribution was due to Gavrić (1994), who formulated a shell finite element that was subsequently used to determine the vibration amplitude and number of half-waves of tubular and I-section members excited in a given frequency domain – this researcher concluded that the analytical results based on Euler–Bernoulli’s classical beam theory do not correlate well with the numerical values, owing to the influence of the in-plane cross-section deformation, an effect that was found to be particularly relevant in the I-section members. Using a similar approach, Li and Ho (1995) also showed that the natural frequencies and vibration modes of rectangular hollow

section members are strongly influenced by the in-plane cross-section deformation.

More recently, Kim and Kim (1999, 2000) developed and validated beam finite elements with closed thin-walled cross-sections that incorporate local deformation effects – the validation procedure showed clearly that, in order to perform accurate vibration analyses, these effects cannot be neglected. Finally, it is worth mentioning the more recent work co-authored by Hamed and Frostig (2005), proposing a beam model that accounts for the cross-section in-plane deformation by ensuring displacement compatibility and stress equilibrium along longitudinal edges joining adjacent walls. The natural frequency values obtained by means of this approach are compared with values yielded by shell FEA performed in a commercial code, for members with several cross-section geometries – good agreement was found in all cases.

### 2.1.2 Finite strip analysis (FSA)

Cheung and Kong (1995) employed the spline finite strip method to analyse the vibration behaviour of U-section ‘short’ cantilevers and determined values for the first five natural frequency values that differ only by 1.6% from similar results yielded by shell FEA – however, the FSA involve only about 1% of the number of degrees of freedom required by FEA. Williams *et al.* (1996) applied the semi-analytical finite strip method to investigate the vibration behaviour of uniaxially compressed simply supported stiffened panels with I-section and semi-circular stiffeners – they concluded that there is a strong correlation between their fundamental frequency and critical buckling load values. On the other hand, semi-analytical FSA was used by (i) Stephen and Steven (1997) to study the local-plate, distortional and global vibration behaviour of simply supported plain channel, lipped channel and hat-section members, and by (ii) Okamura and Fukasawa (1991) to analyse the local and global vibration behaviour of ‘short’ simply supported lipped channel, I-section and square hollow section members – the latter investigation addressed the first five vibration modes and showed that the lipped channel and I-section members are the ones more and least susceptible to exhibit cross-section in-plane deformation.

A few years later, Okamura and Fukasawa (1998) developed a semi-analytical finite strip to analyse the free and forced vibration behaviour of thin-walled members. In the context of the analysis of members acted on by periodic applied loads, these authors carried out a preliminary study concerning the influence of (nonperiodic) compressive normal stresses on the local-plate vibration of I-section and square hollow section members – they drew some important conclusions about the vibration mode configurations and the relation between the member natural frequencies and bifurcation stresses/loads.

Ohga *et al.* (1995, 1998) implemented the ‘transfer matrix method’, which resembles the semi-analytical finite strip method (both adopt sinusoidal functions to approximate the longitudinal variation of the displacements). It uses exact displacement functions in the transverse directions, thus requiring no wall strip discretisation – these functions are obtained by solving the differential equations, ensuring the equilibrium of each wall and satisfying the compatibility conditions along the various longitudinal edges (incorporated in the ‘transfer matrix’). These researchers validated the above method by assessing the local and global vibration behaviour of the ‘short’ simply supported lipped channel, I-section and square hollow section members analysed by Okamura and Fukasawa (1991) a few years earlier, through semi-analytical FEA – the two approaches were found to yield virtually identical results.

More recently, Ohga (2002) applied the ‘transfer matrix method’ to investigate the vibration behaviour of thin-walled members formed by several groups of cylindrical panels joined together through their longitudinal edges. In particular, he studied how the panel length-to-width ratio influences the first five natural frequencies and local vibration mode shapes. He showed that the local deformation effects become gradually more relevant as both the number of panels and the length-to-width ratio of each panel decrease.

### 2.1.3 Generalised beam theory (GBT)

*Generalised beam theory* (GBT), originally developed by Schardt (1966, 1989), has been shown to be a powerful tool to perform a wide variety of structural analyses involving prismatic thin-walled members – e.g. the buckling or the vibration behaviour of cold-formed steel or FRP (fibre-reinforced plastic) composite members (e.g. Davies 2000, Camotim *et al.* 2004). Owing to its unique modal decomposition features, GBT provides a general and unified approach to obtain accurate, elegant and clarifying solutions for several problems – indeed, by (i) decomposing the member deformed configuration (or buckling/vibration mode) into a linear combination of cross-section *deformation modes*, which account for both rigid-body motions and in-plane deformations, and (ii) being able to assess the contribution of each of them, GBT offers possibilities not available even through the use of very potent numerical techniques, such as the finite element or finite strip methods – indeed, this modal decomposition cannot be done in FEA or FSA, since all degrees of freedom are of a *nodal* (not modal) nature (i.e. the GBT-based analyses reveal all the ‘structural ingredients’ of a member deformed configuration or buckling/vibration mode, while retaining a numerical accuracy fully matching that of the FEA or FSA). Therefore, GBT may be viewed as either (i) a *bar* theory that incorporates cross-section in-plane deformation or (ii) a *folded-plate* theory that includes plate rigid-body motions.

In the 1970s, Saal (1974) developed the first GBT formulation to analyse the vibration behaviour of thin-walled members with unbranched open cross-sections and applied it to assess the influence of the local deformations on the dynamic response of such members. Years later, Schardt and Heinz (1991) employed this GBT formulation to analyse the free vibration behaviour of a bridge deck. They concluded that the natural frequency associated with a predominantly torsional vibration mode can be significantly affected (lowered) by the cross-section in-plane deformation. Soon after, C. Schardt (1995) (not the GBT pioneer R. Schardt) used GBT to investigate how the occurrence of coupling phenomena involving local and global deformation modes influences the vibration and dynamic behaviour of open thin-walled members. Recently, Silvestre and Camotim (2004) developed and implemented a novel GBT formulation to analyse the vibration behaviour of arbitrarily orthotropic thin-walled members, still with unbranched open cross-sections. This formulation was then applied to FRP composite lipped channel members.

The objective of this chapter is to present the derivation and illustrate the application and capabilities of a GBT formulation intended to analyse the local and global vibration behaviour of isotropic thin-walled members with open cross-sections. Initially, the main concepts and operations involved in the performance and numerical implementation of a GBT vibration analysis are addressed: (i) the *cross-section analysis*, a procedure that may be viewed as the ‘GBT trademark’ and is described here in the context of arbitrary (i.e. branched or unbranched) open cross-sections, and (ii) the *member analysis*, generally carried out by means of a GBT-based beam finite element specifically developed for that task. The proposed GBT formulation is then employed to present and discuss in-depth studies concerning the vibration behaviour of lipped channel and I-section thin-walled steel members with several end support conditions. The issues addressed include the variation of the member natural frequencies (mostly the fundamental one) and corresponding vibration mode nature and/or shape with (i) its length and, in the case of the I-section members (beams), also with (ii) the bending moment level. For validation purposes, some GBT-based numerical results are compared with values obtained by means of ABAQUS (HKS 2002) and adopting four-node isoparametric shell finite elements to discretise the thin-walled members.

## 2.2 GBT vibration analysis

### 2.2.1 Formulation

In a GBT formulation, the displacement field at a given member cross-section is expressed as a linear combination of orthogonal *deformation modes*, which makes it possible to write the equilibrium equations and boundary conditions in a unique and very convenient fashion – indeed, one is then able

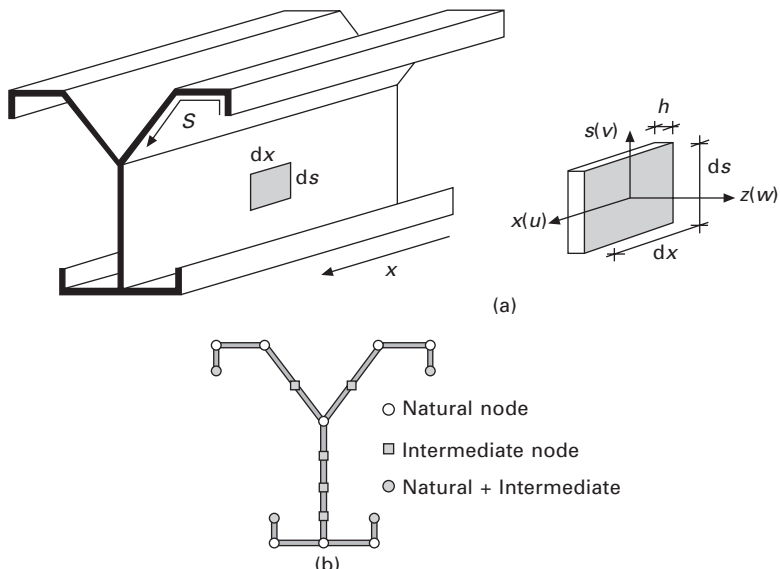
to perform a very easy and ‘natural’ *modal* analysis of the cross-section deformed configuration that contributes to a deeper understanding about the thin-walled member structural behaviour. In order to derive the GBT equilibrium equations, let us consider the coordinate system and displacement components depicted in Fig. 2.2:  $x$ ,  $s$  and  $z$  are coordinates along the member length, cross-section mid-line and wall thickness –  $u$ ,  $v$  and  $w$  are the related displacement components.

To obtain a displacement representation compatible with classical beam theory, the components  $u(x, s, t)$ ,  $v(x, s, t)$  and  $w(x, s, t)$  must be expressed as

$$\begin{aligned} u(x, s, t) &= u_k(s) \phi_{k,x}(x, t), \quad v(x, s, t) = v_k(s) \phi_k(x, t) \\ w(x, s, t) &= w_k(s) \phi_k(x, t) \end{aligned} \quad 2.1$$

where (i)  $(\cdot)_{,x} \equiv \partial(\cdot)/\partial x$ , (ii) the summation applies to subscript  $k$  and (iii) the time-dependent function  $\phi_k(x, t)$  stands for the variation of the displacement profiles  $u_k(s)$ ,  $v_k(s)$  and  $w_k(s)$  along the member length  $L$  and with time. Since the thin-walled member is deemed to be made of an isotropic and elastic material (e.g. steel), the constitutive relation of each wall element is defined by

$$\begin{Bmatrix} \sigma_{xx} \\ \sigma_{ss} \\ \sigma_{xs} \end{Bmatrix} = \frac{E}{1 - \nu^2} \begin{bmatrix} 1 & \nu & 0 \\ \nu & 1 & 0 \\ 0 & 0 & \frac{1}{2}(1 - \nu) \end{bmatrix} \begin{Bmatrix} \epsilon_{xx} \\ \epsilon_{ss} \\ \gamma_{xs} \end{Bmatrix} \quad 2.2$$



2.2 Thin-walled member: (a) geometry, axes/displacements; (b) cross-section discretisation.

where  $E$  and  $\nu$  are Young's modulus and Poisson's ratio. Finally, one considers the plate kinematic relations

$$\begin{aligned}\varepsilon_{xx} &= u_{,x} - zw_{,xx}, \quad \varepsilon_{ss} = -zw_{,ss}, \\ \gamma_{xs} &= \underbrace{u_{,s} + v_{,x}}_{=0} - 2zw_{,xs} = -2zw_{,xs}\end{aligned}\quad 2.3$$

which incorporate Vlasov's assumptions of null membrane shear and transverse extension strains along the cross-section mid-line (Vlasov 1959) – the commas denote partial differentiation. The variation of the member strain energy (virtual work of the internal forces) involves only terms related to the virtual work done by the longitudinal normal stresses  $\sigma_{xx}$ , transverse normal stresses  $\sigma_{ss}$  and shear stresses  $\sigma_{xs}$ . Therefore, one has

$$\delta U = \int_L \int_b \int_h (\sigma_{xx} \delta \varepsilon_{xx} + \sigma_{ss} \delta \varepsilon_{ss} + \sigma_{xs} \delta \gamma_{xs}) dz ds dx \quad 2.4$$

where  $L$ ,  $b$  and  $h(s)$  are the member length, cross-section mid-line length and wall thickness. Taking into account Eqs. (2.1) and (2.3), the virtual strain components are given by

$$\delta \varepsilon_{xx} = (u_i - zw_i) \delta \phi_{i,xx}, \quad \delta \varepsilon_{ss} = -zw_{i,ss} \delta \phi_i, \quad \delta \gamma_{xs} = -2zw_{i,s} \delta \phi_{i,x} \quad 2.5$$

After introducing Eqs. (2.2) and (2.5) into Eq. (2.4) and integrating over the cross-section (coordinates  $s$  and  $z$ ), one obtains the expressions of the three terms of  $\delta U$ , namely

$$\delta U = \int_L (C_{ik} \phi_{k,xx} \delta \phi_{i,xx} + D_{ik} \phi_{k,x} \delta \phi_{i,x} + B_{ik} \phi_k \delta \phi_i) dx \quad 2.6$$

The tensors appearing in the right-hand side of these expressions stem from the cross-section integration of products of  $u_k(s)$ ,  $v_k(s)$ ,  $w_k(s)$  and their derivatives, and are given by

$$\begin{aligned}C_{ik} &= E \int_b (hu_i u_k + \frac{1}{12} h^3 w_i w_k) ds \\ B_{ik} &= \frac{E}{12(1-\nu^2)} \int_b h^3 w_{i,ss} w_{k,ss} ds\end{aligned}\quad 2.7$$

$$D_{ik} = G \int_b \frac{1}{3} h^3 \left[ w_{i,s} w_{k,s} - \frac{\nu}{2(1-\nu)} (w_i w_{k,ss} + w_k w_{i,ss}) \right] ds \quad 2.8$$

It is worth noting that  $C_{ik}$  are stiffness components concerning *generalised warping* and their two terms stand for the cross-section primary ( $u_k(s)$ ) and secondary ( $w_k(s)$ ) warping effects. Notice also that matrix  $B_{ik}$  is associated with *wall transverse bending* (its expression involves curvatures  $w_{k,ss}(s)$ , i.e. second derivatives with respect to coordinate  $s$ ) – this is precisely why the

present ‘beam theory’ bears the designation ‘generalised’: it includes cross-section local deformations and can account for all folded-plate effects. Finally, note that  $D_{ik}$  are stiffness components dealing with *generalised torsion* and their expressions comprise two terms: (i) the first one related to the transverse rotation of the wall mid-lines ( $w_{k,s}(s)$ ) and (ii) the second one concerning the rotation of the fibres aligned along the plate thickness due to coupling between wall transverse bending ( $w_{k,ss}(s)$ ) and Poisson’s effect.

The derivation of the GBT fundamental system of equations also involves the kinetic energy variation

$$\delta T = \int_L \int_b \int_h (\rho u_{,t}^P \delta u_{,t}^P + \rho v_{,t}^P \delta v_{,t}^P + \rho w_{,t}^P \delta w_{,t}^P) dz ds dx \quad 2.9$$

where  $\rho$  is the material mass density and  $u^P$ ,  $v^P$  and  $w^P$  are the displacement components of an arbitrary wall point  $P$ , related to their mid-line ( $z = 0$ ) counterparts  $u$ ,  $v$ ,  $w$  by means of

$$u^P = u - zw_{,x} \quad v^P = v - zw_{,s} \quad w^P = w \quad 2.10$$

Moreover, by introducing Eqs. (2.1) into Eqs. (2.10) and differentiating the displacement components with respect to  $t$ , one is led to the velocity components

$$u_{,t}^P = (u_k - zw_k) \phi_{k,xt} \quad v_{,t}^P = (v_k - zw_{k,s}) \phi_{k,t} \quad w_{,t}^P = w_k \phi_{k,t} \quad 2.11$$

After incorporating Eqs. (2.11) into Eq. (2.9) and integrating over the cross-section area (on  $s$  and  $z$ ), one obtains the thin-walled member kinetic energy variation

$$\delta T = \int_L (Q_{ik} \phi_{i,xt} \delta \phi_{k,xt} + R_{ik} \phi_{i,t} \delta \phi_{k,t}) dx \quad 2.12$$

which includes second-order tensors that read

$$Q_{ik} = \rho \int_b (hu_i u_k + \frac{1}{12} h^3 w_i w_k) ds$$

$$R_{ik} = \rho \int_b \left[ h(v_i v_k + w_i w_k) + \frac{1}{12} h^3 w_{i,s} w_{k,s} \right] ds \quad 2.13$$

It is worth pointing out that  $Q_{ik}$  are mass components that account for the influence of the inertia forces associated with the *out-of-plane cross-section displacements*: their first and second terms, which depend on  $u_k(s)$  and  $w_k(s)$ , correspond to translational and rotational inertia forces, respectively. Note also that  $C_{ik}$  and  $Q_{ik}$  display very similar expressions – indeed, one has  $Q_{ik}/\rho = C_{ik}/E$ , which means that they are directly proportional. On the other hand,  $R_{ik}$  are mass components accounting for the influence of the inertia forces on *in-plane cross-section displacements* – as in the case of  $Q_{ik}$ , their first and second terms are also associated with translational and rotational inertia forces.

Through the application of Hamilton's principle to the strain and kinetic energy variations  $\delta U$  and  $\delta T$ , given in Eqs. (2.6) and (2.12) (note that the  $\delta\phi_i$  are arbitrary), one obtains the GBT equilibrium equation system

$$C_{ik}\phi_{k,xxxx} - D_{ik}\phi_{k,xx} + B_{ik}\phi_k + R_{ik}\phi_{k,tt} - Q_{ik}\phi_{k,xxtt} = 0 \quad 2.14$$

Since Eq. (2.14) involves time derivatives, it is convenient to consider the variable separations

$$\phi_k(x, t) = \varphi_k(x) Y(t) \quad 2.15$$

where  $Y(t)$  is a time-dependent function satisfying the *free vibration* harmonic motion equation  $Y_{,tt} + \omega^2 Y = 0$ , where  $\omega$  is the member frequency parameter – therefore, one may write

$$\phi_{k,tt} = -\omega^2 \phi_k \quad 2.16$$

The insertion of Eq. (2.16) into Eq. (2.14) leads to the final system of equilibrium equations

$$C_{ik}\phi_{k,xxxx} - D_{ik}\phi_{k,xx} + B_{ik}\phi_k - \omega^2(R_{ik}\phi_k - Q_{ik}\phi_{k,xx}) = 0 \quad 2.17$$

which depends exclusively on derivatives with respect to  $x$ . The corresponding system of boundary conditions reads

$$W_i^\sigma \delta\phi_{i,x}|_0^L = 0 \quad W_i^\tau \delta\phi_i|_0^L = 0 \quad 2.18$$

where  $W_i^\sigma$  and  $W_i^\tau$  are generalised *normal* and *shear* stress resultants, given by

$$W_i^\sigma = C_{ik}\phi_{k,xx} + D_{ik}^{II}\phi_k \quad W_i^\tau = -W_{i,x}^\sigma + W_i^{xs} \quad W_i^{xs} = D_{ik}^I\phi_{k,x} \quad 2.19$$

It should be mentioned that, like in other beam theories, the generalised *shear* stress resultant  $W_i^\tau$  involves two terms, (i) one stemming from normal stress equilibrium ( $-W_{i,x}^\sigma$ ) and (ii) the other due to the variation of the shear stresses along the cross-section wall thickness ( $W_i^{xs}$ ).

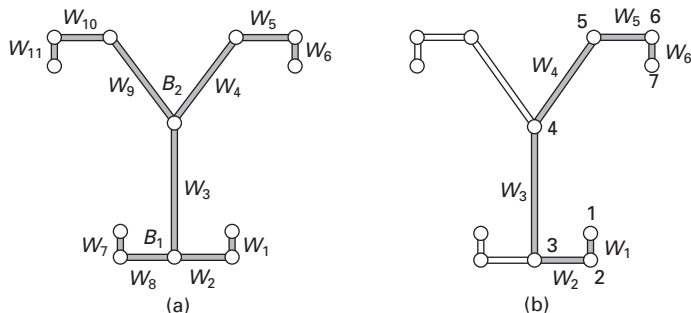
The performance of a GBT vibration analysis involves two main tasks, namely (i) a *cross-section analysis*, which leads to the identification of the GBT deformation modes and determination of the corresponding modal mechanical and mass properties (i.e. full definition of system (2.17) and its boundary conditions (2.18)), and (ii) a *member analysis*, which consists of solving the ensuing vibration eigenvalue problem to obtain the member natural frequencies and associated vibration mode shapes. Next, the main aspects and operations related to the execution of each of these tasks are presented and illustrated, in the context of thin-walled members with arbitrary *open* cross-sections sections (the analysis of the vibration behaviour of closed section members is outside the scope of this chapter.)

## 2.2.2 Cross-section analysis

*Open* cross-sections may be classified as *branched* or *unbranched*, depending on whether they include or not *branching nodes*, i.e. nodes shared by more than two walls – Fig. 2.3 provides examples of unbranched and branched cross-sections. Since the GBT analysis of an unbranched cross-section may be viewed as a particular case of that of a branched one (see the recent work of Dinis *et al.* 2006), this presentation concerns a general branched cross-section and will be illustrated by means of the specific geometry depicted in Fig. 2.4(a) – it has 11 walls ( $W_1$ – $W_{11}$ ) and 12 natural nodes (GBT terminology for nodes corresponding to member wall longitudinal edges), two of which are branching ones ( $B_1$  –  $B_2$ ). The first step of the analysis is the choice of an *unbranched sub-section* that (i) should contain as many branching nodes as possible (a non-mandatory requirement that renders the whole procedure simpler) and (ii) must not include aligned walls sharing the same branching node. This ensures that the branching nodes can be treated as natural nodes of the unbranched sub-section – otherwise, it is no longer always possible to impose unit or null warping values at all the natural nodes of this unbranched sub-section, since the warping displacements are *linear*, and not bilinear, along two aligned walls (Dinis *et al.* 2006). Figure 2.4(b) shows one possible (and convenient) unbranched sub-section that contains all branching nodes ( $B_1$  and  $B_2$ ) and includes no aligned walls sharing a branching node – e.g. this would be the case of the unbranched sub-section formed by walls  $W_1$ ,  $W_2$ ,  $W_8$  and  $W_7$ .



2.3 (a) Unbranched and (b) branched open cross-sections.



2.4 Branched section (a) geometry and (b) one possible unbranched sub-section.

Then, this unbranched sub-section, comprising six walls ( $W_1 - W_6$ ), is treated as an *unbranched cross-section*, i.e. following the procedures involved in the application of the so-called ‘conventional GBT’. Although a detailed description of these procedures cannot be presented here (it can be found elsewhere – e.g. Schardt 1989 or Silvestre and Camotim 2002a), it is important to draw the reader’s attention to the following aspects:

- The cross-section is discretised into seven natural nodes, corresponding to the wall ends.
- To determine the displacement fields  $u(s)$ ,  $v(s)$  and  $w(s)$ , one must begin by imposing unit warping displacements at each natural node ( $u_k = 1$ ,  $k = 1 \dots 7$ ) and null values at all the remaining ones, thus obtaining seven ‘elementary warping functions’  $u_k(s)$ , which either vary linearly or are null along the various walls – for illustrative purposes, Fig. 2.5(a) depicts the elementary warping function  $u_4(s)$ .
- In order to comply with Vlasov’s assumption of null membrane shear strains along the cross-section mid-line, when a unit warping displacement is imposed at node  $k$  (function  $u_k(s)$ ), each wall adjacent to that node is forced to move laterally, thus exhibiting membrane displacements  $v$  defined by

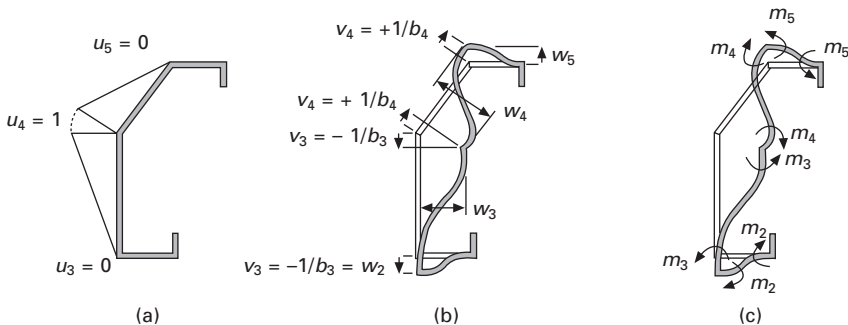
$$\gamma_{xs} = u_{,s} + v_{,x} = 0 \Rightarrow dv = -\frac{du}{ds} dx \quad 2.20$$

In order to ensure nodal compatibility between the transverse membrane ( $v$ ) and flexural ( $w$ ) displacements, the cross-section is ‘constrained’ to deform in its own plan. This is illustrated in Fig. 2.5(b), where the membrane displacements in walls  $W_3$  and  $W_4$  (adjacent to node 4), associated with  $u_4(s)$  are sketched their values are given by

$$v_3 = -\frac{u_4 - u_3}{b_3} = -\frac{1}{b_3} \quad v_4 = -\frac{u_5 - u_4}{b_4} = \frac{1}{b_4} \quad 2.21$$

where (i)  $b_3$  and  $b_4$  are the widths of walls  $W_3$  and  $W_4$ , and (ii)  $u_4 = 1$ ,  $u_3 = u_5 = 0$  – see Fig. 2.4(b).

- Imposing the wall membrane displacements and keeping the nodal rotations null leads to unbalanced transverse bending moments acting in each node, as shown in Fig. 2.5(c). The nodal rotation values that ensure bending moment equilibrium at the various nodes are determined by means of the displacement method. Using the *displacement method* to perform this task is a radical departure from the procedure adopted in the conventional GBT, which was based on the force method (Schardt 1989) – note that the degrees of kinematic and static indeterminacy (nodal rotations and transverse bending moments) are equal in *unbranched* cross-sections, which is no longer true for *branched* cross-sections. When both equilibrium and compatibility are satisfied, the cross-section



2.5 Unbranched cross-section: (a) imposition of unit/null warping displacements, (b) corresponding transverse membrane displacements and (c) determination of the nodal rotations (displacement method).

displacement field obtained is characterised by linear  $u_k(s)$ , constant  $v_k(s)$  and cubic  $w_k(s)$ .

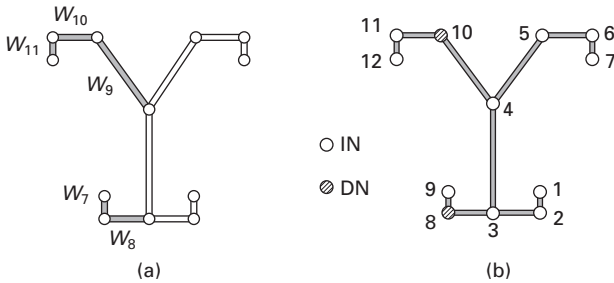
- Next, matrices  $C_{ik}$ ,  $B_{ik}$ ,  $D_{ik}$ ,  $Q_{ik}$  and  $R_{ik}$  must be determined, which is a straightforward but time-consuming task. It can be done by using commercial symbolic manipulation codes or standard numerical computer programs. Nevertheless, it should be pointed that all the above matrices are fully populated, which means that system (2.17) is highly coupled and that the physical meaning of their components is not obvious at all.
- In order to take full advantage of the GBT potential, the coupling of system (2.17) must be reduced as much as possible, a goal that can be achieved through the simultaneous diagonalisation of matrices  $C_{ik}$  and  $B_{ik}$ . This operation is carried out in several stages, requires the solution of three auxiliary eigenvalue problems and leads to the identification of a set of warping eigenvectors  $\tilde{a}_{ik}$  ( $k = 1, \dots, n + 1$ ) that correspond to the cross-section (orthogonal) deformation modes (extension, major/minor axis bending, torsion and distortion). For the cross-section shown in Fig. 2.4(b) ( $n = 6$ ), there are  $7 \times 7$  matrices and, therefore, seven eigenvalues and the corresponding eigenvectors are obtained.
- The evaluation of the cross-section modal properties is performed by means of a transformation matrix  $\tilde{A}_{ik}$ , which assembles the eigenvectors  $\tilde{a}_k$ . The transformed matrices  $\tilde{C}_{ik}$ ,  $\tilde{B}_{ik}$  and  $\tilde{D}_{ik}$  are diagonal (rigorously speaking, the last matrix is not diagonal – however, because its off-diagonal components are very small, when compared with their diagonal counterparts, ignoring them entails no meaningful errors, as shown by Schardt 1989) and their components represent such cross-section properties as (i) the member area, moments of inertia, St Venant and warping constants, associated with the global modes, and (ii) several unfamiliar quantities with no obvious mechanical meaning, related to the distortional

modes. Moreover, matrix  $\tilde{Q}_{ik}$  is also diagonal (recall that it is proportional to  $\tilde{C}_{ik}$ ) and matrix  $\tilde{R}_{ik}$  has non-null off-diagonal components – the presence of  $\tilde{R}_{ik}$  makes system (2.17) remain coupled.

In the case of *branched* cross-sections, the presence of the *branching nodes* renders the determination of  $u_k(s)$ ,  $v_k(s)$  and  $w_k(s)$  more complex, because of the need to ensure compatibility between the transverse displacements at the branching nodes. Since such nodes are shared by more than two walls, it is no longer possible to impose *independent* (unit or null) warping displacements at all nodes – thus, the number of elementary warping functions that must be considered is *lower* than the number of natural nodes (in unbranched cross-sections, these two numbers are equal). Recently, Dinis *et al.* (2006) developed a GBT formulation to analyse the buckling behaviour of members with arbitrarily branched open cross-sections – it concerns mainly the choice and definition of the elementary warping functions to be considered. First, the authors provide a systematic and sequential procedure to choose the most convenient set of *independent* natural nodes, i.e. nodes where unit or null warping displacement values are imposed. Then, the warping displacement values at the remaining *dependent* natural nodes are evaluated, in order to ensure transverse displacement compatibility at all branching nodes.

A general and systematic procedure to select the most convenient *independent natural nodes* is described and illustrated by means of its application to the branched cross-section depicted in Fig. 2.2(a):

- As mentioned and illustrated earlier (see Fig. 2.4(b)), the first step consists of choosing an *unbranched sub-section* that should contain as many branching nodes as possible and must not include aligned walls sharing the same branching node.
- Definition of a set of *first-order branches*, which are the whole or part of the various wall assemblies linked to the branching nodes belonging to the unbranched sub-section – note that all the remaining cross-section branching nodes (if any) are contained in these wall assemblies. A first-order branch either (a) coincides with a wall assembly, if it contains no branching node, or (b) is a part of a wall assembly, if it contains one or more branching nodes. In the latter case, the first-order branch must be chosen in a similar way to the unbranched sub-section, i.e. fulfilling the conditions described in the previous item. Figure 2.6(a) displays the first-order branches associated with the unbranched sub-section defined in Fig. 2.4(b) – note that none of the wall assemblies contains branching nodes.
- If necessary, definition of sets of *higher-order branches*, which (i) are the whole or part of the wall assemblies linked to the branching nodes belonging to the ‘previous-order’ branches and (ii) are defined according



2.6 Branched section: (a) first-order branches and (b) independent/dependent nodes (IN/DN).

to the guidelines given in the first bullet point. Obviously, the cross-section depicted in Fig. 2.4(a) only displays first-order branches.

- Once the whole cross-section is covered by the unbranched sub-section and the various sets of branches are completely defined, it is a straightforward matter to identify the *dependent natural nodes* (DN): all the second nodes of the various branches (i.e. the ones located immediately after the corresponding branching node). The number of DN is equal to  $\sum(m_{wi} - 2)$ , where the summation extends to all branching nodes and  $m_{wi}$  is the number of walls emerging from branching node  $i$ . For the cross-section depicted in Fig. 2.4(a), there are two DN (nodes 8 and 10 – see Fig. 2.5(b)).
- The number of *elementary warping functions* is equal to the number of independent natural nodes (IN). For the cross-section depicted in Fig. 2.4(a), there are ten IN (nodes 1–7, 9 and 11–12 – see Fig. 2.5(b)). Each function is characterised by (i) a unit warping value at one IN, (ii) null values at all the remaining IN and (iii) warping values at the DN that must be specifically determined. For instance, when  $u_4 = 1$ ,  $u_3 = u_5 = u_{11} = 0$  and  $u_{10}$  must be determined. The determination of these warping values is addressed in the next paragraphs.

The determination of the warping values at the DN is based on the fact that (i) Vlasov's null membrane shear strain assumption has to be satisfied in all the walls emerging from a given branching node and (ii) the compatibility between the transverse displacements must be ensured at that same branching node. At this point, it is worth mentioning that the *warping displacement* value at a given DN is obtained on the basis of (i) the warping value at the associated branching node and (ii) the membrane displacement value of the wall connecting these two nodes, which is obtained from geometric relations. For the cross-section shown in Fig. 2.4(a), the membrane displacement of wall 9 ( $v_9$  – see Fig. 2.6(a)) is the displacement of the branching node 4 in the  $W_9$  direction and is obtained directly from the  $v_3$  and  $v_4$  values (see

Eq. (2.21) and Fig. 2.5(b)). On the other hand, the satisfaction of Vlasov's assumption implies that the value of  $v_9$  is given by (see Fig. 2.7(a))

$$v_9 = -\frac{u_{10} - u_4}{b_9} \quad 2.22$$

Since  $u_4 = 1$  and  $v_9$  are known, Eq. (2.22) can be readily used to obtain the warping displacement at the DN 10 (see Fig. 2.7 (b)),

$$u_{10} = 1 - v_9 \cdot b_9 \quad 2.23$$

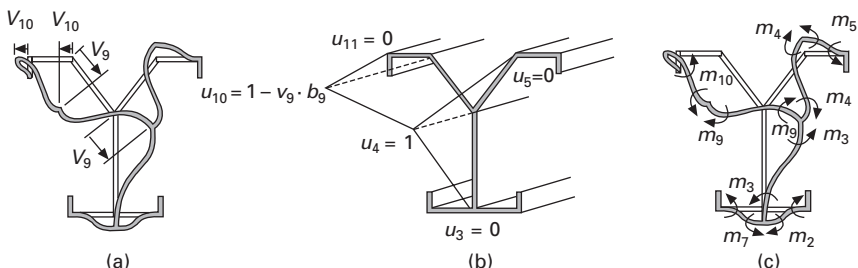
where it should be noted that the coordinate  $s$  points from node 4 to node 10, one has  $v_9 < 0$  and  $u_{10} > 1$ .

Aside from the choice and characterisation of the elementary warping functions, the GBT analyses of branched and unbranched cross-sections are virtually identical. Concerning the first step, its application to a general branched cross-section involves the following tasks:

- Use a systematic and sequential procedure to discretise the cross-section into  $n_I$  independent nodes and  $n_D$  dependent nodes. Note that there may exist several ways to perform this task and that, most likely, they will not be equally convenient from a computational point of view.
- The  $n_I$  elementary warping functions correspond to (a) the imposition of a unit warping displacement at one independent node, (b) the imposition of null warping displacements at the remaining  $(n_I - 1)$  independent nodes and (c) the evaluation of the warping displacements at the  $n_D$  dependent nodes. All these elementary warping functions vary linearly between consecutive nodes.

#### *Intermediate nodes – local-plate modes*

It is well known that the cross-section (local) deformation of thin-walled members may involve either (i) a combination of wall warping and bending effects (folded-plate behaviour) or (ii) exclusively wall bending effects

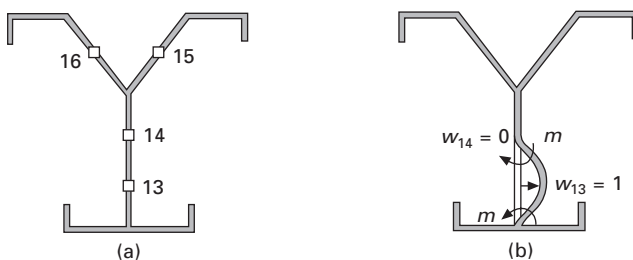


2.7 Branched section: (a) membrane transverse displacements, (b) warping displacement at DN 10 and (c) determination of the nodal rotations (displacement method).

(individual plate behaviour). The previous sub-section dealt essentially with the analysis of the wall warping effects and it was shown that its features depend on whether the cross-section shape is branched or unbranched. As for the cross-section deformation due to wall bending (local-plate deformation), it does not depend on the cross-section shape, i.e. its mechanics are the same for branched or unbranched cross-sections) and its inclusion in a GBT analysis is briefly addressed next.

Since local-plate deformation is characterised by (i) the occurrence of transverse plate bending (flexural displacements  $w$ ) and (ii) the absence of fold-line motions, its incorporation in a GBT analysis requires the cross-section discretisation to include *intermediate nodes*: nodes located within the wall widths, i.e. in between the *natural nodes*, which always correspond to wall ends. At this point, it is worth noting that local-plate deformation involves neither warping displacements  $u$  nor membrane displacements  $v$ . Figure 2.8(a) shows a possible discretisation of the cross-section depicted in Fig. 2.4(a), which involves four intermediate nodes (13–16) located in the slender walls. In order to define the GBT deformation modes that account for local-plate deformation, the displacement fields due to the imposition of unit flexural displacements must be determined at each intermediate node ( $w_k = 1$ ,  $k = 13 \dots 16$ ), while preventing all the other intermediate nodal displacements and intermediate/natural nodal rotations. In the illustrative example, this means four ‘elementary flexural functions’ – the one associated with node 13 is shown in Fig. 2.8(b). Then, in order to determine the corresponding displacement fields  $w_k(s)$ , the displacement method is again used to evaluate the nodal rotations values that ensure equilibrium and compatibility (see Fig. 2.7(c)).

Once the displacement fields stemming from the elementary flexural functions are known, the local-plate deformation modes may be determined either (i) separately or (ii) together with the deformation modes due to warping. The second approach is adopted in this work: the cross-section is discretised into natural and intermediate nodes and the joint mechanical and mass matrices  $\tilde{C}_{ik}$ ,  $\tilde{B}_{ik}$ ,  $\tilde{D}_{ik}$ ,  $\tilde{Q}_{ik}$  and  $\tilde{R}_{ik}$  are determined. These are associated with (i)

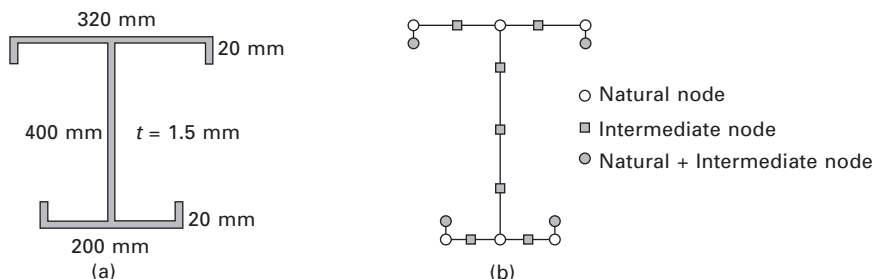


2.8 (a) Intermediate nodes and (b) elementary flexural function associated with  $w_{13}(s)$ .

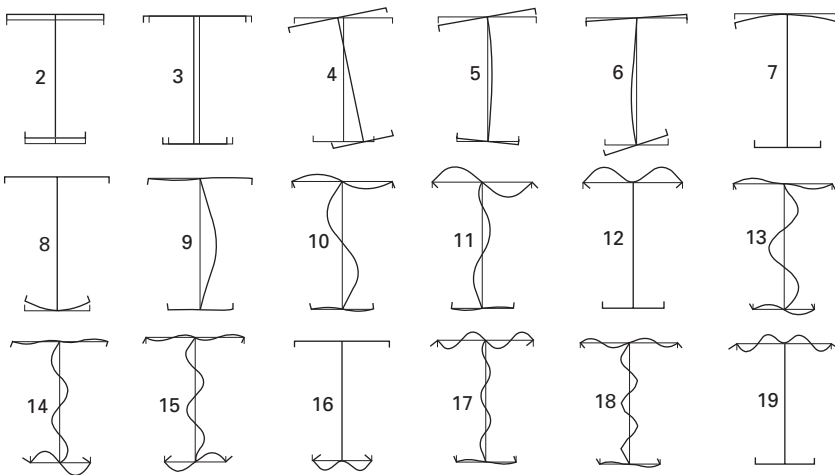
equilibrium equations and boundary conditions as uncoupled as possible and (ii) deformation modes belonging to an ‘expanded’ vector space, i.e. written in a ‘mixed’ coordinate system that consists of displacement fields stemming from elementary warping functions (one per independent natural node) and elementary flexural functions (one per intermediate node) – for more details, the interested reader is referred to the work by Silvestre (2005). Obviously, the wall bending exhibited by some of these deformation modes is due to a combination of warping and local-plate effects.

### *Illustration*

In order to illustrate graphically the outcome of a GBT cross-section analysis, Fig. 2.10 shows the in-plane configurations of the deformation modes of the particular I-shape cross-section depicted in Fig. 2.9(a) and discretised as shown in Fig. 2.9(b). This discretisation involves (i) ten natural nodes, two of which are *branching* ones, and (ii) 11 intermediate nodes, four of which correspond to wall free ends – note that these last four nodes are natural and intermediate at the same time, since they are associated with both elementary warping functions and elementary flexural functions. Since only eight out of the ten natural nodes are *independent*, the performance of the GBT cross-section analysis yields 19 deformation modes – with one single (and trivial) exception, all their in-plane deformed configurations are depicted in Fig. 2.10. As far as the nature of these deformation modes is concerned, one has (i) four rigid-body *global* modes, corresponding to axial extension (mode **1**, not shown – no in-plane deformation), major axis bending (mode **2**), minor axis bending (mode **3**) and torsion (mode **4**), (ii) four *distortional* modes (**5–8**), invariably associated with fold-line motions, and (iii) 11 *local plate* modes (**9–19**), which involve exclusively wall bending.



2.9 Illustrative example: I-section (a) dimensions and (b) GBT discretisation.



2.10 In-plane deformed configurations of all but the first I-section deformation modes: major axis bending (2), minor axis bending (3), torsion (4), distortional (5–8) and local plate (9–19).

### 2.2.3 Member analysis

Before addressing the methods that can be used to carry out exact or approximate member vibration analyses, the following remarks are appropriate:

- Incorporating the cross-section mechanical and mass properties, i.e. matrices  $\tilde{C}_{ik}$ ,  $\tilde{B}_{ik}$ ,  $\tilde{D}_{ik}$ ,  $\tilde{Q}_{ik}$  and  $\tilde{R}_{ik}$  into (2.17) and (2.18), results in a *one-dimensional* eigenvalue problem defined by a system of differential equilibrium equations (one per deformation mode) and boundary conditions expressed in terms of the modal amplitude functions  $\tilde{\phi}_k(x)$ . The solution of this problem yields the member natural frequencies (eigenvalues) and corresponding vibration mode shapes (eigenfunctions).
- A major advantage of the GBT analysis resides in the possibility of performing vibration analyses involving an arbitrary set of deformation modes – i.e. one may consider only the deformation modes known to be relevant for a certain problem. Then, only the ‘sub-system’ of (2.17) and (2.18) corresponding to those modes needs to be solved, in order to obtain *upper bounds* of the member natural frequencies and *approximate* vibration modes – if all relevant modes are selected, these results are virtually ‘exact’.

The methods that have already been employed to solve the GBT-based eigenvalue problem are fairly standard in structural analysis (Camotim *et al.* 2004). They include (i) the Galerkin and Rayleigh–Ritz methods (e.g. Saal 1974) and (ii) the finite element method, using a beam element that was specifically developed to perform GBT analyses (Silvestre and Camotim 2003) – its formulation is briefly outlined in the next sub-section. Concerning

the suitability of the above methods to solve a given vibration problem, it is worth pointing the following out:

- In members with pinned (locally and globally) and free-to-warp end sections, the Galerkin and/or Rayleigh–Ritz techniques are extremely advantageous – indeed, since the eigenfunctions are known to display pure sinusoidal shapes, these techniques can be readily used to obtain *exact* vibration results.
- In members with other end support conditions, for which there are no *exact* eigenfunctions available, the finite element method provides the most powerful and versatile numerical tool – regardless of the particular problem under consideration, highly accurate results are always obtained through analyses that involve only a fairly moderate number of degrees of freedom.

The GBT-based vibration results presented in this paper have been obtained through the application of either (i) Galerkin's method (simply supported lipped channel members and I-section beams) or (ii) the beam finite element (non-simply supported lipped channel members).

### *Beam finite element*

Silvestre and Camotim (2003) formulated, implemented and validated an efficient *beam finite element* intended to perform GBT-based buckling analyses in the context of arbitrarily orthotropic thin-walled members. The most relevant steps involved in the formulation of this finite element, specialised for the vibration analysis of *isotropic* thin-walled members, are described briefly in the following paragraphs.

First, rewrite the system of equilibrium equations (2.17) and boundary conditions (2.18), which define the vibration eigenvalue problem, in variational form,

$$\int_{L_e} \left( (\tilde{C}_{ik} \tilde{\phi}_{k,xx} \delta\tilde{\phi}_{i,xx} + \tilde{D}_{ik} \tilde{\phi}_{k,x} \delta\tilde{\phi}_{i,x} + \tilde{B}_{ik} \tilde{\phi}_k \delta\tilde{\phi}_i) - \omega^2 (\tilde{R}_{ik} \tilde{\phi}_k \delta\tilde{\phi}_i + \tilde{Q}_{ik} \tilde{\phi}_{k,x} \delta\tilde{\phi}_{i,x}) \right) dx = 0 \quad 2.24$$

where  $L_e$  is the finite element length and  $i, k$  are indices related to the deformation modes.

Second, adopt linear combinations of standard Hermitean cubic polynomials to approximate the deformation mode amplitude functions  $\tilde{\phi}_k(x)$ . Thus, one has

$$\tilde{\phi}_k(x) = Q_1 \psi_1(\xi) + Q_2 \psi_2(\xi) + Q_3 \psi_3(\xi) + Q_4 \psi_4(\xi) \quad 2.25$$

where  $Q_1 = \tilde{\phi}_{k,x}(0)$ ,  $Q_2 = \tilde{\phi}_k(0)$ ,  $Q_3 = \tilde{\phi}_{k,x}(L_e)$ ,  $Q_4 = \tilde{\phi}_k(L_e)$ ,  $\xi = x/L_e$

and

$$\begin{aligned}\psi_1 &= L_e(\xi^3 - 2\xi^2 + \xi) & \psi_2 &= 2\xi^3 - 3\xi^2 + 1 \\ \psi_3 &= L_e(\xi^3 - \xi^2) & \psi_4 &= -2\xi^3 + 3\xi^2\end{aligned}\quad 2.26$$

Finally, incorporate Eq. (2.25) into Eq. (2.24) and carry out the integrations, in order to obtain the usual finite element matrix equation

$$([K^{(e)}] - \omega^2[M^{(e)}]) \{d^{(e)}\} = \{0\} \quad 2.27$$

where  $[K^{(e)}$ ,  $[M^{(e)}$ ] and  $\{d^{(e)}$  are the finite element stiffness matrix, mass matrix and generalised displacement vector, all having dimension  $4n_m$ , where  $n_m$  is the number of deformation modes included in the analysis. These matrices and vector are of the form

$$[K^{(e)}] = \begin{bmatrix} [K^{11}] & [0] & [0] & [0] & [0] & \dots \\ & [K^{22}] & [0] & [0] & [0] & \dots \\ & & [K^{33}] & [0] & [0] & \dots \\ & & & [K^{44}] & [0] & \dots \\ \text{sym.} & & & & [K^{55}] & \dots \\ & & & & & \dots \end{bmatrix} \quad 2.28$$

$$[M^{(e)}] = \begin{bmatrix} [M^{11}] & [0] & [0] & [0] & [0] & \dots \\ & [M^{22}] & [M^{23}] & [M^{24}] & [M^{25}] & \dots \\ & & [M^{33}] & [M^{34}] & [M^{35}] & \dots \\ & & & [M^{44}] & [M^{45}] & \dots \\ \text{sym.} & & & & [M^{55}] & \dots \\ & & & & & \dots \end{bmatrix} \quad 2.28$$

$$\{d^{(e)}\} = \{\{d^2\}^T \{d^3\}^T \{d^4\}^T \{d^5\}^T \dots\} \quad 2.29$$

where superscripts  $i, j$  concern the various deformation modes and the components of each sub-matrix or sub-vector ( $p, r = 1\dots 4$  – finite element degrees of freedom) are obtained from the expressions

$$\begin{aligned}K_{pr}^{ik} &= \tilde{C}_{ik} \int_{L_e} \psi_{p,xx} \psi_{r,xx} dx + \tilde{D}_{ik} \int_{L_e} \psi_{p,x} \psi_{r,x} dx \\ &\quad + \tilde{B}_{ik} \int_{L_e} \psi_p \psi_r dx\end{aligned}\quad 2.30$$

$$M_{pr}^{ik} = \tilde{R}_{ik} \int_{L_e} \psi_p \psi_r dx + \tilde{Q}_{ik} \int_{L_e} \psi_{p,x} \psi_{r,x} dx \quad d_r^k = Q_r \quad 2.31$$

## 2.3 Illustrative examples

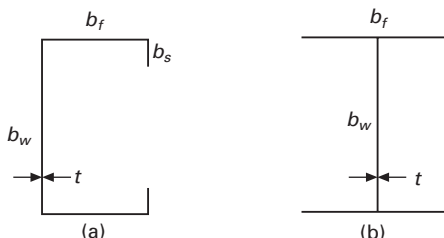
The objective of this section is to illustrate the application of the GBT formulation described earlier to analyse the vibration behaviour of thin-walled members with lipped channel and I cross-sections. Initially, simply supported lipped channel members (locally and globally pinned end sections that may warp freely) are analysed – the variation of the lower natural frequency values and vibration mode shapes with the member length is studied. Then, using the vibration behaviour of the simply supported members as reference, the end support conditions are altered to investigate how such behaviour is influenced. Finally, the chapter deals with the vibration behaviour of I-section members under major axis bending – an assessment is made of how the applied moment level affects the beam natural frequencies and vibration mode shapes.

The cross-section geometries of all the members analysed in this work are displayed in Fig. 2.11 and their dimensions and material properties (Young's modulus, Poisson's ratio and mass density) are as follows (note that the wall thickness is now designated by  $t$ , instead of  $h$  – in the development of the GBT vibration formulation,  $h$  was used to avoid confusion with the time variable):

- Lipped channel members (Fig. 2.11(a)):  $b_w = 100$  mm,  $b_f = 60$  mm,  $b_s = 10$  mm,  $t = 2$  mm,  $E = 210$  GPa,  $\nu = 0.3$  and  $\rho = 7.85 \times 10^{-3}$  g/mm<sup>3</sup>.
- I-section beams under major axis bending (Fig. 2.11(b)) :  $b_w = 80$  mm,  $b_f = 70$  mm,  $t = 2$  mm,  $E = 200$  GPa,  $\nu = 0.3$  and  $\rho = 7.85 \times 10^{-3}$  g/mm<sup>3</sup>.

### 2.3.1 Lipped channel members

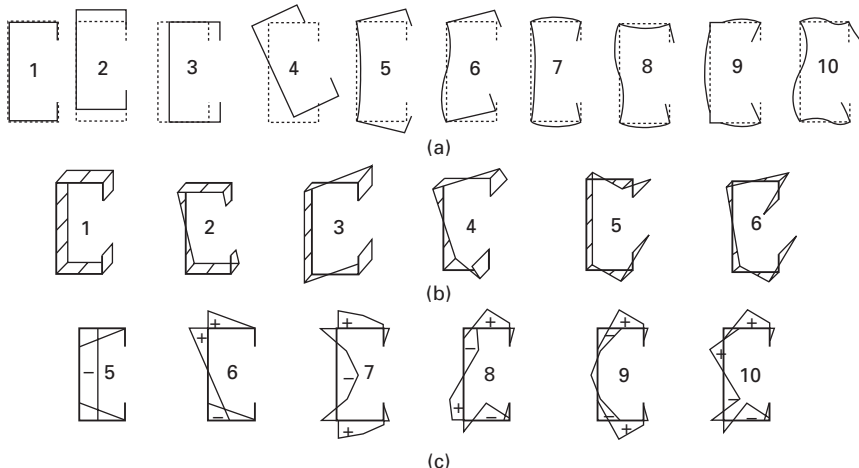
The cross-section discretisation adopted involves a total of 13 nodes (six natural nodes, three web intermediate nodes, one intermediate node in each flange and one intermediate node in each lip free end), which means that it leads to the identification of 13 deformation modes and to the determination of the corresponding modal mechanical and mass properties.



2.11 Cross-section geometries of the (a) lipped channel and (b) I-section members.

The in-plane deformed configurations of the most relevant global, distortional and local plate deformation modes are displayed in Fig. 2.12(a). Figures 2.12(b) and (c) provide, respectively, (i) the warping displacement profiles of the global and distortional modes and (ii) the transverse bending moment diagrams associated with the two distortional modes and four (out of seven) local plate modes. On the other hand, the mechanical and mass properties of the cross-section (components of matrices  $\tilde{C}_{ik}$ ,  $\tilde{B}_{ik}$ ,  $\tilde{D}_{ik}$ ,  $\tilde{Q}_{ik}$  and  $\tilde{R}_{ik}$ ) are given in Table 2.1.

The first four deformation modes, i.e. axial extension axial (**1** –  $\tilde{C}_{11}$  is the axial stiffness  $EA$ ), major axis bending (**2** –  $\tilde{C}_{22}$  is the bending stiffness  $EI_y$ ), minor axis bending (**3** –  $\tilde{C}_{33}$  is the bending stiffness  $EI_z$ ) and torsion (**4** –  $\tilde{C}_{44}$  is the warping stiffness  $E\Gamma$  and  $\tilde{D}_{44}$  is the St Venant stiffness  $GJ$ ), concern only rigid-body motions, which means that one has  $\tilde{B}_{kk} = 0$  ( $k = 1 \dots 4$ ). These deformation modes are precisely the ones taken into account by Vlasov's classical theory (Vlasov 1959) and the associated properties correspond to the shaded area in Table 2.1. Since the remaining nine deformation modes (symmetric and antisymmetric distortional modes **5** and **6**, as well as local-plate modes **7–13**) involve in-plane cross-section deformations, one has  $\tilde{B}_{kk} \neq 0$  ( $k = 5 \dots 13$ ). Finally, note also that  $\tilde{D}_{11} = \tilde{D}_{22} = \tilde{D}_{33} = 0$ , since no wall rotations occur in modes **1**, **2** and **3**. On the other hand, Table 2.1 makes it possible to confirm the validity of relation  $\tilde{Q}_{ik}/\rho = \tilde{C}_{ik}/E$  mentioned earlier. Moreover, it is still worth noting that a member vibration mode may either (i) coincide with a deformation mode, if all the diagonal components  $\tilde{Q}_{kk}$  and  $\tilde{R}_{kk}$  are non-null, or (ii) combine several even or odd-numbered deformation modes –  $k = 2, 4, 6, 8, 10$  or  $k = 3, 5, 7, 9$ , respectively.



2.12 Lipped channel cross-section deformation modes: (a) in-plane deformed configurations, (b) warping displacement profiles and (c) transverse bending moment diagrams.

Table 2.1 Components of matrices  $\tilde{C}_{ik}$ ,  $\tilde{B}_{ik}$ ,  $\tilde{D}_{ik}$ ,  $\tilde{Q}_{ik}$  and  $\tilde{R}_{ik}$

Mode	$\tilde{C}_{ik}$	$\tilde{D}_{ik}$	$\tilde{B}_{ik}$	$\tilde{Q}_{ik}$	1	2	3	4	5	6	7	8	9	10	$\tilde{R}_{ik}$	
1	$1.008 \times 10^8$	0	0	3.768	0	0	0	0	0	0	0	0	0	0	0	
2	$1.781 \times 10^{11}$	0	0	6657.7	3.768	0	-181.6	0	0.1363	0	-1.149	0	0	0	0.4318	
3	$5.042 \times 10^{10}$	0	0	1884.7	3.768	0	0	0.0567	0	0.9222	0	-0.3663	0	-0.3663	0	
4	$1.013 \times 10^{14}$	$5.169 \times 10^7$	0	$3.787 \times 10^7$	17301.3	0	-9.1836	0	57.894	0	57.894	0	-52.966	0	-52.966	0
5	$3.129 \times 10^6$	146.9	0.01793	0.1166	0.014514	0	0.04764	0	0.0529	0	0.0529	0	0	0	0	
6	$3.393 \times 10^6$	157.0	0.04317	0.1265	0.01350	0	-0.0629	0	0	0	-0.0629	0	0	0	0.01748	
7	$7.927 \times 10^6$	$1.943 \times 10^4$	16.962	0.2671	0.8016	0	0	0	0	0	0	-0.0080	0	0	0	
8	$1.134 \times 10^7$	$8.106 \times 10^4$	109.68	0.3817	Sym.	1.14649	0	1.14649	0	0	0	0.0035	0	0.0035	0	
9	$1.020 \times 10^7$	$7.470 \times 10^4$	135.32	0.3440	0.3008	1.0334	0	1.0334	0	0	0	0	0	0	0	
10	$8.853 \times 10^6$	$8.124 \times 10^4$	262.53	0.3008	0.9037	0	0	0	0	0	0	0	0	0	0	

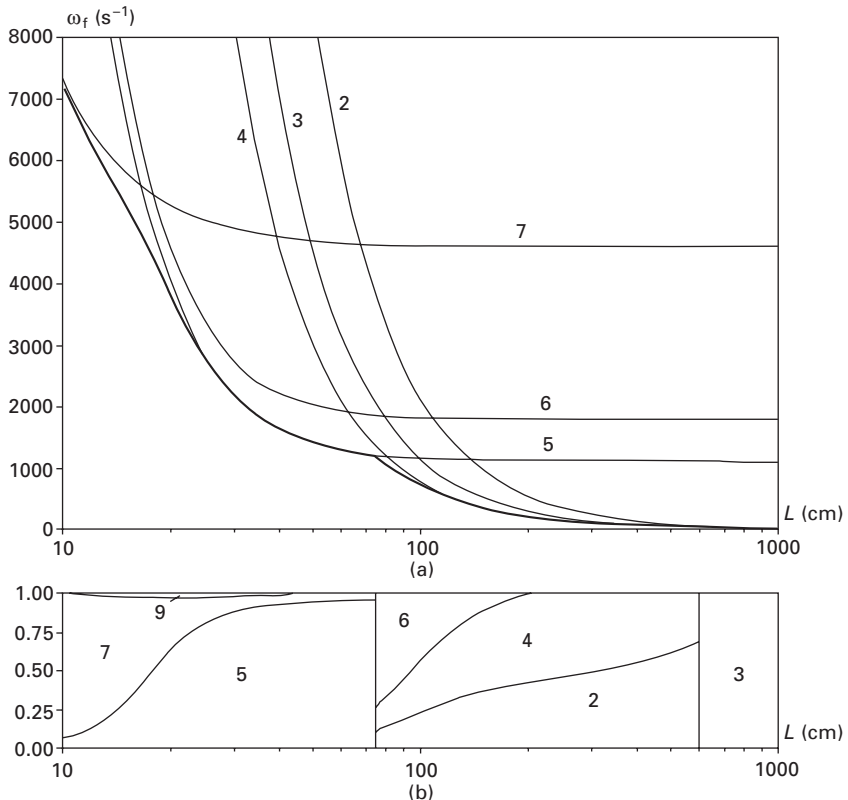
When analysing the vibration behaviour of simply supported members, due account is taken of the fact that the fundamental vibration mode shapes are sinusoidal and exhibit a single half-wave ( $n_s = 1$ ). The curves depicted in Fig. 2.13(a) provide the variation of the fundamental frequency value  $\omega_f$  with the member length  $L$  (in logarithmic scale), for vibration in (i) *individual* deformation modes (upper thinner curves) and (ii) any combination of *all* deformation modes (lower thicker curve). Moreover, it should be noted that, whenever a vibration mode (i) coincides with an individual deformation mode  $k$  and (ii) exhibits  $n_s$  half-waves, the corresponding curve  $\omega_{k,n_s}(L)$  is given by the analytical expression

$$\omega_{k,n_s} = \sqrt{\frac{\tilde{C}_{kk} \left(\frac{n_s \pi}{L}\right)^4 + \tilde{D}_{kk} \left(\frac{n_s \pi}{L}\right)^2 + \tilde{B}_{kk}}{\tilde{Q}_{kk} \left(\frac{n_s \pi}{L}\right)^2 + \tilde{R}_{kk}}} \quad 2.32$$

Finally, the modal participation diagram shown in Fig. 2.13(b) provides information about the contribution of each deformation mode to the member vibration mode shape.

The observation of Fig. 2.13 leads to the following conclusions:

- The individual mode curves decrease monotonically with  $L$  and tend to the value  $(\tilde{B}_{kk}/\tilde{R}_{kk})^{1/2}$  – the analytical expressions of the various curves are obtained by making  $n_s = 1$  in Eq. (2.32). Since one has  $\tilde{B}_{kk} = 0$  for the rigid-body bending and torsion deformation modes (2–4), the corresponding curves tend to null fundamental frequency ( $\omega_f$ ).
- The exact (all mode) curve decreases monotonically with  $L$  and, inside some length intervals, practically coincides with some of the individual mode curves. This means that, for those length intervals, the  $\omega_f$ -estimates provided by Eq. (2.32) are extremely accurate.
- For  $10 < L < 20$  cm,  $20 < L < 75$  cm and  $75 < L < 200$  cm, the members vibrate respectively in local plate modes (LPM  $\equiv$  7 + bits of 5 and 9), distortional modes (DM  $\equiv$  5 + bits of 7 and 9) and mixed flexural-torsional-distortional modes (FTDM  $\equiv$  6 + 4 + 2). The modal participation diagram presented in Fig. 2.13(b) shows that there exist (i) a smooth transition between the LPM and DM, and (ii) a fairly abrupt one between the DM and FTDM.
- For  $200 < L < 600$  cm and  $L > 600$  cm, the value of  $\omega_f$  decreases again continuously and the members vibrate respectively in global flexural-torsional modes (FTM  $\equiv$  2 + 4) and purely flexural modes (FM  $\equiv$  3). The transitions FTDM–FTM and FTM–FM are smooth and abrupt.
- As mentioned above, the modal decomposition of the member vibration shapes changes abruptly for  $L = 75$  cm and  $L = 600$  cm. This implies



2.13 (a) Individual and combined  $\omega_f(L)$  curves and (b) modal participation diagram.

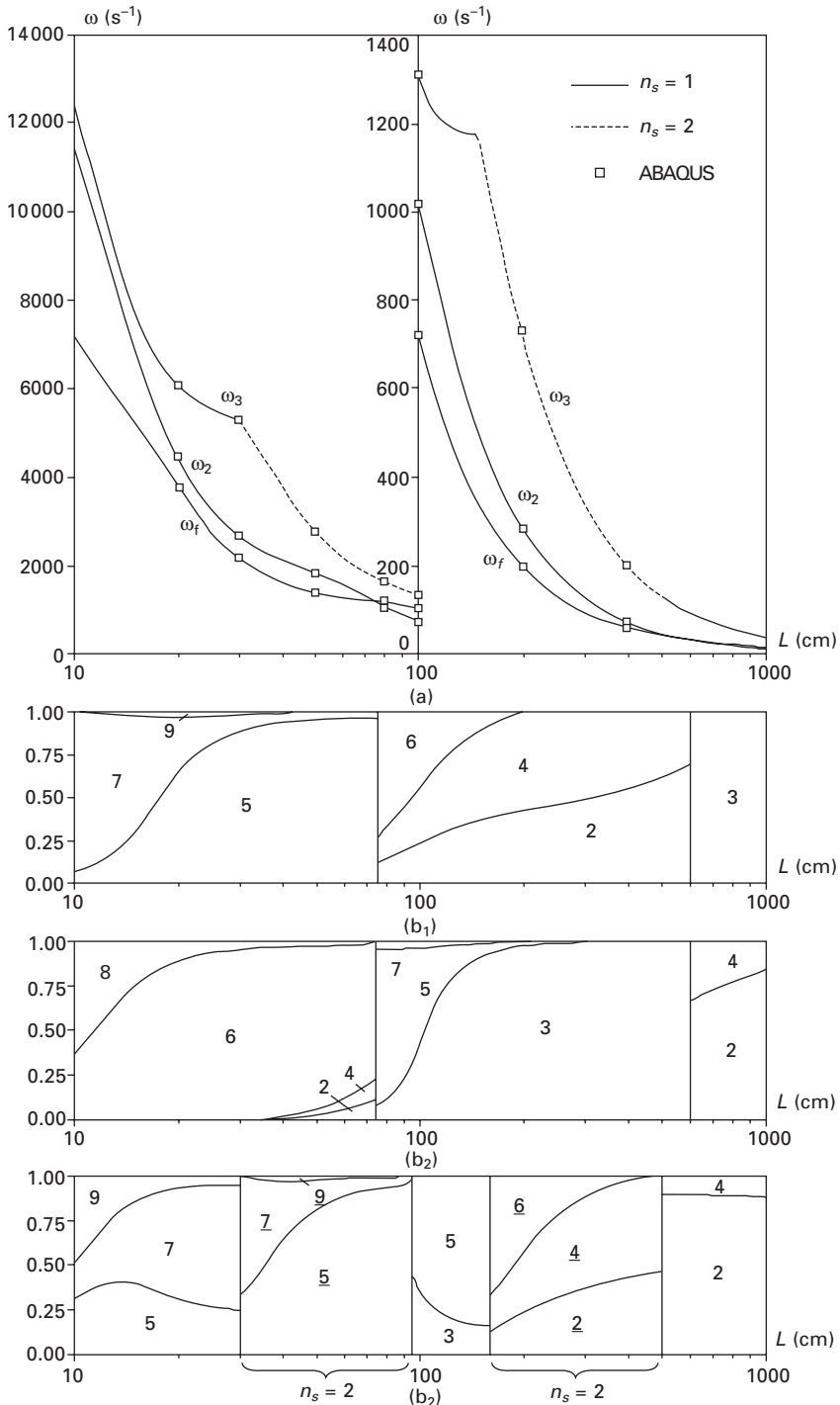
that, in the vicinity of these length values, the two first natural frequency values are very close – the fundamental vibration mode suddenly becomes the second vibration mode and vice versa.

- The assumption of no in-plane cross-section deformation yields accurate results only for  $L > 200$  cm. Since laterally unrestrained members with  $L < 200$  cm (or laterally restrained ones with lengths larger than 200 cm) are often used in practical applications, this assumption, implicitly adopted by all classical beam theories (e.g. Gere 1954 or Vlasov 1959), may lead to the evaluation of natural frequency values that are incorrect to a smaller or larger extent.
- For very long members, the individual curves concerning modes **5**, **6** and **7** become virtually horizontal, which means that the higher-order natural frequencies (associated with vibration modes that involve local deformations) are practically independent of  $L$ .

Next, one assumes that the sinusoidal vibration mode shapes may exhibit several half-waves ( $n_s = 1, 2, 3, \dots$ ) and determines the member higher-order

natural frequency values, as well as the shapes of the corresponding vibration modes. The curves displayed in Fig. 2.14(a) provide the variation of the three first natural frequencies ( $\omega_f$ ,  $\omega_2$  and  $\omega_3$ ) with  $L$  and the modal participation diagrams included in Figs 2.14(b<sub>1</sub>)–(b<sub>3</sub>) give information about the associated vibration mode shapes. To enable a clearer visualisation of the three curves in Fig. 2.14(a), different vertical scales are adopted for  $10 < L < 100$  cm and  $100 < L < 1000$  cm. In order to validate the GBT-based vibration results, some are compared with values yielded by four-node shell finite element analyses performed in the code ABAQUS (HKS 2002) – these values are also presented in Fig. 2.14(a) and they concern members with  $L = 20, 30, 50, 80, 100, 200, 400$  cm. The observation of Figs 2.14(a)–(b<sub>3</sub>) prompts the following comments:

- Although combinations of sinusoidal functions with several half-waves were considered, it was found that the fundamental frequencies are always associated with  $n_s = 1$ , i.e. the curves  $\omega_f(L)$  shown in Figs 2.13(a) and 2.14(a) are identical. This means that, unlike the column critical buckling modes (which may exhibit several half-waves – e.g. Silvestre and Camotim 2002b) the member *fundamental* vibration modes invariably have a *single* half-wave. Because of this, the conclusions drawn by Okamura and Fukasawa (1998) are not completely correct – indeed, the similarity between the column critical buckling modes and the member fundamental vibration modes does not occur for all lengths, but only for those associated with single half-wave critical buckling modes.
- Like their fundamental counterparts, the second vibration modes always exhibit a single half-wave, regardless of the member length. The third vibration modes, on the other hand, may have either one or two half-waves, depending on the member length – see Figs 2.14(a) and (b<sub>2</sub>)–(b<sub>3</sub>).
- For  $L < 12$  cm,  $12 < L < 35$  cm and  $35 < L < 75$  cm, the second natural frequency corresponds to local-plate (**8** + bit of **6**), distortional (**6** + bit of **8**) and flexural-torsional-distortional (**6** + bits of **4** and **2**) vibration modes with *antisymmetric* configurations and having smooth transitions between them – see Fig. 2.14(b<sub>2</sub>).
- For  $75 < L < 100$  cm,  $100 < L < 300$  cm and  $300 < L < 600$  cm, the second natural frequency corresponds to distortional (**5** + bits of **3** and **7**), flexural-distortional (**3** + bits of **5**) and flexural (**3**) vibration modes, all with *symmetric* configurations and having again smooth transitions between them – see Fig. 2.14(b<sub>2</sub>).
- For  $L > 600$  cm, the second natural frequency corresponds to *antisymmetric* flexural-torsional (**2** + **4**) vibration modes – see Fig. 2.14(b<sub>2</sub>).
- Like its fundamental counterpart, the second vibration mode experiences sudden changes for  $L = 75$  cm and  $L = 600$  cm. The joint observation of Figs 2.14(b<sub>1</sub>)–(b<sub>2</sub>) provides a clear view of these facts: combining the

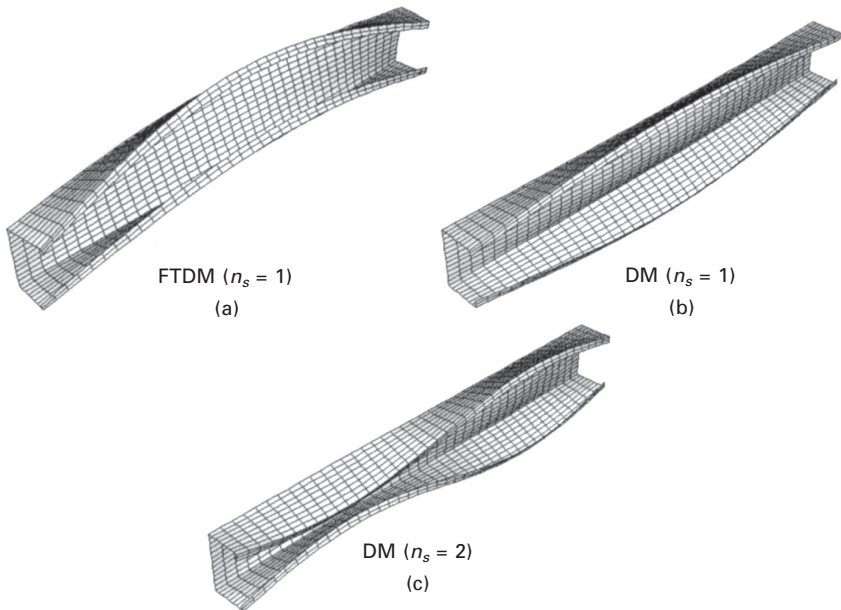


2.14 (a) Curves  $\omega_f(L)$ ,  $\omega_2(L)$  and  $\omega_3(L)$  and (b) corresponding modal participation diagrams.

length intervals (i)  $10 < L < 75$  cm and  $600 < L < 1000$  cm of Fig. 14(b<sub>1</sub>) and (ii)  $75 < L < 600$  cm of Fig. 2.14(b<sub>2</sub>), one observes that there exist smooth transitions between the vibration modes involving *symmetric* GBT modes (**3, 5, 7, 9**). On the other hand, combining the length intervals (i)  $75 < L < 600$  cm of Fig. 2.14(b<sub>1</sub>) and (ii)  $10 < L < 75$  cm and  $600 < L < 1000$  cm of Fig. 2.14(b<sub>2</sub>), similar smooth transitions occur between the vibration modes involving *antisymmetric* GBT modes (**2, 4, 6, 8**).

- For  $10 < L < 30$  cm,  $95 < L < 150$  cm and  $500 < L < 1000$  cm, the third natural frequency corresponds to local-plate-distortional (**5 + 7 + 9**), flexural-distortional (**3 + 5**) and flexural-torsional (**2 + bit of 4**) single-wave vibration modes – see Fig. 2.14(b<sub>3</sub>).
- For  $30 < L < 50$  cm,  $50 < L < 95$  cm and  $150 < L < 500$  cm, the third natural frequency corresponds to local-plate-distortional (**5 + 7 + bit of 9**), distortional (**5 + bit of 7**) and flexural-torsional-distortional (**2 + 4 + 6**) two half-wave vibration modes – see Fig. 2.14(b<sub>3</sub>).
- The local (local-plate or distortional) deformation modes **5, 6, 7, 8, 9** cease to participate in the member vibration modes for  $L > 200$  cm (fundamental),  $L > 300$  cm (second) and  $L > 500$  cm (third) – thus, it is fair to say that the in-plane cross-section rigidity assumption is valid only for the lower-order vibration modes of long enough members, a conclusion also reached by Cheung and Cheung (1971) and Ohga *et al.* (1995).
- The maximum difference between the  $\omega_f$ ,  $\omega_2$  and  $\omega_3$  values obtained by means of GBT and shell FEM (ABAQUS) analyses never exceeded 1.3%. The values associated with the highest differences are: (i)  $\omega_{f,FEM} = 1382.8 \text{ s}^{-1}$  and  $\omega_{f,GBT} = 1388.4 \text{ s}^{-1}$  ( $L = 50$  cm), (ii)  $\omega_{2,FEM} = 1151.2 \text{ s}^{-1}$  and  $\omega_{2,GBT} = 1166.4 \text{ s}^{-1}$  ( $L = 80$  cm) and (iii)  $\omega_{3,FEM} = 1606.8 \text{ s}^{-1}$  and  $\omega_{3,GBT} = 1617.4 \text{ s}^{-1}$  ( $L = 80$  cm). For illustrative purposes, Fig. 2.15 shows the shapes of the first three vibration modes of the  $L = 80$  cm member yielded by the ABAQUS analysis.

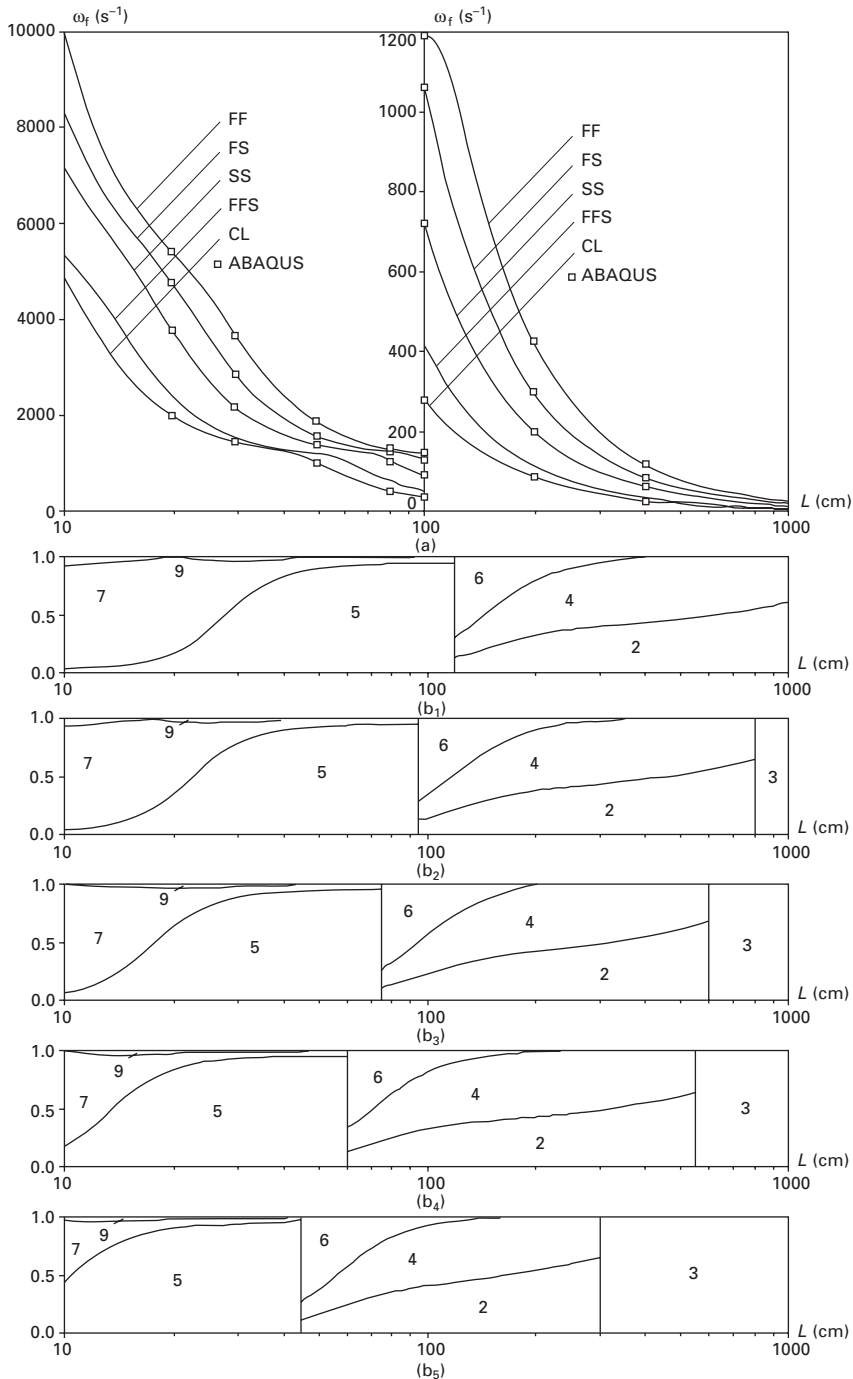
Finally, the GBT-based beam finite element described earlier was employed to assess the vibration behaviour of members with five distinct end support conditions, namely (i) pinned and free-to-warp end sections (SS members, i.e. the simply supported members analysed earlier, included as a reference case), (ii) fixed and warping-prevented end sections (FF members), (iii) one end section fixed and warping-prevented and the other pinned and free-to-warp (FS members), (iv) fixed and warping-prevented end sections, one of which is free to slide laterally (FFS members) and (v) one end section fixed and warping-prevented and the other fully free (CL members, i.e. cantilevers). Their  $\omega_f(L)$  curves and modal participation diagrams are presented in Figs 2.16(a) and 2.16(b<sub>1</sub>)–(b<sub>5</sub>) – all these results were obtained adopting the same cross-section discretisation as before and a longitudinal discretisation into



2.15 FEM-based shapes of the three first vibration modes of the member with  $L = 80$  cm.

10 finite elements. Additionally, members with all the above support conditions and lengths  $L = 20, 30, 50, 80, 100, 200, 400$  cm were analysed using ABAQUS (members discretised by means of fine S4 shell finite element meshes) – the corresponding  $\omega_f$  values are the white squares in Fig. 2.16(a). The observation of the fundamental vibration results displayed in these figures leads to the following comments:

- In *all* members and regardless of the length value, the fundamental vibration mode always exhibits a *single* half-wave. In particular, there is a perfect coincidence between the SS member  $\omega_f(L)$  curves depicted in Figs 2.14(a) and 2.16(a) – recall that the former was obtained by means of Galerkin's method, using single-wave sinusoidal functions to approximate the member vibration modes (i.e. exact solutions of the vibration eigenvalue problem).
- Since all the fundamental vibration modes exhibit a single half-wave, it would have been possible to obtain very accurate  $\omega_f$  values with a much smaller number of finite elements (e.g. three finite elements lead to practically exact  $\omega_f$  estimates – errors always below 1%).
- Regardless of the member length, the  $\omega_f$  values always decrease according to the end support sequence FF–FS–SS–FFS–CL. Cheung and Cheung (1971) reached a similar conclusion on the basis of finite strip vibration analyses performed in stiffened panels and I-section bars.

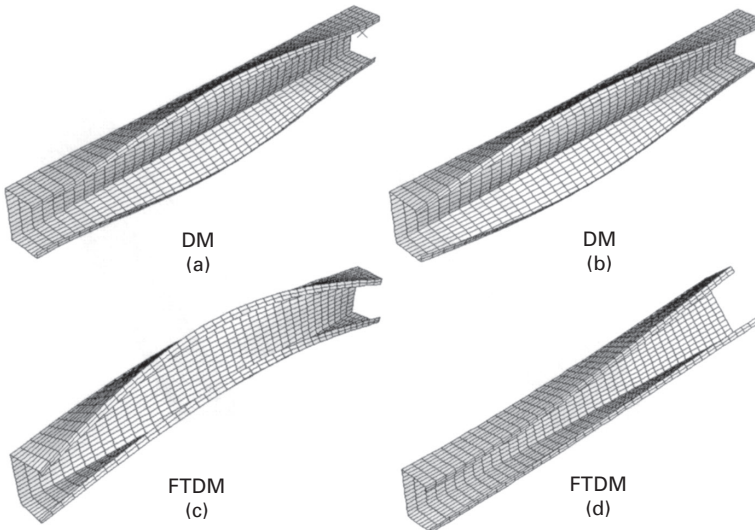


2.16 (a) Curves  $\omega_f(L)$  and (b) modal participation diagrams (FF, FS, SS, FFS and CL members).

- In view of the fact that the global critical buckling loads of SS and FFS columns are identical, it is fairly surprising to observe that the fundamental frequencies of the FFS members are considerably lower than their SS member counterparts – indeed, the end section transverse displacements influence the member vibration behaviour, but not the column buckling behaviour.
- The various modal participation diagrams are qualitatively similar: for  $L < L_1$ ,  $L_1 < L < L_2$ ,  $L_2 < L < L_3$ ,  $L_3 < L < L_4$  and  $L > L_4$ , the members vibrate in local plate, distortional, flexural-torsional-distortional, flexural-torsional and flexural modes. Moreover, the corresponding modal contributions exhibit smooth transitions for  $L = L_1$  and  $L = L_3$ , and change abruptly for  $L = L_2$  and  $L = L_4$ . However, the length values associated with the transitions ( $L_i$ ) decrease significantly according to the end support sequence FF–FS–SS–FFS–CL: for instance, the values of  $L_2$  and  $L_4$  read, respectively, 120, 95, 75, 60, 45 cm and 1200, 800, 600, 550, 300 cm – see Figs 2.16(b<sub>1</sub>)–(b<sub>5</sub>). In other words, restraining the member end section local/global displacements and rotations makes its vibration behaviour more susceptible to local-plate and distortional deformation modes.
- The  $\omega_f$  values yielded by the GBT and ABAQUS analyses are never more than 0.8% apart. Besides, the largest differences are as follows:  $\omega_{f,FEM} = 1382.8 \text{ s}^{-1}$  and  $\omega_{f,GBT} = 1388.4 \text{ s}^{-1}$  (SS +  $L = 50 \text{ cm}$ ), (b)  $\omega_{f,FEM} = 1304.6 \text{ s}^{-1}$  and  $\omega_{f,GBT} = 1295.5 \text{ s}^{-1}$  (FF +  $L = 80 \text{ cm}$ ), (c)  $\omega_{f,FEM} = 1234.0 \text{ s}^{-1}$  and  $\omega_{f,GBT} = 1224.2 \text{ s}^{-1}$  (FS +  $L = 80 \text{ cm}$ ) and (d)  $\omega_{f,FEM} = 1979.2 \text{ s}^{-1}$  and  $\omega_{f,GBT} = 1988.1 \text{ s}^{-1}$  (CL +  $L = 20 \text{ cm}$ ).
- Finally, Fig. 2.17 shows the vibration mode shapes concerning members of length  $L = 80 \text{ cm}$  and four end support conditions. It becomes clear that the end support conditions may significantly alter the local and global vibration behaviour of thin-walled members.

### 2.3.2 I-section beams

The vibration analyses are almost always performed under the assumption that the thin-walled member is not loaded. However, since those members are invariably subjected to applied loads (at least the permanent ones), a more realistic vibration analysis should take into account the loading effects, namely the ones due to the stiffness erosion stemming from the acting compressive stresses. Although there exists a vast amount of research work on the influence of the axial compression level ( $N$ ) on the *global* (flexural-torsional) vibration behaviour of thin-walled members, the same does not apply when either (i) the *local* vibration behaviour is involved and/or (ii) the members are subjected to bending moments. As far as the influence of the bending moment level ( $M$ ) on the *local* vibration behaviour of thin-walled



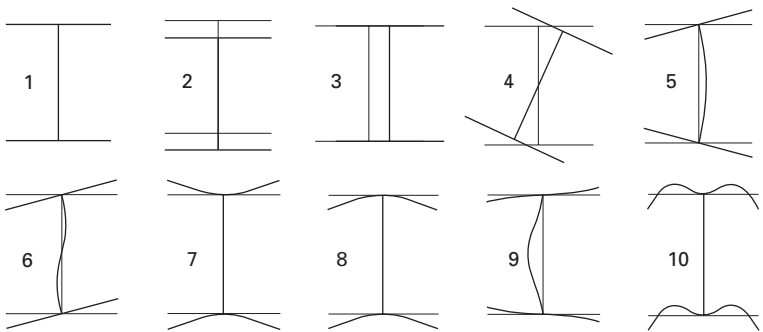
2.17 FEM-based fundamental vibration mode shapes of FF, FS, SS and CL members with  $L = 80$  cm.

members is concerned, very few studies are available in the literature – in this context, it is worth noting the recent works by Silvestre and Camotim (2006a,b), who address the vibration behaviour of thin-walled steel and FRP composite with open unbranched cross-sections and subjected to axial compression and major axis bending. Next, numerical results concerning the vibration behaviour of I-section members under uniform major axis bending are presented and discussed – in particular, the influence of the bending moment level on the beam fundamental frequency value and vibration mode nature is assessed.

In order to investigate the vibration behaviour of bended I-section beams, one must begin by studying their buckling behaviour – indeed, the vibration analyses are performed in beams subjected to bending moments that correspond to a certain percentage of their *critical buckling moments*  $M_{cr}$ . The I-section discretisation involves 17 nodes (six natural nodes, two of which are *dependent*, three web intermediate nodes and four intermediate nodes in each flange) and leads to 15 deformation modes (four global and 11 local-plate) – the in-plane configurations of the ten most relevant ones are depicted in Fig. 2.18.

When performing vibration analyses of *loaded members*, the system of equilibrium equations (2.17) must be replaced by (Silvestre and Camotim 2006a,b)

$$\tilde{C}_{ik} \tilde{\phi}_{k,xxxx} - \tilde{D}_{ik} \tilde{\phi}_{k,xx} + \tilde{B}_{ik} \tilde{\phi}_k - \tilde{W}_j^o \tilde{X}_{jik} \tilde{\phi}_{k,xx} - \omega^2 (\tilde{R}_{ik} \tilde{\phi}_k - \tilde{Q}_{ik} \tilde{\phi}_{k,xx}) = 0 \quad 2.33$$



2.18 In-plane configurations of the ten most relevant global and local-plate deformation modes.

which includes an additional term corresponding to the member *stiffness degradation* due to the presence of the generalised internal forces  $\tilde{W}_j^o(\tilde{X}_{jik})$  is the geometric stiffness matrix associated with  $\tilde{W}_j^o$ ). This system defines linear eigenvalue problems corresponding to vibration analysis of members acted by *known* generalised internal forces  $\tilde{W}_j^o - \omega^2$  are the problem eigenvalues. Since the beams analysed in this work are subjected to uniform major axis bending (mode 2 – see Fig. 2.18), the only non-null generalised internal force is  $\tilde{W}_2^o = M_1$ . Finally, note that only simply supported beams (end sections locally/globally pinned and free-to-warp) are dealt with, which means that all the *exact solutions* of Eqs. (2.33) are of the form

$$\tilde{\phi}_k(x) = d_k \sin\left(\frac{n_s \pi}{L} x\right) \quad 2.34$$

The curves shown in Fig. 2.19(a) show the variation of the beam single half-wave bifurcation moment  $M_{b,1}$  and critical buckling moment  $M_{cr}$  with the length  $L$  (in logarithmic scale). On the other hand, the modal participation diagrams presented in Figs 2.19(b<sub>1</sub>) and (b<sub>2</sub>) make it possible to assess the contribution of each individual deformation mode to the corresponding beam buckling modes – note that a bar under a mode number indicates a two half-wave ( $n_s = 2$ ) contribution and that the subsequent vertical lines separate length ranges associated with critical buckling modes exhibiting a growing number of half-waves. Finally, Figs 2.19(c<sub>1</sub>) and (c<sub>2</sub>) display the buckled mid-span cross-sections of the beams with  $L = 10$  cm and  $L = 300$  cm. The observation of these results prompts the following remarks:

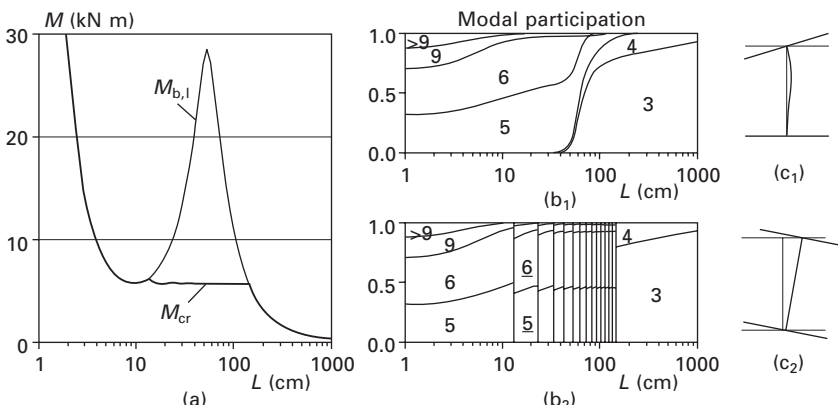
- Both the single half-wave and critical buckling curves exhibit a local minimum value equal to  $M_{min} = 5.73$  kN m), occurring for  $L = 10$  cm in the former case and for  $L = 10n_s$  ( $n_s \leq 14$  is the half-wave number) in the latter one. The two curves  $M_{b,1}(L)$  and  $M_{cr}(L)$  differ only for  $12 < L < 150$  cm: while the second one is associated with 2–14 half-wave local-

plate buckling modes, the first one corresponds to a stiffer beam behaviour and is associated with local-plate or flexural-torsional buckling modes – this difference can be easily visualised by looking at Figs 2.19(b<sub>1</sub>) and (b<sub>2</sub>).

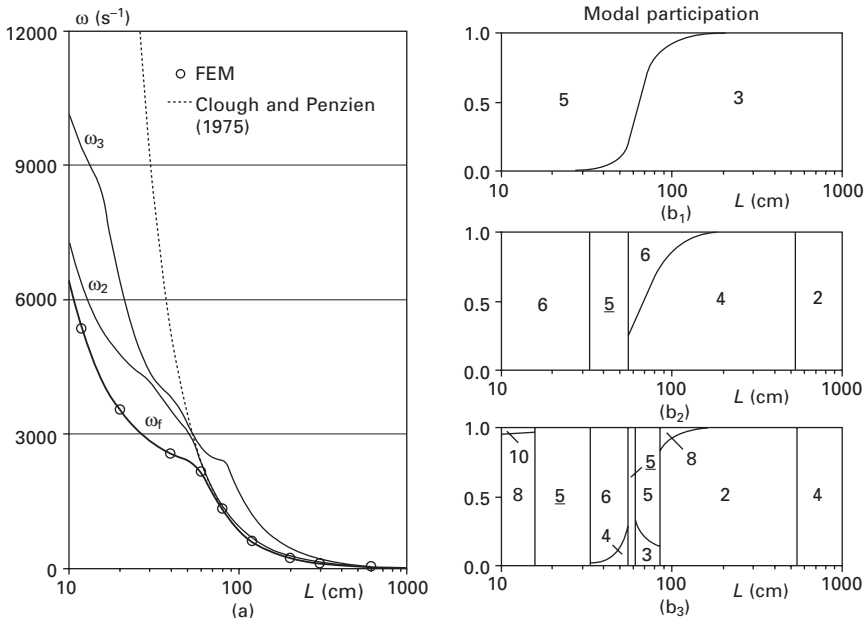
- Critical buckling occurs (i) in 1–14 half-wave local-plate modes for  $L < 150$  cm and (ii) in single half-wave flexural-torsional modes for  $L > 150$  cm. Figures 2.19(c<sub>1</sub>) and (c<sub>2</sub>) show the buckled configurations of the mid-span cross-section of a short ( $L = 10$  cm) and a long ( $L = 300$  cm) beam. In the first case, buckling (i) is triggered by the compressed (top) flange and (ii) combines deformation modes 5, 6 and 9 – note that the joint participation of modes 5 and 6 (see Fig. 2.18) accounts for the null rotation of the bottom flange and for a larger rotation of the top one. In the long beam, flexural-torsional buckling (or lateral-torsional buckling) combines modes 3 (minor axis bending) and 4 (torsion) – note that the top flange lateral displacement is much larger than its bottom flange counterpart.

Now, let us consider the vibration behaviour of the I-section beams. The curves shown in Fig. 2.20(a) provide the variation of the first three natural frequencies of the *unloaded* beam with its length  $L$  (logarithmic scale). Moreover, the modal participation diagrams of the associated vibration modes are given in Figs 2.20(b<sub>1</sub>)–(b<sub>3</sub>). For validation purposes, Fig 2.20(a) also includes natural frequencies (i) yielded by the analytical expression

$$\omega_f = \left(\frac{\pi}{L}\right)^2 \sqrt{\frac{EI_{II}}{\rho A}} \quad 2.35$$



2.19 (a) Curves  $M_{b,1}(L)$  and  $M_{cr}(L)$ , (b) modal participation diagrams of the (b<sub>1</sub>) single half-wave and (b<sub>2</sub>) critical buckling modes and (c) buckled mid-span cross-sections for (c<sub>1</sub>)  $L = 10$  cm and (c<sub>2</sub>)  $L = 300$  cm.



2.20 (a) Curves  $\omega_f(L)$ ,  $\omega_2(L)$  and  $\omega_3(L)$  and (b) corresponding modal participation diagrams.

which concerns the minor axis flexural vibration of simply supported members (e.g. Clough and Penzien 1975), and (ii) obtained by means of vibration analyses performed in the code ABAQUS (HKS 2002), adopting S4 shell element beam discretisations. The observation of the results presented in these figures makes it possible to draw the following conclusions:

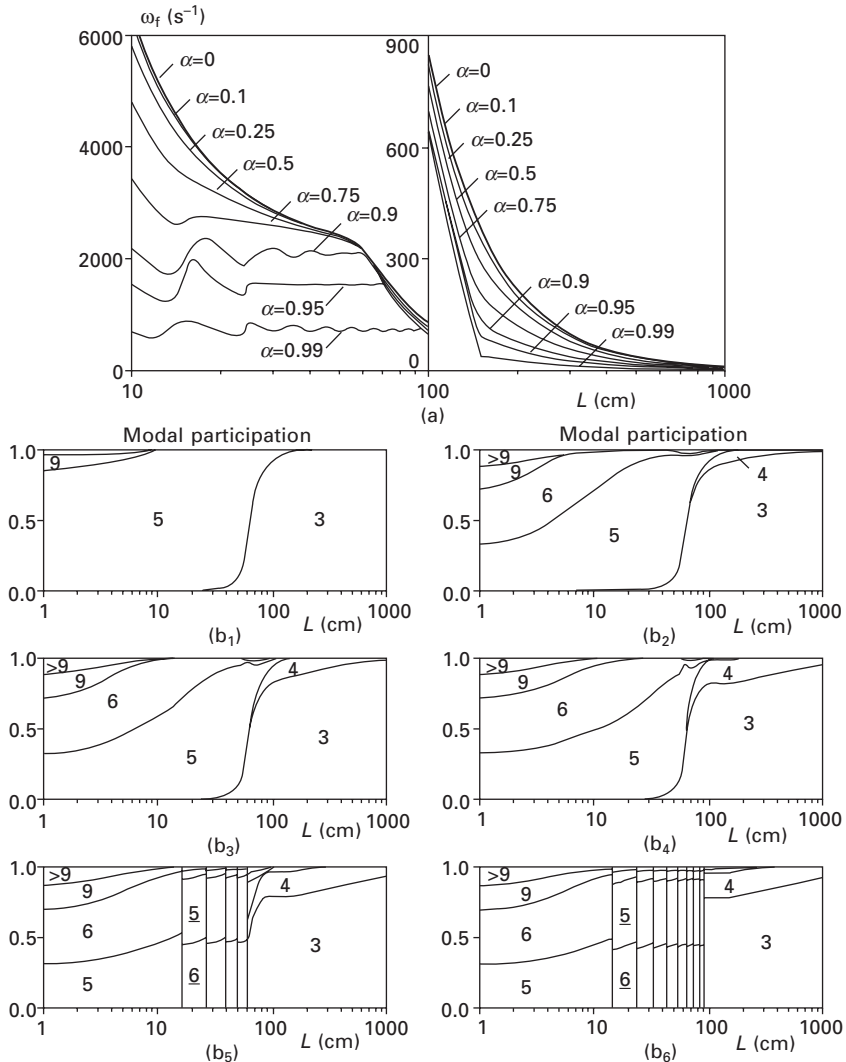
- As expected, the three natural frequencies decrease monotonically with  $L$ , eventually tending to zero. For  $L > 80$  cm, mode 3 is predominant and the differences between the GBT-based results and the estimates provided by Eq. (2.35) (dashed curve in Fig. 2.20(a)) never exceed 2%. Furthermore, one notices that there exists a virtually perfect agreement with the values yielded by the ABAQUS analyses (white circles in Fig. 2.20(a)) – the differences are always lower than 1%.
- The fundamental vibration mode always exhibits a single half-wave and its main contribution comes from either the local-plate mode 5 (short beams), the minor axis bending mode 3 (long beams) or a combination of both (beams with intermediate lengths). In the last case, there is a smooth transition between the participations of modes 5 and 3 for length values close to  $L = 65$  cm (see Fig. 2.20(b<sub>1</sub>)).
- The modal decomposition of the second and third vibration modes exhibit a more pronounced variation with  $L$ , both in terms of the deformation modes involved and the number of half-waves of their contributions –

concerning this last aspect, note that, for (i)  $32 < L < 55$  cm and for (ii)  $16 < L < 32$  cm and  $55 < L < 60$  cm, the member second and third vibration modes exhibit two half-waves. Moreover, the number of local plate and global deformation modes appearing in the modal participation diagrams increases with the vibration mode order – indeed, (a) the fundamental vibration modes involve only modes **5** and **3**, (b) the second vibration modes involve modes **5 + 6** and **2 + 4**, and (c) the third vibration modes involve modes **5 + 6 + 8 + 10** and **2 + 3 + 4**.

- For  $60 < L < 85$  cm, only deformation modes **3** and **5** participate in both the fundamental and third vibration modes. However, while **3** governs the former, mode **5** is predominant in the latter – this fact explains the considerable difference between the two corresponding natural frequencies.

Finally, the vibration behaviour of beams subjected to uniform major axis bending moment diagrams of value  $M = \alpha M_{\text{cr}}$  is analysed, where  $0 \leq \alpha \leq 1$  and  $M_{\text{cr}}$  is the corresponding critical buckling moment – recall that the curve  $M_{\text{cr}}(L)$  was plotted in Fig. 2.19(a). The curves  $\omega_f(L)$  presented in Fig. 2.21(a) make it possible to assess the influence of the applied moment level on the beam fundamental frequency – note that, for the sake of clarity, different vertical scales were used for  $10 < L < 100$  cm and  $100 < L < 1000$  cm. Moreover, Figs 2.21(b<sub>1</sub>)–(b<sub>6</sub>) provide the modal decomposition diagrams of the fundamental vibration modes concerning beams subjected to six different applied moment levels ( $\alpha = 0, 0.1, 0.25, 0.75, 0.90, 0.99$  – note that the  $\alpha = 0$  diagram was presented in Fig. 2.20(b<sub>1</sub>), but only for  $10 < L < 1000$  cm, instead of  $1 < L < 1000$  cm). Once again, a bar under a mode number indicates a two half-wave ( $n_s = 2$ ) contribution and the subsequent vertical lines separate length ranges associated with fundamental vibration modes exhibiting a growing number of half-waves. From the observation of the results displayed in Figs 2.21(a)–(b<sub>6</sub>), it is possible to draw the following conclusions:

- The presence of the bending moments only causes noticeable fundamental frequency drops for  $\alpha \geq 0.25$ , i.e. whenever the applied moment level is ‘high enough’.
- Even for very small bending moments (e.g.  $\alpha = 0.1$ ), the shape of the fundamental vibration mode may change considerably, with respect to that of an unloaded member with the same length – compare the modal participation diagram of Fig. 2.21(b<sub>1</sub>) with the ones shown in Figs 2.21(b<sub>2</sub>)–(b<sub>6</sub>).
- For  $0.25 < \alpha < 0.75$ , the decrease of  $\omega_f$  becomes quite relevant and a noticeable change in the shape of the curve  $\omega_f(L)$  occurs between  $\alpha = 0.5$  and  $\alpha = 0.75$ : it ceases to decrease monotonically with  $L$  and exhibits a small ascending branch in the vicinity of  $L = 12$  cm.



2.21 (a) Curves  $\omega_f(L)$  for  $\alpha = 0, 0.1, 0.25, 0.5, 0.75, 0.90, 0.95, 0.99$  and (b) modal participation diagrams for (b<sub>1</sub>)  $\alpha = 0$ , (b<sub>2</sub>)  $\alpha = 0.10$ , (b<sub>3</sub>)  $\alpha = 0.25$ , (b<sub>4</sub>)  $\alpha = 0.75$ , (b<sub>5</sub>)  $\alpha = 0.90$  and (b<sub>6</sub>)  $\alpha = 0.99$ .

- For  $0.10 < \alpha < 0.75$  and regardless of the beam length  $L$ , the shape of the fundamental vibration mode remains practically unaltered, a statement that can easily be attested by the high similarity of the modal participation diagrams shown in Figs 2.21(b<sub>2</sub>)–(b<sub>4</sub>).
- For  $0.75 < \alpha < 1.0$ , the fundamental frequency drop is rather severe and, moreover, the shape of the curve  $\omega_f(L)$  changes considerably with the applied moment level  $\alpha$  – (i) the variation of  $\omega_f$  with  $L$  becomes very

‘irregular’ for a length range between 12 cm and an upper limit that is lower than 150 cm and varies with  $\alpha$  (e.g.  $12 < L < 95$  cm for  $\alpha = 0.99$ ), and (ii) a ‘kink’ is clearly visible close to  $L = 150$  cm. For a beam length range that increases with  $\alpha$  and reaches  $12 < L < 150$  cm for  $\alpha = 1.0$ , (i)  $\omega_f$  tends to a constant value and (ii) the shape of the fundamental vibration mode changes drastically. The above length range is precisely the one in which the beams *buckle* in modes exhibiting a growing number of half-waves (see Figs 2.19(a) and 2.19(b<sub>2</sub>)). Thus, it seems fair to conclude that, as the applied moment level approaches its critical value (i.e.  $\alpha$  approaches 1.0), the fundamental vibration mode tends to the corresponding critical buckling mode (i.e. same shape and number of half-waves). Indeed, while for  $\alpha \leq 0.75$  there are always single half-wave beam fundamental vibration modes, for larger applied moments half-wave numbers varying between 1 and the associated critical buckling mode  $n_s$  value are exhibited (e.g. Figs 2.21(b<sub>5</sub>) and (b<sub>6</sub>) show that, for  $\alpha = 0.90$  and  $\alpha = 0.99$ , these numbers vary from 1 to 4 and 1 to 9 – note that, for  $\alpha = 1.0$ , they would vary from 1 to 14, maximum half-wave number in a beam critical buckling mode, which occurs for  $L = 150$  cm).

## 2.4 Conclusions

This chapter has addressed the assessment and characterisation of the local and global vibration behaviour of thin-walled members displaying fully arbitrary open cross-sections by means of a formulation based on GBT (generalised beam theory) that provides a general approach to obtain accurate and clarifying solutions for a wide range of vibration problems. This is mostly due to the unique modal features of the GBT analyses, which make it possible (i) to express the member vibration modes as linear combinations of structurally meaningful cross-section *deformation modes*, (ii) to determine the individual contributions of each of those modes and, last but not least, (iii) to obtain very accurate results with discretisations that involve fairly small numbers of degrees of freedom. Initially, the GBT system of equilibrium equations and corresponding boundary conditions was derived and physical interpretations were provided for all the terms appearing in it. Next, the main concepts and procedures involved in the performance of the cross-section and member analyses were described in some detail – in this context, it is worth mentioning that (i) the GBT cross-section analysis was developed for arbitrarily branched open cross-sections (the unbranched cross-sections were handled as a particular case) and that (ii) a GBT-based beam finite element was formulated and numerically implemented to solve the vibration eigenvalue problems (member analysis).

In order to illustrate the application and capabilities of the proposed GBT formulation, in-depth studies about the local and global vibration behaviour

of (i) lipped channel members with several end support conditions and (ii) simply supported I-section beams (under uniform major axis bending) were presented and discussed in great detail – the numerical results were obtained either by employing Galerkin's method (simply supported members) or through GBT-based beam finite element analyses (members with other end support conditions). The lipped channel results concerned mostly the variation of the lower natural frequencies and corresponding vibration mode natures/shapes with the member length – for validation purposes, some of these results were compared with values yielded by shell finite element analyses performed in ABAQUS and a perfect agreement was found. The chapter concluded with an investigation on the influence of uniform major axis bending on the local and global vibration behaviour of I-section beams, which revealed that the presence of the bending moments may significantly alter the beam fundamental frequency value and vibration mode nature/shape – in particular, it was shown that, whenever the applied bending moment level approaches its critical value, the beam fundamental vibration mode configuration tends to the one exhibited by its critical buckling mode.

## 2.5 References

- Budiansky B and Fralich RW (1954). *Effects of Panel Flexibility on Natural Vibration Frequencies of Box Beams*, NACA Technical Note TN-3070.
- Camotim D, Silvestre N, Gonçalves R and Dinis PB (2004). GBT Analysis of Thin-walled Members: New Formulations and Applications, *Thin-Walled Structures: Recent Advances and Future Trends in Thin-Walled Structures Technology*, J. Loughlan (Ed.), Canopus Publishing, Bath, 137–168.
- Cheung YK and Cheung MS (1971). Natural Vibrations of Thin, Flat-walled Structures with Different Boundary Conditions, *Journal of Sound and Vibration*, **18**(3), 325–337.
- Cheung YK and Kong J (1995). Vibration and Buckling of Thin-walled Structures by a New Finite Strip, *Thin-Walled Structures*, **21**(4), 327–343.
- Clough RW and Penzien J (1975). *Dynamics of Structures*, McGraw-Hill Kogakusha, Tokyo.
- Davies JM (2000). Recent Research Advances in Cold-formed Steel Structures, *Journal of Constructional Steel Research*, **55**(1–3), 267–288.
- Dinis PB, Camotim D and Silvestre N (2006). GBT Formulation to Analyse the Buckling Behaviour of Thin-walled Members with Arbitrarily ‘Branched’ Open Cross-Sections, *Thin-Walled Structures*, **44**(1), 20–38.
- Fitcher WB and Kordes EE (1959). *Investigation of Vibration Characteristics of Circular Arc Monocoque Beams*, NACA Report D-59.
- Gavrić L (1994). Finite Element Computation of Dispersion Properties of Thin-walled Waveguides, *Journal of Sound and Vibration*, **173**(1), 113–124.
- Gere JM (1954). *Bending and Torsional Vibrations of Thin-walled Bars of Open Cross-section*, Ph.D. Thesis, Stanford University, USA.
- Hamed E and Frostig Y (2005). Free Vibrations of Multi-girder and Multi-cell Box Bridges with Transverse Deformations Effects, *Journal of Sound and Vibration*, **279**(3–5), 699–722.

- HKS (Hibbit, Karlsson and Sorensen Inc.) (2002). *ABAQUS Standard* (version 6.3-1).
- Kim YY and Kim JH (1999). Thin-walled Closed Box Beam Element for Static and Dynamic Analysis, *International Journal for Numerical Methods in Engineering*, **45**(4), 473–490.
- Kim JH and Kim YY (2000). One-dimensional Analysis of Thin-walled Closed Beams Having General Cross-sections, *International Journal for Numerical Methods in Engineering*, **49**(5), 653–668.
- Klausbruckner MJ and Pryputniewicz RJ (1995). Theoretical and Experimental Study of Coupled Vibrations of Channel Beams, *Journal of Sound and Vibration*, **183**(2), 239–252.
- Li WY and Ho WK (1995). A Displacement Variational Method for the Free Vibration Analysis of Thin-walled Members, *Journal of Sound and Vibration*, **181**(3), 503–513.
- Liu WH and Huang CC (1992). Vibration Analysis of Folded Plates, *Journal of Sound and Vibration*, **157**(1), 123–137.
- Noor AK, Hadian MJ and Andersen CM (1993). Hybrid Analytical Technique for Nonlinear Vibration Analysis of Thin-walled Beams, *Journal of Engineering Mechanics* (ASCE), **119**(4), 786–800.
- Ohga M (2002). Natural Frequencies and Mode Shapes of Thin-walled Members with Shell Type Cross Section, *Steel and Composite Structures*, **2**(3), 223–236.
- Ohga M, Nishimoto K, Shigematsu T and Hara T (1998). Natural Frequencies and Mode Shapes of Thin-walled Members under In-plane Forces, *Thin-walled Structures – Research and Development*, N.E. Shamugam, J.Y. Liew and V. Thevendran (Eds.), Elsevier, Amsterdam, 501–508.
- Ohga M, Takao H and Hara T (1995). Natural Frequencies and Mode Shapes of Thin-walled Members, *Computer and Structures*, **55**(6), 971–978.
- Okamura M and Fukasawa Y (1991). Natural Frequencies Analysis of Steel Thin-walled Beams, *46<sup>th</sup> Annual Conference of Japanese Society of Civil Engineers (JSCE)*, **46**, 998–999.
- Okamura M and Fukasawa Y (1998). Characteristics of Instability of Local Vibration of the Thin-walled Members Under Periodic Axial Forces, *Structural and Earthquake Engineering* (JSCE), **15**(2), 215s–223s.
- Saal G (1974). *A Contribution to the Dynamic Analysis of Thin Walled Prismatic Structures with Unbranched Sections*, Ph.D. Dissertation, Technische Hochschule Darmstadt, Germany. (In German.)
- Schardt C (1995). *A Contribution to the Analysis of Coupled Eigenvibrations of Prismatic Rods Considering Cross-Section Distortions*. Ph.D. Dissertation, Technische Hochschule Darmstadt, Germany. (In German.)
- Schardt R (1966). Extension of the Engineer's Theory of Bending to the Analysis of Folded Plate Structures. *Der Stahlbau*, **35**, 161–171. (In German.)
- Schardt R (1989). *Verallgemeinerte Technische Biegetheorie*, Springer-Verlag, Berlin. (In German.)
- Schardt R and Heinz DA (1991). Vibrations of Thin-walled Prismatic Structures under Simultaneous Static Load Using Generalized Beam Theory, *Structural Dynamics* (Eurodyn '90), W.B. Krätsig *et al.* (Eds.), Balkema, Rotterdam, 921–927.
- Silvestre N (2005). *Generalised Beam Theory: New Formulations, Numerical Implementation and Applications*, Ph.D. Thesis, IST-Technical University of Lisbon, Portugal. (In Portuguese.)
- Silvestre N and Camotim D (2002a). First Order Generalised Beam Theory for Arbitrary Orthotropic Materials, *Thin-walled Structures*, **40**(9), 755–789.

- Silvestre N and Camotim D (2002b). Unified GBT Approach to the Stability and Vibration Analysis of Thin-walled Structural Members, *Proceedings of Second International Conference on Structural Stability and Dynamics* (ICSSD 2002 – Singapore, 16–18 December), C.M. Wang, G.R. Liu and K.K. Ang (Eds.), World Scientific, Singapore, 489–495.
- Silvestre N and Camotim D (2003). GBT Stability Analysis of Pultruded FRP Lipped Channel Members, *Computers and Structures*, **81**(18–19), 1889–1904.
- Silvestre N and Camotim D (2004). Generalised Beam Theory to Analyse the Vibration Behaviour of Orthotropic Thin-walled Members, *Thin-walled Structures: Advances in Research, Design and Manufacturing Technology* (ICTWS 2004 – Loughborough, 22–24 June), J. Loughlan (Ed.), Institute of Physics Publishing, Bristol, 919–926.
- Silvestre N and Camotim D (2006a). Vibration Behaviour of Axially Compressed Cold-formed Steel Members, *Steel and Composite Structures*, **6**(3), 221–236.
- Silvestre N and Camotim D (2006b). GBT-based Local and Global Vibration Analysis of Loaded Composite Thin-walled Members, *International Journal of Structural Stability and Dynamics*, **6**(1), 1–29.
- Stephen DB and Steven GP (1997). Error Measures for the Finite Strip Vibration Analysis Method, *Journal of Sound and Vibration*, **200**(2), 139–149.
- Thomson RG and Kruszewski ET (1961). *Cross-Sectional Deformations of Monocoque Beams and Their Effects on the Natural Vibration Frequencies*, NACA Report D-987.
- Vlasov VZ (1959). *Thin-Walled Elastic Bars*, Fizmatgiz, Moscow. (In Russian – English translation: Israel Program for Scientific Translation, Jerusalem, 1961.)
- Williams FW, Bennett PN and Kennedy D (1996). Curves for Natural Frequencies of Axially Compressed Prismatic Plate Assemblies, *Journal of Sound and Vibration*, **194**(1), 13–24.

## Dynamics of nonprismatic thin-walled composite members of generic section

S R A J A S E K A R A N, PSG College of Technology, India

### 3.1 Introduction

Fibre reinforced plastic (FRP) has been increasingly used over the past few decades in variety of structures that require high stiffness and strength to weight ratios. In the construction industry, recent applications have proved the structural and cost efficiency of FRP structural shapes such as thin-walled open and closed sections. Thin-walled open section members, made from isotropic materials, have been studied by many investigators such as Vlasov (1961), Timoshenko (1945), Gjelsvik (1981) and Murray (1984). With the current emphasis on structural optimization, tapered members such as haunches are increasingly used in composite construction. Uniform beams are not always the most efficient choice. Often, greater material economy is achieved by using non-uniform beams. The economy may even be greater if the beam has adequate external supports.

The behaviour of uniform thin-walled bars in bending and torsion has been well known since the early works of Vlasov (1961). The corresponding behaviour of non-uniform thin-walled bars has been investigated by Rajasekaran (1971, 1994a,b) and Rajasekaran and Padmanabhan (1989) and Murray and Rajasekaran (1975) by using the finite element method. Before this, a straightforward and commonly used technique for analysing a tapered beam for flexural behaviour was to divide the member into a number of uniform elements (Chini and Wolde-Tinsae 1988, Shiomi and Kurata 1984). Yang and Yau (1987) have investigated the stability of beams with tapered I sections using the finite element method but their analysis is restricted to doubly symmetric wide flange sections. They extended the work of Yang and McGuire (1986a,b) on the geometric nonlinear analysis of three-dimensional framed structures with uniform I-section.

Bradford and Cuk (1988) presented a finite element method for the elastic flexural torsional buckling of nonprismatic I-section beam-columns. Chan (1990) performed the buckling analysis of structures composed of tapered members. His formulation was based on an updated Lagrangian description

and he derived flexural and geometric stiffness matrices. But the formulation is limited to wide flange sections. Kitipornchai and Trahair (1972) addressed the problem of linear stability of doubly symmetric wide flange beams by considering more general tapering and loading conditions and differential flexure of two flanges to derive the equilibrium equation. Later, Kitipornchai and Trahair (1975) extended the work to singly symmetric wide flange beams and reported numerical results by using the finite integral method. Wekezer's (1985) work is concerned with the lateral torsional buckling of thin-walled tapered beam with arbitrary cross-section and loading. He treated the walls as membranes and neglected both the in-plane cross-section deformations and mid-surface shear strain. He did not consider the variation of the shear centre location along the beam longitudinal axes. More recently, Andrade and Camotim (2005) presented a general variational formulation for the elastic lateral torsional buckling of singly symmetric thin-walled tapered beams.

The closed form solutions for small amplitude vibrations of thin-walled open and constant cross-sections were published by Vlasov (1963) and the explicit formula to determine the lowest natural frequencies of the thin-walled bars of open cross-sections are also found in Timoshenko and Gere (1961). Other investigators such as Gupta (1985, 1986) and Mei (1970) presented explicitly mass and stiffness matrices for thin-walled beams of constant cross-sections. Wekezer (1987) considered thin-walled bars of variable open cross-section by using a finite element method. Krishnan and Singh (1991) studied the vibration of thin-walled open section. Rajasekaran (1994a) has presented the equations for tapered thin-walled beams of generic open sections and studied the static and dynamic instability of thin-walled beams of generic section (1994b).

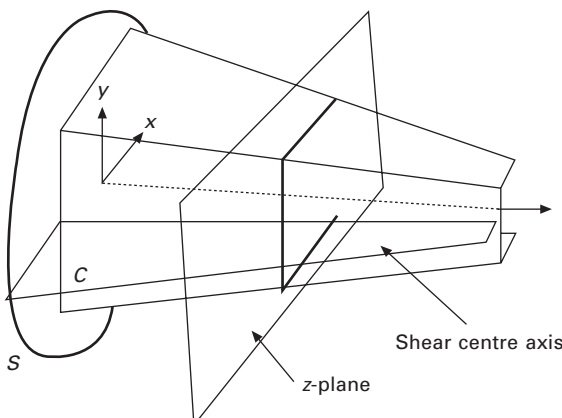
A Vlasov-type theory for composite thin-walled beams of open sections was established by Bauld and Tzeng (1984), Kobelev and Lerichev (as cited in Wu and Sun (1992) considered thin-walled beams with closed sections. This theory was also based on the assumptions that the cross-section of the beam does not deform in its own plane and the laminate has symmetric lay up. Libove (1988) established a simple theory for composite thin-walled beams with a single cell cross-section. Mansfield and Sobey (cited in Wu and Sun 1992) developed theories for one or two cell beams. Bauchau (1985) developed a thin-walled beam theory based on the assumption that the cross-section does not deform in its own plane, the out-of-plane cross-sectional warping is arbitrary. Giavotto *et al.* (1983), Bauchau and Hung (1987), Stemple and Lee (1989) and Wu and Sun (1992) proposed some other finite element techniques.

Although the original theory was restricted to members with symmetrical laminated plates neglecting shear deformations, Chandra and Chopra (1991) and Song and Librescu (1993) incorporated shear deformation. Silvestre and

Camotim (2002a,b) formulated a generalized beam theory to analyse the structural behaviour of composite thin-walled members made of laminated plates and displaying arbitrary orthotropy. They also addressed the influence of local deformations. Rajesekaran (2005a,c) has developed a procedure for finding the mechanical properties of thin-walled sections and also applied evolution strategies to find the optimal laminate sequence of thin-walled composite beams of generic cross-section (2005b). This chapter presents a detailed treatment of the formulation of vibration analysis of tapered thin-walled composite spatial members of generic open and/or closed section using beam and plate/shell elements and the solution of some simple numerical examples.

### 3.2 Remarks on approach

In a classical elastic theory, to get a closed form for displacement equations of equilibrium it is normally advantageous to uncouple the equations by defining the lateral displacements at the shear centre and axial displacement at the centroid. Therefore these axes have become the standard reference. But when a transverse load is applied to the prismatic I-shaped composite beam at a point other than (mechanical) shear centre, the load can be replaced by a statically equivalent load system at the (mechanical) shear centre as a transverse load and a torsional moment. This enables the flexural and torsional stresses to be computed separately and then superimposed to obtain the complete stress distribution. The behaviour of tapered unsymmetric beams is so complex that it cannot be analysed easily because of the locations of (mechanical) shear centre and (mechanical) centroid vary along the beam's longitudinal axis as shown in Fig. 3.1. Hence it is necessary to define lateral



3.1 Location of shear centre axis of undeformed tapered thin-walled beam and fixed Cartesian reference system.

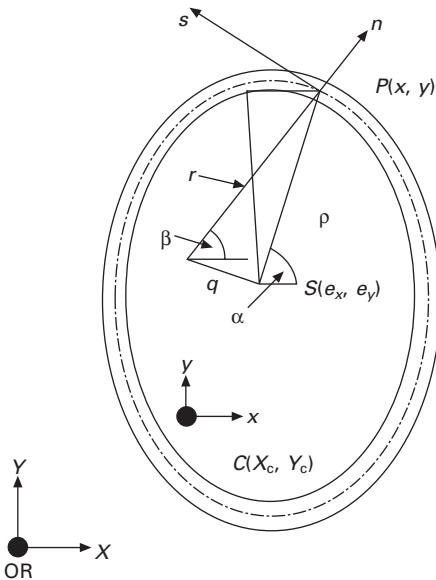
and axial displacement at an arbitrary point regardless of the strain of the cross-sections. The governing equations are nonlinear.

The simplest method of analysing a thin-walled spatially curved beam is based on approximating the beam by a series of straight beam elements including warping contribution. The beam element used in this work has two nodes with seven degrees of freedom at each node. The spatially curved beam is modelled into a number of these straight elements and the displacements of these straight elements are transformed into that of ‘Frenet’ axis by using the transformation matrices. In the second approach the spatial curved beam is modelled into degenerated plate/shell elements.

### 3.3 Geometric description of undeformed beam

The present work is aimed at developing a geometrically nonlinear theory valid for open/closed section with one or many cells. To be specific, the theory accounts for an-isotropy, transverse shear deformation, constrained warping and bending stiffness of the beam as well. The undeformed configuration of spatial thin-walled beam can be generated by the rigid body translation along a curved line of a plane figure (i) which remains perpendicular to the above curved line throughout the whole motion and (ii) has shape and dimensions that are allowed to vary smoothly. When a curved beam is idealized as straight beam elements, the curved line becomes a straight segment for each element. A fixed rectangular right-hand coordinate system is introduced as shown in Fig. 3.1 so that the  $z$  axis is parallel to the straight line segment used to generate the beam for straight element. The cross-section is defined as the projected section of the beam on  $z$ -plane (i.e. the plane perpendicular to  $z$  axis) as shown in Fig. 3.1.

Theoretical developments presented require three sets of coordinate systems, which are mutually interrelated. The first coordinate system is the orthogonal Cartesian system ( $x, y, z$ ) for which the  $x$  and  $y$  axes lie in the plane of the cross-section passing through reference point  $C$  and the  $z$  axis parallel to the line segment of the beam as explained above. The second coordinate system is the local plane ( $n, s, z$ ) system as shown in Fig. 3.2 where the  $n$  axis is normal to the middle surface of the thin wall, the  $s$  axis is tangent to the middle surface and is directed along the contour line of the cross-section. The ( $n, s, z$ ) and ( $x, y, z$ ) systems are in the same plane related through an angle of orientation  $\beta$  as defined in Fig. 3.2.  $\beta$  is the angle of orientation of the  $n$  axis with respect to the  $x$  axis at any point  $P$ . The third coordinate set is the contour coordinate  $s$  along the profile of the section with its origin at any point  $O$  on the profile of the section. Point  $S$  is the pole at which all displacements are defined. In this paper, wall thickness, material properties are assumed to vary along the length of the beam as well as with respect to  $s$ .



3.2 Definitions of coordinates of thin-walled section.

### 3.4 Assumptions

The following assumptions are made:

1. The flexural displacements  $u$  and  $v$  in the  $x$  and  $y$  directions respectively and the twist  $\phi$  of the cross-section are finite.
2. The axial displacement  $w$  is much smaller than  $u$  and  $v$  so that the products of the derivatives of  $w$  can be neglected in the strain displacement relation.
3. In the beam formulation, the projections of the cross-section on a plane normal to the  $z$  axis does not distort during deformation, whereas in the plate formulation this restriction is not adhered to.
4. The torsional shear strain  $\gamma_{sz}$  on the middle surface of the beam wall is zero for an open contour while it corresponds to a constant shear flow (with respect to  $s$ ) for a closed contour.
5. Strains are small so that a linear constitutive law can be used to relate the second Piola Kirchhoff's stress tensor to Green's strain tensor.
6. The ratio of wall thickness to the ratio of curvature at any point of the beam wall is small compared to unity so that it can be neglected in the expression of the strains. It should be noted that this is exact for cross-sections composed of linear segments.
7. The shell force and moment resultants corresponding to the circumferential normal stress  $\sigma_{ss}$  and the force resultant corresponding to  $\gamma_{ns}$  are negligibly small.

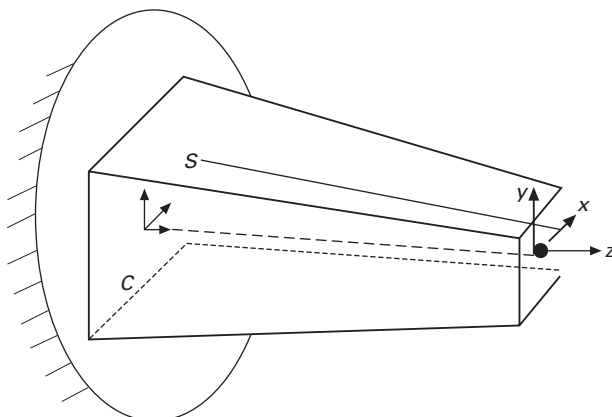
8.  $\sigma_{nn}$  can be neglected when deriving the stress–strain law of any layer of the beam wall.
9. The Kirchhoff–Love assumption in classical theory remains valid for each laminated plate component of a thin-walled beam.

### 3.5 Kinematics

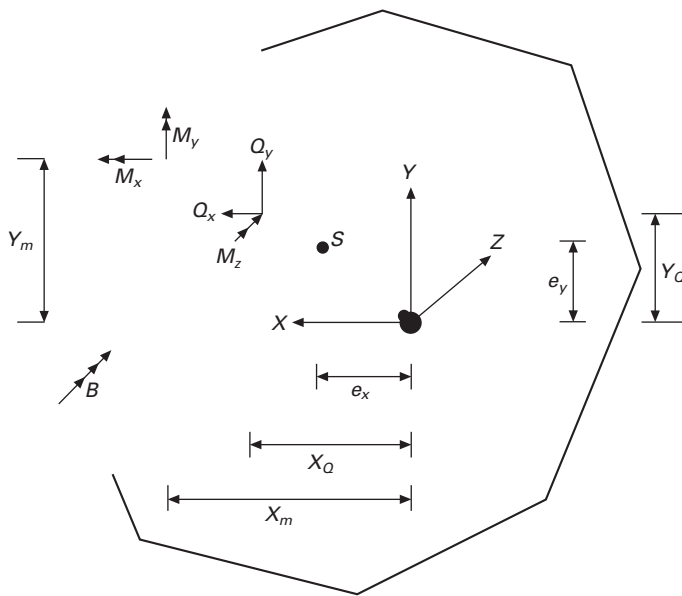
The member of length  $L$  shown in Fig. 3.3 is of a thin-walled nonprismatic beam of generic open section and is straight and untwisted. The Cartesian axes pass through an arbitrary point  $C$  of every section such that the longitudinal axis is straight. The transverse displacements are specified at arbitrary point  $S$  of every section such that it is parallel to the  $C$  axis (as  $u_s$ ,  $v_s$  and the actual axial displacement  $w_c$  at the point  $C$ ). The beam is subjected to a generic system of applied loads and end moments as shown in Fig. 3.4. The loading considered may include any combination of conservative applied forces (concentrated)  $Q_x$ ,  $Q_y$  and  $Q_z$  acting through  $(X_{QK}, Y_{QK})$  and moments  $M_x$ ,  $M_y$  and  $M_z$  and bi-moment  $B$  through  $(X_{MK}, Y_{MK})$  ( $k = 1\dots N$ ) and distributed applied forces ( $q_x$ ,  $q_y$ ,  $q_z$ ) acting through  $(x_q, y_q)$  and moments at  $(x_m, y_m)$ . All the loads are proportional to a single parameter  $\lambda$ . The end reactions are shown in Fig. 3.4. For a prismatic composite beam,  $S$  may be the mechanical shear centre and  $C$  may be the mechanical centroid but for a non-prismatic beam  $S$  and  $C$  vary along the longitudinal axis of the beam and hence  $C$  and  $S$  can be any arbitrary points. They may or may not be the same point.

#### 3.5.1 Displacements, rotations, curvatures and twist

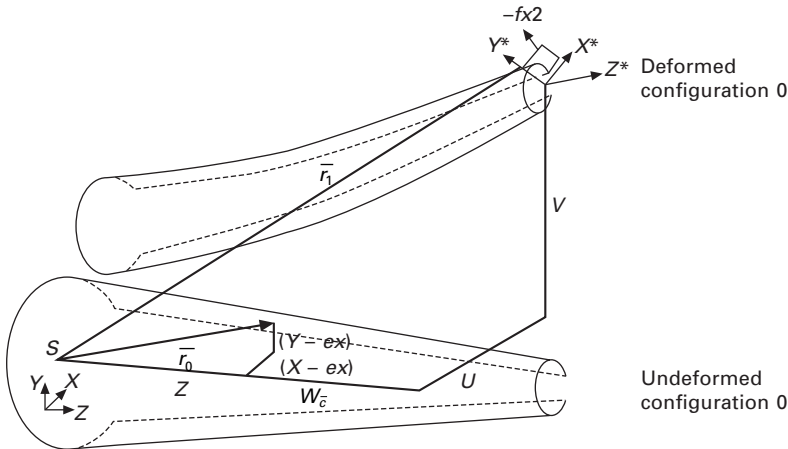
A right-hand coordinate system  $x$ ,  $y$ ,  $z$  is chosen such that they coincide with the axes passing through  $C$  as shown in Fig. 3.5. The position vector of any



3.3 Nonprismatic beam ( $C$ -axis = reference axis).



3.4 End actions.



3.5 Nonprismatic beam in deformed and undeformed configurations.

arbitrary point  $P$  with respect to  $S$  (at  $z = 0$ ) located on the mid-surface of the beam in the undeformed configuration may be expressed as

$$\bar{r}_0 = (x - e_x)\bar{i} + (y - e_y)\bar{j} + z\bar{k} \quad 3.1$$

where  $\bar{i}, \bar{j}, \bar{k}$  are unit vectors along the  $x, y, z$  axes respectively.

For a nonprismatic beam both  $x$  and  $y$  coordinates at any generic point on the contour are functions of  $z$  and, therefore, the derivatives of  $\bar{r}_0$  with respect to the  $x$ ,  $y$  and  $z$  axes may be expressed as

$$\bar{r}_0, x = \bar{i} \quad 3.2a$$

$$\bar{r}_0, y = \bar{j} \quad 3.2b$$

$$\bar{r}_0, z = x' \bar{i} + y' \bar{j} + \bar{k} \quad 3.2c$$

where ('') prime denotes differentiation with respect to  $z$ . After the beam deforms, it attains a deformed configuration  $\Gamma_1$  from undeformed configuration  $\Gamma_0$ . After an increment in set of actions the displacements of the points  $S$  and  $C$  will be  $u_s$ ,  $v_s$  and  $w_{\bar{c}}$  parallel to the  $x$ ,  $y$  and  $z$  axes through  $S$  and  $C$  and rotations by  $\theta_x$ ,  $\theta_y$  and  $\theta_z$ . In addition, the cross-section warps by ' $f_1 k_z$ ' one of its plane as shown in Fig. 3.5 where  $k_z$  denotes the rate of change of twist in the  $z$  direction. The rotations  $\theta_x$ ,  $\theta_y$  and  $\theta_z$  about the  $x$ ,  $y$  and  $z$  axes are given by

$$\begin{Bmatrix} \theta_x \\ \theta_y \\ \theta_z \end{Bmatrix} = \begin{Bmatrix} -v'_s \\ u'_s \\ \phi \end{Bmatrix} \quad 3.3$$

Then the direction cosine matrix between fixed  $x$ ,  $y$  and  $z$  and rotate  $x^*$ ,  $y^*$  and  $z^*$  is given by Love (1944) as

$$\begin{Bmatrix} \bar{e}_1 \\ \bar{e}_2 \\ \bar{e}_3 \end{Bmatrix} = [T_R]^T \begin{Bmatrix} \bar{i} \\ \bar{j} \\ \bar{k} \end{Bmatrix} \quad 3.4a$$

$$[T_R] = \begin{bmatrix} L_x & L_y & L_z \\ M_x & M_y & M_z \\ N_x & N_y & N_z \end{bmatrix} \quad 3.4b$$

where  $\bar{e}_1$ ,  $\bar{e}_2$  and  $\bar{e}_3$  are the unit vectors in the deformed directions of  $x$ ,  $y$  and  $z$ .

Assume moderate deflection and small rotation of twist and approximating

$$\cos \theta_x = 1 - \frac{\theta_x^2}{2}; \sin \theta_x = \theta_x \quad 3.5a$$

and similarly

$$\cos \theta_y = 1 - \frac{\theta_y^2}{2}; \sin \theta_y = \theta_y \quad 3.5b$$

$T_R$  is given by Van Erp *et al.* (1988) as

$[T_R]$

$$[T_R] = \begin{bmatrix} \left(1 - \frac{\theta_y^2}{2}\right) \cos \phi + \theta_x \theta_y \sin \frac{\phi}{2} & \left(1 - \frac{\theta_y^2}{2}\right) \sin \phi + \theta_x \theta_y \cos \frac{\phi}{2} & \theta_y \\ \left(1 - \frac{\theta_x^2}{2}\right) \sin \phi + \theta_x \theta_y \cos \frac{\phi}{2} & \left(1 - \frac{\theta_x^2}{2}\right) \cos \phi + \theta_x \theta_y \sin \frac{\phi}{2} & -\theta_x \\ -\theta_y \cos \phi + \theta_x \sin \phi & (\theta_y \sin \phi + \theta_x \cos \phi) & \left(1 - \frac{\theta_x^2}{2} - \frac{\theta_y^2}{2}\right) \end{bmatrix}$$

3.5c

The rotations and curvatures of the axes  $x^*$ ,  $y^*$  and  $z^*$  can be obtained as shown in Love (1944), Trahair and Bild (1990) and Bild *et al.* (1992):

$$\begin{Bmatrix} \kappa_x \\ \kappa_y \\ \kappa_z \end{Bmatrix} = \begin{Bmatrix} L'_y L_z + M'_y M_z + N'_y N_z \\ L'_z L_x + M'_z M_x + N'_z N_x \\ L'_x L_y + M'_x M_y + N'_x N_y \end{Bmatrix} \quad 3.6$$

$\kappa_z$  is given by

$$\kappa_z = \phi' + (v'_s u''_s - u'_s v''_s) \quad 3.7$$

Hence the triad  $\bar{e}_1, \bar{e}_2$  and  $\bar{e}_3$  in the deformed configuration is related to the triad  $\bar{i}, \bar{j}, \bar{k}$  in the undeformed configuration as

$$<\bar{e}_1 \bar{e}_2 \bar{e}_3> = <\bar{i} \bar{j} \bar{k}> [T_R] \quad 3.8$$

for small rotations

$$\cos \phi = 1 - \frac{\phi^2}{2} \quad 3.9a$$

$$\sin \phi = \phi \quad 3.9b$$

Hence transformation matrix  $T_R$  is written as,

$$[T_R] = \begin{bmatrix} \left(1 - u'^2_s - \frac{\phi^2}{2}\right) & (-\phi - u'_s v''_s)/2 & u'_s \\ \left(\phi - \frac{u'_s v'_s}{2}\right) & \left(1 - v'^2_s - \frac{\phi^2}{2}\right) & v'_s \\ (-u'_s - v'_s \phi) & (-v'_s + u'_s \phi) & \left(1 - \frac{u'^2_s}{2} - \frac{v'^2_s}{2}\right) \end{bmatrix}$$

3.10

After deformation, the position vector  $\bar{r}_l$  is given by

$$\bar{r}_l = \langle \bar{i} \quad \bar{j} \quad \bar{k} \rangle \begin{Bmatrix} u_s \\ v_s \\ w_e + z \end{Bmatrix} + \langle \bar{e}_1 \quad \bar{e}_2 \quad \bar{e}_3 \rangle \begin{Bmatrix} (x - e_x) \\ (y - e_y) \\ f_1 \kappa_z \end{Bmatrix} \quad 3.11$$

Hence displacements  $u_p$ ,  $v_p$  and  $w_p$  at a point  $P$  on the mid-line of the contour is given by

$$\bar{u} = PP' = \bar{r}_l - \bar{r}_0 = \langle \bar{i} \quad \bar{j} \quad \bar{k} \rangle \begin{Bmatrix} u_p \\ v_p \\ w_p \end{Bmatrix} \quad 3.12$$

The displacements are explicitly given by

$$u_p = u_s - (y - e_y)\phi + \frac{1}{2}[(x - e_x)(u_s'^2 + \phi^2) - (y - e_y)u_s'v_s' + 2f_1\kappa_zu_s'] \quad 3.13a$$

$$v_p = v_s + (y - e_x)\phi + \frac{1}{2}[-(x - e_x)u_s'v_s' - (y - e_y)(v_s' + \phi^2) + 2f_1\kappa_zv_s'] \quad 3.13b$$

$$w_p = w_c - xu_s' - yv_s' + f_1\kappa_z + (-xv_s'\phi + yu_s'\phi) - \frac{f_1\kappa_z}{2}(u_s'^2 - v_s'^2) \quad 3.13c$$

where

$$w_c = w_{\bar{c}} + e_x(u_s' + v_s'\phi) + e_y(v_s' - u_s'\phi) \quad 3.14$$

### 3.5.2 Finite strains

Since the cross-section of the tapered beam may vary in a linear or nonlinear manner along the axis, the mid-surface coordinates ‘z’ and ‘s’ are in general curvilinear. According to the theory of elasticity (Green and Zerna, 1968), the Green Lagrange strain tensor in its linear form is

$$e_{mn} = \frac{1}{2}(\bar{r}_{0,m} \cdot \bar{u}_{,n} + \bar{r}_{0,n} \cdot \bar{u}_{,m}) \quad \text{for } m, n = x, y, z \quad 3.15$$

Hence the strain tensors can be written as

$$e_{zz} = x'u_{p,z} + y'v_{p,z} + w_{p,z} \quad 3.16a$$

or

$$e_{zz} = x'u_p' + y'v_p' + w_p' \quad 3.16b$$

$$e_{xz} = \frac{1}{2}(u_p' + y'v_{p,x} + w_{p,x}) \quad 3.16c$$

$$e_{yz} = \frac{1}{2} (v'_p + x'u_{p,y} + w_{p,y}) \quad 3.16d$$

It should be noted that

$$e_{xx} = u_{p,x} + \frac{1}{2} (u_{p,x}^2 + v_{p,x}^2 + w_{p,x}^2) \quad 3.17a$$

$$e_{yy} = v_{p,y} + \frac{1}{2} (u_{p,y}^2 + v_{p,y}^2 + w_{p,y}^2) \quad 3.17b$$

$$e_{xy} = \frac{1}{2} (u_{p,y} + v_{p,x}) \quad 3.17c$$

Substituting for displacements, we get

$$e_{xx} = e_{yy} = e_{xy} = 0 \quad 3.18$$

This also implies that assumptions 2 and 3 are mutually compatible. The shear strain along the mid-surface of the contour can be obtained as follows.

Referring to Fig. 3.2, the relationship between unit vectors  $\bar{i}, \bar{j}, \bar{k}$  along the  $x, y, z$  axes can be written in terms of unit vectors along the  $n, s, z$  axes as

$$\begin{Bmatrix} \bar{i} \\ \bar{j} \\ \bar{k} \end{Bmatrix} = \begin{bmatrix} \cos \beta & -\sin \beta & 0 \\ \sin \beta & \cos \beta & 0 \\ 0 & 0 & 1 \end{bmatrix} \begin{Bmatrix} \bar{e}_n \\ \bar{e}_s \\ \bar{k} \end{Bmatrix} \quad 3.19$$

or

$$\begin{Bmatrix} \bar{e}_n \\ \bar{e}_s \\ \bar{k} \end{Bmatrix} = \begin{bmatrix} \cos \beta & \sin \beta & 0 \\ -\sin \beta & \cos \beta & 0 \\ 0 & 0 & 1 \end{bmatrix} \begin{Bmatrix} \bar{i} \\ \bar{j} \\ \bar{k} \end{Bmatrix} \quad 3.20$$

The displacements  $\bar{u}$  and  $\bar{v}$  along the  $n$  and  $s$  axes can be written as

$$\bar{u} = u_p \cos \beta + v_p \sin \beta \quad 3.21a$$

$$\begin{aligned} \bar{u} = u_s \cos \beta + v_s \sin \beta + q\phi + \frac{1}{2} \{-(x - e_x) \cos \beta (u'_s)^2 + \phi^2 \\ -(y - e_y) \cos \beta u'_s v'_s + 2 \cos \beta f_1 \kappa_z u'_s - (x - e_x) \sin \beta u'_s v'_s \\ -(y - e_y) \sin \beta (v'_s)^2 + \phi^2 + 2 \sin \beta f_1 \kappa_z v'_s\} \end{aligned} \quad 3.21b$$

$$\bar{v} = v_p \cos \beta - u_p \sin \beta \quad 3.21c$$

$$\begin{aligned} \bar{v} = -u_s \sin \beta + v_s \cos \beta + r\phi + \frac{1}{2} \{(x - e_x) \sin \beta (u'_s)^2 + \phi^2 \\ +(y - e_y) \sin \beta u'_s v'_s - 2 f_1 \sin \beta \kappa_z u'_s - (x - e_x) \cos \beta u'_s \phi \\ -(y - e_y) (v'_s)^2 + \phi^2 \cos \beta + 2 f_1 \cos \beta \kappa_z v'_s\} \end{aligned} \quad 3.21d$$

where

$$r = (x - e_x) \cos \beta + (y - e_y) \sin \beta \quad 3.22a$$

$$q = (x - e_x) \sin \beta + -(y - e_y) \cos \beta \quad 3.22b$$

as shown in Fig. 3.2.

The axial strain in the  $z$ -direction can be obtained by considering the shear strain  $\gamma_{sz}$  and  $\gamma_{hz}$ . Consider  $h(s)$  as the thickness of the wall considering of many layers of composite laminates and  $N_{sz}(z, n)/G_{sz}(s)$  be the torsional shear flow and the effective in-plane shear stiffness of the laminate respectively with respect to the closed contour. Then the shear strain  $\gamma_{sz}$  at any point  $P$  of the mid-surface of the contour is given by:

$$\begin{aligned} \gamma_{zs} &= 2e_{zs} = 2\left(e_{xz}\frac{\partial x}{\partial s} + e_{yz}\frac{\partial y}{\partial s}\right) \\ &= 0 + \delta_c \frac{\bar{N}_{sz}(z, n)}{h(s)\bar{G}_{sz}(s)} \end{aligned} \quad 3.23$$

In Eq. (3.23),  $\delta_c$  is a tracer as defined by Bhaskar and Librescu (1995) and Lee (2001) to indicate the closed section. For the sake of clarity, mid-surface quantities are indicated by (\*) whenever applicable.

Simplifying we get,

$$w^* = w_c - x^*u'_s - y^*v'_s + \phi' \left( \omega^* + \frac{\delta_c \int r^* ds \int \frac{ds}{hG_{sz}}}{\int \frac{ds}{hG_{sz}}} \right) \quad 3.24a$$

$$w^* = w_c - x^*u'_s - y^*v'_s + \phi'(\omega^* + \delta_c \int \psi ds) \quad 3.24b$$

Comparing Eq. (3.13c) with Eq. (3.24b), it is shown that  $f_1 = \omega$  = warping coordinate. The linear part of the strain in terms of displacements may be written as

$$(e_{zz}^*)_1 = (\varepsilon_{zz}^*)_1 = (x'u'_p + yv'_p + w'_p) \quad 3.25$$

or

$$(\varepsilon_{zz}^*)_1 = w'_c - x^*u''_s - y^*v''_s + \bar{\omega}^*\phi'' + \eta^*\phi' \quad 3.26a$$

$$\text{where } \bar{\omega}^* = \bar{\omega} = \omega^* + \delta_c \int \psi ds \quad 3.26b$$

$\bar{\omega}$  is called the modified warping constant.

$$\eta^* = \omega' + y'(x - e_x) - x'(y - e_y) \quad 3.27$$

and the torsional strains

$$e_{xz}^* = \frac{1}{2} \left[ \frac{\partial w}{\partial x} - (y - e_y) \right] \phi' \quad 3.28a$$

$$e_{yz}^* = \frac{1}{2} \left[ \frac{\partial w}{\partial y} + (x - e_x) \right] \phi' \quad 3.28b$$

The nonlinear component of Green Lagrange strain may be written as

$$\eta_{mn} = \frac{1}{2} [u_{,m} u_n]; m, n = x, y, z \quad 3.29a$$

$$\eta_{zz}^* = \frac{1}{2} [u_p'^2 + v_p'^2 + w_p'^2] \quad 3.29b$$

where  $w_p'$  is small and can be neglected in Eq. (3.29b):

$$\eta_{zz}^* = \frac{1}{2} \{ [u_s' - (y - e_y) \phi' - y' \phi]^2 + [v_s' + (x - e_x) \phi' + x' \phi]^2 \} \quad 3.30$$

with  $\eta_{zz}$ , adding quadratic terms of  $w_p'$ , the nonlinear term  $e_{zz}$  is given as:

$$(e_{zz})_{nl} = (e_{zz})_{nl} \\ = \frac{1}{2} \left[ \begin{array}{l} u_s'^2 + v_s'^2 + (x^2 + y^2) \phi^2 + (e_x^2 + e_y^2) \phi'^2 - 2x e_x \phi'^2 \\ - 2y e_y \phi'^2 + (x'^2 + y'^2) \phi^2 + 2e_y u_s' \phi' - 2e_x v_s' \phi' \\ + 2 \{(y - e_y) y' + (x - e_x) x'\} \phi \phi' - 2x v'' \phi \\ + 2y u_s'' \phi + \bar{\omega} (v' u''' - u' v''') \end{array} \right] \quad 3.31$$

Using assumption 9, the displacements  $u, v, w$  at any generic point on the projected cross-section are given in terms of mid-surface displacements  $u^*$ ,  $v^*$  and  $w^*$  as (see Fig. 3.6):

$$u(s, z, n) = \bar{u}^*(s, z) \quad 3.32a$$

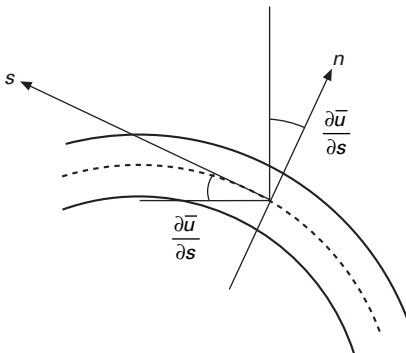
$$v(s, z, n) = \bar{v}^*(s, z) - \frac{n \partial \bar{u}(s, z)}{\partial s} \quad 3.32b$$

$$w(s, z, n) = w^*(s, z) - \frac{n \partial \bar{u}^*(s, z)}{\partial z} \quad 3.32c$$

The strains are given by

$$\epsilon_{zz} = (\epsilon_{zz}^*)_L + n \bar{k}_z + (\epsilon_{zz}^*)_{NL} \quad 3.33a$$

$$\gamma_{sz} = (\gamma_{sz}^*)_L + (\gamma_{sz}^*)_{NL} n \bar{k}_{sz} \quad 3.33b$$



### 3.6 Definition of slope.

where

$$\bar{k}_z = -\frac{\partial^2 \bar{u}^*}{\partial z^2} \quad 3.34a$$

$$\bar{k}_{sz} = -\frac{2\partial^2 u^*}{\partial s \partial z} \quad 3.34b$$

Substituting Eq. (3.34) in Eq. (3.33), we get

$$\varepsilon_{zz} = w'_c - x^* u''_s - y^* v''_s + \bar{\omega} \phi'' - n \bar{u}^{*'} + \eta^* \phi' + (\varepsilon_{zz})_{NL} \quad 3.35a$$

$$\begin{aligned} \varepsilon_{zz} = & w'_c - (x^* + n \cos \beta) u''_s - (y^* + n \sin \beta) v_s \\ & + (\bar{\omega} - nq) \phi'' + \eta^* \phi' + (\varepsilon_{zz})_{NL} \end{aligned} \quad 3.35b$$

and

$$\gamma_{sz} = (\delta_c \psi - z n) \phi' - n (u''_s v'_s - v''_s u'_s) \quad 3.35c$$

or

$$\begin{Bmatrix} \varepsilon_{zz} \\ \gamma_{sz} \end{Bmatrix} = [R] \{ \varepsilon_r \} \quad 3.36$$

where

$$[R] = \begin{bmatrix} 1 & -(x^* + n) & -(y^* + n) & (\bar{\omega} - nq) & -2x^* & -2y^* & \eta^* & (x^{*2} + y^{*2}) & 2x^* x' & 2y^* y' & 0 \\ \cos \beta & \sin \beta & 0 & 0 & 0 & 0 & 0 & 0 & 0 & 0 & 0 & -2n \\ 0 & 0 & 0 & 0 & 0 & 0 & (\delta_c \psi & 0 & 0 & 0 & 0 & -2n) \end{bmatrix} \quad 3.37$$

$$\{\varepsilon_r\} = \begin{bmatrix} w'_c \\ u''_s \\ v''_s \\ \phi'' \\ 0 \\ 0 \\ \phi' \\ 0 \\ 0 \\ 0 \\ 0 \\ 0 \end{bmatrix} + 1/2 \begin{bmatrix} u'^2_s + v'^2_s + (e_x^2 + e_y^2) \phi'^2 + 2e_y u'_s \phi' - 2e_x v'_s \phi' + (x'^2 + y'^2) \phi^2 \\ 2v''_s \phi + 2e_x \phi'^2 \\ -2u''_s \phi' + 2e_y \phi'^2 \\ v'_s u'''_s - u'_s v'''_s \\ e_x \phi \phi' \\ e_y \phi \phi' \\ 0 \\ \phi'^2 \\ \phi \phi' \\ \phi \phi'' \\ v'_s u''_s - u'_s v''_s \end{bmatrix} \quad 3.38$$

In Eq. (3.38),  $\{\varepsilon_r\}$  is called the generalized strain and its first component in Eq. (3.38) consists of linear strains associated with axial strain  $w'$ , the curvatures about the  $y$  and  $x$  axes ( $u''_s, v''_s$ ) a term  $\phi''$  associated with warping strain that might be called as ‘twistature’ and twist  $\phi$ . The second component of  $\{\varepsilon_r\}$  contains quadrature terms as

$$\begin{Bmatrix} \varepsilon_{zz} \\ \gamma_{sz} \end{Bmatrix} = [[B_L] + [B_Q]] \bar{\phi} \quad 3.39a$$

$$\begin{Bmatrix} \varepsilon_{zz} \\ \gamma_{sz} \end{Bmatrix} = \{\varepsilon_r\}_L + \{\varepsilon_r\}_{NL} \quad 3.39b$$

where  $[B_L]$  and  $[B_Q]$ , the linear and nonlinear strain displacement matrices can be identified from Uma (1992) and Anandavalli (1993) generalized displacement is given as

$$\langle \phi \rangle = \langle u_s \ u'_s \ u''_s \ u'''_s \ v_s \ v'_s \ v''_s \ v'''_s \ w_c \ w'_c \ \phi \ \phi' \ \phi'' \rangle \quad 3.40$$

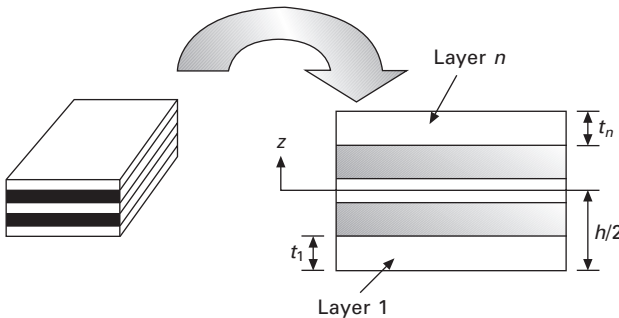
Zienkiewicz (1971) showed that

$$[B_Q]\{\Delta_\phi\} = [\Delta B_Q]\{\bar{\phi}\} \quad 3.41$$

in which  $\Delta$  is termed to indicate small change in quantities.

### 3.6 Constitutive equations

A thin-walled beam can be considered to be made of  $n$  orthotropic layers of total thickness  $h$  as shown in Fig. 3.7. The coordinates  $L, T, Z$  are principal coordinate directions with  $Z$  axes ( $z$  axis) is taken positive upward in the



3.7 Coordinate system and layer numbering.

middle plane (see Fig. 3.7). In addition to the assumptions made in Section 3.4 the following additional assumptions are made:

- The layers are perfectly bonded together with each layer of uniform thickness.
- Kirchhoff's assumptions hold good.
- The transverse normal does not suffer any elongation.
- The transverse normal rotates such that it remains perpendicular to the mid-surface even after deformation.

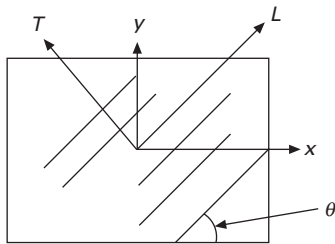
Considering a laminate as shown in Fig. 3.8 and using the notations commonly adopted in composite literature given by Kaw (1997) and Rajasekaran *et al.* (2003), the stresses in the  $x, y$  co-ordinate system in terms of the  $L, T$  system can be shown as

$$\begin{Bmatrix} \sigma_{xx} \\ \sigma_{yy} \\ \sigma_{xy} \end{Bmatrix} = [T] \begin{Bmatrix} \sigma_{LL} \\ \sigma_{TT} \\ \sigma_{LT} \end{Bmatrix} \quad 3.42$$

where  $[T]$  is the strain transformation matrix. Using the constitutive law, the stress-strain relationship in  $LT$  system can be written as

$$\begin{Bmatrix} \sigma_{LL} \\ \sigma_{TT} \\ \sigma_{LT} \end{Bmatrix} = \begin{Bmatrix} Q_{11} & Q_{12} & Q_{16} \\ Q_{21} & Q_{22} & Q_{26} \\ Q_{61} & Q_{62} & Q_{66} \end{Bmatrix} \begin{Bmatrix} \varepsilon_{LL} \\ \varepsilon_{TT} \\ \gamma_{LT} \end{Bmatrix} \quad 3.43$$

$$[Q] = \frac{1}{(1 - \gamma_{LT}\gamma_{TL})} \begin{bmatrix} E_L & \gamma_{LT}E_T & 0 \\ \gamma_{LT}E_T & 0 & 0 \\ 0 & 0 & G_{LT}(1 - \gamma_{LT}\gamma_{TL}) \end{bmatrix} \quad 3.44$$

3.8  $x, y, L, T$  system.

using the transformation law, the constitutive matrix in the  $x, y$  system is obtained as:

$$\begin{Bmatrix} \sigma_{xx} \\ \sigma_{yy} \\ \sigma_{xy} \end{Bmatrix} = \begin{bmatrix} S_{11} & S_{12} & S_{16} \\ S_{21} & S_{22} & S_{26} \\ S_{61} & S_{62} & S_{66} \end{bmatrix} \begin{Bmatrix} \varepsilon_{LL} \\ \varepsilon_{TT} \\ \gamma_{LT} \end{Bmatrix} \quad 3.45$$

or

$$[S] = [T][Q][T]^T \quad 3.46$$

where

$$[T] = \begin{bmatrix} \cos^2 \theta & \sin^2 \theta & -\sin 2\theta \\ \sin^2 \theta & \cos^2 \theta & \sin 2\theta \\ \frac{\sin 2\theta}{2} & \frac{-\sin 2\theta}{2} & \cos 2\theta \end{bmatrix} \quad 3.47$$

where  $\theta$  is the fibre orientation of laminate with respect to the  $x$  axis of the plate. The  $X$  axis of the plate (lamina) corresponds to the  $z$  ( $Z$ ) axis of the beam and  $\theta$  is the fibre orientation with respect to the  $Z$  axis of the beam. The constitutive equation of  $R$ , the orthotropic lamina in the beam coordinate system, is given as:

$$\begin{Bmatrix} \sigma_{zz} \\ \tau_{sz} \end{Bmatrix}^k = \begin{bmatrix} S_{11} & S_{16} \\ S_{61} & S_{66} \end{bmatrix} \begin{Bmatrix} \varepsilon_{zz} \\ \gamma_{sz} \end{Bmatrix} \quad 3.48$$

It is seen from Eq. (3.48) that  $\sigma_z$  and  $\tau_{sz}$  are the normal and shear stresses at any point of the thin-walled contour and they are the same as  $\sigma_{xx}$  and  $\sigma_{xy}$  given in Eq. (3.45).

From Eq. (3.36),

$$\begin{Bmatrix} \varepsilon_{zz} \\ \gamma_{sz} \end{Bmatrix} = [R]\{\varepsilon_r\}_L \quad 3.49$$

and using the contragradient law we get the generalized forces corresponding to  $\{\varepsilon_r\}_L$  as

$$\{Q\} = \int (R)^T \{\sigma\} dA \quad 3.50$$

where  $\{Q\}$  are generalized forces corresponding to  $q$  where

$$\{Q\}^T = \langle P \ M_y \ M_x \ M_\omega \ 0 \ 0 \ T \ 0 \ 0 \ 0 \ 0 \ 0 \rangle \quad 3.51a$$

$$\text{and } \{q\} = \langle w'_c \ u''_s \ v''_s \ \phi'' \ 0 \ 0 \ \phi' \ 0 \ 0 \ 0 \ 0 \ 0 \rangle \quad 3.51b$$

where  $P$  = axial load;  $M_y, M_x$  = moments about the  $y$  and  $x$  axes passing through  $C$  and  $M_\omega$  denotes the warping moment (bi-moment) as defined by Vlasov (1961) and the  $T$ -torsional moment. Hence generalized forces are written in terms of stresses as:

$$\begin{bmatrix} p \\ M_y \\ M_x \\ M_\omega \\ 0 \\ 0 \\ T \\ 0 \\ 0 \\ 0 \\ 0 \\ 0 \end{bmatrix} = \sum_{k=1}^n \int [R]^T \begin{Bmatrix} \sigma_{zz} \\ \tau_{sz} \end{Bmatrix} dn ds \quad 3.52$$

or

$$= \sum_{k=1}^n \int [R]^T \begin{bmatrix} S_{11} & S_{16} \\ S_{61} & S_{66} \end{bmatrix} [R] dn ds \begin{Bmatrix} w'_c \\ v''_s \\ u''_s \\ \phi'' \\ 0 \\ 0 \\ \phi' \\ 0 \\ 0 \\ 0 \\ 0 \\ 0 \end{Bmatrix} \quad 3.53$$

$$\{Q\} = \begin{bmatrix} E_{11} & E_{12} & E_{13} & E_{14} & 0 & 0 & E_{17} & 0 & 0 & 0 & 0 \\ E_{21} & E_{22} & E_{23} & E_{24} & 0 & 0 & E_{27} & 0 & 0 & 0 & 0 \\ E_{31} & E_{32} & E_{33} & E_{34} & 0 & 0 & E_{37} & 0 & 0 & 0 & 0 \\ E_{41} & E_{42} & E_{43} & E_{44} & 0 & 0 & E_{47} & 0 & 0 & 0 & 0 \\ 0 & 0 & 0 & 0 & E_{55} & 0 & 0 & 0 & 0 & 0 & 0 \\ 0 & 0 & 0 & 0 & 0 & 0 & E_{66} & 0 & 0 & 0 & 0 \\ E_{71} & E_{72} & E_{73} & E_{74} & 0 & 0 & E_{77} & 0 & 0 & 0 & 0 \\ 0 & 0 & 0 & 0 & 0 & 0 & 0 & 0 & 0 & 0 & 0 \\ 0 & 0 & 0 & 0 & 0 & 0 & 0 & 0 & 0 & 0 & 0 \\ 0 & 0 & 0 & 0 & 0 & 0 & 0 & 0 & 0 & 0 & 0 \\ 0 & 0 & 0 & 0 & 0 & 0 & 0 & 0 & 0 & 0 & 0 \end{bmatrix} \begin{Bmatrix} w'_c \\ v''_s \\ u''_s \\ \phi'' \\ 0 \\ 0 \\ \phi' \\ 0 \\ 0 \\ 0 \\ 0 \end{Bmatrix}$$

or  $[E]\{\epsilon_r\}_L$  3.54

where  $E_{ij}$  is the mechanical stiffness of a thin-walled composite beam cross-section, which it is symmetric and defined by:

$$E_{11} = \int A_{11} ds \quad 3.55a$$

$$E_{12} = - \int (A_{11}x^* + B_{11} \cos \beta) ds \quad 3.55b$$

$$E_{13} = - \int (A_{11}y^* + B_{11} \sin \beta) ds \quad 3.55c$$

$$E_{14} = \int (A_{11}\bar{\omega} - B_{11}q) ds \quad 3.55d$$

$$E_{17} = -2 \int B_{16} ds + \delta_c \int A_{16} \psi ds + \int A_{11} \eta^* ds \quad 3.55e$$

$$E_{22} = \int (A_{11}x^{*2} + 2B_{11}x^*\cos \beta + D_{11}\cos^2 \beta) ds \quad 3.55f$$

$$E_{23} = \int (A_{11}x^*y^* + B_{11}(x^*\sin \beta + y^*\cos \beta) + D_{11}\sin \beta \cos \beta) ds \quad 3.55g$$

$$E_{24} = - \int (A_{11}\bar{\omega}x^* - B_{11}qx^* + B_{11}\bar{\omega}\cos \beta - D_{11}q\cos \beta) ds \quad 3.55h$$

$$E_{27} = 2 \int (B_{16}x^* + D_{16}\cos \beta) ds + \delta_c \int (A_{16}x^*\psi + B_{16}\psi \cos \beta) ds \quad 3.55i$$

$$E_{33} = \int (A_{11} y^{*2} + 2B_{11} y^* \sin \beta + D_{11} \sin^2 \beta) ds \quad 3.55j$$

$$E_{34} = - \int (A_{11} \bar{\omega} y^* - B_{11} q y^* + B_{11} \bar{\omega} \sin \beta - D_{11} q \sin \beta) ds \quad 3.55k$$

$$E_{37} = 2 \int (B_{16} y^* + D_{16} \sin \beta) ds + \delta_c \int (A_{16} y^* \psi + B_{16} \psi \sin \beta) ds \quad 3.55l$$

$$E_{44} = \int (A_{11} \bar{\omega}^2 - 2B_{11} q \bar{\omega} + D_{11} q^2) ds \quad 3.55m$$

$$E_{37} = -2 \int (B_{16} \bar{\omega} - D_{16} q) ds + \delta_c \int (A_{16} \bar{\omega} \psi - B_{16} \psi q) ds \quad 3.55n$$

$$E_{77} = 4 \int D_{66} ds + \delta_c \left[ \int (A_{66} \psi^2 - 4B_{66} \psi) ds \right] + \int A_{16} \eta^2 * ds \quad 3.55o$$

For the mechanical properties the reader may refer to the paper by Rajasekaran (2005a)  $A_{ij}$ ,  $B_{ij}$ ,  $D_{ij}$  matrices are extensional and coupling and bending stiffnesses respectively defined by (see Kaw 1997 and Rajasekaran *et al.* 2003)

$$A_{ij}, B_{ij}, D_{ij} = \int S_{ij}(1, n, n^2) dn \quad 3.56$$

and are explicitly given by

$$A_{ij} = \sum \int S_{ij} dn = \sum_{k=1}^n S_{ij}^k (Z_{k+1} - Z_k) \quad 3.57a$$

$$B_{ij} = \sum \int S_{ij} nds = \frac{1}{2} \sum_{k=1}^n S_{ij}^k (Z_{k+1}^2 - Z_k^2) \quad 3.57b$$

$$D_{ij} = \sum \int S_{ij} n^2 ds = \frac{1}{3} \sum_{k=1}^n S_{ij}^k (Z_{k+1}^3 - Z_k^3) \quad 3.57c$$

Knowing the stress resultants, one can solve for generalized strains and curvatures as:

$$\begin{bmatrix} w'_c \\ u''_s \\ v''_s \\ \phi'' \\ \phi' \end{bmatrix} = [E]^{-1} \begin{bmatrix} p \\ M_y \\ M_x \\ M_\omega \\ T \end{bmatrix} \quad 3.58$$

There is no point in making the  $[E]$  matrix uncoupled by choosing reference axes through mechanical centroid  $C$  and pole at mechanical shear centre  $S$ , since for nonprismatic beam the position of  $C$  and  $S$  changes from section to section. Hence, for prismatic beams displacements are specified at  $S$  and  $C$  whereas for nonprismatic beams they are referred at arbitrary reference point  $C$ .

The generalized stress resultants are given by:

$$\mu = \int [R]^T \begin{Bmatrix} \sigma_{xx} \\ \sigma_{xy} \end{Bmatrix} dA \quad 3.59$$

$$\text{where } \mu_1 = p = \int \sigma_{xx} dA; \mu_2 = M_y = - \int \sigma_{xx} (x^* + n \cos \beta) dA \quad 3.60a$$

$$\mu_3 = M_x = - \int \sigma_{xx} (y^* + n \sin \beta) dA \quad 3.60b$$

$$\mu_4 = M_\omega = \int \sigma_{xx} (\bar{\omega} - nq) dA \quad 3.60c$$

$$\mu_5 = -2 \int \sigma_{xx} x' dA \quad 3.60d$$

$$\mu_6 = -2 \int \sigma_{xx} y' dA \quad 3.60e$$

$$\mu_7 = \int \sigma_{xx} n^* dA + \int \sigma_{xy} \delta_c (\psi - 2n) dA \quad 3.60f$$

$$\mu_8 = M_\rho = \int \sigma_{xx} (x^{*2} + y^{*2}) dA \quad 3.60g$$

$$\mu_9 = 2 \int \sigma_{xx} x^* x' dA \quad 3.60h$$

$$\mu_{10} = 2 \int \sigma_{xx} y^* y' dA \quad 3.60i$$

$$\mu_{11} = -2 \int \sigma_{xy} n dA \quad 3.60j$$

### 3.7 Equations of equilibrium

#### 3.7.1 Total equilibrium equation

The principle of virtual work (virtual displacement) may be used to write the equilibrium requirements for any stress field (Fung 1965), neglecting the

body forces, expressing the internal virtual work as the product of associated component of Kirchhoff's stress tensor,  $\sigma$  and Green Lagrange strain tensor,  $\varepsilon$ , we get

$$\int \delta\varepsilon^T \sigma dv = \int_L \delta\varepsilon_r^T dz = \int_s \delta U^T T ds \quad 3.61$$

When the generalized strain  $\{\varepsilon_r\}$  is given by

$$\{\varepsilon_r\} = [[B]_L + [B]_Q] \bar{\phi} \quad 3.62a$$

$$\{\delta\varepsilon_r\} = ([B]_L + 2[B]_Q) \delta \bar{\phi} \quad 3.62b$$

and  $\{\delta^2\varepsilon_r\} = (2[dB]_Q) \delta \bar{\phi}$  3.62c

Considering initial deformations and initial stress,  $\mu$  can be written as

$$\mu = E(\varepsilon_r - \varepsilon_{ri}) + \sigma_{oi} \quad 3.63$$

where  $[E]$  is defined in Eq. (3.54),  $\varepsilon_{ri}$  is the generalized strain due to initial deformations and  $\sigma_{oi}$  is the initial stress resultant.

$$\int \delta U^T T ds = \int <\delta r_q> q dz + \sum <\delta r_Q> Q dz \quad 3.64$$

in which

$$(q) = (q_x \quad q_y \quad q_z \quad m_x \quad m_y \quad m_z \quad b) \quad 3.65a$$

$$(Q) = (Q_{xi} \quad Q_{yi} \quad Q_{zi} \quad M_{xi} \quad M_{yi} \quad M_{zi} \quad B_i) \quad 3.65b$$

and

$$r = r_L + r_Q \quad 3.66$$

Where  $r_L$  and  $r_Q$  denote the linear and nonlinear parts of the displacements respectively can be identified from Eq. (3.13) and written as

$$r = r_L + r_Q = (A_L + A_Q)\phi \quad 3.67$$

$$\delta_r = (A_L + 2A_Q)\delta\phi \quad 3.68$$

where  $[A_L]$  and  $[A_Q]$  are written similarly to  $[B_L]$  and  $[B_Q]$ . Hence Eq. (3.61) may be written as

$$\begin{aligned} \int \delta\phi^T (B_L^T + 2B_Q^T) \{[E](B_L + B_Q) \bar{\phi} - [E](\varepsilon_{ri}) + \sigma_{oi}\} dz \\ = \int \delta\phi^T (A_L^T + 2A_Q^T) q dz + \sum (\delta\bar{\phi}_k) (A_{Lk}^T + 2A_{Qk}^T) Q_k \end{aligned} \quad 3.69$$

### 3.7.2 Incremental equilibrium equation

Considering Eq. (3.61) and differentiating once again we get

$$\int \delta \varepsilon_r^T \Delta \mu dz + \delta^2 \varepsilon_r^T \mu dz = \int \delta^2 U^T ds \quad 3.70$$

$$\begin{aligned} &= \int \delta \phi^T [ (B_L^T + 2B_Q^T) ] [E] (B_L + 2B_Q) \Delta \bar{\phi} dz + \delta \phi^T 2dB_Q \mu dz \\ &= \int \delta r_q^T \Delta q dz + \delta^2 r_q^T q dz + \sum \delta r_{Qk}^T \Delta Q_k + \sum \delta^2 r_{Qk} Q_k \end{aligned} \quad 3.71$$

Substituting for

$$2dB_Q^T \mu = M_\mu \Delta \bar{\phi} \quad 3.72a$$

$$2dA_Q^T Q = M_Q \Delta \bar{\phi} \quad 3.72b$$

$$2dA_q^T q = M_q \Delta \bar{\phi} \quad 3.72c$$

where  $M_\mu$ ,  $M_Q$  and  $M_q$  are symmetric matrices. For example  $M_\mu$  is given by

$$\begin{aligned} M_\mu(2, 2) &= \mu_1; M_\mu(2, 7) = -\mu_{12}/2; M_\mu(2, 8) = -\mu_{11}/2; M_\mu(2, 12) = \mu_1 ey \\ M_\mu(3, 6) &= \mu_{12}/2; M_\mu(3, 11) = -\mu_3; M_\mu(4, 6) = \mu_4/2; M_\mu(6, 6) = \mu_1 \\ M_\mu(6, 12) &= -\mu_1 ex; M_\mu(7, 11) = \mu_2; M_\mu(11, 11) = \mu_{11} \\ M_\mu(11, 12) &= \mu_{10}/2 + \mu_6 ey/2 + \mu_5 ex/2 \\ M_\mu(12, 11) &= \mu_{11}(ex^2 + ey^2) + 2\mu_2 ex + 2\mu_3 ey + \mu_8 \end{aligned} \quad 3.73$$

### 3.7.3 Dynamic equations of equilibrium

The equations of motion for an  $N$  degrees of freedom system can be derived directly from the variational statement of dynamics, namely Hamilton's principle, and expressed as

$$\delta L = \int_{t1}^{t2} \delta(T - \Pi) dt + \int_{t1}^{t2} \delta W_{nc} dt = 0 \quad 3.74$$

where  $T$  = kinetic energy,  $\Pi$  = total potential including both strain energy and potential of any conservative external forces,  $W_{nc}$  = Work done by non-conservative forces acting on system including damping and any arbitrary external loads.

By taking variation taken during time interval and assuming sine functions for displacements we get

$$(K - K_G) \Delta \bar{d} = \rho p^2 \bar{M} \Delta \bar{d} \quad 3.75$$

where  $[K]$  and  $[K_G]$  are the flexural and geometric stiffness matrices given by Eq. (3.84a) and (3.84b) respectively. The mass matrix is given by

$$\bar{M} = [TR]^T \left( \int_L N_r^T M N_r dz \right) [TR] \quad 3.76$$

and the  $[TR]$  matrix is given in Eq. (3.81), The  $[N_r]$  matrix is defined as

$$\begin{aligned} \bar{\phi} &= N_r \bar{r} \\ \bar{r} &= < \bar{u}_s^T \bar{v}_s^T \bar{w}^T \bar{\phi}^T > \end{aligned} \quad 3.77$$

and the elements of  $M$  are given by

$$\left[ \begin{array}{lll} M_{1,1} = A & M_{5,5} = A & M_{9,12} = S_w \\ M_{1,11} = -A\bar{y} - Ae_y & M_{5,11} = A\bar{x} - Ae_x & \\ M_{2,2} = I_{yy} & M_{6,6} = I_{xx} & M_{12,12} = I_\omega \\ M_{2,6} = I_{xy} & M_{6,9} = -A\bar{y} & M_{2,9} = -A\bar{x} \\ M_{6,12} = S_{\omega y} & M_{2,12} = S_{\omega y} & M_{9,9} = A \end{array} \right] \quad 3.78$$

$$M_{11,11} = I_{xx} - 2A\bar{y}e_y + Ae_y^2 + I_y - 2A\bar{x}e_x + Ae_x^2$$

$\lambda = p^2$  (eigenvalue is the square of the natural frequency) and  $\bar{M}$  is the consistent mass matrix since same displacement function is used to formulate the stiffness and mass matrices. Hence the potential and kinetic energies have the same basis.

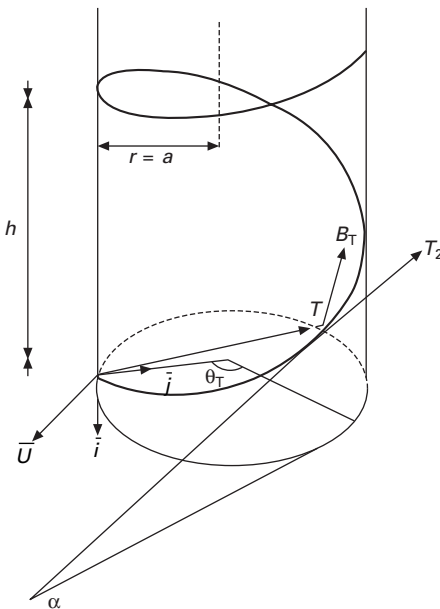
## 3.8 Finite element beam model

### 3.8.1 Derivation of secant and tangent stiffness matrices

The element used in this chapter is a three-dimensional nonprismatic straight element with seven degrees of freedom (three displacements,  $u$ ,  $v$ ,  $w$ , three rotations,  $\theta_x$ ,  $\theta_y$  and  $\theta_z = \phi$ , and the rate of twist  $\dot{\phi}$  at each node).  $u_s$ ,  $v_s$ , and  $\phi$  are written in terms of nodal displacements using well-known cubic shape functions and the axial displacement  $w$  is written in terms of nodal displacements using linear shape function and the details of finite element formulation; the reader may refer to the paper by the author (Rajasekaran, 1994a).

### 3.8.2 Transformation matrix in spatial girder

The spatial girder can be analysed using straight beam elements. The helicoids are shown in Fig. 3.9. A global reference coordinate system is established at



3.9 Helicoidal girder.

the point  $O$ . The relation between axes of the straight beam element coordinate system with respect to global system is given as:

$$\begin{Bmatrix} \bar{e}_1 \\ \bar{e}_2 \\ \bar{e}_3 \end{Bmatrix} = \begin{bmatrix} a_{11} & a_{12} & a_{13} \\ a_{21} & a_{22} & a_{23} \\ a_{31} & a_{32} & a_{33} \end{bmatrix} \begin{Bmatrix} \bar{i} \\ \bar{j} \\ \bar{k} \end{Bmatrix} \quad 3.79$$

where  $a_{11}, a_{12}\dots$  are given in terms of the ratios of the helicoids  $\alpha$  and which are the angles subtended in plan of points  $I$  and  $J$  of the element. Using the transformation given by Baki and Shukair (1973), the relationship between the  $\bar{i}, \bar{j}, \bar{k}$  system with respect to the helicoid system  $\bar{B}, N, \bar{T}$  is:

$$\begin{Bmatrix} \bar{e}_1 \\ \bar{e}_2 \\ \bar{e}_3 \end{Bmatrix} = \begin{bmatrix} a_{11} & a_{12} & a_{13} \\ a_{21} & a_{22} & a_{23} \\ a_{31} & a_{32} & a_{33} \end{bmatrix} \begin{bmatrix} \cos \alpha & 0 & -\sin \alpha \\ \sin \alpha \sin \theta & \cos \theta & \cos \alpha \sin \theta \\ \sin \alpha \cos \theta & -\sin \theta & \cos \alpha \cos \theta \end{bmatrix} \begin{Bmatrix} \bar{B} \\ \bar{N} \\ \bar{T} \end{Bmatrix} \quad 3.80$$

Hence at two nodes  $I, J$  the transformation matrices are given as

$$\begin{Bmatrix} \bar{e}_1 \\ \bar{e}_2 \\ \bar{e}_3 \end{Bmatrix}_I = [R]_I \begin{Bmatrix} \bar{B} \\ \bar{N} \\ \bar{T} \end{Bmatrix}_I \quad 3.81a$$

$$\begin{Bmatrix} \bar{e}_1 \\ \bar{e}_2 \\ \bar{e}_3 \end{Bmatrix}_J = [R]_J \begin{Bmatrix} \bar{B} \\ \bar{N} \\ \bar{T} \end{Bmatrix}_J \quad 3.81b$$

Combining the transformation matrix  $[TR]$  yields

$$[TR] = \begin{bmatrix} [R]_I & \\ & [R]_J \end{bmatrix} \quad 3.82a$$

Hence the stiffness matrix of the helicoidal elements is given as

$$[K]_{\text{helicoidal}} = [TR]^T [K]_{\text{straight}} [TR] \quad 3.82b$$

For more details the reader can refer to Anandavalli (1993). For the vibration problem, we get eigenvalue problem as

$$K \Delta \bar{d} = p M \Delta \bar{d} \quad 3.83$$

where  $p$  is the square of the natural frequency.

### 3.8.3 Linear behaviour theory

The simplest approximation to the behaviour of the thin-walled member is given by the linear theory according to which the deformations ( $u_s, v_s, w, \phi$ ) are always proportional to loads:

$$K = [TR]^T \left( \int L N_r^T (B_L^T E B_L) dz \right) [TR] \quad 3.84a$$

and the geometric stiffness  $[K_G]$  is given by

$$\begin{aligned} \bar{K}_G = -T^T \left[ \int L N_r^T M_\mu N_r dz \right] T + T^T \left[ \int L N_r^T M_q N_r dz \right] T \\ + \sum T_k^T N_{rk}^T M_Q N_{rk} T_k \end{aligned} \quad 3.84b$$

As already seen,  $T$  denotes the transformation matrix between local coordinates of the elements to the global coordinates. The warping degrees of freedom remains unchanged since the transformation of warping between members are joint dependent (Vacharazittiphan and Trahair 1974) and cannot be generalized. The type of joint, if specified, could be incorporated by putting an equivalent stiffness.

## 3.9 Numerical integration for finding properties and stress resultants at a cross-section

The closed form integration for the computation of mechanical properties of any thin-walled open or closed composite cross-section of a beam is difficult.

Figure 3.10 shows a cross-section consisting of four elements and five nodes. Any one typical element is considered and integration with respect to thickness direction is carried out to find axial coupled and bending stiffness properties. Then the integral is carried out along the contour of the cross-section to find the mechanical properties and stress resultants of the cross-section. Hence numerical integration using Gaussian quadrature is used to find the properties and stiffness matrices. For horizontal curved beams the radius of curvature of the beam is accounted for in the denominator of the integral to calculate the properties in the form of  $(1-y/R)$ . The reader may refer, for details, to the paper by the author (Rajasekaran 1994a).

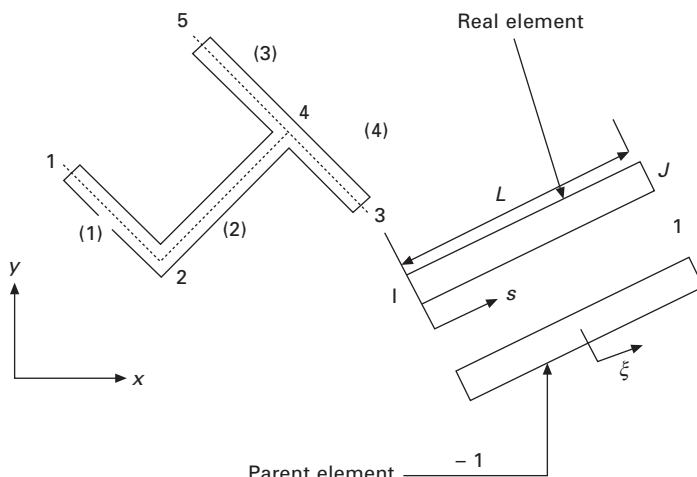
### 3.9.1 Computer program

The FORTRAN computer programs FUNGEN and CLPROP may be used to compute geometric properties and stress resultants. HYDYN may be used to compute stiffness and mass matrices using the numerical integration of Gaussian quadrature. Using the Jacobi iteration method, the classical eigenvalue problem is solved for natural frequency and the mode shapes for composite spatial nonprismatic member of generic cross-section.

## 3.10 Alternative formulation using plate elements (anon, 1995)

### 3.10.1 Strain in terms of displacement

The analysis of layered curved/straight panels and shells is generally carried out by employing doubly curved degenerated shell elements. For completeness



3.10 Cross-section of thin-walled beam.

the formulation is given and the reader may refer to Bathe (1996) for details. The coordinates  $\bar{X}, \bar{Y}, \bar{Z}$  of a point anywhere in a shell element are expressed as (see Fig. 3.11):

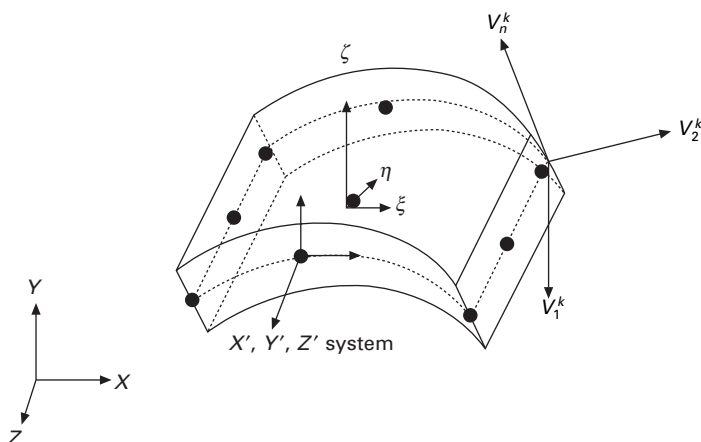
$$\begin{aligned}\bar{X} &= \sum N_i X_i + \frac{\zeta}{2} \sum t_i N_i V_{nX}^i \\ \bar{Y} &= \sum N_i Y_i + \frac{\zeta}{2} \sum t_i N_i V_{nY}^i \\ \bar{Z} &= \sum N_i Z_i + \frac{\zeta}{2} \sum t_i N_i V_{nZ}^i\end{aligned}\quad 3.85$$

where  $N_i$  are the shape functions,  $t_i$ , nodal thickness and the summation is over a number of nodes per element. The normal vector  $V_n$  at a point on the mid surface  $\zeta = 0$  is computed by taking the cross-product of the first two rows  $J_1, J_2$  of the Jacobian matrix given by

$$[J] = \begin{bmatrix} \frac{\partial X}{\partial \xi} & \frac{\partial Y}{\partial \xi} & \frac{\partial Z}{\partial \xi} \\ \frac{\partial X}{\partial \eta} & \frac{\partial Y}{\partial \eta} & \frac{\partial Z}{\partial \eta} \\ \frac{\partial X}{\partial \zeta} & \frac{\partial Y}{\partial \zeta} & \frac{\partial Z}{\partial \zeta} \end{bmatrix} \quad 3.86$$

and  $\bar{V}_n$  is given by

$$\bar{V}_n = \frac{J_1 \times J_2}{|J_1 \times J_2|} \quad [3.87]$$



3.11 Shell mid-surface.

Subtracting the  $X, Y, Z$  coordinates of any point in the undeformed configuration from the deformed configuration we obtain the displacements (for details, refer to Bathe 1996):

$$\begin{aligned}\bar{u} &= \sum N_i u_i + \frac{\zeta}{2} \sum t_i N_i (-V_{nY}^i \theta_{Zi} + V_{nZ}^i \theta_{Yi}) \\ \bar{v} &= \sum N_i v_i + \frac{\zeta}{2} \sum t_i N_i (-V_{nZ}^i \theta_{Xi} + V_{nX}^i \theta_{Zi}) \\ \bar{w} &= \sum N_i w_i + \frac{\zeta}{2} \sum t_i N_i (-V_{nX}^i \theta_{Yi} + V_{nY}^i \theta_{Xi})\end{aligned}\quad 3.88$$

The local coordinate system ( $X', Y', Z'$ ) is constructed as explained in Bathe (1996). In the local coordinate system,  $\varepsilon_{Z'}$  is neglected as only first-order shear deformation theory is employed. Now the strain in the local system can be related to the strain in the global system as

$$\{\varepsilon'\} = [T]\{\varepsilon\} \quad 3.89$$

The global strain vector may be written as

$$\langle \varepsilon \rangle = \langle \frac{\partial u}{\partial X} \frac{\partial v}{\partial Y} \frac{\partial w}{\partial Z} \left( \frac{\partial u}{\partial Y} + \frac{\partial v}{\partial X} \right) \left( \frac{\partial u}{\partial Z} + \frac{\partial w}{\partial X} \right) \left( \frac{\partial v}{\partial Z} + \frac{\partial w}{\partial Y} \right) \rangle \quad 3.90$$

The global strain vector may be written in another form in terms of  $\langle \bar{\varepsilon} \rangle$  as

$$\langle \bar{\varepsilon} \rangle = \langle \frac{\partial u}{\partial X} \frac{\partial u}{\partial Y} \frac{\partial u}{\partial Z} \frac{\partial v}{\partial X} \frac{\partial v}{\partial Y} \frac{\partial v}{\partial Z} \frac{\partial w}{\partial X} \frac{\partial w}{\partial Y} \frac{\partial w}{\partial Z} \rangle \quad 3.91$$

Hence  $\langle \varepsilon \rangle$  may be written in terms of  $\langle \bar{\varepsilon} \rangle$  as

$$\{\varepsilon\} = [L] \{\bar{\varepsilon}\} \quad 3.92$$

Hence  $\{\bar{\varepsilon}\}$  is written in terms of  $\{\varepsilon_n\}$  as

$$\{\bar{\varepsilon}\} = [J^*]\{\varepsilon_n\} \quad 3.93$$

where

$$[J^*] = \begin{bmatrix} [J]^{-1} & [0] & [0] \\ [0] & [J]^{-1} & [0] \\ [0] & [0] & [J]^{-1} \end{bmatrix} \quad 3.94$$

Substituting for displacements in  $\{\varepsilon_n\}$  we can write in terms of nodal displacements as

$$\{\varepsilon_n\} = \{[S_0] + \zeta[S_1]\} \{r\} \quad 3.95$$

where  $r$  represents the nodal displacements.

Combining Eqs 3.83, 3.88 and 3.93 we can write strains in local system in terms of nodal displacements of global system as

$$\{\varepsilon'\} = [T][L][J^*]\{[S_0] + \zeta[S_1]\} (r) \quad 3.96a$$

or

$$\{\varepsilon'\} = \{[B_0] + \zeta[B_1]\} \{\underline{r}\} \quad 3.96b$$

### 3.10.2 Stiffness matrix for composite lamina

Consider a composite lamina as shown in Fig. 3.8. The fibres are oriented at an angle of  $\theta$  with respect to the  $X'$  axis. The constitutive properties of the composite lamina with respect to the  $LT$  system is given by

$$\{\sigma\}_{LT} = [Q] \{\varepsilon\}_{LT} \quad 3.97$$

where  $[Q]$  is the constitutive matrix with respect to the  $LT$  system. The stresses with respect to the  $X' Y'$  system can be written as

$$\{\sigma'\} = [R]\{\sigma\}_{LT} \quad 3.98$$

and the strain with respect to the  $LT$  system can be obtained with respect to strain in the  $X' Y'$  system as

$$\{\varepsilon\}_{LT} = [R]^T \{\varepsilon'\} \quad 3.99$$

Substituting Eqs (3.97) and (3.99) in Eq. (3.98) we get

$$\{\sigma'\} = [R][Q][R]^T \{\varepsilon'\} = [\bar{Q}] \{\varepsilon'\} \quad 3.100$$

where  $[\bar{Q}]$  represents the constitutive matrix for a composite lamina wherein the properties have been transformed from material principal to the local coordinate system.

The strain energy for a composite plate is written as

$$U = \frac{1}{2} \sum_1^{n_{\text{layer}}} \int_V \{\varepsilon'\}^T [\bar{Q}] \{\varepsilon'\} dv \quad 3.101$$

Substituting Eq. (3.96b) in Eq. (3.101) we get

$$U = \frac{1}{2} \{\underline{r}\}^T \sum \int ([B_0] + \zeta[B_1])^T [\bar{Q}] ([B_0] + \zeta[B_1]) dv \{\underline{r}\} \quad 3.102$$

$dv = dt \times dA$  and carrying out the integration in thickness direction we get

$$U = \frac{1}{2} \{\underline{r}\}^T [k] \{\underline{r}\} \quad 3.103$$

Considering the variation of strain energy with respect to nodal displacements we get  $[k]$  in Eq. (3.103) as

$$[k] = \int \{[B_0]^T [A] [B_0] + [B_0]^T [B] [B_1] + [B_1]^T [B] [B_0] + [B_1]^T [D] [B_1]\} dA \quad 3.104$$

where

$$[A] = \sum_{h_k}^{h_{k+1}} \int [\bar{Q}] dt = \sum_{k=1}^{n \text{ layer}} [\bar{Q}](h_{k+1} - h_k) \quad 3.105a$$

$$[B] = \sum \int_{h_k}^{h_{k+1}} [\bar{Q}] \varsigma dt = \frac{1}{2} \sum_{n=1}^{n \text{ layer}} [\bar{Q}](h_{k+1}^2 - h_k^2) \quad 3.105b$$

$$[D] = \sum_{h_k}^{h_{k+1}} \int [\bar{Q}] \varsigma^2 dt = \frac{1}{3} \sum_{n=1}^{n \text{ layer}} [\bar{Q}](h_{k+1}^3 - h_k^3) \quad 3.105c$$

where  $h_k$  is the normalized height of the  $k$ th layer from the bottom surface.  $[A]$ ,  $[B]$  and  $[D]$  are the axial, coupled and bending stiffness matrices of the composite plate respectively. To arrive at the stiffness matrix numerical integration is carried out using Gaussian quadrature. In the case of coplanar elements the assembled stiffness matrix will contain a large number of zero diagonals corresponding to  $\theta_X$ ,  $\theta_Y$ ,  $\theta_Z$  depending on the plane of the plate. This makes global stiffness matrix singular or ill conditioned. To avoid this problem, a small stiffness of 1/1000th smallest diagonal is placed at the corresponding locations.

### 3.10.3 Mass matrix

The kinetic energy is written as

$$Y = \frac{1}{2} \int \rho (\bar{u}_{,t}^2 + \bar{v}_{,t}^2 + \bar{w}_{,t}^2) dv \quad 3.106$$

where  $,t$  denotes differentiation with respect to time ' $t$ '.

Using kinematics Eq. 3.31 for a layered plate/shell

$$T = -\frac{\omega^2}{2} \int \{r\}^T \{[R_0]^T + \varsigma [R_1]^T\} \rho \{[R_0] + \varsigma [R_1]\} dv \quad 3.107$$

where

$$[R_0] = \begin{bmatrix} N_i & 0 & 0 & 0 & 0 & 0 \\ 0 & N_i & 0 & 0 & 0 & 0 \\ 0 & 0 & N_i & 0 & 0 & 0 \end{bmatrix} \quad 3.108$$

and

$$[R_1] = \frac{1}{2} \begin{bmatrix} 0 & 0 & 0 & 0 & t_i V_{nZ} N_i & -t_i V_{nY} N_i \\ 0 & 0 & 0 & t_i V_{nZ} N_i & 0 & t_i V_{nX} N_i \\ 0 & 0 & 0 & t_i V_{nY} N_i & -t_i V_{nX} N_i & 0 \end{bmatrix} \quad 3.109$$

The variation of kinetic energy leads to

$$-\omega^2 [M]\{\underline{r}\} = -\omega^2 \left\{ \int \rho [R_0]^T [R_0] + \rho \zeta ([R_0]^T [R_1] + [R_1]^T [R_0]) + \rho \zeta^2 [R_1]^T [R_1] d\nu \right\} \quad 3.110$$

Once again integration is carried out in the thickness direction as shown below.

Denoting

$$R = \int_{h_k}^{h_{k+1}} \rho d\zeta = \sum_{i=1}^{NL} \rho_i (h_{k+1} - h_k) \quad 3.111a$$

$$S = \int_{h_k}^{h_{k+1}} \rho \zeta d\zeta = \frac{1}{2} \sum_{i=1}^{NL} \rho_i (h_{k+1}^2 - h_k^2) \quad 3.111b$$

$$I = \int_{h_k}^{h_{k+1}} \rho \zeta^2 d\zeta = \frac{1}{3} \sum_{i=1}^{NL} \rho_i (h_{k+1}^3 - h_k^3) \quad 3.111c$$

Substituting Eq. (3.111) in Eq. (3.110), we get

$$[M] = \int \{ R [R_0]^T [R_0] + S ([R_0]^Y [R_1] + [R_1]^T [R_0]) + I [R_1]^T [R_1] \} dA \quad 3.112$$

## 3.11 Numerical examples

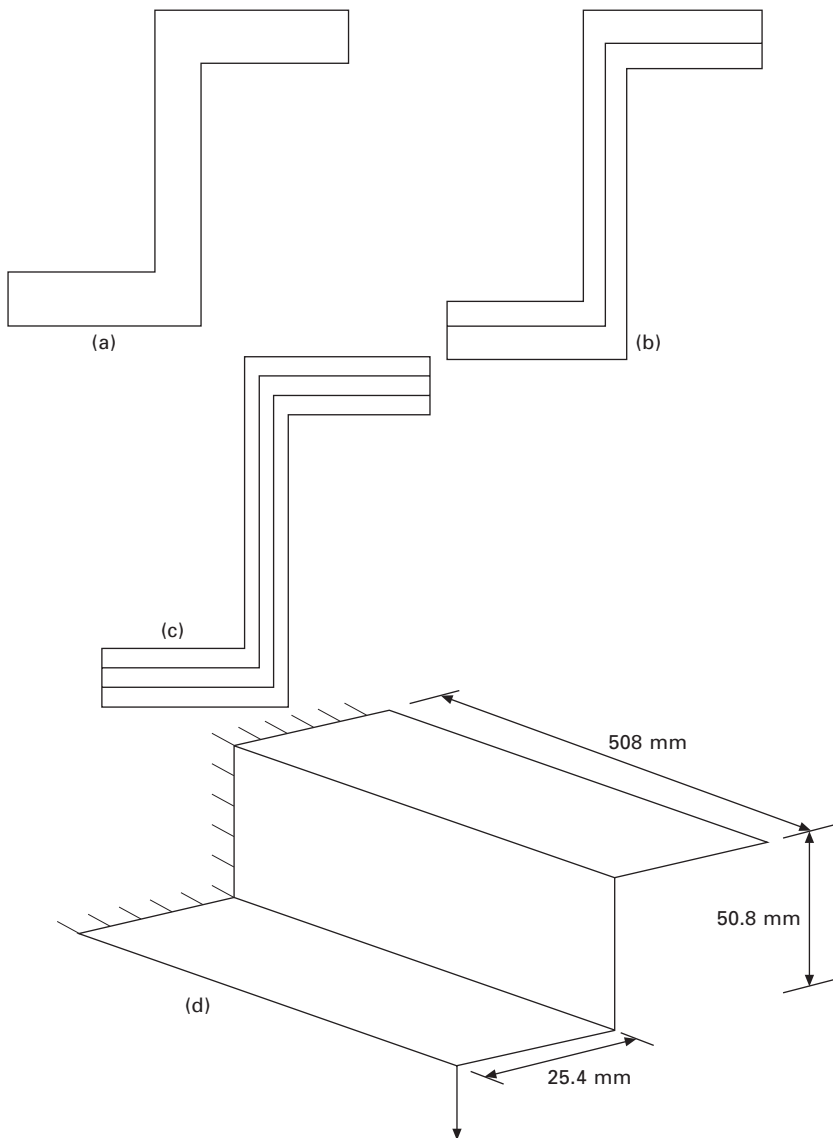
### 3.11.1 Example 1

A straight cantilever beam used by Oden (1967) made from boron epoxy is subjected to load as shown in Fig. 3.12(d). Three types of analyses have been performed:

- 1 single layer  $0^\circ$  composite (Fig. 3.12a)
- 2 two layer  $45^\circ/-45^\circ$  composite (Fig. 3.12b)
- 3 three layer  $0^\circ/45^\circ/0^\circ$  composite (Fig. 3.12c)

The properties of boron epoxy are  $E_L = 206.8$  GPa;  $E_T = 103.4$  GPa;  $\nu_{LT} = 0.3$ ;  $G_{LT} = 51.7$  GPa. (The wall thickness is assumed to be 3.175 mm.)

The results of the analysis are presented as shown in Table 3.1 and compared with FEAST-C, Oden (1967) and Gupta *et al.* (1985). FEAST-C is the package for Finite Element Analysis of Structures – Composites developed by Vikram Sarabhai Space Centre VSSC, Trivandrum in 1995. The beam is idealized with four elements and the results obtained by the beam element compare very well with the results obtained by the other investigators.



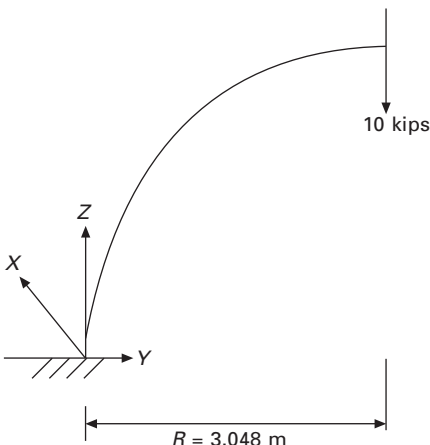
3.12 (a)  $0^\circ$  composite. (b)  $45^\circ/-45^\circ$  composite. (c)  $0^\circ/45^\circ/0^\circ$  composite. (d) Cantilever beam.

### 3.11.2 Example 2

A  $90^\circ$  curved beam with circular arc fixed at one end and free at the other end ( $R = 3.048$  m (10 feet)) is subjected to force in  $Y$  direction as shown in Fig. 3.13. Static analysis is performed using four element approximation. The results of the analysis are shown in Table 3.2 and compared with Palani

Table 3.1 Comparison of tip deflection of beam model with FEAST-C (Example 1)

Fibre angles	Analysis	$U$ (mm)	$V$ (mm)	$W$ (mm)	Rotation about $Y$	Twist
0°	This paper	0.023	0.0147	$0.34 \times 10^{-3}$	$0.435 \times 10^{-4}$	$0.569 \times 10^{-3}$
	FEAST-C	0.0216	0.0156	$0.24 \times 10^{-3}$	$0.454 \times 10^{-4}$	$0.554 \times 10^{-3}$
	Oden (1967)	0.0215	0.0144	0	$0.427 \times 10^{-4}$	$0.567 \times 10^{-3}$
	Gupta <i>et al.</i> (1985)	0.0215	0.0144	0	$0.426 \times 10^{-4}$	$0.566 \times 10^{-3}$
45°/-45°	This paper	0.0214	0.0303	$0.498 \times 10^{-3}$	$0.632 \times 10^{-4}$	$0.548 \times 10^{-3}$
	FEAST-C	0.0236	0.0341	$0.366 \times 10^{-3}$	$0.812 \times 10^{-4}$	$0.582 \times 10^{-3}$
	Oden (1967)	0.021	0.0312	0	$0.62 \times 10^{-4}$	$0.541 \times 10^{-3}$
	Gupta <i>et al.</i> (1985)	0.0209	0.0312	0	$0.619 \times 10^{-4}$	$0.564 \times 10^{-3}$
0°/45°/0°	This paper	0.0164	0.0227	$0.383 \times 10^{-3}$	$0.485 \times 10^{-4}$	$0.588 \times 10^{-3}$
	FEAST-C	0.01766	0.0247	$0.2452 \times 10^{-3}$	$0.544 \times 10^{-4}$	$0.5779 \times 10^{-3}$
	Oden (1967)	0.0162	0.024	0	$0.477 \times 10^{-4}$	$0.585 \times 10^{-3}$
	Gupta <i>et al.</i> (1985)	0.0161	0.0239	0	$0.475 \times 10^{-4}$	$0.584 \times 10^{-3}$



3.13 Circular beam.

Table 3.2 Free end deflection and fixed end stress resultants (Example 2)

Model	$V$	$W$	Rotation	$F_Y$	$F_X$	$M_X$
Present study	0.2023	0.1321	0.026	0	-10.0	100.0
Palani and Rajasekaran (1992)	0.2185	0.1389	0.0278	0	-10.0	100.0

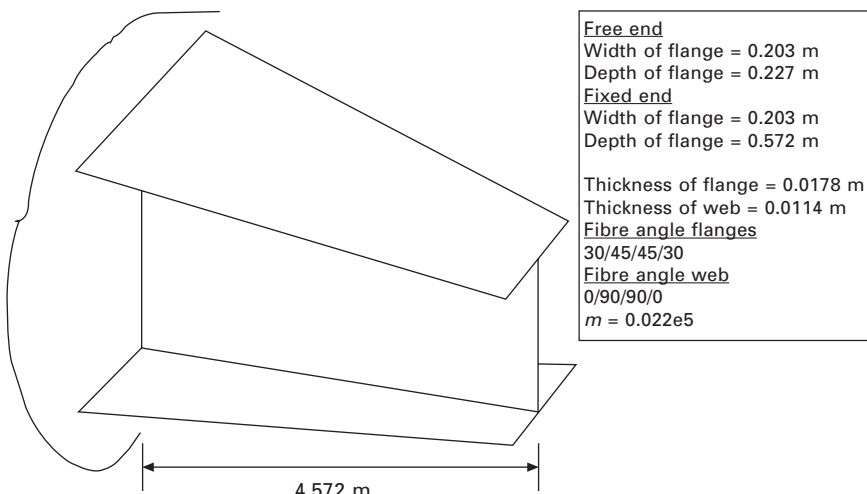
and Rajasekaran (1992). The comparison is quite good. The properties of the section are  $E = 20.684 \text{ GPa}$  (432 000 kips/sq ft);  $G = 98.6189 \text{ GPa}$  (180 000 kips/sq ft);  $I_{xx} = I_{yy} = 7.1896 \times 10^{-4} \text{ m}^4$  (0.0833 ft<sup>4</sup>);  $A = 0.092 \text{ m}^2$  (1 sq ft);  $J = 1.2135 \times 10^{-4} \text{ m}^4$  (0.1406 ft<sup>4</sup>);  $I_\omega = 0$ .

### 3.11.3 Example 3

Free vibration analysis is performed for a simply supported wide flange beam of span 8 m and the natural frequencies for vibration in the  $y$  direction,  $x$  direction and axial vibration are obtained as 5570 rad/s, 1403 rad/s and 11018 rad/s as against the closed form solution of 5642 rad/s, 1414 rad/s and 9395 rad/s.

### 3.11.4 Example 4

Free vibration of the nonprismatic composite beam of graphite epoxy shown in Fig. 3.14 was performed. The dimensions and the cross-section are shown in Fig. 3.14. The natural frequency of vibration is obtained as 49.6 rad/s both for thin-walled open and closed sections. If the beam is made up of isotropic material, instead of graphite epoxy, with  $E = 206.8 \text{ GPa}$ , mass density of



3.14 Free vibration of nonprismatic cantilever beam.

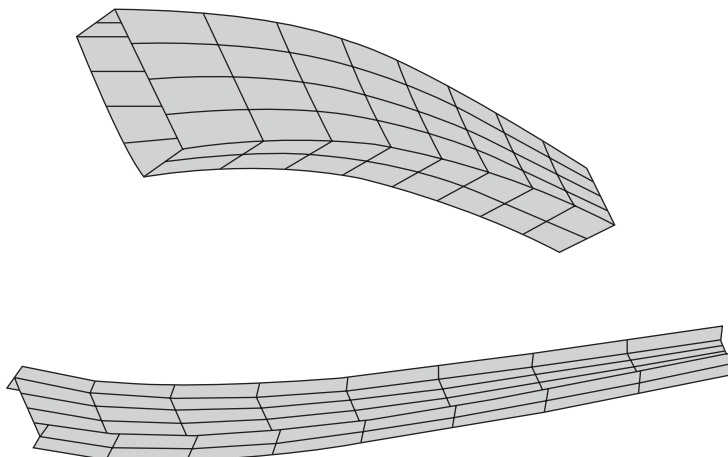
7997 kg m and Poissson ratio of 0.33, the natural frequency obtained using COMPOPT is 43.5 rad/s as compared with 42.0 obtained by Wekezer (1989). But the values obtained by FEAST-C are 106.36 rad/s both for open and closed sections and 82.76 rad/s for steel beam. The mode shapes are shown in Fig. 3.15.

### 3.11.5 Example 5

Free vibration analysis is performed on a curved beam shown in Fig. 3.16 with the fibre (graphite) angles  $30^\circ/45^\circ/45^\circ/30^\circ$  in the flanges and  $0^\circ/90^\circ/90^\circ/0^\circ$  in the web with a layer thickness of 0.000 389 m with a mass density of 2200 kg m. The natural fundamental frequency of vibration is  $\sqrt{108} = 10.392$  rad/s as compared with  $\sqrt{114} = 10.688$  rad/s obtained in FEAST-C. The mode shape is also shown in Fig. 3.16 and in Table 3.3.

## 3.12 Conclusions

Equations for tapered thin-walled spatial composite beams of generic cross-section have been formulated. The displacements are defined with respect to any reference point not necessarily at shear centre and centroid since the shear centre and centroid are the functions of longitudinal axis. Nonlinear strain displacement relation is obtained, using the membrane theory of shells through which the effect of tapering is considered. The section properties, stress resultants, flexural stiffness, geometric stiffness and mass matrices are computed using the numerical integration of Gaussian quadrature.



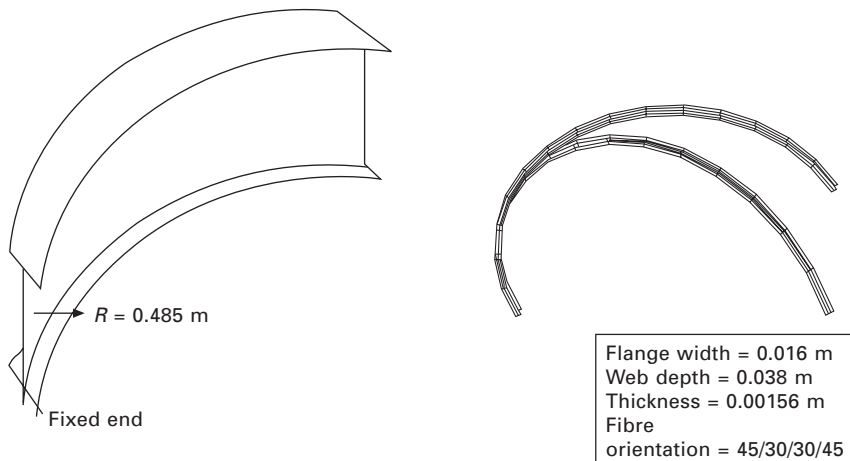
3.15 Mode shapes for cantilever beam.

Table 3.3 Mode shape for Example 5 (semicircular beam)

Node	<i>u</i>	<i>v</i>	<i>w</i>	Twist	<i>x</i> -rotn	<i>y</i> -rotn	Change of twist
1	0	0	0	0	0	0	0
2	0.0088	0	0	-2.2	0.96	0	-7.6
3	0.663	0	0	-2.86	3.1	0	-3.76
4	2.105	0	0	-0.506	4.53	0	-0.896
5	3.76	0	0	2.73	3.6	0	-0.12

The principle of virtual work utilizing the total Lagrangian concept is used to obtain nonlinear equilibrium and incremental equilibrium equations. In all the problems, the beam is idealized with only four elements. An alternative formulation of solving composite beam using degenerated plate/shell element as given in general purpose program FEAST-C has also been discussed. If packages such as FEAST-C are used, the beam is idealized with plate elements and hence the degrees of freedom increase, whereas in beam element at every node there are only seven degrees of freedom and hence the size of the equations for equilibrium or eigenvalue solution is substantially reduced.

The validity, adequacy and accuracy of the theory have been verified by many numerical examples through comparisons obtained by other investigators or solved by using a general purpose package such as FEAST-C. The cross-sectional properties with respect to any reference axes can be obtained for any generic section consisting of plies of symmetrical/antisymmetrical/unsymmetrical orientation of fibres. Numerical examples are solved for free vibration problems to find the natural frequency of nonprismatic spatial



3.16 Mode shape of cantilever semicircular beam.

girder of composite open/closed generic section. However, local buckling cannot be investigated using the beam formulation although this is possible in plate/shell formulation; in practice one uses compact sections and hence this may not be the critical issue. The author (Rajasekaran, 2005a,b) combined HYDYN with evolution strategies to obtain lay-up for optimal design of nonprismatic composite spatial thin-walled beams of generic section (open/closed) subjected to deflection, buckling and frequency constraints.

### 3.13 References

- Anandavalli, P.L. (1993). 'Static and dynamic instability analysis of nonprismatic thin-walled spatial members of generic open section,' *M. Eng. Thesis*, Bharathiar University, Coimbatore, India.
- Andrade, A. and Camotim, D. (2005). 'Lateral torsional buckling of singly symmetric tapered beams, theory and applications,' *J. Engng Mech. ASCE*, **131**(6), 586–597.
- Anon (1995). 'FEAST-C, User Manual, SEG, SDS Group, ISRO,' Vikram Sarabai Space Centre (VSSC), Trivandrum.
- Baki, A.A. and Shukair, A. (1973). 'Continuous helicoidal girders,' *J. Struct. Div., ASCE*, **99**(10), 2183–2203.
- Bathe, K.J. (1996). *Finite Element Procedures*, Prentice-Hall of India, New Delhi.
- Bauchau, O.A. (1985). 'A beam theory for anisotropic materials,' *J. Appl. Mech.*, **52**(2), 416–422.
- Bauchau, O.A. and Hung, C.H. (1987). 'Finite element approach to rotor blade modeling,' *J. Amer. Helicopter Soc.*, **32**(1), 60–67.
- Bauld, N.R. and Tzeng, L.S. (1984). 'A Vlasov theory for fiber reinforced beams with thin-walled open cross sections,' *Int. J. Solids Struct.*, **20**(3), 277–297.
- Bhaskar, K. and Librescu, L.A. (1995). 'Geometrically non-linear theory for laminated anisotropic thin-walled beams,' *Int. J. Engng Sci.*, **33**(9), 1331–1344.

- Bild, S., Chen, G. and Trahair, N.S. (1992). 'Out of plane strengths of steel beams,' *J. Struct. Engng, ASCE*, **118**, 1987–2003.
- Bradford, M.A. and Cuk, P.E. (1988). 'Elastic buckling of tapered monosymmetric I-beams,' *J. Struct. Div., ASCE*, **114**(5), 977–996.
- Chan, S.L. (1990). 'Buckling analysis of structures composed of tapered members,' *J. Struct. Div., ASCE*, **116**(7), 1893–1906.
- Chandra, R. and Chopra, I. (1991). 'Experimental and theoretical analysis of composite I beams with elastic couplings,' *AIAA J.*, **29**(12), 2197–2206.
- Chini, S.A. and Wolde-Tinsae, A.M. (1988). 'Critical load and post buckling of arch frameworks,' *J. Engng Mech., ASCE*, **114**(9), 1435–1453.
- Fung, Y.C. (1965). *Foundations of Solid Mechanics*, Prentice-Hall, Inc., Englewood Cliffs, New Jersey.
- Giavotto, V., Borri, M., Mantegazza, P., Chirungelli, G., Caramaschi, V., Maffioli, G.C. and Mussi, F. (1983). 'Anisotropic beam theory and applications,' *Comp. Struct.*, **16**(1–4), 403–413.
- Gjelsvik, A. (1981). *The Theory of Thin-walled Bars*, Wiley, New York.
- Green, A.E. and Zerna, W. (1968). *Theory of Elasticity*, 2nd Ed., Oxford University Press, London.
- Gupta, A.K. (1985). 'Vibration of tapered beams,' *J. Struct. Engng, ASCE*, **111**(1), 19–36.
- Gupta, A.K. (1986). 'Frequency-dependent matrices for tapered beams,' *J. Struct. Engng, ASCE*, **112**(1), 85–103.
- Gupta, R.K., Venkatesh, S. and Rao, K.P. (1985). 'Finite element analysis of laminated an-isotropic thin-walled open section beams,' *Composite Struct.*, **3**(1), 19–31.
- Kaw, A.K. (1997). *Mechanics of Composite Materials*, CRC Press, Boca Raton, FL.
- Kitipornchai, S. and Trahair, N.S. (1972). 'Elastic stability of tapered I beams,' *J. Struct. Div., ASCE*, **98**(3), 713–728.
- Kitipornchai, S. and Trahair, N.S. (1975). 'Elastic behaviour of tapered monosymmetric I beams,' *J. Struct. Div., ASCE*, **101**(8), 1661–1678.
- Krishnan, A. and Singh, V.K. (1991). 'Some studies on vibration of thin-walled open section,' *J. Sound Vibration*, **49** (2) 297–310.
- Lee, J. (2001). 'Centre of gravity and shear centre of thin-walled open cross section composite beam,' *Composite Struct.*, **52**, 255–260.
- Libove, C. (1988). 'Stresses and rate of twist in single-cell thin-walled beams with anisotropic walls,' *AIAA J.*, **26**(9), 1107–1118.
- Love, A.E.H. (1944). *A Treatise on the Mathematical Theory of Elasticity*, 4th Ed, Dover Publications, New York.
- Mei, C. (1970). 'Coupled vibrations of thin-walled beams of open section using finite element method,' *Int. J. Mech. Sci.*, **12**, 883–891.
- Murray, D.W. and Rajasekaran, S. (1975). 'Technique for formulating beam equations,' *J. Engng Mech. Div., ASCE*, **101**(5), 561–573.
- Murray, N.W. (1984). *Introduction to the Theory of Thin-walled Structures*, Clarendon Press, Oxford.
- Oden, J.T. (1967). *Mechanics of Elastic Structures*, McGraw-Hill, New York.
- Palani, G.S. and Rajasekaran, S. (1992). 'Finite element analysis thin-walled curved beam of open cross section made of composites,' *J. Struct. Engng, ASCE*, **118**(8), 2039–2062.
- Rajasekaran, S. (1971). 'Finite Element Analysis of Thin-walled Beams of Open Cross Section,' PhD thesis, University of Alberta, Canada.

- Rajasekaran, S. (1994a). 'Equations for tapered thin-walled beams of generic open section,' *J. Engng Mech., ASCE*, **120**(8), 1607–1629.
- Rajasekaran, S. (1994b). 'Instability of tapered thin-walled beams of generic sections,' *J. Engng Mech., ASCE*, **120**(8), 1630–1640.
- Rajasekaran, S. (2005a). 'Mechanical properties of thin-walled composite beams of generic open and closed sections,' *Struct. Engng Mech.*, **21**(5), 591–620.
- Rajasekaran, S. (2005b). 'Optimal laminate sequence of non-prismatic thin-walled composite spatial members of generic section,' *Composite Struct.*, **70**(2), 200–211.
- Rajasekaran, S. and Padmanabhan, S. (1989). 'Equations for curved beams,' *J. Engng Mech., ASCE*, **115**(5), 1094–1111.
- Rajasekaran, S., Nalinaa, K., Greeshma, S., Poornima, N.S. and Kumar, V. (2003). 'Optimal lay-up of hybrid composite beams, plates and shells using cellular genetic algorithm,' *Struct. Engng Mech.*, **16**(5), 557–580.
- Shiomi, H. and Kurata, M. (1984). 'Strength formula for tapered beam-columns,' *J. Struct. Engng., ASCE*, **110**(7), 1630–1643.
- Silvestre, N. and Camotim, D. (2002a). 'First-order generalized beam theory for arbitrary orthotropic materials,' *Thin-walled Struct.*, **40**, 755–789.
- Silvestre, N. and Camotim, D. (2002b). 'Second-order generalized beam theory for arbitrary orthotropic materials,' *Thin-walled Struct.*, **40**, 791–820.
- Song, O. and Liberescu, L. (1993). 'Free vibration of anisotropic composite thin-walled beams of closed cross section contour,' *J. Sound Vibration*, **167**(1), 129–147.
- Stemple, A.D. and Lee, S.W. (1989). 'A finite element modeling for composite beams undergoing large deflections with arbitrary cross sectional warping,' *Int. J. Num. Meth. Engng.*, **28**(9), 2143–2163.
- Timoshenko, S.P. (1945). 'Theory of bending, torsion and buckling of thin-walled members of open cross section,' *J. Franklin Institute*, **239**(3–5), 201–219, 249–268, 343–361.
- Timoshenko, S.P. and Gere, J.M. (1961). *Theory of Elastic Stability*, McGraw-Hill, New York.
- Trahair, N.S. and Bild, S. (1990). 'Elastic biaxial bending and torsion of thin-walled members,' *Thin-walled Struct.*, **9**, 269–307.
- Uma, K. (1992). 'Static and dynamic instability analysis of non-prismatic members of open section,' *M. Eng. Thesis, Bharathiar University*, Coimbatore, India.
- Vacharazitiphan, P. and Trahair, N.S. (1974). 'Warping and distortion of I-section joints,' *J. Struct. Div., ASCE*, **100**(3), 547–564.
- Van Erp, G.M., Menken, C.M. and Veldpaus, F.E. (1988). 'The nonlinear flexural torsional behaviour of straight slender elastic beams with arbitrary cross section,' *Thin-walled Struct.*, **6**(5), 385–404.
- Vlasov, V.Z. (1961). *Thin-walled Elastic Beams*, 2nd Ed., Israel Program for Scientific Translations, Jerusalem, Israel.
- Wekezer, J. (1985). 'Instability of thin-walled bars,' *J. Engng Mech., ASCE*, **111**(7), 923–935.
- Wekezer, J. (1987). 'Free vibrations of thin-walled bars with open cross section,' *J. Engng Mech., ASCE*, **113**(10), 1441–1453.
- Wekezer, J.W. (1989). 'Vibration analysis of thin-walled bars of open cross section,' *J. Struct. Div., ASCE*, **115**(2), 2965–2978.
- Wu, X.X. and Sun, C.T. (1992). 'Simplified theory for composite thin-walled beams,' *AIAA J.*, **30**(12), 2945–2951.

- Yang, Y.B. and McGuire, W. (1986a). 'Stiffness matrix for geometric nonlinear analysis,' *J. Struct. Engng, ASCE*, **112**(4), 853–878.
- Yang, Y.B. and McGuire, W. (1986b). 'Joint rotations and geometric nonlinear analysis,' *J. Struct. Engng, ASCE*, **112**(4), 879–905.
- Yang, Y.B. and Yau, J.D. (1987). 'Stability of beams with tapered I-sections,' *J. Engng. Mech., ASCE*, **113**(9), 1337–1357.
- Zienkiewicz, O.C. (1971). *The Finite Element Method in Engineering Science*, McGraw-Hill, New York.

## Least squares finite difference method for vibration analysis of plates

C S H U, W X W U and C M WANG,  
National University of Singapore, Singapore

### 4.1 Introduction

In the classical thin plate and shear deformable plate theories for free vibration of plates (Timoshenko and Woinowsky-Krieger 1959; Leissa 1969; Mindlin 1951; Liew *et al.* 1998), the governing equations of motion and boundary conditions are expressed as partial differential equations (PDEs). Analytical vibration solutions are possible only for a very few simple plate shapes and boundary conditions. Rectangular plates with all edges simply supported, circular plates with homogeneous boundary conditions and circular sectorial plates with two radial edges simply supported are examples that have analytical vibration solutions (Leissa 1969; Wang *et al.* 2004). Usually, numerical methods are used to solve approximately plate vibration problems.

If the plate shape is rectangular, the traditional finite difference method (FDM) and generalized differential quadrature (GDQ) method can be readily used to compute the vibration solutions (Shu and Du 1997a,b). FDM and GDQ can also be easily applied to plates with circular or circular sectorial domains because these shapes can be readily mapped into rectangles by using the polar coordinate system. However, for irregularly shaped domains, FDM and GDQ cannot be easily applied because their straight mesh lines do not fit the domain boundaries. A better choice is to use mesh-free numerical methods for solving these problems. In this chapter, the least squares-based finite difference (LSFD) method is presented for solving vibration problems of arbitrarily shaped plates. It will be shown that the LSFD method is a powerful mesh free approach for solving the strong form of PDEs.

### 4.2 Least squares-based finite difference (LSFD) method

The LSFD method was originally developed by Ding *et al.* (2004) who employed the method for solving fluid flow problems. This method is further

extended in some respects as shown in this chapter, and applied to solve plate vibration problems.

#### 4.2.1 Formulations for derivative approximation

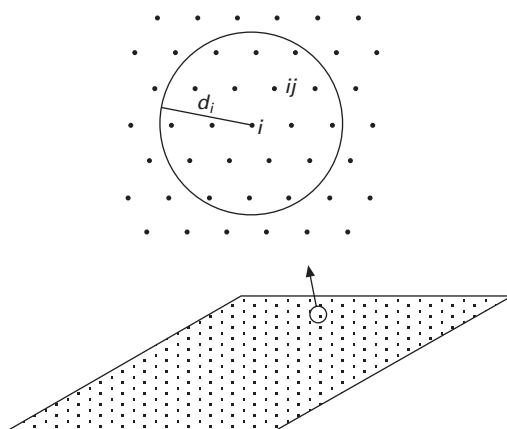
For the unstructured distribution of points in a problem domain  $\Omega$  as shown in Fig. 4.1, the index  $i$  represents a typical point and  $ij$  a group of points surrounding the point  $i$  (hereafter  $ij$  is referred as the supporting points for the point  $i$ ). A 2D Taylor series expansion in the  $\Delta$ -form for a continuous and differentiable function  $f(x, y)$  is given by

$$\begin{aligned}\Delta f_{ij} = & \Delta x_{ij} \frac{\partial f_i}{\partial x} + \Delta y_{ij} \frac{\partial f_i}{\partial y} + \frac{\Delta x_{ij}^2}{2} \frac{\partial^2 f_i}{\partial x^2} + \frac{\Delta y_{ij}^2}{2} \frac{\partial^2 f_i}{\partial y^2} + \Delta x_{ij} \Delta y_{ij} \frac{\partial^2 f_i}{\partial x \partial y} \\ & + \frac{\Delta x_{ij}^3}{6} \frac{\partial^3 f_i}{\partial x^3} + \frac{\Delta y_{ij}^3}{6} \frac{\partial^3 f_i}{\partial y^3} + \frac{\Delta x_{ij}^2 \Delta y_{ij}}{2} \frac{\partial^3 f_i}{\partial x^2 \partial y} + \frac{\Delta x_{ij} \Delta y_{ij}^2}{2} \frac{\partial^3 f_i}{\partial x \partial y^2} + O(h^4)\end{aligned}$$

4.1

where  $\Delta f_{ij} = f_{ij} - f_i$ ,  $\Delta x_{ij} = x_{ij} - x_i$ ,  $\Delta y_{ij} = y_{ij} - y_i$ ,  $(x_{ij}, y_{ij})$  and  $(x_i, y_i)$  are the Cartesian coordinates of the points  $i$  and  $ij$ , respectively.  $f_i$  and  $f_{ij}$  are the function values at the points  $i$  and  $ij$ , respectively.  $\partial f_i / \partial x$  represents the value of  $\partial f / \partial x$  at the point  $i$ , and other expressions for derivatives in (4.1) have similar meaning.  $h$  in  $O(h^4)$  is the mean distance from the supporting points  $ij$  to the point  $i$ .

In the LSFD method, the derivatives in the Taylor series expansion are considered as unknowns. Equation (4.1) has nine unknowns, that is, two first-order derivatives, three second-order derivatives and four third-order derivatives. In order to solve for the nine unknowns, we need nine equations



4.1 Computational domain with an unstructured distribution of points.

to close the system. This can be done by applying Eq. (4.1) at nine supporting points. As a result, a system of equations is obtained in a compact form:

$$\Delta \mathbf{f}_i = \mathbf{S}_i d\mathbf{f}_i \quad 4.2$$

where

$$\Delta \mathbf{f}_i = [\Delta f_{i1} \quad \Delta f_{i2} \quad \dots \quad \Delta f_{i9}]^T \quad 4.3$$

$$d\mathbf{f}_i = \left[ \frac{\partial f_i}{\partial x} \quad \frac{\partial f_i}{\partial y} \quad \frac{\partial^2 f_i}{\partial x^2} \quad \frac{\partial^2 f_i}{\partial y^2} \quad \frac{\partial^2 f_i}{\partial x \partial y} \quad \frac{\partial^3 f_i}{\partial x^3} \quad \frac{\partial^3 f_i}{\partial y^3} \quad \frac{\partial^3 f_i}{\partial x^2 \partial y} \quad \frac{\partial^3 f_i}{\partial x \partial y^2} \right]^T \quad 4.4$$

$$\mathbf{S}_i = \begin{bmatrix} \Delta x_{i1} & \Delta y_{i1} & \frac{\Delta x_{i1}^2}{2} & \frac{\Delta y_{i1}^2}{2} & \Delta x_{i1} \Delta y_{i1} & \frac{\Delta x_{i1}^3}{6} & \frac{\Delta y_{i1}^3}{6} & \frac{\Delta x_{i1}^2 \Delta y_{i1}}{2} & \frac{\Delta x_{i1} \Delta y_{i1}^2}{2} \\ \Delta x_{i2} & \Delta y_{i2} & \frac{\Delta x_{i2}^2}{2} & \frac{\Delta y_{i2}^2}{2} & \Delta x_{i2} \Delta y_{i2} & \frac{\Delta x_{i2}^3}{6} & \frac{\Delta y_{i2}^3}{6} & \frac{\Delta x_{i2}^2 \Delta y_{i2}}{2} & \frac{\Delta x_{i2} \Delta y_{i2}^2}{2} \\ \vdots & \vdots \\ \Delta x_{i9} & \Delta y_{i9} & \frac{\Delta x_{i9}^2}{2} & \frac{\Delta y_{i9}^2}{2} & \Delta x_{i9} \Delta y_{i9} & \frac{\Delta x_{i9}^3}{6} & \frac{\Delta y_{i9}^3}{6} & \frac{\Delta x_{i9}^2 \Delta y_{i9}}{2} & \frac{\Delta x_{i9} \Delta y_{i9}^2}{2} \end{bmatrix} \quad 4.5$$

In the matrix  $\mathbf{S}_i$ , the entries are the coefficient factors of the derivatives in the Taylor series expansion (4.1).

In order to solve Eq. (4.2), we need to invert the matrix  $\mathbf{S}_i$ . It was observed that the matrix  $\mathbf{S}_i$  tends to become ill-conditioned numerically when one or more of the supporting points are very close to the reference point, i.e.  $\Delta x_{ij} \approx 0$ ,  $\Delta y_{ij} \approx 0$  for some  $j$ . In addition, it was found that the matrix  $\mathbf{S}_i$  may become ill-conditioned or even singular when some supporting points are very close to each other. To overcome this difficulty, the radius  $d_i$  of the supporting region (see Fig. 4.1) is used to scale the local distance  $\Delta x_{ij}$ ,  $\Delta y_{ij}$ , that is

$$\Delta \bar{x}_{ij} = \frac{\Delta x_{ij}}{d_i}, \quad \Delta \bar{y}_{ij} = \frac{\Delta y_{ij}}{d_i} \quad 4.6$$

The local scaling process is equivalent to introducing a diagonal matrix  $\mathbf{D}_i$  of the form

$$\mathbf{D}_i = \text{diag}(d_i, d_i, d_i^2, d_i^2, d_i^2, d_i^3, d_i^3, d_i^3, d_i^3) \quad 4.7$$

In view of Eq. (4.2), we can write

$$\Delta \mathbf{f}_i = \bar{\mathbf{S}}_i d\bar{\mathbf{f}}_i \quad 4.8$$

where

$$\bar{\mathbf{S}}_i = \mathbf{S}_i \mathbf{D}_i^{-1}, d\bar{\mathbf{f}}_i = \mathbf{D}_i d\mathbf{f}_i \quad 4.9a,b$$

The local scaling improves the condition number of the matrix  $\mathbf{S}_i$ . On the other hand, the point distribution in LSFD method could be random. The irregular point distribution may also cause the matrix  $\mathbf{S}_i$  to be ill-conditioned or even singular, which cannot be improved by the local scaling. To remove this difficulty, we can introduce the weighted least-square optimization to determine the unknown vector  $d\bar{\mathbf{f}}_i$  in the approximate equation (4.8). This process is given in detail as follows.

Apply Eq. (4.1) at  $m$  supporting points  $ij$  ( $j = 1, 2, \dots, m; m > 9$ ) of the reference point  $i$  to approximate the values of  $\Delta f_{ij}$ . Then the same form of Eqs. (4.2) to (4.9) can be obtained by following a procedure that is similar to the one discussed above, except that the vector  $\Delta\mathbf{f}_i$  in Eq. (4.3) and the matrix  $\mathbf{S}_i$  in Eq. (4.5) have to be modified, i.e.

$$\Delta\mathbf{f}_i = [\Delta f_{i1} \quad \Delta f_{i2} \quad \dots \quad \Delta f_{im}]^T \quad 4.10$$

$$\mathbf{S}_i = \begin{bmatrix} \Delta x_{i1} & \Delta y_{i1} & \frac{\Delta x_{i1}^2}{2} & \frac{\Delta y_{i1}^2}{2} & \Delta x_{i1}\Delta y_{i1} & \frac{\Delta x_{i1}^3}{6} & \frac{\Delta y_{i1}^3}{6} & \frac{\Delta x_{i1}^2\Delta y_{i1}}{2} & \frac{\Delta x_{i1}\Delta y_{i1}^2}{2} \\ \Delta x_{i2} & \Delta y_{i2} & \frac{\Delta x_{i2}^2}{2} & \frac{\Delta y_{i2}^2}{2} & \Delta x_{i2}\Delta y_{i2} & \frac{\Delta x_{i2}^3}{6} & \frac{\Delta y_{i2}^3}{6} & \frac{\Delta x_{i2}^2\Delta y_{i2}}{2} & \frac{\Delta x_{i2}\Delta y_{i2}^2}{2} \\ \vdots & \vdots \\ \Delta x_{im} & \Delta y_{im} & \frac{\Delta x_{im}^2}{2} & \frac{\Delta y_{im}^2}{2} & \Delta x_{im}\Delta y_{im} & \frac{\Delta x_{im}^3}{6} & \frac{\Delta y_{im}^3}{6} & \frac{\Delta x_{im}^2\Delta y_{im}}{2} & \frac{\Delta x_{im}\Delta y_{im}^2}{2} \end{bmatrix} \quad 4.11$$

The unknown vector  $d\bar{\mathbf{f}}_i$  in Eq. (4.8) is obtained by minimizing the summation of weighted squares of the approximation errors. This summation of errors is given by

$$\begin{aligned} J_i &= \sum_{j=1}^m V_{ij} \left[ \Delta f_{ij} - \sum_{k=1}^9 (\bar{\mathbf{S}}_i)_{j,k} \cdot (d\bar{\mathbf{f}}_i)_k \right]^2 \\ &= (\Delta\mathbf{f}_i - \bar{\mathbf{S}}_i d\bar{\mathbf{f}}_i)^T \mathbf{V}_i (\Delta\mathbf{f}_i - \bar{\mathbf{S}}_i d\bar{\mathbf{f}}_i) \end{aligned} \quad 4.12$$

where

$$\mathbf{V}_i = \text{diag}(V_{i1}, V_{i2}, \dots, V_{im}) \quad 4.13$$

is the weighting function matrix with compact support, i.e. the values of  $V_{ij}$  ( $j = 1, 2, \dots, m$ ) are chosen in such a way that the supporting point closer to the reference point  $i$  has a greater influence on the function value at the point  $i$ . The weighting function that is normally adopted is

$$V_{ij} = \sqrt{4/\pi} (1 - \bar{r}_{ij}^2)^4 \quad 4.14$$

where  $\bar{r}_{ij} = \sqrt{\Delta x_{ij}^2 + \Delta y_{ij}^2}/d_i \leq 1$ , and  $d_i$  is the radius of supporting region of point  $i$ . Other forms of weighting functions can also be used, such as

$$V_{ij} = 1/\bar{r}_{ij} \quad 4.15a$$

$$V_{ij} = 1 - 6\bar{r}_{ij}^2 + 8\bar{r}_{ij}^3 - 3\bar{r}_{ij}^4 \quad 4.15b$$

$$V_{ij} = 1/\bar{r}_{ij}^4 \quad 4.15c$$

In order to find  $d\bar{\mathbf{f}}_i$ , we need to minimize  $J_i$  by making

$$\begin{aligned} \frac{\partial J_i}{\partial (d\bar{\mathbf{f}}_i)} &= -2\bar{\mathbf{S}}_i^T \mathbf{V}_i (\Delta \mathbf{f}_i - \bar{\mathbf{S}}_i d\bar{\mathbf{f}}_i) \\ &= -2(\bar{\mathbf{S}}_i^T \mathbf{V}_i \Delta \mathbf{f}_i - \bar{\mathbf{S}}_i^T \mathbf{V}_i \bar{\mathbf{S}}_i d\bar{\mathbf{f}}_i) = \mathbf{0} \end{aligned} \quad 4.16$$

From this equation, we have

$$d\bar{\mathbf{f}}_i = (\bar{\mathbf{S}}_i^T \mathbf{V}_i \bar{\mathbf{S}}_i)^{-1} \bar{\mathbf{S}}_i^T \mathbf{V}_i \Delta \mathbf{f}_i \quad 4.17$$

In Eq. (4.17), it is observed that the number of supporting points  $m$  of each point  $i$  should be sufficiently large so as to ensure the matrices  $(\bar{\mathbf{S}}_i^T \mathbf{V}_i \bar{\mathbf{S}}_i)$  are invertible at all points  $i$  in the domain  $\Omega$ .

The final LSFD formulations can be derived from Eqs. (4.9b) and (4.17) as

$$d\mathbf{f}_i = \mathbf{D}_i^{-1} (\bar{\mathbf{S}}_i^T \mathbf{V}_i \bar{\mathbf{S}}_i)^{-1} \bar{\mathbf{S}}_i^T \mathbf{V}_i \Delta \mathbf{f}_i \quad 4.18$$

In order to simplify this formulation, the following matrices are defined

$$\mathbf{T}^i = \mathbf{D}_i^{-1} (\bar{\mathbf{S}}_i^T \mathbf{V}_i \bar{\mathbf{S}}_i)^{-1} (\bar{\mathbf{S}}_i^T \mathbf{V}_i) \quad 4.19$$

In view of Eq. (4.19), Eq. (4.18) may be rewritten as

$$d\mathbf{f}_i = \mathbf{T}^i \Delta \mathbf{f}_i \quad 4.20$$

where  $\Delta \mathbf{f}_i$  and  $d\mathbf{f}_i$  are vectors given by expressions (4.10) and (4.4), respectively, and  $\mathbf{T}^i \in R^{9 \times m}$ .

From the foregoing process, we can observe that for the 2D case, LSFD formulation (4.20) is derived by using the 2D Taylor series expansion with the first nine truncated terms. Higher-order LSFD schemes (which approximate derivatives of a function with a higher order of accuracy) can be derived by using the 2D Taylor series expansions with more terms. The formulations for higher-order schemes have the same form as that of Eq. (4.20).

The significance of the formulation (4.20) is that it expresses/approximates the derivatives at a point  $i$  with the forms of weighted summations of the function values at the point  $i$  itself and a set of its supporting points  $ij$ , for  $j = 1, 2, \dots, m$ . It should be noted that any set of points  $i$  and  $ij$ , and even all the points in the problem domain, can be scattered. There is no specified connection between the points. Hence no mesh is required for discretization of the

derivatives and PDEs. Furthermore, no mesh is required for solving the strong form of PDEs because there is no necessity for numerical integration. Therefore, this method is indeed mesh-free. As this method originates from a 2D Taylor series expansion (akin to the traditional FDM that originates from 1D Taylor series expansion) and the least squares technique is used, the approach has been named the least squares-based finite difference (LSFD) method.

#### 4.2.2 Chain rule for discretization of derivatives

In the LSFD method, PDEs are solved directly. The derivatives in the strong form PDEs are discretized by using the formulation (4.20), and the resulting algebraic equations that are collocated at all interior points in the domain form an equation system. With the proper implementation of boundary conditions, the equation system can be solved by using common solvers.

For some physical phenomena, the governing equations are high-order PDEs in which high-order derivatives appear. One example of high-order PDEs is the governing equation for free vibration of plates based on the classical thin plate theory. The governing equation may be expressed as

$$\frac{\partial^4 W}{\partial x^4} + 2 \frac{\partial^4 W}{\partial x^2 \partial y^2} + \frac{\partial^4 W}{\partial y^4} = \frac{\rho h}{D} \omega^2 W \quad 4.21$$

where  $W$  is the modal deflection of the vibrating plate,  $\rho$  the mass density,  $h$  the plate thickness,  $\omega$  the angular frequency of vibration,  $D = Eh^3/[12(1 - \nu^2)]$  the flexural rigidity per unit length,  $E$  Young's modulus and  $\nu$  the Poisson ratio. It is well known that accurate approximation of high-order derivatives is usually difficult when using FEM and other numerical methods. To overcome this difficulty, a chain rule for discretization of derivatives is proposed in this chapter. Without any loss of generality, the fourth-order derivative  $\partial^4 W / \partial x^4$  is used as an example to illustrate the use of chain rule. The value of  $\partial^4 W / \partial x^4$  at a point  $i$  can be discretized in the following way:

$$\begin{aligned} \frac{\partial^4 W_i}{\partial x^4} &= \frac{\partial^2}{\partial x^2} \left( \frac{\partial^2 W_i}{\partial x^2} \right) = \sum_{j=1}^m T_{3,j}^i \left( \frac{\partial^2 W_{ij}}{\partial x^2} - \frac{\partial^2 W_i}{\partial x^2} \right) \\ &= \sum_{j=1}^m T_{3,j}^i \left[ \sum_{k=1}^m T_{3,k}^{ij} (W_{ijk} - W_{ij}) - \sum_{k=1}^m T_{3,k}^i (W_{ik} - W_i) \right] \end{aligned} \quad 4.22$$

where  $W_{ijk}$  is to be understood as the function value at the point  $ijk$ , and the subscript  $ijk$  means the index of the  $k$ th supporting point of the point  $ij$ . In Eq. (4.22), the formulation (4.20) is applied twice successively to discretize the fourth-order derivative which has been treated as a second-order derivative of another second order derivative. It is evident that  $\partial^4 W_i / \partial x^4$  can also be discretized in other ways. For example,

$$\begin{aligned}
\frac{\partial^4 W_i}{\partial x^4} &= \frac{\partial^2}{\partial x^2} \left( \frac{\partial^2 W_i}{\partial x^2} \right) = \sum_{j=1}^m T_{3,j}^i \left[ \frac{\partial}{\partial x} \left( \frac{\partial W_{ij}}{\partial x} \right) - \frac{\partial^2 W_i}{\partial x^2} \right] \\
&= \sum_{j=1}^m T_{3,j}^i \left[ \sum_{k=1}^m T_{1,k}^{ij} \left( \frac{\partial W_{ijk}}{\partial x} - \frac{\partial W_{ij}}{\partial x} \right) - \sum_{k=1}^m T_{3,k}^i (W_{ik} - W_i) \right] \\
&= \dots
\end{aligned} \tag{4.23}$$

In LSFD method, different ways of discretization may be chosen so that the boundary conditions can be easily implemented. It will be shown in the following sections that the boundary conditions of plates, possibly after some transformations, can be directly substituted into the governing equations of plate vibration in the process of discretization.

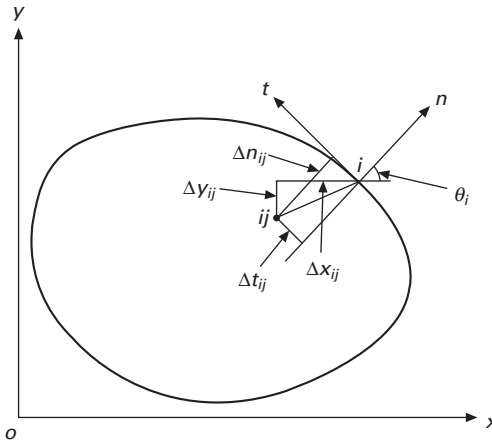
Another function of the chain rule is that it increases the order of accuracy of discretization of high-order derivatives. For example, if Eq. (4.22) is used, then the order of accuracy of discretization of this fourth-order derivative should be the same as that of a second-order derivative. This function is similar to that of a weak form of plate vibration equation in FEM or other mesh-free methods, in which by using the integration by parts technique, the fourth-order derivatives are transformed into the product of two second-order derivatives.

#### 4.2.3 LSFD formulations in local ( $n, t$ )-coordinates at boundary

If the PDEs for boundary conditions involve derivatives of function with reference to  $n$  and/or  $t$  (where  $n$  and  $t$  are the coordinates along the outer normal and tangential directions respectively to the boundary  $\Gamma$ , e.g.  $\partial w/\partial n = 0$  at  $\Gamma$ ), then we can use the LSFD method to derive the formulations for approximating the derivatives of function in  $n$ - and  $t$ -local directions at a boundary point.

The procedure for deriving aforementioned formulations is similar to that of Eqs. (4.1) to (4.20). At a boundary point  $i$ , firstly a local ( $n, t$ )-coordinate system is defined with the  $n$ -axis in the direction outer normal to  $\Gamma$ , and the  $t$ -axis in the direction tangential to  $\Gamma$ , as shown in Fig. 4.2. At the boundary point  $i$  with supporting points  $ij$  ( $j = 1, 2, \dots, m$ ; and  $m > 9$ ), the Taylor series expansion can be written as

$$\begin{aligned}
\Delta f_{ij} &= \Delta n_{ij} \frac{\partial f_i}{\partial n} + \Delta t_{ij} \frac{\partial f_i}{\partial t} + \frac{\Delta n_{ij}^2}{2} \frac{\partial^2 f_i}{\partial n^2} + \frac{\Delta t_{ij}^2}{2} \frac{\partial^2 f_i}{\partial t^2} \\
&\quad + \Delta n_{ij} \Delta t_{ij} \frac{\partial^2 f_i}{\partial n \partial t} + \frac{\Delta n_{ij}^3}{6} \frac{\partial^3 f_i}{\partial n^3} + \frac{\Delta t_{ij}^3}{6} \frac{\partial^3 f_i}{\partial t^3} + \frac{\Delta n_{ij}^2 \Delta t_{ij}}{2} \frac{\partial^3 f_i}{\partial n^2 \partial t} \\
&\quad + \frac{\Delta n_{ij} \Delta t_{ij}^2}{2} \frac{\partial^3 f_i}{\partial n \partial t^2} + O(h^4)
\end{aligned} \tag{4.24}$$

4.2 Local  $(n, t)$ -coordinate system.

where

$$\Delta f_{ij} = f_{ij} - f_i \quad 4.25$$

$$\begin{cases} \Delta n_{ij} = n_{ij} - n_i = \Delta x_{ij} \cos \theta_i + \Delta y_{ij} \sin \theta_i \\ \Delta t_{ij} = t_{ij} - t_i = -\Delta x_{ij} \sin \theta_i + \Delta y_{ij} \cos \theta_i \end{cases} \quad 4.26a,b$$

The relations in Eqs. (4.26a) and (4.26b) can be easily verified by referring to Fig. 4.2.

Following a similar process to that used for deriving the formulation (4.20), one obtains

$$d\mathbf{f}_i = \tilde{\mathbf{T}}^i \Delta \mathbf{f}_i \quad 4.27$$

where

$$d\mathbf{f}_i = \left[ \frac{\partial f_i}{\partial n} \quad \frac{\partial f_i}{\partial t} \quad \frac{\partial^2 f_i}{\partial n^2} \quad \frac{\partial^2 f_i}{\partial t^2} \quad \frac{\partial^2 f_i}{\partial n \partial t} \quad \frac{\partial^3 f_i}{\partial n^3} \quad \frac{\partial^3 f_i}{\partial t^3} \quad \frac{\partial^3 f_i}{\partial n^2 \partial t} \quad \frac{\partial^3 f_i}{\partial n \partial t^2} \right]^T \quad 4.28$$

$$\Delta \mathbf{f}_i = [\Delta f_{i1} \quad \Delta f_{i2} \quad \cdots \quad \Delta f_{im}]^T \quad 4.29$$

$$\tilde{\mathbf{T}}^i = \mathbf{D}_i^{-1} (\bar{\mathbf{S}}_i^T \mathbf{V}_i \bar{\mathbf{S}}_i)^{-1} (\bar{\mathbf{S}}_i^T \mathbf{V}_i), \quad \tilde{\mathbf{T}}^i \in R^{9 \times m} \quad 4.30$$

$$\mathbf{S}_i = \begin{bmatrix} \Delta n_{i1} & \Delta t_{i1} & \frac{\Delta n_{i1}^2}{2} & \frac{\Delta t_{i1}^2}{2} & \Delta n_{i1} \Delta t_{i1} & \frac{\Delta n_{i1}^3}{6} & \frac{\Delta t_{i1}^3}{6} & \frac{\Delta n_{i1}^2 \Delta t_{i1}}{2} & \frac{\Delta n_{i1} \Delta t_{i1}^2}{2} \\ \Delta n_{i2} & \Delta t_{i2} & \frac{\Delta n_{i2}^2}{2} & \frac{\Delta t_{i2}^2}{2} & \Delta n_{i2} \Delta t_{i2} & \frac{\Delta n_{i2}^3}{6} & \frac{\Delta t_{i2}^3}{6} & \frac{\Delta n_{i2}^2 \Delta t_{i2}}{2} & \frac{\Delta n_{i2} \Delta t_{i2}^2}{2} \\ \vdots & \vdots \\ \Delta n_{im} & \Delta t_{im} & \frac{\Delta n_{im}^2}{2} & \frac{\Delta t_{im}^2}{2} & \Delta n_{im} \Delta t_{im} & \frac{\Delta n_{im}^3}{6} & \frac{\Delta t_{im}^3}{6} & \frac{\Delta n_{im}^2 \Delta t_{im}}{2} & \frac{\Delta n_{im} \Delta t_{im}^2}{2} \end{bmatrix} \quad 4.31$$

$$\mathbf{D}_i^{-1} = \text{diag}(d_i^{-1}, d_i^{-1}, d_i^{-2}, d_i^{-2}, d_i^{-2}, d_i^{-3}, d_i^{-3}, d_i^{-3}, d_i^{-3}) \quad 4.32$$

$$\mathbf{V}_i = \text{diag}(V_{i1}, V_{i2}, \dots, V_{im}),$$

$$V_{ij} \text{ takes one form from (4.14) or (4.15a, b, c)} \quad 4.33$$

$$\bar{\mathbf{S}}_i = \mathbf{S}_i \mathbf{D}_i^{-1}, \bar{\mathbf{S}}_i^T = \mathbf{D}_i^{-1} \mathbf{S}_i^T \quad 4.34$$

### 4.3 Governing equation and boundary conditions for free vibration of thin plates

According to the classical thin plate theory, the governing equation of motion for a freely vibrating, elastic, isotropic, thin plate may be expressed in a nondimensional form given by Timoshenko and Woinowsky-Krieger (1959):

$$\frac{\partial^4 W}{\partial X^4} + 2 \frac{\partial^4 W}{\partial X^2 \partial Y^2} + \frac{\partial^4 W}{\partial Y^4} = \Omega^2 W \quad 4.35$$

where  $W = W(X, Y)$  is the modal deflection of the plate;  $X = x/a$ ,  $Y = y/a$  are the non-dimensional Cartesian coordinates in the mid-plane of the plate;  $a$  is a characteristic length dimension in the  $x-y$  plane.  $\Omega$  is the nondimensional frequency parameter defined as

$$\Omega = \omega a^2 \sqrt{\frac{\rho h}{D}} \quad 4.36$$

where  $\omega$  (rad/s) is the angular frequency of vibration,  $\rho$  the mass density of plate material;  $h$  the plate thickness; and  $D = Eh^3/[12(1 - \nu^2)]$  the flexural rigidity per unit length of the plate;  $E$  and  $\nu$  being respectively the Young's modulus and Poisson's ratio of the plate material.

The boundary conditions considered are those of simply supported (SS), clamped (C) and free (F) edges. They are given as follows:

- Simply supported edge (SS)

$$W = 0, \frac{\partial^2 W}{\partial n^2} + \nu \frac{\partial^2 W}{\partial t^2} = 0 \quad 4.37a,b$$

- Clamped edge (C)

$$W = 0, \frac{\partial W}{\partial n} = 0 \quad 4.38a,b$$

- Free edge (F)

$$\frac{\partial^2 W}{\partial n^2} + \nu \frac{\partial^2 W}{\partial t^2} = 0, \frac{\partial}{\partial n} (\nabla^2 W) + (1 - \nu) \frac{\partial}{\partial s} \left( \frac{\partial^2 W}{\partial n \partial t} \right) = 0 \quad 4.39a,b$$

where  $n$  and  $t$  are the outer normal and tangential coordinates to the plate edge, respectively; the notation  $\partial/\partial s$  denotes the differentiation along the edge curve of plate.

#### 4.4 Discretization of the governing equation by the LSFD method

In the two-dimensional domain of the problem,  $N_t$  points  $(X_i, Y_i)$ ,  $i = 1, 2, \dots, N_t$  are generated using the software GAMBIT, in which points  $i = 1, 2, \dots, N_i$  are the interior points, and the rest  $(N_t - N_i) = N_b$  points  $i = N_i + 1, N_i + 2, \dots, N_t$  are the boundary points. Another data file is also generated in which the global indices of  $m$  nearest supporting points of each point  $i$  ( $i = 1, 2, \dots, N_t$ ) are given as  $ij$  ( $j = 1, 2, \dots, m$ ). The radius  $d_i$  of the supporting region associated to the point  $i$  is calculated using

$$d_i = \max \{ \sqrt{(X_{ij} - X_i)^2 + (Y_{ij} - Y_i)^2} \} \times 1.2, \text{ for } j = 1, 2, \dots, m; \text{ and } i = 1, 2, \dots, N_t \quad 4.40$$

Based on the generated point distribution, the matrices  $\mathbf{T}^i$  ( $i = 1, 2, \dots, N_t$ ) can be evaluated by using the formulation (4.19). Then the vector  $\mathbf{c}^i$  ( $i = 1, 2, \dots, N_t$ ) is computed by

$$\mathbf{c}_j^i = T_{3,j}^i + T_{4,j}^i \quad \text{for } j = 1, 2, \dots, m \quad 4.41$$

Note that  $\mathbf{c}^i$  is the combination of the weighting coefficients for the second-order derivatives  $\partial^2 W / \partial X^2$  and  $\partial^2 W / \partial Y^2$ . Using  $\mathbf{c}^i$ , the Laplacian operator

$$\nabla^2 = \frac{\partial^2}{\partial X^2} + \frac{\partial^2}{\partial Y^2} \quad 4.42$$

can be discretized as

$$\nabla^2 W_i = \sum_{j=1}^m c_j^i \Delta W_{ij} = \sum_{j=1}^m c_j^i W_{ij} + \left( - \sum_{j=1}^m c_j^i \right) W_i \quad 4.43$$

The spatial operator in the governing equation may be written as

$$\nabla^2(\nabla^2) = \left( \frac{\partial^2}{\partial X^2} + \frac{\partial^2}{\partial Y^2} \right) \left( \frac{\partial^2}{\partial X^2} + \frac{\partial^2}{\partial Y^2} \right) = \frac{\partial^4}{\partial X^4} + 2 \frac{\partial^4}{\partial X^2 \partial Y^2} + \frac{\partial^4}{\partial Y^4} \quad 4.44$$

Using the chain rule, this operator can be discretized as

$$\nabla^2(\nabla^2 W_i) = \sum_{j=1}^m c_j^i \nabla^2 W_{ij} + \left( - \sum_{j=1}^m c_j^i \right) \nabla^2 W_i \quad 4.45a$$

$$\begin{aligned} &= \sum_{j=1}^m \sum_{k=1}^m c_j^i c_k^{ij} W_{ijk} + \sum_{j=1}^m c_j^i \left( - \sum_{k=1}^m c_k^{ij} \right) W_{ij} \\ &\quad + \sum_{j=1}^m \left( - \sum_{k=1}^m c_k^i \right) c_j^i W_{ij} + \left( - \sum_{j=1}^m c_j^i \right)^2 W_i \end{aligned} \quad 4.45b$$

where  $W_{ijk}$  is the function value at the point  $ijk$ , and the subscript  $ijk$  means the index of the  $k$ th supporting point of the point  $ij$ . Thus, Eq. (4.35) can be discretized as

$$\begin{aligned} & \sum_{j=1}^m \sum_{k=1}^m c_j^i c_k^{ij} W_{ijk} + \sum_{j=1}^m c_j^i \left( -\sum_{k=1}^m c_k^{ij} \right) W_{ij} \\ & + \sum_{j=1}^m \left( -\sum_{k=1}^m c_k^i \right) c_j^i W_{ij} + \left( -\sum_{j=1}^m c_j^i \right)^2 W_i = \Omega^2 W_i \end{aligned} \quad 4.46$$

for interior points  $i = 1, 2, \dots, N_i$ .

Collocation of Eq. (4.46) at all interior points forms a system of algebraic equations, in which the function values  $W_i$  are those at the interior points, whereas  $W_{ij}$  and  $W_{ijk}$  may be those at the interior points or at the boundary points. Therefore, the number of unknowns is more than the number of equations. In order to solve this system of equations, we need to implement the boundary conditions. In the following, we will present an efficient way for implementing the simply supported, clamped and free boundary conditions, which can be applied for any irregularly shaped plates.

## 4.5 Numerical implementation of boundary conditions

As shown in Eqs. (4.45a) and (4.45b), the two-step discretization of the fourth-order differential operator in the governing PDE is carried out for two purposes. One purpose is to obtain a high degree of accuracy for the discretization of the fourth-order derivatives. Another purpose is for the implementation of one boundary condition at the intermediate step of discretization and another boundary condition at the final step of discretization. In the plate vibration analysis using the LSFD method, this approach for implementation of multiple boundary conditions is found to yield good accuracy for the solutions. In the following sub-sections, we shall illustrate the transformation and the implementation of the two PDEs for the three classical boundary conditions by using this two-step approach.

### 4.5.1 Simply supported edge

Consider a plate with all its edges simply supported. The boundary conditions for a simply supported edge are given by Eqs. (4.37a,b), i.e. the deflection is zero, and the normal bending moment is zero. It is obvious that if  $W = 0$  along the plate edge, then  $\partial^2 W / \partial t^2 = 0$  holds for a rectilinear edge. However, if the simply supported edge is curved, then it can be shown that  $\partial^2 W / \partial t^2 = \pm r^{-1}(\partial W / \partial n)$  instead, where  $t$  is the tangential direction of the edge,  $r$  the radius of curvature of the curvilinear edge in the mid-plane of the plate, the

‘+’ sign is for a convex curvilinear edge and the ‘–’ sign is for a concave curvilinear edge. Therefore, from Eqs. (4.37a,b), we have

$$\nabla^2 W = \frac{\partial^2 W}{\partial n^2} + \frac{\partial^2 W}{\partial t^2} = 0 \quad 4.47a$$

along a rectilinear simply supported edge, while

$$\nabla^2 W = \frac{\partial^2 W}{\partial n^2} + \frac{\partial^2 W}{\partial t^2} = \pm \frac{1-\nu}{r} \frac{\partial W}{\partial n} \quad 4.47b$$

along a curvilinear simply supported edge.

In sum, the boundary conditions (4.37a,b) for a simply supported edge can be rewritten as

$$W_i = 0 \quad 4.48a$$

$$\nabla^2 W_i = 0 \quad \text{along a rectilinear edge} \quad 4.48b$$

$$\nabla^2 W_i = \pm \frac{1-\nu}{r_i} \frac{\partial W_i}{\partial n} \quad \text{along a curvilinear edge} \quad 4.48c$$

for  $i = N_i + 1, N_i + 2, \dots, N_t$ .

Let us examine the discretized form of the spatial operator  $\nabla^2(\nabla^2 W)$  in Eq. (4.45). We may observe that the simply supported condition (4.48b) for the rectilinear edge can be directly implemented without further discretization of the derivatives in the boundary condition. That is, if a supporting point  $ij$  is a boundary point on a rectilinear edge, then  $\nabla^2 W_{ij} = 0$  can be directly substituted into Eq. (4.45a). It is not necessary to discretize  $\nabla^2 W_{ij}$  further. If the point  $ij$  is on a curved edge,  $\nabla^2 W_{ij} = \pm [(1-\nu)/r_{ij}] (\partial W_{ij}/\partial n)$  can be substituted into Eq. (4.45a) instead. We only need to discretize the first-order derivatives  $\partial W_{ij}/\partial X$  and  $\partial W_{ij}/\partial Y$  since  $\partial W_{ij}/\partial n = (\partial W_{ij}/\partial X) \cos \theta_{ij} + (\partial W_{ij}/\partial Y) \sin \theta_{ij}$ . It is essential to discretize the first-order derivatives instead of the second-order derivatives on the boundary because the discretization errors of lower-order derivatives are much smaller. If the supporting points  $ij$  and  $ijk$  are the boundary points, the terms that contain  $W_{ij}$  and  $W_{ijk}$  are set to zero in Eq. (4.45b). By using this approach, the equation system (4.46) will only be left with terms that contain the function values  $W_i$  at all interior points, and it can be written in a compact form as

$$\mathbf{Aw} = \Omega^2 \mathbf{w} \quad 4.49$$

where  $\mathbf{w} = [W_1 \ W_2 \ \dots \ W_{N_i}]^T$ , and  $\mathbf{A}$  is a coefficient matrix of size  $N_i \times N_i$ . The frequency parameters  $\Omega$  and the mode shapes can be obtained by calculating the eigenvalues and eigenvectors of matrix  $\mathbf{A}$ .

#### 4.5.2 Clamped edge

Consider a plate with all its edges clamped. The boundary conditions for a

clamped edge are given by Eqs. (4.38a,b), i.e. the deflection is zero and the rotation normal to the edge is zero. Now, assume that  $(X, Y)$  is a point on the boundary  $\Gamma$ , then

$$\frac{\partial W}{\partial n} = \frac{\partial W}{\partial X} \cdot \frac{\partial X}{\partial n} + \frac{\partial W}{\partial Y} \cdot \frac{\partial Y}{\partial n} = \frac{\partial W}{\partial X} \cos \theta + \frac{\partial W}{\partial Y} \sin \theta \quad 4.50a$$

$$\frac{\partial W}{\partial t} = \frac{\partial W}{\partial X} \cdot \frac{\partial X}{\partial t} + \frac{\partial W}{\partial Y} \cdot \frac{\partial Y}{\partial t} = -\frac{\partial W}{\partial X} \sin \theta + \frac{\partial W}{\partial Y} \cos \theta \quad 4.50b$$

where the relations  $\partial X/\partial n = \cos \theta$ ,  $\partial Y/\partial n = \sin \theta$ ,  $\partial X/\partial t = -\sin \theta$  and  $\partial Y/\partial t = \cos \theta$  can be verified from Fig. 4.2. From Eqs. (4.38a,b), we can derive  $\partial W/\partial n = \partial W/\partial t = 0$  along the clamped edge. Then from Eqs. (4.50a,b), we obtain  $\partial W/\partial X = \partial W/\partial Y = 0$ . Therefore, the clamped boundary condition given by Eqs. (4.38a,b) can be equivalently written as

$$W_i = 0 \quad 4.51a$$

$$\frac{\partial W_i}{\partial X} = \frac{\partial W_i}{\partial Y} = 0 \quad 4.51b$$

for  $i = N_i + 1, N_i + 2, \dots, N_t$ .

As shown in Eq. (4.45), the spatial operator in the governing equation can be discretized as

$$\nabla^2(\nabla^2 W_i) = \sum_{j=1}^m c_j^i \nabla^2 W_{ij} + \left( -\sum_{j=1}^m c_j^i \right) \nabla^2 W_i \quad 4.52$$

For a boundary point  $ij$ , the term  $c_j^i \nabla^2 W_{ij}$  in Eq. (4.52) can be further discretized as

$$\begin{aligned} c_j^i \nabla^2 W_{ij} &= c_j^i \left( \frac{\partial^2 W_{ij}}{\partial X^2} + \frac{\partial^2 W_{ij}}{\partial Y^2} \right) \\ &= c_j^i \left[ \sum_{k=1}^m T_{1,k}^{ij} \left( \frac{\partial W_{ijk}}{\partial X} - \frac{\partial W_{ij}}{\partial X} \right) + \sum_{k=1}^m T_{2,k}^{ij} \left( \frac{\partial W_{ijk}}{\partial Y} - \frac{\partial W_{ij}}{\partial Y} \right) \right] \end{aligned} \quad 4.53$$

Then the boundary condition (4.51b) can be directly substituted into Eq. (4.53). For an interior point  $ij$ , Eq. (4.52) can be further discretized as shown in Eq. (4.45b). The zero deflection condition ( $W = 0$ ) can be substituted into the final form of discretized governing equation. As a result, the final discretized system of equations only involves the function values at interior points, and a similar matrix form to Eq. (4.49) can be obtained.

### 5.5.3 Free edge

Consider a plate with all its edges free. The boundary conditions for a free edge are given by Eqs. (4.39a,b), i.e. the normal bending moment is zero and the normal effective shear force is zero. First, we need to transform Eq. (4.39a). By using Eq. (4.27), Eq. (4.39a) can be discretized as

$$\sum_{j=1}^m (\tilde{T}_{3,j}^i + v \tilde{T}_{4,j}^i) W_{ij} + \left[ -\sum_{j=1}^m (\tilde{T}_{3,j}^i + v \tilde{T}_{4,j}^i) \right] W_i = 0 \quad 4.54$$

From Eq. (4.54), we have

$$W_i = -\frac{\left[ \sum_{j=1}^m (\tilde{T}_{3,j}^i + v \tilde{T}_{4,j}^i) W_{ij} \right]}{\left[ -\sum_{j=1}^m (\tilde{T}_{3,j}^i + v \tilde{T}_{4,j}^i) \right]} \quad 4.55$$

Second, we need to transform Eq. (4.39b). Noting that  $\nabla^2 W = \partial^2 W / \partial n^2 + \partial^2 W / \partial t^2$ , Eq. (4.39a) is equivalent to

$$\nabla^2 W_i = (1 - v) \frac{\partial^2 W_i}{\partial t^2} \quad \text{for point } i \text{ on a free edge.} \quad 4.56$$

In addition, Eq. (4.39b) can be reduced to

$$\begin{aligned} & \frac{\partial}{\partial n} (\nabla^2 W_i) \\ & + (1 - v) \frac{\partial}{\partial s} \left[ \cos 2\theta_i \frac{\partial^2 W_i}{\partial X \partial Y} + \frac{1}{2} \sin 2\theta_i \left( \frac{\partial^2 W_i}{\partial Y^2} - \frac{\partial^2 W_i}{\partial X^2} \right) \right] = 0 \end{aligned} \quad 4.57$$

By performing the differentiation  $\partial/\partial s$  of the expression in the square brackets and using the relations

$$\begin{aligned} & \cos 2\theta_i \frac{\partial}{\partial s} \left( \frac{\partial^2 W_i}{\partial X \partial Y} \right) + \frac{1}{2} \sin 2\theta_i \frac{\partial}{\partial s} \left( \frac{\partial^2 W_i}{\partial Y^2} - \frac{\partial^2 W_i}{\partial X^2} \right) \\ & = \cos 2\theta_i \frac{\partial}{\partial t} \left( \frac{\partial^2 W_i}{\partial X \partial Y} \right) + \frac{1}{2} \sin 2\theta_i \frac{\partial}{\partial t} \left( \frac{\partial^2 W_i}{\partial Y^2} - \frac{\partial^2 W_i}{\partial X^2} \right) \\ & = \frac{\partial}{\partial t} \left[ \cos 2\theta_i \frac{\partial^2 W_i}{\partial X \partial Y} + \frac{1}{2} \sin 2\theta_i \left( \frac{\partial^2 W_i}{\partial Y^2} - \frac{\partial^2 W_i}{\partial X^2} \right) \right] \\ & = \frac{\partial}{\partial t} \left( \frac{\partial^2 W_i}{\partial n \partial t} \right) = \frac{\partial^2 W_i}{\partial n \partial t^2} \end{aligned}$$

Eq. (4.57) can be further reduced to

$$\begin{aligned} & \frac{\partial}{\partial n} \left[ \nabla^2 W_i + (1 - \nu) \frac{\partial^2 W_i}{\partial t^2} \right] \\ & + (1 - \nu) \frac{\partial \theta_i}{\partial s} \left[ -2 \sin 2\theta_i \cdot \frac{\partial^2 W_i}{\partial X \partial Y} + \cos 2\theta_i \cdot \left( \frac{\partial^2 W_i}{\partial Y^2} - \frac{\partial^2 W_i}{\partial X^2} \right) \right] = 0 \end{aligned} \quad 4.58$$

By using the formulation (4.27), Eq. (4.58) can be discretized into the following form:

$$\begin{aligned} & \sum_{j=1}^m \tilde{T}_{1,j}^i \left[ \nabla^2 W_{ij} + (1 - \nu) \frac{\partial^2 W_{ij}}{\partial t^2} \right] + \left( - \sum_{j=1}^m \tilde{T}_{1,j}^i \right) \left[ \nabla^2 W_i + (1 - \nu) \frac{\partial^2 W_i}{\partial t^2} \right] \\ & + (1 - \nu) \frac{\partial \theta_i}{\partial s} \left[ -2 \sin 2\theta_i \cdot \frac{\partial^2 W_i}{\partial X \partial Y} + \cos 2\theta_i \cdot \left( \frac{\partial^2 W_i}{\partial Y^2} - \frac{\partial^2 W_i}{\partial X^2} \right) \right] = 0 \end{aligned} \quad 4.59$$

The substitution of Eq. (4.56) into Eq. (4.59) yields

$$\nabla^2 W_i = \frac{\left\{ \begin{array}{l} \sum_{j=1}^m \tilde{T}_{1,j}^i \left[ \nabla^2 W_{ij} + (1 - \nu) \begin{pmatrix} \sin^2 \theta_i \frac{\partial^2 W_{ij}}{\partial X^2} + \cos^2 \theta_i \frac{\partial^2 W_{ij}}{\partial Y^2} \\ - \sin 2\theta_i \frac{\partial^2 W_{ij}}{\partial X \partial Y} \end{pmatrix} \right] \\ + (1 - \nu) \frac{\partial \theta_i}{\partial s} \left[ -2 \sin 2\theta_i \cdot \frac{\partial^2 W_i}{\partial X \partial Y} + \cos 2\theta_i \cdot \left( \frac{\partial^2 W_i}{\partial Y^2} - \frac{\partial^2 W_i}{\partial X^2} \right) \right] \end{array} \right\}}{-2 \left( - \sum_{j=1}^m \tilde{T}_{1,j}^i \right)} \quad 4.60$$

We have used the relation

$$\frac{\partial^2 W_{ij}}{\partial t^2} = \sin^2 \theta_i \frac{\partial^2 W_{ij}}{\partial X^2} + \cos^2 \theta_i \frac{\partial^2 W_{ij}}{\partial Y^2} - \sin 2\theta_i \frac{\partial^2 W_{ij}}{\partial X \partial Y}$$

to obtain Eq. (4.60), which is a second-order differential equation reduced from the original third-order differential equation (4.57). In sum, we have transformed Eqs. (4.39a,b) into Eqs. (4.55) and (4.60). For easy reference, the latter equations are listed together:

$$W_i = - \frac{\sum_{j=1}^m (\tilde{T}_{3,j}^i + v \tilde{T}_{4,j}^i) W_{ij}}{\sum_{j=1}^m (\tilde{T}_{3,j}^i + v \tilde{T}_{4,j}^i)} \quad 4.61a$$

$$\nabla^2 W_i = \left\{ \begin{array}{l} \sum_{j=1}^m \tilde{T}_{1,j}^i \left[ \nabla^2 W_{ij} + (1-v) \begin{pmatrix} \sin^2 \theta_i \frac{\partial^2 W_{ij}}{\partial X^2} + \cos^2 \theta_i \frac{\partial^2 W_{ij}}{\partial Y^2} \\ -\sin 2\theta_i \frac{\partial^2 W_{ij}}{\partial X \partial Y} \end{pmatrix} \right] \\ + (1-v) \frac{\partial \theta_i}{\partial s} \left[ -2 \sin 2\theta_i \cdot \frac{\partial^2 W_i}{\partial X \partial Y} + \cos 2\theta_i \cdot \left( \frac{\partial^2 W_i}{\partial Y^2} - \frac{\partial^2 W_i}{\partial X^2} \right) \right] \end{array} \right\} \left[ -2 \left( -\sum_{j=1}^m \tilde{T}_{1,j}^i \right) \right] \quad 4.61b$$

Eqs. (4.61a,b) will be used as the alternative form for the boundary conditions of a free edge.

A further inspection on the equivalent boundary condition equations (4.61a,b) reveals a trick that allows easy implementation of the free edge boundary conditions, i.e. we may define  $m$  nearest *interior* points as the supporting points  $ij$  of each boundary point  $i$ . Then Eq. (4.61b) shows that  $\nabla^2 W_i$  may be expressed as a linear combination of the second-order derivatives of  $W$  at the point  $i$  itself and its  $m$  interior supporting points  $ij$ ; and Eq. (4.61a) shows that the function value  $W_i$  may be expressed as a linear combination of the function values  $W_{ij}$  at  $m$  interior supporting points  $ij$ .

The boundary conditions of free edges are now ready to be implemented by using Eqs. (4.61a,b). First, Eq. (4.61b) can be substituted into the first step of discretization of governing PDE as shown in (4.45a) if a point  $ij$  happens to be a boundary point. Next, the second step of discretization of governing PDE is performed; a process similar to that shown in Eq. (4.45b). Then Eq. (4.61a) can be substituted into the final expression of the second step of discretization.

Finally, the fully discretized governing equation collocated at an interior point  $i$  contains only function values at interior points. For all the interior points  $i = 1, \dots, N_i$ , the fully discretized governing equations of this kind can be collectively expressed as

$$\mathbf{Aw} = \Omega^2 \mathbf{w} \quad 4.62$$

where  $\mathbf{w} = [W_1 \ W_2 \ \dots \ W_{N_i}]^T$ , the coefficient matrix  $\mathbf{A}$  is of dimension

$N_i \times N_i$ , the frequency parameters  $\Omega$  and the mode shapes  $\mathbf{w}$  of the plates can be derived by calculating eigenvalues and eigenvectors of the matrix  $\mathbf{A}$ .

It should be noted that the procedures described in the foregoing subsections can be used together so that any combination of boundary conditions can be implemented.

## 4.6 Computation of stress resultants

Apart from being able to obtain accurate results for frequency parameters and mode shapes, the LSFD method also allows the determination of accurate modal stress resultants which many numerical methods will not be able to do. This is due to the capability of the method in ensuring the complete satisfaction of the boundary conditions and the higher accuracy of approximation of the higher-order derivatives throughout the plate domain.

The stress resultants are computed by using the following expressions (Timoshenko and Woinowsky-Krieger 1959):

$$M_x = -D\left(\frac{\partial^2 W}{\partial x^2} + \nu \frac{\partial^2 W}{\partial y^2}\right), \quad M_y = -D\left(\frac{\partial^2 W}{\partial y^2} + \nu \frac{\partial^2 W}{\partial x^2}\right) \quad 4.63a$$

$$M_{xy} = D(1 - \nu) \frac{\partial^2 W}{\partial x \partial y} \quad 4.63b$$

$$Q_x = -D \frac{\partial}{\partial x} (\nabla^2 W), \quad Q_y = -D \frac{\partial}{\partial y} (\nabla^2 W) \quad 4.63c$$

$$V_n = Q_n - \frac{\partial M_{nt}}{\partial s} \quad 4.63d$$

$$M_{x'} = M_x \cos^2 \alpha + M_y \sin^2 \alpha - 2M_{xy} \sin \alpha \cos \alpha \quad 4.63e$$

$$M_{x'y'} = M_{xy} (\cos^2 \alpha - \sin^2 \alpha) + (M_x - M_y) \sin \alpha \cos \alpha \quad 4.63f$$

$$Q_{x'} = Q_x \cos \alpha + Q_y \sin \alpha \quad 4.63g$$

In Eqs. (4.63e,f,g),  $x'$  denotes the direction which makes an angle  $\alpha$  with respect to the  $x$  axis. By setting  $\partial M_{x'}/\partial \alpha = 0$ , one obtains

$$\alpha_1 = \frac{1}{2} \arctan \frac{2M_{xy}}{-M_x + M_y}, \quad \alpha_2 = \frac{1}{2} \arctan \frac{2M_{xy}}{-M_x + M_y} + \frac{\pi}{2} \quad 4.64a$$

By back-substituting Eq. (4.64a) into Eq. (4.63e), the principal bending moments at a point of interest can be obtained. By setting  $\partial M_{x'y'}/\partial \alpha = 0$ , we have

$$\alpha_3 = \frac{1}{2} \arctan \frac{M_x - M_y}{2M_{xy}}, \quad \alpha_4 = \frac{1}{2} \arctan \frac{M_x - M_y}{2M_{xy}} + \frac{\pi}{2} \quad 4.64b$$

The back-substitution of Eq. (4.64b) into Eq. (4.63f) furnishes the maximum and minimum twisting moments at the point of interest. By setting  $\partial Q_x / \partial \alpha = 0$ , one obtains

$$\alpha_5 = \arctan \frac{Q_y}{Q_x} \quad 4.64c$$

The back-substitution of Eq. (4.64c) into Eq. (4.63g) yields the maximum absolute shear forces at a point of interest.

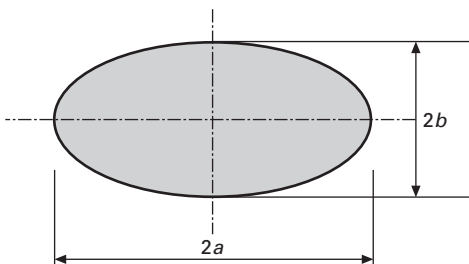
## 4.7 Numerical examples

In this section, the high accuracy and effectiveness of the LSFD method will be demonstrated via some plate vibration problems. In the following LSFD computations, the symbol  $N_t$  represents the total number of mesh points and the symbol  $N$  the number of truncated terms in the Taylor series expansions (4.1) and (4.24).

### 4.7.1 Circular and elliptical plates

Figure 4.3 shows an elliptical plate which covers the special case of a circular plate when  $b = a$ . The LSFD scheme with  $N_t = 2468$  and  $N = 27$  is used in the case of a completely free circular plate while  $N_t = 2504$  and  $N = 35$  is used for a completely free elliptical plate.

Table 4.1 presents the first six vibration frequency parameters  $\Omega = \omega a^2 \sqrt{\rho h/D}$  of the completely free circular and elliptical plates. (Note that for the completely free plates, the first three modes correspond to rigid body motions and the frequencies of these rigid modes are zero.) For the completely free circular plate with Poisson's ratio  $\nu = 0.33$ , LSFD results were checked against exact frequency parameters that were published by Itao and Crandall (1979) who used the Bessel functions for solutions. The LSFD results are in excellent agreement with the exact results, thereby confirming the validity, convergence and accuracy of the method.



4.3 Elliptical plate.

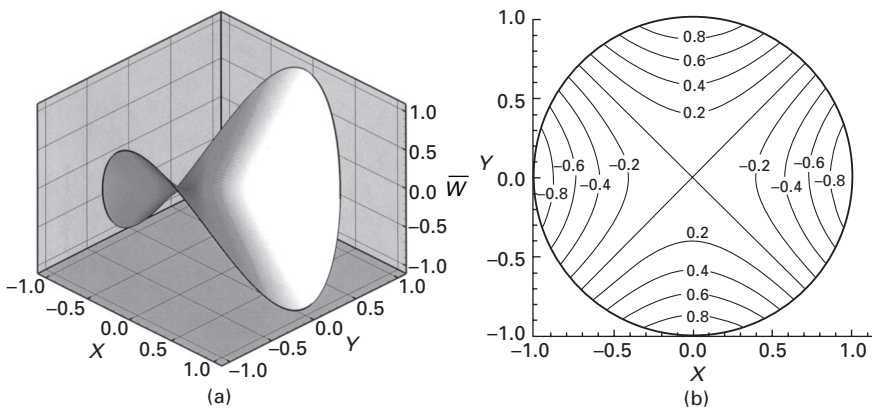
Table 4.1 First six vibration frequency parameters  $\Omega = \omega a^2 \sqrt{\rho h/D}$  of completely free circular and elliptical plates

Source	$N_t$	N	Mode sequence					
			1	2	3	4	5	6
<b>Circular plate, <math>a/b = 1.0</math> (<math>v = 0.33</math>)</b>								
LSFD	2468	27	5.2620	5.2620	9.0687	12.243	12.245	20.511
Itao and Crandall (1979)*			5.2620	9.0689	12.244	12.244	12.244	20.513
<b>Circular plate, <math>a/b = 1.0</math> (<math>v = 0.3</math>)</b>								
LSFD	2468	27	5.3583	5.3583	9.0030	12.439	12.440	20.473
Lam <i>et al.</i> (1992)			5.3583	5.3583	9.0732	12.439	12.439	20.521
Sato (1973)			5.3592	5.3592	9.0120	—	—	—
Narita (1985)			5.3583	5.3583	9.0031	12.439	12.439	20.475
<b>Elliptical plate, <math>a/b = 2.0</math> (<math>v = 0.3</math>)</b>								
LSFD	2504	35	6.6705	10.547	16.922	22.015	27.765	31.521
Lam <i>et al.</i> (1992)			6.6704	10.548	16.923	22.021	27.777	31.523
Sato (1973)			6.6667	—	—	—	27.773	31.517
Narita (1985)			6.6705	10.548	16.921	22.015	27.768	31.513

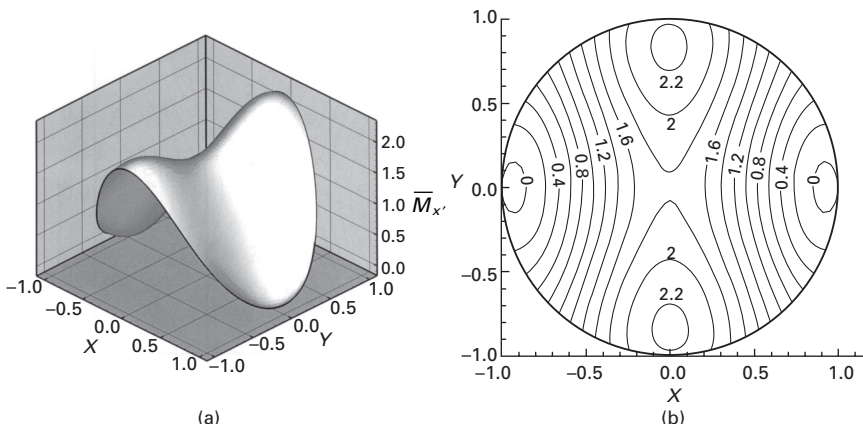
\*Exact solutions.

The LSFD results for elliptical and circular plates (with  $\nu = 0.3$ ) are also compared with those obtained by Lam *et al.* (1992) and Narita (1985) using the Rayleigh-Ritz method, and by Sato (1973) who employed the Mathieu functions and modified Mathieu functions. Again, the results are in close agreement with each other.

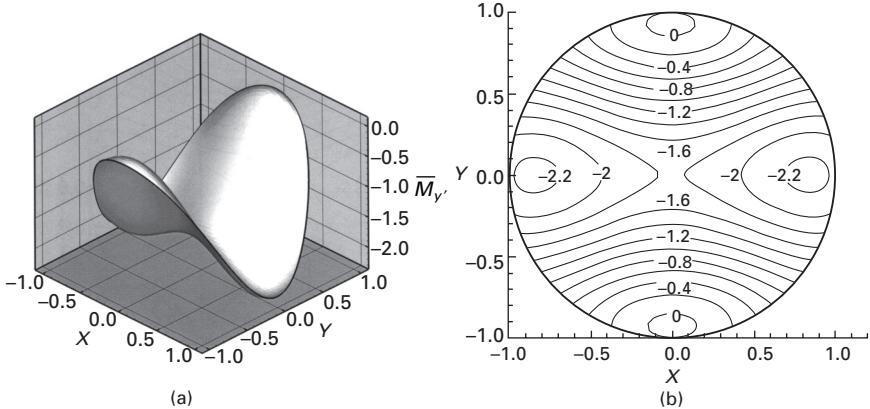
By normalizing  $\bar{W}_{\max} = |W_{\max}/a| = 1$ , the fundamental vibration mode shape and the corresponding non-dimensionalized modal stress resultants (i.e. the principal bending moments  $\bar{M}_{x'} = M_{x'}a/D$ ,  $\bar{M}_{y'} = M_{y'}a/D$ , the maximum twisting moment  $\bar{M}_{x''y''} = M_{x''y''}a/D$ , the maximum absolute shear forces  $\bar{Q}_{x'''} = |Q_{x'''}|a^2/D$ ) of the completely free vibrating circular plate are presented in 3D and contour plots in Figs 4.4 to 4.8. The distributions of



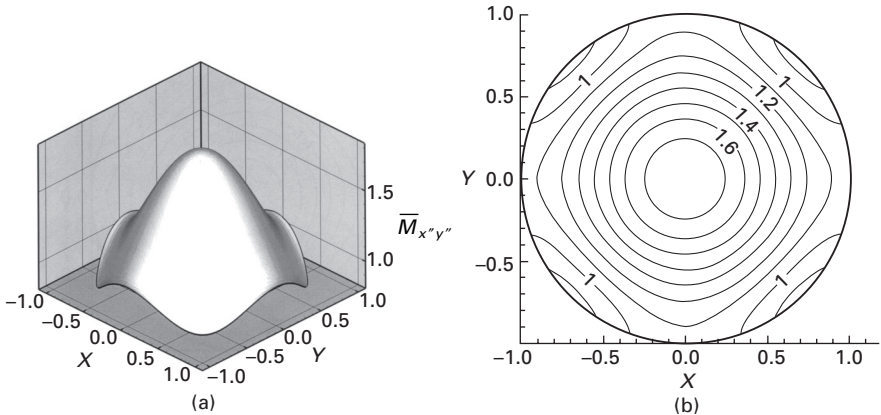
4.4 Modal deflections  $\bar{W}$  for free circular plate vibrating in fundamental mode.



4.5 Principal modal bending moment  $\bar{M}_{x'}$  for free circular plate vibrating in fundamental mode.



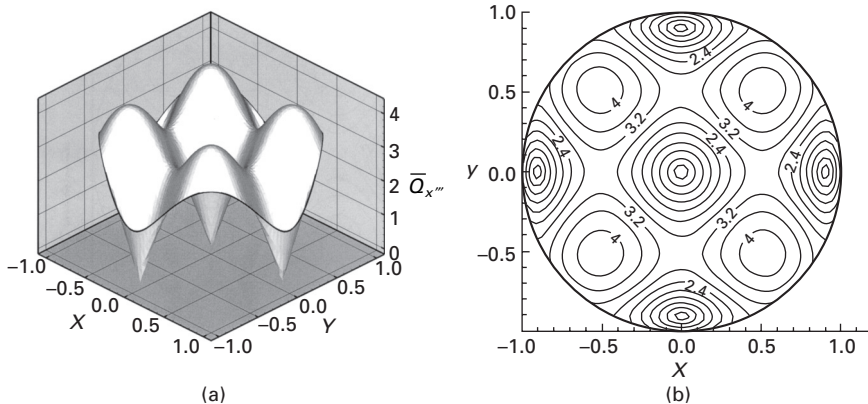
4.6 Principal modal bending moment  $\bar{M}_{y'}$  for free circular plate vibrating in fundamental mode.



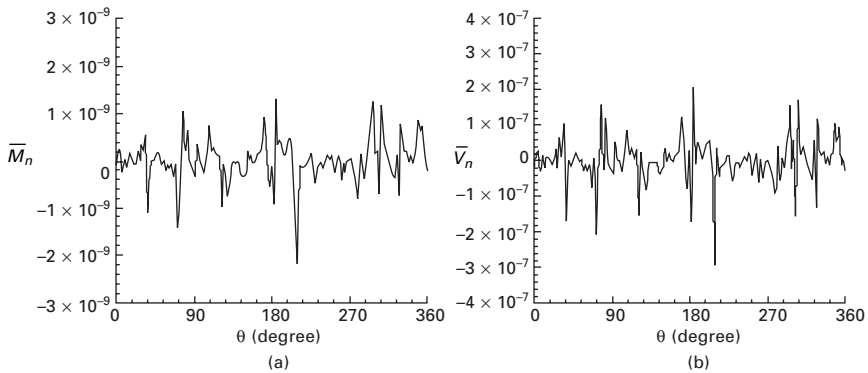
4.7 Maximum modal twisting moment  $\bar{M}_{x''y''}$  for free circular plate vibrating in fundamental mode.

the modal stress resultants are smooth over the domain. Moreover the stress resultants satisfy the natural boundary conditions as shown in Fig. 4.9. In this figure,  $|\bar{M}_n|_{\max} = 2.2042 \times 10^{-9}$  and  $|\bar{V}_n|_{\max} = 2.9302 \times 10^{-7}$  at the plate free edge. Noting that in the plate domain,  $|\bar{M}_{x'}|_{\max} = 2.2451$  and  $|\bar{Q}_{x'''}|_{\max} = 4.2350$ , the relative errors of  $\bar{M}_n$  and  $\bar{V}_n$  are very small, i.e.  $|\bar{M}_n|_{\max} / |\bar{M}_{x'}|_{\max} = 9.82 \times 10^{-10}$  and  $|\bar{V}_n|_{\max} / |\bar{Q}_{x'''}|_{\max} = 6.92 \times 10^{-8}$ . In view of such small magnitudes of the absolute and relative errors of  $\bar{M}_n$  and  $\bar{V}_n$ , one can regard that the natural boundary conditions  $\bar{M}_n = 0$  and  $\bar{V}_n = 0$  are strictly satisfied. A literature search reveals that such accurate modal stress resultants obtained by other numerical methods are not available.

This plate example illustrates that it is not only frequencies and mode shapes that can be obtained accurately by using the LSFD method, but also the modal stress resultants.



4.8 Maximum modal shear force  $\bar{Q}_{x''}$  for free circular plate vibrating in fundamental mode.



4.9 Verification of satisfaction of natural boundary conditions ( $\bar{M}_n = 0$ ,  $\bar{V}_n = 0$ ) at free edge of circular plate vibrating in fundamental mode.

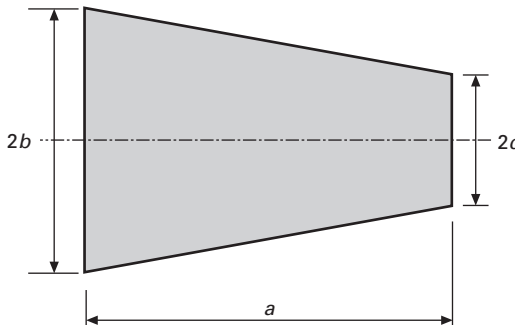
#### 4.7.2 Symmetric trapezoidal plate

Next, a symmetric trapezoidal plate as shown in Fig. 4.10 is considered. Three combinations of simply supported and clamped boundary conditions, viz. SS-SS-SS-SS, C-C-C-C and SS-C-SS-C, are treated. The designation SS-C-SS-C denotes that the two parallel opposite edges are simply supported while the other two edges are clamped. In the LSFD scheme employed for computing the numerical results for the three cases of boundary conditions,  $N_t = 2954$  and  $N = 14$  are adopted. For SS-SS-SS-SS and C-C-C-C plates, the approaches for implementation of simply supported and clamped boundary conditions introduced in Sections 4.5.1 and 4.5.2 are applied, respectively. For SS-C-SS-C plate, the above two approaches are used together.

Table 4.2 presents the first six vibration frequencies of this plate shape. It can be seen that the LSFD results are in excellent agreement with those

Table 4.2 First six vibration frequency parameters  $\Omega = \omega(a/\pi)^2 \sqrt{\rho h/D}$  of a symmetric trapezoidal plate ( $a/b = 3.0$ ,  $b/c = 2.5$ )

Source	$N_t$	$N$	Mode Sequence					
			1	2	3	4	5	6
<b>SS-SS-SS-SS plate</b>								
LSFD	2954	14	5.3891	9.4223	14.682	15.908	21.690	23.140
Bert and Malik (1996)	$25 \times 25$		5.3890	9.4219	14.680	15.908	21.689	23.140
Chopra and Durvasula (1971)			5.3896	9.424	14.685	15.911	21.700	23.146
Wang and Cheng-Tzu (1994)			5.3906	9.4311	14.727	15.936	21.909	23.205
<b>C-C-C-C plate</b>								
LSFD	2954	14	10.428	15.567	21.481	23.905	28.827	32.552
Bert and Malik (1996)	$17 \times 17$	10.427	15.563	21.476		23.905	28.842	32.540
<b>SS-C-SS-C plate</b>								
LSFD	2954	14	9.4431	14.386	19.896	22.473	26.328	30.879
Bert and Malik (1996)	$17 \times 17$	9.4431	14.386	19.897		22.472	26.331	30.879



4.10 Symmetrical trapezoidal plate.

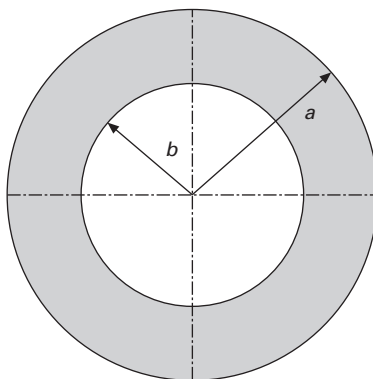
obtained by Bert and Malik (1996), who used the DQ method, by Chopra and Durvasula (1971), who used the Galerkin method, and by Wang and Cheng-Tzu (1994), who used the  $B_3$ -spline functions.

#### 4.7.3 Annular plate

The foregoing examples involve plates with convex and single-connected domain shapes. Usually, numerical problems with concave or multiconnected domain shapes are more difficult to solve accurately (Kang and Lee 2000). In order to demonstrate the applicability of the LSFD method for solving plate problems with concave and multiconnected domain shapes, an annular plate is considered next. Figure 4.11 shows the considered annular plate with  $a/b = 2.0$ . Table 4.3 presents the first four vibration frequency parameters for this annular plate with four combinations of boundary conditions, i.e. C-outside and inside edges, C-outside edge and SS-inside edge, SS-outside edge and C-inside edge, and SS-outside and inside edges. All these results are computed by using the LSFD scheme with  $N_t = 2357$  and  $N = 27$ . It is shown that the LSFD results compare very well with those exact and numerical solutions presented in Leissa's book (1969). The findings confirm the applicability of LSFD for concave and multiconnected plate shapes.

### 4.8 Conclusions

In this chapter, the mesh-free LSFD method is presented for the free vibration analysis of isotropic, thin plates with arbitrary shapes and any boundary conditions. In this method, the chain rule of derivative discretization is used to discretize the fourth-order governing PDE for plate vibration. The discretization is carried out in two steps. In the first step, the fourth-order PDE is reduced to a second-order PDE. In the second step, the second-order PDE is converted into an algebraic equation. The boundary conditions (for simply supported, clamped or free plate edge) can be successively implemented



4.11 Annular plate.

Table 4.3 First four vibration frequency parameters  $\Omega = \omega a^2 \sqrt{\rho h/D}$  of an annular plate ( $a/b = 2.0$ ,  $v = 0.3$ )

Source	$N_t$	$N$	Mode sequence			
			1	2	3	4
<b>C-outside and inside edges</b>						
LSFD	2357	27	89.26	90.24	93.95	98.99
Leissa (1969)			89.30*	90.2	93.3	99.0
<b>C-outside edge and SS-inside edge</b>						
LSFD	2357	27	63.86	65.37	70.04	78.10
Leissa (1969)			64.06*	65.4	70.0	78.1
<b>SS-outside edge and C-inside edge</b>						
LSFD	2357	27	59.90	61.07	64.72	71.21
Leissa (1969)			59.91*	61.0	64.6	71.0
<b>SS-outside and inside edges</b>						
LSFD	2357	27	40.01	41.77	47.07	55.95
Leissa (1969)			40.01*	41.8	47.1	56.0

\*Exact solutions.

during the two-step discretization of the governing equation. The LSFD formulations for approximating derivatives in terms of the local  $nt$ -coordinates at the boundary are proposed as an alternative way to discretizing the boundary condition equations in which the derivatives are given in terms of a local  $nt$ -coordinate system. Numerical simulations show that the chain rule is a very convenient and effective way for approximating high-order derivatives in the LSFD discretization.

The present approach has advantages over the traditional methods such as FDM and DQM. For example, by using the LSFD method, numerical errors caused by discretizing derivatives in the boundary conditions can be completely

avoided in the case of clamped edge and considerably reduced in the case of simply supported edge.

The LSFD method is able to accurately predict the vibration frequencies for any plate shape and boundary conditions as demonstrated by solving the various plate examples that involve circular, elliptical, trapezoidal and annular plates. The latter plate shape serves as an example of a plate with concave and multiconnected domain shape.

In addition, the high accuracy and effectiveness of the LSFD method were established with the yielding of not only accurate frequency parameters and mode shapes, but also accurate modal stress resultants for completely free circular plates. It should be pointed out that the accurate stress resultants for completely free vibrating plates are important to engineers performing hydroelastic analysis of pontoon-type, very large floating structures (Watanabe *et al.* 2004, 2006).

## 4.9 References

- Bert, C.W. and Malik, M. (1996). 'The differential quadrature method for irregular domains and application to plate vibration,' *International Journal of Mechanical Sciences*, **38**(6), 589–606.
- Chopra, I. and Durvasula, S. (1971). 'Vibration of simply-supported trapezoidal plates I. Symmetric trapezoids,' *Journal of Sound and Vibration*, **19**, 379–392.
- Ding, H., Shu, C., Yeo, K.S. and Xu, D. (2004). 'Development of least square-based two-dimensional finite difference schemes and their application to simulate natural convection in a cavity,' *Computers and Fluids*, **33**, 137–154.
- Itao, K. and Crandall, S.H. (1979). 'Natural modes and natural frequencies of uniform, circular, free-edge plates,' *ASME, Journal of Applied Mechanics*, **46**, 448–453.
- Kang, S.W. and Lee, J.M. (2000). 'Application of free vibration analysis of membranes using the non-dimensional dynamic influence function,' *Journal of Sound and Vibration*, **234**, 455–470.
- Lam, K.Y., Liew, K.M. and Chow, S.T. (1992). 'Use of two-dimensional orthogonal polynomials for vibration analysis of circular and elliptical plates,' *Journal of Sound and Vibration*, **154**, 261–269.
- Leissa, A.W. (1969). *Vibration of Plates*, NASA SP-160, US Government Printing Office, Washington, DC.
- Liew, K.M., Wang, C.M., Xiang, Y. and Kitipornchai S. (1998). *Vibration of Mindlin Plates: Programming the p-version Ritz Method*, Elsevier Science, Oxford.
- Mindlin, R.D. (1951). 'Influence of rotatory inertia and shear on flexural motion of isotropic elastic plates,' *Trans. ASME, Journal of Applied Mechanics*, **18**, 31–38.
- Narita, Y. (1985). 'Natural frequencies of free, orthotropic elliptical plates,' *Journal of Sound and Vibration*, **100**, 83–89.
- Sato, K. (1973). 'Free flexural vibration of an elliptical plate with free edge,' *Journal of the Acoustical Society of America*, **54**, 547–550.
- Shu, C. and Du, H. (1997a). 'Implementation of clamped and simply supported boundary conditions in the GDQ free vibration analysis of beams and plates,' *International Journal of Solids and Structures*, **34**(7), 819–835.

- Shu, C. and Du, H. (1997b). 'A generalized approach for implementing general boundary conditions in the GDQ free vibration analysis of plates,' *International Journal of Solids and Structures*, **34**(7), 837–846.
- Timoshenko, S.P. and Woinowsky-Krieger, S. (1959). *Theory of Plates and Shells*. McGraw-Hill, New York.
- Wang, C.M., Xiang, Y., Watanabe, E. and Utsunomiya, T. (2004). 'Mode shapes and stress resultants of circular Mindlin plates with free edges,' *Journal of Sound and Vibration*, **276**, 511–525.
- Wang, G. and Cheng-Tzu, T.H. (1994). 'Static and dynamic analysis of arbitrary quadrilateral flexural plates by  $B_3$ -spline functions,' *International Journal of Solids and Structures*, **31**(5), 657–667.
- Watanabe, E., Utsunomiya, T. and Wang, C.M. (2004). 'Hydroelastic analysis of pontoon-type VLFS: A literature survey,' *Engineering Structures*, **26**, 245–256.
- Watanabe, E., Utsunomiya, T., Wang, C.M. and Le Thi Thu Hang (2006). 'Benchmark hydroelastic responses of a circular VLFS under wave action,' *Engineering Structures*, **28**, 423–430.

# 5

## Analytical $p$ -elements for vibration of plates/plated structures

A Y T L E U N G, City University of Hong Kong,  
People's Republic of China and B Z H U, Zhejiang University,  
People's Republic of China

### 5.1 Introduction

The accuracy of solutions using the finite element method (FEM) may be improved in two ways. The first is by the  $h$ -version to refine the finite element mesh and the second is by the  $p$ -version to increase the order of polynomial shape functions for a fixed mesh. The  $p$ -version elements have several advantages over the  $h$ -version: (i) they have better conditioned matrices; (ii) they do not require a change in the mesh and can be easily used in the adaptive analysis (Peano *et al.* 1979, Papadrakakis and Babilis 1994); (iii) just one  $p$ -version element can predict accurate solutions for a simple structure; (iv)  $p$ -version elements tend to give the same accurate results with far fewer degrees of freedom (DOF) than the  $h$ -version (Houmat 1997a,b, 2000, 2001a, b, 2004); (v) the  $p$ -version elements can overcome some locking problems (Zienkiewicz and Taylor 1989). The new contributions for  $p$ -elements here include the use of Fourier series as well as orthogonal power series and their analytical integration.

Rectangular elements can be used for the vibration analysis of structures with rectangular,  $L$ - and  $H$ -shapes. For irregular polygonal shapes, triangular elements are useful. The existing triangular  $p$ -element (Houmat 2000) cannot be integrated analytically and error from the numerical integration will be introduced. The problem becomes obvious for higher oscillating terms in the shape functions (Woo *et al.* 2003). Fortunately, one can always break a triangle into three trapezoids by drawing three lines parallel to the edges from any point inside the triangle. With analytical integration, the trapezoidal  $p$ -version elements can produce very high vibration modes of the polygonal structures.

The concept of the  $p$ -version elements are presented in detail in Woo *et al.* (2003) and Zienkiewicz *et al.* (1983). Early  $p$ -version elements mainly adopted shape functions of the Lagrange family, the Jacobi family and the 'serendipity' family (Zienkiewicz and Taylor 1989). Recently, researchers are interested in the hierarchical and Fourier  $p$ -elements using the Legendre orthogonal

polynomials and trigonometric functions as the shape functions, respectively. The former converges fast to some lowest frequency modes, and the latter not only can avoid the ill-conditioning problem but also are more effective in predicting the medium- and high-frequency modes (Zienkiewicz *et al.* 1983). The chapter covers the Legendre and Fourier families to generate  $p$ -elements analytically.

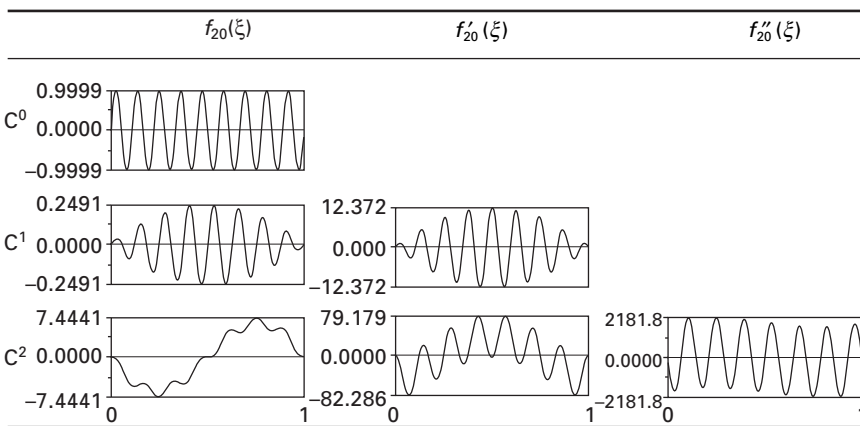
The original  $p$ -version beam elements using Lagrangian polynomials as shape functions have been applied to the free vibration analysis of structures (Martini and Vitaliani 1988). The shape functions satisfy only  $C^0$  continuity, leading easily to an ill-conditioning problem if high-degree polynomials are involved. Bardell (1996) used the  $C^1$  hierarchical straight beam element to analyze the transverse deformation of Euler–Bernoulli beams and Leung and Chan (1998) introduced  $C^0$  and  $C^1$  Fourier  $p$ -elements for the axial and transverse vibration of straight beams, respectively. Houmat (2000) has done much work in the vibration of membranes using both hierarchical and Fourier  $p$ -elements. The rectangular and the sectorial elements are applied to the analysis of irregular polygonal membranes.

For the vibration of plates, the existing hierarchical elements (Woo *et al.* 2003, Bardell 1991, 1992) and Fourier  $p$ -elements (Houmat 1997a,b, 2001a,b, Leung and Chan 1998, Beslin and Nicolas 1997, Bardell *et al.* 1999), using Legendre orthogonal polynomials or trigonometric functions as shape functions respectively are usually based on 16- or 36-DOF rectangular thin plate element (Mindlin 1951). Unfortunately, since the application of these two conforming elements is limited to rectangular and skew elements (Zienkiewicz *et al.* 1983), the above  $p$ -version elements are valid just for these two shapes. Actually, the sectorial element (Houmat 2001a,b) can be seen as a rectangular one in the polar coordinates.

We discuss the ill-conditioning problem in Section 5.2, trapezoidal Mindlin plates in Section 5.3, plates on Pasternak foundations in Section 5.4 and nonlinear vibration in Section 5.5. Recent development can be found in Leung *et al.* (2003a,b, 2004, 2005, Leung and Zhu (2004a,b,c,d, 2005) and Zhu and Leung (2004).

## 5.2 Condition number

Leung and Chan (1998) presented the  $C^0$  Fourier-enriched shape functions  $f_1(\xi) = 1 - \xi$ ,  $f_2(\xi) = \xi$ ,  $f_i(\xi) = \sin(i - 2)\pi\xi$  ( $i \geq 3$ ). The sine functions represent the internal DOF. The  $C^0$ ,  $C^1$  and  $C^2$  Fourier  $p$  shape functions can easily be obtained (Houmat 1997a,b). As an example, the 20th  $C^0$ ,  $C^1$  and  $C^2$  shape functions  $f_{20}(\xi)$  and their first and second derivatives are shown in Table 5.1. On the other hand, the  $C^0$  Legendre orthogonal polynomials are widely used in formulation of  $p$ -version hierarchical elements (Houmat 1997a,b, 2001a,b, Bardell 1992).

Table 5.1 The  $C^0$ ,  $C^1$  and  $C^2$  shape functions  $f_{20}(\xi)$  and their first two derivatives.

The Rodrigues formula for the Legendre polynomials in  $\xi = (-1, 1)$  is given by  $f_k = \frac{1}{2^k k!} \frac{d^k}{d\xi^k} (\xi^2 - 1)^k$ . The condition number CN defined in Cook *et al.* (1989) is used to measure the ill-conditioning in a coefficient matrix. The smaller CN, the more stable is the matrix. The mass matrices of a uniform beam vibrating axially for a Fourier  $p$ -element and a Legendre  $p$ -element are respectively,

$$\begin{bmatrix} \frac{1}{3} & \frac{1}{6} & \left[ \frac{1}{j\pi} \right] \\ & \frac{1}{3} & \left[ \frac{(-1)^{j+1}}{j\pi} \right] \\ \text{sym} & & [\delta_{ij}/2] \end{bmatrix}$$

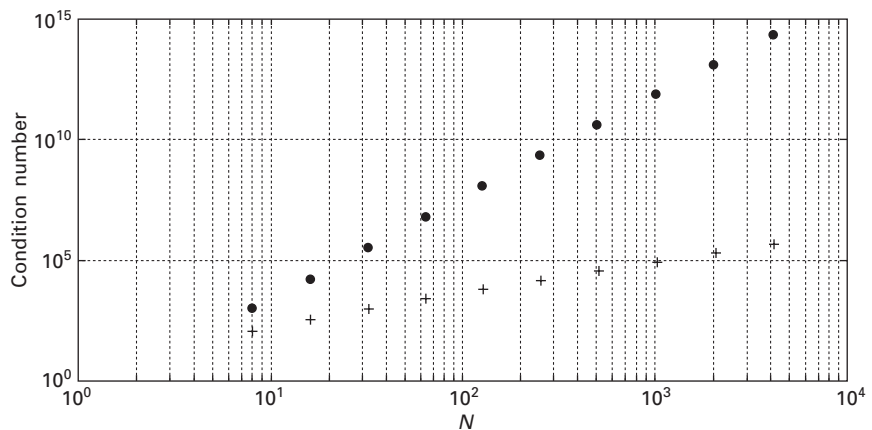
and

$$\begin{bmatrix} \frac{1}{3} & \frac{1}{6} & -\frac{1}{6} & \frac{1}{30} & 0 & 0 \\ \frac{1}{3} & -\frac{1}{6} & -\frac{1}{30} & 0 & 0 & \\ \frac{2}{5 \times 3 \times 1} & 0 & \frac{-1}{9 \times 7 \times 5} & 0 & \\ \frac{2}{7 \times 5 \times 3} & 0 & \frac{-1}{11 \times 9 \times 7} & \\ \ddots & \ddots & \ddots & \ddots \end{bmatrix}$$

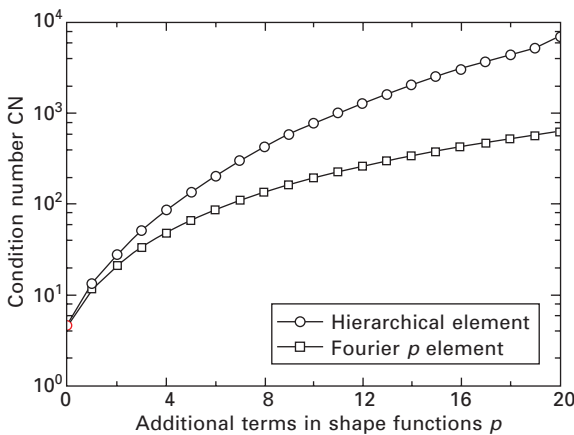
where  $\lfloor \cdot \rfloor$  denotes a row vector and  $\delta_{ij}$  is the Kronecker delta which is 1 when  $i = j$  and 0 otherwise. The condition numbers of the Fourier and the Legendre mass matrices denoted by ‘+’ and ‘.’ respectively are given in Fig. 5.1 for various matrix size  $N$ . It is evident that the Fourier  $p$ -mass matrix is much more stable than that of the Legendre  $p$ -element.

The CN of the mass matrices of both elements for bending of a simply supported beam are compared in Fig. 5.2 with various  $p$ . In fact, using double precision, the mass matrix of the Legendre  $p$ -element will be ill-conditioning when  $p = 41$  and any software will fail to find eigenvectors. A similar phenomenon was also found in Beslin and Nicolas (1997).

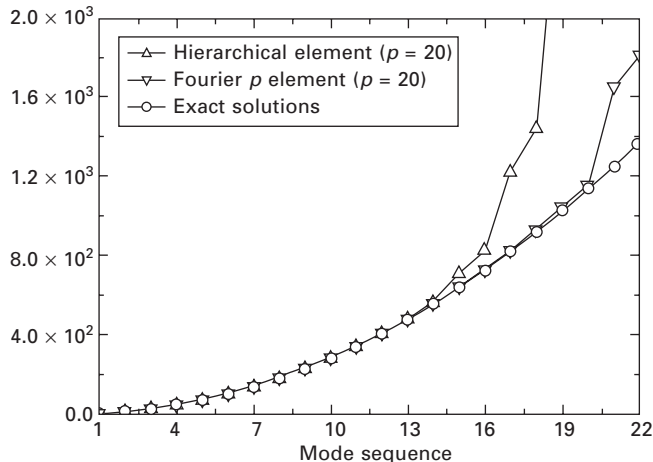
The computed natural frequencies with  $p = 20$  are compared in Fig. 5.3 along with the exact solutions. The Fourier  $p$ -element using trigonometric



5.1 Condition numbers of the Fourier and the Legendre mass matrices.



5.2 Comparison of the condition number CN of the mass matrices.



### 5.3 Comparison of the computed natural frequencies.

shape functions is indeed more effective in predicting the medium- and high-frequency modes.

## 5.3 Trapezoidal Mindlin plate elements

The coordinate systems used to define trapezoidal elements are shown in Fig. 5.4 for the Cartesian plane coordinates and the mapped  $\xi$ - $\eta$  square plane region. The Jacobian matrix is defined in terms of the Cartesian coordinates at the four corner nodes as

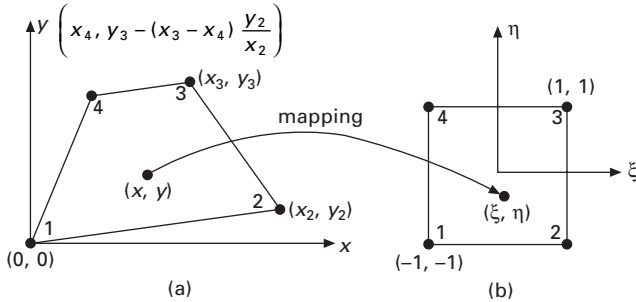
$$\mathbf{J} = \begin{bmatrix} \frac{\partial x}{\partial \xi} & \frac{\partial y}{\partial \xi} \\ \frac{\partial x}{\partial \eta} & \frac{\partial y}{\partial \eta} \end{bmatrix} = \begin{bmatrix} a + b\eta & d + e\eta \\ c + b\xi & f + e\xi \end{bmatrix} \quad 5.1$$

where  $a = 0.25(x_2 + x_3 - x_4)$ ,  $b = 0.25(-x_2 + x_3 - x_4)$ ,  $c = 0.25(-x_2 + x_3 + x_4)$ ,  $d = 0.25y_2$ ,  $e = -0.25y_2$ ,  $f = 0.25(-y_2 + 2y_3)$ .

The Jacobian is  $|\mathbf{J}| = \frac{y_4}{8} [(-x_2 + x_3 - x_4)\eta + (x_2 + x_3 - x_4)]$ , and

$$\mathbf{J}^{-1} = \frac{1}{|\mathbf{J}|} \begin{bmatrix} f + e\xi & -(d + e\eta) \\ -(c + b\xi) & a + b\eta \end{bmatrix} \quad 5.2$$

The deflection  $w$  and the rotations  $\theta_x$ ,  $\theta_y$  are interpolated using the  $C^0$  Legendre or Fourier hierarchical shape functions



5.4 The trapezoidal elements coordinate transformation.

$$\mathbf{u} = \begin{Bmatrix} w \\ \theta_x \\ \theta_y \end{Bmatrix} = \begin{bmatrix} N_1 & 0 & 0 & N_2 & 0 & 0 & N_i & 0 & 0 & \dots \\ 0 & N_1 & 0 & 0 & N_2 & 0 & 0 & N_i & 0 & \dots \\ 0 & 0 & N_1 & 0 & 0 & N_2 & 0 & 0 & N_i & \dots \end{bmatrix} \boldsymbol{\delta}^e$$

$$= \mathbf{N} \cdot \boldsymbol{\delta}^e \quad 5.3$$

where  $\boldsymbol{\delta}^e$  is the vector of generalized DOF, and  $N_i(\xi, \eta) = f_j(\xi)f_k(\eta)$ ,  $i = 1, 2, \dots, (p+2)(q+2)$  in which  $f_j(\xi)$  and  $f_k(\eta)$  are the one-dimensional shape functions of either the Fourier or the Legendre forms. The first 10 Legendre functions are

$$\begin{aligned} f_1 &= (1 - \xi)/2 \\ f_2 &= (\xi + 1)/2 \\ f_3 &= (\xi^2 - 1)/2 \\ f_4 &= (\xi^3 - x)/2 \\ f_5 &= (5\xi^4 - 6\xi^2 + 1)/8 \\ f_6 &= (7\xi^5 - 10\xi^3 + 3\xi)/8 \\ f_7 &= (63\xi^6 - 105\xi^4 + 45\xi^2 - 3)/48 \\ f_8 &= (99\xi^7 - 189\xi^5 + 105\xi^3 - 15\xi)/48 \\ f_9 &= (429\xi^8 - 924\xi^6 + 630\xi^4 - 140\xi^2 + 5)/128 \\ f_{10} &= (715\xi^9 - 1716\xi^7 + 1386\xi^5 - 420\xi^3 + 35\xi)/128 \end{aligned}$$

and the Fourier functions are

$$\begin{aligned} f_1 &= (1 - \xi)/2 \\ f_2 &= (\xi + 1)/2 \\ f_{i+2} &= \sin [i\pi(1 + \xi)/2] \quad i = 1, 2, \dots \end{aligned}$$

Substituting Eqs. (5.2) and (5.3) into the strain equations of the Mindlin theory (Mindlin 1951, Wang *et al.* 2001) gives

$$\chi = \begin{Bmatrix} \frac{\partial \theta_x}{\partial x} \\ \frac{\partial \theta_y}{\partial y} \\ \frac{\partial \theta_x}{\partial y} + \frac{\partial \theta_y}{\partial x} \end{Bmatrix} = \begin{bmatrix} 0 & \partial/\partial x & 0 \\ 0 & 0 & \partial/\partial y \\ 0 & \partial/\partial y & \partial/\partial x \end{bmatrix} \mathbf{u} = \mathbf{B}_b \cdot \boldsymbol{\delta}^e \quad 5.4a$$

$$\gamma = \begin{Bmatrix} \frac{\partial w}{\partial x} + \theta_x \\ \frac{\partial w}{\partial y} + \theta_y \end{Bmatrix} = \begin{bmatrix} \partial/\partial x & 1 & 0 \\ \partial/\partial y & 0 & 1 \end{bmatrix} \mathbf{u} = \mathbf{B}_s \cdot \boldsymbol{\delta}^e \quad 5.4b$$

In view of the coordinate mapping, the derivatives in  $\mathbf{B}_b$  and  $\mathbf{B}_s$  should be replaced by

$$\begin{Bmatrix} \partial/\partial x \\ \partial/\partial y \end{Bmatrix} = \mathbf{J}^{-1} \begin{Bmatrix} \partial/\partial \xi \\ \partial/\partial \eta \end{Bmatrix} \quad 5.5$$

For the harmonic vibration, the stiffness and the mass matrices of the element are obtained by applying the principle of minimum potential energy and Hamilton's principle respectively as follows

$$\begin{aligned} \mathbf{K}^e &= \int_A \mathbf{B}_b^T \mathbf{D}_b \mathbf{B}_b dA + \int_A \mathbf{B}_s^T \mathbf{D}_s \mathbf{B}_s dA \\ &= \int_{-1}^1 \int_{-1}^1 \mathbf{B}_b^T \mathbf{D}_b \mathbf{B}_b \cdot |\mathbf{J}| d\xi d\eta \\ &\quad + \int_{-1}^1 \int_{-1}^1 \kappa G t \cdot \mathbf{B}_s^T \text{diag}[1, 1] \mathbf{B}_s \cdot |\mathbf{J}| d\xi d\eta \end{aligned} \quad 5.6a$$

$$\begin{aligned} \mathbf{M}^e &= \int_A \rho t \cdot \mathbf{N}^T \text{diag}[1, t^2/12, t^2/12] \mathbf{N} dA \\ &= \int_{-1}^1 \int_{-1}^1 \rho t \cdot \mathbf{N}^T \text{diag}[1, t^2/12, t^2/12] \mathbf{N} \cdot |\mathbf{J}| d\xi d\eta \end{aligned} \quad 5.6b$$

where  $\rho$  is the density,  $t$  is the thickness of the element,  $\kappa$  is the shear correction factor,  $G$  is the shear modulus, and  $\mathbf{D}_b$  is defined as

$$\mathbf{D}_b = \frac{Et^3}{12(1-\nu^2)} \cdot \begin{bmatrix} 1 & \nu & 0 \\ \nu & 1 & 0 \\ 0 & 0 & (1-\nu)/2 \end{bmatrix} = D_0 \cdot \begin{bmatrix} 1 & \nu & 0 \\ \nu & 1 & 0 \\ 0 & 0 & (1-\nu)/2 \end{bmatrix} \quad 5.7$$

in which  $E$  is Young's modulus and  $\nu$  is Poisson's ratio. For the trapezoidal element, since the determinant of Jacobian  $|J|$  is only related to  $\eta$ , so that  $\xi$  and  $\eta$  can be integrated independently in Eq. (5.6).

The coefficients of the stiffness matrix the trapezoidal plate element are: if  $m = 3[j + (i - 1)(q + 2)] - 2$  and  $n = 3[l + (k - 1)(q + 2)] - 2$

$$K_{m,n} = cGt \cdot A_{(1)i,k}^{1,1} B_{(1)j,l}^{0,0} + \frac{Gt}{c} \cdot A_{(3)i,k}^{1,1} B_{(1)j,l}^{0,0} - \frac{Gt}{c} \cdot A_{(2)i,k}^{1,0} B_{(2)j,l}^{0,1} \\ - \frac{Gt}{c} \cdot A_{(2)i,k}^{0,1} B_{(2)j,l}^{1,0} + \frac{Gt}{c} \cdot A_{(1)i,k}^{0,0} B_{(3)j,l}^{1,1}$$

else if  $m = 3[j + (i - 1)(q + 2)] - 2$  and  $n = 3[l + (k - 1)(q + 2)] - 1$

$$K_{m,n} = cGt \cdot A_{(1)i,k}^{1,0} B_{(2)j,l}^{0,0}$$

else if  $m = 3[j + (i - 1)(q + 2)] - 2$  and  $n = 3[l + (k - 1)(q + 2)]$

$$K_{m,n} = Gt \cdot A_{(1)i,k}^{0,0} B_{(3)j,l}^{1,0} - Gt \cdot A_{(2)i,k}^{1,0} B_{(2)j,l}^{0,0}$$

else if  $m = 3[j + (i - 1)(q + 2)] - 1$  and  $n = 3[l + (k - 1)(q + 2)] - 2$

$$K_{m,n} = cGt \cdot A_{(1)i,k}^{0,1} B_{(2)j,l}^{0,0}$$

else if  $m = 3[j + (i - 1)(q + 2)] - 1$  and  $n = 3[l + (k - 1)(q + 2)] - 1$

$$K_{m,n} = cD_0 \cdot A_{(1)i,k}^{1,1} B_{(1)j,l}^{0,0} + \frac{(1 - \nu)D_0}{2c} \cdot A_{(3)i,k}^{1,1} B_{(1)j,l}^{0,0} \\ - \frac{(1 - \nu)D_0}{2c} \cdot A_{(2)i,k}^{1,0} B_{(2)j,l}^{0,1} - \frac{(1 - \nu)D_0}{2c} \cdot A_{(2)i,k}^{0,1} B_{(2)j,l}^{1,0} \\ + \frac{(1 - \nu)D_0}{2c} \cdot A_{(1)i,k}^{0,0} B_{(3)j,l}^{1,1} + cGt \cdot A_{(1)i,k}^{0,0} B_{(3)j,l}^{0,0}$$

else if  $m = 3[j + (i - 1)(q + 2)] - 1$  and  $n = 3[l + (k - 1)(q + 2)]$

$$K_{m,n} = D_0\nu \cdot A_{(1)i,k}^{1,0} B_{(2)j,l}^{0,1} - D_0\nu \cdot A_{(2)i,k}^{1,1} B_{(1)j,l}^{0,0} \\ - \frac{(1 - \nu)D_0}{2} \cdot A_{(2)i,k}^{1,1} B_{(1)j,l}^{0,0} + \frac{(1 - \nu)D_0}{2} \cdot A_{(1)i,k}^{0,1} B_{(2)j,l}^{1,0}$$

else if  $m = 3[j + (i - 1)(q + 2)]$  and  $n = 3[l + (k - 1)(q + 2)] - 2$

$$K_{m,n} = Gt \cdot A_{(1)i,k}^{0,0} B_{(3)j,l}^{0,1} - Gt \cdot A_{(2)i,k}^{1,1} B_{(2)j,l}^{0,0}$$

else if  $m = 3[j + (i - 1)(q + 2)]$  and  $n = 3[l + (k - 1)(q + 2)] - 1$

$$K_{m,n} = D_0\nu \cdot A_{(1)i,k}^{0,1} B_{(2)j,l}^{1,0} - D_0\nu \cdot A_{(2)i,k}^{1,1} B_{(1)j,l}^{0,0} \\ - \frac{(1 - \nu)D_0}{2} \cdot A_{(2)i,k}^{1,1} B_{(1)j,l}^{0,0} + \frac{(1 - \nu)D_0}{2} \cdot A_{(1)i,k}^{1,0} B_{(2)j,l}^{0,1}$$

else if  $m = 3[j + (i - 1)(q + 2)]$  and  $n = 3[l + (k - 1)(q + 2)]$

$$\begin{aligned} K_{m,n} = & \frac{D_0}{c} \cdot A_{(3)i,k}^{1,1} B_{(1)j,l}^{0,0} - \frac{D_0}{c} \cdot A_{(2)i,k}^{1,0} B_{(2)j,l}^{0,1} - \frac{D_0}{c} \cdot A_{(2)i,k}^{0,1} B_{(2)j,l}^{1,0} \\ & + \frac{D_0}{c} \cdot A_{(1)i,k}^{0,0} B_{(3)j,l}^{1,1} + \frac{cD_0(1-\nu)}{2} \cdot A_{(1)i,k}^{1,1} B_{(1)j,l}^{0,0} \\ & + cGt \cdot A_{(1)i,k}^{0,0} B_{(3)j,l}^{0,0} \end{aligned}$$

The coefficients of the mass matrix are

if  $m = 3[j + (i - 1)(q + 2)] - 2$  and  $n = 3[l + (k - 1)(q + 2)] - 2$ , or  $m = 3[j + (i - 1)(q + 2)] - 1$  and  $n = 3[l + (k - 1)(q + 2)] - 1$ , or  $m = 3[j + (i - 1)(q + 2)]$  and  $n = 3[l + (k - 1)(q + 2)]$

$$M_{m,n} = \rho tc \cdot A_{(1)i,k}^{0,0} B_{(1)j,l}^{0,0}$$

else then

$$M_{m,n} = 0$$

The integration formulae are

$$\begin{aligned} A_{(\mu)i,k}^{\alpha,\beta} &= \int_0^1 (b + e\xi)^{\mu-1} f_i^\alpha f_k^\beta d\xi \text{ and } B_{(\mu)i,k}^{\alpha,\beta} \\ &= \int_0^1 \frac{1}{(a + e\eta)^{2-\mu}} \cdot f_i^\alpha f_k^\beta d\eta \end{aligned}$$

where  $i, k = 1, 2, \dots, p+2, j, l = 1, 2, \dots, q+2, \mu = 1 \sim 3$  and the superscripts  $\alpha$  and  $\beta$  ( $\alpha, \beta = 0, 1$ ) denote the order of the derivatives.

For an arbitrary quadrilateral element, the two coordinates  $\xi$  and  $\eta$  cannot be integrated independently. The problem in integrating the coefficients of stiffness and mass matrices reduces to the integration of  $\xi^i \eta^j / (A\xi + B\eta + C)$  with  $A, B$  and  $C$  are constants. Using some commercial packages such as *MAPLE*, *MATLAB* and *MATHEMATICA*, the exact formula of the above integration can also be easily obtained. For example

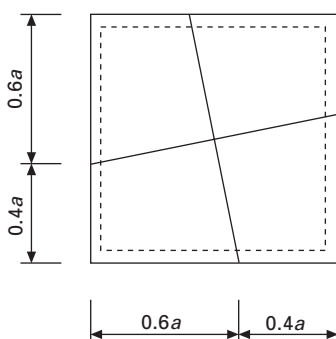
$$\begin{aligned} & \int_{-1}^1 \int_{-1}^1 \xi \eta^2 / (A\xi + B\eta + C) d\xi d\eta \\ &= \frac{1}{12A^2B^3} \{ 12AB^3 - 4ABC^2 - 12A^3B \\ & \quad - \log(A + B + C) \cdot [-3A^4 + 3B^4 + C^4 - 6A^2C^2 - 8A^3C + 4B^3C] \\ & \quad - \log(-A + B + C) \cdot [3A^4 - 3B^4 - C^4 - 6A^2C^2 - 8A^3C - 4B^3C] \\ & \quad - \log(A - B + C) \cdot [3A^4 - 3B^4 - C^4 + 6A^2C^2 + 8A^3C + 4B^3C] \\ & \quad - \log(-A - B + C) \cdot [-3A^4 + 3B^4 + C^4 - 6A^2C^2 + 8A^3C - 4B^3C] \} \end{aligned}$$

Since no exact integration of  $\exp(ji\pi\xi)/(A\xi + B\eta + C)$  or  $\exp(ki\pi\eta)/(A\xi + B\eta + C)$  is available, the quadrilateral Fourier  $p$ -element is not developed herein.

Consider the boundary conditions with the combination of free (F), hard type simply supported (S) and clamped (C) for some numerical examples. Unless stated otherwise, the shear correction factor  $\kappa$  and Poisson's ratio  $\nu$  are taken to be 5/6 and 0.3 respectively. To simplify computation and presentation, the number of hierarchical terms  $p$  is taken to be the same as  $q$  in this chapter.

### 5.3.1 Vibration of square plates

Analytical solutions are available for the out-of-plane vibration of hard type simply supported (S-S-S-S) square plates (Han and Petyt 1997). In order to examine the accuracy and the convergence of the computed solutions by the present quadrilateral hierarchical finite element method (QHFE-P) for out-of-plane vibration of plates, S-S-S-S square plates are meshed by four identical elements of QHFE-P as shown in Fig. 5.5. With increasing number of hierarchical terms  $p$ , the computed frequency parameters  $\lambda = (\omega a^2)/\pi^2 \sqrt{pt/D_0}$  of the lowest eight modes are shown in Table 5.2 along with the solutions from analytical method (Han and Petyt 1997) and the pb-2 Ritz method (Liew *et al.*, 1993 a,b). Excellent agreement can be observed. In the analysis of plates by the conventional finite elements, the shear constraint is too strong if the terms in element matrices are fully integrated, so the shear locking problem occurs. The solutions for a very thin plate with  $a/t = 1000$  demonstrate that the present hierarchical element is free from shear locking.



5.5 Mesh for simply supported square plates.

Table 5.2 Frequency parameters  $\lambda = (\omega a^2 / \pi^2) \sqrt{\rho t / D_0}$  for out-of-plane vibration of simply supported square plates ( $\kappa = 5/6$ ,  $\nu = 0.3$ )

$a/t$	Method	Mode number						
		1	2	3	4	5	6	7
1000	QHFE-P ( $p = 4$ )	2.000	5.001	5.001	8.005	10.085	13.137	13.137
	QHFE-P ( $p = 5$ )	2.000	5.000	5.000	8.000	10.002	13.004	13.004
	QHFE-P ( $p = 6$ )	2.000	5.000	5.000	8.000	10.000	13.000	13.000
	Liew <i>et al.</i> (1993a)	2.000	5.000	5.000	8.000	10.000	13.000	13.000
	<sup>a</sup> Exact; Han and Petyt (1997)	2.000	5.000	5.000	8.000	10.000	13.000	13.000
	<sup>b</sup> Exact; Han and Petyt (1997)	2.000	5.000	5.000	8.000	10.000	13.000	13.000
100	QHFE-P ( $p = 4$ )	1.999	4.997	4.997	7.991	10.009	12.996	12.996
	QHFE-P ( $p = 5$ )	1.999	4.995	4.995	7.988	9.984	12.972	12.972
	QHFE-P ( $p = 6$ )	1.999	4.995	4.995	7.988	9.982	12.969	12.969
	<sup>b</sup> Exact; Han and Petyt (1997)	1.999	4.995	4.995	7.988	9.982	12.969	12.969
	Petyt (1997)							
10	QHFE-P ( $p = 4$ )	1.932	4.609	4.609	7.072	8.623	10.816	10.816
	QHFE-P ( $p = 5$ )	1.932	4.608	4.608	7.072	8.616	10.810	10.810
	QHFE-P ( $p = 6$ )	1.932	4.608	4.608	7.072	8.616	10.809	10.809
	Liew <i>et al.</i> (1993a)	1.932	4.608	4.608	7.072	8.616	10.809	10.809
	<sup>b</sup> Exact; Han and Petyt (1997)	1.932	4.608	4.608	7.072	8.616	10.809	10.809
	Petyt (1997)							

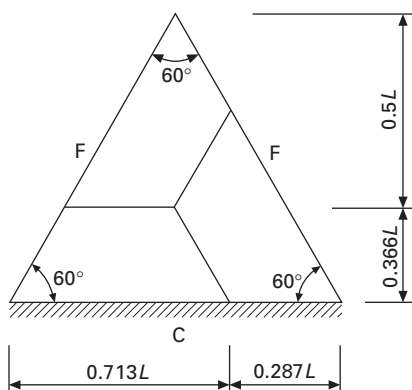
<sup>a</sup> Kirchhoff thin plate theory;  
<sup>b</sup> Mindlin thick plate theory.

### 5.3.2 Vibration of C-F-F equilateral triangular plates

Table 5.3 presents the first six natural frequencies for the C-F-F equilateral triangular plate shown in Fig. 5.6 with different thickness compared with those of Ritz method (Kitipornchai *et al.* 1993). The same value  $p = q = 7$  is used in the computation. The computed results by three elements of THFE-P are in excellent agreement with those in Kitipornchai *et al.* (1993). So the trapezoidal  $p$ -version element with analytic quadrature can be applied to the vibration analysis of plates with arbitrary polygonal shapes without numerical integration.

Table 5.3 Frequency parameters  $\lambda = \omega a^2 / (2\pi) \sqrt{\rho h/D_0}$  for C-F-F equilateral triangular plates ( $\kappa = 0.823$ ,  $v = 0.3$ )

$a/t$	Method	Mode number					
		1	2	3	4	5	6
1000	QHFE-P	1.420	5.585	6.125	14.26	14.82	17.16
	Kitipornchai <i>et al.</i> (1993)	1.420	5.585	6.125	14.26	14.82	17.15
20	QHFE-P	1.404	5.387	5.929	13.50	13.86	15.99
	Kitipornchai <i>et al.</i> (1993)	1.404	5.387	5.929	13.50	13.86	15.99
10	QHFE-P	1.376	4.999	5.540	12.00	12.12	13.85
	Kitipornchai <i>et al.</i> (1993)	1.376	4.999	5.540	12.00	12.12	13.85
6.67	QHFE-P	1.339	4.529	5.066	10.34	10.43	11.77
	Kitipornchai <i>et al.</i> (1993)	1.339	4.529	5.066	10.34	10.43	11.77
5	QHFE-P	1.295	4.051	4.586	8.802	9.060	10.06
	Kitipornchai <i>et al.</i> (1993)	1.295	4.051	4.586	8.802	9.060	10.06



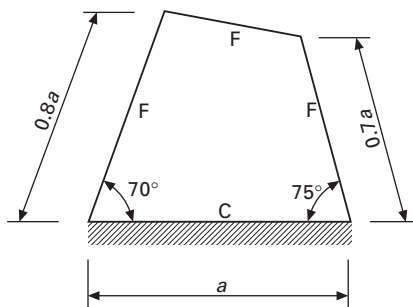
5.6 Geometric sizes and mesh for a C-F-F triangular plate.

### 5.3.3 Vibration of a quadrilateral plate

To study the convergence rate of the present QHFE-P for the vibration of arbitrary quadrilateral plates, a cantilever quadrilateral plate shown in Fig. 5.7 as presented by Karunasena *et al.* (1996) is analyzed herein using a single QHFE-P. A very accurate global method named pb-2 Ritz method is used in that paper. The accuracy of this method for a simple supported square plate is verified in Table 5.4. However, as a global method, it is difficult to analyze plates with composite domains using the pb-2 Ritz method. With the aid of the plot tools of *MATLAB*, the first eight mode shapes of this cantilever quadrilateral plate are plotted in Fig. 5.8.

### 5.3.4 Vibration of a pentagonal plate with a central cut-out

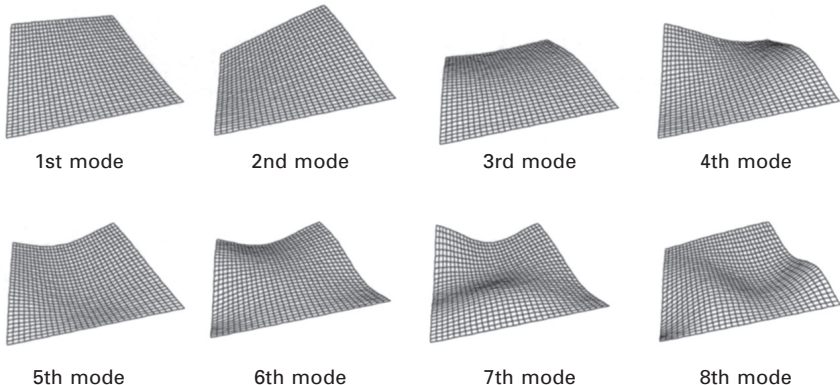
To test the performance of the proposed elements for a problem having an internal discontinuity, a thick pentagonal plate with a central pentagonal cut-out is meshed with five THFE-P as shown in Fig. 5.9(a). The length of outer



5.7 A cantilever quadrilateral plate for out-of-plane vibration analysis.

Table 5.4 Frequency parameters  $\lambda = (\omega a^2/\pi^2)\sqrt{\rho t/D_0}$  for a C-F-F-F quadrilateral plate ( $a/t = 5$ ,  $\kappa = 5/6$ ,  $\nu = 0.3$ )

Method		Mode number							
		1	2	3	4	5	6	7	8
QHFE-P	$p=1$	0.804	2.009	4.071	5.393	5.754	9.835	16.893	17.538
	$p = 2$	0.748	1.737	3.506	4.921	5.109	7.730	8.894	9.818
	$p = 3$	0.745	1.708	3.184	4.482	4.548	6.810	7.968	8.880
	$p = 4$	0.744	1.698	3.173	4.431	4.514	6.503	7.261	7.870
	$p = 5$	0.744	1.697	3.169	4.423	4.504	6.467	7.219	7.802
	$p = 6$	0.744	1.696	3.169	4.421	4.503	6.457	7.205	7.768
Ritz method Karunasena <i>et al.</i> (1996)		0.744	1.696	3.169	4.421	4.503	6.456	7.203	7.765

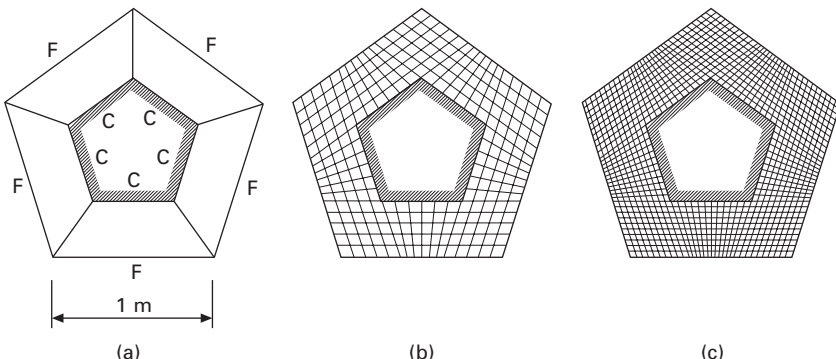


5.8 First eight out-of-plane mode shapes of a cantilever quadrilateral plate.

sides of the plate is twice as that of the inner ones, and the thickness of the plate is  $t = 0.2$  m. The five sides of the cut-out are clamped and the outer five sides of the plate are free. The plate is also meshed with different number of linear elements to obtain the compared data with  $h$ -mesh as shown in Fig. 5.9(b) and (c). The linear element represents a special case of the present  $p$ -version element with no additional hierarchical terms in shape functions ( $p = q = 0$ ). To avoid the shear locking problem, the reduced numerical integration is introduced to the  $h$ -mesh vibration analysis. Comparison between solutions of the present hierarchical finite element (HFE) with different hierarchical terms and the linear finite element (LFE) with different meshes is carried out in Table 5.5. It is observed that the convergence rate of the present hierarchical element is much faster than that of the LFE, and the results of the first six natural frequencies computed by the proposed element with total 735 DOFs are more accurate than those of LFE with total 3450 DOFs.

### 5.3.5 Vibration of fully clamped regular polygonal plates

Most of the studies for the free vibration analysis of polygonal plates are based on the point matching method, the collocation method, the Ritz method and so on. The considerable accurate natural frequencies of the polygonal plates can also be easily obtained using the hierarchical finite element method (HFEM) by assembling the proposed QHFE-P. The  $p$ -version meshes of the fully clamped polygonal plates with three sides to eight sides are shown in Fig. 5.10, in which  $R$  is the common circumscribing radius of the regular polygons. Their frequency parameters  $\lambda$  of the first eight modes are presented in Table 5.6. A common value of the additional hierarchical terms  $p = 6$  is used in the computation. It should be noted that the value of the shear correction factor  $\kappa$  in Kitipornchai *et al.* (1993) is  $\pi^2/12$ , and its results are



5.9 Meshes for out-of-plane vibration analysis of a pentagonal plate with a central cutout: (a)  $p$ -mesh with QHFE-P; (b).  $h$ -mesh-I with linear elements; (c)  $h$ -mesh-II with linear elements.

smaller than the present solutions for the thick triangular plates. The theory in Irie *et al.* (1978) and Liew and Lam (1991) is based on the Kirchhoff thin plate theory, and the method used in Karunasena *et al.* (1996) and Kitipornchai *et al.* (1993) is the pb-2 Ritz method. From Table 5.6, it can be found that the solutions of QHFE-P are in excellent agreement with the results computed by the pb-2 Ritz method, and are smaller than those of other methods. The present results of regular polygonal plates may serve as the benchmark data for the development of new methods.

### 5.3.6 Vibration of fully clamped pentagonal-star plates

Several fully clamped pentagonal-star plates with different ratios of  $a/t$  are meshed into the same five hierarchical elements (see Fig. 5.11). The ratio  $r/R = 0.6$ , and six additional hierarchical terms are introduced in the analysis. Frequency parameters of the first six modes are listed in Table 5.7.

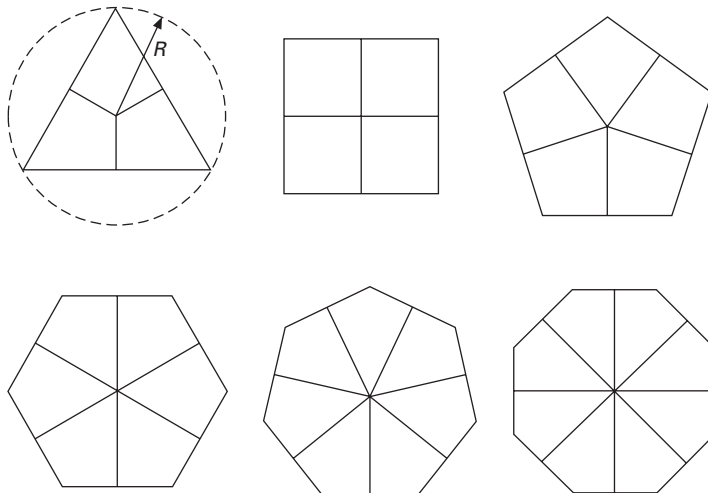
### 5.3.7 Effect of numerical integration

It is well known that numerical integration errors influence the results computed by  $p$ -version elements and the problem becomes obvious for highly oscillating shape functions such as the higher-order Legendre polynomials. Numerical integration softens the stiffness. This is the reason that most of the results in Zienkiewicz *et al.* (1983) are smaller than those of Liew *et al.* (1993a,b). The numerical quadrature should only be used to predict several lowest frequencies with few shape functions (Houmat 2000). Two numerical examples are chosen to substantiate the above viewpoints.

Consider a simply supported square plate as the first example. The exact solutions can be compared with the computed natural frequencies using

Table 5.5 Frequency parameters  $\lambda = (\omega/\pi^2)\sqrt{\rho t/D_0}$  for a pentagonal plate with a cutout ( $\kappa = 5/6$ ,  $\nu = 0.3$ )

Method	DOFs	Mode number					
		1	2	3	4	5	6
THFE-P ( $p$ -mesh, $p = 2$ )	135	1.9327	1.9327	1.9547	1.9555	1.9555	2.7637
THFE-P ( $p$ -mesh, $p = 3$ )	240	1.9045	1.9045	1.9205	1.9421	1.9421	2.7095
THFE-P ( $p$ -mesh, $p = 4$ )	375	1.8996	1.8996	1.9194	1.9328	1.9328	2.7038
THFE-P ( $p$ -mesh, $p = 5$ )	540	1.8973	1.8973	1.9166	1.9314	1.9314	2.7006
THFE-P ( $p$ -mesh, $p = 6$ )	735	1.8966	1.8966	1.9164	1.9298	1.9298	2.6993
LFE ( $h$ -mesh-I)	900	1.9046	1.9107	1.9284	1.9420	1.9490	2.7100
LFE ( $h$ -mesh-II)	3450	1.8975	1.9006	1.9186	1.9320	1.9333	2.7001



5.10 Meshes for out-of-plane vibration analysis of regular polygonal plates.

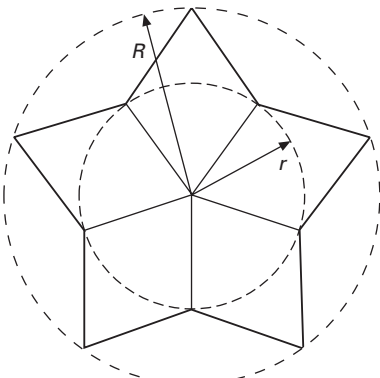
analytic integration, e.g. the results of Woo *et al.* (2003) and Liew *et al.* (1998) can be compared with the exact solutions. The second example is the comparison of three methods for C-F-F-F skew plates with different skew angles (see Fig. 5.12). Only one  $p$ -element with  $p = 7$  are used in the computation. From Table 5.8, one can see that the thin plate results of Woo *et al.* (2003) are in good agreement with the exact solutions but the thick plate results are all smaller than the exact solutions and the results of Liew *et al.* (1993b). The difference between the results of Woo *et al.* (2003) and the exact solutions (Ribeiro and Petyt 1999) increases with an increasing number of  $p$ . On the other hand, the analytic  $p$ -version finite element works well when compared with the exact solutions whatever the plates are ‘thin’ or ‘thick’. The convergence is always from above. The same problem can also be observed in Table 5.8. Two series of shape functions are used in the present solutions with analytic integration. From Table 5.9, it can be observed that the solutions using Legendre orthogonal polynomials as shape functions (Houmat 1997) are more accurate than those using shape functions in Woo *et al.* (2003). Most results of Woo *et al.* (2003) are smaller than those of Liew *et al.* (1993b). Though the difference between them is small in the table, it will become increasingly large for modal frequencies higher than five.

### 5.3.8 Conclusions and discussion

A trapezoidal hierarchical element and an arbitrary quadrilateral hierarchical element for the out-of-plane vibration of plates are presented. The two versatile

Table 5.6 Frequency parameters  $\lambda = (4\omega R^2/\pi^2)\sqrt{pt/D_0}$  for fully clamped polygonal plates ( $\kappa = 5/6$ ,  $v = 0.3$ ,  $\rho = 6$ )

Polygon	2R/t	Method	Mode number							
			1	2	3	4	5	6	7	8
Triangle	1154.7	QHFE-P	13.38	25.53	25.53	39.89	42.58	42.58	59.22	59.22
		Kitipornchai <i>et al.</i> (1993)	13.38	25.53	25.53	39.88	42.58	42.58	—	—
	11.547	Irie <i>et al.</i> (1978)	13.43	25.81	26.01	42.64	43.17	—	—	—
		QHFE-P	10.53	17.93	17.93	25.55	26.70	26.70	34.28	34.28
Square	1414.2	Kitipornchai <i>et al.</i> (1993)	10.51	17.87	17.87	25.48	26.61	26.61	—	—
		QHFE-P	7.292	14.87	14.87	21.93	26.66	26.79	33.44	33.44
	14.142	Liew <i>et al.</i> (1993a)	7.292	14.87	14.87	21.93	26.66	26.79	33.44	33.44
		Irie <i>et al.</i> (1978)	7.317	14.93	14.97	22.11	26.83	27.04	33.6	33.6
Pentagon	1000	QHFE-P	6.591	12.57	12.57	17.62	20.76	20.96	25.11	25.11
		Liew <i>et al.</i> (1993a)	6.591	12.57	12.57	17.62	20.76	20.96	25.11	25.11
	10	QHFE-P	5.803	11.98	11.98	19.37	22.16	22.60	28.60	28.60
		Irie <i>et al.</i> (1978)	5.827	12.05	12.08	19.44	19.52	22.20	28.84	28.84
Hexagon	1000	QHFE-P	5.014	9.410	9.410	13.97	13.97	15.61	18.96	18.96
		QHFE-P	5.184	10.75	10.75	17.54	17.54	20.01	24.49	26.82
	10	Liew & Lam (1991)	5.289	10.85	10.85	17.75	17.78	20.23	24.85	27.22
		Irie <i>et al.</i> (1978)	5.212	10.85	10.88	17.73	17.75	20.13	24.80	27.10
Heptagon	1000	QHFE-P	4.550	8.624	8.624	12.95	12.95	14.46	16.95	18.08
		QHFE-P	4.861	10.10	10.10	16.52	16.52	18.84	24.06	24.06
	10	Irie <i>et al.</i> (1978)	4.884	10.16	10.17	16.62	16.64	18.93	24.21	24.21
		QHFE-P	4.305	8.200	8.200	12.37	12.37	13.82	16.72	16.72
Octagon	1000	QHFE-P	4.670	9.706	9.706	15.90	15.90	18.13	23.22	23.22
		Liew & Lam (1991)	4.723	9.880	9.880	16.12	16.12	18.31	23.55	23.55
	10	Irie <i>et al.</i> (1978)	4.696	9.784	9.816	15.99	16.04	18.24	23.40	23.40
		QHFE-P	4.159	7.942	7.942	12.01	12.01	13.42	16.28	16.28



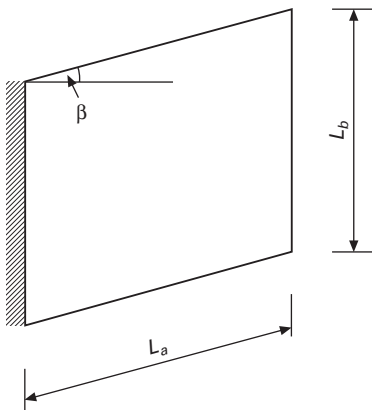
5.11 Mesh for out-of-plane vibration analysis of pentagonal-star plates.

Table 5.7 Frequency parameters  $\lambda = (\omega R^2/\pi^2)\sqrt{pt/D_0}$  for fully clamped pentagonal-star plate ( $\kappa = 5/6$ ,  $v = 0.3$ ,  $p = 6$ ,  $r/R = 0.6$ )

$a/t$	Mode number					
	1	2	3	4	5	6
1000	2.547	5.078	5.078	7.559	7.559	8.818
500	2.500	5.002	5.002	7.518	7.518	8.736
250	2.439	4.903	4.903	7.460	7.460	8.631
100	2.396	4.829	4.829	7.405	7.405	8.547
50	2.380	4.792	4.792	7.348	7.348	8.476
25	2.348	4.701	4.701	7.168	7.168	8.255
10	2.192	4.236	4.236	6.269	6.269	7.133

elements can be applied to the vibration analysis of plates with complicated shapes. With the analytical integration formulae, the analysis using the proposed elements is more accurate than those by using the similar elements involving Gaussian quadrature.

Comparison with the exact solutions for the out-of-plane vibration of simply supported square plates with different thickness validates the present elements. The results of the sequential numerical cases show that not only is the convergence rate of the proposed elements very fast with respect to the number of hierarchical terms, but also that they produce much higher accurate modes than the linear finite elements per DOF. The present numerical data are in excellent agreement with those of a very accurate global method termed the pb-2 Ritz method. The elements can be easily used for vibration analysis of plates with complicated shapes just by assembling elements, although it is rather difficult for the pb-2 Ritz method. The results of new studied cases may be served as the benchmark data for other numerical methods. Comparison with the results computed by the hierarchical elements



5.12 Geometry of skew plates.

with numerical integration show that numerical integration for highly oscillating shape functions will soften the stiffness of the element in general and that the monotonic convergence of the predicted natural frequencies cannot be guaranteed. With analytic integration, the problems are eliminated.

## 5.4 Transverse vibration of plates on Pasternak foundations

The simple Winkler model does not represent accurately the characteristics of many practical foundations. Two-parameter foundation models are more accurate than the Winkler model and simpler than the semi-infinite elastic continuum foundation models presented by Richart *et al.* (1970). The second foundation parameter of the two-parameter foundation model represents the tension value of the membrane connecting the top of the Winkler springs or the stiffness of the shear layer resting on the Winkler springs. By introducing an arbitrary parameter  $\gamma$ , the two foundation parameters are correlated to the soil behavior, and they can be expressed with the Young's modulus and the Poisson ratio of the soil (Valasov and Leont'ev 1996, Jones and Xenophontos 1977, Vallabhan and Das 1991).

For the plates resting on two-parameter elastic foundations, the stiffness matrix and mass matrix of THFE-P and QHFE-P are

$$\begin{aligned} \mathbf{K}^e = & \int_{-1}^1 \int_{-1}^1 \mathbf{B}_b^T \mathbf{D}_b \mathbf{B}_b \cdot |\mathbf{J}| d\xi d\eta \\ & + \int_{-1}^1 \int_{-1}^1 \kappa G_t \mathbf{B}_s^T \text{diag}[1, 1] \mathbf{B}_s \cdot |\mathbf{J}| d\xi d\eta \end{aligned}$$

Table 5.8 Frequency parameters  $\lambda = (\omega b^2/\pi^2)\sqrt{pt/D_0}$  for simply supported square plates ( $\kappa = 0.833$  33,  $\nu = 0.3$ ), figures in parentheses are percentage errors)

$h/b$	Mode	Methods			
		Present	Woo et al. (2003)	Liew et al. (1993b)	Exact <sup>a</sup>
0.001	1	2.0000	1.9999	2.0000	2.0000
	2	5.0144	4.9999	5.0000	5.0000
	3	5.0144	5.0000	5.0000	5.0000
	4	8.0211	7.9999	8.0000	8.0000
	5	10.144	10.0000	9.9999	10.0000
0.2	1	1.7679 (0.00)	1.7637 (-0.04)	1.7679	1.7679
	2	3.8678 (0.06)	3.8497 (-0.41)	3.8656	3.8656
	3	3.8678 (0.06)	3.8497 (-0.41)	3.8656	3.8656
	4	5.5911 (0.06)	5.4989 (-1.59)	5.5879	5.5879
	5	6.6505 (0.76)	6.5681 (-0.49)	6.6006	6.6006

<sup>a</sup> Kirchhoff thin plate theory (Ribeiro and Petyt 1999); <sup>b</sup> Mindlin thick plate theory (Ribeiro and Petyt 1999).

Table 5.9 Frequency parameters  $\lambda = (\omega b^2/\pi^2)\sqrt{\rho t/D_0}$  for C-F-F-F skew plates ( $a/b = 1.0$ ,  $h/b = 0.2$ ,  $\kappa = 0.83333$ ,  $\nu = 0.3$ )

$\beta$	Methods	Modes				
		1	2	3	4	5
0°	Present <sup>a</sup>	0.3384	0.7452	1.7807	2.2767	2.4234
	Present <sup>b</sup>	0.3384	0.7447	1.7807	2.2768	2.4209
	Woo <i>et al.</i> (2003)	0.3383	0.7432	1.7797	2.2712	2.4097
	Liew <i>et al.</i> (1993b)	0.3382	0.7437	1.7779	2.2741	2.4163
15°	Present <sup>a</sup>	0.3482	0.7601	1.8331	2.1923	2.6369
	Present <sup>b</sup>	0.3482	0.7597	1.8330	2.1916	2.6355
	Woo <i>et al.</i> (2003)	0.3479	0.7579	1.8309	2.1863	2.6242
	Liew <i>et al.</i> (1993b)	0.3479	0.7588	1.8299	2.1886	2.6309
30°	Present <sup>a</sup>	0.3776	0.8175	1.9825	2.1661	3.1048
	Present <sup>b</sup>	0.3774	0.8171	1.9818	2.1656	3.1033
	Woo <i>et al.</i> (2003)	0.3768	0.8146	1.9752	2.1606	3.0925
	Liew <i>et al.</i> (1993b)	0.3768	0.8161	1.9772	2.1627	3.0974
45°	Present <sup>a</sup>	0.4246	0.9676	2.1160	2.3915	3.6922
	Present <sup>b</sup>	0.4241	0.9671	2.1136	2.3911	3.6870
	Woo <i>et al.</i> (2003)	0.4225	0.9644	2.1001	2.3855	3.6684
	Liew <i>et al.</i> (1993b)	0.4226	0.9650	2.1059	2.3869	3.6789
60°	Present <sup>a</sup>	0.4831	1.3477	2.2651	2.9529	4.1954
	Present <sup>b</sup>	0.4816	1.3449	2.2561	2.9500	4.1755
	Woo <i>et al.</i> (2003)	0.4791	1.3415	2.2427	2.9414	4.1418
	Liew <i>et al.</i> (1993b)	0.4781	1.3370	2.2387	2.9411	4.1599

<sup>a</sup> Using shape functions from Woo *et al.* (2003); <sup>b</sup> Using shape functions from Houmat (1997a).

$$\begin{aligned}
 & + \int_{-1}^1 \int_{-1}^1 K_1 \cdot \mathbf{N}^T \mathbf{N} \cdot |\mathbf{J}| d\xi d\eta \\
 & + \int_{-1}^1 \int_{-1}^1 K_2 \cdot \mathbf{B}_k^T \text{diag}[1, 1] \mathbf{B}_k \cdot |\mathbf{J}| d\xi d\eta
 \end{aligned} \quad 5.8a$$

$$\mathbf{M}^e = \int_{-1}^1 \int_{-1}^1 \rho t \cdot \mathbf{N}^T \text{diag}[1, t^2/12, t^2/12] \mathbf{N} \cdot |\mathbf{J}| d\xi d\eta \quad 5.8b$$

where the two foundation parameters  $(K_1, K_2) = (k_1 L_a^4, k_2 L_a^2) \pi^4 D_0$  with  $L_a$  is the side length of the plate, and  $k_1$  and  $k_2$  are the two nondimensional foundation parameters. The definitions of matrix  $\mathbf{B}_k$  are defined as

$$\begin{bmatrix} \frac{\partial w}{\partial x} \\ \frac{\partial w}{\partial y} \end{bmatrix} = \begin{bmatrix} \partial/\partial x & 0 & 0 \\ \partial/\partial y & 0 & 0 \end{bmatrix} \mathbf{u} = \mathbf{B}_k \cdot \boldsymbol{\delta}^e \quad 5.9$$

The stiffness matrix and the mass matrix of QHFE-P can be formulated from Eqs. (5.8) straightforwardly as mentioned in Section 5.3. The coefficients of

the stiffness matrix and the mass matrix for the trapezoidal element for plates resting on two-parameter foundations are:

$$\begin{aligned}
 K_{m,n} = & cGt \cdot A_{(1)i,k}^{1,1} B_{(1)j,l}^{0,0} + \frac{Gt}{c} \cdot A_{(3)i,k}^{1,1} B_{(1)j,l}^{0,0} - \frac{Gt}{c} \cdot A_{(2)i,k}^{1,0} B_{(2)j,l}^{0,1} \\
 & - \frac{Gt}{c} \cdot A_{(2)i,k}^{0,1} B_{(2)j,l}^{1,0} + \frac{Gt}{c} \cdot A_{(1)i,k}^{0,0} B_{(3)j,l}^{1,1} + cK_1 \cdot A_{(1)i,k}^{0,0} B_{(3)j,l}^{0,0} \\
 & + cK_2 \cdot A_{(1)i,k}^{1,1} B_{(1)j,l}^{0,0} + \frac{K_2}{c} \cdot A_{(3)i,k}^{1,1} B_{(1)j,l}^{0,0} - \frac{K_2}{c} \cdot A_{(2)i,k}^{1,0} B_{(2)j,l}^{0,1} \\
 & - \frac{K_2}{c} \cdot A_{(2)i,k}^{0,1} B_{(2)j,l}^{1,0} - \frac{K_2}{c} \cdot A_{(1)i,k}^{0,0} B_{(3)j,l}^{1,1}
 \end{aligned}$$

for  $m = 3[j + (i-1)(q+2)] - 2$ ,  $n = 3[l + (k-1)(q+2)] - 2$ ; integrations  $A_{(\mu)i,k}^{\alpha,\beta}$ ,  $B_{(\mu)i,k}^{\alpha,\beta}$  and other coefficients of the stiffness matrix and the mass matrix are same as those of the trapezoidal plate element as expressed in the last section.

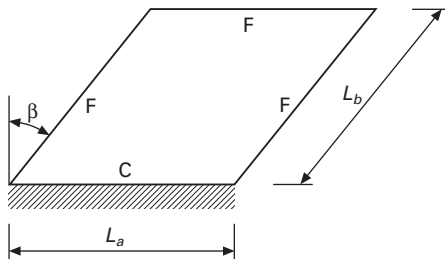
The first five doubly symmetric modes of an F-F-F-F square plate resting on a two-parameter foundation are computed by the QHFE-P with various values of  $p$  ( $= q$ ) and the LFE with different meshes, respectively. The LFE represents a special case of the present elements without the additional hierarchical shape functions ( $p = q = 0$ ). The computed results are given in Table 5.10. The lowest frequencies in the table are the rigid-body translations on the elastic foundation. Very fast convergence is possible for the present hierarchical elements. The solution of the QHFE-P is much more accurate than those of the LFE with the same number of DOFs, and the first five doubly symmetric natural frequencies computed by the QHFE-P just with 147 DOFs ( $p = 5$ ) are more accurate than those of LFE with 1083 DOFs. The present solutions are in good agreement with those of the Rayleigh–Ritz method (Shen *et al.* 2001) but a little smaller.

Table 5.10 Doubly symmetric frequency parameters  $\lambda = (\omega L_a^2 / \pi^2) \sqrt{pt/D_0}$  for F-F-F-F square plates on foundations;  $L_a/L_b = 1.0$ ,  $L_a/t = 10$ ,  $\kappa = \pi^2/12$ ,  $v = 0.15$ ,  $k_1 = 2.0$  and  $k_2 = 0.4$

Method	DOF	Doubly symmetric modes				
		1	2	3	4	5
QHFE-P ( $p = 3$ )	75	1.4142	2.8715	3.0322	6.6581	17.5020
QHFE-P ( $p = 5$ )	147	1.4142	2.8530	3.0081	6.4690	11.2749
QHFE-P ( $p = 7$ )	243	1.4142	2.8530	3.0080	6.4514	10.7469
QHFE-P ( $p = 8$ )	300	1.4142	2.8530	3.0080	6.4511	10.7385
LFE ( $8 \times 8$ )	243	1.4142	3.3190	3.4665	7.1019	14.7089
LFE ( $9 \times 9$ )	300	1.4142	3.2250	3.3739	6.9765	13.8863
LFE ( $20 \times 20$ )	1083	1.4142	2.9309	3.0847	6.5663	11.3761
Shen <i>et al.</i> (2001)		1.4142	2.8533	3.0086	6.6673	10.7468

Shown in Fig. 5.13 is a cantilevered skew plate ( $L_a = L_b = 1$ ,  $L_a/t = 10$ ,  $\nu = 0.3$  and  $\beta = 15^\circ$ ) on two-parameter foundations. Only one skew hierarchical element ( $\kappa = 0.86667$  and  $p = 8$ ) is used to compute the natural frequencies as listed in Table 5.11. Figures 5.14 and 5.15 present the effects of the foundation parameters  $k_1$  and  $k_2$  to the first six modes, respectively. The frequency parameters  $\Omega = \omega L_a^2 \sqrt{\rho t / D_0}$  increase as the foundation parameters are increased. When the foundation parameter  $k_1$  or  $k_2$  is large enough, the first six natural frequencies are almost the same as each other, and each of them approaches a constant value.

With the  $3 \times 3$  mesh shown in Fig. 5.16, a number of C-C-C-C trapezoidal plates resting on a Pasternak foundation with parameters  $k_1 = 2.0$  and  $k_2 = 0.4$  are analyzed here. A common value of  $p = q = 5$  is used in each element. With different values of the skew angle  $\beta$  and the ratio  $L_a/t$ , the first six frequency parameters  $\Omega = \omega L_a^2 \sqrt{\rho t / D_0}$  are listed in Table 5.12. The skew

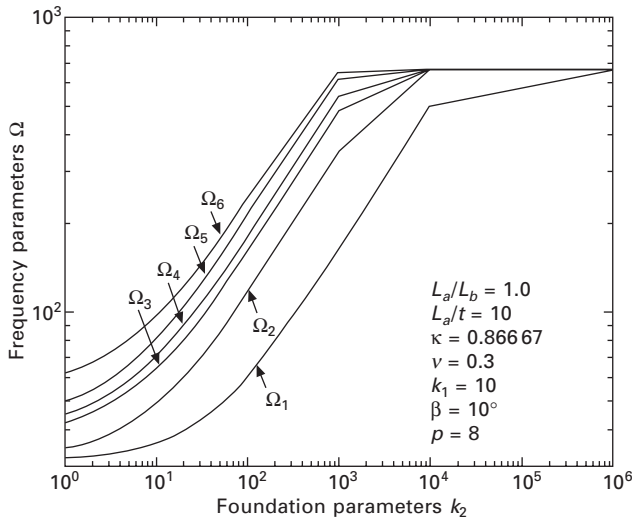
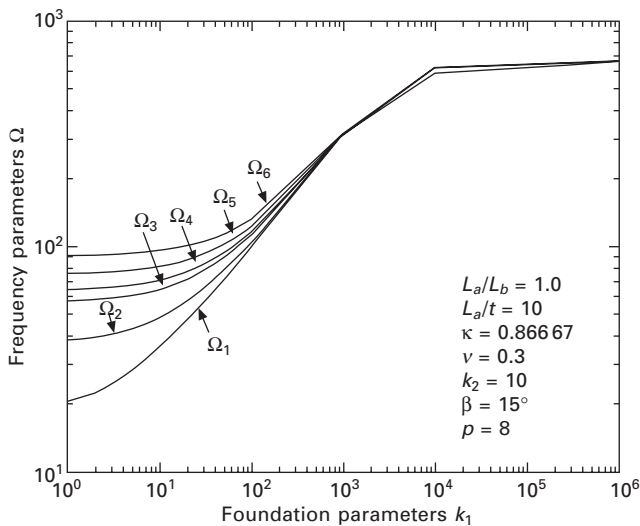


5.13 Geometric size of C-F-F-F skew plate.

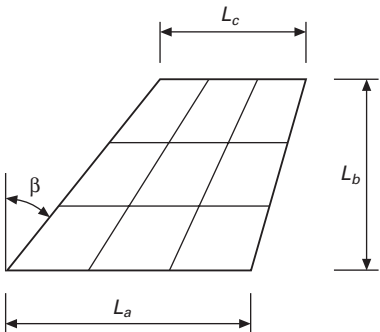
Table 5.11 Frequency parameters  $\Omega = \omega L_a^2 \sqrt{\rho t / D_0}$  for C-F-F-F skew plates on foundations;  $L_a/L_b = 1.0$ ,  $L_a/t = 10$ ,  $\nu = 0.3$ ,  $\beta = 15^\circ$ ,  $\kappa = 0.86667$  and  $p = 8$

$k_1$	$k_2$	Modes <sup>a</sup>					
		1	2	3	4	5	6
0	0	3.538 (3.536)	8.243 (8.228)	20.90 (20.84)	24.70 (24.64)	30.87 (30.77)	46.30 (46.12)
	0.5	5.788	11.89	24.67	28.45	34.60	49.72
	2.0	9.155	18.67	32.70	37.05	43.93	58.56
	10	17.51	37.01	56.20	63.41	75.24	90.67
	100	50.87	111.1	155.8	177.1	212.3	242.2
	10 000	499.3	660.1	662.4	663.3	666.9	667.6
0.5	$\infty$	661.3	662.9	663.6	667.3	668.5	670.0
	0	7.782	10.77	22.00	25.63	31.62	46.80
	2.0	14.37	16.14	25.02	28.26	33.77	48.26
	10	31.35	32.09	37.19	39.41	43.48	55.42
	100	98.34	98.47	99.40	100.2	101.6	106.8
	10 000	571.9	608.5	609.7	611.9	614.9	615.9
$\infty$	0	661.3	662.9	663.6	667.3	668.5	670.0

<sup>a</sup> Values in parentheses are from the literature (Liew *et al.* 1998).

5.14 Effects of foundation parameter  $k_2$ .5.15 Effects of foundation parameter  $k_1$ .

angle  $\beta$  varies from  $0^\circ$  to  $45^\circ$  including the angle corresponding to the symmetric trapezoidal plates ( $\beta = 11.31^\circ$ ), and the plates vary from a very thin plate with  $L_a/t = 1000$  to a thick plate with  $L_a/t = 5$ . The data are arranged to demonstrate the roles of the ratio of  $L_a/t$  and the skew angle  $\beta$ . The effects of the skew angles  $\beta$  are shown in Fig. 5.17 more clearly. It can be observed that frequency parameters increase with an increasing value of skew angle  $\beta$  approximately. With the aid of ANSYS, the first six mode shapes of the symmetric Kirchhoff trapezoidal plate ( $\beta = 11.31^\circ$ ,



5.16 Ecometric size of trapezoidal plate.

$L_a/t = 100$ ) resting on a Winkler foundation ( $k_1 = 2.0$ ,  $k_2 = 0$ ) are plotted in Fig. 5.18.

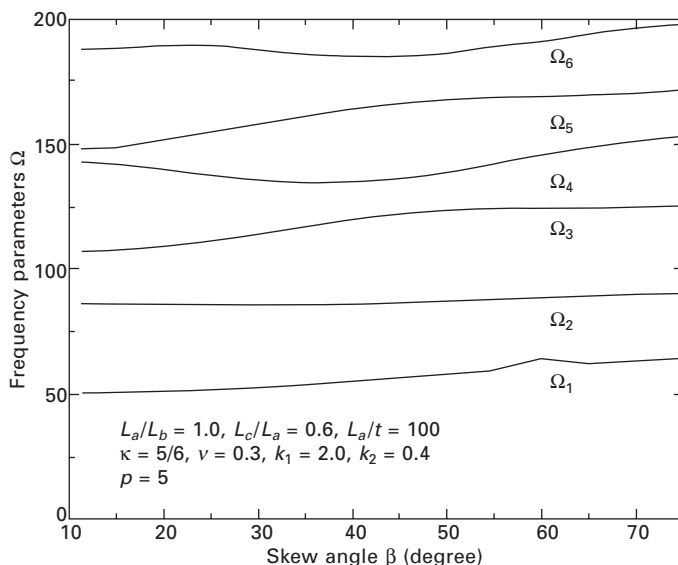
A triangle can be divided into three trapezoids by drawing three lines parallel to the three edges from any point inside the triangle. Based on this viewpoint, any triangular plate can be analyzed by trapezoidal elements. The trapezoidal elements can also be applied to the analysis of any polygonal plate with the irregular shape. Using the present hierarchical plate element, the solutions are very accurate and a larger number of DOFs can be saved than with most other types of finite elements. The two most important characteristics needed for FEM analysis are thus satisfied by the proposed element.

In this section, for brevity, only a few fully clamped equilateral triangular plates with different  $L_a/t$  and foundation parameters  $k_1$  and  $k_2$  are analyzed. Each triangular plate is meshed into three trapezoidal elements. Since there are DOFs along each edge of the trapezoidal hierarchical elements, the direction of the edge between adjacent elements should be the same to ensure continuity along an edge (see Fig. 5.19). The first six frequency parameters  $\Omega = \omega L_a^2 \sqrt{\rho t/D_0}$  are listed in Table 5.13. The data computed without foundation are compared with those of the Ritz method Liew *et al.* 1998 and are found to be in good agreement.

A clamped annular plate meshed as 24 trapezoidal hierarchical elements is shown in Fig. 5.20. Figure 5.21 presents the convergence of six frequency parameters  $\Omega_{ns} = \omega L_a^2 \sqrt{\rho t/D}$  computed by present elements. The subscript  $n$  represents the number of nodal diameters appearing on the mode shapes of the vibration. The subscript  $s$  represents the number of nodal circles of the mode shapes in Kirchhoff plate theory (Irie *et al.* 1978). It can be observed that very fast convergence to the solutions is possible by present elements. The solutions with six additional Legendre orthogonal polynomials ( $p = q = 6$ ) are in good agreement with those in Irie *et al.*, which are 70.28, 70.90, 72.96, 159.78, 160.60 and 163.08 respectively. With finer mesh, the straight

Table 5.12 Frequency parameters  $\Omega = \omega L_a^2 \sqrt{\rho t/D_0}$  for C-C-C-C trapezoidal plates on foundations;  $L_a/L_b = 1.0$ ,  $L_c/L_a = 0.6$ ,  $v = 0.3$ ,  $\kappa = 5/6$ ,  $p = 5$ ,  $k_1 = 2.0$ , and  $k_2 = 0.4$

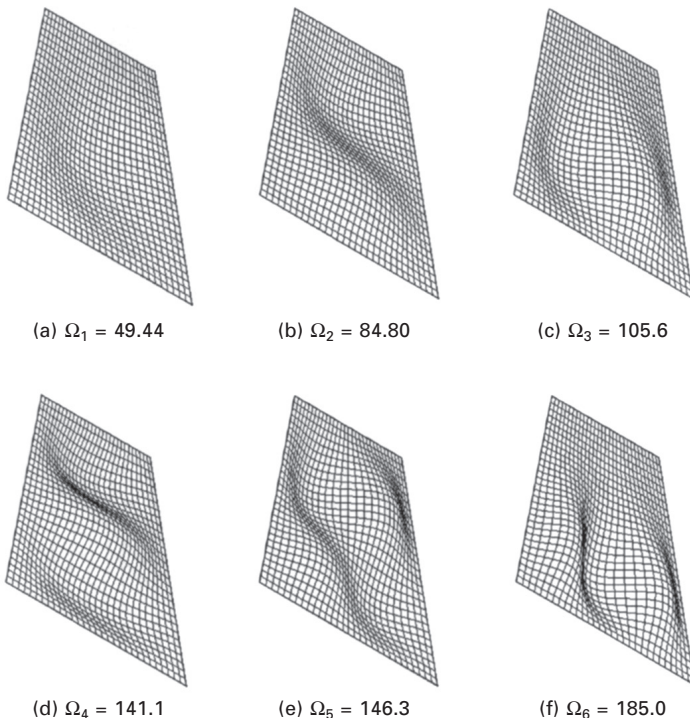
$L_a/t$	$\beta$ (degree)	Modes					
		1	2	3	4	5	6
1000	0	51.65	86.29	110.6	138.5	154.5	189.9
	11.31	50.75	86.59	107.5	143.6	148.7	188.8
	30	52.82	86.21	114.6	136.5	158.6	189.3
	45	56.86	86.91	123.4	136.2	137.7	186.8
10	0	45.92	72.17	88.74	107.8	117.5	139.1
	11.31	45.22	72.44	86.56	111.2	113.5	137.7
	30	46.79	72.02	91.19	106.2	120.0	138.4
	45	49.80	72.37	96.83	105.9	124.8	135.8
5	0	37.29	54.48	63.96	76.11	81.55	93.93
	11.31	36.87	54.71	62.79	78.36	79.17	92.79
	30	37.82	54.32	65.38	75.05	82.89	92.31
	45	39.62	54.33	68.87	74.25	85.49	92.00



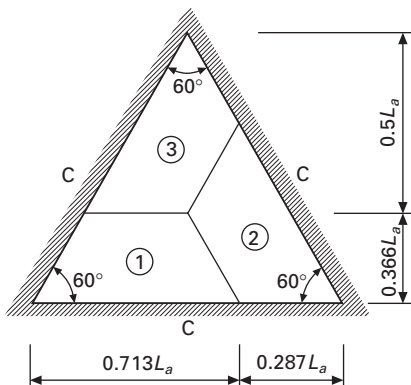
5.17 Effects of skew angle  $\beta$ .

boundaries can approximate the original curved ones more accurately, and the present elements will produce more close solutions compared with those of Irie *et al.*

The natural frequencies of the polygonal plates can also be easily obtained using FEM by assembling quadrilateral or triangular elements. Figure 5.22 shows a hexagonal plate and an octagonal plate meshed by trapezoidal and



5.18 First six mode shapes of C-C-C-C symmetric trapezoidal plate on Winkler foundation.



5.19 Geometric size and mesh of C-C-C triangular plate.

quadrilateral hierarchical elements. With various  $L_a/t$  and foundation parameters, several lowest non-zero natural frequencies of a number of hexagonal plates and octagonal plates with clamped and free boundary conditions are presented in Tables 5.14–5.17. The first three modes of a free

Table 5.13 Frequency parameters  $\Omega = \omega L_a^2 \sqrt{\rho t/D_0}$  for C-C-C equilateral triangular plates on foundations;  $\nu = 0.3$ ,  $\kappa = \pi^2/12$  and  $p = 8$

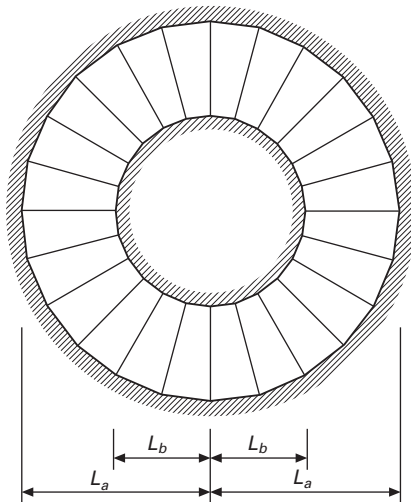
$L_a/t$	$k_1$	$k_2$	Modes <sup>a</sup>					
			1	2	3	4	5	6
1000	0	0	99.02 (99.02)	189.0 (189.0)	189.0 (189.0)	295.2 (295.2)	315.2 (315.2)	315.2 (315.2)
	10	0	103.8	191.6	191.6	296.9	316.7	316.7
	0	5.0	113.9	206.9	206.9	314.5	334.8	334.8
	5.0	1.0	104.5	194.0	194.0	300.0	319.9	319.9
	10	0	77.76 (77.79)	132.4 (132.3)	132.4 (132.3)	188.5 (188.6)	197.0 (197.0)	197.0 (197.0)
	10	0	83.65	135.8	135.8	191.0	199.3	199.3
10	0	5.0	93.87	153.6	153.6	213.4	222.7	222.7
	5.0	1.0	84.15	138.6	138.6	194.9	203.5	203.5

<sup>a</sup>Values in parentheses are from Liew *et al.* (1998).

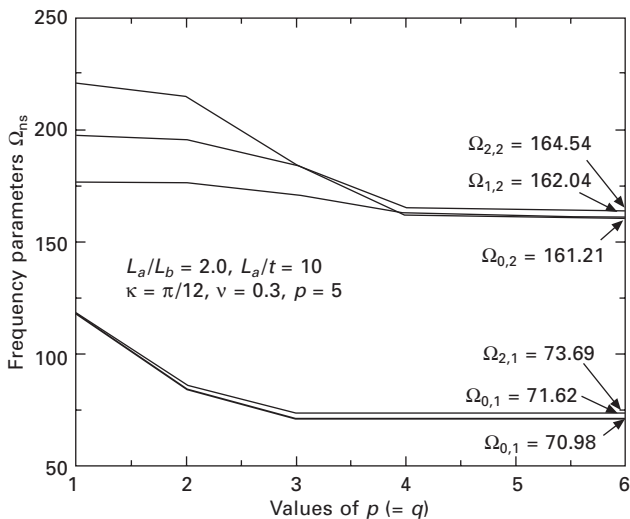
plate represent the rigid-body translations on foundations. For thin plates with  $L_a/t = 1000$ , comparison with results of existing literature based on the Kirchhoff plate theory and computation of ANSYS is carried out. Good agreement between them can be observed. The computation of ANSYS adopts the quadrilateral thin plate element attached to a Winkler foundation, and 2430, 2796, 4839, 5319 DOFs are used for clamped hexagonal, free hexagonal, clamped octagonal and free octagonal plates respectively.

Plate structures usually rest on column supports. The supports can be modeled as point supports with zero DOFs. A concrete clamped plate with eight point supports is coarsely meshed into 16 trapezoidal hierarchical elements (see Fig. 5.23). To compare the solutions with ANSYS using the Kirchhoff thin plate element, the foundation is assumed as a Winkler foundation with a fixed parameter  $K_1 = 1 \times 10^6 \text{ N/m}^3$ . There are 6399 DOFs in the computation of ANSYS. The first six natural frequencies (Hz) of the present method and the computation of ANSYS are presented in Fig. 5.24 for different plate thicknesses. The present solutions are in good agreement with those of ANSYS for the thin plates ( $t < 0.25 \text{ m}$ ), but the difference between the two methods increases with increasing plate thickness. The thin plate elements are only suitable for analysis of plate thickness  $t < 0.25 \text{ m}$ .

Two proposed  $p$ -version elements, THFE-P and QHFE-P, are extended for vibration analysis of plates resting on two-parameter foundations. The present elements produce very accurate modes when compared with the linear finite elements with the same number of DOFs. Plates with other shapes such as skew, trapezoidal, triangular, annular and polygonal ones are analyzed in this section as well. The effects of foundation parameters are considerable in relation to the natural frequencies of plates. Frequency parameters increase as foundation parameters are increased, and each frequency



5.20 Geometric size and mesh of annular plate.

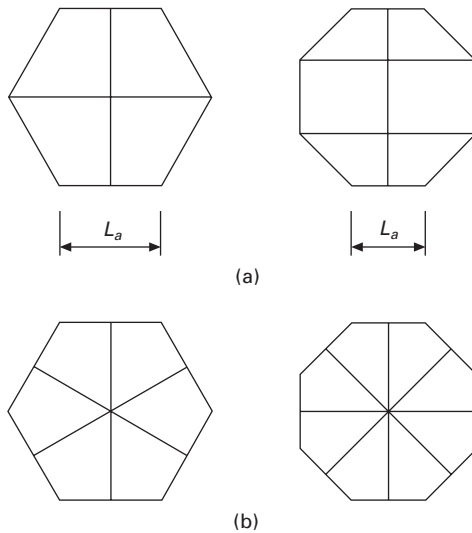


5.21 Convergence for annular plate without foundation.

parameter approaches a constant value when the foundation parameters are large enough. The present elements are suitable for the analysis of both thin and thick plates; furthermore, they have a fast convergence characteristic.

## 5.5 Geometric nonlinear vibration of clamped plates

In the trapezoidal hierarchical element (THFE-P) developed in Section 5.3,



5.22 Geometric size and mesh of hexagonal and octagonal plates:  
(a) THFE-P mesh; (b) QHFE-P mesh.

the membrane strain components taking into account the nonlinear terms are defined by (Zienkiewicz and Taylor 1989):

$$\begin{aligned}\varepsilon_x &= \frac{\partial u}{\partial x} + \frac{1}{2} \left( \frac{\partial w}{\partial x} \right)^2, \quad \varepsilon_y = \frac{\partial v}{\partial y} + \frac{1}{2} \left( \frac{\partial w}{\partial y} \right)^2 \\ \gamma_{xy} &= \frac{\partial u}{\partial y} + \frac{\partial v}{\partial x} + \left( \frac{\partial w}{\partial x} \right) \left( \frac{\partial w}{\partial y} \right)\end{aligned}\quad 5.10$$

The transverse displacement  $w$ , rotations  $\theta_x$  and  $\theta_y$  and membrane displacements  $u$  and  $v$  of the Mindlin plate are interpolated by

$$\begin{Bmatrix} u \\ v \end{Bmatrix} = \begin{bmatrix} \mathbf{N}^i & 0 \\ 0 & \mathbf{N}^i \end{bmatrix} \begin{Bmatrix} \mathbf{q}_u \\ \mathbf{q}_v \end{Bmatrix} \quad 5.11a$$

$$\begin{Bmatrix} w \\ \theta_x \\ \theta_y \end{Bmatrix} = \begin{bmatrix} \mathbf{N}^o & 0 & 0 \\ 0 & \mathbf{N}^o & 0 \\ 0 & 0 & \mathbf{N}^o \end{bmatrix} \begin{Bmatrix} \mathbf{q}_w \\ \mathbf{q}_{\theta_x} \\ \mathbf{q}_{\theta_y} \end{Bmatrix} \quad 5.11b$$

where  $\mathbf{q}_u$ ,  $\mathbf{q}_v$  are the vectors of generalized membrane displacements,  $\mathbf{q}_w$  is the vector of generalized transverse displacement and  $\mathbf{q}_{\theta_x}$  and  $\mathbf{q}_{\theta_y}$  are the vectors of generalized rotations. For the sake of simplicity, the number of the additional  $C^0$  Legendre orthogonal polynomials in the  $\xi$  direction is taken to be the same as that in the  $\eta$  direction. Parameters  $p_o$ ,  $p_\theta$  and  $p_i$  are the number of Legendre orthogonal polynomials used in shape functions for the transverse displacement, rotations and the membrane displacements respectively.

Table 5.14 Frequency parameters  $\Omega = \omega L_a^2 \sqrt{\rho t/D_0}$  for clamped hexagonal plates on foundations;  $\nu = 0.3$ ,  $\kappa = 5/6$  and  $p = 8$

$L_a/t$	$k_1$	$k_2$	Method	Modes <sup>a</sup>					
				1	2	3	4	5	6
1000	0	0	THFE-P	12.79	26.52	26.52	43.29	43.29	49.37
			QHFE-P	12.79	26.52	26.52	43.29	43.29	49.38
			Liew and Lam (1991)	13.05	26.78	26.79	43.80	43.87	49.92
			Irie <i>et al.</i> (1978) Prabhakara and Chia (1977)	12.86	26.77	26.85	43.75	43.80	49.68
			ANSYS	12.78	26.48	26.50	43.18	43.22	49.28
			THFE-P	13.66	27.04	27.04	43.67	43.68	49.74
			QHFE-P	13.66	27.04	27.04	43.68	43.68	49.74
			THFE-P	18.93	29.97	29.97	45.48	45.49	51.31
			QHFE-P	18.93	29.97	29.97	45.49	45.49	51.31
			ANSYS	18.92	29.91	29.96	45.37	45.41	51.21
2	0.04	THFE-P	19.81	31.31	31.31	47.03	47.04	52.87	
		QHFE-P	19.81	31.31	31.31	47.04	47.04	52.87	
		THFE-P	49.41	58.84	58.84	72.41	72.42	77.53	
		QHFE-P	49.41	58.84	58.84	72.42	72.42	77.53	
20	0.4	THFE-P	12.31	24.79	24.79	39.19	39.19	44.36	
		QHFE-P	12.31	24.79	24.79	39.20	39.20	44.36	
		THFE-P	13.20	25.33	25.33	39.61	39.61	44.74	
		QHFE-P	13.20	25.33	25.33	39.61	39.61	44.75	
2	0.4	THFE-P	19.45	29.75	29.75	43.15	43.15	48.07	
		QHFE-P	19.45	29.75	29.75	43.15	43.15	48.07	
		THFE-P	49.06	57.53	57.53	69.16	69.16	73.45	
		QHFE-P	49.06	57.53	57.53	69.16	69.16	73.45	

Table 5.15 Frequency parameters  $\Omega = \omega L_a \sqrt{pt/D_0}$  for free hexagonal plates on foundations;  $v = 0.3$ ,  $\kappa = 5/6$  and  $p = 8$

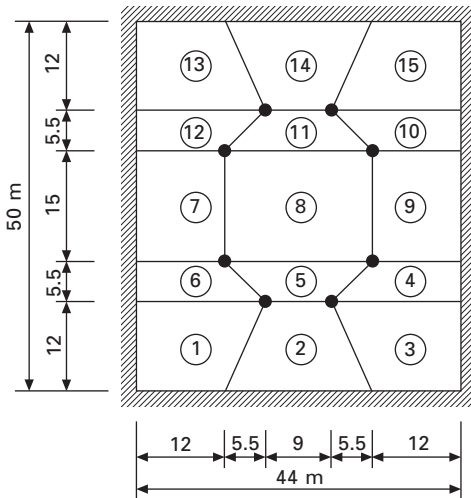
$L_a/t$	$k_1$	$k_2$	Method	Modes <sup>a</sup>					
				1	2	3	4	5	6
1000	0	0	THFE-P	—	—	—	6.376	6.384	10.67
			QHFE-P	—	—	—	6.375	6.384	10.67
			Liew and Lam (1991)	—	—	—	6.384	6.404	10.67
			ANSYS	—	—	—	6.385	6.386	10.67
0.2	0.04	0.04	THFE-P	4.409	4.624	4.629	8.083	8.083	11.92
			QHFE-P	4.409	4.624	4.629	8.083	8.083	11.92
2	0	0	THFE-P	13.96	13.96	13.96	15.35	15.35	17.57
			QHFE-P	13.96	13.96	13.96	15.35	15.35	17.58
			ANSYS	13.96	13.99	13.99	15.39	15.39	17.62
2	0.4	0.4	THFE-P	13.96	14.60	14.60	16.90	16.90	19.85
			QHFE-P	13.96	14.60	14.60	16.90	16.90	19.85
20	4	4	THFE-P	44.41	46.01	46.01	49.53	49.53	53.29
			QHFE-P	44.41	46.01	46.01	49.54	49.54	53.29
10	0	0	THFE-P	—	—	—	6.257	6.257	10.48
			QHFE-P	—	—	—	6.257	6.257	10.48
			THFE-P	4.414	4.613	4.613	7.966	7.966	11.73
0.2	0.04	0.04	QHFE-P	4.414	4.613	4.613	7.967	7.967	11.73
2	0.4	0.4	THFE-P	13.96	14.57	14.57	16.78	16.78	19.61
			QHFE-P	13.96	14.57	14.57	16.78	16.78	19.62
20	4	4	THFE-P	44.14	45.93	45.93	49.27	49.27	52.81
			QHFE-P	44.14	45.93	45.93	49.27	49.27	52.82

Table 5.16 Frequency parameters  $\Omega = \omega L_a^2 \sqrt{\rho t/D_0}$  for clamped octagonal plates on foundations;  $\nu = 0.3$ ,  $\kappa = 5/6$  and  $\rho = 8$

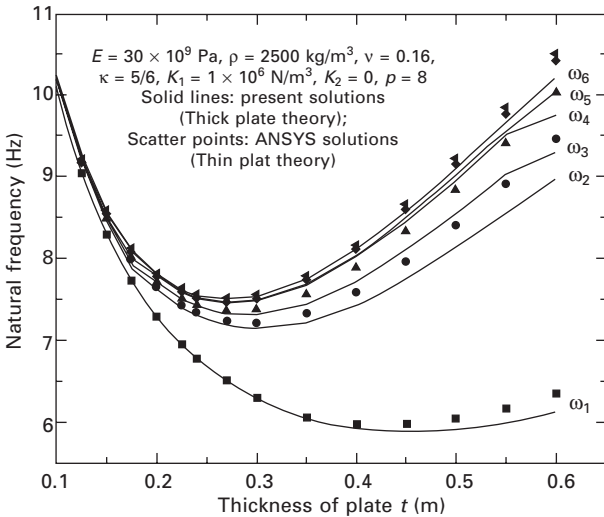
$L_a/t$	$k_1$	$k_2$	Method	Modes <sup>a</sup>					
				1	2	3	4	5	6
1000	0	0	THFE-P	6.750	14.03	14.03	22.98	22.98	26.21
			QHFE-P	6.751	14.03	14.03	22.99	22.99	26.21
			Liew and Lam (1991)	6.826	14.28	14.28	23.30	23.30	26.46
			Irie <i>et al.</i> (1978)	6.787	14.14	14.18	23.11	23.18	26.37
			Prabhakara and Chia (1977)	6.747	14.02	14.02	22.96	22.96	26.18
			ANSYS	6.750	—	—	—	—	—
			THFE-P	8.175	14.86	14.86	23.57	23.57	26.74
			QHFE-P	8.175	14.86	14.86	23.57	23.57	26.74
			THFE-P	15.50	19.79	19.79	26.89	26.89	29.70
			QHFE-P	15.50	19.79	19.79	26.89	26.89	29.69
2	0.04	0	ANSYS	15.50	19.78	19.79	26.87	26.88	29.66
			THFE-P	16.07	20.86	20.86	28.27	28.27	31.12
			QHFE-P	16.07	20.86	20.86	28.28	28.28	31.13
			THFE-P	46.54	50.71	50.71	56.82	56.82	59.13
			QHFE-P	46.54	50.71	50.71	56.83	56.83	59.13
			THFE-P	6.614	13.52	13.52	21.74	21.74	24.68
			QHFE-P	6.614	13.52	13.52	21.75	21.75	24.68
			THFE-P	8.058	14.37	14.37	22.35	22.35	25.23
			QHFE-P	8.058	14.37	14.37	22.36	22.36	25.23
			THFE-P	15.98	20.46	20.46	27.18	27.18	29.75
2	0.4	0	QHFE-P	15.98	20.46	20.46	27.19	27.19	29.76
			THFE-P	46.41	50.30	50.30	55.86	55.86	57.94
			QHFE-P	46.41	50.30	50.30	55.86	55.86	57.94
			THFE-P	—	—	—	—	—	—

Table 5.17 Frequency parameters  $\Omega = \omega L_a^2 \sqrt{\rho t/D_0}$  for free octagonal plates on foundations;  $\nu = 0.3$ ,  $\kappa = 5/6$ , and  $\rho = 8$

$L_a/t$	$k_1$	$k_2$	Method	Modes <sup>a</sup>					
				1	2	3	4	5	6
1000	0	0	THFE-P	—	—	—	3.466	3.473	5.823
			QHFE-P	—	—	—	3.465	3.473	5.823
			Liew and Lam (1991)	—	—	—	3.469	3.469	5.823
			ANSYS	—	—	—	3.469	3.469	5.825
			THFE-P	4.414	4.524	4.530	5.848	5.856	7.627
			QHFE-P	4.413	4.524	4.530	5.848	5.856	7.628
2	0	0.04	THFE-P	13.96	13.96	13.96	14.38	14.38	15.12
			QHFE-P	13.96	13.96	13.96	14.39	14.39	15.12
			ANSYS	13.96	13.97	13.97	14.40	14.41	15.15
			THFE-P	13.96	14.30	14.30	15.29	15.29	16.58
			QHFE-P	13.96	14.30	14.30	15.29	15.29	16.59
			THFE-P	44.14	45.14	45.14	47.01	47.01	48.90
20	4	0.4	QHFE-P	44.14	45.14	45.14	47.02	47.02	48.90
			THFE-P	—	—	—	3.429	3.429	5.768
			QHFE-P	—	—	—	3.429	3.429	5.769
			THFE-P	4.414	4.523	4.523	5.821	5.821	7.566
			QHFE-P	4.414	4.523	4.523	5.822	5.822	7.566
			THFE-P	13.96	14.29	14.29	15.24	15.24	16.48
20	4	4	QHFE-P	13.96	14.29	14.29	15.24	15.24	16.48
			THFE-P	44.14	45.10	45.10	46.89	46.89	48.68
			QHFE-P	44.14	45.10	45.10	46.89	46.89	48.69



5.23 Geometric size and mesh for clamped plate with point supports.



5.24 Effects of plate thickness to first six natural frequencies of plate with point supports.

Taking into account the effects of the transverse shear deformation and rotatory inertia, and neglecting the in-plane inertia, the principle of minimum potential energy with the Hamilton principle gives (Han and Petyt 1997)

$$\mathbf{M}_l \begin{Bmatrix} \ddot{\mathbf{q}}_w \\ \ddot{\mathbf{q}}_{\theta_x} \\ \ddot{\mathbf{q}}_{\theta_y} \end{Bmatrix} + \mathbf{K}_l \begin{Bmatrix} \mathbf{q}_w \\ \mathbf{q}_{\theta_x} \\ \mathbf{q}_{\theta_y} \end{Bmatrix} + \begin{bmatrix} \mathbf{K}_4 - \mathbf{K}_3 \mathbf{K}_l^{-1} \mathbf{K}_2 & 0 & 0 \\ 0 & 0 & 0 \\ 0 & 0 & 0 \end{bmatrix} \begin{Bmatrix} \mathbf{q}_w \\ \mathbf{q}_{\theta_x} \\ \mathbf{q}_{\theta_y} \end{Bmatrix} = \{P\}$$

5.12

where  $\mathbf{K}_l$  and  $\mathbf{M}_l$  are the linear stiffness and mass matrices for the out-of-plane vibration,  $\mathbf{K}_{1,p}$  is the linear stiffness matrix for the in-plane vibration. These three linear matrices have been obtained previously in Section 5.3. In Eq. (5.12)  $\mathbf{K}2$ ,  $\mathbf{K}3$  are linear functions of  $\mathbf{q}_w$ ;  $\mathbf{K}4$  is a quadratic function of  $\mathbf{q}_w$ . The three nonlinear matrices can be expressed as (Zienkiewicz and Taylor 1989, Han and Petyt 1997):

$$\mathbf{K}2 = \frac{1}{2} \int_{-1}^1 \int_{-1}^1 \mathbf{B}_0^T \mathbf{E} \mathbf{B}_b \cdot |\mathbf{J}| d\xi d\eta \quad 5.13a$$

$$\mathbf{K}3 = 2\mathbf{K}2^T \quad 5.13b$$

$$\mathbf{K}4 = \frac{1}{2} \int_{-1}^1 \int_{-1}^1 \mathbf{B}_0^T \mathbf{E} \mathbf{B}_b \cdot |\mathbf{J}| d\xi d\eta \quad 5.13c$$

where  $\mathbf{B}_0$ ,  $\mathbf{B}_b$  and  $\mathbf{E}$  are defined by

$$\mathbf{B}_0 = \begin{bmatrix} \frac{\partial \mathbf{N}}{\partial x} & 0 \\ 0 & \frac{\partial \mathbf{N}}{\partial y} \\ \frac{\partial \mathbf{N}}{\partial y} & \frac{\partial \mathbf{N}}{\partial x} \end{bmatrix}, \mathbf{B}_b = \begin{bmatrix} \frac{\partial w}{\partial x} & 0 \\ 0 & \frac{\partial w}{\partial y} \\ \frac{\partial w}{\partial y} & \frac{\partial w}{\partial x} \end{bmatrix} \begin{bmatrix} \frac{\partial \mathbf{N}}{\partial x} \\ \frac{\partial \mathbf{N}}{\partial y} \end{bmatrix}$$

$$\mathbf{E} = \frac{Et}{(1 - \nu^2)} \begin{bmatrix} 1 & \nu & 0 \\ \nu & 1 & 0 \\ 0 & 0 & (1 - \nu)/2 \end{bmatrix} \quad 5.14$$

where  $E$  is Young's modulus,  $l$  is the thickness of the plate and  $\nu$  is Poisson's ratio. The coefficients of the matrices  $\mathbf{K}2$  and  $\mathbf{K}4$  are formed by integrations

$$k2_{i,j,r}^e = \int_{-1}^1 \int_{-1}^1 N'_i N'_j N'_r \cdot |\mathbf{J}| d\xi d\eta \quad 5.15a$$

$$k4_{i,j,r,s}^e = \int_{-1}^1 \int_{-1}^1 N'_i N'_j N'_r N'_s \cdot |\mathbf{J}| d\xi d\eta \quad 5.15b$$

where  $N'$  is the derivatives of the shape functions  $N(\xi, \eta)$  to  $x$  or  $y$ . The determinant of Jacobian  $|\mathbf{J}|$  is only related to  $\eta$  so that  $\xi$  and  $\eta$  can be integrated independently in Eq. 5.15.

The ability to integrate  $\xi$  and  $\eta$  independently is important for nonlinear analysis with  $p$ -version elements. Although the use of hierarchical elements can effectively reduce the required number of DOFs in a nonlinear vibration analysis, the element matrices should be integrated analytically to eliminate the numerical integration errors when high-order oscillating polynomials are

involved as shape functions (Woo *et al.* 2003). Only Mindlin plates of rectangular, skew and trapezoidal shapes can be easily integrated analytically when hierarchical elements are employed in nonlinear vibration analysis. The results of integrations in Eq. (5.15) can be stored in individual files for the later use.

### 5.5.1 Arc-length iteration for free and forced nonlinear vibration

When the excitation force considered per unit area is given by  $P_0 \cos(\omega t)$ , the vector of generalized force has the form

$$\{P\} = \begin{Bmatrix} \int_{-1}^1 \int_{-1}^1 P_0 \cos(\omega t) \mathbf{N} \cdot |\mathbf{J}| d\xi d\eta \\ 0 \end{Bmatrix} \quad 5.16$$

where  $\omega$  is the circular frequency. The nonlinearity of the system is cubic with respect to displacement and only the odd harmonics are considered in the solution (Prabhakara and Chia 1977). Most of the existing work has been carried out using one harmonic (Prabhakara and Chia 1977, Han and Petyt 1997) for weakly nonlinear analysis. Then, the periodic solution is expressed in Fourier series

$$\mathbf{q}_w = \mathbf{q}_{wc} \cos \omega t + \mathbf{q}_{ws} \sin \omega t \quad 5.17$$

Since the vibration considered herein is undamped, the sine terms in Eq. (5.17) is not necessary. From Eqs. (5.12) and (5.17), applying HBM and neglecting the higher-order harmonic component lead to the following nonlinear eigenvalue problem:

$$\begin{aligned} \{F\} &= (-\mathbf{M}_I \omega^2 + \mathbf{K}_I) \mathbf{q} + \frac{3}{4} (\mathbf{K}4 - 2\mathbf{K}2^T \mathbf{K}1_p^{-1} \mathbf{K}2) \mathbf{q}_{wc} - \{P\} \\ &= \{0\} \end{aligned} \quad 5.18$$

where  $\mathbf{q} = [\mathbf{q}_{wc}, \mathbf{q}_{\theta_x}, \mathbf{q}_{\theta_y}]^T$ . In this section, the arc-length iterative method originally proposed by Crisfield (1981) is used to solve the nonlinear eigenvalue problem. The first point in the backbone curve and FRF curve is obtained by the Newton–Raphson method. Then, iterations of Eq. (5.18) are repeated by the arc-length method to achieve convergence to get the solutions of the next equilibrium state  $^{m+1}\mathbf{q}$  and  $^{m+1}\omega^2$ . During the computation from  $^m\mathbf{q}$  and  $^m\omega^2$  to  $^{m+1}\mathbf{q}$  and  $^{m+1}\omega^2$ , the following constraint equation controls each iteration:

$$(\mathbf{q} - ^m\mathbf{q})^T (\mathbf{q} - ^m\mathbf{q}) = \Delta\mathbf{q}^T \Delta\mathbf{q} = s^2 \quad 5.19$$

where  $\Delta\mathbf{q}$  is the total increment of  $\mathbf{q}$ .

The following parameters of the plates are used in this section:  $E = 21 \times 10^{10}$  Pa,  $\rho = 7800$  kg/m<sup>3</sup>,  $\kappa = 5/6$ ,  $v = 0.3$ ,  $x_2 = 0.5$  m,  $y_2 = 0$ . Nonlinear free

and forced vibrations of both the skew and trapezoidal plates with all edges immovable and clamped are analyzed. The parameter  $w_m = \mathbf{N} \cdot \mathbf{q}_{wc}$  for the first nonlinear modes represents the displacement amplitude of vibration at the origin of the mapped coordinates (0, 0). The parameters for the second and third nonlinear modes represent the amplitude of vibration displacements at the point with mapped coordinates (0, 0.5).

As mentioned above, since the nonlinear stiffness matrices should be reconstructed during iterations, the computational time in an arc-length iteration increases considerably with the number of DOFs. Therefore, the property of using fewer DOFs while satisfying the accuracy requirement is important for the nonlinear vibration analysis by FEM. To demonstrate the fast convergence of the present element, the first three out-of-plane and in-plane natural frequencies of a trapezoidal thin plate are computed in Table 5.18. The frequency parameters  $\lambda$  are  $\omega x_2^2/(2\pi)\sqrt{\rho t/D_0}$  and  $\omega x_2/(2\pi)\sqrt{\rho/E}$  for out-of-plane and in-plane vibration, respectively. A comparison with the results of Ritz method (Kitipornchai *et al.* 1994) and linear finite elements (LFE) is made. The linear finite element is a special case of the present element for out-of-plane and in-plane vibration respectively when no additional hierarchical shape functions are employed in its shape functions. Reduced integration is used in LFE for out-of-plane vibration in order to avoid the shear locking problem.

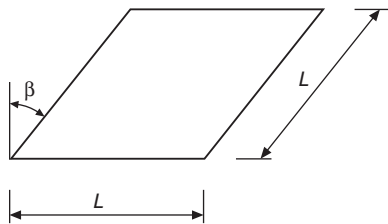
It can be observed that the solutions of the present element are more accurate than those of LFE for the same number of DOFs. The present solutions of in-plane vibration with  $p_i = 8$  are in excellent agreement with those of LFE with  $50 \times 50$  mesh. For the out-of-plane vibration of this very thin plate ( $x_2/t = 1000$ ), the good agreement between the present solutions with those of Ritz method (Kitipornchai *et al.* 1994) and LFEM demonstrates that the present element is free of shear locking just as verified in Section 5.3.

A rhombic plate with a skew angle  $\beta$  is shown in Fig. 5.25. The values  $L = 0.5$  m,  $t = 0.005$  m ( $L/t = 100$ ) are used for the vibration analysis of skew plates. To study the convergence of THFE-P for nonlinear analysis, the free vibration of the rhombic plate ( $\beta = 15^\circ$ ) is analyzed with different number of out-of-plane and in-plane shape functions. Their backbone curves describing the relation between amplitude of vibration and frequency are plotted in Figs 5.26 and 5.27 respectively. In the plots  $w_{l1}$  denotes the first linear frequency of the plate computing by the element with  $p_o = p_\theta = 5$  and  $p_i = 8$ . It can be seen that the hardening spring effect is shown clearly and the present hierarchical element with  $p_o = p_\theta = 5$  and  $p_i = 8$  can achieve excellent convergence. So  $p_o = p_\theta = 5$ ,  $p_i = 8$  are used in the rest of this section.

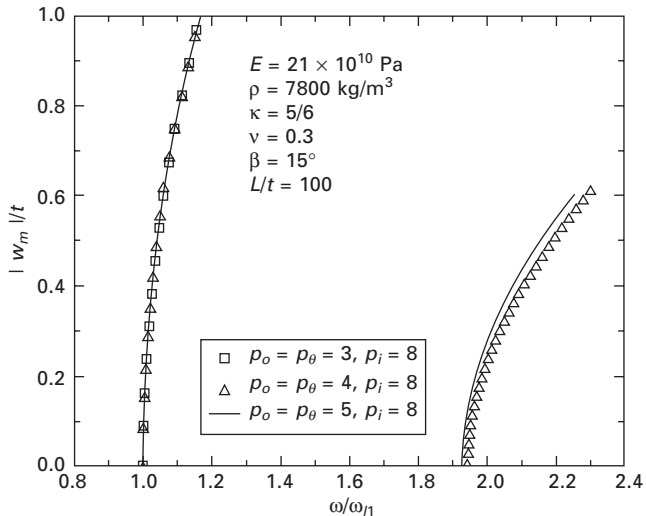
The backbone curves for the first nonlinear mode of the plate with different skew angles varying from  $0^\circ$  to  $45^\circ$  are shown in Fig. 5.28. The first linear frequencies of the plates increase with increasing skew angles  $\beta$  and the

Table 5.18 Convergence of frequency parameters  $\lambda$  for a symmetric trapezoidal plate ( $x_2 = 0.5, x_4 = 0.05, x_3 = 0.45, y_3 = 0.5, t = 0.0005$ )

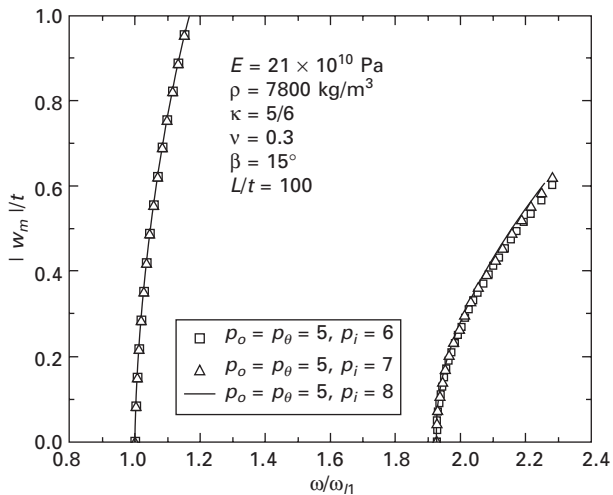
Method	DOF	Out-of-plane modes			In-plane modes		
		1	2	3	DOF	1	2
HFEM $p_o = p_\theta = 3, p_j = 6$	27	12.78			72	0.6126	0.6417
HFEM $p_o = p_\theta = 4, p_j = 7$	48	6.46	14.16	21.46	98	0.6126	0.6417
HFEM $p_o = p_\theta = 5, p_j = 8$	75	6.45	12.55	14.12	128	0.6126	0.6417
LFEM $10 \times 10$	243	6.59	13.05	14.87	162	0.6166	0.6460
LFEM $50 \times 50$	7203	6.45	12.30	13.92	4802	0.6128	0.6419
Ritz method Kitipornchai et al. 1994		6.44	12.27	13.89			0.7489



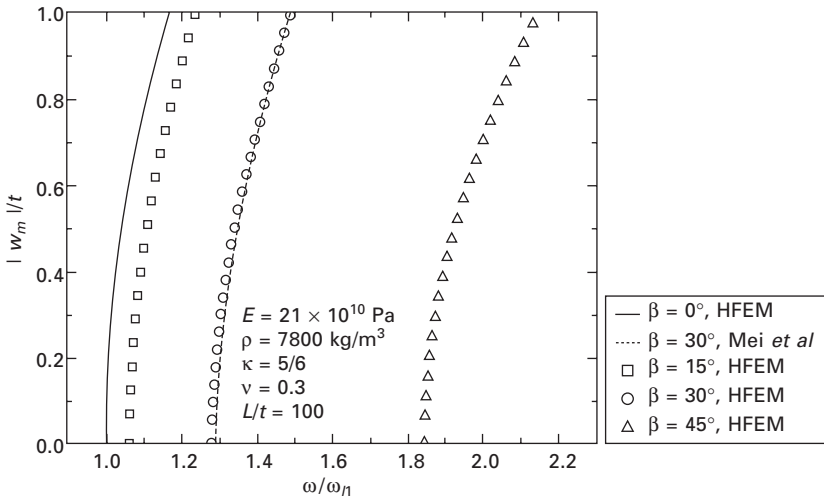
5.25 Geometric size of a skew plate.



5.26 Convergence study of out-of-plane shape functions for nonlinear free vibration of a skew plate.



5.27 Convergence study of in-plane shape functions for nonlinear free vibration of a skew plate.



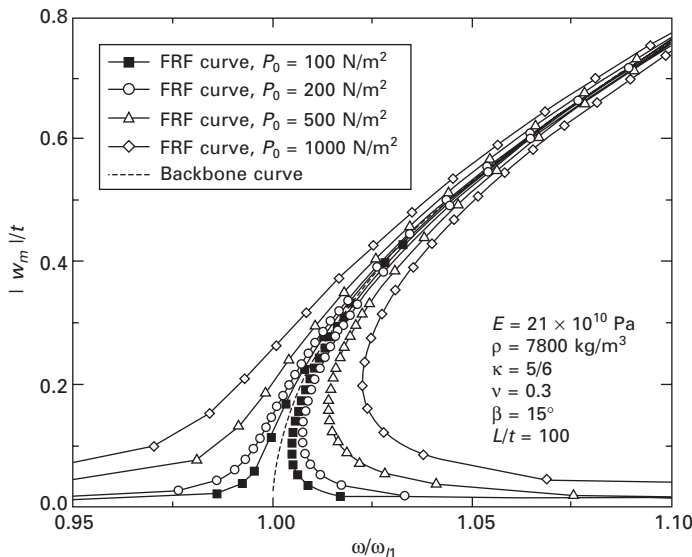
5.28 Backbone curves of a skew plate with different skew angles.

shape of the backbone curves is almost same for the plates with different skew angles. The present solutions of the plate with  $\beta = 30^\circ$  are in good agreement with the results of Mei *et al.* (1985). They analyzed a quarter of the plate with 16 triangular elements. The frequency response function (FRF) curves of a rhombic plate with  $\beta = 15^\circ$  in the vicinity of the first nonlinear mode subject to uniform harmonic loads  $P_0 = 100, 200, 500$  and  $1000 \text{ N/m}^2$  are shown in Fig. 5.29.

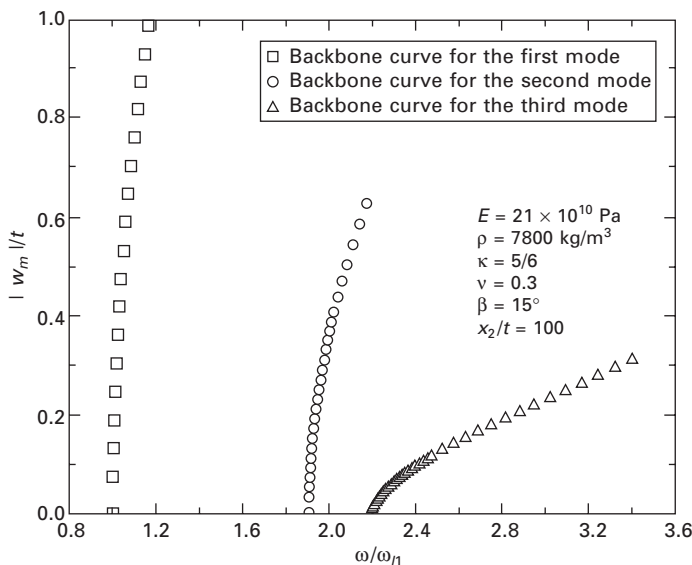
For a trapezoidal plate with  $x_2 = 0.5 \text{ m}$ ,  $y_2 = 0 \text{ m}$ ,  $x_3 = 0.4 \text{ m}$ ,  $y_3 = 0.5 \text{ m}$ ,  $x_4 = 0 \text{ m}$ ,  $y_4 = 0.5 \text{ m}$  and  $t = 0.005 \text{ m}$  ( $x_2/t = 100$ ), the backbone curves for the first three nonlinear modes can be obtained using the arc-length iterative method without difficulty and the results are plotted in Fig. 5.30. Using fixed values  $x_2 = 0.5 \text{ m}$ ,  $x_4 = 0 \text{ m}$ ,  $y_3 = 0.5 \text{ m}$  and different values of  $x_3$  gives the backbone curves for the first mode shown in Fig. 5.31. Using fixed values of  $x_2$ ,  $y_2$ ,  $y_3$ ,  $y_4$ ,  $x_3 - x_4 = 0.3 \text{ m}$  and different values of  $x_4$  gives the backbone curves for the first mode shown in Fig. 5.32. It can be observed that the skew angles of the trapezoidal plates hardly affect the backbone curves of the first nonlinear vibration mode, but the hardening spring effect in the backbone curves increases when the chord ratio  $(x_3 - x_4)/x_2$  decreases. The FRF curves of a symmetric trapezoidal plate with  $(x_3 - x_4)/x_2 = -0.2$  in the vicinity of the first nonlinear mode subject to uniform harmonic loads  $P_0 = 100, 200, 500$  and  $1000 \text{ N/m}^2$  are shown in Fig. 5.33.

## 5.6 Conclusions

The trapezoidal hierarchical finite element (THFE-P) is applied for the nonlinear free and forced vibration of skew and trapezoidal plates. The analytic integration

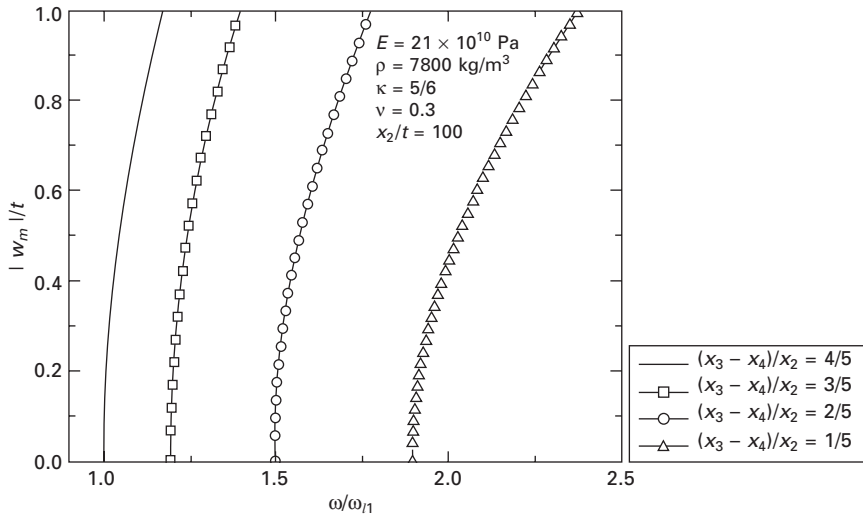


5.29 FRF curves of a skew plate subjected to different uniform harmonic loads.

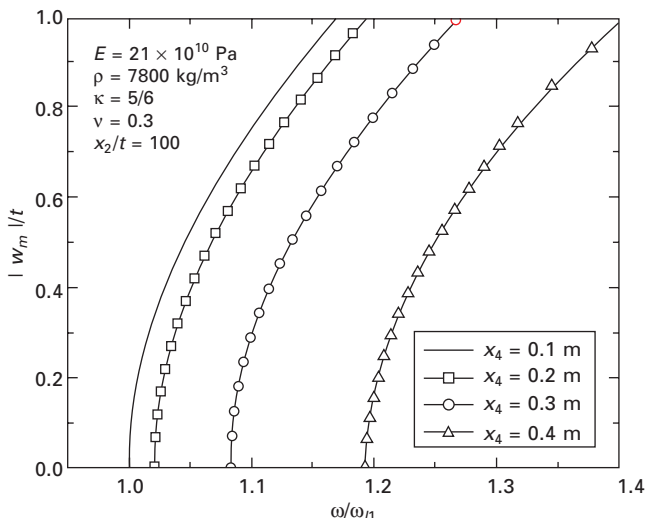


5.30 Backbone curves of the first nonlinear modes for a trapezoidal plate.

of arbitrary quadrilateral hierarchical element (QHFE-P) is time-consuming, so the element with analytic integration is not easy in nonlinear analysis. The convergence of the fundamental and higher linear and nonlinear modes is investigated. It is concluded that this hierarchical element is free of the shear

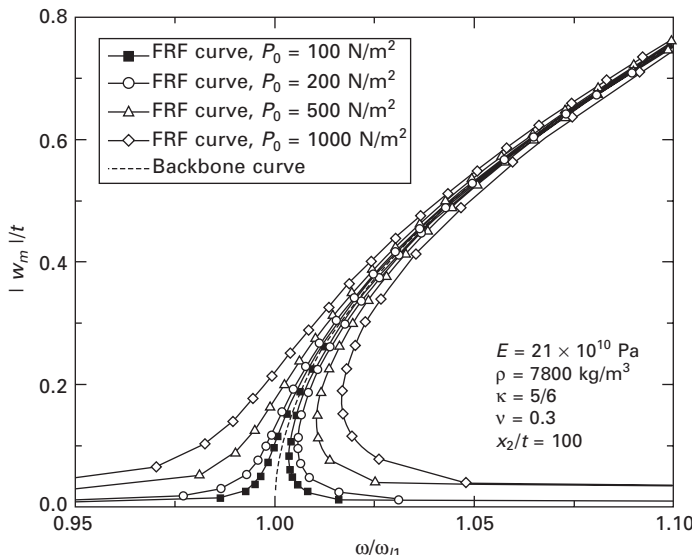


5.31 Backbone curves of a trapezoidal plate with different ratios  $(x_3 - x_4)/x_2$ .



5.32 Backbone curves of a trapezoidal plate with different skew angles.

locking and nonlinear vibration of very thin plates can be analyzed without difficulty. The parametric studies show that the skew angles hardly influence the shape of the backbone curves, but the decreasing of chord ratios of trapezoidal plates increases the hardening spring effect of the backbone curves. The forced vibration of skew and trapezoidal plates subjected to different uniform harmonic loads is also studied



5.33 FRF curves of a trapezoidal plate subjected to different uniform harmonic loads.

## 5.7 References and further reading

- Bardell N.S., Free vibration analysis of a flat plate using the hierarchical finite element method, *Journal of Sound and Vibration* **151** (2) (1991) 263–289.
- Bardell N.S., The free vibration of skew plates using the hierarchical finite element method, *Computers & Structure* **45** (5–6) (1992) 841–874.
- Bardell N.S., An engineering application of the *h-p* version of the finite element method to the static analysis of an Euler–Bernoulli beam, *Computers and Structures* **59** (1996) 195–211.
- Bardell N.S., Dunsdon J.N. and Langley R.S., Free vibration of coplanar sandwich panels, *Composite Structures* **38** (1997) 463–475.
- Bardell N.S., Langley R.S., Dunsdon J.M. and Aglietti G.S., An *h-p* finite element vibration analysis of open conical sandwich panels and conical sandwich frusta, *Journal of Sound and Vibration* **226** (2) (1999) 345–377.
- Beslin O. and Nicolas J., Hierarchical functions set for predicting very high order plate bending modes with any boundary conditions, *Journal of Sound and Vibration* **202** (5) (1997) 633–655.
- Cook R.D., Malkus D.S. and Plesha M.E., *Concepts and Applications of Finite Element Analysis*, 4th Edition, John Wiley & Sons, New York, 1989.
- Crisfield M.A., A fast incremental/iterative solution procedure that handles snap through, *Computers & Structures* **13** (1981) 55–62.
- Han W. and Petyt M., Geometrically nonlinear vibration analysis of thin, rectangular plates using the hierarchical finite element method – I: The fundamental mode of isotropic plates, *Computers & Structures* **63** (1997) 295–308.
- Houmat A., Hierarchical finite element analysis of the vibration of membranes, *Journal of Sound and Vibration* **201** (4) (1997a) 465–472.

- Houmat A., An alternative hierarchical finite element formulation applied to plate vibrations, *Journal of Sound and Vibration* **206** (2) (1997b) 201–215.
- Houmat A., A triangular Fourier  $p$ -element for the analysis of membrane vibrations, *Journal of Sound and Vibration* **230** (1) (2000) 31–43.
- Houmat A., A sector Fourier  $p$ -element for free vibration analysis of sectorial membranes, *Computers & Structures* **79** (2001a) 1147–1152.
- Houmat A., A sector Fourier  $p$ -element applied to free vibration analysis of sectorial plates, *Journal of Sound and Vibration* **243** (2) (2001b) 269–282.
- Houmat A., Three-dimensional hierarchical finite element free vibration analysis of annular sector plates, *Journal of Sound and Vibration* **276** (2004) 181–193.
- Irie T., Yamada G. and Narita Y., Free vibration of clamped polygonal plates, *Bulletin of the JSME* **21** (162) (1978) 1696–1702.
- Jones R. and Xenophontos J., The Valsov foundation model, *International Journal of Mechanical Sciences*, **19** (1977) 317–323.
- Karunasena W., Liew K.M. and Al-Bermani F.G.A., Natural frequencies of thick arbitrary quadrilateral plates using the pb-2 Ritz method, *Journal of Sound and Vibration* **196** (4) (1996) 371–385.
- Kitipornchai S., Liew K.M., Xiang Y. and Wang C.M., Free flexural vibration of triangular Mindlin plates, *International Journal of Mechanical Sciences* **35** (2) (1993) 89–102.
- Kitipornchai S., Xiang Y., Liew K.M. and Lim M.K., A global approach for vibration of thick trapezoidal plates, *Computers and Structures* **53** (1) (1994) 83–92.
- Leung A.Y.T. and Chan J.K.W., Fourier  $p$ -element for the analysis of beams and plates, *Journal of Sound and Vibration* **212** (1998) 179–185.
- Leung A.Y.T. and Zhu B., Transverse vibration of thick polygonal plates using analytically integrated trapezoidal Fourier  $p$ -element, *Computers & Structures* **82** (2–3) (2004a) 109–119.
- Leung A.Y.T. and Zhu B., Hexahedral Fourier  $p$ -elements for vibration of prismatic solids, *International Journal of Structural Stability and Dynamics*, **4** (1) (2004b) 125–138.
- Leung A.Y.T. and Zhu B., Geometric nonlinear vibration of clamped Mindlin plates by analytically integrated trapezoidal  $p$ -element, *Thin-walled Structures*, **42** (7) (2004c) 931–945.
- Leung A.Y.T. and Zhu B., Comments on ‘Free vibration of skew Mindlin plates by  $p$ -version of F.E.M.’, *Journal of Sound and Vibration* **278** (2004d) 699–703.
- Leung A.Y.T. and Zhu B., Transverse vibration of Mindlin plates on two parameter foundations by analytical trapezoidal  $p$ -elements, *ASCE Journal of Engineering Mechanics*, **131** (11) (2005) 1140–1145.
- Leung A.Y.T., Xiao C., Zhu B. and Yuan S., Free vibration of laminated composite plates subjected to in-plane stresses using trapezoidal  $p$ -element, *Journal of Composite Structures*, **68** (2005) 167–175.
- Leung A.Y.T., Zhu B., Zheng J. and Yang H., A trapezoidal Fourier  $p$ -element for membrane vibrations, *Thin-walled Structures*, **41** (5), (2003a) 479–491.
- Leung A.Y.T., Zhu B., Zheng J. and Yang H., Two-dimensional viscoelastic vibration by analytic Fourier  $p$ -elements, *Thin-walled Structures*, **41**(12) (2003b) 1159–1170.
- Leung A.Y.T., Zhu B., Zheng J.J. and Yang H., Analytic trapezoidal Fourier  $p$ -element for vibrating plane problems, *Journal of Sound and Vibration* **271** (2004) 67–81.
- Liew K.M. and Lam K.Y., A set of orthogonal plate functions for flexural vibration of regular polygonal plates, *Journal of Vibration and Acoustics* **113** (3) (1991) 182–186.

- Liew K.M., Wang C.M., Xiang Y. and Kitipornchai S., *Vibration of Mindlin Plates*, Elsevier, Oxford, 1998.
- Liew K.M., Xiang Y. and Kitipornchai S., Transverse vibration of thick rectangular plates – I. Comprehensive sets of boundary conditions, *Computers & Structures* **49** (1) (1993a) 1–29.
- Liew K.M., Xiang Y., Kitipornchai S. and Wang C.M., Vibration of thick skew plates based on Mindlin shear deformation plate theory, *Journal of Sound and Vibration* **168** (1) (1993b) 36–69.
- Martini L. and Vitaliani R., On the polynomial convergent formulation of a  $C^0$  isoparametric skew beam element, *Computers and Structures* **29** (1988) 437–449.
- Mei C. and Decha-Umphai K., A finite element method for nonlinear forced vibrations of beams, *Journal of Sound and Vibration* **102** (1985) 369–380.
- Mindlin R.D., Influence of rotatory inertia and shear on flexural motions of isotropic, elastic plates, *Journal of Applied Mechanics – Transaction ASME* **18** (1951) 31–38.
- Papadrakakis M. and Babilis G.P., Solution techniques for the  $p$ -version of the adaptive finite element method, *International Journal for Numerical Methods in Engineering* **37** (1994) 1413–1431.
- Peano A., Pasini A., Riccioni R. and Sardella L., Adaptive approximations in finite element structural analysis, *Computers & Structures* **10** (1979) 333–342.
- Prabhakara M.K. and Chia C.Y., Nonlinear flexural vibrations of orthotropic rectangular plates, *Journal of Sound and Vibration* **52** (4) (1977) 511–518.
- Ribeiro P. and Petyt M., Non-linear vibration of beams with internal resonance by the hierarchical finite-element method, *Journal of Sound and Vibration* **224** (4) (1999) 591–624.
- Richart F.E., Jr, Hall J.R. and Woods R.D., *Vibration of Soils and Foundations*, Prentice-Hall, Englewood Cliffs, NJ, 1970.
- Shen H.S., Yang J. and Zhang L., Free and forced vibration of Reissner–Mindlin plates with free edges resting on elastic foundations, *Journal of Sound and Vibration* **244** (2) (2001) 299–320.
- Valasov V.Z. and Leont'ev N.N., Beams, plates and shells on elastic foundations (translated from Russian), *NTIS Accession*, (1966) No. N67–14238.
- Vallabhan C.V.G. and Das Y.C., A refined model for beams on elastic foundations, *International Journal of Solids and Structures* **27** (5) (1991) 629–637.
- Wang C.M., Lim G.T., Reddy J.N. and Lee K.H., Relationships between bending solutions of Reissner and Mindlin plate theories, *Engineering Structures* **23** (7) (2001) 838–849.
- Wang C.M., Reddy J.N. and Lee K.H., *Shear Deformable Beams and Plates*, Elsevier, Oxford, 2000.
- Woo K.S., Hong C.H., Basu P.K. and Seo C.G., Free vibration of skew Mindlin plates by  $p$ -version of F.E.M., *Journal of Sound and Vibration* **268** (4) (2003) 637–656.
- Zhu B. and Leung A.Y.T., Fourier  $p$ -elements for curved beam vibrations, *Thin-walled Structures*, **42** (1) (2004) 39–57.
- Zienkiewicz O.C. and Taylor R.L., *The Finite Element Method*, 4th Edition, McGraw-Hill, New York, 1989.
- Zienkiewicz O.C., De J.P., Gago S.R. and Kelly D.W., The hierarchical concept in finite element analysis, *Computers & Structures* **16** (4) (1983) 53–65.

# 6

## The extended Kantorovich method for vibration analysis of plates

---

M E I S E N B E R G E R and I S H U F R I N,  
Technion – Israel Institute of Technology, Israel

### 6.1 Introduction

Plate elements are used in civil, mechanical, aeronautical and marine structures. The consideration of vibration frequencies and modes for such plates is essential to an efficient and reliable design. Exact solutions for the dynamic characteristics of rectangular plates are available only for a limited number of boundary conditions on the four edges of the plate (Leissa 1973). These include all combinations of plates in which two opposite edges are simply supported, and those with one edge free to slide while the rotation is restrained, and on the opposite side simply supported or sliding. For all other combinations only approximate results are available. In this chapter the solution is obtained using the Kantorovich method. The method uses the sum of the multiplications of functions in one direction by functions in the second direction. Then, one assumes a solution in one direction, and upon substitution of this solution into the partial equation of the plate, an ordinary differential equation is obtained. By solving this equation, the natural frequencies and modes are found. This solution is approximate, and the accuracy is dependent on the assumed solution. In the extended Kantorovich method (Kerr 1969), this solution is a starting point for another cycle, where the derived solution is used as the assumed solution in the second direction, and a solution is sought in the first direction using the same procedure. After repeating this process several times convergence is obtained: the solution is still an approximate solution, but with a very small relative error.

The extended Kantorovich method has been used by several researchers for vibration analysis of rectangular plates. Kerr (1969) and Dalaei and Kerr (1996) used the method to obtain converged values of natural frequencies for rectangular plates. Lee and Kim (1995), Sakata *et al.* (1996), Rajalingham *et al.* (1996, 1997) and Bercin (1996), have all used the extended Kantorovich method for vibration analysis of plates, with different starting assumed functions. Eisenberger and Moyal (2000) used the method for the solution of variable thickness plates, using the exact beam solution as an assumed solution

in the first iteration. Shufrin and Eisenberger (2005, 2006) have extended the solution to thick plates with constant and variable thickness using first- and higher-order shear deformation theories.

In all these studies, only one term was used in the assumed solution. These solutions showed high accuracy compared with results from other approximate numerical methods such as finite difference and finite elements. In this chapter the solution is derived as a multifunction expansion using several terms. The results are more accurate than with one-term expansion as in previous work (Eisenberger and Moyal 2000, Shufrin and Eisenberger 2005, 2006). The contribution of the additional terms is demonstrated in several examples. The objective is to obtain a highly accurate solution for the free vibration frequencies of rectangular plates with several combinations of boundary restraints on the four edges of the plate. The principle of minimum of potential energy is adopted in the derivation of the governing equations of motion and the boundary conditions for the rectangular plate. The results are compared with exact results for the relevant cases, and to approximate results from other numerical methods as have been presented over the years in a large number of studies. In many cases, values of higher accuracy for the upper bound of the frequencies are presented in this chapter.

## 6.2 Vibrations of rectangular plates

### 6.2.1 Basic equations

According to the classical thin plate theory the assumptions for the displacement field are

$$\bar{u}(x, y, z, t) = u(x, y, t) + zw_{,x}(x, y, t) \quad 6.1a$$

$$\bar{v}(x, y, z, t) = v(x, y, t) + zw_{,y}(x, y, t) \quad 6.1b$$

$$\bar{w}(x, y, z, t) = w(x, y, t) \quad 6.1c$$

where  $(\bar{u}, \bar{v}, \bar{w})$  are the displacement components along the  $(x, y, z)$  coordinate directions, respectively,  $u$  and  $v$  are the displacements in the plane and  $w$  is the transverse deflection of a point on the middle plane of the plate. Then, the total energy of the transverse harmonic vibrations of the plate is (Reddy 1999)

$$\Pi = \frac{1}{2} \iint_A D \left[ \begin{aligned} & \left( \frac{\partial^2 w}{\partial x^2} \right)^2 + 2\nu \frac{\partial^2 w}{\partial x^2} \frac{\partial^2 w}{\partial y^2} + \left( \frac{\partial^2 w}{\partial y^2} \right)^2 \\ & + 2(1-\nu) \left( \frac{\partial^2 w}{\partial x \partial y} \right)^2 - \omega^2 \frac{\rho h}{D} w^2 \end{aligned} \right] dx dy \quad 6.2$$

where  $D = Eh^3/12(1 - \nu^2)$  is the bending rigidity of the plate,  $E$  denotes Young's modulus of elasticity,  $h$  is the thickness, and  $\nu$  is Poisson's ratio.

### 6.2.2 The Kantorovich procedure

According to the Kantorovich solution procedure (Kerr 1969), the solution is assumed as

$$w(x, y) = \sum_{i=1}^N X_i(x) Y_i(y) \quad 6.3$$

and  $N$  is the number of functions in the expansion. In the extended Kantorovich method the functions in the  $y$  direction are assumed known. Hence, the substitution of the assumed solution into the energy functional will result in a set of coupled ordinary differential equations after variation, as shown below.

### 6.2.3 Derivation of equations of motion

The substitution of the assumed displacements and their derivatives in the energy function for the plate furnishes:

$$\Pi = \frac{D}{2} \int_0^{L_x} \int_0^{L_y} \left( \begin{array}{l} \{X\}_{,xx}^T \{Y\} \{X\}_{,xx}^T \{Y\} + 2\nu \{X\}_{,xx}^T \{Y\} \{X\}^T \{Y\}_{,yy} \\ + \{X\}^T \{Y\}_{,yy} \{X\}^T \{Y\}_{,yy} + 2(1-\nu) \{X\}_{,x}^T \{Y\}_{,y} \{X\}_{,x}^T \{Y\}_{,y} \\ - \frac{\omega^2 \rho h}{D} \{X\}^T \{Y\} \{X\}^T \{Y\} \end{array} \right) dx dy \quad 6.4$$

or

$$\Pi = \frac{D}{2} \int_0^{L_x} \left( \begin{array}{l} \underbrace{\{X\}_{,xx}^T \{Y\} \{Y\}^T dy}_{[S^{(1)}]} \{X\}_{,xx} + \underbrace{\{X\}_{,xx}^T \int_0^{L_y} 2\nu \{Y\} \{Y\}_{,yy}^T dy}_{[S^{(2)}]} \{X\} \\ \times \underbrace{+ \{X\}^T \int_0^{L_y} \{Y\}_{,yy} \{Y\}_{,yy}^T dy}_{[S^{(3)}]} \{X\} + \underbrace{\{X\}_{,x}^T \int_0^{L_y} 2(1-\nu) \{Y\}_{,y} \{Y\}_{,y}^T dy}_{[S^{(4)}]} \{X\}_{,x} \\ \underbrace{- \frac{\omega^2 \rho h}{D} \{X\}^T \int_0^{L_y} \{Y\} \{Y\}^T dy}_{[\bar{\Omega}^2]} \{X\} \end{array} \right) dx \quad 6.5$$

and integration in the  $y$  direction yields

$$\Pi = \frac{D}{2} \int_0^{L_x} \left( \{X\}_{,xx}^T [S^{(1)}] \{X\}_{,xx} + \{X\}_{,xx}^T [S^{(2)}] \{X\} + \{X\}_x^T [S^{(3)}] \{X\} \right. \\ \left. + \{X\}_{,x}^T [S^{(4)}] \{X\}_x - \bar{\Omega}^2 \{X\}_x^T [S^{(1)}] \{X\} \right) dx \quad 6.6$$

where the coefficients  $S_1$  through  $S_4$  are defined as

$$S_1 = \int_0^{L_y} \{Y\} \{Y\}_y^T dy \quad 6.7$$

$$S_2 = 2\nu \int_0^{L_y} \{Y\} \{Y\}_{,yy}^T dy \quad 6.8$$

$$S_3 = \int_0^{L_y} \{Y\}_{,yy} \{Y\}_{,yy}^T dy \quad 6.9$$

$$S_4 = 2(1 - \nu) \int_0^{L_y} \{Y\}_{,y} \{Y\}_{,y}^T dy \quad 6.10$$

and the frequency factor defined as  $\bar{\Omega}^2 = \omega^2 \rho h/D$ .

According to the principle of minimum energy, the first variation of the function should be equal to zero. Thus,

$$\delta \Pi = \frac{1}{2} \int_0^{L_x} \left( \{\delta X\}_{,xx}^T [S^{(1)}] \{X\}_{,xx} + \{X\}_{,xx}^T [S^{(1)}] \{\delta X\}_{,xx} \right. \\ \left. + \{\delta X\}_{,xx}^T [S^{(2)}] \{X\} + \{X\}_{,xx}^T [S^{(2)}] \{\delta X\} \right. \\ \left. + \{\delta X\}_x^T [S^{(3)}] \{X\} + \{X\}_x^T [S^{(3)}] \{\delta X\} \right. \\ \left. + \{\delta X\}_{,x}^T [S^{(4)}] \{X\}_x + \{X\}_{,x}^T [S^{(4)}] \{\delta X\}_x \right. \\ \left. - \bar{\Omega}^2 \{\delta X\}_x^T [S^{(1)}] \{X\} - \bar{\Omega}^2 \{X\}_x^T [S^{(1)}] \{\delta X\} \right) dx = 0 \quad 6.11$$

and

$$\delta \Pi = \int_0^{L_x} \left( \{X\}_{,xx}^T ([S^{(1)}]^T + [S^{(1)}]) + \{X\}_x^T [S^{(2)}]^T \{\delta X\}_{,xx} \right. \\ \left. + \{X\}_{,x}^T ([S^{(4)}]^T + [S^{(4)}]) \{\delta X\}_x + (\{X\}_{,xx}^T [S^{(2)}] \right. \\ \left. + \{X\}_x^T ([S^{(3)}]^T + [S^{(3)}]) - \bar{\Omega}^2 \{X\}_x^T ([S^{(1)}]^T \right. \\ \left. + [S^{(1)}]) \{\delta X\} \right) dx = 0 \quad 6.12$$

The integration by parts leads to the following system of coupled differential equations:

$$\begin{aligned} & ([S^{(1)}] + [S^{(1)}]^T) \{X\}_{xxxx} + ([S^{(2)}] + [S^{(2)}]^T - [S^{(4)}] - [S^{(4)}]^T) \{X\}_{xx} \\ & + ([S^{(3)}] + [S^{(3)}]^T - \bar{\Omega}^2 ([S^{(1)}] + [S^{(1)}]^T)) \{X\} = 0 \end{aligned} \quad 6.13$$

and the boundary conditions

$$\{M\}|_{x=0} = -(([S^{(1)}] + [S^{(1)}]^T) \{X\}_{xx} + [S^{(2)}] \{X\})|_{x=0} \quad 6.14$$

$$\{M\}|_{x=L_x} = (([S^{(1)}] + [S^{(1)}]^T) \{X\}_{xx} + [S^{(2)}] \{X\})|_{x=L_x} \quad 6.15$$

$$\begin{aligned} \{Q\}|_{x=0} & = (([S^{(1)}] + [S^{(1)}]^T) \{X\}_{xxx} \\ & + ([S^{(2)}] - [S^{(4)}] - [S^{(4)}]^T) \{X\}_{,x})|_{x=0} \end{aligned} \quad 6.16$$

$$\begin{aligned} \{Q\}|_{x=L_x} & = -(([S^{(1)}] + [S^{(1)}]^T) \{X\}_{xxx} \\ & + ([S^{(2)}] - [S^{(4)}] - [S^{(4)}]^T) \{X\}_{,x})|_{x=L_x} \end{aligned} \quad 6.17$$

#### 6.2.4 The solution procedure

The solution will be performed using the exact element method (Eisenberger 1991, 1995). For the solution, we use the following dimensionless coordinates:  $\xi = x/L_x$  and  $\eta = y/L_y$ . So the equation of motion in dimensionless coordinates is

$$\begin{aligned} & ([S^{(1)}] + [S^{(1)}]^T) \{X\}_{,\xi\xi\xi\xi} + ([S^{(2)}] + [S^{(2)}]^T - [S^{(4)}] - [S^{(4)}]^T) \{X\}_{,\xi\xi} L_x^2 \\ & + ([S^{(3)}] + [S^{(3)}]^T - \bar{\Omega}^2 ([S^{(1)}] + [S^{(1)}]^T)) \{X\} L_x^4 = 0 \end{aligned} \quad 6.18$$

Equation (6.18) can be written as

$$[A^{(4)}] \{X\}_{,\xi\xi\xi\xi} + [A^{(2)}] \{X\}_{,\xi\xi} + [A^{(0)}] \{X\} = 0 \quad 6.19$$

with

$$[A^{(4)}] = ([S^{(1)}] + [S^{(1)}]^T) \quad 6.20$$

$$[A^{(2)}] = L_x^2 ([S^{(2)}] + [S^{(2)}]^T - [S^{(4)}] - [S^{(4)}]^T) \quad 6.21$$

$$[A^{(0)}] = L_x^4 ([S^{(3)}] + [S^{(3)}]^T - \bar{\Omega}^2 ([S^{(1)}] + [S^{(1)}]^T)) \quad 6.22$$

Now we assume the solution of the system as  $N$  infinite power series of the following form:

$$\{X\} = \left\{ \sum_{i=0}^{\infty} \bar{x}_i \xi^i \right\} = \sum_{i=0}^{\infty} \{\bar{X}\}_i \xi^i \quad 6.23$$

For the solution we have to find the appropriate coefficients of the polynomials in Eq. (6.23). By calculating all the derivatives and substituting them back into Eq. (6.19), we obtain

$$\begin{aligned} & [A^{(4)}] \sum_{i=0}^{\infty} \{\bar{X}\}_{i+4} (i+1)(i+2)(i+3)(i+4) \xi^i \\ & + [A^{(2)}] \sum_{i=0}^{\infty} \{\bar{X}\}_{i+2} (i+1)(i+2) \xi^i + [A^{(0)}] \sum_{i=0}^{\infty} \{\bar{X}\}_i \xi^i = \{0\} \quad 6.24 \end{aligned}$$

Then, the recurrence formula for calculating the  $\{\bar{X}\}_{i+4}$  terms in Eq. (6.23) as a function of the first four vector terms of the each series can be obtained in the following form (Eisenberger 1991, 1995, Eisenberger and Alexandrov 2003):

$$\begin{aligned} \{\bar{X}\}_{i+4} = & -\frac{1}{(i+1)(i+2)(i+3)(i+4)} \\ & \times [A^{(4)}]^{-1} [[A^{(2)}]\{\bar{X}\}_{i+2} (i+1)(i+2) + [A^{(0)}]\{\bar{X}\}_i] \quad 6.25 \end{aligned}$$

The first four terms should be found using the boundary conditions (Shufrin and Eisenberger 2005, Eisenberger and Alexandrov 2003). The terms of the stiffness matrix are the holding actions at the ends of the strip element due to unit displacement in the desired direction when all other degrees of freedom are restrained. The detailed derivation of the terms in the stiffness matrix is similar to that given in Eisenberger and Alexandrov (2003) and is not repeated here.

The vibration frequencies for the plate are found as the values that cause the determinant of the corresponding stiffness matrix to become zero. Having the stiffness matrix for the natural frequency, the generalized displacements of the vibration mode are found (see Shufrin and Eisenberger 2005).

## 6.3 Numerical examples and discussion

The vibration frequencies of square plates are studied using the proposed method. In all calculations, Poisson's ratio  $\nu$  is taken as 0.3. The natural frequencies are presented in nondimensional form as  $\omega = \Omega \pi^2 D/L_y^2$ . Two types of boundary conditions are investigated: a plate clamped on all four edges, and a completely free plate. These two types of boundary conditions are considered as there are no exact vibration solutions.

### 6.3.1 Clamped plate – CCCC boundary conditions

In Table 6.1, a comparison is made between the results of the extended Kantorovich solution and published results for thin plates with clamped boundary conditions. Results are given for the first ten natural frequencies.

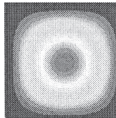
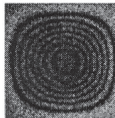
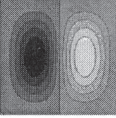
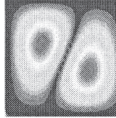
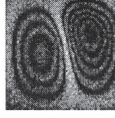
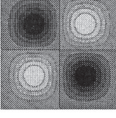
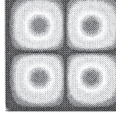
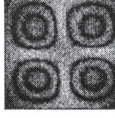
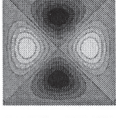
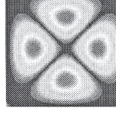
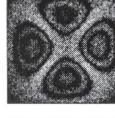
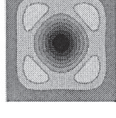
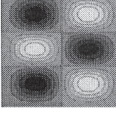
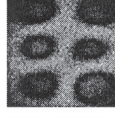
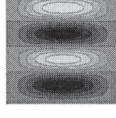
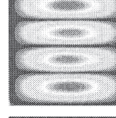
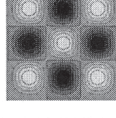
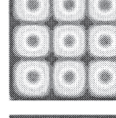
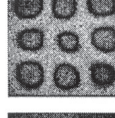
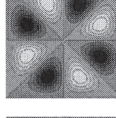
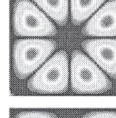
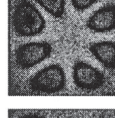
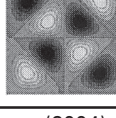
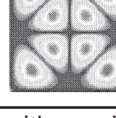
Table 6.1 The first ten normalized natural frequencies of a square CCCC plate

<i>N</i>	1	2	3	4	Best value	Reference
1	35.999	35.986	35.985	35.985	35.984	Rajalingham et al. (1997)
2	73.405	73.394	73.394	73.394	73.394	Leissa (1973)
3	108.236	108.218	108.217	108.217	108.200	Gorman (1984)
4	131.902	131.581	131.581	131.581	131.581	FE-ANSYS
5	131.902	132.215	132.205	132.205	132.205	FE-ANSYS
6	165.023	165.005	165.001	165.000	165.000	Gorman (1984)
7	210.526	210.527	210.522	210.522	210.520	FE-ANSYS
8	220.059	220.037	220.035	220.033	220.039	FE-ANSYS
9	242.667	242.154	242.154	242.154	242.154	FE-ANSYS
10	242.667	243.166	243.146	243.144	243.151	FE-ANSYS

The number of functions in the expansion (*N*) is taken between 1 and 4. In Table 6.2 the mode shapes are given for the calculated frequencies together with the modes that were obtained from a very fine finite element analysis with 10201 degrees of freedom using ANSYS, and results from experiments performed by Ma and Huang (2004). The similarity of the calculated and measured modes is evident. The results for the seventh mode are obtained by adding the mode shape with the same mode rotated by 90° (as the plate is symmetric) as is shown in Table 6.3. From the results in Table 6.1 it can be seen that the convergence of the frequency values is very rapid. Also, with four function expansion the best results are duplicated or exceeded in accuracy.

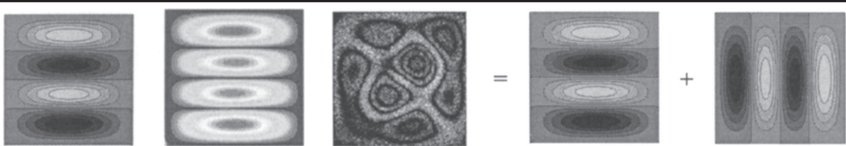
In Tables 6.4–6.8 the composition of the modes from the *N* functions is presented for the first five modes. For each contribution a top view of the plate and a side view are given to represent the mode completely. The improvement in the first mode (Table 6.4) is very small. The contribution of the second function is smaller by three orders of magnitude and the third and fourth functions are four and six orders of magnitude smaller, respectively. The same behavior is seen for the second and third modes. For the fourth and fifth modes a different phenomenon is revealed: using just one term we have a repeated frequency, and the modes are rotated by 90°. For the fourth mode the second function serves to correct this and the sum of the two mode shapes is almost exactly as the experimental and the FE analysis mode shapes. The third and fourth functions have small correcting effect. For the fifth mode the second function adds a shape that is different from that added in the fourth mode. This correction is not as good as in the fourth mode. Then the third function almost completes the generation of the mode by adding as the second function the rotated mode, in negative values with respect to what was added in the fourth mode, and as the third function a relatively small higher oscillating function. The fourth function serves for fine tuning of the frequency and mode. The same also happens for some of

Table 6.2 The first ten normalized modes of a square CCCC plate

Mode number	Present 4 terms	Ansys 10201 DOF	Experimental modes
1			
2			
3			
4			
5			
6			
7			
8			
9			
10			

From Ma and Huang (2004). Reproduced with permission of Elsevier.

Table 6.3 Composition of the seventh mode for CCCC plate



From Ma and Huang (2004). Reproduced with permission of Elsevier.

Table 6.4 Additional terms contribution for the first mode of CCCC plate

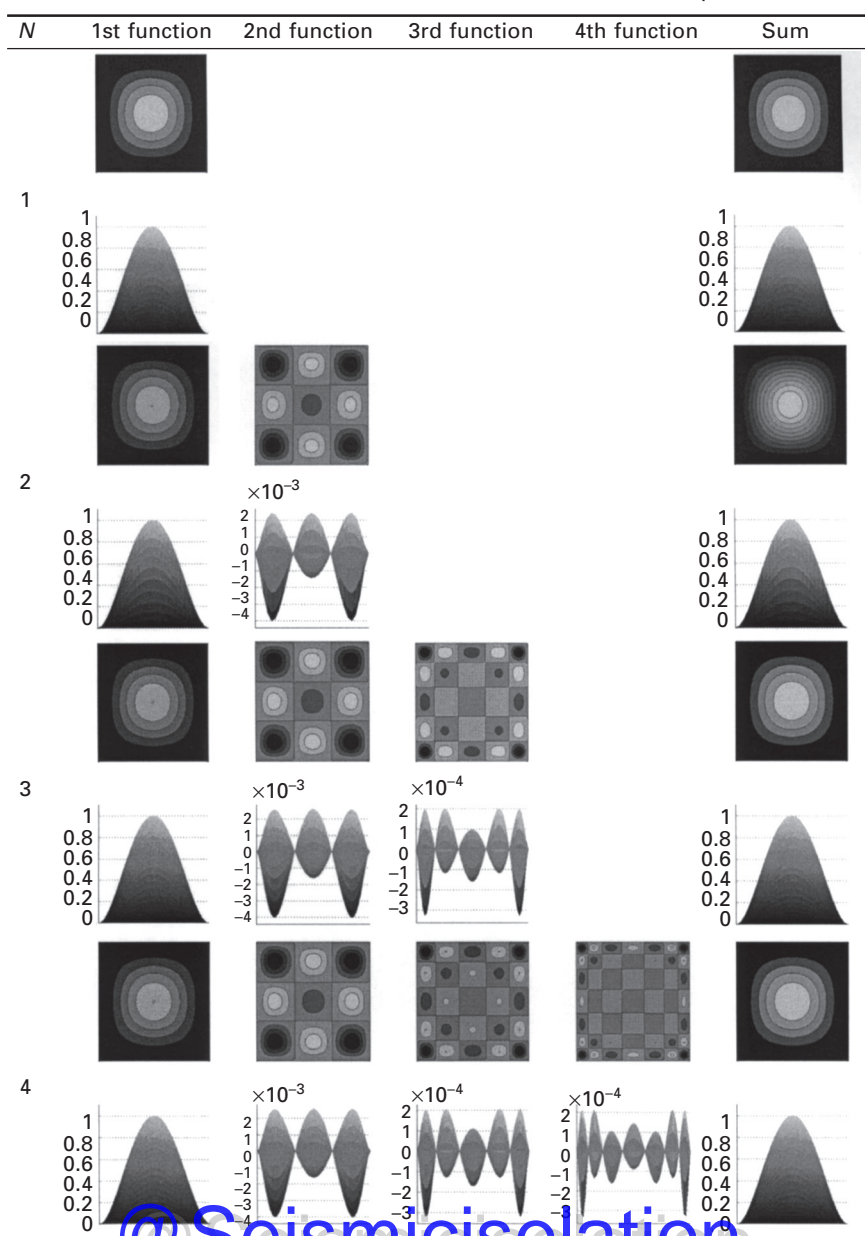


Table 6.5 Additional terms contribution for the second mode of CCCC plate

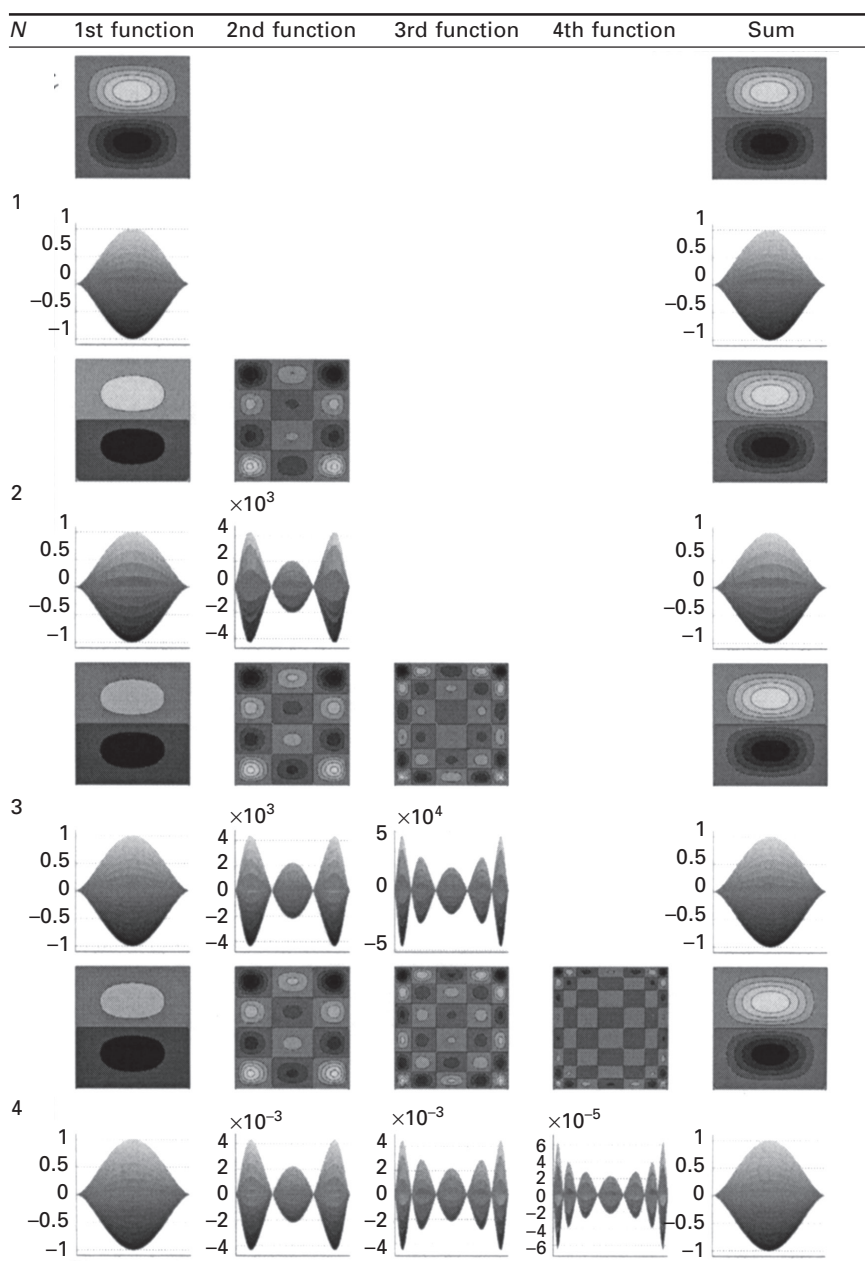


Table 6.6 Additional terms contribution for the third mode of CCCC plate

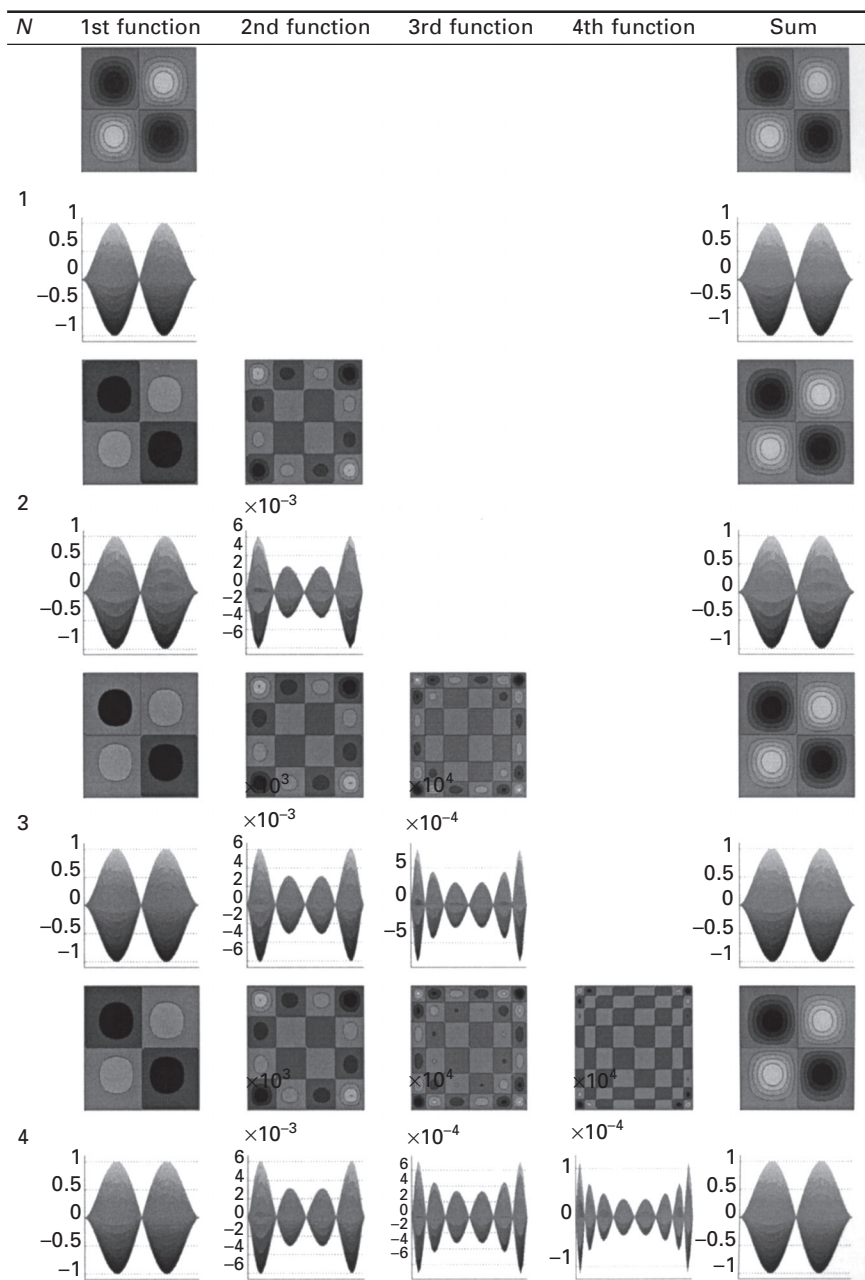


Table 6.7 Additional terms contribution for the fourth mode of CCCC plate

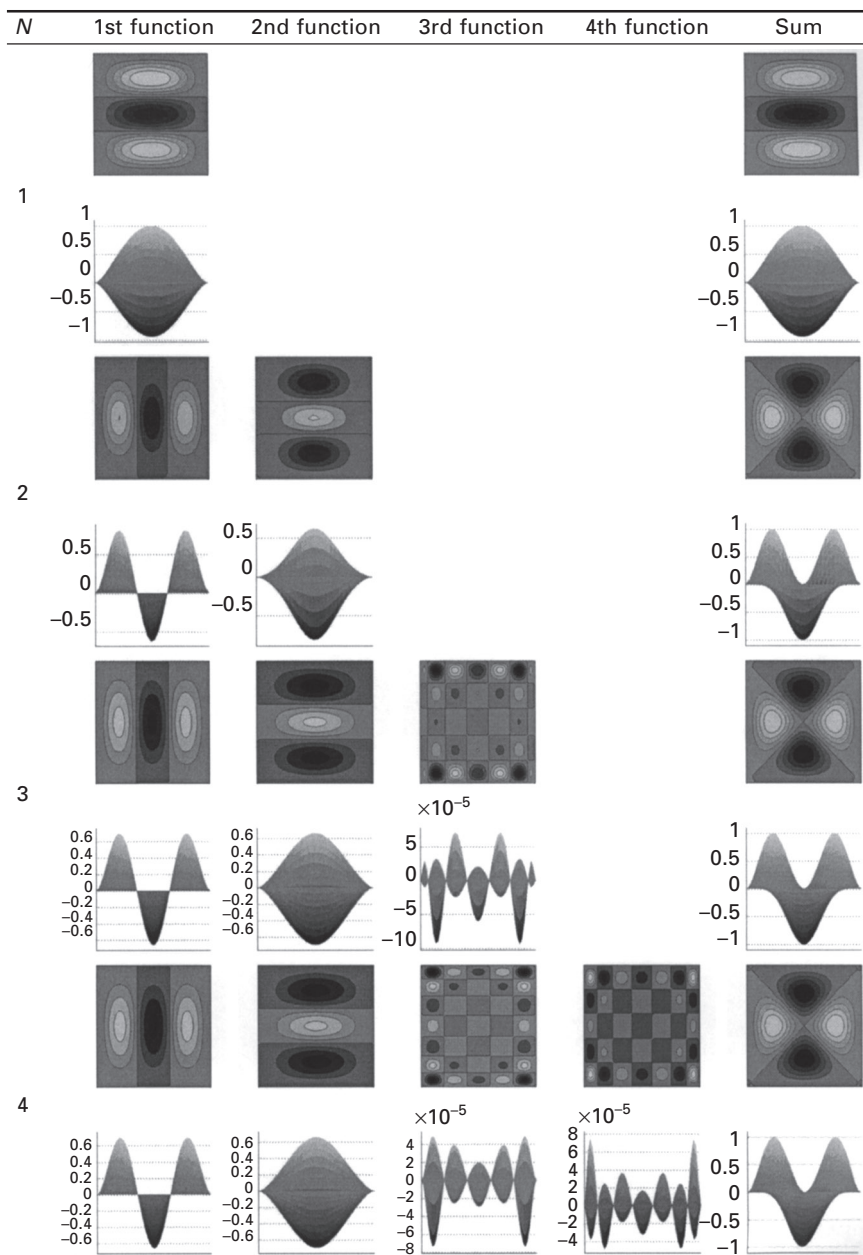
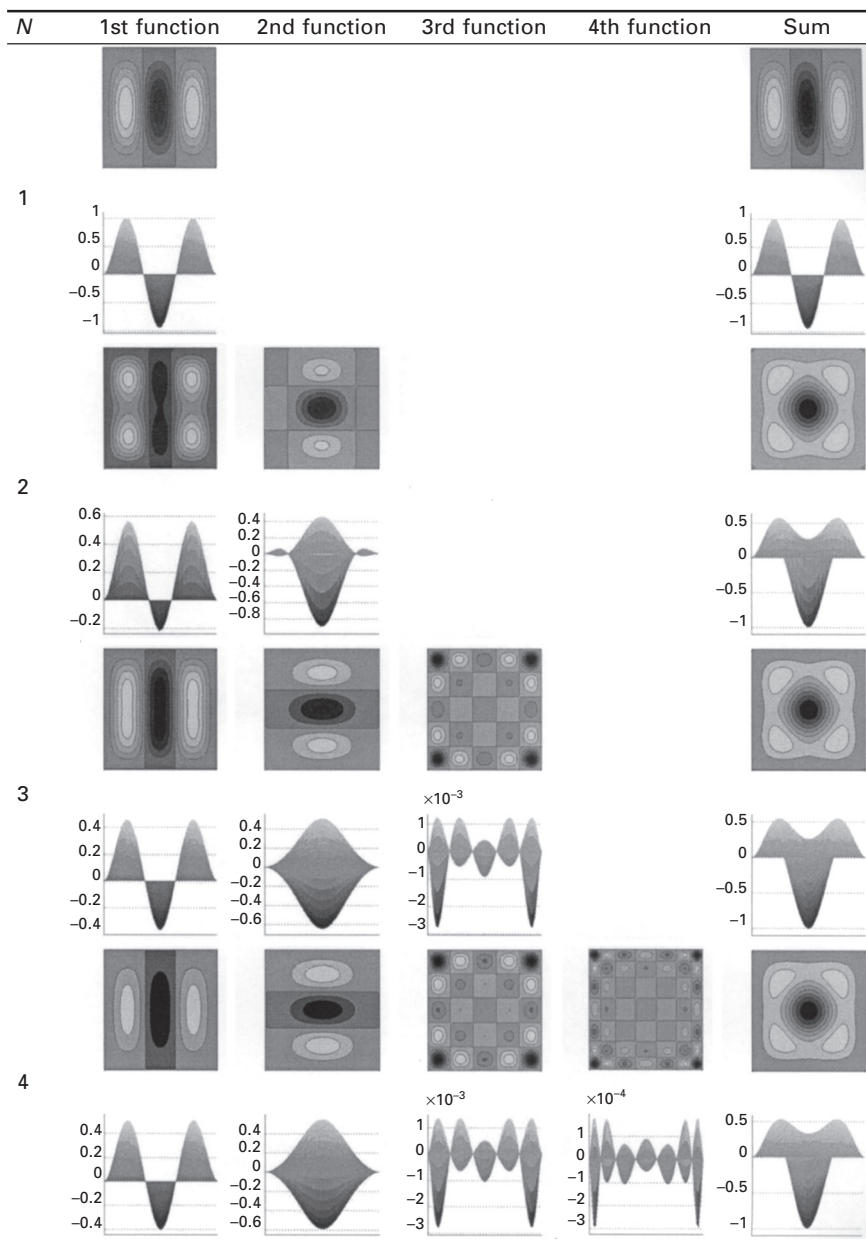


Table 6.8 Additional terms contribution for the fifth mode of CCCC plate



the higher modes for which the single function solution produces repeated frequencies, such as the ninth and tenth frequencies in the CCCC plate.

The distributions of the nondimensional modal bending moment  $\bar{M}_x = M_x L_y / D$  and modal effective shear force  $\bar{V}_x = V_x L_y^2 / D$  in the plate are given in Tables 6.9 and 6.10, and the mid-edge values for the first,

Table 6.9 Variation of the nondimensional modal moments  $\bar{M}_x$  and modal shear  $\bar{V}_x$  in CCCC plate – Modes 1–3

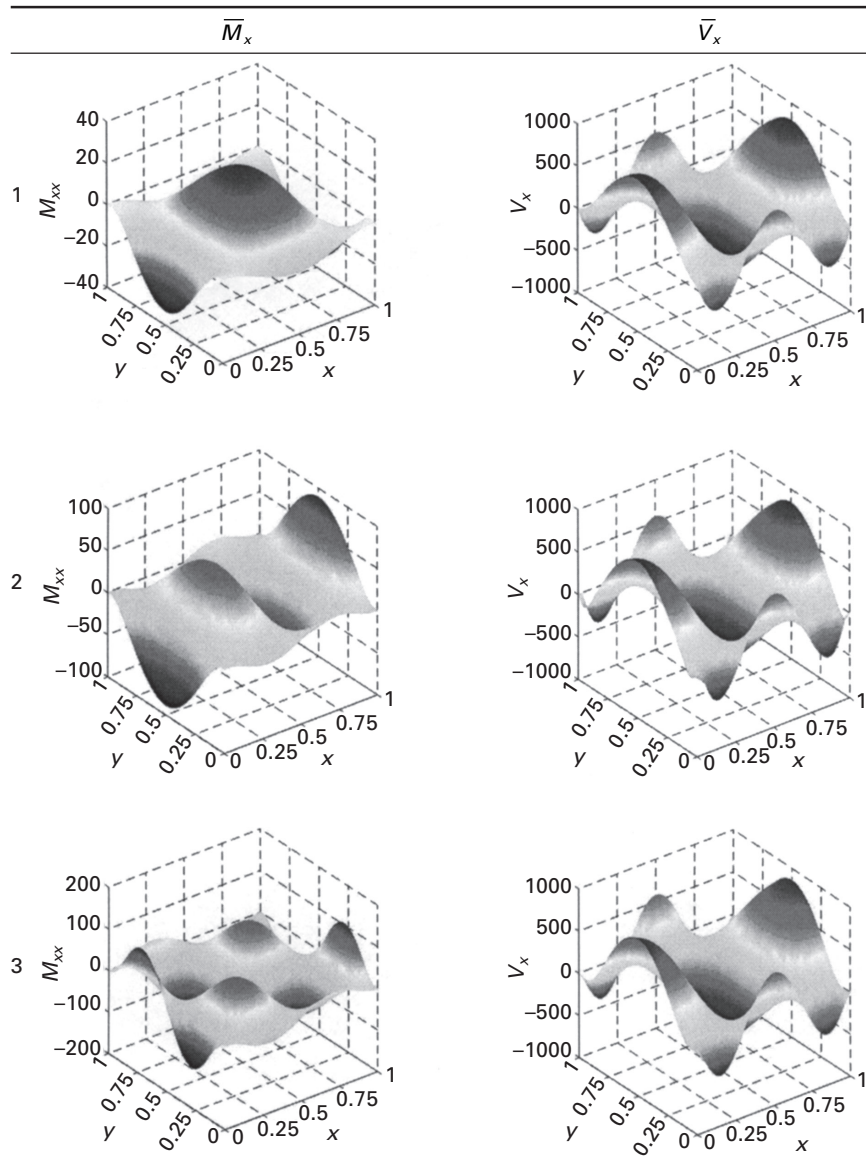
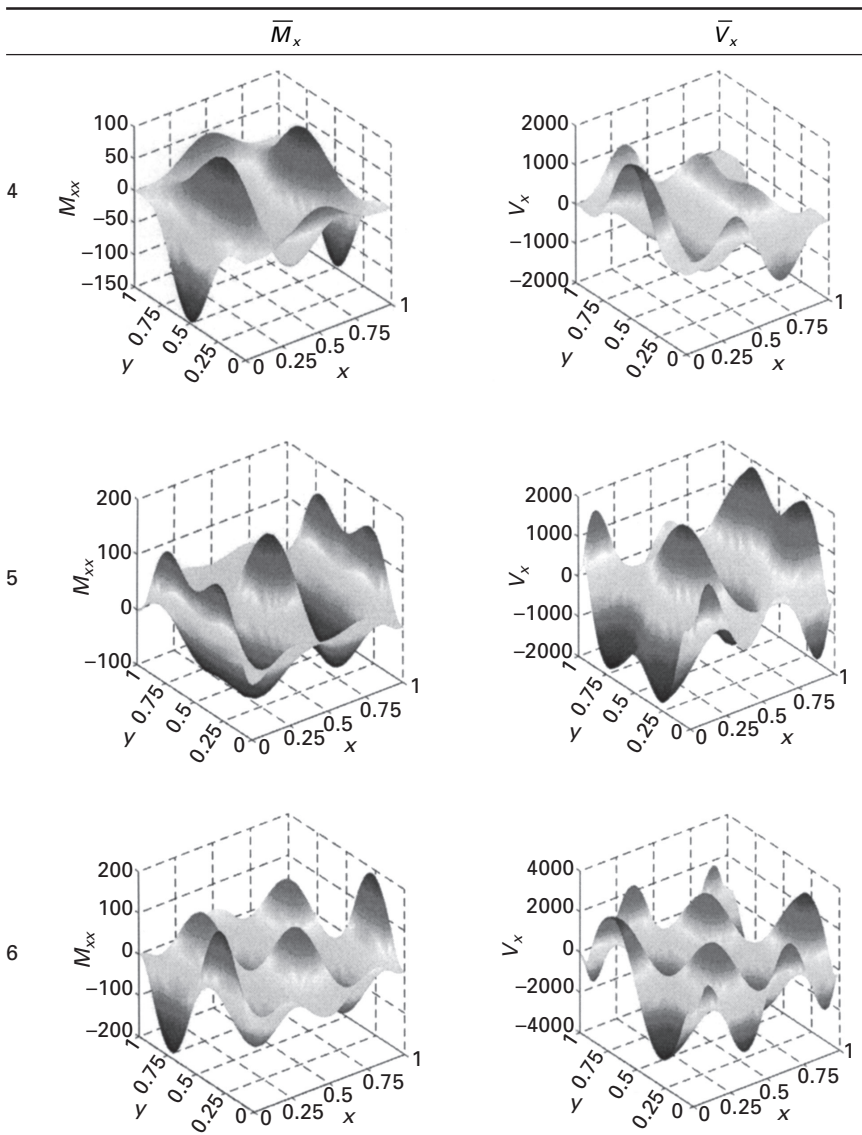


Table 6.10 Variation of the nondimensional modal moments  $\bar{M}_x$  and modal shear  $\bar{V}_x$  in CCCC plate – Modes 4–6



second, fourth, fifth and seventh, modes are given in Tables 6.11 and 6.12. The values of the modal bending moment  $\bar{M}_x$  and modal effective shear  $\bar{V}_x$  for the third and the sixth modes are identically zero as these are antisymmetric modes. The modal stress resultants are normalized by setting  $\bar{W}_{\max} = |W_{\max}/L_y| = 1$ . Note that the stress resultants are given by (Reddy 1999)

Table 6.11 Mid-edge nondimensional modal moments  $\bar{M}_x$  for CCCC plate

$N$	Mode				
	1	2	4	5	7
1	-32.4266	87.4782	-166.9741	-51.3381	-271.6063
2	-33.6081	89.0161	-147.5655	105.2676	-272.7852
3	-33.3285	88.5882	-147.6841	97.0645	-272.6045
4	-33.3833	88.7482	-147.6813	102.6208	-273.0250

Table 6.12 Mid-edge nondimensional modal shear  $\bar{V}_x$  for CCCC plate

$N$	Mode				
	1	2	4	5	7
1	-210.9710	792.9960	-1984.6018	-744.9636	-4029.76
2	-248.6847	852.3010	-1907.4509	1144.1299	-4073.49
3	-231.8182	819.1559	-1915.8974	937.9111	-4039.66
4	-237.3304	834.6731	-1914.3559	1058.5553	-4087.24

$$M_x = -D \left( \frac{\partial^2 W}{\partial x^2} + \nu \frac{\partial^2 W}{\partial y^2} \right) \quad 6.26$$

$$V_x = -D \left[ \frac{\partial}{\partial x} (\nabla^2 W) + (1 - \nu) \frac{\partial^3 W}{\partial x \partial y^2} \right] \quad 6.27$$

It can be seen that as the number of terms in the expansion is increased, the normalized resultants converge.

### 6.3.1 Completely free plate – FFFF boundary conditions

In Table 6.13, a comparison is made between the results of the extended Kantorovich solution and published results for completely free thin plates. Results are given for the first ten natural frequencies. The number of functions in the expansion ( $N$ ) is taken between 1 and 4. In Table 6.14 the mode shapes are given for the calculated frequencies together with the modes that were obtained from a very fine finite element analysis with 10201 degrees of freedom using ANSYS, and results from experiments performed by Ma and Huang (2004). The results for the fourth and ninth modes are obtained by adding the mode shapes which are shown, with the same modes rotated by 90°, as the plate is symmetric, as is shown in Table 6.15. In Tables 6.16–6.20 the composition of the modes from the  $N$  functions is presented, for the first five modes. The same type of behavior as for the clamped plate can be observed for the completely free plate modes.

Table 6.13 The first ten normalized natural frequencies of a square FFFF plate

	1	2	3	4	Best value	
1	13.249	13.166	13.166	13.165	13.156	FE-ANSYS
2	22.277	19.221	19.220	19.220	19.220	FE-ANSYS
3	22.277	24.441	24.424	24.424	24.423	FE-ANSYS
4	34.957	34.244	34.227	34.227	34.203	FE-ANSYS
5	61.329	60.954	60.931	60.930	60.920	Gorman (1984)
6	63.330	63.000	62.779	62.767	62.689	FE-ANSYS
7	73.491	68.122	68.119	68.117	68.072	FE-ANSYS
8	73.491	77.129	76.969	76.968	76.938	FE-ANSYS
9	105.452	104.266	104.193	104.189	104.094	FE-ANSYS
10	120.263	116.609	116.381	116.378	116.396	FE-ANSYS

Table 6.14 The first ten normalized modes of a square FFFF plate

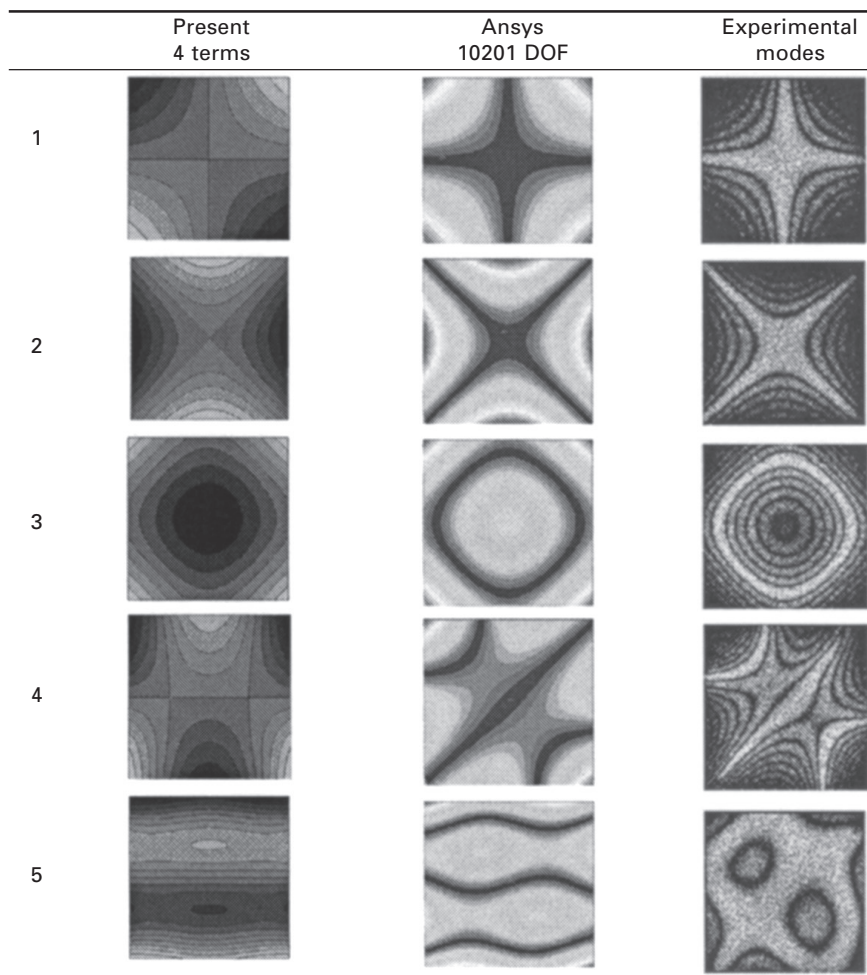
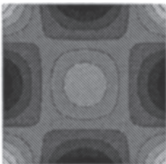
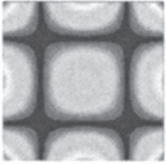
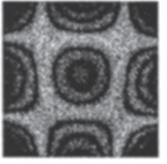
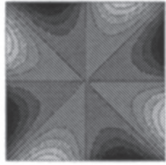
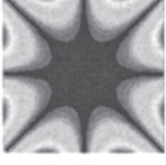
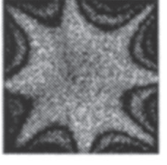
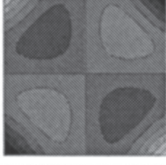
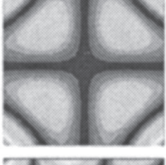
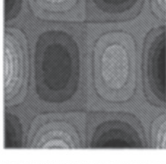
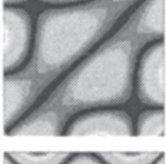
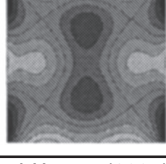
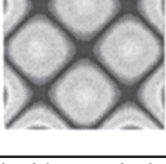
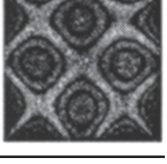
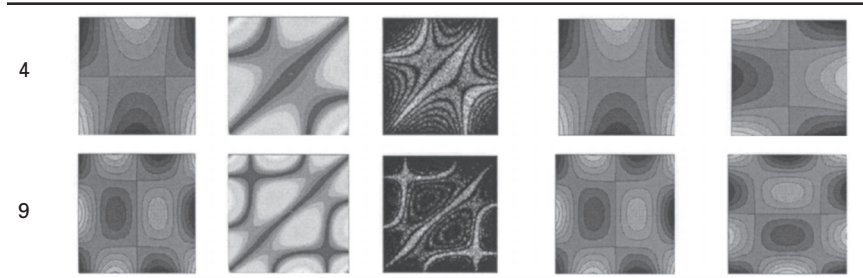


Table 6.14 Continued

	Present 4 terms	Ansys 10201 DOF	Experimental modes
6			
7			
8			
9			
10			

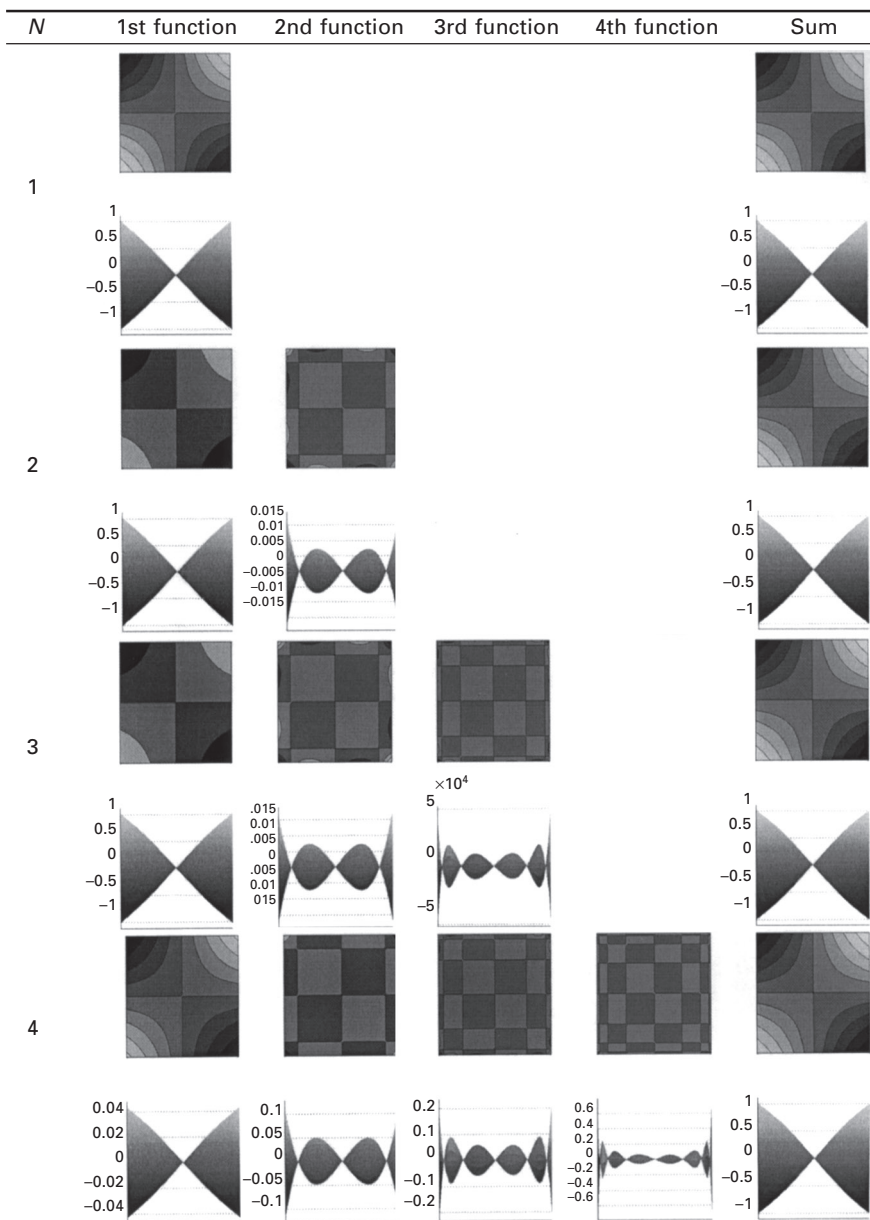
From Ma and Huang (2004). Reproduced with permission of Elsevier.

Table 6.15 Composition of the fourth and ninth modes of FFFF plate



From Ma and Huang (2004). Reproduced with permission of Elsevier.

Table 6.16 Additional terms contribution for the first modes of FFFF plate



The distributions of the nondimensional modal bending moment  $\bar{M}_x$  and modal effective shear force  $\bar{V}_x$  in the plate is given in Tables 6.21 and 6.22, and the mid-edge values for the second, third, fifth and ninth modes are given in Tables 6.23 and 6.24. The values of the modal bending moment  $\bar{M}_x$

Table 6.17 Additional terms contribution for the second mode of FFFF plate

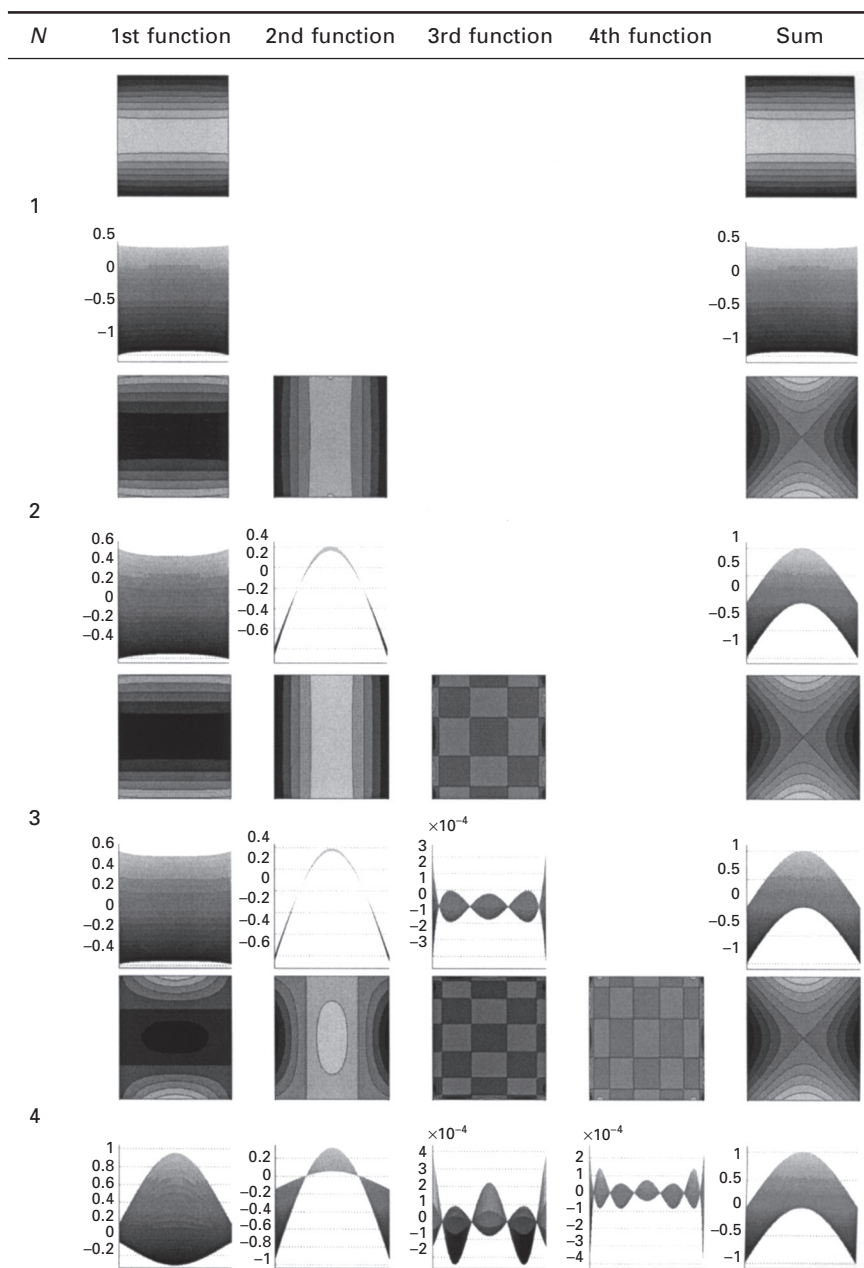


Table 6.18 Additional terms contribution for the third mode of FFFF plate

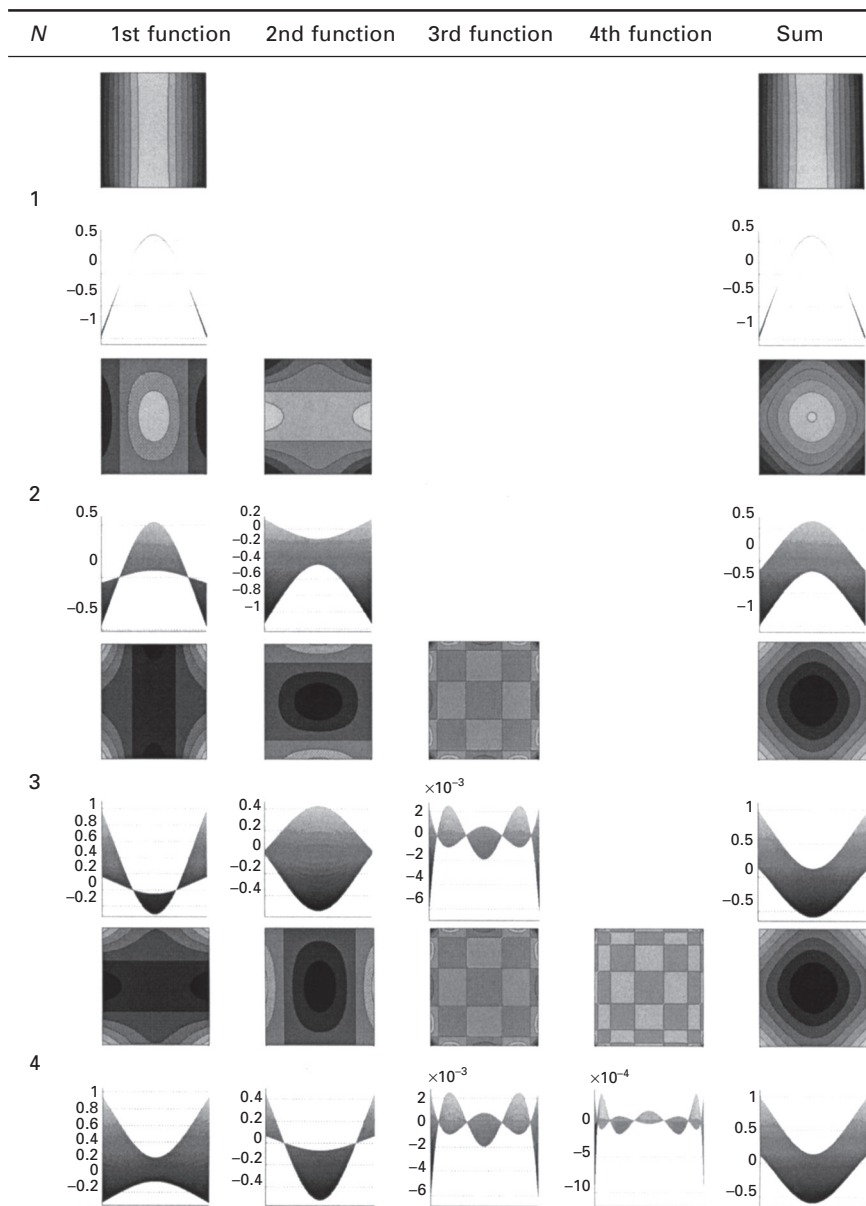


Table 6.19 Additional terms contribution for the fourth mode of FFFF plate

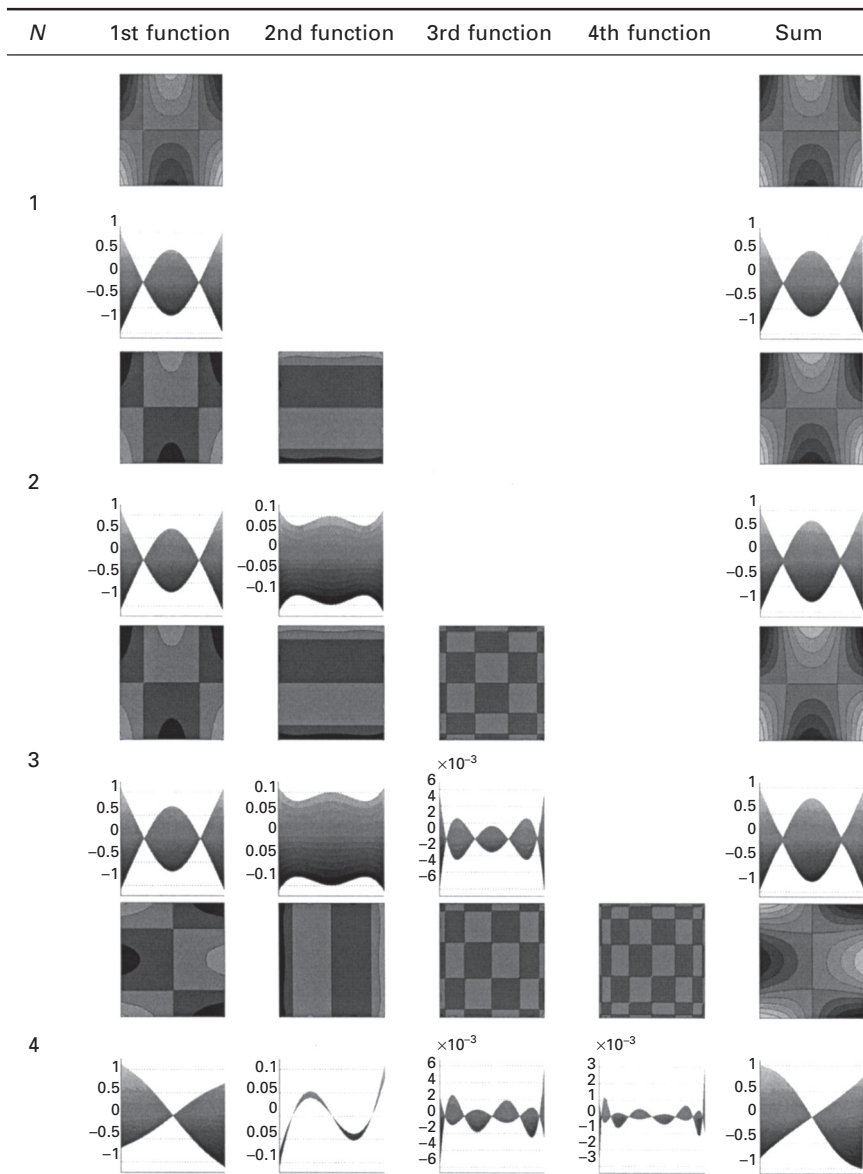


Table 6.20 Additional terms contribution for the fifth mode of FFFF plate

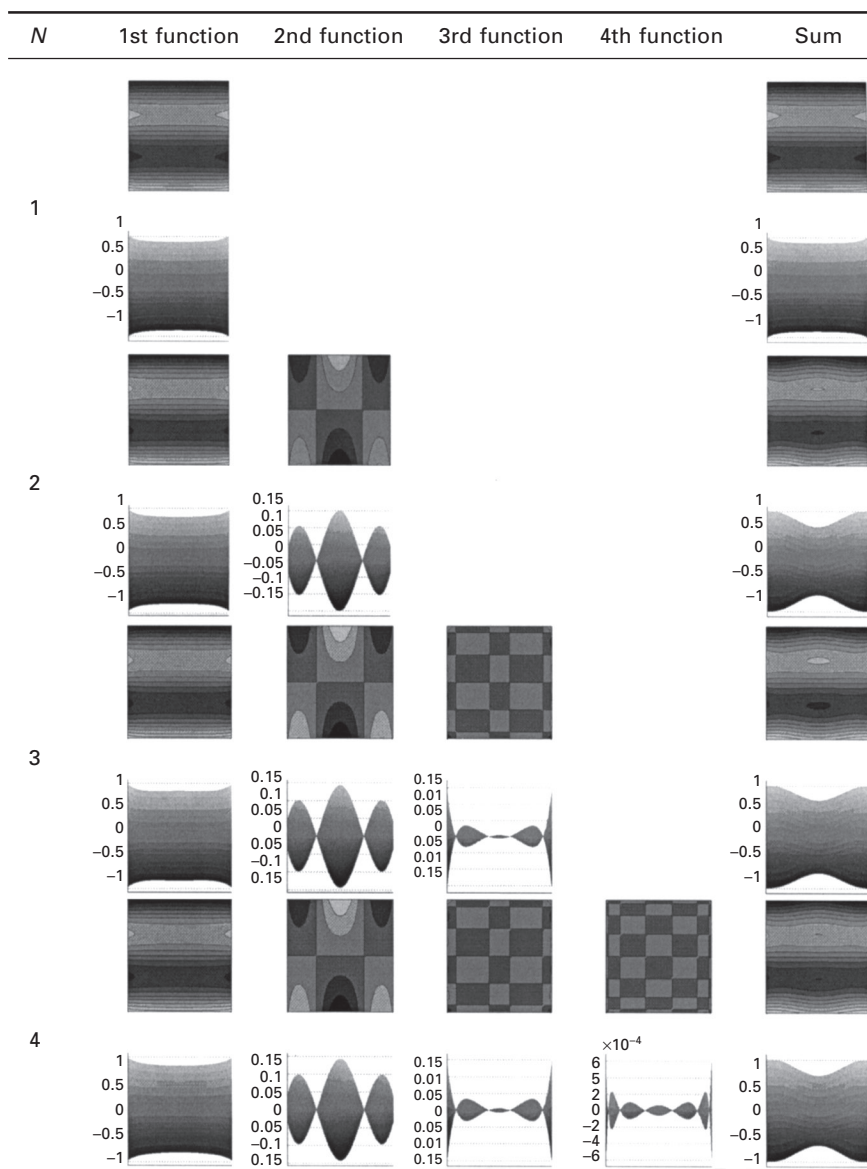
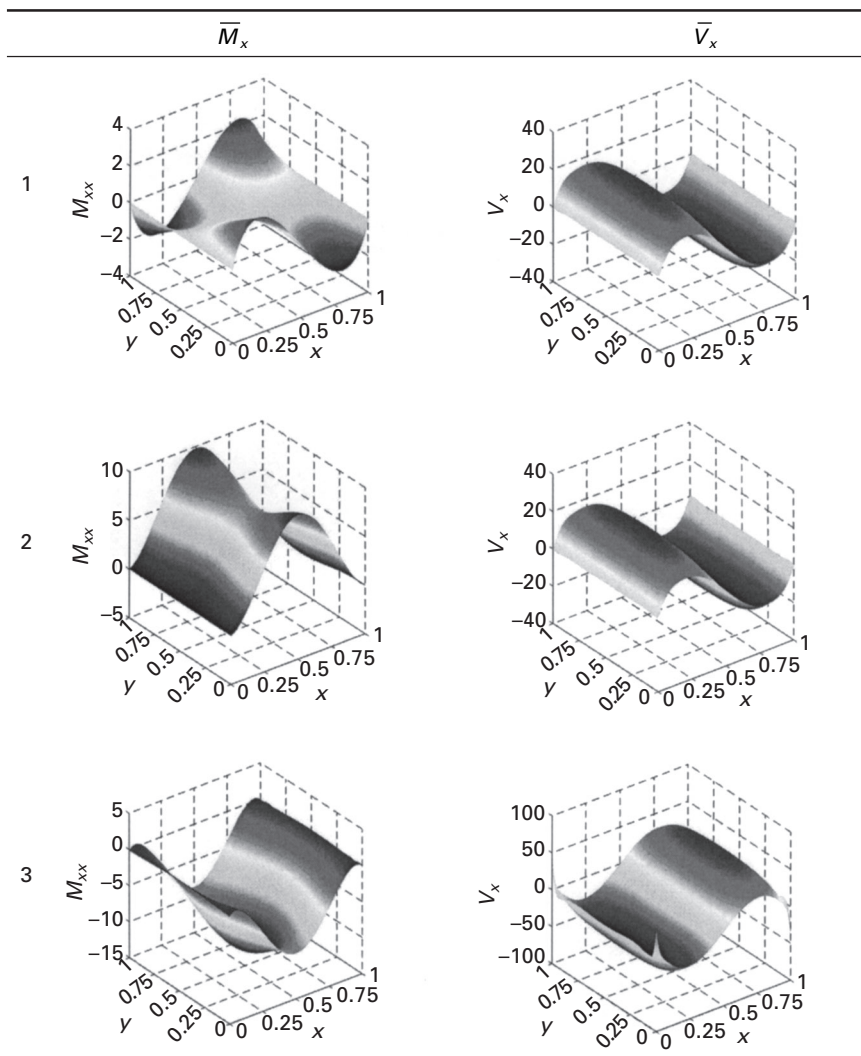


Table 6.21 Variation of the nondimensional modal moments  $\bar{M}_x$  and modal shear  $\bar{V}_x$  in FFFF plate – Modes 1–3

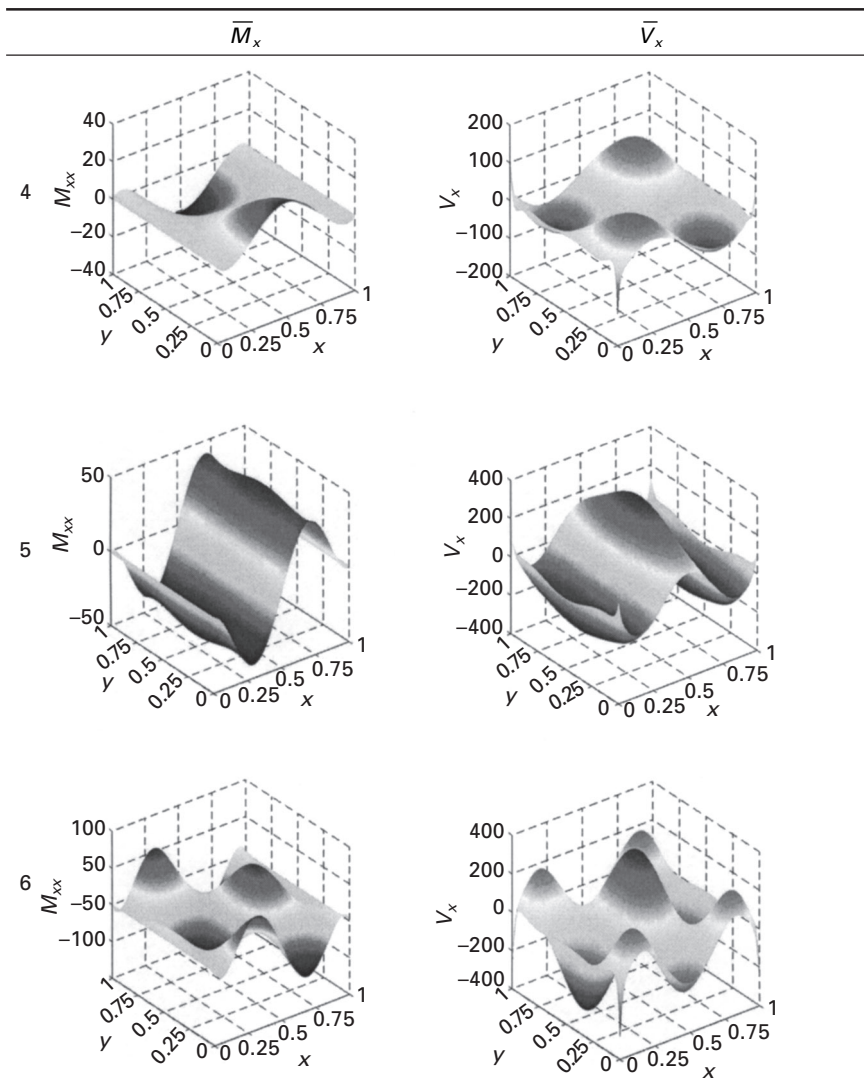


and modal effective shear  $\bar{V}_x$  for the first and the fourth modes are identically zero as these are antisymmetric modes.

## 6.4 Conclusions

The equations of motion for thin rectangular plates were derived. Using the extended Kantorovich method the equations were reduced to a set of ordinary differential equations. This method yields exact solution for several cases of

Table 6.22 Variation of the nondimensional modal moments  $\bar{M}_x$  and modal shear  $\bar{V}_x$  in FFFF plate – Modes 4, 5, 9



boundary conditions and highly accurate results for other cases. The results for the CCCC and FFFF plates were presented in detail. From these one can draw the following conclusions:

- The solution using only one function has relatively large errors.
- It is observed that the three function expansion gave almost complete convergence. In this chapter, four functions were used in the solution process to ensure correct modes.

Table 6.23 Nondimensional modal moments  $\bar{M}_x$  for FFFF plate

$\bar{M}_x$ – mid-edge: mode				
<i>N</i>	2	3	5	9
1	-0.3706	0.3704	-0.6103	-3.6184
2	-0.1254	-0.3132	0.0305	-0.3729
3	-0.0002	0.2660	-0.0383	0.0768
4	-0.0067	0.0781	-0.6677	-0.0722

$\bar{M}_x$ – corner: mode				
	1	2	3	
	4			
1	0.7125	1.3824	-1.3826	2.1827
2	0.0971	-0.3320	-1.1653	0.5323
3	0.0464	0.2012	-0.1799	0.1666
4	0.0306	0.0051	0.0356	0.2044

Table 6.24 Nondimensional modal shear  $\bar{V}_x$  for FFFF plate

$\bar{V}_x$ – mid-edge: mode				
<i>N</i>	2	3	5	9
1	-0.0138	0.0132	-1.4024	28.5479
2	0.3643	9.9280	10.6041	-50.7820
3	2.4728	4.0531	3.1737	-15.8075
4	-0.0223	1.9665	-32.3553	9.4381

$\bar{V}_x$ – corner: mode				
	1	2	3	
	4			
1	28.6697	46.1868	-46.1873	101.4821
2	24.8767	2.1352	-56.8484	106.8348
3	32.2002	24.8452	-17.8322	90.3651
4	42.0345	0.0176	-40.4438	123.7121

- The values of frequency that were obtained are lower than the reference values and they are closer to the exact results, as these are upper bounds to the exact result.
- The convergence of the nondimensional modal bending moment  $\bar{M}_x$  and modal effective shear force  $\bar{V}_x$  in the plate is fast. As expected, for the FFFF plate the convergence of the nondimensional modal bending moment  $\bar{M}_x$  to zero on the free edges is almost satisfied, but the convergence of the modal effective shear forces  $\bar{V}_x$ , which involves a higher-order derivative, is slower.

## 6.5 References

- Bercin, A.N. (1996). Free vibration solution for clamped orthotropic plates using the Kantorovich method. *Journal of Sound and Vibration*, **196** (2), 243–247.
- Dalaei, M. and Kerr, A.D. (1996). Natural vibration analysis of clamped rectangular orthotropic plates. *Journal of Sound and Vibration*, **189** (3), 399–406.
- Eisenberger, M. (1991). Buckling loads for variable cross-section members with variable axial forces. *International Journal of Solids and Structures*, **27**(2), 135–143.
- Eisenberger, M. (1995). Dynamic stiffness matrix for variable cross-section Timoshenko beams, *Communications in Numerical Methods in Engineering*, **11**, 507–513.
- Eisenberger, M. and Alexandrov, A. (2003). Buckling loads of variable thickness thin isotropic plates, *Thin-Walled Structures*, **41**(9), 871–889.
- Eisenberger, M. and Moyal, H. (2000). Vibration frequencies of variable thickness plates. *Proc. Advances in Structural Dynamics 2000*, Hong Kong, China, 645–650, Vol. 1.
- Gorman, D.J. (1984). An exact analytical approach to the free vibration analysis of rectangular plates with mixed boundary conditions. *Journal of Sound and Vibration*, **93**, 235–247.
- Kerr, A.D. (1969). An extended Kantorovich method for the solution of eigenvalue problem. *International Journal of Solids and Structures*, **15**, 559–572.
- Lee, J.M. and Kim, K.C. (1995). Vibration analysis of rectangular isotropic thick plates using Mindlin plate characteristic functions. *Journal of Sound and Vibration*, **187** (5), 865–877.
- Leissa, A.W. (1973). The free vibrations of rectangular plates. *Journal of Sound and Vibration*, **31**, 257–293.
- Ma, C.C. and Huang, C.H. (2004). Experimental whole-field interferometry for transverse vibration of plates. *Journal of Sound and Vibration*, **271** (3–5), 493–506.
- Rajalingham, C., Bhat, R.B. and Xistris, G.D. (1996). Closed form approximations of vibration modes of rectangular cantilever plates by the variational reduction method. *Journal of Sound and Vibration*, **197** (3), 263–281.
- Rajalingham, C., Bhat, R.B. and Xistris, G.D. (1997). Vibration of rectangular plates by reduction of the plate partial differential equation into simultaneous ordinary differential equations. *Journal of Sound and Vibration*, **203** (1), 169–180.
- Reddy, J.N. (1999). *Theory and Analysis of Elastic Plates*. Taylor & Francis, Philadelphia, PA.
- Sakata, T., Takahashi, K. and Bhat, R.B. (1996). Natural frequencies of orthotropic rectangular plates obtained by iterative reduction of the partial differential equation. *Journal of Sound and Vibration*, **189** (1), 89–101.
- Shufrin, I. and Eisenberger, M. (2005). Stability and vibration of shear deformable plates – first order and higher order analyses. *International Journal of Solid and Structures*, **42** (3–4), 1225–1251.
- Shufrin, I. and Eisenberger, M. (2006). Vibration of shear deformable plates with variable thickness – first order and higher order analyses. *Journal of Sound and Vibration*, **290** (1–2), 465–489.

# A closed-form approach to modeling and dynamic analysis of beams, plates and shell

B Y A N G, University of Southern California, USA

## 7.1 Introduction

Dynamics and vibration of plates and shells play an important role in design and development of many structures, machines and devices in aerospace, civil, mechanical, and marine engineering (Timoshenko, 1940; Flügge, 1957; Leissa, 1973; Donnell, 1976; Soedel, 1993), and thus have been extensively studied for years. The finite element method (FEM), because of its versatility in describing complex geometric and physical properties, is most commonly used in modeling and analysis of plates and shells (Kardestuncer and Norrie, 1987; Zienkiewicz and Taylor, 1989). The utility of the FEM, however, is computationally intensive, demands large computer memory and CPU time, and sometimes becomes unrealizable when real time computations are required, as in the case of active vibration and noise control of flexible structures.

Analytical solutions for plates and shells, on the other hand, are desirable because they provide more physical insight, and are more accurate and efficient than numerical methods in computation. Unfortunately, exact analytical solutions are limited to a few simple cases. So, approximate methods using series of continuous functions have been developed, which include Ritz method, Galerkin method, Fourier series, eigenfunction expansion (Meirovitch, 1980), and the finite strip method (Cheung, 1976). Series solution methods have been shown to require less computational effort than the FEM, and to be able to deliver accurate results in many cases studied. Nonetheless, these methods in general are problem-dependent, lack the capability of modeling multi-body structures, and need a large number of continuous functions in a series to describe the effects of concentrated loads and abrupt changes in geometric and material properties.

In this chapter, a semi-analytical method, namely the distributed transfer function method (DTFM), is presented for dynamic analysis of plates and shells. The word ‘semi-analytical’ is used because the DTFM delivers exact closed-form analytical solutions at least in one coordinate direction. The thrust of the method is that it is capable of modeling multi-body regions like

the FEM, and at the same time maintains high accuracy and efficiency of analytical solutions. As shall be seen, the method is convenient in predicting dynamic response of plates and shells with complex shapes and abrupt changes in properties.

The remainder of the chapter is organized as follows. The basic concepts of the DTFM for dynamic analysis of one-dimensional continua is given in Section 7.2. The DTFM-based analysis is extended to multidimensional continua in Section 7.3. The application of the DTFM in free vibration analysis of plates and shells is presented to demonstrate the advantages of the DTFM through numerical examples in Section 7.4.

## 7.2 DTFM for one-dimensional continua

The DTFM was originally developed for modeling, analysis, and control of one-dimensional distributed dynamic systems, including axially moving strings and beams, constrained and combined structures, and flexible rotors (Yang and Mote, 1991; Yang, 1992, 1994, 1995; Yang and Tan, 1992; Fang and Yang, 1998). The distributed transfer function of a flexible system is the Laplace transform of the Green's function of the system (Butkoviskiy, 1983). The DTFM is able to yield closed-form analytical solutions for a variety of static and dynamic problems of structures and flexible mechanical systems (Yang, 2005). In this section, the basic concepts of the DTFM for one-dimensional continua are presented, to prepare the reader for modeling and dynamic analysis of plate and shell structures in the subsequent sections.

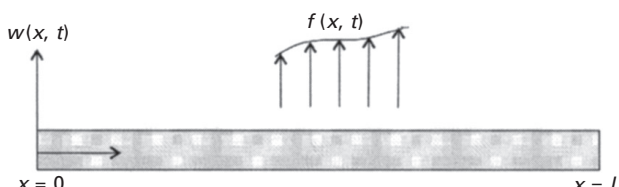
### 7.2.1 Spatial state formulation

Consider a uniform one-dimensional continuum as shown in Fig. 7.1. The generalized displacement  $w(x, t)$  of the continuum is governed by the partial differential equation

$$\sum_{k=0}^n \left( a_k \frac{\partial^2}{\partial t^2} + b_k \frac{\partial}{\partial t} + c_k \right) \frac{\partial^k}{\partial x^k} w(x, t) = f(x, t) \quad 0 \leq x \leq L \quad 7.1$$

that is subject to the boundary conditions

$$M_j w(x, t)|_{x=0} + N_j w(x, t)|_{x=L} = \gamma_{Bj}(t), \quad j = 1, 2, \dots, n \quad 7.2$$



7.1 One-dimensional continuum.

and the initial conditions

$$w(x, t)|_{t=0} = u_0(x), \frac{\partial}{\partial t} w(x, t)|_{t=0} = v_0(x) \quad 7.3$$

Here  $L$  is the length of the continuum;  $f(x, t)$  is a generalized force;  $a_k$ ,  $b_k$ , and  $c_k$  describe the spatial distributions of system parameters, such as inertia, damping, gyroscopic forces, stiffness, and axial loading;  $M_j$  and  $N_j$  are differential operators;  $\gamma_{Bj}(t)$  are the boundary disturbances; and  $u_0(x)$  and  $v_0(x)$  are the initial displacement and velocity of the continuum. Equations (7.1) to (7.3) are a mathematical model of one-dimensional flexible systems such as beams, bars, beam-columns, curved beams, beams with viscoelastic layers and elastic foundation, strings, flexible rotating shafts, pipes conveying fluids, and axially moving belts.

In the DTFM, Laplace transform of the governing equation (7.1) with respect to time  $t$  is first performed, which yields

$$\frac{\partial^n}{\partial x^n} \bar{w}(x, s) = \sum_{k=0}^{n-1} d_k(s) \frac{\partial^k}{\partial x^k} \bar{w}(x, s) + \bar{f}(x, s) + \bar{f}_1(x, s), \quad 0 \leq x \leq L \quad 7.4$$

$$\text{with } d_k(s) = -\frac{a_k s^2 + b_k s + c_k}{a_n s^2 + b_n s + c_n}, \quad k = 0, 1, \dots, n-1$$

where the over-bar stands for Laplace transformation with  $s$  being the complex Laplace transform parameter, and  $\bar{f}_1(x, s)$  represents the terms related to the initial conditions (7.3). Also, Laplace transform of the boundary conditions (7.2) gives

$$\begin{aligned} & \bar{M}_j \bar{w}(x, s)|_{x=0} + \bar{N}_j w(x, s)|_{x=L} \\ &= \bar{\gamma}_{Bj}(s) + \bar{\gamma}_{Ij}(s) \equiv \gamma_j(s), \quad j = 1, 2, \dots, n \end{aligned} \quad 7.5$$

where  $\bar{M}_j$  and  $\bar{N}_j$  are operators  $M_j$  and  $N_j$  with  $\partial/\partial t$  contained in them replaced by  $s$ , and  $\bar{\gamma}_{Ij}(s)$  represents the initial disturbances at the boundaries.

Now, define a spatial state vector as follows

$$\eta(x, s) = \left( \bar{w}(x, s) \quad \frac{\partial}{\partial x} \bar{w}(x, s) \quad \dots \quad \frac{\partial^{n-1}}{\partial x^{n-1}} \bar{w}(x, s) \right)^T \quad 7.6$$

Equation (7.4) can be written in the first-order different equation in  $\eta(x, s)$

$$\frac{\partial}{\partial x} \eta(x, s) = F(s) \eta(x, s) + q(x, s), \quad 0 \leq x \leq L \quad 7.7$$

and Eq. (7.5) can be cast into

$$M_b(s) \eta(0, s) + N_b(s) \eta(L, s) = \gamma(s) \quad 7.8$$

where

$$F(s) = \begin{bmatrix} 0 & 1 & & & \\ & 0 & 1 & & \\ & & \ddots & \ddots & \\ & & & 0 & 1 \\ d_0(s) & d_1(s) & \dots & \dots & d_{n-1}(s) \end{bmatrix}$$

$$q(x, s) = \frac{\bar{f}(x, s) + \bar{f}_I(x, s)}{a_n s^2 + b_n s + c_n} \begin{pmatrix} 0 \\ \vdots \\ 0 \\ 1 \end{pmatrix}, \gamma(s) = \begin{pmatrix} \gamma_1(s) \\ \gamma_2(s) \\ \vdots \\ \gamma_n(s) \end{pmatrix}$$

$M_b(s)$  and  $N_b(s)$  are  $n \times n$  matrices composed of the coefficients of the operators  $\bar{M}_j$  and  $\bar{N}_j$ . Hence, the original dynamic problem of the continuum governed by Eqs. (7.1) to (7.3) is converted to an equivalent one described by the state equation (7.7) with the boundary conditions (7.8).

As an example consider an axially compressed Euler–Bernoulli beam (beam-column), whose transverse displacement  $z(x, t)$  is governed by

$$\rho \frac{\partial^2}{\partial t^2} z(x, t) + P \frac{\partial^2}{\partial x^2} z(x, t) + EI \frac{\partial^4}{\partial x^4} z(x, t) = f(x, t), \quad 0 \leq x \leq L \quad 7.9$$

where  $\rho$  and  $EI$  are the linear density (mass per unit length) and bending stiffness of the beam, and  $P$  is the axial load. Equation (7.9) is cast into spatial state equation (7.7) with

$$\eta(x, s) = \begin{pmatrix} \bar{z}(x, s) \\ \bar{z}'(x, s) \\ \bar{z}''(x, s) \\ \bar{z}'''(x, s) \end{pmatrix}, F(s) = \begin{bmatrix} 0 & 1 & 0 & 0 \\ 0 & 0 & 1 & 0 \\ 0 & 0 & 0 & 1 \\ -\frac{\rho s^2}{EI} & 0 & -\frac{P}{EI} & 0 \end{bmatrix}$$

where  $\bar{z}'(x, s) = \partial \bar{z}(x, s) / \partial x$ . Furthermore, if the beam has clamped-hinged boundary conditions, namely,

$$z(0, t) = 0, \quad \frac{\partial}{\partial x} z(0, t) = 0$$

$$z(L, t) = 0, \quad EI \frac{\partial^2}{\partial x^2} z(L, t) = 0$$

the matrices in Eq. (7.8) are

$$M_b(s) = \begin{bmatrix} 1 & 0 & 0 & 0 \\ 0 & 1 & 0 & 0 \\ 0 & 0 & 0 & 0 \\ 0 & 0 & 0 & 0 \end{bmatrix}, N_b(s) = \begin{bmatrix} 0 & 0 & 0 & 0 \\ 0 & 0 & 0 & 0 \\ 1 & 0 & 0 & 0 \\ 0 & 0 & EI & 0 \end{bmatrix}$$

### 7.2.2 Eigenvalue solutions

The spatial state formulation described in the previous section is conveniently applied to eigenvalue problems of one-dimensional continua. To this end, drop the external and boundary disturbances from Eqs. (7.7) and (7.8) to obtain

$$\frac{\partial}{\partial x} \eta(x, s) = F(s) \eta(x, s), \quad 0 \leq x \leq L \quad 7.10a$$

$$M_b(s) \eta(0, s) + N_b(s) \eta(L, s) = 0 \quad 7.10b$$

The solution of Eq. (7.10a) is of the form

$$\eta(x, s) = e^{F(s)x} \eta(0, s), \quad 0 \leq x \leq L \quad 7.11$$

where  $e^{F(s)x}$  is the exponential of matrix  $F(s)x$ . Substitute Eq. (7.11) into Eq. (7.10b) to obtain the homogeneous equation

$$[M_b(s) + N_b(s) e^{F(s)L}] \eta(0, s) = 0 \quad 7.12$$

The eigenvalues of the continuum are the roots of the characteristic equation

$$\det[M_b(s) + N_b(s) e^{F(s)L}] = 0 \quad 7.13$$

Equation (7.12) offers exact eigensolutions in a compact form. If the eigenvalue problem is for free vibration of an undamped flexible system, the roots of Eq. (7.13) are  $s = j\omega_k$ ,  $j = \sqrt{-1}$ ,  $k = 1, 2, \dots$ , where  $\omega_k$  is the  $k$ th natural frequency of the continuum. The mode shape corresponding to  $\omega_k$  can be obtained by solving Eq. (7.12) for a nonzero  $\eta(0, s)$  at  $s = j\omega_k$  and substituting the result into Eq. (7.11). If the eigenvalue problem is for buckling of a flexible system,  $s = 0$  and the roots of the characteristic equation (7.13) are the buckling loads of the system (Yang, 2005).

Another advantage of Eq. (7.12) is that eigensolutions are obtained in a systematic and symbolic manner. Description of various systems (strings, beams, bars, etc.) only requires simple assignment of matrices  $F(s)$ ,  $M_b(s)$ , and  $N_b(s)$ . Unlike a conventional boundary value approach, the spatial space formulation here avoids tedious derivations of different eigen-frequency equations for different boundary conditions, and explicitly expresses eigenfunctions by an exponential matrix as shown in Eq. (7.11).

### 7.2.3 Dynamic response via distributed transfer functions

The solution of Eqs. (7.7) and (7.8) is given by (Yang and Tan, 1992):

$$\hat{\eta}(x, s) = \int_0^L G(x, \xi, s) q(\xi, s) d\xi + H(x, s) \gamma(s) \quad 7.14$$

where  $G(x, \xi, s)$  and  $H(x, s)$ , called the *distributed transfer functions* of the continuum, are of the form

$$G(x, \xi, s) = \begin{cases} H(x, s) M_b(s) e^{-F(s)\xi} & \text{for } x \geq \xi \\ -H(x, s) N_b(s) e^{F(s)(L-\xi)} & \text{for } x \leq \xi \end{cases} \quad 7.15$$

$$H(x, s) = e^{F(s)x} (M_b(s) + N_b(s) e^{F(s)L})^{-1}$$

This transfer function formulation offers an exact and closed-form approach to determination of static and dynamic response of elastic continua, as shown below.

#### *Static response*

To determine the static response of a continuum, simply set  $s = 0$  in Eq. (7.14), and  $G(x, \xi, 0)$  and  $H(x, 0)$  becomes the Green's functions of the continuum. Given external loads, the integral in Eq. (7.14) can be estimated by exact quadrature (Yang, 2005).

#### *Frequency response*

The steady-state response of a continuum subject to a harmonic excitation of frequency  $\omega$  can be computed by Eq. (7.14) if  $s$  is replaced by  $j\omega$ , where  $j = \sqrt{-1}$ . Again, exact quadrature of the integral in Eq. (7.14) can be obtained (Yang, 2005).

#### *Transient response*

To evaluate the transient (time-domain) response of a continuum, either modal expansion or inverse Laplace transform of Eq. (7.14) can be conducted. This eventually leads to a time-domain Green's function formula

$$\hat{\eta}(x, t) = \int_0^t \int_0^L g(x, \xi, t-\tau) \hat{q}(\xi, \tau) d\xi d\tau + \int_0^t h(x, t-\tau) \hat{\gamma}(\tau) d\tau \quad 7.16$$

where  $\hat{\eta}(x, t)$ ,  $\hat{q}(\xi, \tau)$  and  $\hat{\gamma}(\tau)$  are the time-domain counterparts of the  $s$ -

domain quantities  $\eta(x, s)$ ,  $q(\xi, s)$  and  $\gamma(s)$ , respectively; and the Green's functions  $g$  and  $h$  are related to the distributed transfer functions by

$$g(x, \xi, t) = \mathcal{L}^{-1}[G(x, \xi, s)], \quad h(x, t) = \mathcal{L}^{-1}[H(x, s)] \quad 7.17$$

where  $\mathcal{L}^{-1}$  is the inverse Laplace transform operator. Yang and Wu (1997) derived a closed-form transient response solution via an eigenfunction expansion.

#### 7.2.4 Synthesis of multi-body systems

One unique feature of the DTFM is that it can obtain closed-form analytical solutions for flexible structures with multiple components. This system-level analysis takes the following three steps (Yang, 1994).

##### *Step 1. Transfer function representation of components*

Decompose a structure in consideration into a number of one-dimensional components. The points where the components are interconnected are called *nodes*. The response of each component is expressed in terms of nodal displacements by its distributed transfer functions. For instance, for a component with nodes  $i$  and  $j$  as its two ends, its response is represented by Eq. (7.14) with

$$\gamma(s) = \begin{pmatrix} u_i(s) \\ u_j(s) \end{pmatrix} \quad 7.18$$

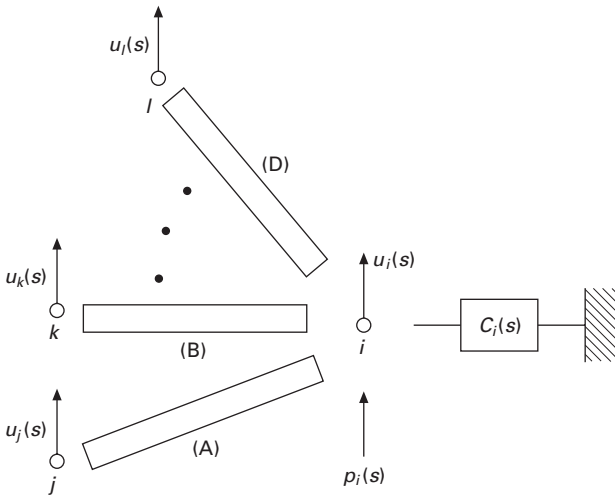
where  $u_i(s)$  and  $u_j(s)$  are vectors of unknown displacements at nodes  $i$  and  $j$ , in the local coordinates of the component.

##### *Step 2. Assembly of components*

In the global coordinates, denote the displacements of the structure at node  $i$  by vector  $U_i(s)$ . The  $U_i(s)$  is related to  $u_i(s)$  in Eq. (7.18) by a coordinate transformation. Suppose that at node  $i$  components (A), (B), ..., (D) are interconnected, as illustrated in Fig. 7.2. Force balance at the node requires

$$Q_A(s) + Q_B(s) + \dots + Q_D(s) - C_i(s)U_i(s) + P_i(s) = 0 \quad 7.19$$

where  $Q_A(s)$ ,  $Q_B(s)$ , ...,  $Q_D(s)$  are vectors of the forces applied to the node by components (A), (B), ..., (D), respectively; the term  $C_i(s)U_i(s)$  describes the forces of any constraints such as springs, dampers, and lumped masses that are imposed at the node; and  $P_i(s)$  is the vector of external forces applied at node  $I$  (not shown in Fig. 7.2). By Eq. (7.14)  $Q_A(s)$ ,  $Q_B(s)$ , ...,  $Q_D(s)$  can be expressed in terms of the nodal displacements  $U_i(s)$ ,  $U_j(s)$ , ...,  $U_l(s)$ . Accordingly, Eq. (7.19) is reduced to

7.2 Interconnection of components (A), (B), ..., (D) at node  $i$ .

$$\begin{aligned} K_{ii}(s)U_i(s) + K_{ij}(s)U_j(s) + \dots + K_{il}(s)U_l(s) \\ = Q_i(s) \equiv P_i(s) + F_i^{\text{TR}}(s) \end{aligned} \quad 7.20$$

where  $K_{ij}(s)$ ,  $K_{ij}(s)$ , ...,  $K_{il}(s)$  are matrices of dynamic stiffness that are composed of the elements of the distributed transfer functions given Eq. (7.15), and  $F_i^{\text{TR}}(s)$  is the vector of transmitted forces that is derived from the integral in Eq. (7.14). Force balance at all nodes leads to a global dynamic equilibrium equation

$$K(s)U(s) = Q(s) \quad 7.21$$

where matrix  $K(s)$  is the global dynamic stiffness matrix;  $U(s)$  is the global nodal displacement vector consisting of the components from  $U_i(s)$  for all  $i$ , and  $Q(s)$  is the corresponding global nodal force vector.

### *Step 3. Static and dynamic analysis*

Solution of Eq. (7.21) gives exact and closed-form solutions for various static and dynamic problems of structures. For instance, setting  $s = 0$ , obtaining the nodal displacements by

$$U(0) = K^{-1}(0)Q(0) \quad 7.22$$

and substituting the result into Eq. (7.14) yields the static response of a structure. For free vibration analysis of a structure, Eq. (7.21) becomes

$$K(s)U(s) = 0 \quad 7.23$$

which defines an eigenvalue problem. The characteristic equation of the structure is

$$\det K(s) = 0 \quad 7.24$$

the roots of which are the eigenvalues of the structure. The mode shape associated with an eigenvalue is determined by solving Eq. (7.21) for a nonzero vector  $U(s)$ . For buckling analysis of a structure, the global stiffness matrix becomes  $K(0; p)$ , where  $p$  is a buckling load parameter. In this case, buckling loads are the roots of the characteristic equation  $K(0; p) = 0$ , and buckling mode shapes can be similarly determined. For a structure under harmonic excitations of frequency  $\omega$ , the nodal displacements are determined as

$$U(j\omega) = K^{-1}(j\omega)Q(j\omega), \quad j = \sqrt{-1} \quad 7.25$$

Substituting (7.25) into Eq. (7.14) gives the steady-state response of the structure at any point. Also, transient response can be estimated via modal expansion using the exact eigen solutions obtained by the DTFM (Yang and Wu, 1997).

The above transfer function synthesis has been applied to dynamic analysis of complex flexible rotor systems (Fang and Yang, 1998), buckling analysis of constrained stepped columns (Yang and Park, 2003), transient response of constrained and combined beam structures (Yang, 2005), and free vibration analysis of three-dimensional frames (Yang *et al.*, 2005).

### 7.2.5 Nonuniformly distributed systems

The DTFM is applicable to those continua whose coefficients, like  $a_k$ ,  $b_k$ , and  $c_k$  in Eq. (7.1), are functions of spatial coordinate  $x$ . For a nonuniform continuum, the transfer function formulation (7.14) is still valid, if  $e^{F(s)x}$  in Eq. (7.15) is replaced by a transition matrix  $\Phi(x, s)$ . Yang and Fang (1994) proposed two techniques for evaluating  $\Phi(x, s)$  and Yang (2005) applied one of the techniques in buckling and free vibration analyses of nonuniform beams.

## 7.3 DTFM for multidimensional continua

### 7.3.1 General concepts

The distributed transfer function formulation can be extended to obtain analytical and semi-analytical solutions for dynamic problems of two- and three-dimensional continua, including plates and shells. The main idea behind this extension is first to reduce a multidimensional problem to a one-dimensional problem, and then to determine the exact closed-form analytical solution of the one-dimensional problem by the DTFM given in the previous section.

Consider a three-dimensional problem governed by the differential equation

$$L[u(x_1, x_2, x_3, t)] = q(x_1, x_2, x_3, t) \quad 7.26$$

where  $L$  is a linear spatial-temporal differential operator,  $u$  is a generalized displacement to be determined,  $q$  is an external force, and  $x_1, x_2$  and  $x_3$  are spatial coordinates. One way to lower the number of dimensions is to assume

$$u(x_1, x_2, x_3, t) = \sum_{i=1}^r u_i(x_1, t) \sum_{j=1}^s N_{ij}(x_2, x_3) \quad 7.27$$

where  $N_{ij}(x_2, x_3)$  are known functions of  $x_2$  and  $x_3$  that satisfy certain conditions, and  $u_i(x_1, t)$  are unknown functions to be determined. The  $N_{ij}$  can be continuous functions used in series solutions, and splines and polynomials used in interpolation or discretization. Substituting Eq. (7.27) into Eq. (7.26) or an equivalent functional and conducting necessary manipulations (integration, variation, minimization of weighted residuals, etc.), produces a one-dimensional differential equation

$$L_1[\{U(x_1, t)\}] = \{Q(x_1, t)\} \quad 7.28$$

where  $L_1$  is a spatial-temporal differential operator, and the vectors

$$\{U(x_1, t)\} = \begin{pmatrix} u_1(x_1, t) \\ u_2(x_1, t) \\ \vdots \\ u_r(x_1, t) \end{pmatrix}, \quad \{Q(x_1, t)\} = \begin{pmatrix} q_1(x_1, t) \\ q_2(x_1, t) \\ \vdots \\ q_r(x_1, t) \end{pmatrix} \quad 7.29$$

with  $u_j(x_1, t)$  defined in Eq. (7.27) and  $q_k(x_1, t)$  related to the forcing function  $q(x_1, x_2, x_3, t)$ . Another way to lower the number of dimensions is to apply finite difference discretization to the original governing equation, in the directions of  $x_2$  and  $x_3$ , which also yields a similar one-dimensional equation.

Equation (7.28) in general has the same format as Eq. (7.1) if  $w(x, t)$  and  $f(x, t)$  are replaced by vectors of displacements and forces, respectively. Thus, the equation is readily solvable by the DTFM as described in Section 7.2. This combination of dimension reduction and analytical formulation makes it possible to obtain highly accurate closed-form semi-analytical solutions for a multidimensional problem.

In the following subsections, four types of DTFM formulations for two-dimensional problems are presented: Fourier series-based DTFM, Ritz-based DTFM, strip DTFM, and finite difference DTFM. For illustrative purposes, we shall only consider a rectangular thin plate in transverse vibration. These methods, of course, can be applied to many other problems defined in domains of different shapes; see Section 7.4.

### 7.3.2 Fourier series-based DTFM

The transverse vibration of a thin rectangular plate in Fig. 7.3 is governed by the differential equation (Timoshenko, 1940)

$$\rho \frac{\partial^2 w(x, y, t)}{\partial t^2} + D \nabla^4 w(x, y, t) = q(x, y, t), \quad 0 \leq x \leq a, 0 \leq y \leq b \quad 7.30$$

where the Laplacian operator  $\nabla^4 = \frac{\partial^4}{\partial x^4} + 2 \frac{\partial^2}{\partial x^2} \frac{\partial^2}{\partial y^2} + \frac{\partial^4}{\partial y^4}$ ;  $\rho$  is mass per unit area; and  $D = \frac{Eh^3}{12(1-\nu^2)}$  is flexural rigidity of the plate, with  $E$ ,  $\nu$ , and  $h$  being the Young's modulus, Poisson's ratio, and thickness of the plate, respectively. Assume that a set of orthogonal functions  $\phi_m(y)$ ,  $m = 1, 2, \dots$ , exists such that the expression

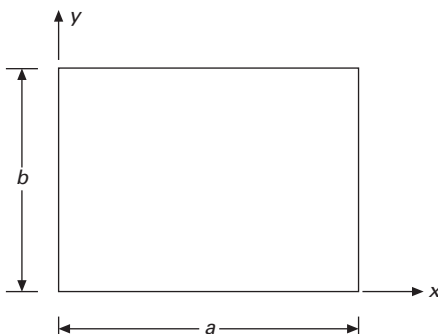
$$w(x, y, t) = \sum_m w_m(x, t) \phi_m(y) \quad 7.31$$

satisfies the boundary conditions of the plate at  $y = 0$  and  $y = b$ , and transforms Eq. (7.30) into a sequence of decoupled differential equations:

$$\rho_m \frac{\partial^2 w_m(x, t)}{\partial t^2} + \sum_{k=0}^4 \sigma_{k,m} \frac{\partial^k}{\partial x^k} w_m(x, t) = q_m(x, t), \quad m = 1, 2, \dots \quad 7.32$$

where  $\rho_m$  and  $\sigma_{k,m}$  are constants, and  $q_m(x, t)$  is the Fourier coefficient of the external load  $q(x, y, t)$  corresponding to  $\phi_m(y)$ . Equation (7.32) is a special case of Eq. (7.1). If functions  $\phi_m(y)$  form a complete basis of the function space in consideration, solution of Eq. (7.31) via the DTFM (Section 7.2) provides analytical prediction of the dynamic response of the plate.

As an example, for a plate simply supported at  $y = 0$  and  $y = b$ , the representation of its transverse displacement is given by



7.3 A rectangular region.

$$w(x, y, t) = \sum_m w_m(x, t) \sin \frac{m\pi y}{b} \quad 7.33$$

where functions  $\sin \frac{m\pi y}{b}$ ,  $m = 1, 2, \dots$ , form a complete basis. Substitute Eq. (7.33) into Eq. (7.30) to obtain

$$\rho \frac{\partial^2 w_m(x, t)}{\partial t^2} + D \left( \frac{\partial^4 w_m(x, t)}{\partial x^4} - 2\alpha_m^2 \frac{\partial^2 w_m(x, t)}{\partial x^2} + \alpha_m^4 w_m(x, t) \right) = q_m(x, t) \quad 7.34$$

with

$$\alpha_m = \frac{m\pi}{b}, \quad q_m(x, t) = \frac{2}{b} \int_0^b q(x, y, t) \sin \frac{m\pi y}{b} dy$$

Equation (7.34) is a special case of Eq. (7.1), and thus can be directly solved by the DTFM given in Section 7.2. The solution of Eq. (7.34) along with the expression (7.33) is often called Lévy-type solution. However, the DTFM is beyond Lévy-type solution in that it can be applied to multi-body structures.

The above method is a combination of the DTFM in one coordinate ( $x$ ) and Fourier series solution in the other ( $y$ ). For this reason, we shall call the method *the Fourier series-based distributed transfer function method* (FS-DTFM). This method gives exact analytical solutions for certain two- and three-dimensional continua.

### 7.3.3 Ritz-based DTFM

The FS-DTFM in the previous section requires that the base functions  $\phi_m(y)$  satisfy *all* the boundary conditions at  $y = 0$  and  $y = b$ , which limits the utility of the method to certain types of boundary conditions. This restriction can be lifted by the following  $N$ -term series approximation of the plate displacement

$$w(x, y, t) \approx w_N(x, y, t) = \sum_{m=1}^N w_m(x, t) \psi_m(y) \quad 7.35$$

where  $\psi_m(y)$  are *admissible functions* that only need to satisfy the geometric boundary conditions at  $y = 0$  and  $y = b$ . Geometric boundary conditions for a plate are those that have terms involving only zero and first spatial derivatives such as  $w$  and  $\partial w/\partial y$ , but not higher derivatives (Meirovitch, 1967). For instance, for a plate clamped at  $y = 0$  and free at  $y = b$ , the boundary conditions are

$$\text{at } y = 0: \quad w = 0, \quad \frac{\partial w}{\partial y} = 0$$

$$\text{at } y = b: \quad \frac{\partial^2 w}{\partial y^2} + v \frac{\partial^2 w}{\partial x^2} = 0, \quad \frac{\partial^3 w}{\partial y^3} + (2 - v) \frac{\partial^3 w}{\partial x^2 \partial y} = 0$$

At  $y = 0$  the geometric boundary conditions are  $w = 0$  and  $\partial w/\partial y = 0$ ; at  $y = b$  there is no geometric boundary condition. For the plate, two sets of admissible functions are  $\psi_j(y) = (y/b)^{j+1}$  and  $\psi_j(y) = 1 - \cos(j\pi y/b)$ ,  $j = 1, 2, \dots$ . The eigenfunctions of a cantilever beam in free vibration can also be chosen as admissible functions for the plate problem.

The generalized Hamilton's principle for a plate is

$$\int_0^t \left\{ \frac{1}{2} \delta \int_A (\{\kappa\}^T [C] \{\kappa\} - \rho w_{,t}^2) dx dy - \int_A q \delta w dx dy \right\} = 0 \quad 7.36$$

where  $A$  denotes the region of the plate,  $\{\kappa\}$  is the curvature vector of the form  $\{\kappa\} = -(w_{,xx} \ w_{,yy} \ 2w_{,xy})^T$ , and  $[C]$  is the constitutive matrix given by

$$[C] = D \begin{bmatrix} 1 & v & 0 \\ v & 1 & 0 \\ 0 & 0 & (1-v)/2 \end{bmatrix}$$

with  $D$  and  $v$  being the flexural rigidity and Poisson's ratio of the plate,  $w_{,t} = \partial w/\partial t$ , and  $w_{,x} = \partial w/\partial x$ , etc. Substitute the series (7.35) into Eq. (7.36) and perform functional variation to obtain the matrix partial differential equation

$$[M] \frac{\partial^2}{\partial t^2} \{W(x, t)\} + \sum_{j=0}^4 [K_j] \frac{\partial^j}{\partial x^j} \{W(x, t)\} = \{Q(x, t)\}, \quad 0 \leq x \leq a \quad 7.37$$

where  $\{W(x, t)\} = [w_1(x, t) \ w_2(x, t) \ \dots \ w_N(x, t)]^T$ ;  $[M]$  and  $[K_i]$  are matrices related to the inertia and stiffness of the plate. Equation (7.37), after Laplace transformation, is cast into a spatial state equation with the same form as Eq. (7.7), in which

$$\eta(x, s) = \begin{pmatrix} \{W(x, s)\} \\ \{W'(x, s)\} \\ \{W''(x, s)\} \\ \{W'''(x, s)\} \end{pmatrix}$$

$$F(s) = \begin{bmatrix} [0] & [I] & [0] & [0] \\ [0] & [0] & [I] & [0] \\ [0] & [0] & [0] & [I] \\ -s^2 [\tilde{M}] - [\tilde{K}_0] & -[\tilde{K}_1] & -[\tilde{K}_2] & -[\tilde{K}_3] \end{bmatrix} \quad 7.38$$

where  $\{W(x, s)\}$  is the Laplace transform of  $\{W(x, t)\}$ ,  $\{W'(x, s)\} = \partial \{W(x, s)\}/\partial x$ ,  $[\tilde{M}] = [K_4]^{-1}[M]$ ,  $[\tilde{K}_j] = [K_4]^{-1}[K_j]$ , and  $[0]$  and  $[I]$  are zero and identity matrices of proper dimensions. It follows that all the formulas in Section 7.2 can be used for static and dynamic analysis of the plate.

The aforementioned method, which combines the DTFM in one coordinate ( $x$ ) and Ritz method in the other ( $y$ ), is called *Ritz-based distributed transfer function method* (R-DTFM). This method delivers semi-analytical solutions of static and dynamic problems of two- and three-dimensional continua.

### 7.3.4 Strip DTFM

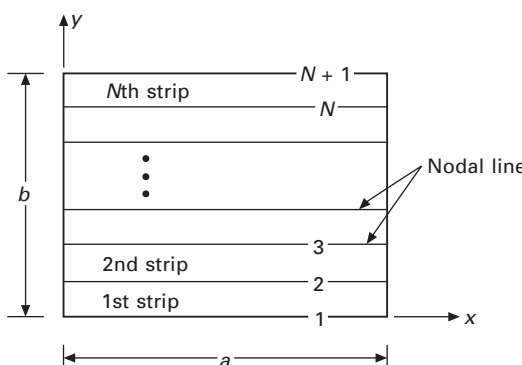
In this method, the rectangular domain of the plate is divided into  $N$  strips by  $N + 1$  lines, which are called *nodal lines*; see Fig. 7.4. Along the  $j$ th nodal line, define a nodal line displacement vector  $\phi_j(x, t)$ , which contains parameters such as transverse displacement and rotation with respect to the  $x$ -axis. Interpolate the displacements of the  $j$ th strip along its lateral ( $y$ -) direction by

$$w(x, y, t) = [N(y)] \begin{pmatrix} \phi_j(x, t) \\ \phi_{j+1}(x, t) \end{pmatrix} \quad 7.39$$

where  $[N(y)]$  is a vector of polynomial functions. The selection of these polynomial functions is similar to that of shape functions in a one-dimensional finite element discretization. The displacement interpolation, by the generalized Hamilton's principle of the plate, reduces the governing equation (7.30) to the matrix partial differential equation

$$[M] \frac{\partial^2}{\partial t^2} \{\Phi(x, t)\} + \sum_{j=0}^4 [K_j] \frac{\partial^j}{\partial x^j} \{\Phi(x, t)\} = \{Q(x, t)\}, \quad 0 \leq x \leq a \quad 7.40$$

where  $[M]$  and  $[K_i]$  are derived from Eq. (7.36), and  $\{\Phi(x, t)\}$  is the vector of independent nodal line displacements. Following Section 7.3.3, a spatial space formulation like (7.7) is obtained, in which the spatial state vector is given by



7.4 A rectangular elastic region divided into strips.

$$\eta(x, s) = \begin{pmatrix} \{\Phi(x, s)\} \\ \{\Phi'(x, s)\} \\ \{\Phi''(x, s)\} \\ \{\Phi'''(x, s)\} \end{pmatrix} \quad 7.41$$

with  $\{\Phi'(x, s)\} = \partial\{\Phi(x, s)\}/\partial x$ , and all the formulas in Section 7.2 can be used.

With combination of the DTFM in one coordinate ( $x$ ) and finite element discretization in the other ( $y$ ), the above method delivers semi-analytical solutions of static and dynamic problems of two- and three-dimensional continua. The method is called *the strip distributed transfer function method* (SDTFM; Zhou and Yang, 1996a).

### 7.3.5 Finite difference DTFM

In this method, the rectangular domain of the plate is also divided into  $N$  strips by  $N + 1$  equally spaced lines that are parallel to the  $x$ -axis. On these lines, which are called *grid lines*, finite difference algorithms are applied to approximate spatial derivatives of  $w$  with respect to  $y$ . For instance, if central finite difference is used, the governing equation (7.30) on the  $k$ th grid line is reduced to the finite difference differential equation

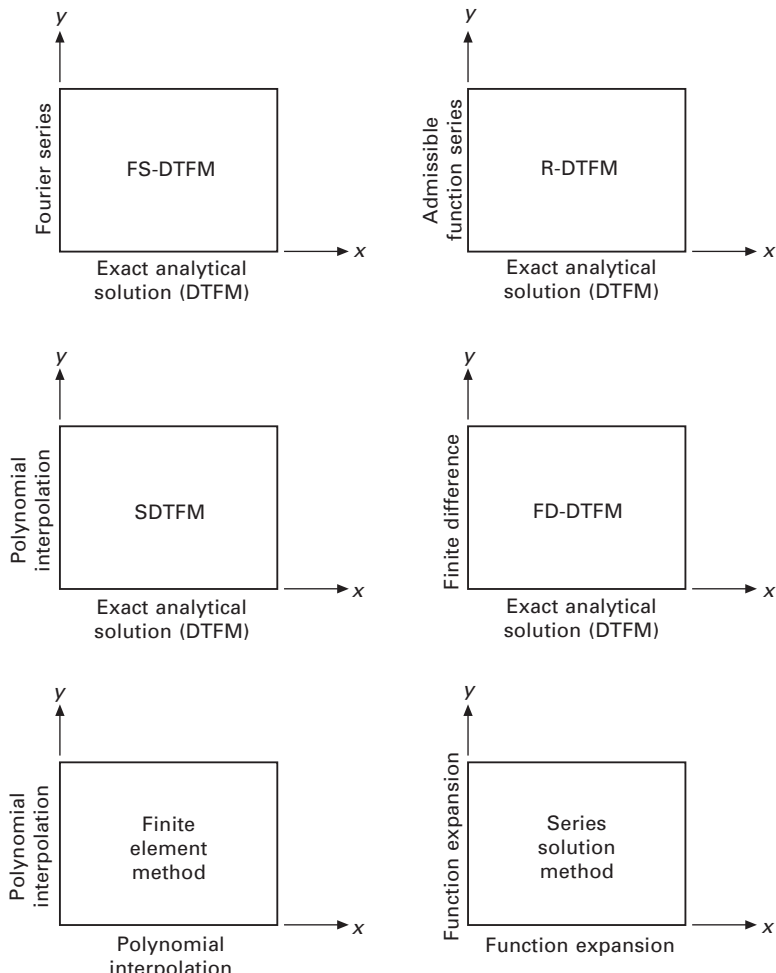
$$\rho \frac{\partial^2 w_k}{\partial t^2} + D \frac{\partial^4 w_k}{\partial x^4} + \frac{2D}{h_g^2} \frac{\partial^2}{\partial x^2} (w_{k+1} - 2w_k + w_{k-1}) + \frac{D}{h_g^4} (w_{k+2} - 4w_{k+1} + 6w_k - 4w_{k-1} + w_{k-2}) = q_k(x, t), \quad 0 \leq x \leq a \quad 7.42$$

where  $h_g$  is the distance between two adjacent grid lines;  $w_k$  is the plate displacement on the  $k$ th grid line, i.e.  $w_k = w(x, kh_g, t)$ ; and  $q_k(x, t) = q(x, kh_g, t)$ . Assembly of the finite difference differential equations on all the grid lines yields a matrix differential equation with the same form as Eq. (7.37) except that the vector  $\{W(x, t)\}$  contains the displacement functions  $w_k$  on the grid lines. Following the previous sections, the exact solution of Eq. (7.42) can be obtained by the DTFM given in Section 7.2.

The above method combines the DTFM in one coordinate ( $x$ ) and finite difference method in the other ( $y$ ), and hence is called *Finite difference-distributed transfer function method* (FD-DTFM). This method gives semi-analytical solutions of static and dynamic problems of two- and three-dimensional continua.

### 7.3.6 Discussion

The four types of the DTFM given in the previous sections are compared in Fig. 7.5. These methods have one thing in common: they all produce exact and closed-form analytical solutions in one coordinate direction ( $x$ ). The FS-DTFM is an exact analytical method because it also presents solutions in Fourier series in the  $y$  direction. The other three types are semi-analytical methods because admissible function series, polynomial interpolation, and finite difference have been used, respectively, to approximate the solution in the  $y$  direction. The R-DTFM and SDTFM are derived based on variation of a functional that is equivalent to the governing differential equation of the



7.5 Comparison of the DTFM and other methods.

problem, while the FS-DTFM and FD-DTFM are established by directly decoupling or discretizing the governing equation.

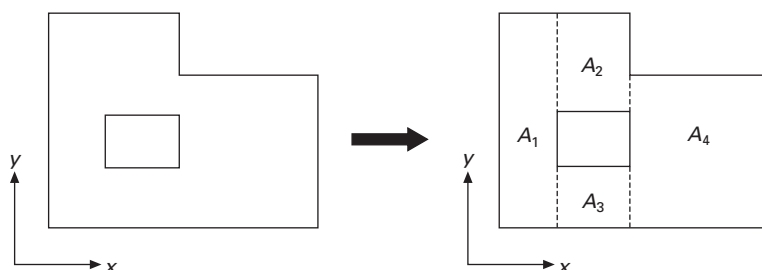
It is interesting to compare the DTFM with the finite element method (FEM) and conventional series solution methods (Galerkin method, Ritz method, assumed-modes method, etc.). The FEM applies polynomial interpolation in both  $x$  and  $y$  directions, while series solution methods adopt expansion of admissible or comparison functions in both  $x$  and  $y$  (Fig. 7.5). The FS-DTFM, R-DTFM, and SDTFM, on the other hand, obtain closed-form analytical solutions in  $x$ , and therefore are more accurate than series solution methods and the FEM. With the same token, the FD-DTFM is more accurate than the standard finite difference method. The high accuracy and efficiency of the DTFM are shown in many examples in Section 7.4.

One unique feature of the DTFM is that it is capable of handling multi-body domains. As an example, consider the multi-region domain in Fig. 7.6, which is composed of four rectangular subregions,  $A_1, A_2, A_3, A_4$ . Following Section 7.2.4, the response of each subregion can be represented by the displacements along its boundaries (dashed lines). This boundary displacement representation automatically guarantees displacement continuity between two adjacent subregions (Yang and Zhou, 1996). As such, assembly of the whole body from all the subregions follows a procedure similar to that of a finite element analysis, though the DTFM yields analytical or semi-analytical solutions for each subregion. Conventional series solution methods lack this multi-body synthesis capability.

Although only a rectangular region is considered here, the DTFM is applicable to domains of various shapes that are described in different coordinate systems (e.g. polar, cylindrical, spherical coordinate systems). This versatility of the DTFM in modeling and analysis will be illustrated in the next section.

## 7.4 Free vibration of plates and shells

In this section, the DTFM is applied to free vibration analysis of certain plates and shells. The interested reader may refer to related publications for further detail.



7.6 A multi-body domain composed of four subregions

### 7.4.1 Rectangular plates

Consider a rectangular thin plate in free vibration that is governed by Eq. (7.30) with  $q(x, y, t) = 0$ . By the SDTFM given in Section 7.3.4, the plate is divided into a number of strips with their longitudinal direction in  $x$  (Fig. 7.4). The plate displacement of the  $j$ th strip is interpolated in the lateral ( $y$ ) direction by (Zhou and Yang, 1996a)

$$w(x, y, t) = [N_w(y)]\{W_j(x, t)\} \quad 7.43$$

where  $\{W_j(x, t)\}$  is the nodal line displacement vector of the strip defined by

$$\{W_j(x, t)\} = \begin{pmatrix} w_j(x, t) \\ \theta_j(x, t) \\ w_{j+1}(x, t) \\ \theta_{j+1}(x, t) \end{pmatrix} \quad 7.44$$

with  $w_j(x, t)$  and  $\theta_j(x, t)$  being the transverse displacement and rotation (with respect to the  $x$ -axis) of the  $j$ th nodal line; and  $[N_w(y)]$  is a vector of shape functions

$$[N_w(y)] = [1 - 3\xi^2 + 2\xi^3 \quad b_j(\xi - 2\xi^2 + \xi^3) \quad 3\xi^2 - 2\xi^3 \quad b_j(-\xi^2 + \xi^3)] \quad 7.45$$

with  $\xi = y/b_j$  and  $b_j$  the strip width. Equation (7.43) assures the continuity of  $w$  and  $\partial w/\partial y$  across the nodal lines. Substituting Eq. (7.43) into the Hamilton's principle given in Eq. (7.36) reduces the original governing equation to a spatial state equation described by Eqs. (7.7) and (7.41), where  $\{\Phi(x, t)\}$  contains the nodal displacements of all the strips. With the spatial state equation, the natural frequencies and mode shapes of the plate can be computed following Section 7.2.2.

Table 7.1 lists the first eight non-dimensional natural frequencies ( $\bar{\omega} = \omega b^2 \sqrt{\rho/D}$ ) of a rectangular plate that is fully clamped and has a

Table 7.1 Nondimensional natural frequencies  $\bar{\omega}$  of a clamped rectangular plate ( $a/b = 1.5$ )

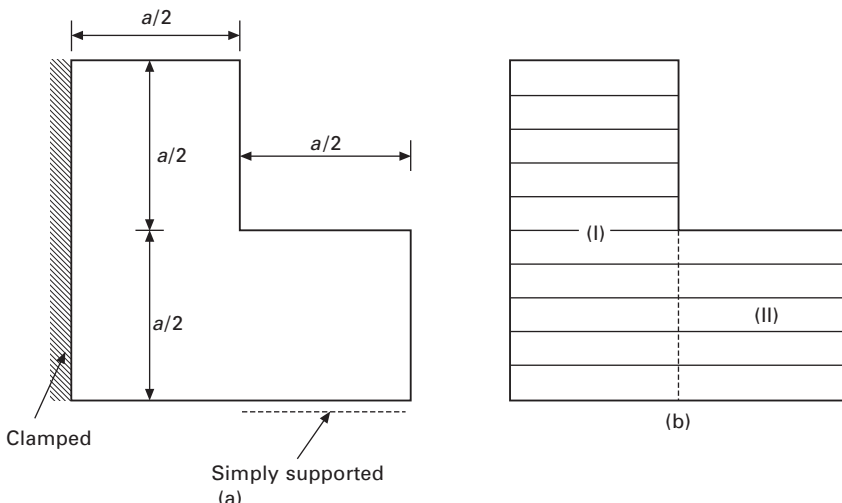
Mode no.	FEM		SDTFM*		FD-DTFM	
	4 × 4	30 × 30	4 strips	8 strips	16 strips	32 strips
1	27.877	27.020	27.036	27.007	26.639	26.912
2	47.284	41.820	41.754	41.708	41.260	41.589
3	71.428	66.259	66.613	66.162	63.996	65.575
4	78.651	67.006	66.685	66.530	65.837	66.345
5	91.561	80.078	80.374	79.842	77.585	79.227
6	115.68	102.16	100.95	100.83	99.606	100.50
7	133.16	103.83	103.77	103.17	100.66	102.48
8	147.92	125.89	127.95	125.58	118.33	123.47

\*Results from Zhou and Yang (1996a).

length-to-width ratio  $a/b = 1.5$  (Zhou and Yang, 1996a). The natural frequencies computed by the SDTFM with eight strips are in good agreement with those obtained by the finite element method (FEM) with a  $30 \times 30$  mesh (900 elements). Because both the SDTFM and the FEM provide a higher estimation of the actual natural frequencies, the eight-strip SDTFM model is more accurate than the  $30 \times 30$  FEM model. Moreover, the four-strip SDTFM prediction is almost the same as that by the  $30 \times 30$  FEM; the  $4 \times 4$  FEM on the other hand only gives the first natural frequency at the same accuracy level.

The above-mentioned plate is also analyzed by the FD-DTFM (Section 7.3.5), with a central finite difference algorithm. The computed results are also given in Table 7.1. The FD-DTFM with 32 strips delivers a good estimation of the natural frequencies. Note that the number of strips for the FD-DTFM is at least twice that for the SDTFM for numerical simulation at the same accuracy level. This is due to the fact that in discretization the SDTFM adopts two displacement parameters ( $w_j(x, t)$ ,  $\theta_j(x, t)$ ) on each nodal line and the FD-DTFM uses only one displacement parameter for each grid line.

To show the multi-body synthesis capability of the DTFM, consider an L-shaped plate in Fig. 7.7(a), which is clamped on its left side, simply supported along half of its bottom side, and free at all other edges. The plate can be viewed as an assemblage of two subregions I and II, as shown in Fig. 7.7(b). Conventional series solution methods cannot deal with this type of multi-body structure because there is no one-to-one mapping between the coefficients of the series for subregions. One way to get around this is to fix the number



7.7 An L-shaped plate: (a) the original domain; (b) the domain divided into two subregions, each of which are future divided into strips.

of terms in each function series. Doing so will change the original format of infinite series solutions into finite element interpolation by continuous functions, which needs an increased number of subregions for the same accuracy level in modeling and analysis.

The SDTFM is capable of handling multi-body domains like the L-shape plate. To this end, the subregions I and II of the plate are divided into  $2N$  and  $N$  strips, respectively. Based on the concept given in Section 7.2.4, the assembly of the subregions by connecting the ends of the strips along the dashed line leads to a global dynamic equilibrium equation like (7.21). Solution of the dynamic equilibrium equation gives the dynamic response of the plate. A similar multi-body synthesis procedure has also been applied to two-dimensional elasticity problems (Yang and Zhou, 1996). The first 10 nondimensional natural frequencies  $\lambda_k = \omega_k a^2 \sqrt{\rho/D}$  of the plate are computed by the SDTFM with 4 + 2 strips and 8 + 6 strips (Park, 1997). The computed results are compared with the reference solution obtained by the FEM with 3675 elements, as shown in Table 7.2, where  $\varepsilon$  gives the percentage deviation of the SDTFM results from the reference solution. The high accuracy of the SDTFM is seen: with just 6 (4 + 2) strips, the SDTFM results have a maximum percentage deviation of 1.09%; with 12 (8 + 4) strips, the SDTFM results have a maximum percentage deviation of 0.28%. Further computation shows that 24 (16 + 8) strips reduces the maximum percentage deviation to 0.11% (Park, 1997).

#### 7.4.2 Circular and sectorial plates

The DTFM is not limited to rectangular regions. Consider a sectorial plate of a subtended angle  $\theta_0$  as shown in Fig. 7.8(a). In the polar coordinate system

Table 7.2 Nondimensional natural frequencies  $\lambda_k$  of an L-shaped plate

k	SDTFM*				FEM 3675 elements	
	4+2 strips		8+4 strips			
	$\lambda_k$	$\varepsilon$	$\lambda_k$	$\varepsilon$		
1	9.9793	0.33%	9.9580	0.12%	9.9463	
2	21.412	0.63%	21.319	0.19%	21.278	
3	35.218	0.28%	35.144	0.07%	35.120	
4	61.286	0.75%	60.910	0.13%	60.830	
5	69.084	0.77%	68.705	0.21%	68.559	
6	75.82	0.93%	75.258	0.18%	75.124	
7	93.361	0.68%	92.949	0.23%	92.732	
8	105.36	1.00%	104.51	0.18%	104.32	
9	122.04	1.09%	121.07	0.28%	120.73	
10	131.03	0.39%	130.71	0.15%	130.52	

\*Results from Park (1997).

$(r, \theta)$ , the transverse vibration of the plate is governed by Eq. (7.30) with the operator

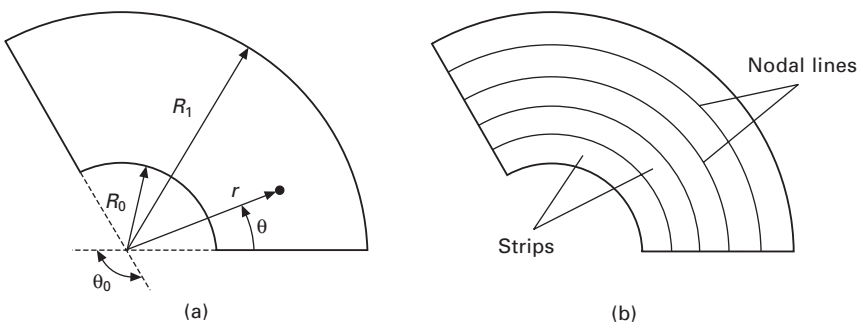
$$\nabla^4 = \left( \frac{\partial^2}{\partial r^2} + \frac{1}{r} \frac{\partial}{\partial r} + \frac{1}{r^2} \frac{\partial^2}{\partial \theta^2} \right) \left( \frac{\partial^2}{\partial r^2} + \frac{1}{r} \frac{\partial}{\partial r} + \frac{1}{r^2} \frac{\partial^2}{\partial \theta^2} \right)$$

If the SDTFM is adopted, the plate can be divided into a number of strips by nodal lines in the circumferential direction as shown in Fig. 7.8(b). (The sectorial plate can be divided by a number of radial lines as well.) The interpolation of the strip displacement is the same as that given by Eqs. (7.43) to (7.45) if  $x$  and  $y$  are replaced by  $r$  and  $\theta$ , which eventually leads to a one-dimensional matrix differential equation:

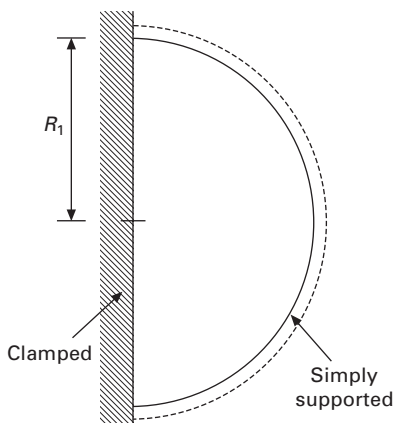
$$[M] \frac{\partial^2}{\partial t^2} \{\Phi(\theta, t)\} + \sum_{j=0}^4 [K_j] \frac{\partial^j}{\partial \theta^j} \{\Phi(\theta, t)\} = \{Q(\theta, t)\}, \quad 0 \leq \theta \leq \theta_0 \quad 7.46$$

The analytical solution of Eq. (7.46) is then determined by the DTFM as discussed in Section 7.3.4. A detailed description of the solution procedure is given in Yang and Zhou (1997).

As an example, consider free vibration of a clamped, simply supported semicircular plate; see Fig. 7.9. The plate parameters are assumed nondimensional, and are chosen as  $R_0 = 0$ ,  $R_1 = 100$ ,  $h = 1$ ,  $\rho = 1$ ,  $E = 10^6$  and  $v = 0.3$ . Table 7.3 shows the first 10 natural frequencies computed by the SDTFM and the FEM. The accuracy of the SDTFM is surprisingly high. With just four strips, the SDTFM prediction has less than 1.2% deviation for the reference solution that is obtained by the FEM with a  $16 \times 64$  mesh (1204 elements). The finite element analyses of  $4 \times 16$ ,  $6 \times 24$  and  $8 \times 32$  meshes give poor results, with much larger deviations (31.4%, 19.1% and 9.6%, respectively) from the reference solution. In fact, the four-strip SDTFM prediction is more accurate than the reference solution because both the SDTFM and the FEM give higher estimation of natural frequencies. The six-



7.8 A sectorial plate: (a) the original domain; (b) the domain divided into strips.



7.9 A clamped, simply supported semicircular plate.

Table 7.3 Natural frequencies of a clamped, simply supported semicircular plate

Mode no.	SDTFM*		FEM			
	4 strips	6 strips	4 × 16	6 × 24	8 × 32	16 × 64
1	0.5903	0.5901	0.6428	0.6055	0.5986	0.5920
2	0.9522	0.9513	1.0191	1.9818	0.9683	0.9552
3	1.4116	1.4105	1.5383	1.4701	1.4442	1.4184
4	1.7790	1.7723	2.1606	1.9520	1.8721	1.7951
5	1.9559	1.9538	2.1749	2.0587	2.0133	1.9676
6	2.4290	2.4127	2.9309	2.6801	2.5619	2.4460
7	2.4290	2.4127	2.9309	2.6801	2.5619	2.4460
8	3.1865	3.1681	3.8048	3.5420	3.3932	3.2198
9	3.2748	3.2685	3.9368	3.5623	3.4273	3.3069
10	3.6166	3.5642	4.8091	4.3585	4.0094	3.6596

\*Results from Yang and Zhou (1997).

strip SDTFM has even higher precision. Although Table 7.3 lists only the first 10 natural frequencies, further numerical simulation shows the SDTFM is even more accurate than the FEM in predicting higher-order natural frequencies.

#### 7.4.3 Plates with curved boundaries

In engineering applications, plates do not always have regular shapes; they may take different shapes and have arbitrarily curved boundaries. The finite element method, of course, is most versatile in modeling this kind of structure. But this method demands large computer storage and CPU time. So, methods using series of comparison or admissible functions have been developed; for instance see Saliba (1986), Geannakakes (1990), Liew and Lam (1991), Kim

and Dickinson (1992). Series solution methods, as mentioned before, are problem-dependent, and are usually limited to single-body domains of simple geometries.

The distributed transfer function formulation can be adopted to obtain closed-form semi-analytical solutions for arbitrary-shaped plates. The isoparametric strip distributed transfer function method (ISDTFM) developed by Yang and Park (1999) is one such modeling and analysis technique. In this method, the SDTFM in Section 7.3.4 is combined with an isoparametric coordinate transformation. To show this, consider the plate in Fig. 7.10(a), whose domain  $A$  has two curved boundaries described by functions  $a_0(y)$  and  $a_1(y)$ . Define an isoparametric coordinate transformation as follows:

$$\begin{aligned}x &= [a_1(Y) - a_0(Y)]X + a_0(Y) \\y &= Y\end{aligned}\quad 7.47$$

which maps the original spatial domain to the rectangular region

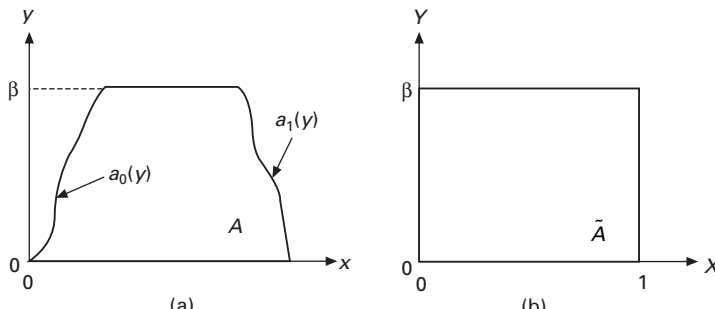
$$\tilde{A} = \{(X, Y) \mid 0 \leq X \leq 1, 0 \leq Y \leq \beta\}$$

as shown in Fig. 7.10(b). With this coordinate transformation, Hamilton's principle given by Eq. (7.36) for the domain  $A$  is reduced to the following one:

$$\int_0^t \left\{ \frac{1}{2} \delta \int_{\tilde{A}} (\{\tilde{\kappa}\}^T [\tilde{C}] \{\tilde{\kappa}\} - \rho w_{,t}^2) |J| dX dY - \int_{\tilde{A}} q \delta w |J| dX dY \right\} = 0 \quad 7.48$$

for the region  $\tilde{A}$ , where  $w = w(X, Y, t)$ ,  $|J|$  is the determinant of the Jacobian matrix given by

$$|J| = \begin{vmatrix} \frac{\partial x}{\partial X} & \frac{\partial y}{\partial X} \\ \frac{\partial x}{\partial Y} & \frac{\partial y}{\partial X} \end{vmatrix} = a_1(Y) - a_0(Y) \quad 7.49(a)$$



7.10 The domains of the plate: (a) the original spatial domain with curved boundaries; (b) the mapped rectangular region.

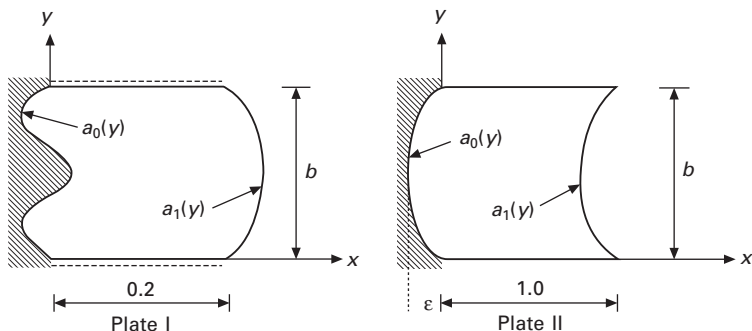
and

$$\{\tilde{\kappa}\} = [T(X, Y)]\{\kappa\}, [\tilde{C}] = [T(X, Y)]^T [C][T(X, Y)] \quad 7.49(b)$$

with  $[T(X, Y)]$  being a matrix that arises from the coordinate transformation. By Eq. (7.48), the SDTFM given in Section 7.3.4 can be applied to obtain a closed-form semi-analytical solution of the equivalent vibration problem defined in the region  $\tilde{A}$ . The dynamic response of the plate in the original spatial domain  $A$  then can be expressed by the solution in  $\tilde{A}$  through the coordinate transformation (7.47).

The ISDTFM is illustrated on the two plates in Fig. 7.11 (Yang and Park, 1999). Plate I is simply supported at the horizontal straight sides, clamped at the left boundary  $a_0(y) = -0.1 \sin(3\pi y/b)$ , and free at the right boundary  $a_1(y) = -1.2y(y - b) + 0.2$ . Table 7.4 gives the first five nondimensional natural frequencies,  $\lambda_k = \omega_k(b/\pi)^2 \sqrt{\rho/D}$ , which are computed by the ISDTFM and the FEM. A fast convergence is seen as the number of strips increases. With just six strips, the ISDTFM prediction is in good agreement with that by the FEM with 3600 elements.

Plate II in Fig. 7.11 has two straight horizontal sides, and two parallel parabolic sides that are described by  $a_0(y) = 4\varepsilon y(y - b)$  and  $a_1(y) = a_0(y) + 1$ .



7.11 Two plates with curved boundaries.

Table 7.4 Nondimensional natural  $\lambda_k$  frequencies of Plate I in Fig. 7.11

k	ISDTFM*				FEM (72 × 50 mesh)
	2 strips	4 strips	6 strips	8 strips	
1	2.9945	2.6014	2.5492	2.5392	2.5407
2	5.5161	4.9872	4.8079	4.7504	4.8422
3	11.3389	9.1674	8.7025	8.5742	8.6978
4	15.8043	14.8989	13.9162	13.5870	13.6843
5	16.4154	14.9081	14.7564	14.7327	14.8493

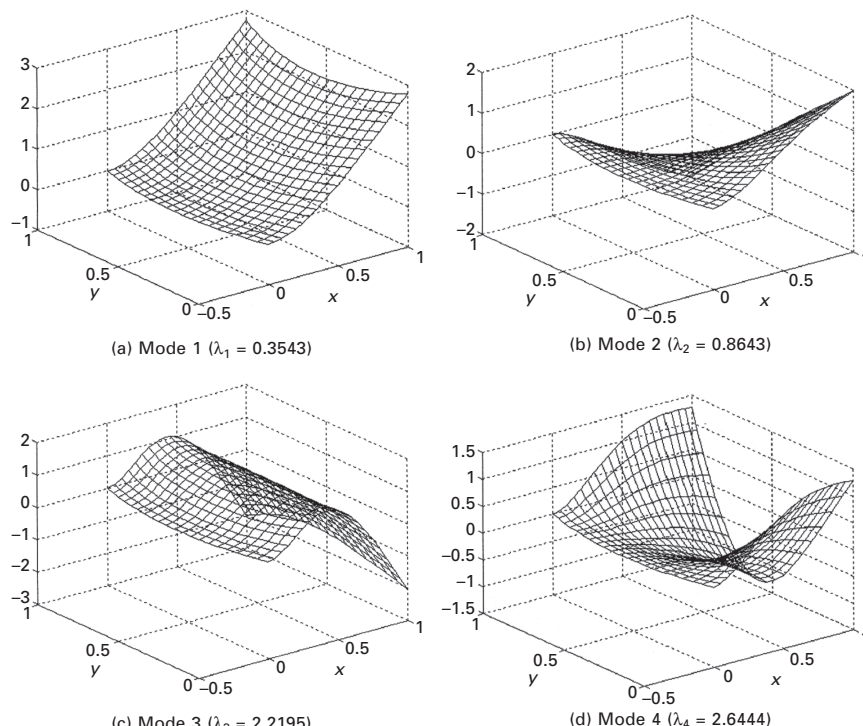
\*Results from Yang and Park (1999).

The plate is clamped at the left parabolic side, and free at all the other sides. The first six nondimensional natural frequencies  $\lambda_k = \omega_k (b/\pi)^2 \sqrt{\rho/D}$  of the plate for  $\epsilon = 0.1$  are computed by the ISDTFM and the FEM, and are shown in Table 7.5. With a few strips, the ISDTFM yields convergent and accurate results, as compared with the FEM prediction with  $3600$  elements. The first four mode shapes of the plate are plotted via the ISDTFM in Fig. 7.12.

Table 7.5 Nondimensional natural frequencies  $\lambda_k$  of Plate II in Fig. 7.11 ( $\epsilon = 0.1$ )

$k$	ISDTFM*				FEM ( $60 \times 60$ mesh)
	2 strips	4 strips	6 strips	8 strips	
1	0.3546	0.3545	0.3543	0.3543	0.3542
2	0.8655	0.8644	0.8643	0.8643	0.8641
3	2.2210	2.2198	2.2196	2.2195	2.2180
4	2.6528	2.6467	2.6447	2.6444	2.6415
5	3.1153	3.1086	3.1081	3.1079	3.1058
6	5.2970	5.2833	5.2780	5.2767	5.2698

\* Results from Yang and Park (1999).



7.12 Mode shapes of Plate II (from Yang and Park, 1999).

The above ISDTFM is also applied to skew, trapezoidal, and elliptical plates (Yang and Park, 1999).

#### 7.4.4 Cylindrical shells

Consider a homogeneous circular cylindrical shell of length  $L$  and radius  $R$  as shown in Fig. 7.13. The equations of motion of the shell with small deformation have the form

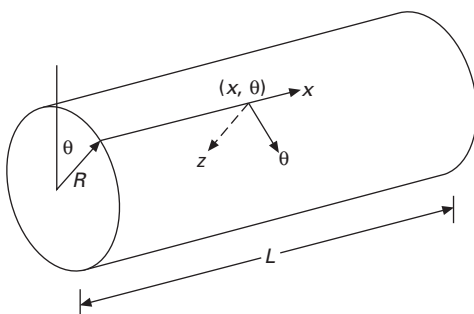
$$\sum_{k=1}^3 \sum_{i=0}^{n_k} \sum_{j=0}^i \frac{\partial^i}{\partial x^{i-j} \partial \theta^j} \left( a_{mkij} \frac{\partial^2}{\partial t^2} + b_{mkij} \frac{\partial}{\partial t} + c_{mkij} \right) u^k(x, \theta, t) \\ = f^m(x, \theta, t), \quad m = 1, 2, 3 \quad 7.50$$

where  $u^1$ ,  $u^2$ , and  $u^3$  are the shell displacements in the longitudinal ( $x$ -), circumferential ( $\theta$ -), and radial ( $z$ -) directions, respectively;  $f^m$  are external loads; and parameters  $a_{mkij}$ ,  $b_{mkij}$ , and  $c_{mkij}$  describe the geometric and material properties of the shell. Equation (7.50) represents various linear models of cylindrical shells (Love type, Donnell–Mushtari type, etc.), and characterizes different physical properties, such as gyroscopic effects from a spinning shell, viscoelastic material, elastic foundation, and passive damping.

Owing to the periodic property of the shell displacements in the circumferential direction, the FS-DTFM given in Section 7.3.2 is convenient for dynamic analysis. In this method, the shell displacements and external loads are first expanded in Fourier series:

$$u^k(x, \theta, t) = \sum_{n=0}^{\infty} \{u_{c,n}^k(x, t) \cos n\theta + u_{s,n}^k(x, t) \sin n\theta\}, \quad k = 1, 2, 3 \\ f^m(x, \theta, t) = \sum_{n=0}^{\infty} \{f_{c,n}^m(x, t) \cos n\theta + f_{s,n}^m(x, t) \sin n\theta\}, \quad m = 1, 2, 3 \quad 7.51$$

where  $u_{c,n}^k(x, t)$  and  $u_{s,n}^k(x, t)$  are unknown displacement functions to be determined. Substituting the above expressions into Eq. (7.50), equating the



7.13 A circular cylindrical shell.

coefficients of the sine and cosine terms, and performing Laplace transform of the resulting equations with respect to time leads to the spatial state equation (Zhou and Yang, 1995):

$$\frac{\partial}{\partial x} \eta_n(x, s) = F_n(s) \eta_n(x, s) + q_n(x, s), \quad x \in (0, L), \quad n = 1, 2, \dots \quad 7.52a$$

where  $n$  is the wave number in the shell circumferential direction; the state vector  $\eta_n$  contains the Laplace transforms of functions  $u_{c,n}^k(x, t)$  and  $u_{s,n}^k(x, t)$ , and their spatial derivatives; and  $q_n(x, s)$  contains the Laplace transforms of the external. The boundary conditions of the shell specified at  $x = 0$  and  $x = L$  can also be written in the state form:

$$M_n(s) \eta_n(0, s) + N_n(s) \eta_n(L, s) = \gamma_n(s) \quad 7.52b$$

where  $\gamma_n(s)$  consists of boundary disturbances or displacement functions.

As an example, the governing equations of a cylindrical shell of the Donnell–Mushtari model are (Markus, 1989)

$$\frac{1}{\gamma_1^2} \frac{\partial^2 u}{\partial x^2} + \frac{1}{2} (1 - \nu) \frac{\partial^2 u}{\partial \theta^2} + \frac{1 + \nu}{2\gamma_1} \frac{\partial^2 v}{\partial x \partial \theta} - \frac{\nu}{\gamma_1} \frac{\partial w}{\partial x} = \bar{p} \frac{\partial^2 u}{\partial t^2} - \bar{q}_x \quad 7.53a$$

$$\frac{1 + \nu}{2\gamma_1} \frac{\partial^2 u}{\partial x \partial \theta} + \frac{1 - \nu}{2\gamma_1^2} \frac{\partial^2 v}{\partial x^2} + \frac{\partial^2 v}{\partial \theta^2} - \frac{\partial w}{\partial \theta} = \bar{p} \frac{\partial^2 v}{\partial t^2} - \bar{q}_\theta \quad 7.53b$$

$$\begin{aligned} \frac{\nu}{\gamma_1} \frac{\partial u}{\partial x} + \frac{\partial v}{\partial \theta} - w - k \left( \frac{1}{\gamma_1^4} \frac{\partial^4 w}{\partial x^4} + \frac{2}{\gamma_1^2} \frac{\partial^4 w}{\partial x^2 \partial \theta^2} + \frac{\partial^4 w}{\partial \theta^4} \right) \\ + \frac{1}{J} \left( N_{x0} \frac{\partial^2 w}{\gamma_1^2 \partial x^2} + 2N_{x\theta 0} \frac{\partial^2 w}{\gamma_1 \partial x \partial \theta} + N_{\theta 0} \frac{\partial^2 w}{\partial \theta^2} \right) = \bar{p} \frac{\partial^2 w}{\partial t^2} - \bar{q}_z \end{aligned} \quad 7.53c$$

where  $(u, v, w) = (u_0, v_0, w_0)/h$  with  $u_0, v_0, w_0$  being the displacements of the shell middle surface in the  $x$ -,  $\theta$ -, and  $z$ -directions, respectively, and  $h$  is the shell thickness. For the demonstrative purpose, assume that the external loads  $\bar{q}_x, \bar{q}_\theta, \bar{q}_z$  are symmetric with respect to  $\theta = 0$ . Thus, the Fourier series of the shell displacements become

$$\begin{Bmatrix} u \\ v \\ w \end{Bmatrix} = \sum_{n=0}^{\infty} \begin{Bmatrix} u_n(x, t) \cos n\theta \\ v_n(x, t) \cos n\theta \\ w_n(x, t) \cos n\theta \end{Bmatrix} \quad 7.54$$

It follows that the state vector  $\eta_n$  and the matrix  $F_n(s)$  in Eq. (7.52a) are of the form

$$\eta_n(x, s) = (\tilde{u}_n \quad \tilde{u}'_n \quad \tilde{v}_n \quad \tilde{v}'_n \quad \tilde{w}_n \quad \tilde{w}'_n \quad \tilde{w}''_n \quad \tilde{w}'''_n)^T \quad 7.55a$$

$$F_n(s) = \begin{bmatrix} F_{11} & F_{12} \\ F_{21} & F_{22} \end{bmatrix} \quad 7.55b$$

with

$$F_{11} = \begin{bmatrix} 0 & 1 & 0 & 0 \\ \gamma_1^2 \left( \frac{1-v}{2} n^2 + s^2 \bar{\rho} \right) & 0 & 0 & -\frac{1+v}{2} n \gamma_1 \\ 0 & 0 & 0 & 1 \\ 0 & \gamma_1 n \frac{1+v}{1-v} & \frac{2n^2 \gamma_1^2}{1-v} + \frac{2\bar{\rho}s^2 \gamma_1^2}{1-v} & 0 \end{bmatrix}$$

$$F_{12} = \begin{bmatrix} 0 & 0 & 0 & 0 \\ 0 & v\gamma_1 & 0 & 0 \\ 0 & 0 & 0 & 0 \\ -\frac{2n\gamma_1^2}{1-v} & 0 & 0 & 0 \end{bmatrix}, \quad F_{21} = \begin{bmatrix} 0 & 0 & 0 & 0 \\ 0 & 0 & 0 & 0 \\ 0 & 0 & 0 & 0 \\ 0 & \gamma_1^3 \frac{v}{k} & \frac{n\gamma_1^4}{k} & 0 \end{bmatrix}$$

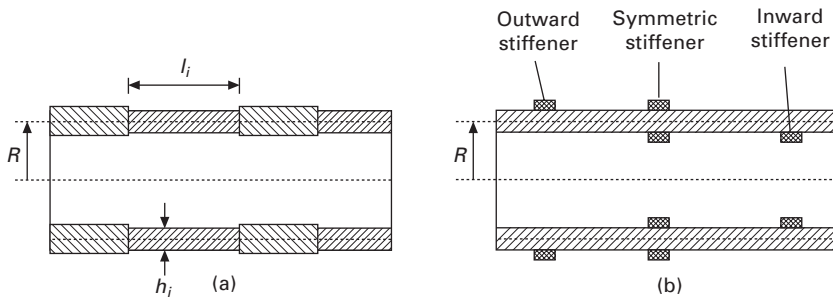
$$F_{22} = \begin{bmatrix} 0 & 1 & 0 & 0 \\ 0 & 0 & 1 & 0 \\ 0 & 0 & 0 & 1 \\ -\gamma_1^4 \left( \frac{1}{k} + n^4 + \frac{\bar{\rho}}{k} s^2 \right) - \frac{n^2 \gamma_1^4 N_{\theta 0}}{kJ} & -\frac{2n\gamma_1^3 N_{x\theta 0}}{kJ} & 2n^2 \gamma_1^2 + \frac{\gamma_1^2 N_{x0}}{kJ} & 0 \end{bmatrix}$$

where the tilde denotes Laplace transformation, and  $(\cdot)' = \partial(\cdot)/\partial x$ . The boundary condition (7.52b) can also be derived through use of the state vector.

With the spatial state formulation (7.52), the distributed transfer functions of the shell are given by Eq. (7.15). This eventually leads to exact analytical solutions about the static and dynamic response of cylindrical shells under arbitrary boundary conditions (Zhou and Yang, 1995; Yang and Zhou, 1998).

#### 7.4.5 Stepped and stiffened cylindrical shells

Because of its multi-body synthesis capability, the FS-DTFM can be applied to stepped cylindrical shells (Fig. 7.14a) and ring-stiffened cylindrical shells (Fig. 7.14b). The key in modeling and analysis of such a shell is to divide the structure into a number of shell elements. The dynamic response of each shell segment can be expressed by distributed transfer functions. Following Section 7.2.4, the structure is assembled from the shell segments, ring stiffeners (for stiffened shells), which produces a global dynamic equilibrium equation. The solution of the global dynamic equilibrium equation yields the dynamic response of the shell structure in exact and closed form (Zhou and Yang, 1995; Yang and Zhou, 1995).



7.14 Stepped and stiffened cylindrical shells: (a) stepped shell; (b) ring-stiffened shell.

Two examples demonstrating the FS-DTFM synthesis are given below, in which the Donnell–Mushtari shell model is used.

*Example 1. A stepped cylindrical shell of three shell segments (Fig. 7.14a)*

A stepped shell of radius  $R = 100$  is composed of three shell segments:

- Segment 1:  $l_1 = 40$ ,  $h_1 = 1$
- Segment 2:  $l_2 = 20$ ,  $h_2 = 3$
- Segment 3:  $l_3 = 40$ ,  $h_3 = 1$

where  $l_i$  and  $h_i$  are the length and thickness of the  $i$ th segment. All the segments are made of the same elastic material with Young's modulus  $E = 100$  and Poisson's ratio  $\nu = 0.3$ . In this example non-dimensional shell parameters are used. Table 7.6 lists the natural frequencies  $\omega_{mn}$  of the shell under five different boundary conditions, where  $m$  and  $n$  are the wave numbers of the shell in the longitudinal and circumferential directions, respectively. The boundary conditions are given below:

- (SS1) Simply supported boundary conditions:

$$w^{(1)} = M_x^{(1)} = u^{(1)} = v^{(1)} = 0 \quad \text{at } x = 0$$

$$w^{(3)} = M_x^{(3)} = u^{(3)} = v^{(3)} = 0 \quad \text{at } x = 100$$

- (SS2) Simply supported boundary conditions:

$$w^{(1)} = M_x^{(1)} = u^{(1)} = N_{x\theta}^{(1)} = 0 \quad \text{at } x = 0$$

$$w^{(3)} = M_x^{(3)} = u^{(3)} = N_{x\theta}^{(3)} = 0 \quad \text{at } x = 100$$

- (SS3) Simply supported boundary conditions:

$$w^{(1)} = M_x^{(1)} = N_x^{(1)} = v^{(1)} = 0 \quad \text{at } x = 0$$

$$w^{(3)} = M_x^{(3)} = N_x^{(3)} = v^{(3)} = 0 \quad \text{at } x = 100$$

Table 7.6 Natural frequencies  $\omega_{mn}$  of the stepped cylindrical shell under various boundary conditions ( $m$  = longitudinal wave number,  $n$  = circumferential wave number)\*

$m$	SS1 ( $n = 5$ )	SS2 ( $n = 2$ )	SS3 ( $n = 5$ )	CC1 ( $n = 5$ )	FF1 ( $n = 2$ )
1	0.032 61	0.020 81	0.029 44	0.033 43	0.002 16
2	0.071 15	0.081 37	0.071 15	0.074 77	0.003 81
3	0.084 72	0.093 74	0.084 71	0.090 46	0.085 57
4	0.111 16	0.108 85	0.111 11	0.118 69	0.099 53
5	0.136 65	0.136 30	0.136 60	0.152 41	0.104 82
6	0.157 53	0.150 88	0.157 20	0.173 42	0.107 37
7	0.219 64	0.209 34	0.219 60	0.244 89	0.118 03
8	0.242 58	0.213 27	0.242 55	0.269 96	0.153 12
9	0.323 88	0.232 86	0.282 63	0.323 90	0.169 13
10	0.333 56	0.236 43	0.333 58	0.364 26	0.219 01

\*Results from Zhou and Yang (1995).

- (CC1) Clamped–clamped boundary conditions:

$$w^{(1)} = w_{,x}^{(1)} = u^{(1)} = v^{(1)} = 0 \quad \text{at } x = 0$$

$$w^{(3)} = w_{,x}^{(3)} = u^{(3)} = v^{(3)} = 0 \quad \text{at } x = 100$$

- (FF1) Free-free boundary conditions

$$Q_x^{(1)} = M_x^{(1)} = N_x^{(1)} = N_{x\theta}^{(1)} = 0 \quad \text{at } x = 0$$

$$Q_x^{(3)} = M_x^{(3)} = N_x^{(3)} = N_{x\theta}^{(3)} = 0 \quad \text{at } x = 100$$

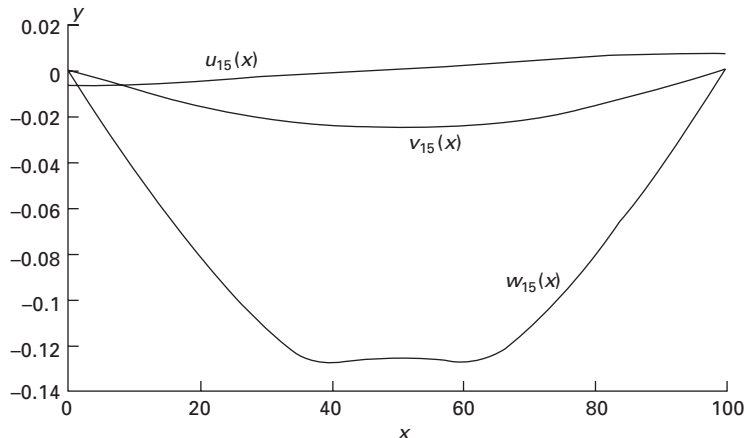
where  $u^{(i)}$ ,  $v^{(i)}$  and  $w^{(i)}$  are the displacements of the  $i$ th shell segment, and  $M_x^{(i)}$ ,  $N_x^{(i)}$  etc. are the internal forces of the segment. The results in the table are the exact solutions obtained via the FS-DTFM (Zhou and Yang, 1995). Furthermore, Figs 7.15 and 7.16 plot the mode shapes of the shell with simply supported boundaries of type SS3, where the eigenfunctions  $u_{mn}(x)$ ,  $v_{mn}(x)$ ,  $w_{mn}(x)$  are associated with the natural frequency  $\omega_{mn}$ .

#### Example 2. A cylindrical shell with ring stiffeners (Fig. 7.14b)

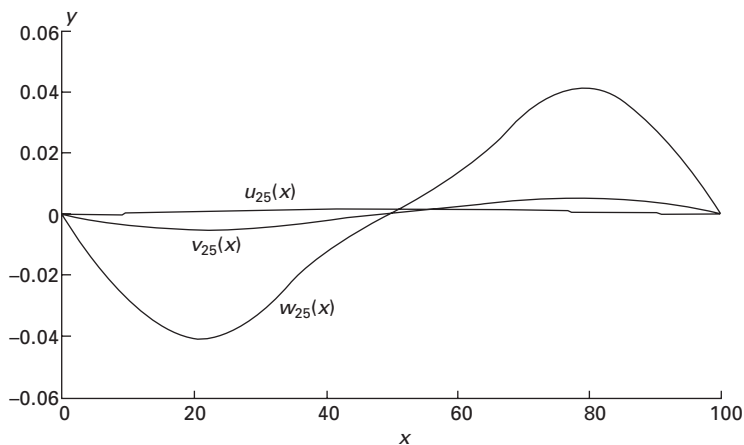
A homogeneous cylindrical shell is stiffened by  $N^r$  identical rings that are equally spaced along the shell longitudinal direction and symmetrically placed with respect to the middle surface of the shell. The shell is simply supported ( $N_x = v = w = M_x = 0$ ) at both ends. The nondimensional parameters of the shell and stiffeners are chosen as follows:

- Shell:  $R = L = 100$ ,  $h = 1$ ,  $E = 10^4$ ,  $\nu = 0.3$
- Rings:  $b_r = 1$ ,  $h_r = 2$ ,  $E_r = 10^4$ ,  $\nu_r = 0.3$

where  $R$ ,  $L$ ,  $h$ ,  $E$  and  $\nu$  are the radius, length, thickness, Young's modulus and Poisson's ratio of the shell, respectively; and  $b_r$ ,  $h_r$ ,  $E_r$ ,  $\nu_r$  are the width,



7.15 The mode shapes of the stepped shell (simply supported SS3):  $\omega_{15} = 0.029\ 44$  (from Yang and Zhou, 1995).



7.16 The mode shapes of the stepped shell (simply supported SS3):  $\omega_{25} = 0.071\ 15$  (from Yang and Zhou, 1995).

height, Young's modulus and Poisson's ratio of the rings, respectively. The fundamental frequency (lowest natural frequency) of the stiffened shell is computed by the FS-DTFM, the finite element method, and an orthotropic approximation that smears the tension and bending stiffness of the rings on the shell. Because symmetric stiffeners are used, the FS-DTFM treats the stiffened shell as a stepped shell. The computed results (Yang and Zhou, 1995) are listed in Table 7.7, where the integer in the brackets is the circumferential wave number  $n$ . As can be seen, the FS-DTFM prediction is in good agreement with that by the FEM. The orthotropic approximation gives a lower estimation of the fundamental frequency as the number stiffeners increases.

Table 7.7 The fundamental frequency of the cylindrical shell with symmetric stiffeners

N <sup>r</sup>	FS-DTFM*	FEM	Orthotropic approximation
1	0.2571 (7)	0.2542 (7)	0.2497 (7)
2	0.2631 (6)	0.2606 (6)	0.2570 (7)
3	0.2676 (6)	0.2650 (6)	0.2603 (6)
4	0.2720 (6)	0.2692 (6)	0.2627 (6)
5	0.2762 (6)	0.2733(6)	0.2650 (6)
6	0.2804 (6)	0.2772 (6)	0.2672 (6)

\* Results from Yang and Zhou (1995).

#### 7.4.6 Other plate and shell structures

Besides the previously mentioned plates and shells, the DTFM has also been applied to laminated cylindrical shells with arbitrary thickness (Zhou and Yang, 1996b), axially moving plates (Park, 1997), conical shells (Zhou and Lei, 1998), and thick plates described by three-dimensional elasticity theory (Park and Yang, 2001). In modeling these structures, a closed-form distributed transfer function formulation is always maintained in one coordinate direction while function expansion or polynomial interpolation is applied in other direction(s). This methodology, as shown in the previous sections, delivers highly accurate analytical or semi-analytical solutions.

### 7.5 Conclusions

The distributed transfer function method (DTFM) presented in this chapter provides new tools for modeling and analysis of a variety of flexible structures including plates and shells. The DTFM has the following special features.

- The DTFM is capable of dealing with multi-body regions, and at the same time delivers highly accurate analytical or semi-analytical solutions, as has been shown in many examples in this chapter. This synthesis capability renders the DTFM applicable to many problems defined in complex domains.
- By providing exact analytical solutions at least in one coordinate direction, the DTFM is much more accurate than the FEM and series solution methods, especially in predicting high-gradient stresses and high-frequency dynamics. Also, the closed form formulation of the DTFM significantly reduces the number of unknowns to be determined.
- Compared with series solution methods, the DTFM is more accurate and efficient in describing the effects of concentrated loads, pointwise constraints, and abrupt changes in geometric and material properties.

- The DTFM treats various models of plates and shells, different geometric and physical properties, and general loads and boundary conditions in a systematic and compact spatial state form. This makes the method convenient in symbolic computation and numerical simulation.

Although only free vibration examples are given in this chapter, the DTFM is certainly applicable to other dynamic problems, including frequency response, transient (time) response, dynamic response due to impact loads, and wave propagation in plates and shells.

The DTFM presented in this chapter is readily applicable to many other plate and shell structures, such as folded plate structures, spinning cylindrical shells, rotating shaft with mounted flexible disks, and plates and shells laminated with viscoelastic damping and piezoelectric layers. The DTFM is naturally useful for feedback control of plate and shell structures. In addition, the DTFM can be extended to plates and shells coupled with thermal, acoustic, hydrodynamic, and electro-magnetic effects.

Besides the four types of the DTFM, reduction of a multidimensional problem to a one-dimensional problem can also be realized by other approaches such as modal expansion, Galerkin method, weight residual method, and boundary integral method. These different strategies will lead to new types of distributed transfer function methods that offer accuracy, efficiency, and flexibility in engineering analysis.

## 7.6 Acknowledgments

The main results presented in this chapter are from the author's previous research partially sponsored by the National Science Foundation, the US Army Research Office, and NASA's Jet Propulsion Laboratory.

## 7.7 References

- Butkoviskiy, A.G., 1983, *Structure Theory of Distributed Systems*, John Wiley & Sons, New York.
- Cheung, Y.K., 1976, *Finite Strip Method in Structural Analysis*, Pergamon Press, Oxford, UK.
- Donnell, L.H., 1976, *Beams, Plates, and Shells*, McGraw-Hill, New York.
- Fang, H., and Yang, B., 1998, 'Modeling, synthesis and dynamic analysis of complex flexible rotor systems,' *Journal of Sound and Vibration*, Vol. 211, No. 4, pp. 571–592.
- Flügge, W., 1957, *Statik und Dynamik der Schalen*, Springer-Verlag, Berlin.
- Geannakakes, G.N., 1990, 'Vibration analysis of arbitrarily shaped plates using beam characteristic orthogonal polynomials in the semi-analytical finite strip method,' *Journal of Sound and Vibration*, Vol. 137, No. 2, pp. 283–303.
- Kardestuncer, H., and Norrie, D.H., 1987, *Finite Element Handbook*, McGraw-Hill Book Company, New York.

- Kim, C.S., and Dickinson, S.M., 1992, 'The free flexural vibration of isotropic and orthotropic general triangular shaped plates,' *Journal of Sound and Vibration*, Vol. 152, No. 3, pp. 383–403.
- Leissa, A.W., 1973, *Vibration of Shells*, NASA SP-288, US Government Printing Office, Washington, DC.
- Liew, K.M., and Lam, K.Y., 1991, 'A set of orthogonal plate functions for vibration analysis of regular polygonal plates,' *ASME Journal of Vibration and Acoustics*, Vol. 113, pp. 182–186.
- Markus, S., 1989, *The Mechanics of Vibrations of Cylindrical Shells*, Elsevier, Amsterdam.
- Meirovitch, L., 1967, *Analytical Methods in Vibrations*, Macmillan Company, London.
- Meirovitch, L., 1980, *Computational Methods in Structural Dynamics*, Sijthoff & Noordhoff, Rockville, MD.
- Park, D.-H., 1997, *Distributed Transfer Function Analysis of Complex Linear Elastic Continua*, Ph.D. Dissertation, University of Southern California, Los Angeles, California.
- Park, D.-H., and Yang, B., 2001, 'Static and vibration analyses of prismatic elastic multi-body solids,' *International Journal of Structures and Structural Dynamics*, Vol. 14, No. 1, pp. 154–162.
- Saliba, H.T., 1986, 'Free vibration analysis of simply supported symmetrical trapezoidal plates,' *Journal of Sound and Vibration*, Vol. 110, pp. 87–97.
- Soedel, W., 1993, *Vibration of Shells and Plates*, Marcel Dekker, New York.
- Timoshenko, S.P., 1940, *Theory of Plates and Shells*, McGraw-Hill, New York.
- Yang, B., 1992, 'Transfer functions of constrained/combined one-dimensional continuous dynamic systems,' *Journal of Sound and Vibration*, Vol. 156, No. 3, pp. 425–443.
- Yang, B., 1994, 'Distributed transfer function analysis of complex distributed systems,' *ASME Journal of Applied Mechanics*, Vol. 61, No. 1, pp. 84–92.
- Yang, B., 1995, 'A transfer function method for modeling and control of gyroscopic dynamic systems,' in *Wave Motion, Intelligent Structures and Nonlinear Mechanics*, edited by Guran, A., and Inman, D.J., World Scientific Publishing Company, New Jersey, pp. 135–162.
- Yang, B., 2005, *Stress, Strain, and Structural Dynamics – An Interactive Handbook of Formulas, Solutions, and MATLAB Toolboxes*, Academic Press, Boston.
- Yang, B., and Fang, H., 1994, 'Transfer function formulation of non-uniformly distributed parameter systems,' *ASME Journal of Vibration and Acoustics*, Vol. 116, No. 4, pp. 426–432.
- Yang, B., and Mote, C.D., Jr., 1991, 'Frequency-domain vibration control of distributed gyroscopic systems,' *ASME Journal of Dynamic Systems, Measurement and Control*, Vol. 113, No. 1, pp. 18–25.
- Yang, B., and Park, D.-H., 1999, 'Analysis of plates with curved boundaries using isoparametric strip distributed transfer functions,' *International Journal of Numerical Methods in Engineering*, Vol. 44, pp. 131–146.
- Yang, B., and Park, D.-H., 2003, 'Exact buckling analysis of constrained stepped columns,' *International Journal of Structural Stability and Dynamics*, Vol. 3, No. 2, pp. 143–167.
- Yang, B., and Tan, C.A., 1992, 'Transfer functions of one dimensional distributed parameter systems,' *ASME Journal of Applied Mechanics*, Vol. 59, No. 4, pp. 1009–1014.
- Yang, B., and Wu, X., 1997, 'Transient response of one-dimensional distributed systems: a closed-form eigenfunction expansion realization,' *Journal of Sound and Vibration*, Vol. 208, No. 5, pp. 763–776.

- Yang, B., and Zhou, J., 1995, 'Analysis of ring-stiffened cylindrical shells,' *ASME Journal of Applied Mechanics*, Vol. 62, No. 4, pp. 1005–1014.
- Yang, B., and Zhou, J., 1996, 'Semi-analytical solution of 2-D elasticity problems by the strip distributed transfer function method,' *International Journal of Solid and Structures*, Vol. 33, No. 27, pp. 3983–4005.
- Yang, B., and Zhou, J., 1997, 'Strip distributed transfer function analysis of circular and sectorial plates,' *Journal of Sound and Vibration*, Vol. 201, No. 5, pp. 641–647.
- Yang, B., and Zhou, J., 1998, 'Distributed transfer function analysis of stepped and ring-stiffened cylindrical shells,' Chapter 6 in *Dynamics and Control of Distributed Systems*, edited by Tzou, H.S. and Bergman, L.A., Cambridge University Press, pp. 264–303.
- Yang, B., Ding, H., Fang, H., and Lou, M., 2005, 'Modeling and vibration analysis of deployable space boom structures,' *Proceedings of ASME 2005 International Design Engineering Technical Conferences & Computers and Information in Engineering Conference*, September 24–28, Long Beach, California. Paper No. DETC2005-84519.
- Zhou, J., and Lei, Y., 1998, 'Asymptotic transfer function analysis of conical shells,' *AIAA Journal*, Vol. 36, No. 5, pp. 848–854.
- Zhou, J., and Yang, B., 1995, 'A distributed transfer function method for analysis of cylindrical shells,' *AIAA Journal*, Vol. 33, No. 9, pp. 1698–1708.
- Zhou, J., and Yang, B., 1996a, 'Strip distributed transfer function method for the analysis of plates,' *International Journal of Numerical Methods in Engineering*, Vol. 39, No. 11, pp. 1915–1932.
- Zhou, J., and Yang, B., 1996b, 'Three-dimensional stress analysis of thick laminated composite cylindrical shells and panels,' *AIAA Journal*, Vol. 34, No. 9, September, pp. 1960–1964.
- Zienkiewicz, O.C., and Taylor, R.L., 1989, *The Finite Element Method*, McGraw-Hill, New York.

## Vibrations of plates with abrupt changes in properties

---

Y X I A N G, University of Western Sydney, Australia

### 8.1 Introduction

Plates are important structural components, widely used in all branches of engineering, i.e. aerospace, marine, mechanical, biomedical and civil engineering. Extensive studies have been carried out on the vibration behaviour of plates by many researchers over the last 100 years because of the vital importance of vibration in designing plate-type structures. Vibration of plates with different shapes, boundary conditions and materials and subjected to various in-plane load distributions has been studied and the results documented in monographs (Leissa 1993, Liew *et al.* 1998), texts (Gorman 1999, Reddy 2003) and technical papers (Young 1950, Leissa 1973, Wang 1997, Shu and Wang 1997, Zhao *et al.* 2002, Xiang and Zhang 2005).

Different analytical and numerical methods have been developed in the past few decades in studying the vibration behaviour of plates. Among a wide range of numerical methods, the finite element method (Hinton and Owen 1984, Petyt 1998), the finite strip method (Cheung 1976, Hinton and Rao 1993, Cheung *et al.* 2000) and the Ritz method (Liew *et al.* 1998, Bhat 1987, Liew and Lam 1990, Dawe and Wang 1993) are three of the most popular numerical approaches employed by many researchers. These numerical methods provide accurate approximate solutions for vibration of plates under various complications/conditions.

Analytical methods, especially the methods that can generate closed form or exact solutions for vibration of plates, play an important role in providing benchmark values for engineers and researchers in designing and analysing plate structures. The Levy approach, which is one of the available analytical methods, can obtain exact solutions for a special class of rectangular plates having two opposite simply supported edges while the other two edges may take any combination of free, simply supported and clamped edges (Khdeir 1988, Chen and Liu 1990, Liew *et al.* 1996). In conjunction with the domain decomposition method and the state-space technique, the Levy approach can be effectively used to study plates with abrupt changes in the geometry and

supports (Xiang and Wang 2002, Wang and Xiang 2002, Xiang *et al.* 2002). In this chapter, the Levy solution method in association with the domain decomposition method and the state-space technique is first presented for a general rectangular plate problem with abrupt changes in properties. Next, exact vibration solutions for some plate problems with an abrupt change in plate thickness (stepped plates), in shear force (multi-span plates) and in slope (hinged plates) are presented. Such benchmark exact solutions should be useful to researchers who develop numerical model and software for plate analysis.

## 8.2 Mathematical modelling

### 8.2.1 Problem definition and governing differential equation

Figure 8.1 shows an isotropic, elastic rectangular plate of length  $aL$  and width  $L$ . The plate consists of  $n$  segments along the  $x$  direction. At the interfaces of the segments, an abrupt change of the properties of the plate may occur, i.e. step thickness variations, intermediate line supports or internal line hinges. The plate is assumed to be simply supported at the edges  $y = 0$  and  $y = L$ , respectively. The vibration behaviour of such a rectangular plate is considered in this chapter.

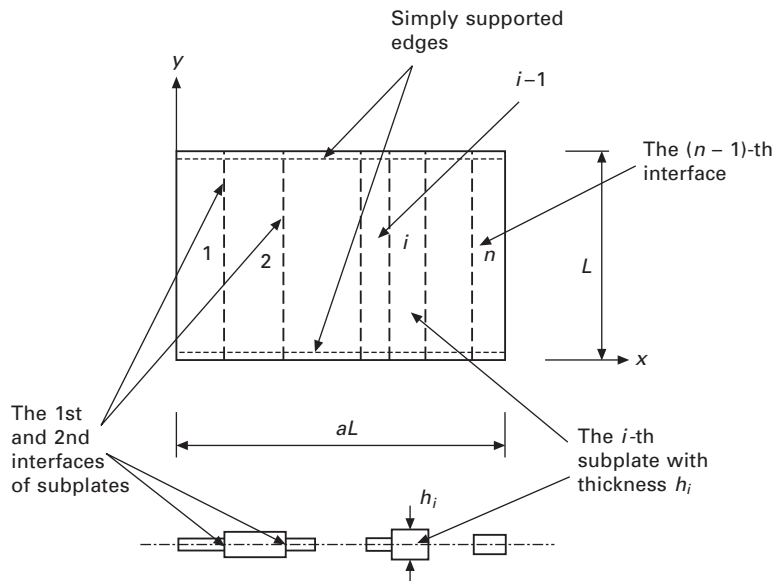
Employing the classical thin plate theory, the governing partial differential equation for the  $i$ th segment of the plate can be expressed as (Leissa 1993):

$$D_i \left( \frac{\partial^4 w_i}{\partial x^4} + 2 \frac{\partial^4 w_i}{\partial^2 x \partial^2 y} + \frac{\partial^4 w_i}{\partial y^4} \right) - \rho h_i \omega^2 w_i = 0, \quad i = 1, 2, \dots, n \quad 8.1$$

where  $x$  and  $y$  are the rectangular Cartesian coordinates,  $w_i(x, y)$  the transverse displacement at the mid-surface of the segment,  $D_i = E_i h_i^3 [12(1 - \nu_i^2)]$  the flexural rigidity,  $E_i$  the modulus of elasticity,  $\nu_i$  the Poisson ratio,  $h_i$  the thickness,  $\rho$  the mass density of the plate, and  $\omega$  the angular frequency of vibration.

### 8.2.2 Levy solution procedure and state-space technique

The Levy solution method and the state-space technique (Xiang and Wang 2002, Wang and Xiang 2002, Xiang *et al.* 2002) are used in this chapter to derive the exact vibration solutions for rectangular plates with abrupt changes of properties. The prescribed simply supported conditions at edges  $y = 0$  and  $y = b$  lead to the following conditions being satisfied:



8.1 Geometry and coordinate system for a multi-segment rectangular plate.

$$w_i = 0$$

8.2

$$(M_y)_i = D_i \left( \frac{\partial^2 w_i}{\partial y^2} + \nu_i \frac{\partial^2 w_i}{\partial x^2} \right) = 0 \quad 8.3$$

where  $(M_y)_i$  is the bending moment along the edges. Using the Levy solution method, the transverse displacement  $w_i(x, y)$  can be expressed as:

$$w_i(x, y) = \sin\left(\frac{m\pi}{L}y\right) X_i(x), \quad i = 1, 2, \dots, n \quad 8.4$$

where  $m$  is the number of half waves of the vibration mode in the  $y$  direction and  $X_i(x)$  is an unknown function to be determined by applying the boundary and interface conditions of the plate.

Substituting Eq. (8.4) into Eq. (8.1) and utilizing the state-space technique, a homogeneous differential equation system for the  $i$ th segment is derived:

$$\Psi'_i - \mathbf{H}_i \Psi_i = 0, \quad i = 1, 2, \dots, n \quad 8.5$$

in which the prime (') denotes differentiation with respect to  $x$ ,

$$\Psi_i = \begin{Bmatrix} X_i \\ X'_i \\ X''_i \\ X'''_i \end{Bmatrix} \quad 8.6$$

and  $\mathbf{H}_i$  is a  $4 \times 4$  matrix with the following non-zero elements

$$(H_{12})_i = 1 \quad 8.7$$

$$(H_{23})_i = 1 \quad 8.8$$

$$(H_{34})_i = 1 \quad 8.9$$

$$(H_{41})_i = -\left(\frac{m\pi}{L}\right)^4 + \frac{\rho h_i \omega^2}{D_i} \quad 8.10$$

$$(H_{43})_i = 2\left(\frac{m\pi}{L}\right)^2 \quad 8.11$$

The general solution of the homogeneous differential equation system Eq. (8.5) can be expressed as (Braun 1993):

$$\Psi_i = e^{\mathbf{H}_i x} \mathbf{c}_i \quad 8.12$$

where  $\mathbf{c}_i$  is a  $4 \times 1$  constant column matrix that is to be determined using the boundary and interface conditions of the plate, and  $e^{\mathbf{H}_i x}$  is a general matrix solution of Eq. (8.5) which can be determined by

$$e^{\mathbf{H}_i x} = \mathbf{Z}(x) \mathbf{Z}^{-1}(0) \quad 8.13$$

in which  $\mathbf{Z}(x)$  is a fundamental matrix solution of Eq. (8.5) and  $\mathbf{Z}^{-1}(0)$  is the inverse of matrix  $\mathbf{Z}(x)$  with the variable  $x = 0$ . Based on the solutions of the eigenvalues of matrix  $\mathbf{H}_i$ , the fundamental matrix solution of Eq. (8.5) can be expressed as follows:

- If all eigenvalues of  $\mathbf{H}_i$  are real and distinctive, i.e.  $r_1, r_2, r_3, r_4$  and the corresponding eigenvectors are  $\mathbf{s}_1, \mathbf{s}_2, \mathbf{s}_3, \mathbf{s}_4$ ,

$$\mathbf{Z}(x) = [\mathbf{Z}_1(x) \quad \mathbf{Z}_2(x) \quad \mathbf{Z}_3(x) \quad \mathbf{Z}_4(x)] \quad 8.14$$

where  $\mathbf{Z}_j(x) = e^{r_j x} \mathbf{s}_j$ ,  $j = 1, 2, 3, 4$ .

- If the matrix  $\mathbf{H}_i$  is of  $q$  (even number) real and distinctive eigenvalues and  $(4 - q)/2$  pairs of conjugate complex eigenvalues, the contribution of the real and distinctive eigenvalues and their corresponding eigenvectors to the fundamental solution of Eq. (8.5) is the same as the term  $\mathbf{Z}_j(x) = e^{r_j x} \mathbf{s}_j$  in Eq. (8.14). While for a pair of conjugate eigenvalues  $r_j = r_j^a + ir_j^b$  and  $r_{j+1} = r_j^a - ir_j^b$  with corresponding eigenvectors

$\mathbf{s}_j = \mathbf{s}_j^a + i\mathbf{s}_j^b$  and  $\mathbf{s}_{j+1} = \mathbf{s}_j^a - i\mathbf{s}_j^b$ , their contribution to the fundamental solution of Eq. (8.5) can be expressed as:

$$\mathbf{Z}_j(x) = e^{r_j^a x} (\mathbf{s}_j^a \cos r_j^b x - \mathbf{s}_j^b \sin r_j^b x) \quad 8.15$$

$$\mathbf{Z}_{j+1}(x) = e^{r_j^a x} (\mathbf{s}_j^a \sin r_j^b x + \mathbf{s}_j^b \cos r_j^b x) \quad 8.16$$

For other cases of eigenvalues of  $\mathbf{H}_i$  (such as repetitive eigenvalues), the formation of  $\mathbf{Z}(x)$  was discussed by Braun (1993). In this study, we have encountered only the two cases of eigenvalues of  $\mathbf{H}_i$  as discussed above.

To determine the constant column matrix  $\mathbf{c}_i$  in Eq. (8.12), the boundary conditions at edges  $x=0$  and  $aL$  and the interface conditions between segments are required. The boundary conditions at these two edges are as follows.

*For a simply supported edge*

$$w_i = 0 \quad 8.17$$

$$(M_x)_i = D_i \left( \frac{\partial^2 w_i}{\partial x^2} + \nu_i \frac{\partial^2 w_i}{\partial y^2} \right) = 0 \quad 8.18$$

*For a clamped edge*

$$w_i = 0 \quad 8.19$$

$$\frac{\partial w_i}{\partial x} = 0 \quad 8.20$$

*For a free edge*

$$(M_x)_i = D_i \left( \frac{\partial^2 w_i}{\partial x^2} + \nu_i \frac{\partial^2 w_i}{\partial y^2} \right) = 0 \quad 8.21$$

$$(V_x)_i = D_i \left( \frac{\partial^3 w_i}{\partial x^3} + (2 - \nu_i) \frac{\partial^3 w_i}{\partial x \partial y^2} \right) = 0 \quad 8.22$$

where  $(M_x)_i$  and  $(V_x)_i$  are the bending moment and the effective shear force along the edge, respectively.

The following interface conditions between the  $i$ th and  $(i+1)$ th segments must be satisfied depending on the case of the abrupt changes of properties:

*For plates with abrupt changes in plate thickness*

$$w_i = w_{i+1} \quad 8.23$$

$$\frac{\partial w_i}{\partial x} = \frac{\partial w_{i+1}}{\partial x} \quad 8.24$$

$$(M_x)_i = (M_x)_{i+1} \quad 8.25$$

$$(V_x)_i = (V_x)_{i+1} \quad 8.26$$

*For plates with abrupt changes in shear force due to the presence of an internal line support*

$$w_i = 0 \quad 8.27$$

$$w_{i+1} = 0 \quad 8.28$$

$$\frac{\partial w_i}{\partial x} = \frac{\partial w_{i+1}}{\partial x} \quad 8.29$$

$$(M_x)_i = (M_x)_{i+1} \quad 8.30$$

*For plates with abrupt changes in slope due to the presence of an intermediate line hinge:*

$$w_i = w_{i+1} \quad 8.31$$

$$(M_x)_i = 0 \quad 8.32$$

$$(M_x)_{i+1} = 0 \quad 8.33$$

$$(V_x)_i = (V_x)_{i+1} \quad 8.34$$

where  $(M_x)_i$ ,  $(M_x)_{i+1}$  and  $(V_x)_i$ ,  $(V_x)_{i+1}$  are the bending moments and effective shear forces at the interface for the  $i$ th and  $(i + 1)$ th segments, respectively.

Based on Eq. (8.12) and applying the boundary and interface conditions for a given case, a homogeneous system of equations can be formed when assembling the segments to form the entire plate

$$\mathbf{K}\{\mathbf{c}\} = \{\mathbf{0}\} \quad 8.35$$

where  $\mathbf{K}$  is a  $4n \times 4n$  matrix and  $\{\mathbf{c}\} = [\mathbf{c}_1^T \ \mathbf{c}_2^T \ \dots \ \mathbf{c}_n^T]^T$  is a  $4n \times 1$  constant column matrix. The angular frequency  $\omega$  is evaluated by setting the determinant of  $\mathbf{K}$  in Eq. (8.35) to be zero.

### 8.3 Case studies

The analytical method is applied to determine exact natural vibration frequencies for rectangular plates with abrupt changes in properties in the  $x$ -direction. The frequencies are expressed in terms of a nondimensional frequency parameter  $\Lambda = (\omega L^2 / \pi^2) \sqrt{\rho h_1 / D_1}$ , where  $h_1$  and  $D_1$  are the thickness and the flexural rigidity of the first segment, respectively.

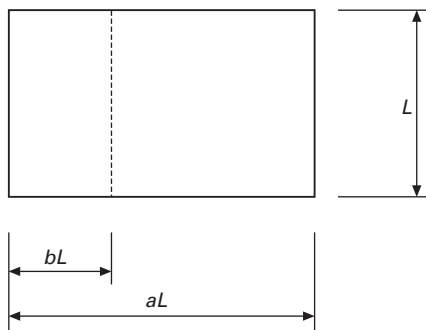
For simplicity and convenience the letters F, S and C are used to denote a free edge, a simply supported edge and a clamped edge at edges  $x = 0$  and  $aL$ , respectively. For example, an SF plate has the edge  $x = 0$  simply supported and edge  $x = aL$  free (see Fig. 8.1). The Poisson ratio  $\nu = 0.3$  is adopted for all cases in this chapter.

### 8.3.1 Rectangular plates with stepped thickness variations

The free vibration of rectangular plates with one-step thickness variation is first considered. The step segment location parameter  $b$  is defined in Fig. 8.2.

The correctness of the method for stepped plates is verified through a comparison study as shown in Table 8.1, where the step thickness ratio  $h_2/h_1 = 0.5$  is used in the calculation. The exact vibration solutions from the present method for one-step SS square and rectangular plates agree well with the results from Yuan and Dickinson (1992).

Table 8.2 presents the exact frequency parameters for one-step square plates. Six combinations of plate boundary conditions are considered and the step thickness ratio  $h_2/h_1 = 2.0$  is used in the calculation. These results can be used as benchmark values for researchers validating their numerical models for such plate vibration problems.



8.2 Rectangular plate with one-step thickness variation.

Table 8.1 Comparison of frequency parameters  $\Lambda$  for one-step SS rectangular plates ( $h_2/h_1 = 0.5$ )

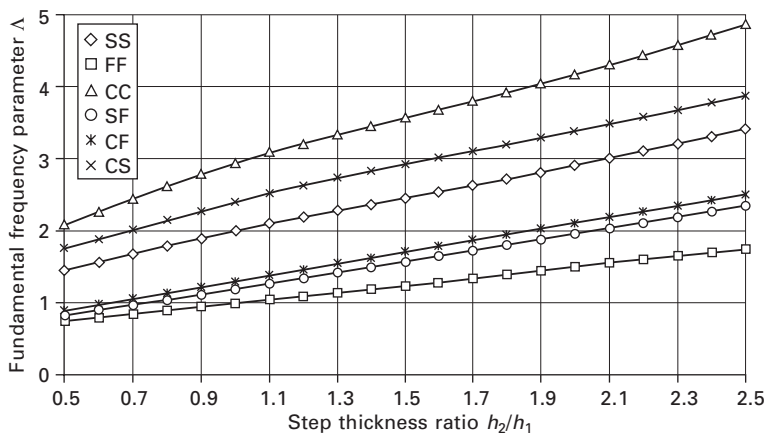
$a$	$b$	Source	Mode sequence			
			1	2	3	4
1	0.25	Present	1.29333	2.87182	2.89981	4.92248
		Yuan and Dickinson (1992)	1.29333	2.87183	2.89981	4.92249
2	0.5	Present	0.89787	1.40673	2.34063	2.50701
		Yuan and Dickinson (1992)	0.89787	1.40673	2.34063	2.50701

Table 8.2 Frequency parameters  $\Lambda$  for square plates with one-step thickness variation ( $h_2/h_1 = 2.0$ )

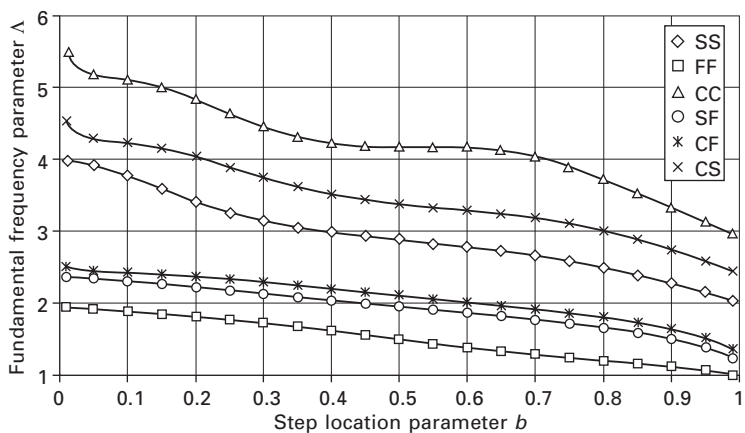
Mode	SS Plate $b$			FF Plate $b$			CC Plate $b$			SF Plate $b$			CF Plate $b$			CS Plate $b$		
	0.3	0.5	0.7	0.3	0.5	0.7	0.3	0.5	0.7	0.3	0.5	0.7	0.3	0.5	0.7	0.3	0.5	0.7
1	3.1452	2.9015	2.6709	1.7251	1.4928	1.2923	4.4503	4.1711	4.0439	2.1252	1.9604	1.7828	2.2938	2.1098	1.9208	3.7451	3.3789	3.1878
2	8.0892	7.1156	5.8447	2.9303	2.4441	2.1574	9.2716	8.0867	6.7397	4.4600	4.2453	3.6734	5.2187	4.9121	4.4271	8.9838	7.8593	6.5543
3	8.4235	7.183	6.0116	5.8006	4.7767	4.3934	11.032	9.9047	8.5478	7.7778	6.8394	5.8298	8.0045	7.294	6.2261	9.2329	8.724	6.9324
4	13.515	11.254	10.082	5.9243	5.1176	4.7678	15.992	13.276	11.568	10.115	8.5568	7.6000	10.780	9.8738	8.5783	14.638	12.509	10.922
5	16.511	12.864	11.088	8.3368	7.7109	6.8686	17.659	13.835	11.951	10.436	9.1223	8.1146	11.744	10.362	8.7032	17.580	13.814	11.538
6	16.536	13.785	12.032	11.133	9.7827	8.9592	21.712	18.045	15.440	16.211	12.850	11.066	17.219	13.78	11.504	19.067	15.439	14.007

Figure 8.3 shows the variation of the fundamental frequency parameter  $\Lambda$  versus the step thickness ratio  $h_2/h_1$  for a one-step square plate with various boundary conditions. The location of the step variation is at the centre of the plate ( $b = 0.5$ ). It is observed that for all cases shown in Fig. 8.3, the fundamental frequency parameter increases as the step thickness ratio varies from 0.5 to 2.5.

The variation of the fundamental frequency parameter  $\Lambda$  against the step location parameter  $b$  is presented in Fig. 8.4 for one-stepped square plates with six different combinations of boundary conditions. The step thickness ratio  $h_2/h_1$  is fixed at 2.0. The fundamental frequency parameter decreases



8.3 Fundamental frequency parameter  $\Lambda$  versus step thickness ratio  $h_2/h_1$  for one-stepped square plates ( $b = 0.5$ ).



8.4 Fundamental frequency parameter  $\Lambda$  versus step location parameter  $b$  for one-stepped square plates ( $h_2/h_1 = 2.0$ ).

for the considered cases when the step location parameter varies from 0.01 to 0.99.

The frequency parameters  $\Lambda$  for two-stepped rectangular plates are presented in Table 8.3. The plate aspect ratio  $a$  is set to be 2.0 and the locations of the two-step variations are at  $x = (1/3) aL$  and  $(2/3) aL$ , respectively. Two sets of thickness ratios are considered in the calculation.

### 8.3.2 Multi-span rectangular plates

The analytical method is also applied to obtain exact natural vibration frequencies for multi-span rectangular plates along the  $x$ -direction. For such plates, a number of intermediate line supports are placed on the plate to impose zero transverse displacement along the line supports. The plate is assumed to have a uniform thickness, i.e.  $h_1 = h_2 = \dots = h_n$ .

The results obtained by the current analytical method are first compared with the available solutions in the open literature. Table 8.4 shows that the present exact solutions agree well with the ones obtained by other researchers (Azimi *et al.* 1984, Liew and Lam 1991) for simply supported rectangular plates with aspect ratio  $a = 4$  and two intermediate line supports at  $x = (1/4) aL$  and  $(3/4) aL$ , respectively.

Table 8.5 presents exact frequency parameters for square plates with one intermediate line support. The location parameter of the line support  $b$  is similarly defined as for the stepped plates shown in Fig. 8.2. These results have important reference values for researchers in checking their numerical methods for such plate vibration problems.

Figures 8.5 and 8.6 present the relationship between the fundamental frequency parameters  $\Lambda$  and the location parameter  $b$  of the intermediate line

*Table 8.3 Frequency parameters  $\Lambda$  for rectangular plates with two-step thickness variations ( $a = 2.0$ , step locations at  $x = 1/3 aL$  and  $2/3 aL$ )*

$h_2/h_1$	$h_3/h_1$	Mode	Cases					
			SS	FF	CC	SF	CF	CS
1.5	1.0	1	1.5251	1.1505	1.6817	1.2078	1.2157	1.5917
		2	2.3348	1.3149	2.7880	1.7479	1.8649	2.5448
		3	3.7993	2.0503	4.6198	2.7461	2.9900	4.1727
		4	5.2516	3.1728	5.4526	4.3216	4.3218	5.3202
		5	5.6235	4.3018	6.0418	4.3412	4.7995	5.8644
		6	5.6469	4.3437	6.7528	5.3891	5.6010	6.1841
1.5	2.0	1	1.7758	1.2433	1.9823	1.6913	1.7783	1.9224
		2	2.9279	1.9031	3.4667	2.2798	2.4306	3.1995
		3	4.6643	2.6029	5.6303	3.5504	3.8911	5.2076
		4	5.4441	4.0619	5.7140	5.3758	5.7113	5.7129
		5	7.0846	4.3250	7.6432	5.4434	5.9659	7.6040
		6	7.3036	6.1626	8.3925	7.2191	7.4516	7.7276

Table 8.4 Comparison of frequency parameters  $\Lambda$  for rectangular plates with two intermediate line supports ( $a = 4$ , line supports at  $x = 1/4 aL$  and  $3/4 aL$ )

Cases	Source	Mode Sequence					
		1	2	3	4	5	6
SS	Present	1.3089	2.0000	2.1818	2.3959	3.5677	4.2798
	Azimi <i>et al.</i> (1984)	1.309	2.000	2.181	2.396	3.568	4.280
	Liew and Lam (1991)	1.3095	2.0000	2.1815	2.3965	3.5749	4.2812
CS	Present	1.3109	2.0362	2.2940	2.6848	3.6063	4.2800
	Azimi <i>et al.</i> (1984)	1.311	2.037	2.294	2.685	3.617	4.280
	Liew and Lam (1991)	1.3132	2.0380	2.3168	2.6864	3.6642	4.2845

support for square plates of various boundary conditions and with one intermediate line support. For SS, FF and CC square plates (see Fig. 8.5), the intermediate line support moves from the left edge to the centre of the plates. The fundamental frequency parameters for these cases increase as the line support moves from the edge to the centre of the plates. The maximum fundamental frequency parameters are obtained when the line support is at the centre of the plates.

For SF, CF and CS square plates (see Fig. 8.6), the intermediate line support moves from the left edge to the right edge. The optimal location of the line support to achieve maximum fundamental frequency parameters is as follows:  $b \approx 0.72$  for the SF square plate,  $b \approx 0.76$  for the CF square plate and  $b \approx 0.55$  for the CS square plate, respectively.

Table 8.6 presents exact frequency parameters  $\Lambda$  for square plates with two intermediate line supports. In this case, the line support location parameter is defined as shown in Fig. 8.7.

The frequency parameters for rectangular plates of aspect ratio  $a = 3$  and with two internal line supports at the locations  $x = (1/3) aL$  and  $(2/3) aL$  are shown in Table 8.7.

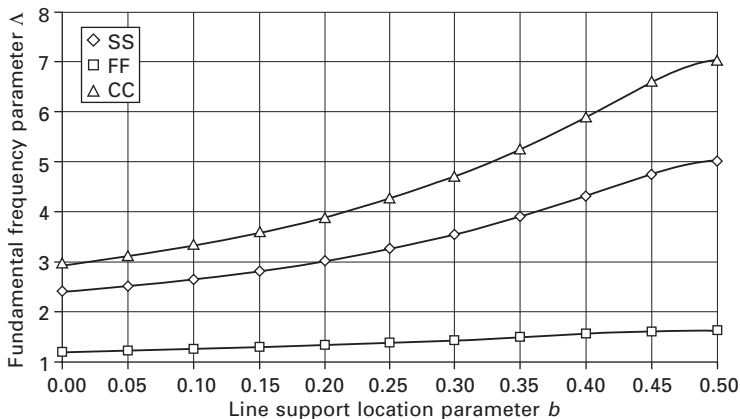
### 8.3.3 Rectangular plates with internal line hinges

Free vibration of plates with internal line hinges along the  $x$  direction is studied in this section by the current analytical method. The plate is assumed to have a uniform thickness, i.e.  $h_1 = h_2 = \dots = h_n$ .

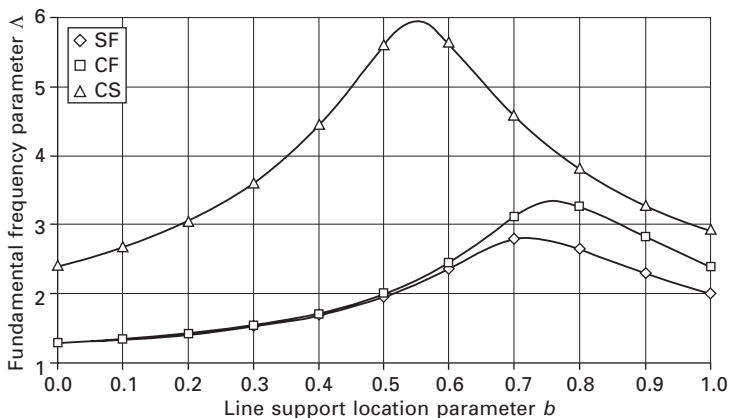
Table 8.8 presents a comparison study for the frequency parameters of SS square and rectangular plates with one internal line hinge at the middle of the plates. The results in Wang *et al.* (2001) were based on the Kirchhoff plate theory and were obtained by the Ritz method. The solutions in Xiang and

Table 8.5 Frequency parameter  $\lambda$  for square plates with one intermediate line support

Mode	SS Plate $b$			FF Plate $b$			CC Plate $b$			SF Plate $b$			CF Plate $b$			CS Plate $b$		
	0.1	0.3	0.5	0.1	0.3	0.5	0.1	0.3	0.5	0.3	0.5	0.7	0.3	0.5	0.7	0.3	0.5	0.7
1	2.6416	3.5358	5.0000	1.2475	1.429	1.6348	3.3229	4.6915	7.0243	1.5238	1.9605	2.7943	1.5393	1.9863	3.1213	3.598	5.5808	4.6003
2	5.4669	6.3655	7.0243	3.2688	3.3039	2.3117	5.8836	7.1588	9.5635	4.4575	4.919	4.294	4.4632	4.9292	5.1218	6.3948	8.4352	7.1152
3	6.7902	9.6986	8.0000	4.2412	4.4324	4.7356	8.1554	11.809	9.6621	5.0738	5.7249	5.9821	5.166	7.3117	6.2567	10.036	8.7318	11.437
4	9.5856	11.288	9.5835	6.5513	5.4957	5.142	10.652	12.06	11.733	8.3285	8.6411	7.0438	8.3854	9.8618	7.5642	11.281	10.991	11.791
5	10.382	12.650	13.000	7.4264	6.4975	7.6278	10.700	14.666	14.206	9.4027	9.1358	10.178	9.4049	9.9009	11.269	12.894	13.326	14.2
6	13.299	14.949	14.206	9.2109	8.6016	9.7309	15.286	18.609	15.842	11.708	9.8584	11.036	12.386	10.166	12.156	17.758	15.289	15.705



8.5 Fundamental frequency parameter  $\Lambda$  versus the line support location parameter  $b$  for SS, FF and CC square plates with one intermediate line support.



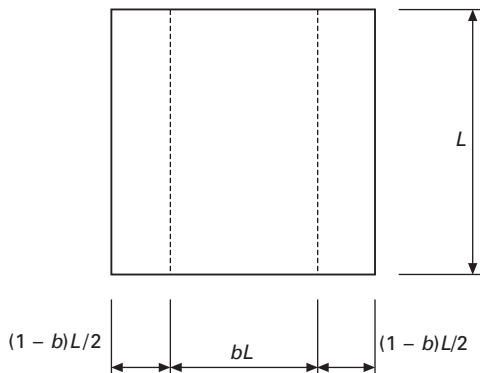
8.6 Fundamental frequency parameter  $\Lambda$  versus the line support location parameter  $b$  for SF, CF and CS square plates with one intermediate line support.

Reddy (2003) were obtained by the Levy solution method. However, the plate theory employed in the study presented in Xiang and Reddy (2003) is the Mindlin shear deformable plate theory with the plate thickness ratio  $h/L$  set to be 0.01. It is seen from Table 8.8 that the current analytical method can generate correct frequency parameters for the hinged plates. As expected, the results in Xiang and Reddy (2003) based on the Mindlin plate theory are slightly lower than the current ones based on the classical thin plate theory.

The exact frequency parameters for square plates of various boundary conditions and with one internal line hinge are presented in Table 8.9. The location parameter of the line hinge  $b$  is similarly defined as for the stepped

Table 8.6 Frequency parameter  $\lambda$  for square plates with two intermediate line supports

Mode	SS Plate $b$			FF Plate $b$			CC Plate $b$			SF Plate $b$			CF Plate $b$			CS Plate $b$		
	0.3	0.5	0.7	0.3	0.5	0.7	0.3	0.5	0.7	0.3	0.5	0.7	0.3	0.5	0.7	0.3	0.5	0.7
1	9.8286	7.0243	4.4387	2.8301	3.2179	13.020	7.3836	4.5727	3.0326	4.1137	3.7483	3.0393	4.138	3.7991	10.423	7.1996	4.505	
2	11.510	9.5835	6.9385	3.2408	4.7464	6.3846	15.658	9.8066	7.0263	5.9778	7.3558	6.6375	5.9798	7.3683	6.6745	13.276	9.6929	6.982
3	12.790	14.206	11.510	5.8661	7.0397	7.5149	16.262	14.325	11.681	10.472	7.7445	8.7311	10.889	7.9153	8.8037	14.687	14.265	11.656
4	14.143	17.000	11.630	6.0954	7.8022	10.636	18.401	19.568	11.827	10.888	10.188	11.494	13.234	10.295	11.517	17.068	17.885	11.667
5	17.745	20.000	14.143	10.825	8.3329	11.177	20.243	21.006	14.392	13.343	12.448	12.062	16.148	12.454	12.118	18.122	20.789	14.267
6	18.765	20.943	18.462	10.954	10.682	11.370	21.718	22.323	18.492	15.044	14.667	13.45	16.484	14.724	13.574	20.725	20.974	18.477



8.7 Square plate with two intermediate line supports.

Table 8.7 Frequency parameters  $\Lambda$  for rectangular plates with two intermediate line supports ( $a = 3$ , line supports at  $x = 1/3 aL$  and  $2/3 aL$ )

Cases	Mode sequence					
	1	2	3	4	5	6
SS	2.0000	2.1887	2.6343	5.0000	5.0000	5.1114
FF	1.2232	1.2392	2.3078	3.0319	3.2485	4.1962
CC	2.1887	2.6343	2.9333	5.1114	5.3778	5.4828
SF	1.231	2.0643	2.4859	3.1542	4.1982	5.0399
CF	1.2311	2.2389	2.7582	3.1751	4.1982	5.1516
CS	2.0492	2.3959	2.844	5.0288	5.1357	5.2357

Table 8.8 Comparison of frequency parameters  $\Lambda$  for SS square and rectangular plates with one internal line hinge ( $b = 0.5$ )

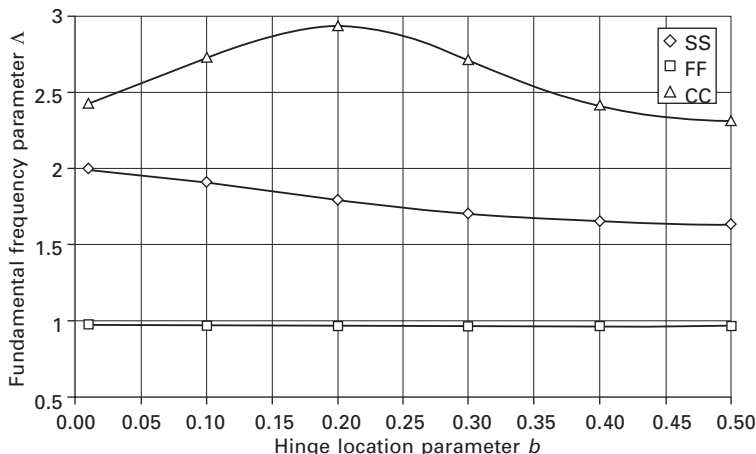
$a$	Source	Mode Sequence					
		1	2	3	4	5	6
1	Present	1.6348	4.7356	5.0000	7.6278	8.0000	9.7309
	Wang <i>et al.</i> (2001)	1.6348	4.7356	5.0000			
	Xiang and Reddy (2003)	1.6309	4.7253	4.9955	7.6042	7.9884	9.7036
2	Present	1.1839	2.0000	2.8123	4.1741	5.0000	5.0000
	Xiang and Reddy (2003)	1.1829	1.9993	2.8069	4.1689	4.9955	4.9955

plates shown in Fig. 8.2. As expected, the presence of the internal line hinge reduces the frequency parameters of the square plates when comparing with the corresponding plates without the line hinge.

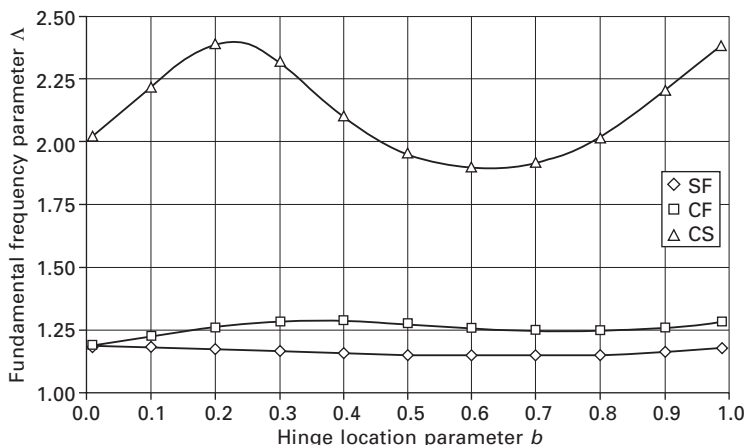
Figures 8.8 and 8.9 depict the variation of the fundamental frequency parameter  $\Lambda$  against the hinge location parameter  $b$  for square plates of

Table 8.9 Frequency parameter  $\Lambda$  for square plates with one internal line hinge

Mode	SS Plate $b$			FF Plate $b$			CC Plate $b$			SF Plate $b$			CF Plate $b$			CS Plate $b$		
	0.1	0.3	0.5	0.1	0.3	0.5	0.1	0.3	0.5	0.3	0.5	0.7	0.3	0.5	0.7	0.3	0.5	0.7
1	1.9068	1.7011	1.6348	0.9717	0.9657	0.9638	2.7225	2.7094	2.3117	1.1667	1.1508	1.1457	1.2711	1.2821	1.2452	2.3151	1.9505	1.9168
2	3.8317	3.3603	4.7356	1.5999	1.6082	1.6348	5.4899	5.3400	5.1420	2.1959	2.3098	2.7037	2.9810	2.5933	3.0133	4.6096	4.9190	4.9131
3	4.9614	4.8047	5.0000	3.7151	3.1910	2.7886	6.9264	5.4641	7.0243	4.1491	4.1169	4.0943	4.2158	4.1730	4.1394	5.1047	5.7249	4.9644
4	7.3600	7.2961	7.6278	3.9254	3.9061	3.9035	9.5633	8.4912	9.5835	5.3566	5.6963	4.4939	5.8402	5.9416	5.3390	7.7900	8.6411	7.9869
5	7.4952	9.7565	8.0000	4.6695	4.6893	4.7356	10.349	10.148	10.008	5.5633	5.8708	5.3801	6.0023	7.3044	6.3472	9.9974	9.1358	9.9212
6	9.9674	9.8062	9.7309	7.0963	5.7295	6.5392	13.046	12.258	10.109	8.9514	9.0680	8.5353	9.1577	9.1037	9.0514	10.313	9.8584	11.445



8.8 Fundamental frequency parameter  $\Lambda$  versus the hinge location parameter  $b$  for SS, FF and CC square plates with one internal line hinge.



8.9 Fundamental frequency parameter  $\Lambda$  versus the hinge location parameter  $b$  for SF, CF and CS square plates with one internal line hinge.

various boundary conditions and with one internal line hinge. It is observed that the optimal location of the hinge for maximizing the fundamental frequency is close to the edge for the SS, FF and SF square plates, at  $b \approx 0.2$  for the CC square plate and  $b \approx 0.36$  for the CF square plates, respectively. There are two optimal locations of the hinge for the CS square plate, i.e.  $b \approx 0.23$  or 0.99.

Table 8.10 presents frequency parameters for square plates with two internal line hinges. The hinge location parameter  $b$  is similarly defined as for square plates with two internal line supports shown in Fig. 8.7.

Table 8.10 Frequency parameters  $\Lambda$  for square plates with two internal line hinges

Mode	SS Plate $b$			FF Plate $b$			CC Plate $b$			SF Plate $b$			CF Plate $b$			CS Plate $b$		
	0.3	0.5	0.7	0.3	0.5	0.7	0.3	0.5	0.7	0.3	0.5	0.7	0.3	0.5	0.7	0.3	0.5	0.7
1	1.5761	1.6348	1.7588	0.9592	0.9603	0.9647	2.4258	2.8309	2.7929	1.1374	1.1405	1.1521	1.2453	1.2269	1.2075	1.8893	1.9540	2.0419
2	2.9956	2.7886	2.9856	1.5872	1.5566	1.5522	4.0344	4.7464	5.5433	2.1915	2.2201	2.3651	2.6873	3.1136	3.3098	3.6153	3.9818	4.2631
3	4.6450	4.7366	4.8655	3.2861	3.2862	3.2868	5.0914	5.3658	6.8340	3.6754	3.9001	4.1010	4.0423	4.1358	4.1458	4.8376	4.9769	5.1188
4	6.8044	6.5392	5.6522	3.8740	3.8780	3.8939	7.6671	7.8022	9.2605	4.0762	4.0810	4.4871	4.1336	4.5134	5.9289	7.2476	7.1969	7.7428
5	9.6151	7.6278	6.8044	4.0491	4.3343	4.5828	9.9026	8.9579	10.339	5.5575	5.5799	5.8934	6.1458	6.3251	9.7452	8.3410	8.5861	
6	9.8861	9.7309	9.8460	4.6668	4.6030	5.6465	12.862	10.114	10.433	8.0221	8.0726	6.7724	8.3343	8.6794	8.9762	10.622	9.8954	10.067

*Table 8.11 Frequency parameters  $\Lambda$  for rectangular plates with two internal line hinges ( $a = 3$ , line hinges at  $x = 1/3 aL$  and  $2/3 aL$ )*

Cases	Mode sequence					
	1	2	3	4	5	6
SS	1.0701	1.3364	2.0000	2.4614	3.1888	4.0478
FF	0.9759	1.0701	1.3364	1.6348	2.4614	3.1888
CC	1.1034	1.4195	2.2345	2.8540	3.4927	4.0634
SF	0.9997	1.1839	1.5147	2.1611	2.8123	3.5435
CF	1.0038	1.2133	1.5487	2.3362	3.0144	3.6291
CS	1.0850	1.3776	2.0919	2.6578	3.3648	4.0552

Finally, the frequency parameters for rectangular plates of aspect ratio  $a = 3$  and with two internal line hinges at the locations  $x = 1/3 (aL)$  and  $2/3 (aL)$  are shown in Table 8.11.

## 8.4 Conclusions

This chapter presents the Levy solution method in association with the domain decomposition method and the state-space technique for analysing the vibration of rectangular plates with abrupt changes in properties. Exact frequency parameters are obtained for Levy plates with stepped thickness variations, intermediate line supports and internal hinges along the  $x$  direction, respectively. The exact vibration solutions presented in this chapter can be used as design references as well as important benchmark values for engineers and researchers. The present method can also be applied to study the vibration of a Levy plate with different combinations of step variations, intermediate line supports or internal hinges within the same plate.

## 8.5 Acknowledgements

The author wishes to thank Professor C.M. Wang and Professor G.W. Wei for their contributions in solving part of the problems in this chapter.

## 8.6 References

- Azimi, S., Hamilton, J.F. and Soedel, W. (1984). ‘The receptance method applied to the free vibration of continuous rectangular plates,’ *Journal of Sound and Vibration*, **93**, 9–29.
- Bhat, R.B. (1987). ‘Flexural vibration of polygonal plates using characteristic orthogonal polynomials in 2 variables,’ *Journal of Sound and Vibration*, **114**, 65–71.
- Braun, M. (1993). *Differential Equations and Their Applications*, 4<sup>th</sup> edition, Springer, New York.
- Chen, W.C. and Liu, W.H. (1990). ‘Deflection and free vibrations of laminated plates – Levy-type solutions,’ *International Journal of Mechanical Sciences*, **32**, 779–793.

- Cheung, Y.K. (1976). *The Finite Strip Method in Structural Analysis*, Pergamon Press, Oxford.
- Cheung, Y.K., Au, F.T.K. and Zheng, D.Y. (2000). 'Finite strip method for the free vibration and buckling analysis of plates with abrupt changes in thickness and complex support conditions,' *Thin-walled Structures*, **36**, 89–110.
- Dawe, D.J. and Wang, S. (1993). 'Free vibration of generally laminated, shear deformable, composite rectangular plates using a spline Rayleigh–Ritz method,' *Composite Structures*, **25**, 77–87.
- Gorman, D.J. (1999). *Vibration Analysis of Plates by the Superposition Method*, World Scientific Publishing, Singapore.
- Hinton, E. and Owen, D.R.J. (1984). *Finite Element Software for Plates and Shells*, Pineridge Press, Swansea.
- Hinton, E. and Rao, N.V.R. (1993). 'Analysis and shape optimization of variable thickness prismatic folded plates and curved shells, 1. Finite strip formulation,' *Thin-walled Structures*, **17**, 81–111.
- Khdeir, A.A. (1988). 'Free vibration and buckling of symmetric cross-ply laminated plates by an exact method,' *Journal of Sound and Vibration*, **126**, 447–461.
- Leissa, A.W. (1973). 'The free vibration of rectangular plates,' *Journal of Sound and Vibration*, **31**, 257–293.
- Leissa, A.W. (1993). *Vibration of Plates*, edition by Acoustical Society of America (originally issued by NASA, 1969).
- Liew, K.M. and Lam, K.Y. (1990) 'Application of 2-dimensional orthogonal plate function to flexural vibration of skew plates,' *Journal of Sound and Vibration*, **139**, 241–252.
- Liew, K.M. and Lam, K.Y. (1991) 'Vibration analysis of multi-span plates having orthogonal straight edges,' *Journal of Sound and Vibration*, **147**, 255–264.
- Liew, K.M., Wang, C.M., Xiang, Y. and Kitipornchai, S. (1998). *Vibration of Mindlin Plates: Programming the p-Version Ritz Method*, Elsevier, Oxford.
- Liew, K.M., Xiang, Y. and Kitipornchai, S. (1996). 'Analytical buckling solutions for Mindlin plates involving free edges,' *International Journal of Mechanical Sciences*, **38**, 1127–1138.
- Petyt, M. (1998). *Introduction to Finite Element Vibration Analysis*, Cambridge University Press, Cambridge.
- Reddy, J.N. (2003). *Mechanics of Laminated Composite Plates and Shells*, 2nd Edition, CRC Press, Boca Raton.
- Shu, C. and Wang, C.M. (1997). 'Implementation of clamped and simply supported boundary conditions in the GDQ free vibration analysis of beams and plates,' *International Journal of Solids and Structures*, **34**, 819–835.
- Wang, C.M. and Xiang, Y. (2002). 'An approach for determining exact Levy solutions for plates with abrupt changes in properties,' *The Second International Symposium on Advances in Structural Engineering and Mechanics (ASEM'02)*, Busan, Korea, 21–23 August 2002.
- Wang, C.M., Xiang, Y. and Wang, C.Y. (2001). 'Buckling and vibration of plates with an internal line-hinge via the Ritz method,' *Proceedings, First Asian-Pacific Congress on Computational Mechanics*, Sydney, pp. 1663–1672.
- Wang, S. (1997). 'A unified Timoshenko beam B-spline Rayleigh–Ritz method for vibration and buckling analysis of thick and thin beams and plates,' *International Journal for Numerical Methods in Engineering*, **40**, 473–491.
- Xiang, Y. and Reddy, J.N. (2003). 'Natural vibration of rectangular plates with an internal line hinge using the first order shear deformation plate theory,' *Journal of Sound and Vibration*, **263**, 285–297.

- Xiang, Y. and Wang, C.M. (2002). 'Exact solutions for buckling and vibration of stepped rectangular plates,' *Journal of Sound and Vibration*, **250**, 503–517.
- Xiang, Y. and Zhang, L. (2005). 'Free vibration analysis of stepped circular Mindlin plates,' *Journal of Sound and Vibration*, **280**, 633–655.
- Xiang, Y., Zhao, Y.B. and Wei, G.W. (2002). 'Levy solutions for vibration of multi-span rectangular plates,' *International Journal of Mechanical Sciences*, **44**, 1195–1218.
- Young, D. (1950). 'Vibration of rectangular plates by the Ritz method,' *Journal of Applied Mechanics, ASME*, **17**, 448–453.
- Yuan, J. and Dickinson, S.M. (1992). 'The flexural vibration of rectangular plate systems approached by using artificial springs in the Rayleigh–Ritz method,' *Journal of Sound and Vibration*, **159**, 39–55.
- Zhao, Y.B., Wei, G.W. and Xiang, Y. (2002). 'Discrete singular convolution for the prediction of high frequency vibration of plates,' *International Journal of Solids and Structures*, **39**, 65–88.

# Relationships between vibration frequencies of higher-order plate theories and classical thin plate theory

---

C M WANG, National University of Singapore, Singapore

## 9.1 Introduction

Ever since the German physicist Ernst Chladni in 1787 first observed nodal patterns (lines of zero amplitude) formed by sprinkled sand on vibrating plates at their resonant frequencies, there has been extensive research conducted on plate vibrations. Abundant thin plate vibration solutions based on the Kirchhoff plate assumptions are available in the literature. Excellent reference sources on this subject include Professor Arthur Leissa's series of review papers (Leissa 1977a,b, 1981a,b, 1987a,b) and his monograph on *Vibration of Plates*, initially published by NASA in 1969 and reprinted by the Acoustical Society of America in 1993 due to great demand. Adoption of the classical thin plate theory, however, leads to an over-prediction of the vibration frequencies for thick and shear deformable plates because the theory neglects the effects of transverse shear deformation and rotary inertia. This shortcoming was eventually overcome by the development of shear deformable plate theories, discussed in the next section.

Recent advances into the subject of plate vibration have focused on shear deformable plates that are somewhat more complicated to analyse compared with classical thin plate theory. Fueled by the availability of powerful computers, researchers have developed computer codes for analysis of shear deformable plated structures which involve a relatively larger number of degrees of freedoms. In order to check the validity, convergence and accuracy of their numerical techniques and software, it is necessary to have exact benchmark vibration frequencies of shear deformable plates. This chapter provides exact vibration frequency relationships that convert the classical plate solutions into their corresponding shear deformable plate solutions.

## 9.2 Plate theories

The simplest plate theory is the classical thin plate theory (CPT) which is based on the following displacement field (Kirchhoff 1850)

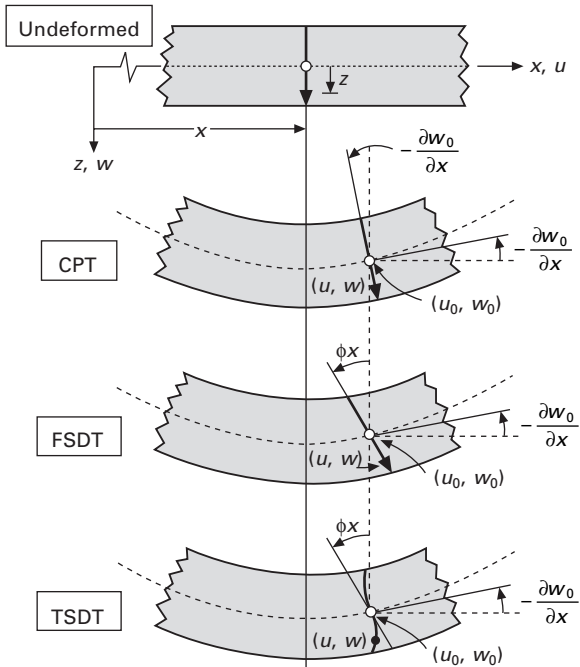
$$u(x, y, z, t) = -z \frac{\partial w_0}{\partial x} \quad 9.1a$$

$$v(x, y, z, t) = -z \frac{\partial w_0}{\partial y} \quad 9.1b$$

$$w(x, y, z, t) = w_0(x, y, t) \quad 9.1c$$

where  $u$ ,  $v$  and  $w$  are the displacement components along the  $x$ ,  $y$  and  $z$  coordinate directions, respectively, of a point on the mid-plane (i.e.  $z = 0$ ). The displacement field given by Eq. (9.1) is written using the Kirchhoff hypothesis which states that straight lines normal to the  $x$ - $y$  plane before deformation remain straight and normal to the mid-surface after deformation (see Fig. 9.1). The Kirchhoff assumption amounts to neglecting both transverse shear and transverse normal effects, i.e. deformation is due entirely to bending and in-plane stretching.

Interestingly, only about 150 years later was the plate theory, which incorporates the effect of transverse deformation formulated by Reissner (1944, 1945), Hencky (1947) and Mindlin (1951). This theory has been



9.1 Deformation of a typical transverse normal line in various beam theories ( $u_0$  denotes displacement due to in-plane stretching which is not considered here).

termed the first-order shear deformation theory (FSDT). It is based on the displacement field:

$$u(x, y, z, t) = z\phi_x(x, y, t) \quad 9.2a$$

$$v(x, y, z, t) = z\phi_y(x, y, t) \quad 9.2b$$

$$w(x, y, z, t) = w_0(x, y, t) \quad 9.2c$$

where  $\phi_x$  and  $\phi_y$  are the rotations about the  $y$  and  $x$  axes, respectively. FSDT relaxes the normality restriction of the CPT by including a gross transverse shear deformation in its kinematic assumptions, i.e. the transverse shear strain is assumed to be constant with respect to the thickness coordinate  $z$  (see Fig. 9.1). This constant shear strain and hence constant shear stress violates the static boundary conditions at the free surfaces of the plate. Thus, FSDT requires the factoring of the transverse shear forces using correction factors which depend not only on material and geometric parameters but also on the loading and boundary conditions.

Higher-order shear deformation theories do away with the shear correction factors. The third-order shear deformation theory (TSDT) of Reddy (1984) with transverse inextensibility is based on the following displacement field:

$$u(x, y, z, t) = z\phi_x(x, y, t) - \frac{4z^3}{3h^2} \left( \phi_x + \frac{\partial w_0}{\partial x} \right) \quad 9.3a$$

$$v(x, y, z, t) = z\phi_y(x, y, t) - \frac{4z^3}{3h^2} \left( \phi_y + \frac{\partial w_0}{\partial y} \right) \quad 9.3b$$

$$w(x, y, z, t) = w_0(x, y, t) \quad 9.3c$$

The displacement field accommodates a quadratic variation of the transverse shear stresses and the vanishing of transverse shear stresses at the top and bottom surfaces of the plate. Thus, there is no need for shear corrections in TSDT. Note that in TSDT, the transverse normal bends in a cubic curve (see Fig. 9.1).

Below, it will be shown that there exist exact relationships between the vibration frequencies of the shear deformation theories (FSDT and TSDT) and the classical thin plate theory (CPT) for simply supported polygonal plates, and the relationship may be applied to other plate shapes and boundary conditions with appropriate modification factors. The relationship allows one to obtain the FSDT and TSDT vibration frequencies just by knowing the corresponding frequencies of the CPT.

### 9.3 Equations of free vibration

Consider an elastic, isotropic plate with thickness  $h$ , and mass density  $\rho$  that is vibrating in a periodic motion. By adopting the foregoing displacement

fields in Eqs. (9.1) to (9.3) and using a consistent variational formulation, the governing equations for free vibration of the plate based on the various plate theories are given by Timoshenko and Woinowsky-Kreiger (1959), Mindlin (1951) and Reddy (1984).

*CPT:*

$$\frac{\partial M_{xx}^C}{\partial x} + \frac{\partial M_{xy}^C}{\partial y} - Q_x^C = 0 \quad 9.4a$$

$$\frac{\partial M_{yy}^C}{\partial y} + \frac{\partial M_{xy}^C}{\partial x} - Q_y^C = 0 \quad 9.4b$$

$$\frac{\partial Q_x^C}{\partial x} + \frac{\partial Q_y^C}{\partial y} = -\rho h \omega_C^2 w^C \quad 9.4c$$

*FSDT:*

$$\frac{\partial M_{xx}^M}{\partial x} + \frac{\partial M_{xy}^M}{\partial y} - Q_x^M = -\frac{\rho h^3}{12} \omega_M^2 \phi_x^M \quad 9.5a$$

$$\frac{\partial M_{yy}^M}{\partial y} + \frac{\partial M_{xy}^M}{\partial x} - Q_y^M = -\frac{\rho h^3}{12} \omega_M^2 \phi_y^M \quad 9.5b$$

$$\frac{\partial Q_x^M}{\partial x} + \frac{\partial Q_y^M}{\partial y} = -\rho h \omega_M^2 w^M \quad 9.5c$$

*TSDT:*

$$\begin{aligned} & \frac{\partial}{\partial x} \left( M_{xx}^R - \frac{4}{3h^2} P_{xx}^R \right) + \frac{\partial}{\partial y} \left( M_{xy}^R - \frac{4}{3h^2} P_{xy}^R \right) - \left( Q_x^R - \frac{4}{h^2} R_x^R \right) \\ &= -\frac{17\rho h^3}{315} \omega_R^2 \phi_x^R + \frac{4\rho h^3}{315} \omega_R^2 \frac{\partial w^R}{\partial x} \end{aligned} \quad 9.6a$$

$$\begin{aligned} & \frac{\partial}{\partial y} \left( M_{yy}^R - \frac{4}{3h^2} P_{yy}^R \right) + \frac{\partial}{\partial x} \left( M_{xy}^R - \frac{4}{3h^2} P_{xy}^R \right) - \left( Q_y^R - \frac{4}{h^2} R_y^R \right) \\ &= -\frac{17\rho h^3}{315} \omega_R^2 \phi_y^R + \frac{4\rho h^3}{315} \omega_R^2 \frac{\partial \omega^R}{\partial y} \end{aligned} \quad 9.6b$$

$$\begin{aligned} & \frac{\partial}{\partial x} \left( Q_x^M - \frac{4}{h^2} R_x^R \right) + \frac{\partial}{\partial y} \left( Q_y^M - \frac{4}{h^2} R_y^R \right) \\ &+ \frac{4}{3h^2} \left( \frac{\partial^2 P_{xx}^R}{\partial x^2} + 2 \frac{\partial^2 P_{xy}^R}{\partial x \partial y} + \frac{\partial^2 P_{yy}^R}{\partial y^2} \right) \\ &= \frac{\rho h^3}{252} \omega_R^2 \nabla^2 w^R - \rho h \omega_R^2 \omega^R - \frac{4\rho h^3}{315} \omega_R^2 \left( \frac{\partial \phi_x^R}{\partial x} + \frac{\partial \phi_y^R}{\partial y} \right) \end{aligned} \quad 9.6c$$

where the superscripts and subscripts  $C$ ,  $M$  and  $R$  denote quantities belonging to CPT, FSDT and TSDT, respectively,  $\omega$  is the natural frequency of the plate (in radians/second) and  $\nabla^2(o) = \partial^2(o)/\partial x^2 + \partial^2(o)/\partial y^2$  the Laplacian operator. The stress-resultants are given by the following.

*CPT:*

$$M_{xx}^C = -D \left( \frac{\partial^2 w^C}{\partial x^2} + \nu \frac{\partial^2 w^C}{\partial y^2} \right) \quad 9.7a$$

$$M_{yy}^C = -D \left( \frac{\partial^2 w^C}{\partial y^2} + \nu \frac{\partial^2 w^C}{\partial x^2} \right) \quad 9.7b$$

$$M_{xy}^C = -D(1 - \nu) \frac{\partial^2 w^C}{\partial x \partial y} \quad 9.7c$$

*FSDT:*

$$M_{xx}^M = D \left( \frac{\partial \phi_x^M}{\partial x} + \nu \frac{\partial \phi_y^M}{\partial y} \right) \quad 9.8a$$

$$M_{yy}^M = D \left( \frac{\partial \phi_y^M}{\partial y} + \nu \frac{\partial \phi_x^M}{\partial x} \right) \quad 9.8b$$

$$M_{xy}^C = \frac{D(1 - \nu)}{2} \left( \frac{\partial \phi_x^M}{\partial y} + \frac{\partial \phi_y^M}{\partial x} \right) \quad 9.8c$$

$$Q_x^M = \kappa^2 G h \left( \phi_x^M + \frac{\partial w^M}{\partial x} \right) \quad 9.8d$$

$$Q_y^M = \kappa^2 G h \left( \phi_y^M + \frac{\partial w^M}{\partial y} \right) \quad 9.8e$$

*TSDT:*

$$M_{xx}^R = \frac{4D}{5} \left( \frac{\partial \phi_x^R}{\partial x} + \nu \frac{\partial \phi_y^R}{\partial y} \right) - \frac{D}{5} \left( \frac{\partial^2 w^R}{\partial x^2} + \nu \frac{\partial^2 w^R}{\partial y^2} \right) \quad 9.9a$$

$$M_{yy}^R = \frac{4h^2 D}{35} \left( \frac{\partial \phi_x^R}{\partial x} + \nu \frac{\partial \phi_y^R}{\partial y} \right) - \frac{h^2 D}{28} \left( \frac{\partial^2 w^R}{\partial x^2} + \nu \frac{\partial^2 w^R}{\partial y^2} \right) \quad 9.9b$$

$$M_{xy}^R = \frac{4D}{5} \left( \frac{\partial \phi_y^R}{\partial y} + \nu \frac{\partial \phi_x^R}{\partial x} \right) - \frac{D}{5} \left( \frac{\partial^2 w^R}{\partial y^2} + \nu \frac{\partial^2 w^R}{\partial x^2} \right) \quad 9.9c$$

$$P_{yy}^R = \frac{4h^2 D}{35} \left( \frac{\partial \phi_y^R}{\partial y} + \nu \frac{\partial \phi_x^R}{\partial x} \right) - \frac{h^2 D}{28} \left( \frac{\partial^2 w^R}{\partial y^2} + \nu \frac{\partial^2 w^R}{\partial x^2} \right) \quad 9.9d$$

$$M_{xy}^R = \frac{(1-\nu)}{2} \left[ \frac{4D}{5} \left( \frac{\partial \phi_x^R}{\partial y} + \frac{\partial \phi_y^R}{\partial x} \right) - \frac{D}{5} \left( 2 \frac{\partial^2 w^R}{\partial x \partial y} \right) \right] \quad 9.9e$$

$$P_{xy}^R = \frac{(1-\nu)}{2} \left[ \frac{4h^2 D}{35} \left( \frac{\partial \phi_x^R}{\partial y} + \frac{\partial \phi_y^R}{\partial x} \right) - \frac{h^2 D}{28} \left( 2 \frac{\partial^2 w^R}{\partial x \partial y} \right) \right] \quad 9.9f$$

$$Q_x^R = \frac{2Gh}{3} \left( \phi_x^R + \frac{\partial w^R}{\partial x} \right) \quad 9.9g$$

$$R_x^R = \frac{Gh^3}{30} \left( \phi_x^M + \frac{\partial w^M}{\partial x} \right) \quad 9.9h$$

$$Q_y^R = \frac{2Gh}{3} \left( \phi_y^R + \frac{\partial w^R}{\partial y} \right) \quad 9.9i$$

$$R_y^R = \frac{Gh^3}{30} \left( \phi_y^M + \frac{\partial w^M}{\partial y} \right) \quad 9.9j$$

in which  $\nu$  is the Poisson ratio,  $G = E/[2(1 + \nu)]$  the shear modulus,  $E$  the modulus of elasticity,  $D = Eh^3/[12(1 - \nu^2)]$  the flexural rigidity per unit length of the plate, and  $\kappa^2$  the shear correction factor. Note that  $(P_{xx}, P_{yy}, P_{xy})$  are the higher-order moments of TSDT and  $(R_x, R_y)$  the higher-order shear forces.

## 9.4 Relationship between frequencies of FSDT and CPT

Below an exact relationship between the natural vibration frequencies of FSDT and CPT is derived for a class of plates, namely polygonal plates with all edges straight and simply supported.

In view of Eqs. (9.7a), (9.7b), (9.7c) and the shear force expressions given in Eqs. (9.4a) and (9.4b), Eq. (9.4c) of CPT can be written as

$$\nabla^4 w^C - \frac{\rho h}{D} \omega_C^2 w^C = 0 \quad 9.10$$

Equation (9.10) of CPT plate may be factored to give

$$(\nabla^2 + \lambda_C)(\nabla^2 - \lambda_C)w^C = 0 \quad 9.11$$

where

$$\lambda_C^2 = \frac{\rho h}{D} \omega_C^2 \quad 9.12$$

For a simply supported polygonal plate, the deflection  $w^C$  and the Marcus moment  $\Phi^C = (M_{xx} + M_{yy})/(1 + \nu) = D\nabla^2 w^C$  are zero at the straight boundary edges, i.e.

$$w^C = 0 \text{ and } \nabla^2 w^C = 0 \quad 9.13$$

As pointed out by Conway (1960) and later proven by Pnueli (1975), the frequency solutions of the fourth differential equation (9.10) and the boundary condition given in Eq. (9.13) are the same as those given by solving simply the following second-order differential equation:

$$(\nabla^2 + \lambda_C^2)w^C = 0 \quad 9.14$$

and the boundary condition  $w^C = 0$ .

Similarly in the case of FSDT, from Eqs. (9.8a), (9.8b), (9.8c), (9.5a) and (9.5b), we can rewrite Eq. (9.5c) as

$$\nabla^2 \Phi^M - \frac{\kappa^2 Gh}{D} (\Phi^M + \nabla^2 w^M) = -\frac{\rho h^3}{12D} \omega_M^2 \Phi^M \quad 9.15$$

where  $\Phi^M$  is the moment sum defined as

$$\Phi^M = \frac{M_{xx} + M_{yy}}{1 + \nu} = D \left( \frac{\partial \phi_x^M}{\partial x} + \frac{\partial \phi_y^M}{\partial y} \right) \quad 9.16$$

By substituting Eqs. (9.8d) and (9.8e) into Eq. (9.5c) and noting Eq. (9.16), we have

$$\kappa^2 Gh(\Phi^M + \nabla^2 w^M) = -\rho h \omega_M^2 w^M \quad 9.17$$

By eliminating  $\Phi^M$  from Eqs. (9.15) and (9.17), one obtains

$$\begin{aligned} \nabla^4 w^M + & \left( \frac{\rho h}{\kappa^2 Gh} + \frac{\rho h^3}{12D} \right) \omega_M^2 \nabla^2 w^M \\ & + \frac{\rho h}{D} \left( \frac{\rho h^3}{12\kappa^2 Gh} \omega_M^2 - 1 \right) \omega_M^2 w^M = 0 \end{aligned} \quad 9.18$$

Equation (9.18) may be factored to give

$$(\nabla^2 + \lambda_1)(\nabla^2 + \lambda_2)w^M = 0 \quad 9.19$$

where

$$\lambda_1 = \frac{1}{2} \left( \frac{\rho h}{\kappa^2 G h} + \frac{\rho h^3}{12 D} \right) \omega_M^2 - \sqrt{\left[ \frac{1}{2} \left( \frac{\rho h}{\kappa^2 G h} + \frac{\rho h^3}{12 D} \right) \omega_M^2 \right]^2 + \frac{\rho h}{D} \omega_M^2} \quad 9.20a$$

$$\lambda_2 = \frac{1}{2} \left( \frac{\rho h}{\kappa^2 G h} + \frac{\rho h^3}{12 D} \right) \omega_M^2 + \sqrt{\left[ \frac{1}{2} \left( \frac{\rho h}{\kappa^2 G h} + \frac{\rho h^3}{12 D} \right) \omega_M^2 \right]^2 + \frac{\rho h}{D} \omega_M^2} \quad 9.20b$$

Alternatively, Eq. (9.19) may be written as two second-order equations (see Pnueli 1975):

$$(\nabla^2 + \lambda_i) w^M = \bar{w} \quad \text{and} \quad (\nabla^2 + \lambda_j) \bar{w} = 0 \quad 9.21$$

where  $i = 1$  if  $j = 2$  and vice versa.

Considering a simply supported polygonal plate, the boundary conditions at each straight simply supported edge are given by

$$w^M = 0, \quad M_{nn}^M = 0, \quad \phi_s^M = 0 \quad 9.22$$

where  $n$  and  $s$  are the normal and tangential coordinates of an edge. Since along the straight edge  $\phi_s^M = 0$  implies that  $\partial \phi_s^M / \partial s = 0$ , then together with the condition  $M_{nn}^M = 0$ , one may deduce that  $\partial \phi_n^m / \partial n = 0$ . In view of this fact and Eq. (9.17), the boundary conditions given in Eq. (9.22) may be expressed as

$$w^M = 0, \quad \Phi^M = 0, \quad \nabla^2 w^M = 0, \quad \bar{w} = 0 \quad 9.23$$

Owing to the mathematical similarity between the governing equations (9.14) and (9.21) and the boundary conditions (9.13) and (9.23), it follows that the FSDT vibration plate problem is analogous to the CPT plate problem. Thus, for a given simply supported, polygonal plate:

$$\lambda_j = \lambda_C \quad 9.24$$

The substitution of Eq. (9.20b) and (9.12) into Eq. (9.24) yields the frequency relationship between FSDT and CPT plates, i.e.

$$\begin{aligned} \omega_M^2 = & \frac{6\kappa^2 G}{\rho h^2} \left\{ \left[ 1 + \frac{1}{12} \omega_C h^2 \sqrt{\frac{\rho h}{D}} \left( 1 + \frac{2}{\kappa^2 (1 - \nu)} \right) \right] \right. \\ & \left. - \sqrt{\left[ 1 + \frac{1}{12} \omega_C h^2 \sqrt{\frac{\rho h}{D}} \left( 1 + \frac{2}{\kappa^2 (1 - \nu)} \right) \right]^2 - \frac{\rho h^2}{3\kappa^2 G} \omega_C^2} \right\} \quad 9.25 \end{aligned}$$

Note that for a CPT frequency value corresponding to a mode sequence, the relationship given in Eq. (9.25) gives the corresponding FSDT frequency value. The relationship given in Eq. (9.25) was first derived by Irschik (1985).

## 9.5 Relationship between frequencies of TSDT and CPT

By differentiating Eq. (9.6a) with respect to  $x$  and Eq. (9.6b) with respect to  $y$ , summing them and using Eq. (9.6c), the governing equations may be expressed as

$$\begin{aligned} \frac{\partial^2 M_{xx}^R}{\partial x^2} + \frac{\partial^2 M_{yy}^R}{\partial y^2} + 2 \frac{\partial^2 M_{xy}^R}{\partial x \partial y} \\ = \frac{\rho h^3}{60} \omega_R^2 \nabla^2 w^R - \rho h \omega_R^2 w^R - \frac{\rho h^3}{15} \omega_R^2 \left( \frac{\partial \phi_x^R}{\partial x} + \frac{\partial \phi_y^R}{\partial y} \right) \end{aligned} \quad 9.26$$

By introducing the moment sum  $\Phi^R$  defined by

$$\Phi^R = \frac{M_{xx}^R + M_{yy}^R}{1 + \nu} = \frac{4D}{5} \left( \frac{\partial \phi_x^R}{\partial x} + \frac{\partial \phi_y^R}{\partial y} \right) - \frac{D}{5} \nabla^2 w^R \quad 9.27$$

and the moment expressions given in Eqs. (9.9a), (9.9c), (9.9e), Eq. (9.26) may be written as

$$\nabla^2 \Phi^R = \frac{\rho h^3}{60} \omega_R^2 \nabla^2 w^R - \rho h \omega_R^2 w^R - \frac{\rho h^3}{15} \omega_R^2 \left( \frac{\partial \phi_x^R}{\partial x} + \frac{\partial \phi_y^R}{\partial y} \right) \quad 9.28$$

Substitution of Eqs. (9.9b), (9.9d), (9.9f), (9.9g)–(9.9j) and (9.27) into Eq. (9.6c) leads to

$$\begin{aligned} K \left( \frac{\partial \phi_x^R}{\partial x} + \frac{\partial \phi_y^R}{\partial y} \right) &= \left( \frac{\rho h^3}{252} \omega_R^2 - \frac{8Gh}{15} \right) \nabla^2 w^R \\ &- \rho h \omega_R^2 w^R - \frac{4}{21} \nabla^2 \Phi^R + \frac{D}{105} \nabla^4 w^R \end{aligned} \quad 9.29$$

where

$$K = \frac{8}{15} Gh + \frac{4}{315} \rho h^3 \omega_R^2 \quad 9.30$$

By substituting Eq. (9.29) into Eq. (9.28), one obtains

$$J\nabla^2\Phi^R = -\rho h \omega_R^2 \left( 1 - \frac{\rho h^3}{15K} \omega_R^2 \right) w^R - \frac{D}{105} \frac{\rho h^3}{15K} \omega_R^2 \nabla^4 w^R + L \nabla^2 w^R \quad 9.31$$

where

$$J = 1 - \frac{4}{315K} \rho h^3 \omega_R^2 \quad 9.32$$

$$L = \frac{\rho h^3}{60} \omega_R^2 - \frac{\rho h^3}{15K} \omega_R^2 \left( \frac{\rho h^3}{252} \omega_R^2 - \frac{8Gh}{15} \right) \quad 9.33$$

Moreover, by substituting Eq. (9.29) into Eq. (9.27), one obtains

$$\begin{aligned} \Phi^R = & -\frac{4D}{5K} \rho h \omega_R^2 w^R - \frac{16D}{105K} \nabla^2 \Phi^R + \frac{4D}{5K} \frac{D}{105} \nabla^4 w^R \\ & + \left[ -\frac{D}{5} + \frac{4D}{5K} \left( \frac{\rho h^3}{252} \omega_R^2 - \frac{8Gh}{15} \right) \right] \nabla^2 w^R \end{aligned} \quad 9.34$$

and noting Eq. (9.31), Eq. (9.34) can be expressed as

$$\begin{aligned} \Phi^R = & \left[ -\frac{4D}{5K} \rho h \omega_R^2 + \frac{16D}{105KJ} \rho h \omega_R^2 \left( 1 - \frac{\rho h^3}{15K} \omega_R^2 \right) \right] w^R \\ & + \left[ -\frac{D}{5} + \frac{4D}{5K} \left( \frac{\rho h^3}{252} \omega_R^2 - \frac{8Gh}{15} \right) - \frac{16DL}{105KJ} \right] \nabla^2 w^R \\ & + \left[ \frac{4D}{5K} \frac{D}{105} + \frac{16D}{105KJ} \frac{D}{105} \frac{\rho h^3}{15K} \omega_R^2 \right] \nabla^4 w^R \end{aligned} \quad 9.35$$

Substitution of Eq. (9.35) into Eq. (9.31) furnishes the governing sixth-order differential equation in terms of  $w^R$ :

$$a_1 \nabla^6 w^R + a_2 \nabla^4 w^R + a_3 \nabla^2 w^R + a_4 w^R = 0 \quad 9.36$$

where

$$a_1 = \frac{4D}{5K} \frac{D}{105} \left[ 1 + \frac{4}{21J} \frac{\rho h^3}{15K} \omega_R^2 \right] \quad 9.37$$

$$a_2 = -\frac{D}{5} \left[ 1 - \frac{4}{K} \left( \frac{\rho h^3}{252} \omega_R^2 - \frac{8Gh}{15} \right) + \frac{16L}{21KJ} - \frac{\rho h^3}{315KJ} \omega_R^2 \right] \quad 9.38$$

$$a_3 = -\frac{4D}{5K} \rho h \omega_R^2 + \frac{16D}{105KJ} \rho h \omega_R^2 \left( 1 - \frac{\rho h^3}{15K} \omega_R^2 \right) - \frac{L}{J} \quad 9.39$$

$$a_4 = \frac{\rho h}{J} \omega_R^2 \left( 1 - \frac{\rho h^3}{15K} \omega_R^2 \right) \quad 9.40$$

The governing equation may be factored to give

$$(\nabla^2 + \lambda_1)(\nabla^2 + \lambda_2)(\nabla^2 + \lambda_3)w^R = 0 \quad 9.41$$

where

$$\lambda_1 = -2\sqrt{\Psi} \cos\left(\frac{\theta}{3}\right) + \frac{a_2}{3a_1} \quad 9.42$$

$$\lambda_2 = -2\sqrt{\Psi} \cos\left(\frac{\theta + 2\pi}{3}\right) + \frac{a_2}{3a_1} \quad 9.43$$

$$\lambda_3 = -2\sqrt{\Psi} \cos\left(\frac{\theta + 4\pi}{3}\right) + \frac{a_2}{3a_1} \quad 9.44$$

and

$$\cos\theta = \frac{\Theta}{\sqrt{\Psi^3}} \quad 9.45a$$

$$\Psi = -\frac{a_3}{3a_1} + \left( \frac{a_2}{3a_1} \right)^2 \quad 9.45b$$

$$\Theta = \frac{a_2 a_3}{6a_1^2} - \frac{a_4}{2a_1} - \left( \frac{a_2}{3a_1} \right)^3 \quad 9.45c$$

The following boundary conditions for a simply supported edge of a TSDT plate have been assumed (Reddy and Phan 1985):

$$w^R = 0, \quad M_{nn}^R = 0, \quad P_{nn}^R = 0, \quad \phi_s^R = 0 \quad 9.46$$

where the subscripts  $n$ ,  $s$  denote, respectively, the normal and tangential directions to the edge. Since  $w^R = 0$  implies that  $\partial^2 w^R / \partial s^2 = 0$  and  $\phi_s = 0$  implies that  $\partial \phi_s / \partial s = 0$ , then together with the conditions  $M_{nn}^R = P_{nn}^R = 0$ , we have  $\partial^2 w^R / \partial n^2 = \partial \phi_s^R / \partial n = 0$  and  $M_{ss}^R = P_{ss}^R = 0$ . Also, it follows that  $\partial^4 w^R / \partial s^2 = \partial^4 w^R / \partial n^2 = 0$ . Thus, for a straight simply supported edge of a TSDT plate, the boundary conditions may be expressed as

$$w^R = 0, \quad \Phi^R = 0, \quad \nabla^2 w^R = 0, \quad \nabla^4 w^R = 0 \quad 9.47$$

In view of the boundary conditions given in Eq. (9.47), the sixth-order governing equation (9.41) may be written as three second-order differential equations given by

$$(\nabla^2 + \lambda_j)w^R = 0, \quad j = 1, 2, 3 \quad 9.48$$

with the boundary condition  $w^R = 0$  along the plate edges. Note that although Pnueli (1975) proved that the frequency solutions of the fourth-order differential equation (9.11) are the same as those given by the second-order differential equation (9.14) for the case of straight, simply supported edges, the same Pnueli proof together with the substitution of variable (for example, let  $v = \nabla^2 w^R + \lambda w^R$ ) can be used to reduce the sixth-order equation to a second-order Eq. (9.48).

In view of the mathematical similarity of Eqs. (9.14) and (9.48) and the boundary conditions for these second-order differential equations, it may be deduced that

$$\lambda_j = \lambda_C \quad 9.49$$

Based on numerical tests, it was found that the first root ( $j=1$ ), yields nonfeasible vibration solutions while the second root ( $j = 2$ ) gives the lowest frequency value when compared with the third root ( $j = 3$ ). Thus, the relationship between TSDT frequency  $\omega_R$  and the CPT frequency  $\omega_C$  is given by

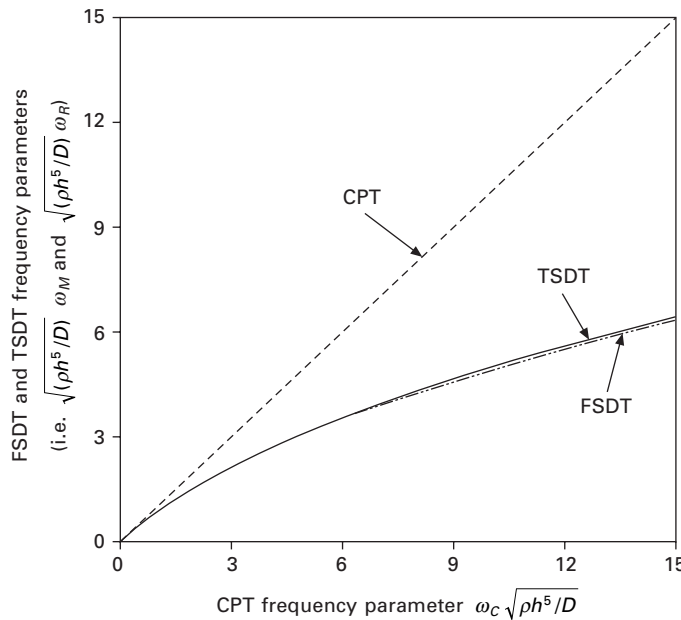
$$-2\sqrt{\Psi} \cos\left(\frac{\theta + 2\pi}{3}\right) + \frac{a_2}{3a_1} = \omega_C \sqrt{\frac{\rho h}{D}} \quad 9.50$$

Upon supplying the CPT frequencies, the foregoing exact relationship (9.50) can be used to compute TSDT frequencies. Note that Eq. (9.50) is an explicit equation for  $\omega_C$  as a function of  $\omega_R$ , but it is a transcendental equation of  $\omega_R$  for given  $\omega_C$ . The transcendental equation may be readily solved by using any root-finding algorithm such as the false position method.

## 9.6 Frequency results

Figure 9.2 shows a graphical representation of the relationships given by Eq. (9.25) with  $\kappa^2 = 5/6$  and Eq. (9.50). The two curves are almost the same and they apply for any polygonal shaped plate with straight, simply supported edges because the frequency parameters are nondimensionalized in a manner so as to exclude side length dimensions. It can be seen that as the frequency parameter increases (i.e. corresponding to increasing plate thickness or higher modes of vibration), the FSDT and the TSDT vibration solutions decrease with respect to the corresponding CPT solutions due to the effects of transverse shear deformation and rotary inertia.

Illustrating the use of Eqs. (9.25) and (9.50), we consider simply supported plates of various shapes. Table 9.1 presents sample vibration frequencies for square and rectangular plates (note that the exact CPT vibration frequency parameter is given by  $\omega_C b^2 \sqrt{\rho h/D} = (mb\pi/a)^2 + (n\pi)^2$ ), Table 9.2 for regular polygonal plates, Table 9.3 for triangular plates, Table 9.4 for skew (or parallelogram) plates and Table 9.5 for symmetric trapezoidal plates.



9.2 Frequency relationships between CPT, FSDT and TSDT simply supported plates.

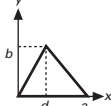
Table 9.1 Natural frequencies  $\omega b^2 \sqrt{\rho h/D}$  of simply supported square ( $a/b = 1$ ) and rectangular ( $a/b = 1/\sqrt{2}$ ) plates with  $h/a = 0.1$  and  $v = 0.3$

Number of half waves $m$	$n$	$a/b = 1$			Number of half waves $m$	$n$	$a/b = 1/\sqrt{2}$		
		CPT: Leissa (1973)	FSDT: Eq. (9.25)	TSDT: Eq. (9.50)			CPT: Leissa (1993)	FSDT: Eq. (9.25)	TSDT: Eq. (9.50)
1	1	19.739	19.065	19.065	1	1	29.609	28.839	28.839
1	2	49.348	45.483	45.487	1	2	59.218	56.274	56.276
2	2	78.957	69.795	69.810	2	1	88.826	82.478	82.484
1	3	98.696	85.038	85.065	1	3	108.57	99.340	99.351
2	3	128.31	106.69	106.74	2	2	118.44	107.60	107.61
1	4	167.78	133.62	133.72	2	3	167.78	147.34	147.38
3	3	177.65	140.06	140.17	1	4	177.65	155.01	155.05
2	4	197.39	152.61	152.75	3	1	187.52	162.58	162.63
3	4	246.74	182.32	182.57	3	2	217.13	184.81	184.88
1	5	256.61	188.01	188.28	2	4	236.87	199.24	199.32
2	5	286.22	204.62	204.96	3	3	266.48	220.33	220.44
4	4	315.83	220.60	221.02	1	5	266.48	220.33	220.44
3	5	335.57	230.93	231.41	2	5	325.70	260.72	260.91

Table 9.2 Fundamental frequencies  $\omega a^2 \sqrt{\rho h/D}$  of simply supported regular polygonal plates with side length  $a$  and  $\nu = 0.3$

Regular polygons	CPT	FSDT		TSDT	
		$h/a = 0.05$	$h/a = 0.15$	$h/a = 0.05$	$h/a = 0.15$
Equilateral triangle	$\frac{16\pi^2}{3} = 52.638$	51.414	44.275	51.415	44.293
Square	$2\pi^2 = 19.739$	19.562	18.328	19.562	18.330
Pentagon	10.863	10.809	10.410	10.809	10.410
Hexagon	7.129	7.106	6.929	7.106	6.929
Octagon	3.624	3.618	3.571	3.618	3.571

Table 9.3 Frequency parameters  $\omega a^2 \sqrt{\rho h/D}$  of simply supported triangular plates ( $h/a = 0.1$ )

Plate shape	Frequency parameters $\omega a^2 \sqrt{\rho h/D}$								
	Mode sequence number								
			CPT: Liew (1993)	FSDT: Eq. (9.25)	TSDT: Eq. (9.50)	CPT: Liew (1993)	FSDT: Eq. (9.25)	TSDT: Eq. (9.50)	
Triangle		$d/a$	$b/a$						
		1/4	2/5	23.75	22.79	22.79	40.80	38.09	38.10
		1/2	1/2	27.12	25.88	25.88	49.47	45.59	45.59
		2/3	33.11	31.29	31.29	65.26	58.78	58.79	
		1.0	46.70	43.21	43.22	100.2	86.17	86.20	
		$2/\sqrt{3}$	53.78	49.24	49.25	115.9	97.78	97.82	
		2.0	101.5	87.15	87.18	195.8	151.6	151.8	
		1/2	2/5	23.61	22.66	22.66	40.70	38.01	38.01
		1/2	1/2	26.91	25.68	25.68	49.33	45.47	42.16
		2/3	32.72	30.94	30.94	65.22	58.75	58.76	
		1.0	45.83	42.46	42.47	102.8	88.12	88.15	
		$2/\sqrt{3}$	52.64	48.28	48.29	122.8	102.8	102.8	
		2.0	98.57	84.94	84.97	197.4	152.6	152.8	

## 9.7 Modification of frequency relationship for complicating effects

If the simply supported, polygonal plate is subjected to a uniform initial stress  $\sigma$  (positive value for tensile stress and negative for compressive stress), the FSDT–CPT relationship is modified to (Irschik 1985, Liew *et al.* 1998):

$$\omega_M^2 = \frac{6\kappa^2 G}{\rho h^2} \left\{ \left[ 1 + \frac{1}{12} \omega_C h^2 \sqrt{\frac{\rho h}{D}} \left( 1 + \frac{2}{\kappa^2(1-\nu)} + \frac{\sigma}{\kappa^2 G} \right) \right] \right\}$$

Table 9.4 Frequencies parameters  $\omega b^2 \sqrt{\rho h/D}$  of simply supported skew plates ( $h/a = 0.1$ )

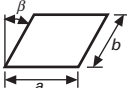
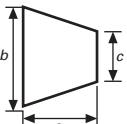
Plate shape	$a/b$	$\beta$	Frequency parameters $\omega b^2 \sqrt{\rho h/D}$					
			Mode sequence number			1		
Skew	CPT: Liew <i>et al.</i> (1993)	FSDT: Eq. (9.25)	TSDT: Eq. (9.50)	CPT: Liew <i>et al.</i> (1993)	FSDT: Eq. (9.25)	TSDT: Eq. (9.50)	2	
	1.0	15	20.87	20.12	20.12	48.20	44.50	44.50
		30	24.96	23.90	23.90	52.63	48.27	48.28
		45	35.33	33.27	33.27	66.27	59.61	59.62
	1.5	15	15.10	14.25	14.25	28.51	25.72	25.72
		30	18.17	16.96	16.96	32.49	28.95	28.95
		45	25.96	23.61	23.61	42.39	36.68	36.69
	2.0	15	13.11	12.03	12.03	20.66	18.17	18.18
		30	15.90	14.35	14.36	23.95	20.71	20.72
		45	23.01	19.99	20.00	32.20	26.76	26.77

Table 9.5 Frequencies parameters  $\omega a^2 \sqrt{\rho h/D}$  of simply supported trapezoidal plates ( $h/a = 0.1$ )

Plate shape	$a/b$	$c/b$	Frequency parameters $\omega a^2 \sqrt{\rho h/D}$					
			Mode sequence number			1		
Symmetric trapezoid	CPT: Liew and Lim (1993)	FSDT: Eq. (9.25)	TSDT: Eq. (9.50)	CPT: Liew and Lim (1993)	FSDT: Eq. (9.25)	TSDT: Eq. (9.50)	FSDT: Eq. (9.25)	TSDT: Eq. (9.50)
	1.0	1/5	37.74	35.40	35.41	79.67	70.36	70.37
		2/5	30.79	29.20	29.20	63.90	57.67	57.67
		3/5	25.64	24.52	24.52	55.96	51.08	51.08
	1.5	1/5	63.08	56.99	57.00	117.81	99.17	99.21
		2/5	53.19	48.75	48.75	92.99	80.70	80.73
		3/5	44.36	41.19	41.20	76.59	67.92	67.93
	2.0	1/5	94.44	81.81	81.83	162.80	130.3	130.4
		2/5	81.74	71.99	72.00	131.07	108.6	108.7
		3/5	69.49	62.22	62.23	105.31	90.00	90.02

$$\left. \begin{aligned} & - \sqrt{\left[ 1 + \frac{1}{12} \omega_c h^2 \sqrt{\frac{\rho h}{D}} \left( 1 + \frac{2}{\kappa^2(1-\nu)} + \frac{\sigma}{\kappa^2 G} \right) \right]^2} \\ & - \frac{\rho h^2}{3\kappa^2 G} \omega_c \left[ \omega_c \left( 1 + \frac{\sigma}{\kappa^2 G} \right) + \frac{\sigma h}{D} \sqrt{\frac{D}{\rho h}} \right] \end{aligned} \right\} \quad 9.51$$

If the simply supported, polygonal plate is resting on a *Pasternak foundation* modeled by lateral springs and shear springs, the FSDT–CPT relationship is modified to (Irschik 1985, Liew *et al.* 1998):

$$\omega_M^2 = \frac{6\kappa^2 G}{\rho h^2} \left\{ \left[ 1 + \frac{kh}{12\kappa^2 G} + \frac{1}{12} \omega_c h^2 \sqrt{\frac{\rho h}{D}} \left( 1 + \frac{2}{\kappa^2(1-\nu)} + \frac{G_b}{\kappa^2 G h} \right) \right] \right. \\ \left. - \sqrt{\left[ 1 + \frac{kh}{12\kappa^2 G} + \frac{1}{12} \omega_c h^2 \sqrt{\frac{\rho h}{D}} \left( 1 + \frac{2}{\kappa^2(1-\nu)} + \frac{G_b}{\kappa^2 G h} \right) \right]^2} \right. \\ \left. - \frac{\rho h^2}{3\kappa^2 G} \left[ \omega_c^2 \left( 1 + \frac{G_b}{\kappa^2 G h} \right) + \frac{k}{\rho h} + \omega_c \sqrt{\frac{D}{\rho h}} \left( \frac{G_b}{D} + \frac{k}{\kappa^2 G h} \right) \right] \right\} \quad 9.52$$

where  $k$  is the modulus subgrade reaction for the foundation and  $G_b$  the shear modulus of the subgrade. If  $G_b$  is viewed as a constant membrane tension, the Pasternak model becomes the Filonenko–Borodich model, while if  $G_b = 0$ , the model reduces to the Winkler foundation model (Horvath 1989).

Consider a simply supported, polygonal plate of a sandwich construction with core thickness  $h_c$ , core modulus of elasticity  $E_c$ , core shear modulus  $G_c$ , core Poisson's ratio  $\nu_c$ , core mass density  $\rho_c$ , facing thickness  $h_f$ , facing modulus of elasticity  $E_f$ , facing shear modulus  $G_f$ , facing Poisson's ratio  $\nu_f$  and facing mass density  $\rho_f$ . For such a sandwich plate, the FSDT–CPT relationship is modified to (Wang 1996):

$$\omega_M^2 = \chi_1 \left\{ \begin{aligned} & \left[ 1 + (1 + \chi_2) \chi_3 \omega_c \sqrt{\frac{\rho h}{D}} \right] \\ & - \sqrt{\left[ 1 + (1 + \chi_2) \chi_3 \omega_c \sqrt{\frac{\rho h}{D}} \right]^2 - 4\chi_2 \chi_3^2 \omega_c^2 \frac{\rho h}{D}} \end{aligned} \right\} \quad 9.53$$

where

$$\chi_1 = \frac{1}{2} \left[ \frac{\kappa^2 (G_c h_c + 2G_f h_f)}{\rho_c I_c + \rho_f I_f} \right] \quad 9.54a$$

$$\chi_2 = \left[ \frac{\rho_c h_c + 2\rho_f h_f}{\kappa^2 (G_c h_c + 2G_f h_f)} \right] \left[ \frac{D_c + D_f}{\rho_c I_c + \rho_f I_f} \right] \quad 9.54b$$

$$\chi_3 = \left[ \frac{\rho_c I_c + \rho_f I_f}{\rho_c h_c + 2\rho_f h_f} \right] \quad 9.54c$$

and

$$D_c = \frac{E_c I_c}{1 - v_c^2}, D_f = \frac{E_f I_f}{1 - v_f^2}, I_c = \frac{h_c^3}{12}, \\ I_f = \frac{2}{3} h_f \left( h_f^2 + \frac{3h_c^2}{4} + \frac{3h_c h_f}{2} \right) \quad 9.55$$

## 9.8 Concluding remarks

In this chapter, exact vibration frequency relationships between CPT and higher-order plate theories FSDT and TSDT are presented. These relationships not only furnish insights into how the various design variables influence the vibration frequencies but they also provide valuable benchmark shear deformable plate frequencies upon supplying the corresponding CPT solutions. Although the relationships are exact for only polygonal plates with straight simply supported plates, they are found to furnish accurate vibration frequencies for simply supported circular and annular sectorial plates (see Wang 1994).

The relationships can also be used as a basic form in which appropriate modification factors may be used to yield approximate formulas for predicting the shear deformable plate frequencies for other plate shapes and boundary conditions. The availability of such simple formulas will save designers from the need to perform tedious and difficult thick plate vibration analysis.

It is important to note that the relationships do not consider transverse shear modes and coupled bending-shear modes which appear at relatively high-order vibration modes (Lim *et al.* 2005).

## 9.9 References

- Conway, H.D. (1960). ‘Analogies between the buckling and vibration of polygonal plates and membranes,’ *Canadian Aeronautical Journal*, **6**, 263.
- Hencky, H. (1947). ‘Über die berücksichtigung der schubverzerrung in ebenen platten,’ *Ingenieur Archiv*, **16**, 72–76.
- Horvath, J.S. (1989). ‘Subgrade models for soil-structure interaction analysis,’ in *Foundation Engineering: Current Principles and Practices*, ASCE, **1**, 599–612.
- Irschik, H. (1985). ‘Membrane-type eigenmotions of Mindlin plates,’ *Acta Mechanica*, **55**, 1–20.
- Kirchhoff, G. (1850), ‘Über das gleichgewich und die bewegung einer elastischen scheibe,’ *Journal fur die Reine und Angewandte Mathematik*, **40**, 51–88.

- Leissa, A.W. (1973). 'The free vibration of rectangular plates,' *Journal of Sound and Vibration*, **31**, 257–293.
- Leissa, A.W. (1977a). 'Recent research in plate vibrations: classical theory,' *The Shock and Vibration Digest*, **9**(10), 13–24.
- Leissa, A.W. (1977b). 'Recent research in plate vibrations: complicating effects,' *The Shock and Vibration Digest*, **9**(10), 25–35.
- Leissa, A.W. (1981a). 'Plate vibration research, 1976–1980: classical theory,' *The Shock and Vibration Digest*, **13**(9), 11–22.
- Leissa, A.W. (1981b). 'Plate vibration research, 1976–1980: complicating effects,' *The Shock and Vibration Digest*, **13**(10), 19–36.
- Leissa, A.W. (1987a). 'Recent studies in plate vibrations, 1981–1985 Part I: classical theory,' *The Shock and Vibration Digest*, **19**(2), 11–18.
- Leissa, A.W. (1987b). 'Recent studies in plate vibrations, 1981–1985 Part II: complicating effects,' *The Shock and Vibration Digest*, **19**(3), 10–24.
- Leissa, A.W. (1993). *Vibration of Plates*, edition by Acoustical Society of America (originally issued by NASA, 1969).
- Liew, K.M. (1993). 'On the use of pb-2 Rayleigh–Ritz method for free flexural vibration of triangular plates with curved internal supports,' *Journal of Sound and Vibration*, **165**, 329–340.
- Liew, K.M. and Lim, M.K. (1993). 'Transverse vibration of trapezoidal plates of variable thickness: symmetric trapezoids,' *Journal of Sound and Vibration*, **165**, 45–67.-
- Liew, K.M., Xiang, Y., Kitipornchai, S. and Wang, C.M. (1993). 'Vibration of thick skew plates based on the Mindlin shear deformation plate theory,' *Journal of Sound and Vibration*, **168**, 39–69.
- Liew, K.M., Wang, C.M., Kitipornchai, S. and Xiang, Y. (1998). *Vibration of Mindlin Plates: Programming the p-Version Ritz Method*, Elsevier, Oxford.
- Lim, C.W., Li, Z.R., Xiang, Y., Wei, G.W. and Wang, C.M. (2005). 'On the missing modes when using the exact frequency relationship between Kirchhoff and Mindlin plates,' *Advances in Vibration Engineering*, **4**(3), 221–248.
- Mindlin, R.D. (1951), 'Influence of rotatory inertia and shear on flexural motions of isotropic, elastic plates,' *Trans. ASME, Journal of Applied Mechanics*, **18**, 31–38.
- Pnueli, D. (1975), 'Lower bounds to the gravest and all higher frequencies of homogeneous vibrating plates of arbitrary shape,' *Trans. ASME, Journal of Applied Mechanics*, **42**, 815–820.
- Reddy, J.N. (1984). 'A simple higher-order theory for laminated composite plates,' *Trans. ASME, Journal of Applied Mechanics*, **51**, 745–752.
- Reddy, J.N. and Phan, N.D. (1985). 'Stability and vibration of isotropic, orthotropic and laminated plates according to a higher-order shear deformation theory,' *Journal of Sound and Vibration*, **98**(2), 157–170.
- Reissner, E. (1944). 'On the theory of bending of elastic plates,' *Journal of Mathematical Physics*, **23**, 184–191.
- Reissner, E. (1945). 'The effect of transverse shear deformation on the bending of elastic plates,' *Trans. ASME, Journal of Applied Mechanics*, **12**, A69–A77.
- Timoshenko, S.P. and Woinowsky-Krieger, S. (1959). *Theory of Plates and Shells*, McGraw-Hill, New York.
- Wang, C.M. (1994). 'Natural frequency formula for simply supported Mindlin plates,' *Trans. ASME, Journal of Vibration and Acoustics*, **116**, 536–540.
- Wang, C.M. (1996). 'Vibration frequencies of simply supported polygonal sandwich plates via Kirchhoff solutions,' *Journal of Sound and Vibration*, **190**(2), 255–260.

## Free vibration analysis of functionally graded ceramic-metal plates

---

J N REDDY, National University of Singapore, Singapore  
and R A ARCIENGA, Texas A&M University, USA

### 10.1 Introduction

Plate structures made of composite materials continue to be used in many engineering applications. In particular, we can cite laminated composite plates and shells made up of fiber-reinforced laminae that are used in many structural applications, ranging from aircraft and automobile components to sports equipment and medical prosthetics (Reddy 2004). A typical lamina is often characterized as orthotropic with the principal material directions of each lamina coinciding with the fiber direction and transverse to it. Among the most attractive properties of composite structures are the high strength-to-weight ratio and high stiffness-to-weight ratio. In spite of their many advantages, laminated composite structures present serious analysis, design, and manufacturing challenges, such as failures due to excessive interlaminar stresses caused by the layer-wise variation of the material properties through the thickness of the laminate. To overcome this problem, new composite materials, called ‘functionally graded materials’ (FGMs) have been proposed (Koizumi 1997, Yamanouchi *et al.* 1990) in which the material properties vary continuously from one surface to the other. These materials are microscopically inhomogeneous and are typically made from isotropic components. The gradation of material properties through the thickness avoids abrupt changes in the stress distributions through the thickness.

A brief review of the technical literature on FGMs shows that few studies have been carried out to investigate the vibration response of FGM structures. Ng *et al.* (2000, 2001) examined the effect of functionally graded materials on the resonance response of plates and Yang *et al.* (2003, 2004) conducted a dynamic stability as well as large amplitude analyses for FGM laminated plates. Moreover, Reddy and Chin (1998) analyzed the dynamic thermoelastic response of functionally graded cylinders and plates. Praveen and Reddy (1998) carried out a nonlinear thermoelastic analysis of functionally graded ceramic–metal plates using a finite element model based on the first-order shear deformation plate theory (FSDT). Further studies of bending and vibration

analyses of FGM plates can be found in the articles of Reddy *et al.* (1999), Loy *et al.* (1999), Reddy (2000) and Della Croce and Venini (2004). These studies were based on classical or first-order plate theories.

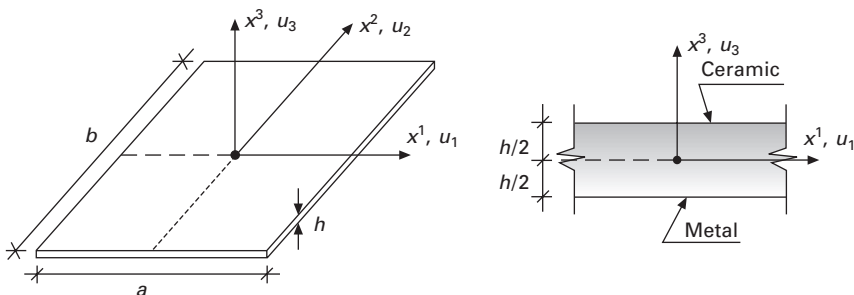
In this chapter, we consider the free vibration analysis of functionally graded plates using the finite element method. The formulation is based on the Reddy third-order shear deformation plate theory (TSDT) (see Reddy 2004) with seven independent parameters, which captures the basic kinematic behavior of composite plates. Results based on the first-order theory are also included for comparison. A displacement finite element model for the third-order theory is developed using high-order Lagrange interpolation functions to avoid shear locking. Numerical results are compared with other formulations found in the literature. Through-the-thickness displacement and stress distributions under mechanical loading for FGM are also presented. Changes in the center deflections and fundamental frequencies of FGM plates due to changes in volume fraction exponent and geometric parameters are discussed.

## 10.2 Theoretical formulation

### 10.2.1 Kinematics of the third-order shear deformation theory

In this section we briefly review the theoretical approach of the present formulation (see Reddy 2004 for additional details). The geometry of the plate is depicted in Fig. 10.1. Let  $\{x^i\}$  be a set of Cartesian coordinates with orthonormal basis  $\{\mathbf{e}_i\}$ . The mid-plane of the plate is defined by the coordinates  $\{x^\alpha\}$ . As usual, the Einstein summation convention is used; repeated Greek indices have the range of 1, 2 and Latin ones have the range 1, 2, 3. The displacement vector is assumed to be of the following form (Reddy 1984, Reddy and Arciniega 2004, Arciniega and Reddy 2005):

$$\mathbf{v}(x^i, t) = \mathbf{u}(x^\alpha, t) + x^3 \underline{\varphi}(x^\alpha, t) + k(x^3)^3 \underline{\psi}(x^\alpha, t) \quad 10.1$$



10.1 Geometry of the plate.

where  $\mathbf{u}$  denotes displacement vector of the point ( $x^\alpha$ ) in the mid-plane;  $\underline{\varphi}$  and  $\underline{\psi}$  are in-plane rotation vectors and  $k$  is a constant,  $k = -4/3h^2$ . These vectors are defined by

$$\mathbf{u}(x^\alpha, t) = u_j \mathbf{e}_j, \quad \underline{\varphi}(x^\alpha, t) = \varphi_\gamma \mathbf{e}_\gamma, \quad \underline{\psi}(x^\alpha, t) = (\varphi_\gamma + u_{3,\gamma}) \mathbf{e}_\gamma \quad 10.2$$

Equation (10.1) contains five independent variables and satisfies the tangential traction-free conditions on the bottom and top planes of the plate. We introduce two auxiliary variables to relax the continuity in the displacement field (from  $C^1$  to  $C^0$ ), namely

$$\psi_\alpha = \varphi_\alpha + u_{3,\alpha} \quad 10.3$$

which are suitable for a straightforward finite element model development.

The components of the infinitesimal strain tensor are expressed as

$$\varepsilon_{ij} = \frac{1}{2} (V_{i,j} + V_{j,i}) \quad 10.4$$

where  $V_i$  are the components of the spatial displacement vector  $\mathbf{v}$ . The kinematics of the plate associated with the displacement field given in Eq. (10.1) is

$$\begin{aligned} \varepsilon_{\alpha\beta} &= \varepsilon_{\alpha\beta}^{(0)} + \varepsilon_{\alpha\beta}^{(1)} x^3 + \varepsilon_{\alpha\beta}^{(3)} (x^3)^3 \\ \varepsilon_{\alpha 3} &= \varepsilon_{\alpha 3}^{(0)} + \varepsilon_{\alpha 3}^{(2)} (x^3)^2 \end{aligned} \quad 10.5$$

where the membrane  $\varepsilon_{\alpha\beta}^{(0)}$  and flexural  $\varepsilon_{\alpha\beta}^{(1)}$  strain components are

$$\begin{aligned} \varepsilon_{11}^{(0)} &= u_{1,1} & \varepsilon_{22}^{(0)} &= u_{2,2} & 2\varepsilon_{12}^{(0)} &= u_{1,2} + u_{2,1} \\ \varepsilon_{11}^{(1)} &= \varphi_{1,1} & \varepsilon_{22}^{(1)} &= \varphi_{2,2} & 2\varepsilon_{12}^{(1)} &= \varphi_{1,2} + \varphi_{2,1} \\ \varepsilon_{11}^{(3)} &= k\psi_{1,1} & \varepsilon_{22}^{(3)} &= k\psi_{2,2} & 2\varepsilon_{12}^{(3)} &= k(\psi_{1,2} + \psi_{2,1}) \end{aligned} \quad 10.6$$

and the transverse shear strain components  $\varepsilon_{\alpha 3}^{(0)}$  and  $\varepsilon_{\alpha 3}^{(1)}$  are defined as

$$\begin{aligned} 2\varepsilon_{13}^{(0)} &= \varphi_1 + \varphi_{3,1} & 2\varepsilon_{23}^{(0)} &= \varphi_2 + u_{3,2} \\ 2\varepsilon_{13}^{(2)} &= 3k\psi_1 & 2\varepsilon_{23}^{(2)} &= 3k\psi_2 \end{aligned} \quad 10.7$$

### 10.2.2 Constitutive equations of functionally graded plates

Functionally graded materials (FGMs) are a special kind of composite in which the material properties vary smoothly and continuously from one surface to the other. These materials are microscopically inhomogeneous and are typically made from isotropic components.

Functionally graded plates considered here are made from a mixture of ceramics and metals which is called two-phase functionally graded material. The material in the bottom and top planes is metal and ceramic respectively (see Fig. 10.1). We also assume a rule of mixtures based on the Voigt model (Suresh and Mortensen 1998). Therefore, any material property is given by the weighted average of the moduli of the constituents, namely

$$\bar{\omega}(x^3) = \bar{\omega}_c f_c + \bar{\omega}_m f_m \quad 10.8$$

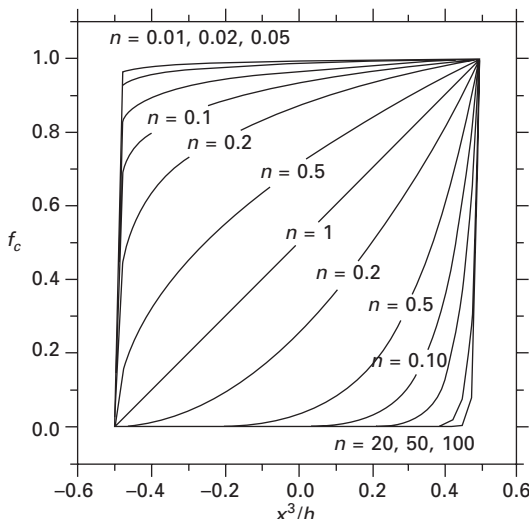
where the subscripts  $m$  and  $c$  refer to the metal and ceramic constituencies and  $f$  is the volume fraction of the phase. The symbol  $\bar{\omega}$  denotes a generic material property like the Young's modulus. The volume fractions of the ceramic  $f_c$  and metal  $f_m$  corresponding to the power law are expressed as (Reddy 2000, Praveen and Reddy 1998)

$$f_c = \left( \frac{z}{h} + \frac{1}{2} \right)^n, \quad f_m = 1 - f_c \quad 10.9$$

where  $n$  is the volume fraction exponent which takes values greater than or equal to zero. The value of  $n$  equal to zero represents a fully ceramic shell. Conversely, we have a fully metal plate as  $n$  goes to infinity (see Fig. 10.2).

By postulating that any plane of the plate (with thickness coordinate  $x^3$ ) is made of linear elastic isotropic material whose constitutive equations are expressed as

$$\sigma_{ij} = E_{ijkl}(x^3)\varepsilon_{kl} \quad 10.10$$



10.2 Variation of the volume fraction function  $f_c$  through the dimensionless thickness for different values of  $n$ .

and under the assumption of zero normal stress  $\sigma_{33} = 0$ , we arrive at the following expression

$$\sigma_{\alpha\beta} = C_{\alpha\beta\lambda\mu}\varepsilon_{\lambda\mu}, \quad \sigma_{\alpha3} = 2C_{\alpha3\lambda3}\varepsilon_{\lambda3} \quad 10.11$$

where

$$C_{\alpha\beta\lambda\mu}(x^3) = E_{\alpha\beta\lambda\mu} - E_{\alpha\beta 33} \frac{E_{33\lambda\mu}}{E_{3333}}, \quad C_{\alpha 3\lambda 3}(x^3) = E_{\alpha 3\lambda 3} \quad 10.12$$

are the reduced components of the elasticity tensor.

Note that the coefficients  $C_{\alpha\beta\lambda\mu}$  are no longer components of a tensor. They can be arranged in a matrix form by defining the matrices  $[C^m] \in \mathbb{M}^{3 \times 3}$  and  $[C^s] \in \mathbb{M}^{2 \times 2}$ . Then, we obtain

$$[C^m] = \begin{bmatrix} C_{1111} & C_{1122} & C_{1112} \\ C_{1122} & C_{2222} & C_{2212} \\ C_{1112} & C_{2212} & C_{1212} \end{bmatrix}, \quad [C^s] = \begin{bmatrix} C_{2323} & C_{2313} \\ C_{2313} & C_{1313} \end{bmatrix} \quad 10.13$$

with

$$\begin{aligned} C_{1111}(x^3) = C_{2222}(x^3) &= \frac{E(x^3)}{1 + \nu^2}, & C_{1122}(x^3) &= \frac{\nu E(x^3)}{1 + \nu^2} \\ C_{1212}(x^3) = C_{2323}(x^3) &= C_{1313}(x^3) = \frac{E(x^3)}{2(1 + \nu)} \end{aligned} \quad 10.14$$

and  $C_{1112} = C_{2212} = C_{2313} = 0$ . For Young's modulus  $E(x^3)$ , the formula given in Eq. (10.8) is used. A constant Poisson ratio of  $\nu = 0.3$  is assumed as it does not vary significantly in an FGM plate.

### 10.2.3 Hamilton's principle and stress resultants

The general form of Hamilton's principle for a continuum deformable body is expressed as (Reddy 2002, 2004)

$$\begin{aligned} \delta \int_{t_1}^{t_2} \mathcal{L} dt &= \int_{t_1}^{t_2} [\delta \mathcal{K} - (\delta \mathcal{W}_I + \delta \mathcal{W}_E)] dt \\ &= \int_{t_1}^{t_2} \left( \delta \int_V \frac{1}{2} \rho \dot{\mathbf{v}} \cdot \dot{\mathbf{v}} dV - \int_V \sigma_{ij} \delta \varepsilon_{ij} dV + \int_{\Omega} P_j \delta V_j d\Omega \right) dt = 0 \end{aligned} \quad 10.15$$

where  $\delta \mathcal{K}$  denotes the virtual kinetic energy,  $\delta \mathcal{W}_I$  is the virtual work of the internal forces,  $\delta \mathcal{W}_E$  the virtual work due to external forces and  $\delta$  is the variational operator. The virtual kinetic energy can be written in terms of the acceleration vector

$$\int_{t_1}^{t_2} \delta \mathcal{H} dt = \int_{t_1}^{t_2} \left( \int_V \rho \dot{\mathbf{v}} \cdot \delta \dot{\mathbf{v}} dV \right) dt = - \int_{t_1}^{t_2} \left( \int_V \rho \ddot{\mathbf{v}} \cdot \delta \mathbf{v} dV \right) dt \quad 10.16$$

where the last expression is arrived by integration-by-parts and using the fact that all virtual variations vanish at the ends of the time interval.

For free vibration, we consider periodic motions of the form

$$\mathbf{v}(x^j, t) = \mathbf{v}^0(x^j) e^{i\omega t}, \quad i = \sqrt{-1} \quad 10.17$$

Substituting Eq. (10.17) into Eq. (10.16) and omitting for simplicity the superscript ‘0’, we obtain

$$\begin{aligned} \int_{t_1}^{t_2} \delta \mathcal{H} dt &= \int_{t_1}^{t_2} e^{2i\omega t} dt \left( \int_V \rho \omega^2 \mathbf{v} \cdot \delta \mathbf{v} dV \right) \\ &= \int_{t_1}^{t_2} e^{2i\omega t} dt \left( \int_V \rho \omega^2 (\mathbf{u} + x^3 \underline{\varphi} + k(x^3)^3 \underline{\psi}) \right. \\ &\quad \times \left. (\delta \mathbf{u} + x^3 \delta \underline{\varphi} + k(x^3)^3 \delta \underline{\psi}) dV \right) \end{aligned} \quad 10.18$$

where  $\int_{t_1}^{t_2} e^{2i\omega t} dt$ , being nonzero, can be factored out when Eq. (10.15) is used. After some manipulations, Eq. (10.18) becomes

$$\begin{aligned} \mathbb{G}_D &= \int_V \rho \omega^2 \mathbf{v} \cdot \delta \mathbf{v} dV = \omega^2 \int_{\Omega} [(\mathbf{u} \cdot \delta \mathbf{u}) I^{(0)} \\ &\quad + (\mathbf{u} \cdot \delta \underline{\varphi} + \underline{\varphi} \cdot \delta \mathbf{u}) I^{(1)} + (\underline{\varphi} \cdot \delta \underline{\varphi}) I^{(2)} + k(\mathbf{u} \cdot \delta \underline{\psi} + \underline{\psi} \cdot \delta \mathbf{u}) I^{(3)} \\ &\quad + k(\underline{\varphi} \cdot \delta \underline{\psi} + \underline{\psi} \cdot \delta \underline{\varphi}) I^{(4)} + k^2 (\underline{\psi} \cdot \delta \underline{\psi}) I^{(6)}] d\Omega \end{aligned} \quad 10.19$$

and the mass inertias  $I^{(j)}$  are defined as

$$I^{(j)} = \int_{-h/2}^{h/2} \rho (x^3)^j dx^3 \quad 10.20$$

In addition, we assume a constant density through the thickness of the plate. This implies that  $I^{(1)} = I^{(3)} = 0$ . Hence, Eq. (10.19) can be written, using tensor component notation, as

$$\begin{aligned} \mathbb{G}_D &= \omega^2 \int_{\Omega} [(u_j \delta u_j) I^{(0)} + (\varphi_{\alpha} \delta \varphi_{\alpha}) I^{(2)} \\ &\quad + k(\varphi_{\alpha} \delta \psi_{\alpha} + \psi_{\alpha} \delta \varphi_{\alpha}) I^{(4)} + k^2 (\psi_{\alpha} \delta \psi_{\alpha}) I^{(6)}] d\Omega \end{aligned} \quad 10.21$$

The internal virtual work can be simplified by using Eqs. (10.5) and (10.17) and the condition  $\varepsilon_{33} = 0$ . Then, we obtain

$$\mathbb{G}_I = \int_V \left( \sigma_{\alpha\beta} \sum_{k=0}^3 (x^3)^{(k)} \delta \epsilon_{\alpha\beta}^{(k)} + 2 \sigma_{\alpha 3} \sum_{k=0}^2 (x^3)^{(k)} \delta \epsilon_{\alpha 3}^{(k)} \right) dV \quad 10.22$$

The pre-integration through the thickness of the plate leads to a two-dimensional integral that is expressed, using stress resultants, as

$$\mathbb{G}_I = \int_{\Omega} \left( \sum_{k=0}^3 N_{\alpha\beta}^{(k)} \delta \epsilon_{\alpha\beta}^{(k)} + 2 \sum_{k=0}^2 Q_{\alpha 3}^{(k)} \delta \epsilon_{\alpha 3}^{(k)} \right) d\Omega \quad 10.23$$

where the index  $k$  takes values of 0, 1, 3 and 0, 2 for the first and second term, respectively. The stress resultants  $N_{\alpha\beta}^{(k)}$  and  $Q_{\alpha 3}^{(k)}$  are defined as

$$\begin{aligned} N_{\alpha\beta}^{(k)} &= \int_{-h/2}^{h/2} \sigma_{\alpha\beta} (x^3)^k dx^3 = \sum_{l=0}^3 C_{\alpha\beta\omega\rho}^{k+l} \epsilon_{\omega\rho}^{(l)}, \quad k, l = 0, 1, 3 \\ Q_{\alpha 3}^{(k)} &= \int_{-h/2}^{h/2} \sigma_{\alpha 3} (x^3)^k dx^3 = 2 \sum_{l=0}^2 C_{\alpha 3\omega 3}^{k+l} \epsilon_{\omega 3}^{(l)}, \quad k, l = 0, 2 \end{aligned} \quad 10.24$$

where  $C_{\alpha\beta\omega\rho}^{k}$  and  $C_{\alpha 3\beta 3}^{k}$  are the material stiffness coefficients of the plate and are computed using

$$\begin{aligned} C_{\alpha\beta\omega\rho}^{k} &= \int_{-h/2}^{h/2} C_{\alpha\beta\omega\rho} (x^3)^k dx^3, \quad k = 0, 1, 2, 3, 4, 6 \\ C_{\alpha 3\beta 3}^{k} &= \int_{-h/2}^{h/2} C_{\alpha 3\beta 3} (x^3)^k dx^3, \quad k = 0, 2, 4 \end{aligned} \quad 10.25$$

The exact formulas of these coefficients for the case of functionally graded plates are presented in the Appendix. Finally, the virtual work of external forces (only surface forces) is written as

$$\mathbb{G}_E = \int_{\Omega} P_j \delta u_j d\Omega \quad 10.26$$

Note that Eqs. (10.21) and (10.23) are symmetric bilinear forms while Eq. (10.26) is a linear functional.

## 10.3 Finite element model

### 10.3.1 Variational formulation

The weak form can be easily constructed from the Hamilton's principle given in Eq. (10.15). Let  $\Theta \equiv (\mathbf{u}, \underline{\varphi}, \underline{\psi})$  be a configuration solution of the plate. We start by introducing the space of test functions  $\mathcal{V}$  (space of admissible variations) defined as (Reddy 2002)

$$\mathcal{V} = \{\Phi \equiv (\mathbf{w}, \underline{\eta}, \underline{\kappa}) \in [H^1(\Omega)]^3 \times [H^1(\Omega)]^2 \times [H^1(\Omega)]^2 \mid \mathbf{w}|_{\Gamma_D} = 0, \underline{\eta}|_{\Gamma_D} = 0, \underline{\kappa}|_{\Gamma_D} = 0\} \quad 10.27$$

where  $H^1(\Omega)$  is the Sobolev space of degree 1 and  $\Gamma_D$  is the Dirichlet boundary. The test function  $\Phi$  can be interpreted as virtual displacements and rotations of the mid-plane. The final expression of the weak form  $\mathcal{J}$  can be written in the following form:

$$\mathcal{J}(\Phi; \lambda, \Theta) = \mathbb{G}_D(\Phi; \lambda, \Theta) - \mathbb{G}_I(\Phi; \Theta) + \mathbb{G}_E(\Phi) \equiv 0 \quad 10.28$$

where

$$\begin{aligned} \mathbb{G}_D(\Phi; \lambda, \Theta) &= \lambda \int_{\Omega} [(\mathbf{w} \cdot \mathbf{u}) I^{(0)} + (\underline{\eta} \cdot \underline{\varphi}) I^{(2)} \\ &\quad + k(\underline{\kappa} \cdot \underline{\varphi} + \underline{\eta} \cdot \underline{\psi}) I^{(4)} + k^2(\underline{\kappa} \cdot \underline{\psi}) I^{(6)}] d\Omega \\ \mathbb{G}_I(\Phi; \Theta) &= \int_{\Omega} \left( \sum_{k=0}^3 \sum_{l=0}^3 C_{\alpha\beta\omega\rho} \epsilon_{\omega\rho}^{(l)}(\Phi) \epsilon_{\alpha\beta}^{(k)}(\Theta) \right. \\ &\quad \left. + 4 \sum_{k=0}^2 \sum_{l=0}^2 C_{\alpha 3 \omega 3} \epsilon_{\omega 3}^{(l)}(\Phi) \epsilon_{\alpha 3}^{(k)}(\Theta) \right) d\Omega \\ \mathbb{G}_E(\Phi) &= \int_{\Omega} (\mathbf{P} \cdot \mathbf{w}) d\Omega \end{aligned} \quad 10.29$$

For static bending problems, the term  $\mathbb{G}_D$  vanishes and we arrive at the following variational problem:

Find  $\Theta = (\mathbf{u}, \underline{\varphi}, \underline{\psi}) \in \mathcal{V}$  such that  $\forall \Phi = (\mathbf{w}, \underline{\eta}, \underline{\kappa}) \in \mathcal{V}$

$$\mathbb{G}_I(\Phi; \Theta) = \mathbb{G}_E(\Phi) \quad 10.30$$

For free vibration problems, the term  $\mathbb{G}_E$  vanishes and the variational problem becomes one of finding

$\lambda \in \mathbb{R}$  and  $\Theta = (\mathbf{u}, \underline{\varphi}, \underline{\psi}) \in \mathcal{V}$  such that  $\forall \Phi = (\mathbf{w}, \underline{\eta}, \underline{\kappa}) \in \mathcal{V}$

$$\mathbb{G}_I(\Phi; \Theta) - \mathbb{G}_D(\Phi; \lambda, \Theta) = 0 \quad 10.31$$

where  $\mathcal{V}$  is given in Eq. (10.27).

### 10.3.2 Discrete finite element model

Consider the computational domain  $\Omega$  be discretized into  $nel$  elements such that

$$\Omega = \bigcup_{e=1}^{nel} \Omega^e \quad 10.32$$

where the closure of  $\Omega$  is obviously understood. Next, we construct the finite-dimensional space of  $\mathcal{V}$  called  $\mathcal{V}^{hp}$  such that  $\mathcal{V}^{hp} \subset \mathcal{V}$ . The discrete finite element model of the problems (10.30) and (10.31) is now written as

$$\text{Find } \Theta^{hp} = (\mathbf{u}^{hp}, \underline{\varphi}^{hp}, \underline{\Psi}^{hp}) \in \mathcal{V}^{hp} \text{ such that } \forall \Phi^{hp}$$

$$= (\mathbf{w}^{hp}, \underline{\eta}^{hp}, \underline{\kappa}^{hp}) \in \mathcal{V}^{hp}$$

$$\mathbb{G}_I^e(\Phi^{hp}; \Theta^{hp}) = \mathbb{G}_E^e(\Phi^{hp}) \quad 10.33$$

for static bending problems, and

$$\text{Find } \lambda^{hp} \in \mathbb{R} \text{ and } \Theta^{hp} = (\mathbf{u}^{hp}, \underline{\varphi}^{hp}, \underline{\Psi}^{hp}) \in \mathcal{V}^{hp}$$

$$\text{such that } \forall \Phi^{hp} = (\mathbf{w}^{hp}, \underline{\eta}^{hp}, \underline{\kappa}^{hp}) \in \mathcal{V}^{hp}$$

$$\mathbb{G}_I^e(\Phi^{hp}; \Theta^{hp}) - \mathbb{G}_D^e(\Phi^{hp}; \lambda^{hp}, \Theta^{hp}) = 0 \quad 10.34$$

for free vibration problem.

Under the isoparametric concept, the same interpolation functions for the coordinates and variables are utilized. Let  $\hat{\Omega}^e \equiv [-1, 1] \times [-1, 1]$  be a parent domain in  $(\xi, \eta)$ -space (e.g. the closed, bi-unit square in  $\mathbb{R}^2$ ). We first map the coordinates  $\underline{x}(\xi, \eta): \hat{\Omega}^e \rightarrow \Omega^e$  such that

$$\underline{x}(\xi, \eta) = \left( \sum_{j=1}^m (x^\alpha)^{(j)} N^{(j)}(\xi, \eta) \right) \mathbf{e}_\alpha \quad 10.35$$

where  $\underline{x} = x^\alpha \mathbf{e}_\alpha$ . The present finite element model requires only  $C^0$ -continuity in all its variables because the weak form involves only the first derivatives of the unknowns. The number of variables to be interpolated in the finite element model is seven for the TSDT and five for the FSDT. The finite element equations are obtained by interpolating the displacements and rotations, namely

$$\begin{aligned} \mathbf{u}^{hp}(\underline{x}) &= \left( \sum_{j=1}^m u_k^{(j)} N^{(j)}(\xi, \eta) \right) \mathbf{e}_k \underline{\varphi}^{hp}(\underline{x}) \\ &= \left( \sum_{j=1}^m \varphi_\beta^{(j)} N^{(j)}(\xi, \eta) \right) \mathbf{e}_\beta, \underline{\Psi}^{hp}(\underline{x}) \\ &= \left( \sum_{j=1}^m \psi_\beta^{(j)} N^{(j)}(\xi, \eta) \right) \mathbf{e}_\beta \end{aligned} \quad 10.36$$

where  $m$  is the number of nodes per element,  $N^{(j)}(\xi, \eta)$  are the Lagrange interpolation functions at the node  $j$  and  $(u_k^{(j)}, \varphi_\alpha^{(j)}, \psi_\alpha^{(j)})$  denote the nodal values of the displacements and rotations. The Lagrange polynomials are given by

$$L_i^1(\xi) = \prod_{\substack{k=1 \\ k \neq i}}^{p+1} \frac{(\xi - \xi_k)}{(\xi_i - \xi_k)}, \quad L_i^2(\eta) = \prod_{\substack{k=1 \\ k \neq i}}^{p+1} \frac{(\eta - \eta_k)}{(\eta_i - \eta_k)}, \quad i = 1, \dots, p+1,$$

10.37

where  $p$  is the polynomial degree. Finally, the interpolation functions are expressed as the tensor product of the Lagrange polynomials as

$$N^{(k)}(\xi, \eta) = L_i^1(\xi) L_j^2(\eta), \quad k = (j-1)(p+1) + i \quad 10.38$$

Here, a family of high-order Lagrange interpolations is used. We have used elements labeled  $Q25$  and  $Q81$  ( $p$  levels equal to 4 and 8, respectively). These higher-order elements are found to be free of shear locking. The family of high-order Lagrange elements and the corresponding number of degrees of freedom for the FSDT and TSDT are presented in Table 10.1.

Substituting interpolations of Eq. (10.36) into Eqs. (10.33) and (10.34), we obtain the following pair of matrix equations at the element level

$$[K^e](d^e) = \{F^e\}, \quad ([K^e] - \lambda[M^e])\{d^e\} = \{0\} \quad 10.39$$

for bending and free vibration analyses, respectively. Here  $[K]$  denotes the stiffness matrix,  $\lambda$  is the eigenvalue (square of the fundamental frequency),  $[M]$  is the mass matrix, and  $\{F\}$  is the load vector (the right-hand side). These element equations are then assembled for the  $nel$  elements of the domain  $\Omega$  (see Reddy 2006). Gauss elimination and inverse iteration methods, respectively, are employed to solve the bending and free vibration problems expressed in Eq. (10.39). These methods are suitable for positive-definite stiffness matrices.

## 10.4 Numerical results

In this section, some numerical examples of composite laminates and functionally graded plates in bending and vibration are presented. An extensive verification is carried out for the present FSDT and TSDT finite element formulations by comparing the present results with those found in the literature. Furthermore, a parametric study is carried out for bending and vibration behavior of functionally graded ceramic–metal plates.

Table 10.1 Number of degrees of freedom per element for different  $p$  levels

Element	$p$ level	FSDT (DOF)	TSDT (DOF)
$Q4$	1	20	28
$Q9$	2	45	63
$Q25$	4	125	175
$Q81$	8	405	567

Uniform meshes of  $4 \times 4Q25$  and  $2 \times 2Q81$  elements with five and seven degrees of freedom per node for the FSDT and TSDT, respectively, were utilized in the finite element analysis (a total of 1445 and 2023 DOF, respectively). The flexibility of these elements (using polynomials of fourth and eighth degree) precludes any possible shear locking in the numerical computation. Consequently, there is no need to use mixed interpolation techniques (for lower-order elements such as assumed strain elements or MITC elements) or reduced integration in the evaluation of the stiffness coefficients (i.e. full Gauss integration rule is employed in all examples). All results are presented in terms of physical components, which in the case of plates, coincide with the tensor components.

#### 10.4.1 Bending analysis

First, the present results are compared with those of Pagano (1970), which are amply used for assessment of the accuracy of plate theories because they represent one of the few analytical 3D solutions for bending of cross-ply laminated plates.

The dimensionless center deflections and in-plane stresses for simply supported cross-ply plates ( $0^\circ/90^\circ/0^\circ$ ) under sinusoidal loading and two different plate aspect ratios,  $a/b = 1$  and  $1/3$  are presented in Tables 10.2 and 10.3. The following nondimensional parameters and lamina properties are employed:

*Table 10.2 Center deflection and stresses of a three-ply ( $0^\circ/90^\circ/0^\circ$ ) laminated square plate under sinusoidal loading ( $4 \times 4Q25$ )*

<i>S</i>	Pagano (1970)	Present TSDT	Present FSDT
$\bar{\sigma}_{<11>} \left( 0, 0, \frac{h}{2} \right)$	4	0.801	0.766 92
	10	0.590	0.584 72
	20	0.552	0.550 70
	50	0.541	0.540 64
	100	0.539	0.539 19
$\bar{\sigma}_{<22>} \left( 0, 0, \frac{h}{6} \right)$	4	-0.556	-0.507 86
	10	-0.288	-0.271 23
	20	-0.210	-0.205 00
	50	-0.185	-0.183 76
	100	-0.181	-0.180 63
$\bar{\sigma}_{<12>} \left( \frac{a}{2}, \frac{b}{2}, \frac{h}{2} \right)$	4	-0.0511	-0.049 93
	10	-0.0289	-0.028 07
	20	-0.0234	-0.023 12
	50	-0.0216	-0.021 58
	100	-0.0213	-0.021 36

Table 10.3 Center deflection and stresses of a cross-ply ( $0^\circ/90^\circ/0^\circ$ ) laminated rectangular plate ( $b = 3a$ ) under sinusoidal loading ( $4 \times 4 Q25$ )

	$S$	Pagano (1970)	Present TSDT	Present FSDT
$\bar{v}_{<3>} (0, 0, 0)$	4	2.820	2.648 38	2.362 56
	10	0.919	0.869 04	0.803 01
	20	0.610	0.595 80	0.578 38
	50	0.520	0.518 21	0.515 39
	100	0.508	0.507 09	0.506 38
$\bar{\sigma}_{<11>} \left( 0, 0, \frac{h}{2} \right)$	4	1.140	1.08110	0.612 99
	10	0.726	0.712 16	0.621 41
	20	0.650	0.646 18	0.622 79
	50	0.628	0.626 97	0.623 19
	100	0.624	0.624 20	0.623 25
$\bar{\sigma}_{<22>} \left( 0, 0, -\frac{h}{6} \right)$	4	-0.1190	-0.103 89	-0.093 42
	10	-0.0435	-0.040 11	-0.037 46
	20	-0.0299	-0.028 98	-0.028 27
	50	-0.0259	-0.025 76	-0.025 64
	100	-0.0253	-0.025 29	-0.025 26
$\bar{\sigma}_{<12>} \left( \frac{a}{2}, \frac{b}{2}, \frac{h}{2} \right)$	4	-0.0269	-0.026 31	-0.020 47
	10	-0.0120	-0.011 67	-0.010 48
	20	-0.0093	-0.009 15	-0.008 84
	50	-0.0084	-0.008 42	-0.008 37
	100	-0.0083	-0.008 32	-0.008 30

$$\bar{v}_{<3>} = \frac{100 E_2}{q_0 h S^4} v_{<3>} , \quad \bar{v}_{<\alpha>} = \frac{100 E_2}{q_0 h S^3} v_{<\alpha>} ,$$

$$\bar{\sigma}_{<\alpha\beta>} = \frac{1}{q_0 S^2} \sigma_{<\alpha\beta>} , \quad S = \frac{a}{h}$$

$$E_1/E_2 = 25, \quad G_{13} = G_{12} = 0.5E_2, \quad G_{23} = 0.2E_2, \quad v_{12} = 0.25$$

The simply supported boundary conditions used are

$$\text{At } x^1 = \pm a/2 \quad u_{<2>} = u_{<3>} = \varphi_{<2>} = \psi_{<2>} = 0$$

$$\text{At } x^2 = \pm b/2 \quad u_{<1>} = u_{<3>} = \varphi_{<1>} = \psi_{<1>} = 0$$

The loading can be expressed as  $P_3 = q_0 \cos(\pi x^1/a) \cos(\pi x^2/b)$ .

It is seen that the results for the present FSDT and TSDT are in close agreement with those of Pagano (1970). However, when the thickness-to-side ratio is increased, the results show greater error. This is evidently because the equivalent single-layer theories do not model a 3D problem adequately. It is also found that the TSDT yields more accurate results than the FSTD for thick plates.

An additional comparison of the dimensionless center deflection of cross-

ply rectangular plate is presented in Table 10.4 for the same geometry, material properties, and boundary conditions as in the previous example. In addition to the results of Pagano (1970) we include the MDT and SDT7 results of Braun (1995) and Braun *et al.* (1994). The MDT is a layer-wise ( $C^0$ -continuous displacement field), so-called multi-director theory, while the SDT7 is an improved first-order theory with thickness stretching and seven parameters (enhanced assumed strain formulation, EAS). The percentage of error computed for the TSDT and FSDT (case  $S = 4$ ) with respect to Pagano's solutions is 6% and 16%, respectively. Naturally, the MDT gives better results for thick plates than other theories, as expected because it is essentially 3D theory. On the other hand, remarkably, the present FSDT shows more accuracy than the SDT7 although Braun's formulation uses thickness stretching with EAS. These results are also illustrated in Fig. 10.3.

Figure 10.4 shows through-the-thickness distribution of the in-plane dimensionless displacement  $\bar{v}_{\langle 1 \rangle}$  for the problem discussed above. We should point out two important facts from these results: first, the zigzag effect arises visibly in thick cross-ply plates, and second, the TSDT (and not the FSDT) can reproduce that effect to some degree.

Next, we consider bending solutions for functionally graded square plates. The boundary conditions are the same as those used for simply supported laminated plates. Young's modulus and Poisson's ratio for zirconia (ceramic) and aluminium (metal) are

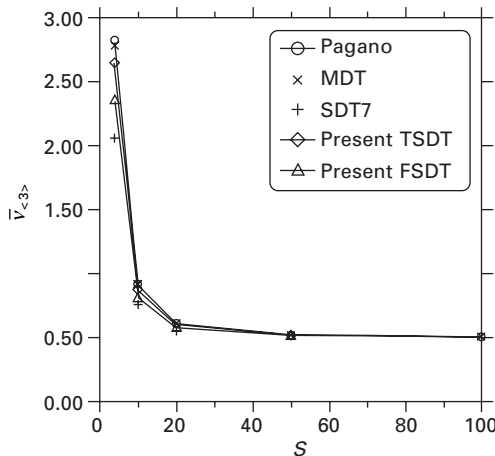
$$E_c = 151 \text{ GPa}, \quad v_c = 0.3$$

$$E_m = 70 \text{ GPa}, \quad v_m = 0.3$$

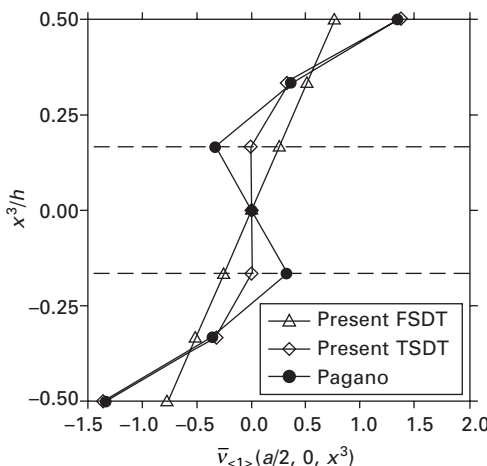
In Table 10.5, center deflection and in-plane stress results for functionally graded plates under sinusoidal loading are tabulated for different side-to-thickness ratios  $S$  and two volume fraction exponents  $n$ . Slight differences

**Table 10.4** Comparison of the center deflection  $\bar{v}_{\langle 3 \rangle}$  of a cross-ply (0°/90°/0°) laminated rectangular plate ( $b = 3a$ ) under sinusoidal loading (4 × 4Q25)

Formulation	Ratio $S = a/h$				
	4	10	20	50	100
Pagano (1970)	2.820	0.919	0.610	0.520	0.508
MDT	2.783 34	0.907 97	0.605 12	0.520 00	0.508 00
	1.3%	1.2%	0.8%	0.0%	0.0%
SDT7	2.061 42	0.753 58	0.566 08	0.513 76	0.505 97
	26.9%	18.0%	7.2%	1.2%	0.4%
Present TSDT	2.648 38	0.869 04	0.595 80	0.518 21	0.507 09
	6.0857%	5.4360%	2.3286%	0.3434%	0.1788%
Present FSDT	2.362 56	0.803 01	0.578 38	0.515 39	0.506 38
	16.2211%	12.6212%	5.1840%	0.8875%	0.3183%



10.3 Central deflection of a three-ply (0°/90°/0°) laminated rectangular plate vs. ratio  $S$ .



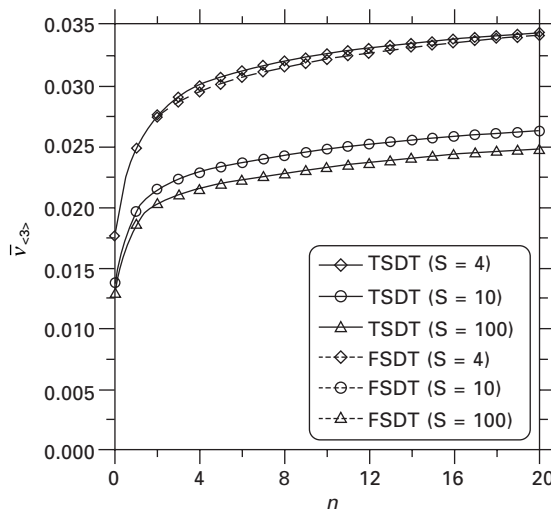
10.4 Displacement distribution through the thickness  $\bar{v}_{<1>}$  of a three-ply (0°/90°/0°) laminated rectangular plate ( $4 \times 4 Q25$ ,  $S = 4$ ).

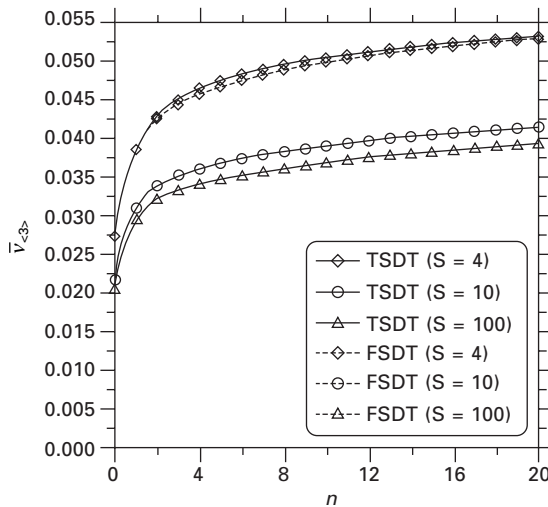
between the present FSDT and TSDT results are observed. The difference increases when the side-to-thickness ratio  $S$  decreases (thick plates). We also illustrate, in Figs 10.5 and 10.6, the effect of the volume fraction exponent on the center deflection of FGM square plates for different ratios  $S$  under sinusoidal and uniformly loading, respectively. Again, the difference in both formulations increases for thick plates ( $S = 4$ ) and volume fraction from 4 to 8.

Finally, Figs 10.7 to 10.14 show through-the-thickness distributions of in-plane displacements, membrane, and transverse shear stresses for FGM square plates under sinusoidal loading for various volume fraction exponents and ratios  $S = 4, 100$ . The nondimensional quantities used are

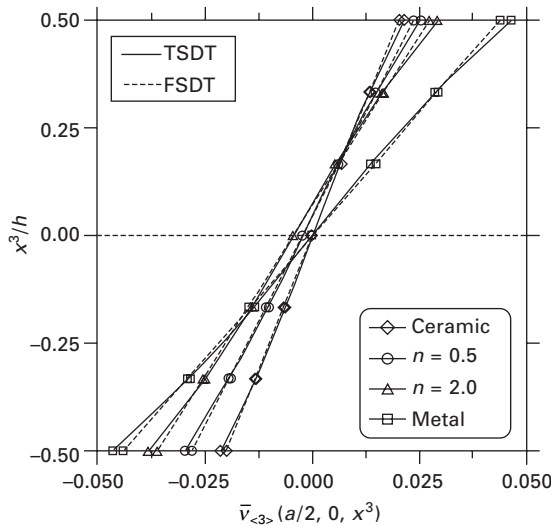
Table 10.5 Center deflection and in-plane stresses of FGM square plates under sinusoidal loading ( $4 \times 4Q25$ )

S	Present TSDT		Present FSDT		
	$n = 0.5$	$n = 2.0$	$n = 0.5$	$n = 2.0$	
$\bar{v}_{<3>} (0, 0, 0)$	4	0.022 114	0.027 577	0.022 189	0.027 404
	10	0.017 496	0.021 448	0.017 505	0.021 415
	20	0.016 834	0.020 568	0.016 836	0.020 560
	50	0.016 648	0.020 321	0.016 648	0.020 320
	100	0.016 622	0.020 286	0.016 622	0.020 286
$\bar{\sigma}_{<11>} \left(0, 0, \frac{h}{2}\right)$	4	0.244 374	0.283 599	0.230 626	0.265 405
	10	0.232 874	0.268 379	0.230 627	0.265 406
	20	0.231 193	0.266 155	0.230 628	0.265 407
	50	0.230 727	0.265 536	0.230 635	0.265 414
	100	0.230 666	0.265 454	0.230 642	0.265 423
$\bar{\sigma}_{<22>} \left(0, 0, -\frac{h}{6}\right)$	4	-0.046 763	-0.063 841	-0.049 238	-0.067 535
	10	-0.048 834	-0.066 931	-0.049 238	-0.067 535
	20	-0.049 137	-0.067 383	-0.049 238	-0.067 535
	50	-0.049 223	-0.067 512	-0.049 240	-0.067 537
	100	-0.049 237	-0.067 533	-0.049 241	-0.067 539
$\bar{\sigma}_{<12>} \left(\frac{a}{2}, \frac{b}{2}, \frac{h}{2}\right)$	4	-0.131 586	-0.152 707	-0.124 183	-0.142 910
	10	-0.125 393	-0.144 511	-0.124 183	-0.142 910
	20	-0.124 487	-0.143 312	-0.124 183	-0.142 910
	50	-0.124 232	-0.142 975	-0.124 184	-0.142 911
	100	-0.124 197	-0.142 928	-0.124 185	-0.142 912

10.5 Central deflection  $\bar{v}_{<3>}$  versus the volume fraction exponent  $n$  for FGM square plates under sinusoidal load.



10.6 Central deflection  $\bar{v}_{<3>}$  versus the volume fraction exponent  $n$  for FGM square plates under uniform load.

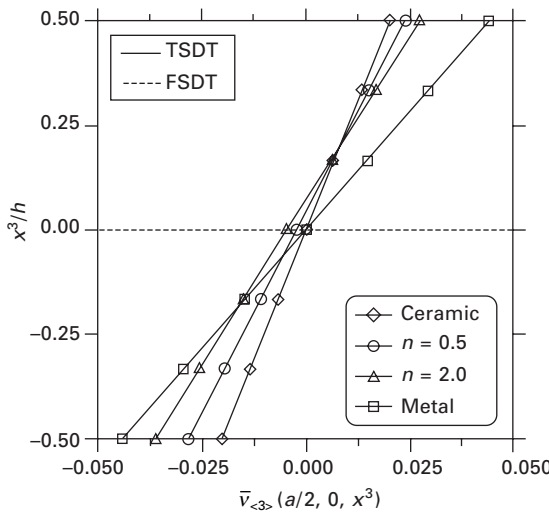


10.7 Displacement distribution through the thickness  $\bar{v}_{<1>}$  for FGM square plates ( $S = 4$ ).

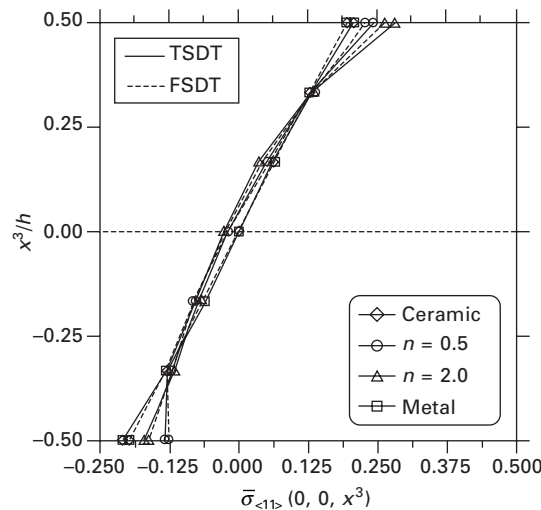
$$\bar{v}_{<3>} = \frac{E_m}{q_0 h S^4} v_{<3>} , \quad \bar{v}_{<\alpha>} = \frac{E_m}{q_0 h S^3} v_{<\alpha>} ,$$

$$\bar{\sigma}_{<\alpha\beta>} = \frac{1}{q_0 S^2} \sigma_{<\alpha\beta>} , \quad \bar{\sigma}_{<\alpha 3>} = \frac{1}{q_0 S} \sigma_{<\alpha 3>} ,$$

It is observed that both theories converge to each other when the ratio  $S$  increases. Also, there is no presence of the zigzag effect in the through-the-

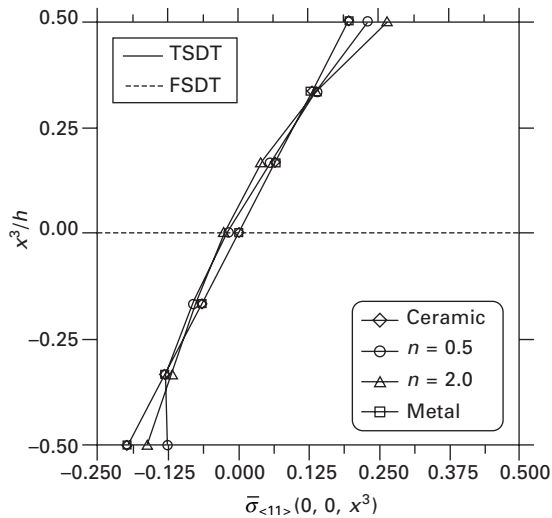


10.8 Displacement distribution through the thickness  $\bar{v}_{<1>}$  for FGM square plates ( $S = 100$ ).

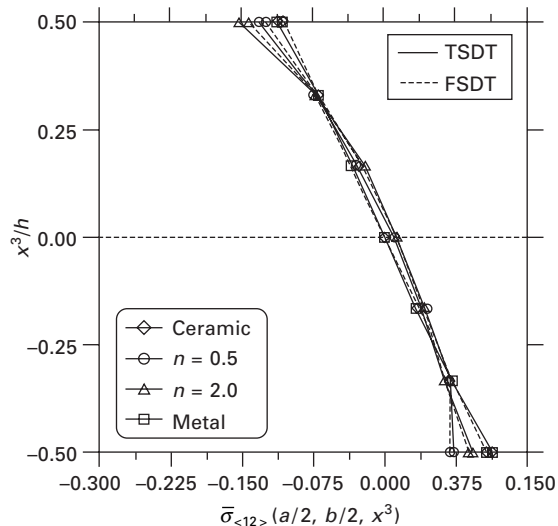


10.9 Stress distribution through the thickness  $\bar{v}_{<11>}$  for FGM square plates ( $S = 4$ ).

thickness distribution of the in-plane displacements even for thick plates. In both theories, thin and thick plates ( $S = 4$  and 100 respectively) show similar pattern of curves. The in-plane stress distribution through the thickness does not exhibit, as expected, any discontinuity (i.e. stress concentrations as in the laminate plates). Major differences between the FSDT and TSDT are observed in the transverse shear stress distribution through the thickness, as illustrated

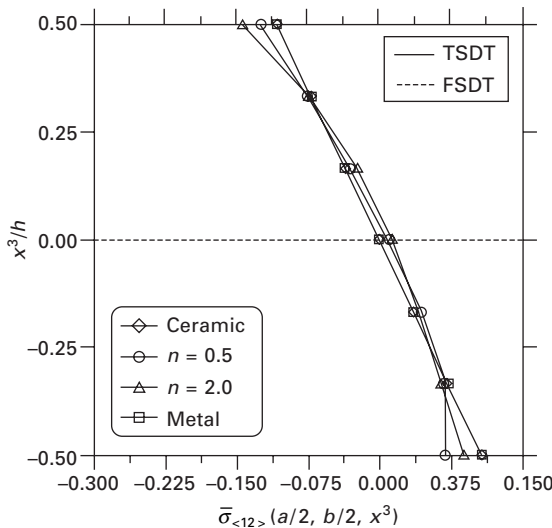


10.10 Stress distribution through the thickness  $\bar{\sigma}_{<11>}$  for FGM square plates ( $S = 100$ ).

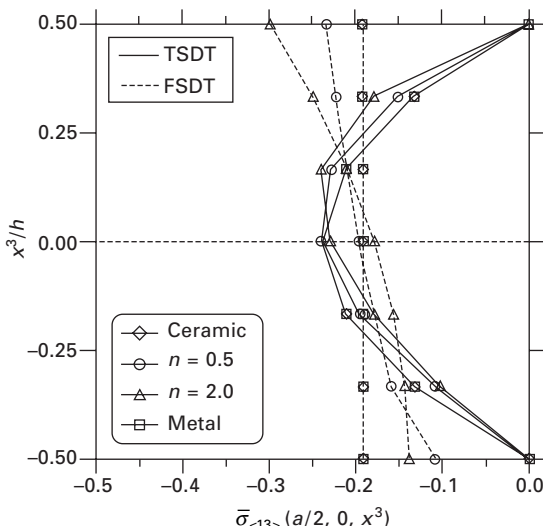


10.11 Stress distribution through the thickness  $\bar{\sigma}_{<12>}$  for FGM square plates ( $S = 4$ ).

in Figs 10.13 and 10.14. Clearly, the FSDT is neither reproduces the quasi-parabolic behavior of the transverse shear stress nor satisfies the tangential traction-free conditions on the surfaces of the plate. This is one of the main advantages of the TSDT over the FSDT.



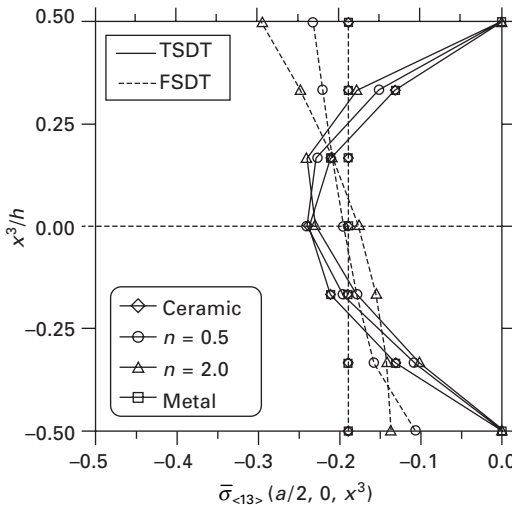
10.12 Stress distribution through the thickness  $\bar{\sigma}_{<12>}$  for FGM square plates ( $S = 100$ ).



10.13 Stress distribution through the thickness  $\bar{\sigma}_{<13>}$  for FGM square plates ( $S = 4$ ).

#### 10.4.2 Free vibration analysis

Next, free vibration analysis of laminated plates is discussed. Table 10.6 contains dimensionless fundamental frequencies for simply supported antisymmetric cross-ply square plates ( $0^\circ/90^\circ$ ) for different degrees of orthotropy ( $E_1/E_2$ ). The present results are compared with 3D analytical



10.14 Stress distribution through the thickness  $\bar{\sigma}_{<13>}$  for FGM square plates ( $S = 100$ ).

solutions of Noor (1973), 3D layerwise FEM results of Setoodeh and Karami (2004) and the analytical Lévy-type solutions of Reddy and Khdeir (1989). The following lamina properties are used in the numerical examples

$$E_1/E_2 = 20, 30, 40, \quad G_{13} = G_{12} = 0.6E_2, \quad G_{23} = 0.5E_2, \quad v_{12} = 0.25$$

Similar results are presented in Table 10.7 for different boundary conditions and side-to-thickness ratios with  $E_1/E_2 = 40$ . In both cases a mesh of  $2 \times 2Q81$  elements in a full plate was used in the analysis. The present results are in good agreement with the corresponding 3D analytical solutions of Noor (1973), the 3D layer-wise FEM results of Setoodeh and Karami (2004) and the analytical Lévy solutions of Reddy and Khdeir (1989).

An additional comparison for dimensionless fundamental frequencies is carried out in Table 10.8 for simply supported symmetric cross-ply square plates ( $0^\circ$  on the outer planes). We include results for the third-order formulation of Nayak *et al.* (2002) and the mixed finite element model of Putcha and Reddy (1986). We can see that the present TSDT and FSDT show a good performance from these comparisons.

The next example deals with free vibration analysis of functionally graded ceramic–metal plates. Table 10.9 shows the effect of the volume fraction exponent and ratio  $S$  on the fundamental frequency of simply supported FGM square plates for aluminum–zirconia materials. Small differences are observed between the present FSDT and TSDT. The difference between both formulations increases for lower ratios  $S$  and FGM plates. However, for fully ceramic or fully metal plates, the differences are negligible.

Finally, we present a parametric study of simply supported FGM square plates using the TSDT and FSDT. In addition to the aluminum–zirconia, we

**Table 10.6** Comparison of fundamental frequency parameter  $\bar{\omega}$  for antisymmetric cross-ply laminated square plates with different ratios  $E_1/E_2$  ( $2 \times 2Q81$ ,  $a/h = 5$ )

Theory	$\bar{\omega} = \omega h \sqrt{\rho/E_2}$		
	$E_1/E_2 = 40$	$E_1/E_2 = 30$	$E_1/E_2 = 20$
Noor (1973)	0.342 50	0.327 05	0.306 98
LW3D	0.347 76	0.330 61	0.308 36
TSDT	0.363 48	0.340 20	0.312 84
FSDT	0.353 33	0.332 84	0.308 24
Present TSDT	0.360 91	0.338 58	0.312 04
Present FSDT	0.353 33	0.332 84	0.308 24

**Table 10.7** Comparison of fundamental frequency parameter  $\bar{\omega}$  for antisymmetric cross-ply laminated square plates with various boundary conditions ( $2 \times 2Q81$ )

		$\bar{\omega} = \omega(b^2/h) \sqrt{\rho/E_2}$		
$h/a$	Theory	SSSS	SCSC	SFSF
0.1	TSDT	10.568	15.709	6.943
	FSDT	10.473	15.152	6.881
	Present TSDT	10.548	15.487	6.928
	Present FSDT	10.473	15.152	6.881
0.2	TSDT	9.087	11.890	6.128
	FSDT	8.833	10.897	5.952
	Present TSDT	9.023	11.373	6.079
	Present FSDT	8.833	10.896	5.952

also utilize the alumina as a ceramic constituent. The material properties of the alumina are

$$E_c = 380 \text{ GPa}, \quad v_c = 0.3$$

The effect of the volume fraction exponent on the fundamental frequency of FGM plates is illustrated in Figs 10.15 and 10.16 (two different ceramic–metal materials). The present FSDT and TSDT are compared for ratios  $S = 4, 20, 100$ . As expected, thinner plates give lower frequencies than thick plates. Also, the difference between both formulations is negligible.

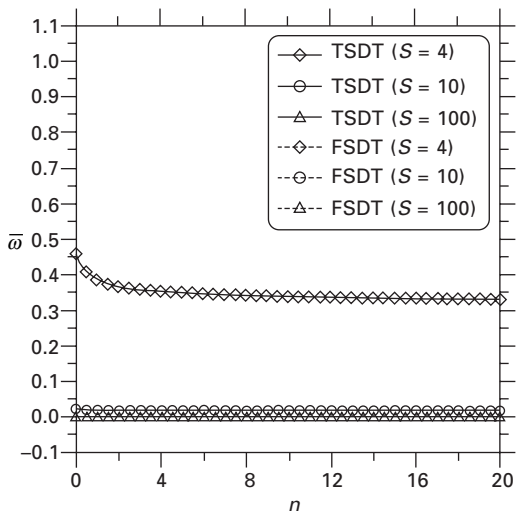
Figures 10.17 and 10.18 show dimensionless fundamental frequencies for functionally graded ceramic–metal square plates versus side-to-thickness ratios  $S$ . Curves are plotted for different volume fraction exponent  $n$  and only for the TSDT. It is noticed that the fundamental frequency tends to reach asymptotically some value (for fully metal) when the ratio  $S$  increases. For  $S = 20$  we can expect constant values. We also note that the fundamental frequency decreases when the volume fraction exponent increases. This is evident since a metal is less stiff than a ceramic material.

*Table 10.8 Effect of degree of orthotropy of the individual layers on the fundamental frequency of simply supported symmetric cross-ply laminated square plates for  $a/h = 5$ ;  $\bar{\omega} = \omega h \sqrt{\rho/E_2}$  ( $2 \times 2Q81$ )*

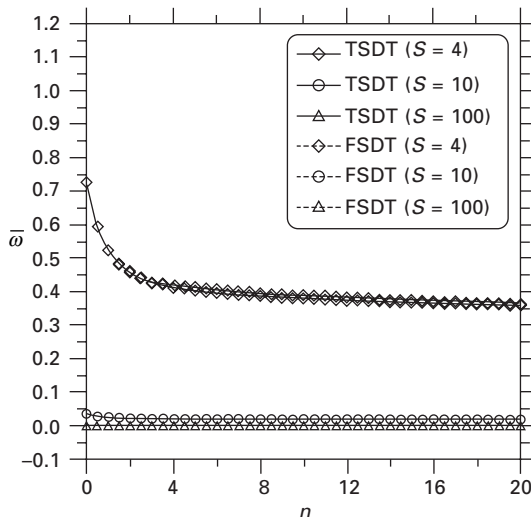
No.	Theory	$E_1/E_2$			
		3	10	20	30
3	Noor (1973)	0.264 74	0.328 41	0.382 41	0.410 89
	Nayak <i>et al.</i> (2002)	0.262 83	0.326 98	0.370 33	0.394 69
	Putcha and Reddy (1986)	0.262 47	0.330 95	0.381 12	0.410 94
	Present TSDT	0.262 09	0.326 03	0.369 34	0.393 71
	Present FSDT	0.262 52	0.327 39	0.371 10	0.395 41
	Noor (1973)	0.265 87	0.340 89	0.397 92	0.431 40
5	Nayak <i>et al.</i> (2002)	0.264 12	0.337 82	0.393 51	0.426 38
	Putcha and Reddy (1986)	0.263 72	0.339 97	0.399 43	0.435 09
	Present TSDT	0.263 37	0.336 74	0.392 25	0.425 08
	Present FSDT	0.263 37	0.336 80	0.393 06	0.427 14
	Noor (1973)	0.266 40	0.344 32	0.405 47	0.442 10
	Nayak <i>et al.</i> (2002)	0.264 12	0.337 82	0.393 51	0.426 38
9	Putcha and Reddy (1986)	0.264 00	0.342 20	0.404 33	0.442 01
	Present TSDT	0.263 81	0.340 91	0.401 48	0.437 96
	Present FSDT	0.263 76	0.340 79	0.401 47	0.438 18
					0.463 15

*Table 10.9* Effect of volume fraction exponent and ratio  $S$  on the fundamental frequency parameter of simply supported FGM square plates  
 $(2 \times 2 Q81)$

		$\bar{\omega} = 100 \omega h \sqrt{\rho/E_m}$												
$S = a/h$	Theory	$n = 0$			$n = 0.5$			$n = 1$			$n = 2$			
		TSDT	FSDT	45.874 329	40.807 276	38.502 949	36.553 900	TSDT	FSDT	45.853 995	40.749 429	38.486 542	36.653 696	31.648 716
10	TSDT	8.473 671		7.503 427		7.090 496		6.775 734		5.859 462				
	FSDT	8.473 526		7.501 538		7.090 380		6.780 666		5.859 618				
20	TSDT	2.173 659		1.922 934		1.817 739		1.739 516		1.503 714				
	FSDT	2.173 657		1.922 810		1.817 737		1.739 862		1.503 731				
50	TSDT	0.350 418		0.309 908		0.292 986		0.280 500		0.242 447				
	FSDT	0.350 418		0.309 905		0.292 986		0.280 509		0.242 448				
100	TSDT	0.087 700		0.077 558		0.073 324		0.070 204		0.060 679				
	FSDT	0.087 700		0.077 558		0.073 324		0.070 205		0.060 679				



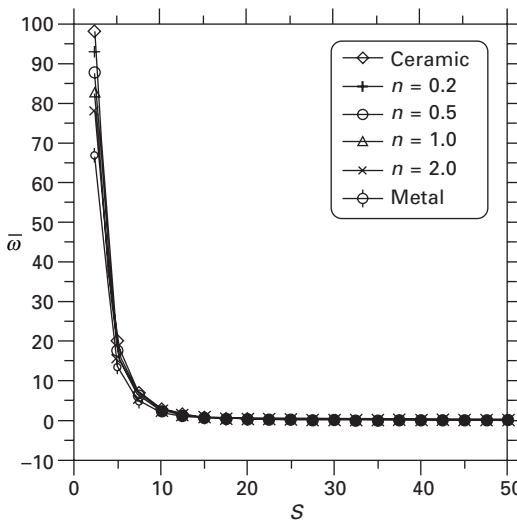
10.15 Effect of the volume fraction exponent on the fundamental frequency parameter for FGM square plates ( $\bar{\omega} = \omega h \sqrt{\rho/E_m}$ , aluminum–zirconia,  $2 \times 2Q81$ ).



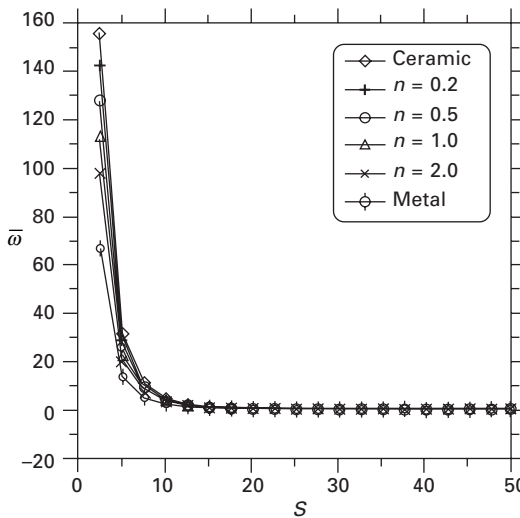
10.16 Effect of the volume fraction exponent on the fundamental frequency parameter for FGM square plates ( $\bar{\omega} = \omega h \sqrt{\rho/E_m}$ , aluminum–alumina,  $2 \times 2Q81$ ).

## 10.5 Conclusions

In this study, bending and free vibration analyses of laminated composite plates as well as functionally graded plates are presented. The third-order shear deformation theory with seven independent variables is used to model



10.17 Effect of the ratio  $a/h$  on the fundamental frequency parameter for FGM square plates ( $\bar{\omega} = 100 \sqrt{\rho/E_m}$ , aluminum-zirconia,  $4 \times 4$  Q25).



10.18 Effect of the ratio  $a/h$  on the fundamental frequency parameter for FGM square plates ( $\bar{\omega} = 100 \sqrt{\rho/E_m}$ , aluminum-alumina,  $4 \times 4$  Q25).

the structural behavior. In FGM plates, the gradation of properties through the thickness is assumed to be of the power-law type. An efficient displacement finite element model with high-order interpolation polynomials is developed. These types of element mitigate shear locking problems observed in shear

deformable finite element models with lower-order interpolation of the field variables. Comparisons of the present results with others found in the literature are excellent and verify the accuracy of the present formulation. As expected, for bending loading, the zig zag effect in the through-the-thickness distribution of the in-plane displacement disappears for functionally graded plates even for thick plates. Stress distributions through the thickness are smooth without any discontinuity (no stress concentration). Only the TSDT is capable of reproducing the parabolic behavior of the transverse shear stress (as shown in Figs 10.13 and 10.14) and satisfying the tangential traction-free conditions on the bottom and top planes of the plate. In general, free vibration analysis of FGM plates indicates that both theories yield almost the same results. It is also found that the fundamental dimensionless frequency of FGM plates lies in between that of the fully ceramic and fully metal plates. The differences between the results predicted by the two theories decrease when the side-to-thickness ratio increases (thin plate).

## 10.6 Acknowledgments

The research results reported herein were obtained while the authors were supported by Structural Dynamics Program of the Army Research Office (ARO) through Grant W911NF-05-1-0122 to Texas A&M University.

## 11.7 References

- Arciniega, R.A. and Reddy, J.N. (2005), ‘Consistent third-order shell theory with applications to composite circular cylinders’, *AIAA Journal*, **43** (9), 2024–2038.
- Braun, M. (1995), *Nichtlineare Analysen von geschichteten, elastischen Flächentragwerken*, PhD dissertation, Bericht Nr. 19, Institut für Baustatik, Universität Stuttgart.
- Braun, M., Bischoff, M. and Ramm, E. (1994), ‘Nonlinear shell formulations for complete three-dimensional constitutive laws including composites and laminates’, *Computational Mechanics*, **15**, 1–18.
- Della Croce, L. and Venini, P. (2004), ‘Finite elements for functionally graded Reissner-Mindlin plates’, *Computer Methods in Applied Mechanics and Engineering*, **193**, 705–725.
- Koizumi, M. (1997), ‘FGM activities in Japan’, *Composites, Part B: Engineering*, **28B**, 1–4.
- Loy, C.T., Lam, K.Y. and Reddy, J.N. (1999), ‘Vibration of functionally graded cylindrical shells’, *International J. Mechanical Sciences*, **41**, 309–324.
- Nayak, A.K., Moy, S.J. and Shenoi, R.A. (2002). ‘Free vibration analysis of composite sandwich plates based on Reddy’s higher-order theory’, *Composites, Part B: Engineering*, **33**, 505–519.
- Ng, T.Y., Lam, K.Y. and Liew, K.M. (2000). ‘Effects of FGM materials on the parametric resonance of plate structures’, *Computer Methods in Applied Mechanics and Engineering*, **190**, 953–962.

- Ng, T.Y., He, X.Q. and Liew, K.M. (2001), 'Finite element modeling of active control of functionally graded shells in frequency domain via piezoelectric sensors and actuators', *Computational Mechanics*, **28**, 1–9.
- Noor, A.K. (1973), 'Free vibrations of multilayered composite plates', *AIAA Journal*, **11**, 1038–1039.
- Pagano, N.J. (1970), 'Exact solutions for rectangular bidirectional composites and sandwich plates', *J. Composite Materials*, **4**, 20–34.
- Praveen, G.N. and Reddy, J.N. (1998), 'Nonlinear transient thermoelastic analysis of functionally graded ceramic–metal plates', *International J. Solids Structures*, **35**, 4457–4476.
- Putcha, N.S. and Reddy, J.N. (1986), 'Stability and natural vibration analysis of laminated plates by using a mixed element based on a refined plate theory', *J. Sound Vibration*, **104**, 285–300.
- Reddy, J.N. (1984), 'A simple higher-order theory for laminated composite plates', *ASME J. Applied Mechanics*, **51**, 745–752.
- Reddy, J.N. (2000), 'Analysis of functionally graded plates', *International J. Numerical Methods in Engineering*, **47**, 663–684.
- Reddy, J.N. (2002), *Energy Principles and Variational Methods in Applied Mechanics*, 2nd ed., John Wiley, New York.
- Reddy, J.N. (2004), *Mechanics of Laminated Composite Plates and Shells: Theory and Analysis*, 2nd ed., CRC Press, Boca Raton, Florida.
- Reddy, J.N. (2006), *An Introduction to the Finite Element Method*, 3rd ed., McGraw-Hill, New York.
- Reddy, J.N. and Arciniega, R.A. (2004), 'Shear deformation plate and shell theories from Stavsky to present', *Mechanics of Advanced Materials Structures*, **11** (6), 535–582.
- Reddy, J.N. and Chin, C.D. (1998), 'Thermomechanical analysis of functionally graded cylinders and plates', *J. Thermal Stresses*, **21**, 593–626.
- Reddy, J.N. and Khdeir, A.A. (1989), 'Buckling and vibration of laminated composite plates using various plate theories', *AIAA Journal*, **27**, 1808–1817.
- Reddy, J.N., Wang, C.M. and Kitipornchai, S. (1999), 'Axisymmetric bending of functionally graded circular and annular plates', *European Journal of Mechanics A – Solids*, **18** (2), 185–199.
- Setoodeh, A.R. and Karami, G. (2004), 'Static, free vibration and buckling analysis of anisotropic thick laminated composite plates on distributed and point elastic supports using a 3-D layerwise FEM', *Engineering Structures*, **26**, 211–220.
- Suresh, S. and Mortensen, A. (1998). *Fundamentals of Functionally Graded Materials*, IOM Commun. Ltd, Cambridge.
- Yamanouchi, M., Koizumi, M., Hirai, T. and Shiota, I. (eds.) (1990), *Proc. First Int. Sypos. Functionally Graded Materials*, Japan.
- Yang, J., Kitipornchai, S. and Liew, K.M. (2003), 'Large amplitude vibration of thermo-electro-mechanically stressed FGM laminated plates', *Computer Methods in Applied Mechanics and Engineering*, **192**, 3861–3885.
- Yang, J., Liew, K.M. and Kitipornchai, S. (2004), 'Dynamic stability of laminated FGM plates based on higher-order shear deformation theory', *Computational Mechanics*, **33**, 305–315.

## 10.8 Appendix

In this appendix, the exact values of the material stiffness coefficients for functionally graded plates are presented. We use the following formula given in Eq. (10.25)

$$\begin{aligned} C_{\alpha\beta\gamma\lambda}^k &= \int_{-h/2}^{h/2} C_{\alpha\beta\gamma\lambda}(x^3)^k dx^3, \quad k = 0, 1, 2, 3, 4, 6 \\ C_{\alpha 3 \gamma 3}^k &= \int_{-h/2}^{h/2} C_{\alpha 3 \gamma 3}(x^3)^k dx^3, \quad k = 0, 2, 4 \end{aligned} \quad 10.40$$

The coefficients  $C_{\alpha\beta\gamma\lambda}$  and  $C_{\alpha 3 \gamma 3}$  are defined by

$$\begin{aligned} C_{\alpha\beta\gamma\lambda} &:= C_{\alpha\beta\gamma\lambda}(x^3) = C_{\alpha\beta\gamma\lambda}^{\text{cm}} f_c + C_{\alpha\beta\gamma\lambda}^{\text{m}}, \\ C_{\alpha 3 \gamma 3} &:= C_{\alpha 3 \gamma 3}(x^3) = C_{\alpha 3 \gamma 3}^{\text{cm}} f_c + C_{\alpha 3 \gamma 3}^{\text{m}} \end{aligned} \quad 10.41$$

which are functions of the thickness coordinate  $x^3$ . In the above equation  $C_{\alpha\beta\gamma\lambda}^{\text{cm}} = C_{\alpha\beta\gamma\lambda}^{\text{c}} - C_{\alpha\beta\gamma\lambda}^{\text{m}}$ ,  $C_{\alpha 3 \gamma 3}^{\text{cm}} = C_{\alpha 3 \gamma 3}^{\text{c}} - C_{\alpha 3 \gamma 3}^{\text{m}}$ , and  $f_c$  is the volume fraction function of the ceramic constituency. Then Eq. (10.40) yields the following bending-membrane material stiffness coefficients:

$$\begin{aligned} {}^0 C_{\alpha\beta\gamma\lambda} &= C_{\alpha\beta\gamma\lambda}^{\text{cm}} \left( \frac{h}{n+1} \right) + C_{\alpha\beta\gamma\lambda}^{\text{m}} h, \\ {}^1 C_{\alpha\beta\gamma\lambda} &= C_{\alpha\beta\gamma\lambda}^{\text{cm}} \left( \frac{nh^2}{2(n+1)(n+2)} \right), \\ {}^2 C_{\alpha\beta\gamma\lambda} &= C_{\alpha\beta\gamma\lambda}^{\text{cm}} \left( \frac{(n^2+n+2)h^3}{4(n+1)(n+2)(n+3)} \right) + C_{\alpha\beta\gamma\lambda}^{\text{m}} \left( \frac{h^3}{12} \right), \\ {}^3 C_{\alpha\beta\gamma\lambda} &= C_{\alpha\beta\gamma\lambda}^{\text{cm}} \left( \frac{(n^2+3n+8)nh^4}{8(n+1)(n+2)(n+3)(n+4)} \right), \\ {}^4 C_{\alpha\beta\gamma\lambda} &= C_{\alpha\beta\gamma\lambda}^{\text{cm}} \left( \frac{(n^4+6n^3+23n^2+18n+24)h^5}{16(n+1)(n+2)(n+3)(n+4)(n+5)} \right) + C_{\alpha\beta\gamma\lambda}^{\text{m}} \left( \frac{h^5}{80} \right), \\ {}^5 C_{\alpha\beta\gamma\lambda} &= C_{\alpha\beta\gamma\lambda}^{\text{cm}} \left( \frac{(n^4+10n^3+55n^2+110n+184)nh^6}{32(n+1)(n+2)(n+3)(n+4)(n+5)(n+6)} \right), \\ {}^6 C_{\alpha\beta\gamma\lambda} &= C_{\alpha\beta\gamma\lambda}^{\text{cm}} \left( \frac{(n^6+15n^5+115n^4+405n^3+964n^2+660n+720)h^7}{64(n+1)(n+2)(n+3)(n+4)(n+5)(n+6)(n+7)} \right) \\ &\quad + C_{\alpha\beta\gamma\lambda}^{\text{m}} \left( \frac{h^7}{448} \right) \end{aligned} \quad 10.42$$

The shear material stiffness coefficients are given by

$$\begin{aligned} C_{\alpha 3 \gamma 3}^0 &= C_{\alpha 3 \gamma 3}^{\text{cm}} \left( \frac{h}{n+1} \right) + C_{\alpha 3 \gamma 3}^{\text{m}} h, \\ C_{\alpha 3 \gamma 3}^2 &= C_{\alpha 3 \gamma 3}^{\text{cm}} \left( \frac{(n^2 + n + 2)h^3}{4(n+1)(n+2)(n+3)} \right) + C_{\alpha 3 \gamma 3}^{\text{m}} \left( \frac{h^3}{12} \right), \\ C_{\alpha 3 \gamma 3}^4 &= C_{\alpha 3 \gamma 3}^{\text{cm}} \left( \frac{(n^4 + 6n^3 + 23n^2 + 18n + 24)h^5}{16(n+1)(n+2)(n+3)(n+4)(n+5)} \right) + C_{\alpha 3 \gamma 3}^{\text{m}} \left( \frac{h^5}{80} \right). \end{aligned} \quad 10.43$$

## Differential quadrature element method for vibration analysis of plates

---

K M LIEW, J YANG and S KITIPORNCHAI,  
City University of Hong Kong, People's Republic of China

### 11.1 Introduction

It is well known that significant geometrical nonlinearity is induced when a plate has deflections of more than approximately one-half of its thickness, especially when there are immovable edge constraints. For composite laminated plates with a bending–stretching coupling effect, the presence of initial stresses will make the problem much more complicated. Numerous studies of nonlinear vibration of isotropic and composite laminated plates have been conducted using various theoretical models and solution approaches (Sathyamoorthy, 1987, 1997). However, research efforts on nonlinear vibration of initially stressed plates are quite limited in number. By using the finite element method, Mei (1978) and Yang and Han (1983) presented large amplitude vibration analyses of isotropic plates under in-plane compression. Based on Mindlin plate theory and higher-order plate theories, Doong and his co-workers derived the nonlinear governing equations for thick plates in a general state of nonuniform initial stresses, and studied the large amplitude vibration of initially stressed isotropic rectangular plates (Chen and Doong, 1983a,b), isotropic circular plates, and cross-ply laminated plates (Chen *et al.*, 2002). Chen and Lin (1992) examined the combined effects of large amplitude and geometric imperfection on the large amplitude vibration behavior of initially stressed isotropic Mindlin plates. In the above-mentioned work, the results were only for simple boundary conditions.

Most of the studies dealing with the nonlinear vibration of isotropic and composite plate structures are based on the assumption that the plates are perfect in shape. In practice, however, these structures can possess globally or locally distributed, small and unavoidable initial geometric imperfections (namely, deviations between the actual shape and the intended shape) during the fabrication process. As revealed by experimental results (Yamaki *et al.*, 1983), these imperfections can have pronounced and complicated effects on the linear and nonlinear dynamic responses of plates in some cases.

There have been quite a few investigations of the dynamics of imperfect, isotropic, homogeneous, thin, and moderately thick plates (see Celep, 1976, 1980; Hui, 1983; Hui and Leissa, 1983; Lin and Chen, 1989; Chen and Lin, 1992). However, research into the nonlinear vibration of imperfect composite plates has been limited. Hui (1985) examined the influence of geometric imperfections on linear and large amplitude vibration of antisymmetrically laminated rectangular thin plates and reported that switch from a ‘hard-spring’ character to ‘soft-spring’ behavior may happen when the imperfection amplitude is of the order of half the plate thickness. By using the finite element method and polynomial functions to model the shape of imperfection modes, Kapania and Yang (1987) obtained the nonlinear vibration frequencies for isotropic and laminated thin plates with more general imperfections. Studies based on shear deformation plate theories include those by Chen and Lin (1992) for initially stressed, imperfect isotropic Mindlin plates, by Chen and Yang (1993) and Bhimaraddi (1993) for antisymmetric angle-ply and symmetric cross-ply rectangular plates, and the one by Bhimaraddi and Chandrashekara (1993) for heated antisymmetric angle-ply rectangular plates.

The above analyses found that for thicker isotropic plates, and even for some thin composite laminated plates, the effects of the transverse shear flexibility and rotary inertia become significant on the nonlinear dynamic response. Furthermore, the existence of a bending–stretching coupling effect in composites makes the vibration frequencies of some laminated plates very sensitive to geometric imperfections and initial stresses. With the exception of Kapania and Yang (1987), the aforementioned authors assumed that the imperfection mode was the same as the vibration mode, and presented results only for simple boundary conditions.

Functionally graded materials (FGMs) are novel inhomogeneous composite materials that were initially designed as thermal barriers for aerospace structures and fusion reactors and are now attracting a lot of research effort as reflected by a great number of studies reported (e.g. Reddy and Chin, 1998; Noda, 1999; Reddy, 2000; Liew *et al.*, 2001, 2002a, 2003a,b, 2004; Vel and Batra, 2002; Ng *et al.* 2002; Yang and Shen, 2003a,b; Yang *et al.*, 2004a,b). Unlike fiber–matrix composites, in which cracking and debonding may occur at high temperatures because of the material property mismatch at the interface of two discrete materials, FGMs have the advantage of being capable of withstanding severe high temperature while maintaining structural integrity. Owing to this superior thermo-mechanical property, FGM plate structures have found a wide range of applications in many industries, especially in space vehicles and aircraft, where they are very often subjected to high levels of thermal and dynamic loading, such as large temperature gradients and acoustic pressure. This may result in complicated large amplitude, nonlinear vibration behavior of the FGM plate due to the bending–stretching coupling and combined external loads. On the other hand, although several metallurgical

techniques have been developed for the fabrication of FGMs, the complexity of the manufacturing process means that initial imperfections are inevitable. Hence, it is of prime importance to understand the large amplitude vibration behavior of FGM plate structures with initial geometrical imperfections and under general loading and boundary supporting conditions.

In recent years, the dynamics of FGM plates have attracted increasing research effort, most of which has been devoted to linear vibration or dynamic response; see, for example, Reddy *et al.* (1999), Cheng and Batra (2000), Yang and Shen (2001, 2002), Vel and Batra (2004), and Qian *et al.* (2004). Investigations into the large amplitude vibration and nonlinear dynamic response of FGM plates are scarce. Praveen and Reddy (1998) analyzed the nonlinear transient response of FGM plates that were subjected to a steady temperature field and lateral dynamic loads by using the first-order shear deformation plate theory (FSDPT) and the finite element method. Reddy (2000) developed both theoretical and finite element formulations for thick FGM plates according to the higher-order shear deformation plate theory (HSDPT). In these two studies, nonlinear vibration and the effect of initial stresses were not discussed. Huang and Shen (2004) investigated the nonlinear vibration and dynamic response of a simply supported functionally graded plate under a uniform temperature field. A perturbation asymptotic technique and HSDPT were used in their analysis. By using Galerkin procedure and Runge–Kutta method, Chen (2005) solved the nonlinear vibration frequencies for a simply supported functionally graded plate subjected to a general state of nonuniform initial stress. The effect of initial geometrical imperfection, however, was not accounted for in these studies.

Since about 1995, vibration control of plate structures through the use of smart materials such as piezoelectrics, shape memory alloys, and rheological fluids has become increasingly important in practical applications. Many studies have been carried out on the modeling and controlling of the vibration behavior of isotropic and composite plates by means of piezoelectric sensors and actuators (Benjeddou, 2000). A number of studies have also been reported on the mechanical response of FGM plates that are integrated with piezoelectric materials (Ootao and Tanigawa, 2000; Elmajid *et al.*, 2001; Lim and He, 2001; Wu *et al.*, 2002). For the dynamics of piezoelectric FGM plates, Liew and his co-workers (Liew *et al.*, 2001, 2002b; He *et al.*, 2001) used classical plate theory (CPT) and the first-order shear deformation plate theory to present the finite element formulation for the shape and vibration control of FGM plates with integrated piezoelectric sensors and actuators. Reddy and Cheng (2001) employed the transfer matrix and asymptotic expansion techniques to obtain three-dimensional asymptotic solutions for functionally graded plates with an active material to suppress the vibration amplitude. On the basis of three-dimensional theory, Chen and Ding (2002) investigated the free vibration problem of a piezoelectric rectangular plate with a functionally

graded property. None of the above papers dealt with the large amplitude vibration of initially stressed FGM plates that were integrated with piezoelectric materials.

The objective of this chapter is to present a comprehensive study on the nonlinear vibration behavior of perfect and imperfect FGM laminated plates with or without thermo-electro-mechanical loads by using Reddy's higher-order shear deformation plate theory (Reddy, 1984) and a semi-analytical solution approach. Extensive numerical results are presented in both dimensionless tabular and graphical forms, and highlight the influence of material composition, vibration amplitude, geometric imperfection mode, prestress state induced by the applied thermo-electro-mechanical load, boundary conditions, as well as plate geometry on the linear and large amplitude vibration behavior of the plate.

## 11.2 The DQ–Galerkin method

A semi-analytical approach that makes use of one-dimensional differential quadrature approximation in conjunction with the Galerkin technique proposed by Yang and Shen (2001, 2002) is used in this section. Its basic idea can be illustrated by solving an unknown smooth function  $\varphi(x_1, x_2)$  from a partial differential system:

$$V(\varphi) - v = 0 \quad \in S_V \quad 11.1a$$

$$G_k(\varphi) - g_k = 0 \quad \in S_G \quad k = 1, \dots, K \quad 11.1b$$

where  $V$  and  $G_k$  are the partial differential operators defined in a normalized rectangular domain  $S_V \in [0 \leq x_1 \leq 1, 0 \leq x_2 \leq 1]$  and on the boundary  $S_G$ ,  $v$  and  $g_k$  are the given functions in the governing equation (11.1a) and boundary conditions (11.1b), and  $K$  is the total number of boundary conditions. We first discretize the rectangular domain along the  $x_1$  axis by a number of nodal lines parallel to the  $x_2$  axis and designate  $\varphi_i (i = 1, \dots, N)$  as the unknown function values at an arbitrary sampling nodal line  $x_1 = x_{1i}$ , where  $N$  is the total number of nodal lines. Based on the one-dimensional differential quadrature rule,  $\varphi$  and its  $r$ th partial derivative with respect to  $x_1$  can be approximated as the linear weighting sums of  $\varphi_i$  by

$$\varphi(x_1, x_2) = \sum_{i=1}^N l_i(x_1) \varphi_i(x_2) \quad 11.2$$

$$\left. \frac{\partial^r \varphi(x_1, x_2)}{\partial x_1^r} \right|_{x_1=x_{1i}} = \sum_{j=1}^N C_{ij}^{(r)} \varphi_j(x_2) \quad 11.3$$

where Lagrange interpolation polynomial  $l_i(x_1)$  and the recursive formula for weighting coefficients  $C_{ij}^{(r)}$  are given in many references, for example,

those by Bert and Malik (1996), Liew and Han (1997), Liu and Liew (1999a,b), and Teo and Liew (1999).

The application of Eqs. (11.2) and (11.3) to the partial differential system (11.1) leads to a set of ordinary differential equation system in terms of  $\varphi_i$ :

$$V_i(\varphi_1, \varphi_2, \dots, \varphi_N) - v_i = 0 \quad 11.4a$$

$$\tilde{G}_k(\varphi_1, \varphi_2, \dots, \varphi_N) - \tilde{g}_k = 0 \quad k = 1, \dots, K \quad 11.4b$$

in which  $V_i$ ,  $v_i$ ,  $\tilde{G}_k$ , and  $\tilde{g}_k$  are the discretized forms of  $V$ ,  $v$ ,  $G_k$ , and  $g_k$ . The solution of  $\varphi_i$  is constructed as a linear series of an analytical function  $\phi_{im}(x_2)$  that satisfies all the boundary conditions at  $x_2 = 0, 1$ , i.e.

$$\varphi_i = \sum_{m=1}^M \mu_{im}(x_2) \quad 11.5$$

where  $\mu_{im}$  is the series coefficient to be determined, and  $M$  is the truncated number of the series.

In general,  $\varphi_i$  cannot satisfy the discretized governing equations (11.4a) and the boundary conditions (11.4b) at every arbitrary point. The Galerkin technique is then applied to minimize the residuals:

$$\int_0^1 \phi_{im}(x_2) \{V_i(\varphi_1, \varphi_2, \dots, \varphi_N) - v_i\} dx_2 = 0 \quad i = 1, \dots, N, \quad m = 1, \dots, M \quad 11.6a$$

$$\int_0^1 \phi_{km}(x_2) \{\tilde{G}_k(\varphi_1, \varphi_2, \dots, \varphi_N) - \tilde{g}_k\} dx_2 = 0 \quad k = 1, \dots, K, \quad m = 1, \dots, M \quad 11.6b$$

Incorporating Eq. (11.6b) into Eq. (11.6a) by the  $\delta$ -method establishes an algebraic equation system from which the unknown coefficients can be solved

$$[G]\{\mu\} = \{R\} \quad 11.7$$

where  $[G]$  is a constant matrix,  $\{R\}$  is the known right-hand vector, and  $\{\mu\}$  is the unknown vector composed of series coefficients  $\mu_{im}(i = 1, \dots, N; m = 1, \dots, M)$ .

The above semi-analytical approach, together with the iteration process, will be used in the following analyses to obtain the nonlinear vibration solutions of the FGM plate. Our attention is focused on FGM laminated plates that are clamped at  $x_2 = 0, 1$ , and free, simply supported, or clamped at  $x_1 = 0, 1$ .

## 11.3 Theoretical formulations

### 11.3.1 Basic equations

Consider an  $N_L$ -layer imperfect FGM laminated plate  $[0 \leq X_1 \leq a, 0 \leq X_2 \leq b, -h/2 \leq X_3 \leq h/2]$  that may contain piezoelectric actuator layers and is defined in the Cartesian coordinate system  $(X_1, X_2, X_3)$  where the  $X_3$ -axis is taken to be positive upward from the  $X_1$ - $X_2$  mid-plane. It is assumed that: (1) before undergoing a time-varying incremental deformation, the plate is in a static equilibrium state under the action of a uniform temperature change  $\Delta T$  from the stress-free temperature  $T_0$ , a constant electric field  $(E_1, E_2, E_3)$ , and uniform edge forces  $\bar{p}_1$  in the  $X_1$  axis and  $\bar{p}_2$  in the  $X_2$  axis (where the tensile membrane stress is negative and the compressive membrane stress is positive); (2) the laminates are perfectly bonded and no debonding will occur; (3) the initial geometrical imperfection in the stress-free state is small and the only transverse initial deflection  $\bar{W}^*$  is considered; and (4) all of the materials involved are linear, elastic.

Since in a laminated composite structure the effect of transverse shear strains is very important and should be properly accounted for, Reddy's higher-order shear deformation theory is used to describe the displacement field because it gives more accurate stress and natural frequency predictions than the FSDPT, requires no shear correction factors, and uses only the same number of variables as the FSDPT. Let  $\bar{U}_k$  denote the displacement in the  $X_k$  direction. The displacement field  $(\bar{U}_1, \bar{U}_2, \bar{U}_3)$  of an arbitrary point in the plate is assumed to be

$$(\bar{U}_1 = \bar{U}(X, Y, t) + X_3 \bar{\Psi}_1(X, Y, t) - c_1 X_3^3 \left( \bar{\Psi}_1(X, Y, t) + \frac{\partial \bar{U}_3}{\partial X_1} \right)) \quad 11.8a$$

$$(\bar{U}_2 = \bar{V}(X, Y, t) + X_3 \bar{\Psi}_2(X, Y, t) - c_1 X_3^3 \left( \bar{\Psi}_2(X, Y, t) + \frac{\partial \bar{U}_3}{\partial X_2} \right)) \quad 11.8b$$

$$\bar{U}_3 = \bar{W}(X, Y, t) + \bar{W}^*(X, Y) \quad 11.8c$$

where  $c_1 = 4/3h^2$ ,  $\bar{U}$ ,  $\bar{V}$ , and  $\bar{W}$  represent the displacements of a point on the mid-plane ( $X_3 = 0$ ) of the plate, and  $\bar{\Psi}_1$  and  $\bar{\Psi}_2$  are the mid-plane rotations of transverse normal about the  $X_2$  and  $X_1$  axes. As the in-plane displacements are small compared with the transverse displacement and the higher-order strain terms are negligible, the von Karman-type nonlinear strains that are associated with the above displacement field are

$$\begin{aligned}\varepsilon_1 &= \varepsilon_1^{(0)} + X_3[\varepsilon_1^{(1)} + X_3^2\varepsilon_1^{(3)}], \quad \varepsilon_2 = \varepsilon_2^{(0)} + X_3[\varepsilon_2^{(1)} + X_3^2\varepsilon_2^{(3)}] \\ \varepsilon_6 &= \varepsilon_6^{(0)} + X_3[\varepsilon_6^{(1)} + X_3^2\varepsilon_6^{(3)}] \\ \varepsilon_4 &= \varepsilon_4^{(0)} + X_3^2\varepsilon_4^{(2)}, \quad \varepsilon_5 = \varepsilon_5^{(0)} + X_3^2\varepsilon_5^{(2)}\end{aligned} \quad 11.9$$

where

$$\begin{aligned}\varepsilon_1^{(0)} &= \frac{\partial \bar{U}}{\partial X_1} + \frac{1}{2} \left( \frac{\partial \bar{W}}{\partial X_1} \right)^2 + \frac{\partial \bar{W}}{\partial X_1} \frac{\partial \bar{W}^*}{\partial X_1}, \quad \varepsilon_1^{(1)} = \frac{\partial \bar{\Psi}_1}{\partial X_1} \\ \varepsilon_1^{(3)} &= -c_1 \left( \frac{\partial \bar{\Psi}_1}{\partial X_1} + \frac{\partial^2 \bar{W}}{\partial X_2^2} + \frac{\partial^2 \bar{W}^*}{\partial X_1^2} \right) \\ \varepsilon_2^{(0)} &= \frac{\partial \bar{U}}{\partial X_2} + \frac{1}{2} \left( \frac{\partial \bar{W}}{\partial X_2} \right)^2 + \frac{\partial \bar{W}}{\partial X_2} \frac{\partial \bar{W}^*}{\partial X_2}, \quad \varepsilon_2^{(1)} = \frac{\partial \bar{\Psi}_2}{\partial X_2} \\ \varepsilon_2^{(3)} &= -c_1 \left( \frac{\partial \bar{\Psi}_2}{\partial X_2} + \frac{\partial^2 \bar{W}}{\partial X_2^2} + \frac{\partial^2 \bar{W}^*}{\partial X_2^2} \right) \\ \varepsilon_6^{(0)} &= \frac{\partial \bar{U}}{\partial X_2} + \frac{\partial \bar{V}}{\partial X_1} + \frac{\partial \bar{W}}{\partial X_1} \frac{\partial \bar{W}}{\partial X_2} + \frac{\partial \bar{W}^*}{\partial X_1} \frac{\partial \bar{W}}{\partial X_2} + \frac{\partial \bar{W}}{\partial X_1} \frac{\partial \bar{W}^*}{\partial X_2} \\ \varepsilon_6^{(1)} &= \frac{\partial \bar{\Psi}_1}{\partial X_2} + \frac{\partial \bar{\Psi}_2}{\partial X_1} \\ \varepsilon_6^{(3)} &= -c_1 \left( \frac{\partial \bar{\Psi}_1}{\partial X_2} + \frac{\partial \bar{\Psi}_2}{\partial X_1} + 2 \frac{\partial^2 \bar{W}}{\partial X_1 \partial X_2} + 2 \frac{\partial^2 \bar{W}^*}{\partial X_1 \partial X_2} \right) \\ \varepsilon_4^{(0)} &= \bar{\Psi}_2 + \frac{\partial \bar{W}}{\partial X_2} + \frac{\partial \bar{W}^*}{\partial X_2}, \quad \varepsilon_4^{(2)} = -3c_1 \left( \bar{\Psi}_2 + \frac{\partial \bar{W}}{\partial X_2} + \frac{\partial \bar{W}^*}{\partial X_2} \right) \\ \varepsilon_5^{(0)} &= \bar{\Psi}_2 + \frac{\partial \bar{W}}{\partial X_1} + \frac{\partial \bar{W}^*}{\partial X_1}, \quad \varepsilon_5^{(2)} = -3c_1 \left( \bar{\Psi}_1 + \frac{\partial \bar{W}}{\partial X_1} + \frac{\partial \bar{W}^*}{\partial X_1} \right)\end{aligned} \quad 11.10$$

Assuming  $\sigma_3 = 0$  and the piezoelectric actuator layers are of the orthorhombic materials of class mm<sup>2</sup> with the poling direction being coincident with the  $X_3$  direction, the linear stress-strain constitutive relation for the  $k$ th layer of the FGM laminated plate is given by

$$\begin{aligned}\sigma_i^{(k)} &= Q_{ij}^{(k)}(\varepsilon_j - \alpha_j^{(k)}\Delta T) - e_{ir}^{(k)}E_r^{(k)} \\ i, j &= 1, 2, 4, 5, 6; \quad r = 1, 2, 3\end{aligned} \quad 11.11$$

where  $Q_{ij}^{(k)}$  denotes the elastic stiffness,  $\sigma_i^{(k)}$  is the coefficients of thermal expansion,  $\sigma_i^{(k)}$  and  $E_r^{(k)}$  are the stress and electric field components,  $e_{ir}^{(k)}$  are the piezoelectric moduli. For the FGM layer, the part containing the

piezoelectric moduli  $e_{ir}^{(k)}$  should be omitted. Furthermore, its Young's modulus  $E_{11}^{(k)} = E_{22}^{(k)} = E^{(k)}$  and Poisson's ratio  $\nu_{12}^{(k)} = \nu_{21}^{(k)} = \nu^{(k)}$ , hence

$$Q_{11}^{(k)} = Q_{22}^{(k)} = \frac{E^{(k)}}{1 - (\nu^{(k)})^2}; Q_{12}^{(k)} = Q_{21}^{(k)} = \frac{\nu^{(k)} E^{(k)}}{1 - (\nu^{(k)})^2}$$

$$Q_{44}^{(k)} = Q_{55}^{(k)} = Q_{66}^{(k)} = \frac{E^{(k)}}{2(1 + \nu^{(k)})}$$

$$Q_{16}^{(k)} = Q_{26}^{(k)} = 0; \alpha_1^{(k)} = \alpha_2^{(k)} = \alpha^{(k)}; \alpha_4^{(k)} = \alpha_5^{(k)} = \alpha_6^{(k)} = 0 \quad 11.12$$

In the present investigation, only a large uniform electric field due to a constant actuator voltage  $V_a$  along the poling direction (i.e.  $X_3$  direction) is considered, that is

$$E_1 = E_2 = 0; \quad E_3 = V_a/h_a \quad 11.13$$

In such a case, the electric field resulting from variations in stress and temperature is assumed to be insignificant compared with the applied field and the so-called direct piezoelectric effect can be neglected (Jonnalagadda *et al.*, 1994).

Note that the material properties of the FGM are position dependent, and its material composition profile varies continuously across the plate thickness in terms of the volume fractions of the constituent materials. Suppose that the FGM layer is made from a mixture of ceramic and metal whose volume fractions are  $V_c$  and  $V_m$  where subscripts c and m stand for ceramic and metal. Its effective material properties  $P_{\text{eff}}$ , such as Young's modulus  $E$ , the coefficient of thermal expansion  $\alpha$ , and mass density  $\rho$  are functions of  $X_3$  and can be determined by

$$P_{\text{eff}} = P_c V_c + P_m V_m \quad 11.14$$

while Poisson's ratio  $\nu$  is assumed to be a constant for simplicity.

The nonlinear equations of motion that are appropriate for the displacement field (11.8) and the constitutive relation (11.11) are

$$\frac{\partial \bar{N}_1}{\partial X_1} + \frac{\partial \bar{N}_6}{\partial X_2} = \frac{\partial}{\partial t^2} \left( I_1 \bar{U} + \bar{I}_2 \bar{\Psi}_1 - c_1 I_4 \frac{\partial \bar{W}}{\partial X_1} \right) \quad 11.15$$

$$\frac{\partial \bar{N}_6}{\partial X_1} + \frac{\partial \bar{N}_2}{\partial X_2} = \frac{\partial}{\partial t^2} \left( I_1 \bar{V} + \bar{I}_2 \bar{\Psi}_2 - c_1 I_4 \frac{\partial \bar{W}}{\partial X_2} \right) \quad 11.16$$

$$\frac{\partial \bar{Q}_1}{\partial X_1} + \frac{\partial \bar{Q}_2}{\partial X_2} - 3c_1 \left( \frac{\partial \bar{R}_1}{\partial X_1} + \frac{\partial \bar{R}_2}{\partial X_2} \right) + c_1 \left( \frac{\partial^2 \bar{P}_1}{\partial X_1^2} + 2 \frac{\partial^2 \bar{P}_6}{\partial X_1 \partial X_2} + \frac{\partial^2 \bar{P}_2}{\partial X_2^2} \right)$$

$$+ \frac{\partial}{\partial X_1} \left( \bar{N}_1 \frac{\partial(\bar{W} + \bar{W}^*)}{\partial X_1} + \bar{N}_6 \frac{\partial(\bar{W} + \bar{W}^*)}{\partial X_2} \right)$$

$$\begin{aligned}
& + \frac{\partial}{\partial X_2} \left( \bar{N}_6 \frac{\partial(\bar{W} + \bar{W}^*)}{\partial X_1} + \bar{N}_2 \frac{\partial(\bar{W} + \bar{W}^*)}{\partial X_2} \right) \\
& = \frac{\partial^2}{\partial t^2} \left[ I_1 \bar{W} - c_1^2 I_7 \left( \frac{\partial^2 \bar{W}}{\partial X_1^2} + \frac{\partial^2 \bar{W}}{\partial X_2^2} \right) + c_1 I_4 \left( \frac{\partial \bar{U}}{\partial X_1} + \frac{\partial \bar{V}}{\partial X_2} \right) \right. \\
& \quad \left. + c_1 \bar{I}_5 \left( \frac{\partial \bar{\Psi}_1}{\partial X_1} + \frac{\partial \bar{\Psi}_2}{\partial X_2} \right) \right] \quad 11.17
\end{aligned}$$

$$\begin{aligned}
& \frac{\partial \bar{M}_1}{\partial X_1} + \frac{\partial \bar{M}_6}{\partial X_2} - \bar{Q}_1 + 3c_1 \bar{R}_1 - c_1 \left( \frac{\partial \bar{P}_1}{\partial X_1} + \frac{\partial \bar{P}_6}{\partial X_2} \right) \\
& = \frac{\partial}{\partial t^2} \left( \bar{I}_2 \bar{U} + \bar{I}_3 \bar{\Psi}_2 - c_1 \bar{I}_5 \frac{\partial \bar{W}}{\partial X_1} \right) \quad 11.18
\end{aligned}$$

$$\begin{aligned}
& \frac{\partial \bar{M}_6}{\partial X_1} + \frac{\partial \bar{M}_2}{\partial X_2} - \bar{Q}_2 + 3c_1 \bar{R}_2 - c_1 \left( \frac{\partial \bar{P}_6}{\partial X_1} + \frac{\partial \bar{P}_2}{\partial X_2} \right) \\
& = \frac{\partial}{\partial t^2} \left( \bar{I}_2 \bar{V} + \bar{I}_3 \bar{\Psi}_2 - c_1 \bar{I}_5 \frac{\partial \bar{W}}{\partial X_2} \right) \quad 11.19
\end{aligned}$$

where  $t$  is the time variable,  $\bar{I}_2 = I_2 - c_1 I_4$ ,  $\bar{I}_3 = I_3 - 2c_1 I_5 + c_1^2 I_7$ ,  $\bar{I}_5 = I_5 - c_1 I_7$ . The inertia terms are calculated by

$$(I_1, I_2, I_3, I_4, I_5, I_7) = \sum_{k=1}^{N_L} \int_{X_3^{(k-1)}}^{X_3^{(k)}} \rho^{(k)} (1, X_3, X_3^2, X_3^3, X_3^4, X_3^6) dX_3 \quad 11.20$$

and the stress resultants  $\bar{N}_i$ ,  $\bar{M}_i$ ,  $\bar{P}_i$  ( $i = 1, 2, 6$ ) and  $\bar{Q}_i$ ,  $\bar{R}_i$  ( $i = 1, 2$ ) are related with the strains by

$$\bar{N}_i = A_{ij} \varepsilon_j^0 + B_{ij} \kappa_j^0 + E_{ij} \kappa_j^2 - \bar{N}_i^P \quad 11.21a$$

$$\bar{M}_i = B_{ij} \varepsilon_j^0 + D_{ij} \kappa_j^0 + F_{ij} \kappa_j^2 - \bar{M}_i^P \quad 11.21b$$

$$\bar{P}_i = E_{ij} \varepsilon_j^0 + F_{ij} \kappa_j^0 + H_{ij} \kappa_j^2 - \bar{P}_i^P \quad (i, j = 1, 2, 6) \quad 11.21c$$

$$\bar{Q}_1 = A_{5j} \varepsilon_j^0 + D_{5j} \kappa_j^2, \quad \bar{Q}_2 = A_{4j} \varepsilon_j^0 + D_{4j} \kappa_j^2 \quad 11.22a$$

$$\bar{R}_1 = D_{5j} \varepsilon_j^0 + F_{5j} \kappa_j^2, \quad \bar{R}_2 = D_{4j} \varepsilon_j^0 + F_{4j} \kappa_j^2 \quad (i, j = 4, 5) \quad 11.22b$$

in which  $A_{ij}$ ,  $B_{ij}$ , etc. are the plate stiffness elements

$$(A_{ij}, B_{ij}, D_{ij}, E_{ij}, F_{ij}, H_{ij})$$

$$\begin{aligned}
& = \sum_{k=1}^{N_L} \int_{X_3^{(k-1)}}^{X_3^{(k)}} Q_{ij}^{(k)} (1, X_3, X_3^2, X_3^3, X_3^4, X_3^6) dX_3 \quad (i, j = 1, 2, 6) \\
& \quad 11.23
\end{aligned}$$

$$(A_{ij}, D_{ij}, F_{ij}) = \sum_{k=1}^{N_L} \int_{X_3^{(k-1)}}^{X_3^{(k)}} Q_{ij}^{(k)}(1, X_3^2, X_3^4) dX_3 \quad (i, j = 4, 5) \quad 11.24$$

In Eq. (11.21),  $\bar{N}_i^P = \bar{N}_i^T + \bar{N}_i^E$ ,  $\bar{M}_i^P = \bar{M}_i^T + \bar{M}_i^E$  and  $\bar{P}_i^P = \bar{P}_i^T + \bar{P}_i^E$  are the total stress resultants due to thermal and electric loading:

$$\begin{aligned} (\bar{N}_i^T, \bar{M}_i^T, \bar{P}_i^T) &= \sum_{k=1}^{N_L} \int_{X_3^{(k-1)}}^{X_3^{(k)}} A_i^{(k)}(1, X_3, X_3^2) \Delta T dX_3 \\ &= (A_i^T, D_i^T, F_i^T) \Delta T \end{aligned} \quad 11.25$$

$$\begin{aligned} (\bar{N}_i^E, \bar{M}_i^E, \bar{P}_i^E) &= \sum_{k=1}^{N_L} \int_{X_3^{(k-1)}}^{X_3^{(k)}} B_i^{(k)}(1, X_3, X_3^2) E_3 dX_3 \\ &= (A_i^E, D_i^E, F_i^E) E_3 \end{aligned} \quad 11.26$$

where, for the material's undercurrent consideration,

$$\begin{aligned} A_1^{(k)} &= A_2^{(k)} = (Q_{11}^{(k)} + Q_{12}^{(k)}) \alpha^{(k)}, A_6^{(k)} = 0 \\ B_1^{(k)} &= -e_{31}^{(k)}, B_2^{(k)} = -e_{32}^{(k)}, B_6^{(k)} = 0 \end{aligned} \quad 11.27$$

### 11.3.2 Nonlinear governing equations

It is convenient to introduce a stress function  $\bar{F}$  for the in-plane stress-related boundary-value problems. As usual, let  $\bar{F}$  be associated with the stress resultants such that (Shen, 1995)

$$\bar{N}_1 = \frac{\partial^2 \bar{F}}{\partial X_2^2}, \quad \bar{N}_2 = \frac{\partial^2 \bar{F}}{\partial X_1^2}, \quad \bar{N}_6 = -\frac{\partial^2 \bar{F}}{\partial X_1 \partial X_2} \quad 11.28$$

The condition of compatibility for the laminated plate requires that

$$\begin{aligned} \frac{\partial^2 \varepsilon_1}{\partial X_2^2} + \frac{\partial^2 \varepsilon_2}{\partial X_1^2} - \frac{\partial^2 \varepsilon_6}{\partial X_1 \partial X_2} &= \left( \frac{\partial^2 (\bar{W} + \bar{W}^*)}{\partial X_1 \partial X_2} \right)^2 \\ - \frac{\partial^2 (\bar{W} + \bar{W}^*)}{\partial X_1^2} \frac{\partial^2 (\bar{W} + \bar{W}^*)}{\partial X_2^2} \end{aligned} \quad 11.29$$

Introduce the following dimensionless quantities:

$$\begin{aligned} x_1 &= X_1/a, \quad x_2 = X_2/b, \quad \beta = a/b \\ (W, W^*) &= (\bar{W}, \bar{W}^*) / (D_{11}^* D_{22}^* A_{11}^* A_{22}^*)^{1/4} \\ F, \bar{F} / (D_{11}^* D_{22}^*)^{1/2}, (\Psi_1, \Psi_2) &= (\bar{\Psi}_1, \bar{\Psi}_2) a / (D_{11}^* D_{22}^* A_{11}^* A_{22}^*)^{1/4} \\ \omega &= \Omega a^2 \sqrt{I_1/D_{11}^*} \end{aligned}$$

$$\begin{aligned}
(\gamma_1, \gamma_2, \gamma_3, \gamma_4, \gamma_5) &= [B_{11}^*, B_{12}^*, B_{21}^*, B_{22}^*, B_{66}^*]/(D_{11}^* D_{22}^* A_{11}^* A_{22}^*)^{1/4} \\
(\gamma_6, \gamma_7, \gamma_8) &= [A_{11}^*, A_{12}^*, A_{66}^*]/A_{22}^* \\
(\gamma_9, \gamma_{10}, \gamma_{11}, \gamma_{12}, \gamma_{13}) &= [B_{11}^* - c_1 E_{11}^*, B_{21}^* - c_1 E_{21}^*, B_{66}^* \\
&\quad - c_1 E_{66}^*, B_{12}^* - c_1 E_{12}^*, B_{22}^* - c_1 E_{22}^*]/(D_{11}^* D_{22}^* A_{11}^* A_{22}^*)^{1/4} \\
\gamma_{14} &= [D_{22}^*/D_{11}^*]^{1/2}, \quad \gamma_{24} = [A_{11}^*/A_{22}^*]^{1/2} \\
(\lambda_1, \lambda_2) &= (\bar{p}_1 b^2, \bar{p}_2 a^2)/(D_{11}^* / D_{22}^*)^{1/2} \\
(N_1^P, N_2^P, N_6^P) &= (\bar{N}_1^P, \bar{N}_2^P, \bar{N}_6^P) a^2 / (D_{11}^* / D_{22}^*)^{1/2} \\
(M_1, M_2, M_6, M_1^P, M_2^P, M_6^P) &= (\bar{M}_1, \bar{M}_2, \bar{M}_6, \bar{M}_1^P, \bar{M}_2^P, \bar{M}_6^P) a^2 / (D_{11}^* (D_{11}^* D_{22}^* A_{11}^* A_{22}^*)^{1/4}) \\
(P_1, P_2, P_6, P_1^P P_2^P P_6^P) &= c_1 (\bar{P}_1, \bar{P}_2, \bar{P}_6, \bar{P}_1^P \bar{P}_2^P \bar{P}_6^P) a^2 / (D_{11}^* (D_{11}^* D_{22}^* A_{11}^* A_{22}^*)^{1/4}) \quad 11.30
\end{aligned}$$

where  $\Omega$  is the natural frequency  $A_{ij}^*$ ,  $B_{ij}^*$ ,  $D_{ij}^*$ ,  $E_{ij}^*$ ,  $F_{ij}^*$ ,  $H_{ij}^*$  ( $i, j = 1, 2, 6$ ) are the reduced stiffness components in semi-inverse form as

$$\begin{aligned}
\mathbf{A}^* &= \mathbf{A}^{-1}, \quad \mathbf{B}^* = -\mathbf{A}^{-1}\mathbf{B}, \quad \mathbf{D}^* = \mathbf{D} - \mathbf{B}\mathbf{A}^{-1}\mathbf{B}, \quad \mathbf{E}^* = -\mathbf{A}^{-1}\mathbf{E}, \quad \mathbf{F}^* \\
&= \mathbf{F} - \mathbf{E}\mathbf{A}^{-1}\mathbf{B}, \quad \mathbf{H}^* = \mathbf{H} - \mathbf{E}\mathbf{A}^{-1}\mathbf{E} \quad 11.31
\end{aligned}$$

Upon substituting Eq. (11.28), dimensionless quantities (11.30), and the partial inverse form of Eq. (11.21) into Eqs. (11.15)–(11.19) and Eq. (11.29), the dimensionless nonlinear governing equations of motion for the imperfect FGM laminated plate under initial thermo-electro-mechanical preloading can be derived as

$$\begin{aligned}
L_{11}(W) - L_{12}(\Psi_1) - L_{13}(\Psi_2) + \gamma_{14} L_{14}(F) - L_{15}(N^P) - L_{16}(M^P) \\
= \gamma_{14} \beta^2 L(W + W^*, F) \\
- \frac{\partial^2}{\partial t^2} \left[ W + \hat{I}_7^* \left( \frac{\partial^2 W}{\partial x_1^2} + \beta^2 \frac{\partial^2 W}{\partial x_2^2} \right) + \hat{I}_5^* \left( \frac{\partial \Psi_1}{\partial x_1} + \frac{\partial \Psi_2}{\partial x_2} \right) \right] \quad 11.32
\end{aligned}$$

$$\begin{aligned}
L_{21}(F) + \gamma_{24} L_{22}(\Psi_1) + \lambda_{24} L_{23}(\Psi_2) - \gamma_{24} L_{24}(W) - L_{25}(N^P) \\
= -\frac{1}{2} \gamma_{24} \beta^2 L(W + 2W^*, W) \quad 11.33
\end{aligned}$$

$$\begin{aligned}
L_{31}(W) + L_{32}(\Psi_1) - L_{33}(\Psi_2) + \gamma_{14} L_{34}(F) - L_{35}(N^*) \\
- L_{36}(M^P, P^P) = -\frac{\partial^2}{\partial t^2} \left( I_3^* \Psi_1 - I_5^* \frac{\partial W}{\partial x_1} \right) \quad 11.34
\end{aligned}$$

$$L_{41}(W) - L_{42}(\Psi_1) + L_{43}(\Psi_2) + \gamma_{14}L_{44}(F) - L_{45}(N^*) \\ - L_{46}(M^P, P^P) = -\frac{\partial^2}{\partial t^2} \left( I_3^* \Psi_2 - I_5^* \frac{\partial W}{\partial x_2} \right) \quad 11.35$$

where the nonlinear partial differential operator  $L() = \frac{\partial^2}{\partial x_1^2} \frac{\partial^2}{\partial x_2^2} - 2 \frac{\partial^2}{\partial x_1 \partial x_2}$   
 $\frac{\partial^2}{\partial x_1 \partial x_2} + \frac{\partial^2}{\partial x_2^2} \frac{\partial^2}{\partial x_1^2}$ , and

$$I'_3 = I_3 - 2c_1 I_5 + c_1^2 I_7 - (I_2 - c_1 I_4)^2 / I_1 \\ I'_5 = c_1 [I_5 - c_1 I_7 - I_4 (I_2 - c_1 I_4) / I_1], \quad I'_7 = c_1^2 (I_4^2 / I_1 - I_7) \\ (I_3^*, I_5^*, I_7^*) = (I'_3, I'_5, I'_7) / a^2 I_1, \quad \hat{I}_5^* = I_3^* + I_5^*, \quad \hat{I}_7^* = I_7^* - I_5^* \quad 11.36$$

the linear partial differential operators  $L_{ij}$  ( $i, j = 1, 2, 3, 4$ ) are given by Yang and Shen (2002), except

$$L_{15}(N^P) = \frac{\partial^2}{\partial x_1^2} (\gamma_1 N_1^P + \gamma_3 N_2^P) + 2\beta \gamma_5 \frac{\partial^2 N_6^P}{\partial x_1 \partial x_2} \\ + \beta^2 \frac{\partial^2}{\partial x_2^2} (\gamma_2 N_1^P + \gamma_4 N_2^P) \\ L_{16}(M^P) = \frac{\partial^2 M_1^P}{\partial x_1^2} + 2\beta \frac{\partial^2 M_6^P}{\partial x_1 \partial x_2} + \beta^2 \frac{\partial^2 M_2^P}{\partial x_2^2} \\ L_{25}(N^P) = \frac{\partial^2}{\partial x_1^2} (\gamma_7 N_1^P + N_2^P) - \beta \gamma_8 \frac{\partial^2 N_6^P}{\partial x_1 \partial x_2} \\ + \beta^2 \frac{\partial^2}{\partial x_2^2} (\gamma_6 N_1^P + \gamma_7 N_2^P) \\ L_{35}(N^P) = \frac{\partial}{\partial x_1} (\gamma_9 N_1^P + \gamma_{10} N_2^P) + \beta \gamma_{11} \frac{\partial N_6^P}{\partial x_2} \\ L_{36}(M^P, P^P) = \frac{\partial M_1^P}{\partial x_1} + \beta \frac{\partial M_6^P}{\partial x_2} - c_1 \left( \frac{\partial P_1^P}{\partial x_1} + \beta \frac{\partial P_6^P}{\partial x_2} \right) \\ L_{45}(N^P) = \frac{\partial}{\partial x_2} \beta (\gamma_{12} N_1^P + \gamma_{13} N_2^P) + \gamma_{11} \frac{\partial N_6^P}{\partial x_1} \\ L_{46}(M^P, P^P) = \frac{\partial M_6^P}{\partial x_1} + \beta \frac{\partial M_2^P}{\partial x_2} - c_1 \left( \frac{\partial P_6^P}{\partial x_1} + \beta \frac{\partial P_2^P}{\partial x_2} \right) \quad 11.37$$

Note that these terms will vanish when both the temperature field and the electric field vary in the  $X_3$  direction only.

The following boundary conditions for simply supported (S), clamped (C) and free (F) edges are considered

$$S \text{ (movable): } W = \Psi_s = M_n = P_n = \frac{\partial^2 F}{\partial n \partial s} = \frac{\partial^2 F}{\partial s^2} + \lambda_n^* = 0 \quad 11.38a$$

$$S \text{ (immovable): } W = \Psi_s = M_n = P_n = \frac{\partial^2 F}{\partial n \partial s} = U_n = 0 \quad 11.38b$$

$$C \text{ (movable): } W = \Psi_s = \Psi_n = \frac{\partial W}{\partial n} = \frac{\partial^2 F}{\partial n \partial s} = \frac{\partial^2 F}{\partial s^2} \lambda_n^* = 0 \quad 11.39a$$

$$C \text{ (immovable): } W = \Psi_s = \Psi_n = \frac{\partial W}{\partial n} = \frac{\partial^2 F}{\partial n \partial s} = U_n = 0 \quad 11.39b$$

$$F \text{ (movable): } Q_n^* = M_{ns}^* = M_n = P_n = \frac{\partial^2 F}{\partial n \partial s} = \frac{\partial^2 F}{\partial s^2} \lambda_n^* = 0 \quad 11.40a$$

$$F \text{ (immovable): } Q_n^* = M_{ns}^* = M_n = P_n = \frac{\partial^2 F}{\partial n \partial s} = U_n = 0 \quad 11.40b$$

where subscripts  $n$  and  $s$  refer to the normal and tangential directions of the plate edge, and  $M_{ns}^*$  and  $Q_n^*$  are the generalized moment and transverse shear force as defined by Reddy (1984). Edge force  $\lambda_n^*$  is a combination of applied in-plane forces and the reactions that stem from the immovable edge constraints.

### 11.3.3 Pre-vibration analysis

Owing to the bending–stretching coupling effect in the FGM laminated plate, the thermo-electro-mechanical preload will bring about deflections, bending curvatures and the nonuniform distribution of initial stresses, which have significant influences on the plate vibration characteristics. To account for this effect, a pre-vibration solution  $(W_b, \Psi_{1b}, \Psi_{2b}, F_b)$  is sought at the first step from the following nonlinear equations:

$$\begin{aligned} L_{11}(W_b) - L_{12}(\Psi_{1b}) - L_{13}(\Psi_{2b}) + \gamma_{14}L_{14}(F_b) \\ = \gamma_{14}\beta^2 L(W_b, F_b) \end{aligned} \quad 11.41$$

$$\begin{aligned} L_{21}(F_b) + \gamma_{24}L_{22}(\Psi_{1b}) + \lambda_{24}L_{23}(\Psi_{2b}) - \gamma_{24}L_{24}(W_b) \\ = -\frac{1}{2}\gamma_{24}\beta^2 L(W_b, W_b) \end{aligned} \quad 11.42$$

$$L_{31}(W_b) + L_{32}(\Psi_{1b}) - L_{33}(\Psi_{2b}) + \gamma_{14}L_{34}(F_b) = 0 \quad 11.43$$

$$L_{41}(W_b) - L_{42}(\Psi_{1b}) + L_{43}(\Psi_{2b}) + \gamma_{14}L_{44}(F_b) = 0 \quad 11.44$$

Eqs. (11.41)–(11.44) are obtained by discarding the dynamic and imperfection terms in Eqs. (11.32)–(11.35).

To include the uniform pre-stress state in the plate, the stress function  $F_b^0$  takes the form of

$$F_b = -\frac{1}{2}(x_2^2 \lambda_1^* + x_1^2 \lambda_2^*) + f_b(x_1, x_2) \quad 11.45$$

The unknown functions  $W_{bi}$ ,  $\Psi_{1bi}$ ,  $\Psi_{2bi}$  and  $f_{bi}$  at  $i$ th nodal line are expressed as

$$(W_{bi}, \Psi_{1bi}, \Psi_{2bi}, f_{bi}) = \sum_{m=1}^M [a_{bim} W_{im}, b_{bim} \Psi_{1im}, c_{bim} \Psi_{2im}, d_{bim} f_{im}] \quad 11.46$$

in which  $a_{bim}$ ,  $b_{bim}$ ,  $c_{bim}$ ,  $d_{bim}$  are the constants to be determined, and  $W_{im}$ ,  $\Psi_{1im}$ ,  $\Psi_{2im}$ , and  $f_{im}$  are chosen to be the following analytical functions that satisfy the boundary conditions in  $x_2$  axis, for example:

$$W_{im} = \sin \alpha_m x_2 - \sinh \alpha_m x_2 - \xi_m (\cos \alpha_m x_2 - \cosh \alpha_m x_2) \quad 11.47a$$

$$\Psi_{1im} = \sin (m\pi x_2); \quad \Psi_{2im} = \sin (m\pi x_2) \quad 11.47b,c$$

$$f_{im} = \sin \alpha_m x_2 - \sinh \alpha_m x_2 - \xi_m (\cos \alpha_m x_2 - \cosh \alpha_m x_2) \quad 11.47d$$

for a plate clamped at both edges  $x_2 = 0$  and 1, and

$$W_{im} = \sin (m\pi x_2) \quad 11.48a$$

$$\Psi_{1im} = \sin (m\pi x_2) \quad 11.48b$$

$$\Psi_{2im} = \cos (m\pi x_2) \quad 11.48c$$

$$f_{im} = \sin \alpha_m x_2 - \sinh \alpha_m x_2 - \xi_m (\cos \alpha_m x_2 - \cosh \alpha_m x_2) \quad 11.48d$$

for a plate simply supported at both edges  $x_2 = 0$  and 1, where  $\xi_m = \frac{(\sin \alpha_m - \sinh \alpha_m)}{(\cos \alpha_m - \cosh \alpha_m)}$ ,  $\alpha_m = \frac{(2m+1)\pi}{2}$ .

According to the semi-analytical solution method given in Section 11.2, the nonlinear algebraic system governing the pre-vibration deformation of the FGM laminated plate under thermo-electro-mechanical preloading can be generated as

$$([G_{b0}] + [G_{b1}(\Delta_b)])\{\Delta_b\} = \{R\} \quad 11.49$$

where the unknown vector  $\{\Delta_b\}$  is composed of  $a_{bim}$ ,  $b_{bim}$ ,  $c_{bim}$ ,  $d_{bim}$  ( $i = 1, \dots, N; m = 1, \dots, M$ ),  $\{R\}$  is the thermo-electro-mechanical load vector,  $[G_{b0}]$  is the linear constant coefficient matrix, and  $[G_{b1}(\Delta_b)]$  is the nonlinear matrix dependent on  $\{\Delta_b\}$ .

The solution of Eq. (11.49) requires an iteration process. A direct iteration scheme that is known as the Picard method is employed herein, in which the solution vector from the previous iteration is used to evaluate  $[G_{NL}(\Delta_b)]$  and the solution at the subsequent iteration is obtained by solving updated Eq.

(11.49). The iteration process is continued until the difference between the two consecutive iterations ( $r$ ) and ( $r + 1$ ) reduces to a prescribed error tolerance. The error criterion is of the form

$$\sqrt{\frac{\sum_{k=1}^N (W_{ck}^{(r+1)} - W_{ck}^{(r)})^2}{\sum_{k=1}^N (W_{ck}^{(r+1)})^2}} \leq 10^{-3} \quad 11.50$$

where  $W_{ck} = W_b(x_{1k}, 0.5)$  is the dimensionless pre-vibration deflection at the central point of the  $k$ th nodal line.

#### 11.3.4 Nonlinear vibration analysis

To determine the final state of an initially stressed FGM laminated plate that is undergoing dynamic deformation, an incremental vibrating state should be added to its pre-vibration state of static equilibrium so that the final solution is

$$\begin{aligned} W &= W^* + W_b + W_d, \quad \Psi_1 = \Psi_{1b} + \Psi_{1d}, \quad \Psi_2 = \Psi_{2b} + \Psi_{2d}, \\ F &= F_b + F_d \end{aligned} \quad 11.51$$

where the subscript  $d$  refers to the dynamic state. The incremental dynamic stress function  $F_d$  is of the form

$$F_d = f_d(x_1, x_2) \quad 11.52$$

Placing Eqs. (11.51) and (11.52) into the nonlinear governing equations of motion (11.32)–(11.35) and noticing that  $W_b$ ,  $\Psi_{1b}$ ,  $\Psi_{2b}$ , and  $F_b$  satisfy Eqs. (11.41)–(11.44), the nonlinear dynamic equations for the plate are derived as

$$\begin{aligned} L_{11}(W_d) - L_{12}(\Psi_{1d}) - L_{13}(\Psi_{2d}) + \gamma_{14}L_{14}(f_d) \\ = \gamma_{14}\beta^2[LW^* + W_b, f_d] + L(W_d, F_b) + L(W_d, f_d) \\ - \frac{\partial^2}{\partial t^2} \left[ W_d + \hat{I}_7^* \left( \frac{\partial^2 W_d}{\partial x_1^2} + \beta^2 \frac{\partial^2 W_d}{\partial x_2^2} \right) + \hat{I}_5^* \left( \frac{\partial \Psi_{1d}}{\partial x_1} + \frac{\partial \Psi_{1d}}{\partial x_2} \right) \right] \end{aligned} \quad 11.53$$

$$\begin{aligned} L_{21}(f_d) + \gamma_{24}L_{22}(\Psi_{1d}) + \lambda_{24}L_{23}(\Psi_{2d}) - \gamma_{24}L_{24}(W_d) \\ = -\frac{1}{2}\gamma_{24}\beta^2 [2L(W^* + W_b, W_d) + L(W_d, W_d)] \end{aligned} \quad 11.54$$

$$\begin{aligned} L_{31}(W_d) + L_{32}(\Psi_{1d}) - L_{33}(\Psi_{2d}) + \gamma_{14}L_{34}(f_d) \\ = -\frac{\partial^2}{\partial t^2} \left( \hat{I}_3^* \Psi_{1d} - I_5^* \frac{\partial W_d}{\partial x_1} \right) \end{aligned} \quad 11.55$$

$$\begin{aligned}
& L_{41}(W_d) - L_{42}(\Psi_{1d}) + L_{43}(\Psi_{2d}) + \gamma_{14}L_{44}(f_d) \\
& = -\frac{\partial^2}{\partial t^2} \left( \hat{I}_3^* \Psi_{2d} - I_5^* \frac{\partial W_d}{\partial x_2} \right)
\end{aligned} \quad 11.56$$

Expanding the incremental dynamic solutions at the  $i$ th nodal line ( $W_{di}$ ,  $\Psi_{1di}$ ,  $\Psi_{2di}$ ,  $f_{di}$ ) in the form of

$$\begin{aligned}
& (W_{di}, \Psi_{1di}, \Psi_{2di}, f_{di}) \\
& = \sum_{m=1}^N [a_{dim} W_{im}(x_2), b_{dim} \Psi_{1im}(x_2), c_{dim} \Psi_{2im}(x_2), d_{dim} f_{im}(x_2)] e^{i\omega t}
\end{aligned} \quad 11.57$$

and using the proposed solution procedure, a nonlinear eigenvalue system is obtained:

$$([G_{d0}] + [G_{d0}^*] + [G_{d1}(\Delta_b)] + [G_{d2}(\Delta_d)])\{\Delta_d\} - \omega^2 [S]\{\Delta_d\} = \{0\} \quad 11.58$$

where  $[G_{d0}] = [G_{b0}]$  and  $[S]$  are the constant matrices,  $[G_{d0}^*]$  and  $G_{d1}(\Delta_b)$  are, respectively, the constant matrices showing the effects of initial geometrical imperfection and the thermo-electro-mechanical pre-stresses, and  $[G_{d2}(\Delta_d)]$  is a nonlinear matrix as a function of the unknown vector  $\Delta_d$ , which is composed of  $a_{dim}$ ,  $b_{dim}$ ,  $c_{dim}$ ,  $d_{dim}$  ( $i = 1, \dots, N$ ;  $m = 1, \dots, M$ ).

The solutions of the following vibration problems can also be determined from Eq. (11.58) as limiting cases:

- Linear vibration of perfect and imperfect plates without pre-stresses

$$([G_{d0}] + [G_{d0}^*])\{\Delta_d\} - \omega^2 [S]\{\Delta_d\} = \{0\} \quad 11.59$$

- Linear vibration of pre-stressed plates

$$([G_{d0}] + [G_{d1}(\Delta_b)])\{\Delta_d\} - \omega^2 [S]\{\Delta_d\} = \{0\} \quad 11.60$$

- Large amplitude vibration of perfect and imperfect plates without pre-stresses

$$([G_{d0}] + [G_{d0}^*] + [G_{d2}(\Delta_d)])\{\Delta_d\} - \omega^2 [S]\{\Delta_d\} = \{0\} \quad 11.61$$

Unlike the iteration process in pre-vibration analysis, the iterative scheme for Eqs. (11.58) and (11.61) begins with a linear vibration solution as the initial guesses for the fundamental frequency and mode shape, and scales up the mode for a given vibration amplitude to calculate  $[G_{d2}(\Delta_d)]$  and then to obtain a new fundamental frequency and mode shape from the updated eigensystem (11.58) or (11.61) as the next guesses. This process is repeated until the difference between the fundamental frequencies that are obtained from the subsequent two iterations is within the specified tolerance, that is

$$\sqrt{\frac{(\omega^{(r+1)} - \omega^{(r)})^2}{(\omega^{(r+1)})^2}} \leq 10^{-3} \quad 11.62$$

## 11.4 Imperfection mode

Unlike the vast majority of the work on the vibration of imperfect plate structures where the imperfection was assumed to have the same shape as the deformed shape, the imperfect mode under current consideration can be of an arbitrary type. A generic model developed from a one-dimensional imperfection model for struts (Wadee, 2000) is employed to describe the various possible imperfection modes, which take the form of the products of trigonometric functions and hyperbolic functions in the  $X_1$ - $X_2$  plane:

$$\begin{aligned} \bar{W}^* &= \eta h \sec h[\delta_1(x_1 - \psi_1)] \cos [\mu_1 \pi (x_1 - \psi_1)] \\ &\quad \sec h[\delta_2(x_2 - \psi_2)] \cos [\mu_2 \pi (x_2 - \psi_2)] \end{aligned} \quad 11.63$$

where  $\eta$  is the maximum dimensionless amplitude of the initially deflected geometry,  $\delta_1$  and  $\delta_2$  are the constants defining the localization degree of the imperfection that is symmetric about  $x_1 = \psi_1$  and  $x_2 = \psi_2$ , and  $\mu_1$  and  $\mu_2$  are the half-wave numbers of the imperfection in the  $X_1$  axis and  $X_2$  axis, respectively. This expression is capable of modeling a wide range of initial imperfection modes, including: (a) the sine type, when  $\delta_1 = \delta_2 = 0$ ,  $\mu_1 = \mu_2 = 1$ ,  $\psi_1 = \psi_2 = 0.5$ ; (b) the localized type, when  $\delta_1 \neq 0$ ,  $\delta_2 \neq 0$ ; and (c) the global type, when  $\delta_1 = \delta_2 = 0$ ,  $\mu_1 \neq 1$  or  $\mu_2 \neq 1$ . A list of nine imperfection modes that will be used in numerical illustrations is given in Table 11.1 where G1, G2, G3 are global imperfection modes while L1, L2, L3, L4, and L5 are localized imperfection modes. The imperfection parameters are

$$\delta_1 = \delta_2 = 0, \mu_1 = \mu_2 = 1, \psi_1 = \psi_2 = 0.5$$

for sine-type imperfection,

$$\text{G1-mode: } \delta_1 = \delta_2 = 0, \mu_1 = \mu_2 = 3, \psi_1 = \psi_2 = 0.5$$

$$\text{G2-mode: } \delta_1 = \delta_2 = 0, \mu_1 = \mu_2 = 5, \psi_1 = \psi_2 = 0.5$$

$$\text{G3-mode: } \delta_1 = \delta_2 = 0, \mu_1 = \mu_2 = 7, \psi_1 = \psi_2 = 0.5$$

for global-type imperfection, and

$$\text{L1-mode: } \delta_1 = 15, \mu_1 = 2, \psi_1 = 0.25, \delta_2 = 0, \mu_2 = 1, \psi_2 = 0.5$$

$$\text{L2-mode: } \delta_1 = 15, \mu_1 = 2, \psi_1 = 0.50, \delta_2 = 0, \mu_2 = 1, \psi_2 = 0.5$$

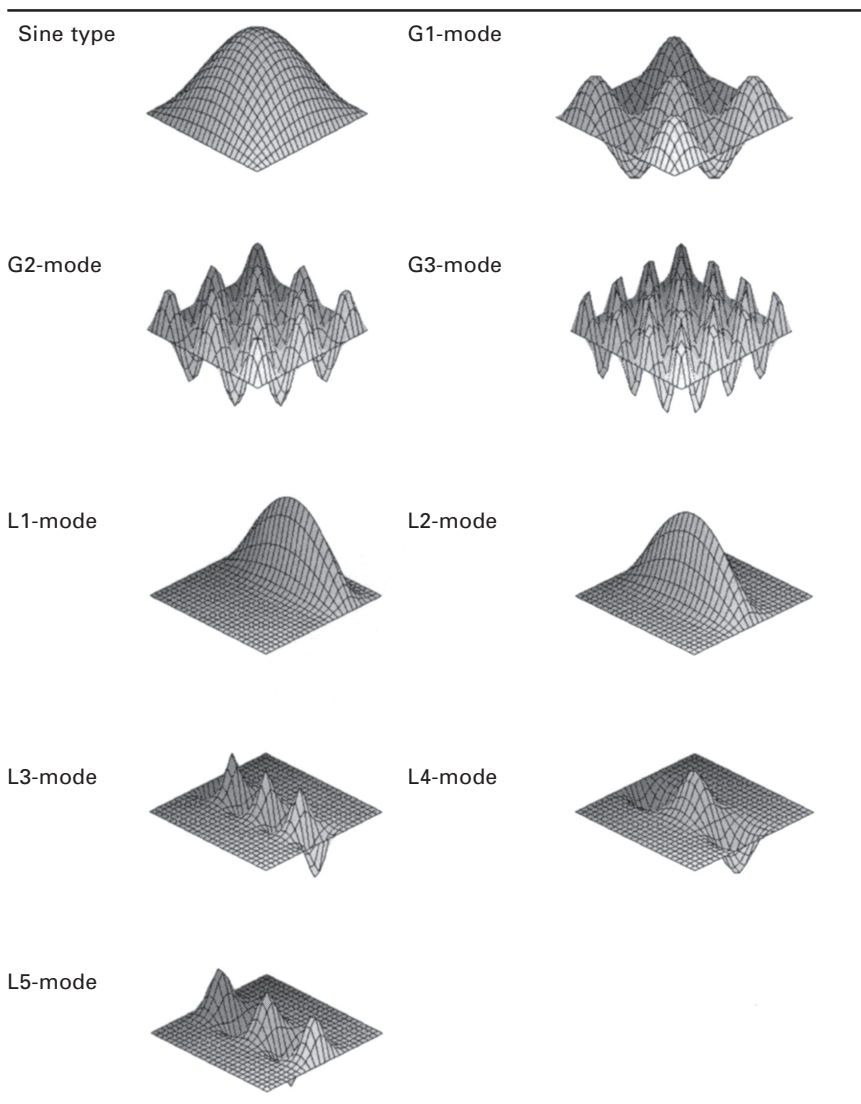
$$\text{L3-mode: } \delta_1 = 15, \mu_1 = 2, \psi_1 = 0.50, \delta_2 = 0, \mu_2 = 3, \psi_2 = 0.5$$

$$\text{L4-mode: } \delta_1 = 15, \mu_1 = 2, \psi_1 = 0.50, \delta_2 = 0, \mu_2 = 5, \psi_2 = 0.5$$

$$\text{L5-mode: } \delta_1 = 15, \mu_1 = 2, \psi_1 = 0.50, \delta_2 = 0, \mu_2 = 7, \psi_2 = 0.5$$

for local-type imperfection.

Table 11.1 Imperfection modes



## 11.5 Validation studies

To validate the present formulation and ensure the accuracy and convergence of the proposed solution method, several linear and nonlinear vibration analyses of isotropic plates, composite laminated plates, and FGM plates with or without geometrical imperfections are first solved and results are compared with those that are available in the open literature. In what follows, a clockwise notation will be used to indicate the out-of-plane support conditions. ‘CSCF’,

for example, refers to a plate that is clamped at  $x_2 = 0, 1$ , simply supported at  $x_1 = 0$ , and free at  $x_1 = 1$ .

*Comparison example 1: Linear vibration of simply supported FGM thin plates*

Table 11.2 gives the first 10 natural frequencies (in Hz) of simply supported aluminum oxide/Ti-6Al-4V square plates ( $a = b = 0.4$  m,  $h = 0.004$  m) with volume fraction exponent  $n = 0, 2000$ . The plates are aluminum oxide-rich at the top surface and Ti-6Al-4V-rich at the bottom surface with the volume fractions

$$V_c = \left( \frac{1}{2} + \frac{X_3}{h} \right)^n, \quad V_m = 1 - \left( \frac{1}{2} + \frac{X_3}{h} \right)^n \quad 11.64$$

It is evident that the top surface of the plate is purely ceramic while its bottom surface is fully metallic. The material properties are evaluated at  $T_0 = 300$  K as

Ti-6Al-4V:  $E = 105.70$  GPa,  $\nu = 0.2981$ ,  $\rho = 4429$  kg/m<sup>3</sup>

Aluminum oxide:  $E = 320.24$  GPa,  $\nu = 0.2600$ ,  $\rho = 3750$  kg/m<sup>3</sup>

The results show that the present solutions are in close correlation with the CPT-based finite element solutions that were given by He *et al.* (2001).

*Comparison example 2: Linear vibration of clamped isotropic thick plates under equal biaxial forces*

The linear frequency parameters  $\omega^* = \Omega b \sqrt{2(1 + \nu) \rho/E}$  of a fully clamped, moderately thick, isotropic square plate ( $a/h = 10$ ,  $\nu = 0.3$ ) under equal biaxial in-plane tension  $\lambda_1 = \lambda_2 = -5\pi^2$  and compression  $\lambda_1 = \lambda_2 = 5\pi^2$  are shown in Table 11.3 together with the FSDPT-based Rayleigh-Ritz solutions of Liew *et al.* (1993) by using the pb-2 polynomials and of Roufaeil and Dawe (1982) by using Timoshenko beam functions. Excellent agreement is observed.

*Comparison example 3: Nonlinear vibration of clamped isotropic thick plates*

Table 11.4 compares the normalized periods (nonlinear period to linear period ratios  $T_{NL}/T_L$ ) for fully clamped, moderately thick isotropic square plates ( $a/h = 20, 10, 5$ ,  $\nu = 0.3$ ) without in-plane stresses and under various vibration amplitudes ( $\bar{W}_c/h = 0.2, 0.4, 0.6, 0.8, 1.0$ ).  $\bar{W}_c$  is the deflection at the center of the plate, i.e.  $\bar{W}_c \bar{W}(0.5, 0.5)$ . A similar analysis was conducted by Raju

Table 11.2 Linear natural frequencies (Hz) of simply supported aluminum oxide/Ti-6Al-4V square plates

Mode sequence	1	2	3	4	5	6	7	8	9	10
<i>Source: n = 0</i>										
N = 9, M = 0	144.97	362.58	362.58	579.44	699.37	723.22	918.78	940.04	1281.31	1791.34
N = 9, M = 3	144.96	362.07	362.07	578.87	723.22	723.22	939.43	939.43	1227.49	1227.49
N = 13, M = 5	144.96	362.08	362.08	578.88	723.23	723.23	929.40	929.40	1227.09	1227.09
N = 17, M = 5	144.96	362.09	362.09	578.88	723.22	723.22	929.41	929.41	1227.05	1227.05
N = 21, M = 7	144.96	360.53	360.53	569.89	720.57	720.57	919.74	919.74	1225.72	1225.72
He et al. (2001)	144.66									
<i>Source: n = 2000</i>										
N = 9, M = 0	244.36	610.45	611.25	976.93	1179.23	1219.43	1549.30	1585.13	2160.94	3026.85
N = 9, M = 3	261.46	653.10	653.10	1044.27	1303.60	1303.60	1693.83	1694.94	2214.41	2269.67
N = 13, M = 5	261.46	653.13	653.13	1044.30	1304.79	1304.79	1694.98	1694.98	2214.41	2214.41
N = 17, M = 5	261.46	653.14	653.14	1044.31	1304.79	1304.79	1694.98	1694.98	2214.34	2214.34
N = 21, M = 7	261.46	669.40	669.40	1052.49	1338.52	1338.52	1695.23	1695.23	2280.95	2280.95
He et al. (2001)	268.92									

Table 11.3 Comparison of linear frequency parameters  $\omega^* = \Omega b \sqrt{2(1+\nu)\rho/E}$  of a clamped, isotropic square plate under equal in-plane forces

In-plane force $\lambda_1 = \lambda_2$	Sources	Mode sequence					
		1	2	3	4	5	6
- $5\pi^2$	$N=9, M=3$ $N=13, M=5$ $N=17, M=5$ $N=21, M=7$ Liew <i>et al.</i> (1993) Roufaeil and Dawe (1982)	2.2621 2.2669 2.2650 2.2660 2.2563 2.280	3.9888 3.9346 3.9349 3.9397 3.9012 3.949	4.8954 5.3347 5.3352 5.3243 5.2345 5.315	5.5494 5.9892 6.1197 6.1235 6.0423 6.112	5.6308 6.2027 6.1425 6.1539 6.0752 6.141	6.6688 7.1535 7.2542 7.2794 7.1631 7.266
$5\pi^2$	$N=9, M=3$ $N=13, M=5$ $N=17, M=5$ $N=21, M=7$ Liew <i>et al.</i> (1993) Roufaeil and Dawe (1982)	1.2536 1.7314 1.7221 1.7230 1.7008 1.624	1.7693 2.9711 2.9694 2.9700 2.8970 2.825	2.3566 3.2603 3.6564 3.6588 3.6435 3.558	2.5225 4.2801 3.7604 3.7624 3.7246 3.648	3.2563 4.4002 4.6988 4.7006 4.6492 4.569	

*Table 11.4 Comparison of normalized periods  $T_{NL}/T_L$  of a clamped isotropic square plate*

$a/h$	$\bar{W}_c/h$	Raju and Hinton (1980)	Present			
			$N = 9,$ $M = 3$	$N = 13,$ $M = 5$	$N = 17,$ $M = 5$	$N = 21,$ $M = 7$
20	0.2	0.9928	0.9723	0.9920	0.9927	0.9929
	0.4	0.9723	0.8977	0.9696	0.9716	0.9728
	0.6	0.9412	0.7965	0.9367	0.9398	0.9423
	0.8	0.9029	0.6801	0.8979	0.9021	0.9042
	1.0	0.8608	0.6787	0.8569	0.8629	0.8647
10	0.2	0.9924	0.9726	0.9921	0.9919	0.9925
	0.4	0.9708	0.9001	0.9699	0.9701	0.9712
	0.6	0.9385	0.8040	0.9374	0.9393	0.9394
	0.8	0.8994	0.6997	0.8991	0.8999	0.9009
	1.0	0.8572	0.6035	0.8584	0.8586	0.8594
5	0.2	0.9903	0.9730	0.9907	0.9904	0.9906
	0.4	0.9636	0.9060	0.9647	0.9637	0.9643
	0.6	0.9248	0.8249	0.9270	0.9250	0.9259
	0.8	0.8795	0.7472	0.8832	0.8799	0.8810
	1.0	0.8318	0.6818	0.8369	0.8327	0.8342

and Hinton (1980) using Mindlin plate theory and Lagrangian, isoparametric quadrilateral elements. Our results agree quite well with their finite element solutions, and the difference increases with the increase in vibration amplitude.

#### *Comparison example 4: Nonlinear vibration of simply supported, imperfect isotropic plates*

For the isotropic square plates ( $\nu = 0.3$   $a/h = 10, 20, 40$ ) with sine-type imperfection ( $\eta = 0.2$ ), present results are compared in Table 11.5 with the analytical solutions of Singh *et al.* (1974) and Lin and Chen (1989). Close correlation is achieved. Some discrepancy is expected because their analyses were based on the FSDT and the in-plane displacement modes that they assumed were slightly different from the movable conditions that are considered in the present investigation.

#### *Comparison example 5: Nonlinear vibration of simply supported imperfect laminated plates*

Since the stiffness matrices of a symmetric cross-ply plate can be regarded as a limiting case of those of the laminated FGM plates and do not contain stretching–bending coupling elements, we further compare in Table 11.6 normalized frequencies  $\omega_{NL}/\omega_L$  of both  $90^\circ/0^\circ/90^\circ$  and  $0^\circ/90^\circ/0^\circ/90^\circ/0^\circ$

*Table 11.5 Comparisons of nonlinear periods for simply supported imperfect isotropic square plates*

$a/h$	$W_c/h$	Singh et al. (1974)	Lin and Chen (1989)	(N, M)			
		(9, 3)	(13, 5)	(17, 5)	(23, 7)		
10	0.0	10.269	10.0353	8.1746	10.092	10.298	10.307
	0.1	10.24	9.98	8.1510	10.063	10.112	10.123
	0.2	10.15	9.87	8.1030	10.004	10.019	10.042
	0.4	9.67	9.23	7.6411	9.4001	9.4571	9.4602
	0.6	8.81	8.10	6.6197	8.1712	8.3370	8.3547
	0.8	7.85	6.97	5.5467	6.8478	6.9876	6.9916
	1.0	6.99	5.99	4.6636	5.7575	5.8750	5.8769
20	0.0	20.044	21.2688	18.285	21.017	21.446	21.468
	0.1	19.99	19.47	16.745	19.243	19.636	19.656
	0.2	19.81	19.30	16.583	19.060	19.443	19.469
	0.4	18.90	18.70	16.086	18.488	18.862	18.881
	0.6	17.27	15.89	13.647	15.684	16.001	16.023
	0.8	15.55	13.78	11.911	13.695	13.971	13.985
	1.0	13.77	12.02	10.429	11.987	12.232	12.244
40	0.0	39.840	42.2041	34.419	40.159	41.404	41.526
	0.1	39.74	38.73	32.309	37.700	38.866	38.983
	0.2	39.39	38.38	31.959	37.282	38.435	38.551
	0.4	37.59	35.94	29.931	34.925	36.006	36.114
	0.6	34.37	31.63	26.363	30.762	31.717	31.809
	0.8	30.75	27.44	22.970	26.803	27.632	27.715
	1.0	27.45	23.97	19.987	23.317	24.038	24.106

*Table 11.6 Comparisons of normalized frequencies for simply supported imperfect symmetric cross-ply square plates*

$W_c/h$	0°/90°/0°		0°/90°/0°/90°/0°	
	Present	Bhimaraddi (1993)	Present	Bhimaraddi (1993)
0.0	1.000	1.000	1.000	1.000
0.2	1.034	1.030	1.036	1.030
0.4	1.142	1.130	1.134	1.125
0.6	1.301	1.289	1.291	1.278
0.8	1.496	1.482	1.476	1.465
1.0	1.708	1.694	1.683	1.671
1.2	1.933	1.917	1.897	1.888

symmetric cross-ply graphite/epoxy plates ( $a/h = 10$ ) with Bhimaraddi's (1993) parabolic shear deformation theory-based results where  $\omega_L$  and  $\omega_{NL}$  denote linear and nonlinear fundamental frequency of the plate with sine-type imperfection ( $\eta = 0.1$ ), respectively. The material constants used in this example are:

$$E_{11} = 181 \text{ GPa}, E_{22} = 10.3 \text{ GPa}, G_{12} = G_{13} = 7.17 \text{ GPa}$$

$$G_{23} = 6.21 \text{ GPa}, \nu_{12} = 0.28$$

### Convergence study

By varying the number of nodal lines  $N$  and truncated series number  $M$ , the convergence characteristic of the proposed method is also examined in the first three examples. Like other conventional differential quadrature approaches, the present method does not converge in a monotonic way. However, as shown in Tables 11.2–11.4, it converged well enough to produce sufficiently accurate results when  $N = 17$ ,  $M = 5$ . Thus,  $N = 17$ ,  $M = 5$  is used for all of the following computations.

## 11.6 Numerical results

### 11.6.1 Vibrational behavior of imperfect FGM laminated plates

The linear and nonlinear vibrational behavior of an imperfect FGM laminated rectangular plate that consists of a homogeneous substrate of thickness  $h_c$  and two inhomogeneous FGM layers of the same layer thickness  $h_F$  is analyzed in this section. Both the top surface ( $X_3 = h_c/2$ ) and the bottom surface ( $X_3 = -h_c/2$ ) of the substrate are perfectly bonded to an FGM layer to form a symmetrically laminated plate structure, as shown in Fig. 11.1(a). The ceramic volume fraction  $V_c$  is described by

$$V_c = \begin{cases} \left( \frac{2X_3 - h_c}{2h_F} \right)^n & X_3 \geq h_c/2 \\ \left( -\frac{2X_3 - h_c}{2h_F} \right)^n & X_3 \leq -h_c/2 \end{cases}, \quad V_m = 1 - V_c \quad 11.65$$

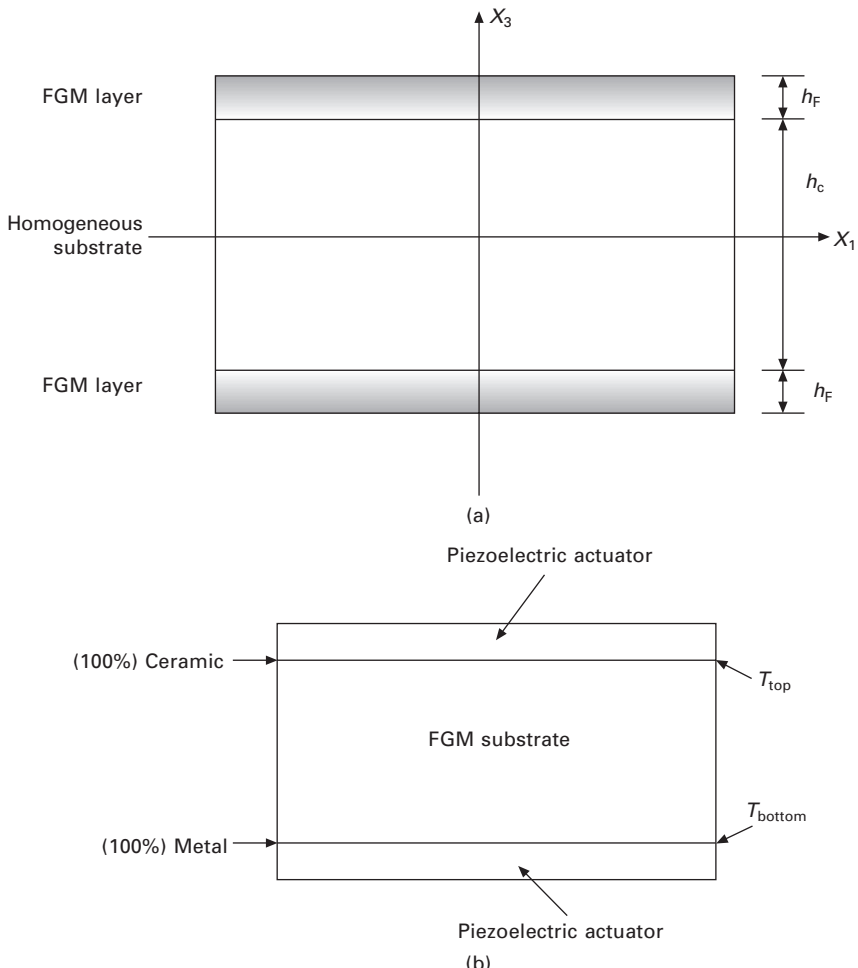
The homogeneous substrate is made of stainless steel (SUS304) and the FGM layers are a mixture of silicon nitride and stainless steel, with material constants at  $T = 300$  K being

$$E = 322.272 \text{ GPa}, v = 0.24, \alpha = 7.4746 \times 10^{-6} \text{ 1/K}, \rho = 2370 \text{ kg/m}^3$$

for silicon nitride and

$$E = 207.79 \text{ GPa}, v = 0.3178, \alpha = 15.321 \times 10^{-6} \text{ 1/K}, \rho = 8166 \text{ kg/m}^3$$

for stainless steel. The thickness ratio between the homogeneous substrate and the FGM layer is  $h_c/h_F = 3$  and the side-to-thickness ratio is  $a/h = 5$  except in Table 11.7 and Fig. 11.2. The values of  $I_1$  and  $D_{11}^*$  of an isotropic steel plate with  $a/h = 10$  are selected to serve as the reference inertia  $I_0$  and the reference stiffness  $D_0$ . This section is focused on the imperfection sensitivity of the vibration of an FGM laminated plate, the thermo-electro-mechanical load is not taken into consideration.



11.1 Configuration of FGM laminated plates: (a) a symmetrically FGM laminated plate; (b) a piezoelectric FGM laminated plate.

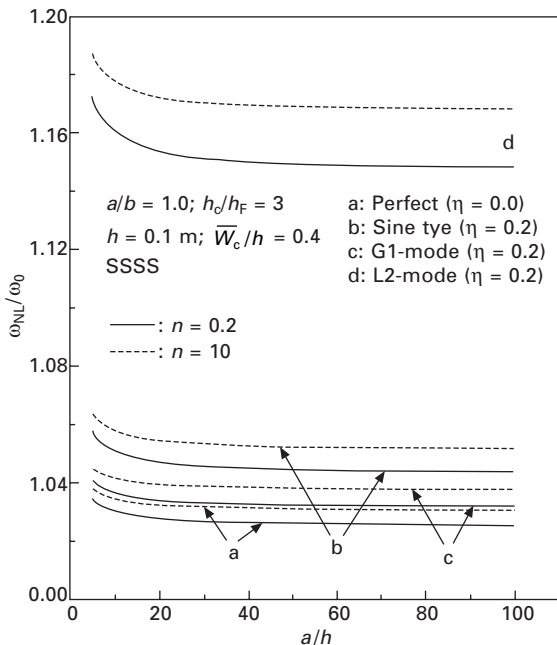
#### *Linear vibration of imperfect FGM laminated plates*

Tables 11.7–11.10 present the first six dimensionless linear frequencies  $\omega = \Omega a^2/\pi^2 \sqrt{I_0/D_0}$  for imperfect ( $\eta = 0.2$ ) laminated square plates with three types of initial imperfections, together with those for perfect ( $\eta = 0.0$ ) plates to demonstrate the effect of imperfection. The temperature is assumed to be  $T = 300$  K.

Table 11.7 compares the linear results of simply supported, moderately thick ( $a/h = 40, 10$ ) and thick ( $a/h = 5$ ), FGM laminated ( $n = 0.2, 2.0, 10$ ), and fully stainless steel plates with sine-type imperfection. The linear frequency is the maximum for laminated plates of  $n = 0.2$  and becomes smaller as  $n$

Table 11.7 Linear frequency parameters for simply supported laminated square plates with sine type imperfection

$a/h$	Mode no.	Perfect			Imperfect				
		$n = 0.2$	$n = 2.0$	$n = 10$	SUS304	$n = 0.2$	$n = 2.0$	$n = 10$	SUS304
5	1	6.4388	5.6094	5.1983	4.9959	6.4636	5.6313	5.2192	5.0165
	2	13.902	12.183	11.338	10.922	13.917	12.196	11.350	10.934
	3	13.902	12.183	11.338	10.922	13.917	12.196	11.350	10.934
	4	19.937	17.546	16.374	15.796	19.948	17.555	16.383	15.805
	5	23.460	20.692	19.338	18.669	23.470	20.700	19.345	18.675
	6	23.460	20.692	19.338	18.669	23.470	20.700	19.345	18.675
10	1	2.5120	2.1792	2.0131	1.9310	2.5201	2.1865	2.0200	1.9379
	2	5.9606	5.1826	4.7958	4.6052	5.9649	5.1865	4.7995	4.6088
	3	5.9606	5.1827	4.7958	4.6052	5.9649	5.1865	4.7995	4.6088
	4	9.1059	7.9328	7.3515	7.0652	9.1087	7.9353	7.3539	7.0676
	5	11.066	9.6515	8.9519	8.6076	11.068	9.6535	8.9538	8.6094
	6	11.066	9.6515	8.9519	8.6076	11.068	9.6535	8.9538	8.6094
40	1	0.3256	0.2821	0.2602	0.2494	0.3266	0.2830	0.2611	0.2502
	2	0.8110	0.7026	0.6482	0.6214	0.8116	0.7031	0.6487	0.6219
	3	0.8110	0.7026	0.6482	0.6214	0.8116	0.7031	0.6487	0.6219
	4	1.2927	1.1201	1.0337	0.9909	1.2931	1.1204	1.0339	0.9912
	5	1.6120	1.3969	1.2892	1.2359	1.6122	1.3971	1.2894	1.2361
	6	1.6120	1.3969	1.2892	1.2359	1.6122	1.3971	1.2894	1.2361



11.2 Effect of side-to-thickness ratio on the nonlinear vibration behavior of simply supported laminated square plates with different initial imperfections.

increases. This can be expected because the Young's modulus for silicon nitride is much greater than that of stainless steel, and the volume of silicon nitride declines when  $n$  increases. The linear frequency also decreases dramatically with increases in the side-to-thickness ratio  $a/h$ . The effect of the initial imperfections is to increase the vibration frequency. This effect, however, tends to be very weak as  $a/h$  increases to 40, which indicates that the geometric imperfection has much stronger influence on the vibration behavior of thicker plates.

Table 11.8 examines the effect of the location of local-type imperfection on the linear frequencies of FGM laminated plates with different boundary supporting conditions (CCCC, SCSC, SSSS, CFCF and SFSF). Given the same parameters, the plate with an imperfection locally centered at  $x_1 = 0.5$  (L2-mode) has higher frequencies than the one whose imperfection is deviated from the plate center and located at  $x_1 = 0.25$  (L1-mode). The fully clamped laminated plate has the highest linear frequencies among the plates considered.

Table 11.9 investigates the effect of the global imperfection mode on the linear vibration of SSSS and CCCC FGM laminated plates. The half-wave number is taken to be the same along  $x_1$  and  $x_2$  axes, and is 3, 5, and 7 for G1-mode, G2-mode and G3-mode, respectively. The linear frequency increases as the half-wave number increases. This effect is much more pronounced for

Table 11.8 Linear frequency parameters for laminated square plates with localized imperfection

Plate type	Mode no.	Perfect		L1-mode		L2-mode	
		$n = 0.2$	$n = 2.0$	$n = 0.2$	$n = 2.0$	$n = 10$	$n = 2.0$
CCCC	1	9.7131	8.5588	7.9958	9.7564	8.5971	8.0320
	2	16.866	14.930	13.996	16.974	15.025	14.085
	3	17.134	15.153	14.196	17.252	15.257	14.293
	4	22.916	20.307	19.047	23.200	20.555	19.280
	5	25.955	23.042	21.639	26.034	23.116	21.711
	6	26.759	23.683	22.172	26.940	23.834	22.306
SCSC	1	8.1526	7.1646	6.6825	8.1828	7.1911	6.7074
	2	14.505	12.744	11.882	14.603	12.829	11.962
	3	16.171	14.302	13.401	16.246	14.368	13.462
	4	21.209	18.743	17.546	21.425	18.931	17.723
	5	23.708	20.925	19.565	23.881	21.076	19.706
	6	25.586	22.713	21.331	25.629	22.751	21.367
SSSS	1	6.4388	5.6094	5.1983	6.4914	5.6560	5.2428
	2	13.902	12.183	11.338	13.984	12.255	11.406
	3	13.902	12.183	11.338	14.020	12.287	11.436
	4	19.937	17.546	16.374	20.158	17.739	16.556
	5	23.460	20.692	19.338	23.502	20.729	19.372
	6	23.460	20.692	19.338	23.663	20.869	19.503
CFCF	1	6.4849	5.6942	5.3055	6.5514	5.7531	5.3613
	2	7.4929	6.5464	6.0836	7.5672	6.6122	6.1461
	3	11.8946	10.349	9.5899	11.901	10.355	9.5958
	4	14.8668	13.129	12.287	14.988	13.234	12.386
	5	16.2188	14.273	13.329	16.369	14.402	13.450
	6	20.132	17.550	16.281	20.198	17.608	16.335
SFSF	1	3.3602	2.9055	2.6787	3.4372	2.9741	2.7441
	2	5.3156	4.5702	4.2029	5.3789	4.6265	4.2567
	3	10.957	9.4870	8.7603	10.961	9.4907	8.7639
	4	11.499	10.032	9.3075	11.610	10.129	9.3977
	5	13.308	11.580	10.728	13.431	11.686	10.827
	6	18.355	16.011	14.854	18.372	16.026	14.869

Table 11.9 Linear frequency parameters for laminated square plates with global imperfection

Imperfection	Mode no.	SSSS			CCCC		
		n = 0.2	n = 2.0	n = 10	n = 0.2	n = 2.0	n = 10
Perfect	1	6.4388	5.6094	5.1983	9.7131	8.5588	7.9958
	2	13.902	12.183	11.338	16.866	14.930	13.996
	3	13.902	12.183	11.338	17.134	15.153	14.196
	4	19.937	17.546	16.374	22.916	20.307	19.047
	5	23.460	20.692	19.338	25.955	23.042	21.639
	6	23.460	20.692	19.338	26.759	23.683	22.172
G1-mode	1	6.5166	5.6785	5.2641	9.7606	8.6024	8.0381
	2	14.034	12.299	11.448	16.939	14.993	14.055
	3	14.067	12.328	11.475	17.202	15.212	14.250
	4	20.157	17.738	16.554	23.010	20.387	19.122
	5	23.987	21.150	19.766	26.605	23.604	22.162
	6	23.987	21.150	19.766	27.506	24.331	22.776
G2-mode	1	6.5871	5.7414	5.3241	9.8215	8.6561	8.0887
	2	13.947	12.222	11.375	16.919	14.976	14.039
	3	13.983	12.255	11.406	17.339	15.334	14.367
	4	19.936	17.545	16.373	22.963	20.346	19.083
	5	23.654	20.861	19.496	26.913	23.818	22.296
	6	24.519	21.614	20.201	27.184	24.088	22.605
G3-mode	1	8.4370	7.3813	6.8790	11.143	9.8274	9.2005
	2	14.760	12.939	12.052	17.998	15.939	14.957
	3	15.437	13.535	12.614	19.233	17.003	15.943
	4	20.796	18.300	17.083	24.548	21.752	20.416
	5	24.548	21.635	20.214	27.414	24.317	22.837
	6	25.262	22.265	20.812	29.328	25.920	24.261

SSSS laminated plates where a maximum of 31.2–32.5% gain in fundamental frequencies can be obtained with G3-mode imperfections.

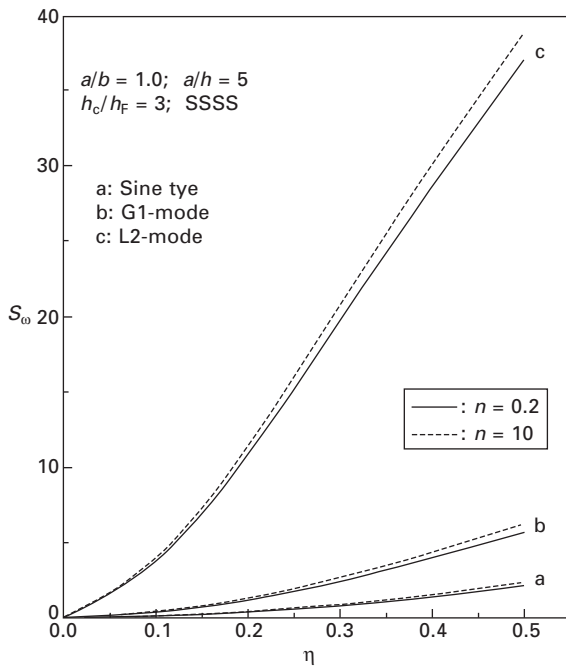
The sensitivity of linear fundamental frequency to geometric imperfection is studied in Fig. 11.3 by comparing the sensitivity indicator  $S_\omega$  of simply supported, FGM laminated square plates with sine type, G1-mode, or L2-mode imperfections. Here,  $S_\omega$  is calculated by

$$S_\omega = \frac{\omega_{\text{imperfect}} - \omega_{\text{perfect}}}{\omega_{\text{perfect}}} \times 100\% \quad 11.66$$

where  $\omega_{\text{perfect}}$  and  $\omega_{\text{imperfect}}$  denote the dimensionless fundamental frequencies for perfect plates and imperfect plates, respectively. Among the imperfection modes under consideration, the linear frequency is most sensitive to localized imperfection, but is comparatively less sensitive to sine-type imperfection. The results also confirm that the linear frequency increases steadily as the imperfection amplitude increases.

Table 11.10 Normalized frequencies of laminated square plates with initial imperfection

Imperfection type	$\bar{W}_c/h$	CCCC		SSSS		SCSC	
		$n = 0.2$	$n = 2$	$n = 0.2$	$n = 2$	$n = 10$	$n = 0.2$
Sine type	0.0	1.0029	1.0029	1.0030	1.0039	1.0040	1.0030
	0.2	1.0224	1.0226	1.0231	1.0251	1.0256	1.0216
	0.4	1.0577	1.0581	1.0593	1.0631	1.0644	1.0662
	0.6	1.1048	1.1057	1.1076	1.1153	1.1175	1.1206
	0.8	1.1607	1.1621	1.1650	1.1784	1.1818	1.1866
	1.0	1.2238	1.2257	1.2296	1.2495	1.2542	1.2607
L2-mode	0.0	1.0956	1.0959	1.0977	1.1060	1.1084	1.1114
	0.2	1.1430	1.1439	1.1464	1.1584	1.1618	1.1661
	0.4	1.1953	1.1967	1.2001	1.2193	1.2238	1.2295
	0.6	1.2531	1.2551	1.2592	1.2877	1.2933	1.3005
	0.8	1.3177	1.3201	1.3251	1.3625	1.3691	1.3779
	1.0	1.3906	1.3931	1.3989	1.4426	1.4503	1.4605
G1-mode	0.0	1.0089	1.0090	1.0093	1.0103	1.0105	1.0108
	0.2	1.0218	1.0222	1.0230	1.0179	1.0183	1.0188
	0.4	1.0462	1.0472	1.0487	1.0422	1.0431	1.0443
	0.6	1.0809	1.0826	1.0848	1.0816	1.0833	1.0856
	0.8	1.1257	1.1278	1.1309	1.1339	1.1366	1.1403
	1.0	1.1812	1.1836	1.1875	1.1972	1.2011	1.2065

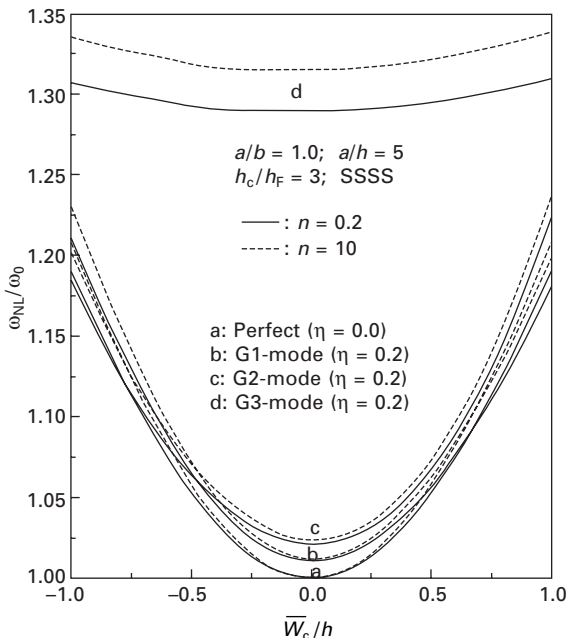


11.3 Geometric imperfection sensitivity of linear fundamental frequency for simply supported laminated square plates.

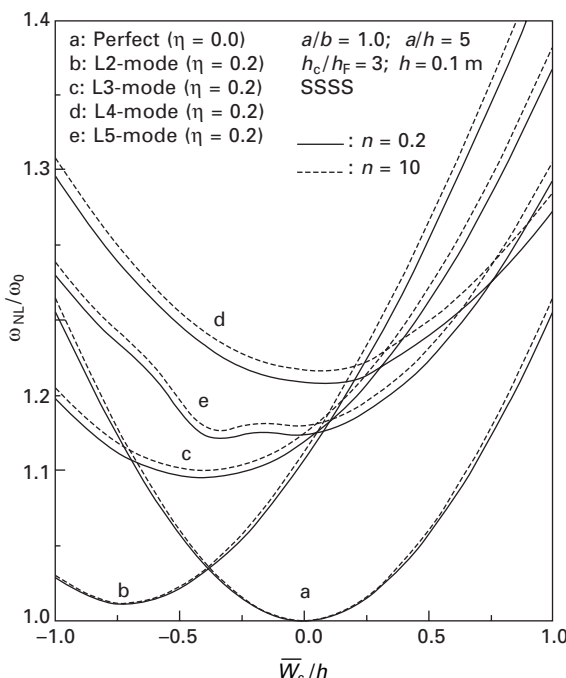
#### *Nonlinear vibration of imperfect FGM laminated plates*

Only nonlinear results for the fundamental vibration mode are presented here although the analysis is also applicable to the non-fundamental modes. Unless otherwise specified, numerical results in the form of normalized frequency  $\omega_{NL}/\omega_0$ , given in Table 11.10 and Fig. 11.2 and 11.4–11.9, are for simply supported, FGM laminated square plates ( $n = 0.2, 10$ ) at  $T = 300$  K, where  $\omega_{NL}$  is the nonlinear fundamental frequency of an imperfect plate and  $\omega_0$  is the linear fundamental frequency of its perfect counterpart, which is determined from the linear form of Eq. (11.59) by neglecting the imperfection-related matrix  $[G_{d0}^*]$ .

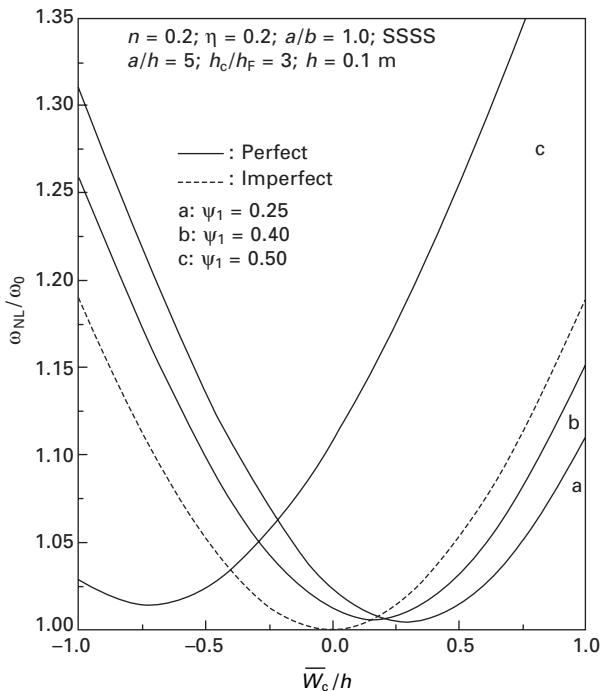
The normalized frequencies of CCCC, SCSC, and SSSS imperfect laminated plates ( $\eta = 0.2$ ) at various vibration amplitudes ( $\bar{W}_c/h = 0.0, 0.2, 0.4, 0.6, 0.8, 1.0$ ) and with three types of initial imperfections (sine type, L2-mode, and G1-mode) are listed in Table 11.10. Note that the results at  $\bar{W}_c/h = 0.0$  are virtually the frequency ratios between the linear fundamental frequency and  $\omega_0$ . The normalized frequency rises with the increase of vibration amplitude, thus displaying the typical characteristic of the well-known ‘hard-spring’ vibration behavior. The plate with L2-mode imperfection has the highest values of normalized frequency  $\omega_{NL}/\omega_0$ , but unlike the linear case



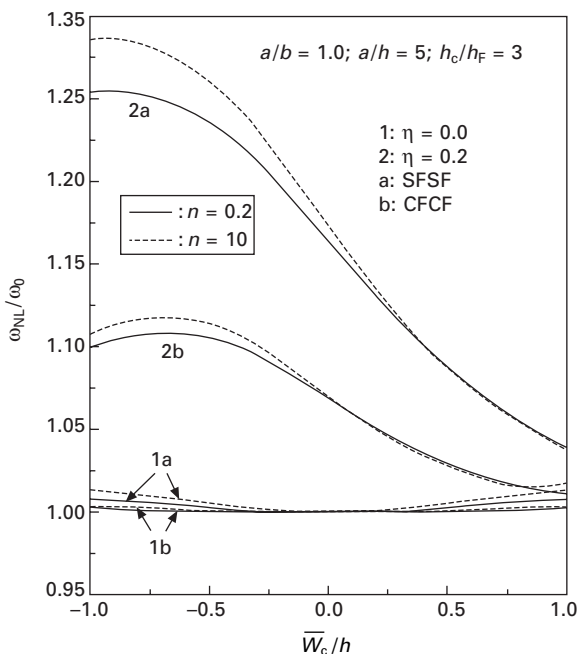
11.4 Normalized frequencies versus vibration amplitude curves for simply supported laminated square plates with global imperfection.



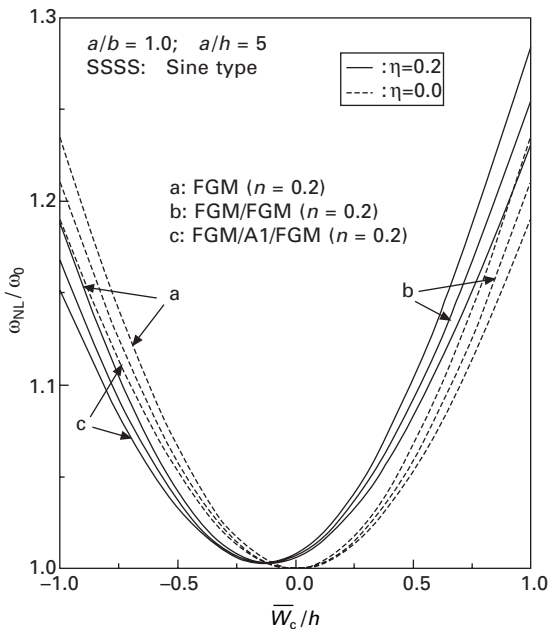
11.5 Normalized frequencies versus vibration amplitude curves for simply supported laminated square plates with localized imperfection.



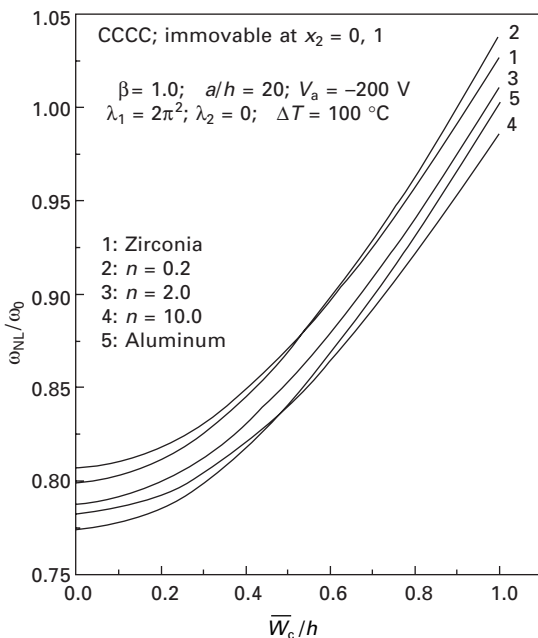
11.6 Effect of imperfection location on the nonlinear vibration behavior of simply supported laminated square plates.



11.7 Normalized frequencies versus vibration amplitude for SFSF and CFCF laminated square plates with localized imperfections (L2-mode).



11.8 Normalized frequencies versus vibration amplitude curves for simply supported laminated square plates with different material compositions.



11.9 Normalized frequencies versus vibration amplitudes for thermo-electro-mechanically pre-stressed CCCC FGM laminated plates.

discussed in Fig. 11.3, the values of  $\omega_{NL}/\omega_0$  for the plate with sine-type imperfections are greater than those with G1-mode imperfections.

Figures 11.4 and 11.5 show the normalized frequency versus vibration amplitude curves for perfect and imperfect FGM laminated plates with global and localized imperfections. Curves a, which are for perfect plates, are exactly symmetric with  $\bar{W}_c/h = 0.0$ . For an imperfect plate, however, the minima, rising as the half-wave number increases, deviate from  $\bar{W}_c/h = 0.0$ , and the symmetry of the curves does not exist. Such a tendency is much more obvious in Fig. 11.5 for plates with localized imperfections.

We next investigate the effect of imperfection location on the nonlinear vibration of FGM laminated plate. To this end, normalized frequency versus vibration amplitude curves with the center of L1-mode imperfection located at  $x_1 = 0.25, 0.40, 0.50$  are given in Fig. 11.6. As can be observed, the minima of the curves increase slightly and move further to the left-hand side as the imperfection location gets closer to the plate center.

Figure 11.7 depicts the nonlinear vibration behavior of FGM laminated plates with free edges. The numerical results show that both CFCF and SFSF imperfect plates change to ‘soft-spring’ vibration behavior from their inherent ‘hard-spring’ behavior as the magnitude of central localized imperfection reaches a certain level ( $\eta \geq 0.095$  for SFSF plates and  $\eta \geq 0.055$  for CFCF plates). A similar phenomenon is found in all of the other examples involving free edges. This suggests that the vibration behavior of laminated plates containing free edges is very much dependent on the existence and amplitude of initial imperfection.

Figure 11.8 gives the normalized frequency versus vibration amplitude curves for plates with sine-type imperfection and having different material composition. Curves a, b, and c are for a fully FGM plate, a symmetrically laminated FGM/FGM plate, and an FGM/Al/FGM plate, respectively. The material profile of the first two plates can be characterized by ceramic volume fraction defined as

$$\text{FGM/FGM: } V_c = (2X_3/h)^n \quad X_3 \geq 0; \quad V_c = (-2X_3/h)^n \quad X_3 \leq 0 \quad 11.67a$$

$$\text{Fully FGM: } V_c = (0.5 + X_3/h)^n \quad 11.67b$$

The fully FGM plate has the highest  $\omega_{NL}/\omega_0$  at negative vibration amplitudes, but has the lowest  $\omega_{NL}/\omega_0$  at positive vibration amplitudes. In contrast, the normalized frequency of an FGM/Al/FGM laminated plate is the minimum when  $\bar{W}_c/h < 0.0$ , but becomes the maximum when  $\bar{W}_c/h > 0.0$ . Figure 11.9 examines the variation of  $\omega_{NL}/\omega_0$  with side-to-thickness ratio  $a/h$  for simply supported laminated plates. For all plates, perfect and imperfect,  $\omega_{NL}/\omega_0$  decreases with the increase of  $a/h$ , and tends to be a constant when  $a/h \geq 20$ .

### 11.6.2 Vibrational behavior of FGM laminated plates under thermo-electro-mechanical loading

We now turn our attention to the linear and nonlinear vibration of FGM laminated plates subjected to a combined thermo-electro-mechanical preload which involves a uniform temperature change  $\Delta T$ , a constant electric field  $E_3$ , and uniform edge forces. The plates considered herein are composed of an intermediate FGM substrate of thickness  $h$ , a top piezoelectric actuator layer, and a bottom piezoelectric actuator layer of equal thickness  $h_a$ , as shown in Fig. 11.1(b).

Numerical results are obtained for laminated plates with either an isotropic substrate layer (that is, the substrate is purely metallic or purely ceramic) or a graded substrate layer ( $n = 0.2, 2, 10$ ). Here, zirconia ( $\text{ZrO}_2$ ) and aluminum (Al) are chosen to be the constituent materials of the FGM substrate layer, and piezoceramic PZT G-1195N is selected as the piezoelectric material for actuator films. The material properties used are

$$\begin{aligned} \text{Zirconia: } & E = 151.0 \text{ GPa}, \nu = 0.3, \alpha = 1.0 \times 10^{-5}/^\circ\text{C}, \rho = 3000 \text{ kg/m}^3 \\ \text{Aluminum: } & E = 70.0 \text{ GPa}, \nu = 0.3, \alpha = 2.3 \times 10^{-5}/^\circ\text{C}, \rho = 2707 \text{ kg/m}^3 \\ \text{G-1195N: } & E_{11} = E_{22} = 63.0 \text{ GPa}, \nu_{12} = \nu_{13} = \nu_{32} = 0.3, \\ & \alpha_{11} = \alpha_{22} = 1.2 \times 10^{-4}/^\circ\text{C}, \varepsilon_{31} = \varepsilon_{32} = 22.8429 \text{ N/m V}, \\ & \rho = 7600 \text{ kg/m}^3 \end{aligned}$$

In Tables 11.11–11.14 and Figs 11.9–11.16, the values of the reference inertia  $I_0$  and bending stiffness  $D_0$  are chosen to be the  $I_1$  and  $D_{11}^*$  of the laminated plate with purely zirconia layer of  $h = 0.02 \text{ m}$ .

#### *Linear vibration of thermo-electro-mechanically stressed FGM laminated plates*

Table 11.11 gives the first eight linear frequency parameters  $\omega = (\Omega a^2/\pi^2) \sqrt{I_0/D_0}$  for the fully immovable CCCC and CSCS laminated square plates ( $a = 0.4 \text{ m}$ ,  $a/h = 20$ ,  $h_a = 0.001 \text{ m}$ ) that are initially stressed by different thermo-electric loads ( $\Delta T = 0 \text{ }^\circ\text{C}$ ,  $300 \text{ }^\circ\text{C}$ ,  $V_a = \pm 200 \text{ V}$ ), among which  $\Delta T = 0 \text{ }^\circ\text{C}$  corresponds to the case that the plate is electrically loaded only.

Table 11.12 displays the first eight linear frequency parameters for CCCC laminated square plates ( $a = 0.4 \text{ m}$ ,  $a/h = 5, 20$ ,  $h_a = 0.001 \text{ m}$ ) that are immovable at  $x_2 = 0, 1$  and subjected to uniform temperature rise  $\Delta T = 300 \text{ }^\circ\text{C}$ , negative applied actuator voltage  $V_a = -200 \text{ V}$ , and uniaxial edge force ( $\lambda_1 = 0, \pm 3\pi^2$ ,  $\lambda_2 = 0$ ).

It is shown that the frequency is the maximum for a plate with purely zirconia layer, the minimum for a plate with purely aluminum layer, and

Table 11.11 Linear frequency parameters  $\omega = (\Omega a^2/\pi^2)\sqrt{I_0 D_0}$  for initially stressed FGM laminated square plates immovable at all edges ( $a/h = 20$ )

Boundary condition	$V_a$	Material mixture	Mode sequences							
			1	2	3	4	5	6	7	8
CCCC	-200 V	Zirconia	3.5257	7.0667	7.0667	10.288	11.149	12.394	14.102	15.325
		$n = 0.2$	3.2156	6.4553	6.4553	9.4109	10.041	11.342	12.775	14.038
		$n = 2.0$	2.9324	5.8913	5.8913	8.5424	9.3338	10.290	11.774	12.719
		$n = 10.0$	2.8377	5.6647	5.6647	8.2245	9.1019	9.8969	11.420	12.215
		Aluminum	2.5360	5.0958	5.0958	7.3859	8.0063	8.8959	10.128	10.997
	200 V	Zirconia	3.5028	7.0394	7.0394	10.259	11.113	12.364	14.066	15.294
		$n = 0.2$	3.1905	6.4254	6.4254	9.3783	9.9986	11.309	12.733	14.003
		$n = 2.0$	2.9035	5.8369	5.8369	8.5052	9.2880	10.252	11.725	12.680
		$n = 10.0$	2.8071	5.6281	5.6281	8.1850	9.0548	9.8564	11.373	12.172
		Aluminum	2.5013	5.0345	5.0345	7.3413	7.9505	8.8505	10.067	10.950
CSCS	-200 V	Zirconia	2.8420	5.3427	6.7258	9.0976	9.8407	10.894	13.217	13.217
		$n = 0.2$	2.5926	4.8728	6.1448	8.3147	8.9908	9.8027	11.949	11.949
		$n = 2.0$	2.3714	4.4436	5.5870	7.5563	8.1876	9.1238	11.036	11.036
		$n = 10.0$	2.2953	4.3005	5.3925	7.2878	7.8976	8.9046	10.628	10.628
		Aluminum	2.0475	3.8425	4.8317	6.5336	7.0675	7.8237	9.4880	9.4880
	200V	Zirconia	2.8165	5.3105	6.6974	9.0666	9.8068	10.857	13.178	13.178
		$n = 0.2$	2.5635	4.8371	6.1137	8.2802	8.9529	9.7598	11.905	11.905
		$n = 2.0$	2.3386	4.4025	5.5515	7.5163	8.1440	9.0778	10.992	10.992
		$n = 10.0$	2.2605	4.2569	5.3547	7.2454	7.8513	8.8573	10.582	10.582
		Aluminum	2.0081	3.7932	4.7890	6.4857	7.0151	7.7671	9.4301	9.4301

Table 11.11 Continued

Boundary condition	$V_a$	Material mixture	Mode sequences						
			1	2	3	4	5	6	7
$\Delta T = 300^\circ\text{C}$									
CCCC	-200 V	Zirconia	2.8148	6.2907	9.4371	10.057	11.538	13.036	13.436
	$n = 0.2$	2.3142	5.4628	5.4628	8.3678	8.5919	10.295	11.408	12.955
	$n = 2.0$	1.7251	4.6287	4.6287	7.2480	7.6718	8.9996	10.165	11.384
	$n = 10.0$	1.5397	4.3279	4.3279	6.8347	7.4034	8.5134	9.7514	10.789
	Aluminum	1.0112	3.6125	3.6125	5.8874	5.9506	7.4086	8.2070	9.4672
	Zirconia	2.7861	6.2334	6.2334	9.4055	10.010	11.507	12.992	14.404
200 V	$n = 0.2$	2.2782	5.4264	5.4264	8.3313	8.5376	10.258	11.358	12.917
	$n = 2.0$	1.7011	4.5843	4.5843	7.2038	7.6108	8.9562	10.109	11.340
	$n = 10.0$	1.4795	4.2792	4.2792	6.7867	7.3415	8.4666	9.6934	10.734
	Aluminum	0.9147	3.5529	3.5529	5.8309	5.9065	7.3539	8.1320	9.4121
	Zirconia	1.9937	4.3487	5.8925	8.1752	8.8313	9.7808	12.097	12.319
	$n = 0.2$	1.4790	3.6196	5.1136	7.1789	7.7459	8.3277	10.512	10.964
CSCS	$n = 2.0$	0.7869	2.8403	4.2944	6.1449	6.6482	7.4381	9.3593	9.5657
	$n = 10.0$	0.4194	2.5716	4.0110	5.7805	6.2557	7.1974	9.0029	9.0596
	Aluminum	0.3592	2.2968	3.6023	5.1950	5.6024	6.1557	7.8552	8.1506
	Zirconia	1.9568	4.3093	5.8607	8.1406	8.7936	9.7379	12.055	12.281
	$n = 0.2$	1.4277	3.5712	5.0763	7.1387	7.7018	8.2723	10.460	10.922
	$n = 2.0$	0.6830	2.7776	4.2489	6.0969	6.5962	7.3775	9.3016	9.5177
200 V	$n = 10.0$	0.3878	2.4835	4.0004	5.7461	6.2264	7.1305	8.9553	9.0154
	Aluminum	0.2856	2.1303	3.5443	5.1344	5.5361	6.0741	7.7802	8.0903

Table 11.12 Linear frequency parameters  $\omega = (\Omega a^2/\pi^2)\sqrt{J_0 D_0}$  for initially stressed CCCC FGM laminated square plates immovable at  $x_2 = 0$ ,  
 $1$  ( $\Delta T = 300$  °C,  $V_a = -200$  V)

$a/h$	Material mixture	Mode sequences					
		1	2	3	4	5	6
$\lambda_1 = -3\pi^2$ , $\lambda_2 = 0$							
5	Zirconia	14.268	23.534	24.536	31.762	35.243	41.948
	$n = 0.2$	13.091	21.678	22.599	29.298	32.389	38.627
	$n = 2.0$	11.805	19.442	20.337	26.294	29.175	30.670
	$n = 10.0$	11.261	18.406	19.308	24.869	27.621	29.008
	Aluminum	10.179	16.758	17.559	22.685	25.104	26.483
20	Zirconia	4.0581	7.4704	7.9826	10.992	11.514	14.714
	$n = 0.2$	3.6426	6.7025	7.2593	9.9683	10.185	12.345
	$n = 2.0$	3.2489	5.9411	6.5677	8.9506	9.2313	11.183
	$n = 10.0$	3.1179	5.6762	6.3277	8.5851	8.9285	10.758
	Aluminum	2.7295	4.9708	5.6362	7.6282	7.6586	9.6399
$\lambda_1 = 0$ , $\lambda_2 = 0$							
5	Zirconia	10.986	19.479	19.479	26.487	30.287	36.101
	$n = 0.2$	10.133	18.074	18.074	24.594	28.100	33.588
	$n = 2.0$	9.0647	16.124	16.124	21.892	25.085	29.897
	$n = 10.0$	8.5446	15.091	15.091	20.429	23.398	27.823
	Aluminum	7.8115	13.906	13.906	18.887	21.633	25.805

Table 11.12 Continued

$a/h$	Material mixture	Mode sequences					
		1	2	3	4	5	6
20	Zirconia	3.2918	6.6521	6.9492	9.9868	10.463	12.321
	$n = 0.2$	2.9306	5.9430	6.3145	9.0466	9.1468	11.255
	$n = 2.0$	2.5804	5.2266	5.7009	8.0976	8.3217	10.186
	$n = 10.0$	2.4610	4.9722	5.4832	7.7496	8.0709	9.7884
	Aluminum	2.1301	4.3301	4.8820	6.7900	6.8806	8.7766
$\lambda_1 = 3\pi^2, \lambda_2 = 0$							
5	Zirconia	5.7984	12.3010	14.526	19.732	21.709	25.082
	$n = 0.2$	5.5342	11.756	13.656	18.641	20.667	23.367
	$n = 2.0$	4.6963	10.123	11.891	16.238	17.943	20.668
	$n = 10.0$	4.0314	8.8737	10.728	14.585	15.931	18.885
	Aluminum	4.0307	8.7621	10.228	14.011	15.529	17.755
20	Zirconia	2.2473	5.7090	5.7150	8.8599	9.2296	10.987
	$n = 0.2$	1.9442	5.0628	5.1849	7.8820	8.0125	10.040
	$n = 2.0$	1.6267	4.3893	4.6614	7.1366	7.2359	9.0744
	$n = 10.0$	1.5090	4.1420	4.4675	6.8053	7.0632	8.6993
	Aluminum	1.2377	3.5686	3.9747	5.7172	6.0349	7.8132

decreases as the volume fraction exponent  $n$  increases because aluminum has a much smaller Young's modulus than zirconia. The frequency is also seen to decrease with the application of uniform temperature rise, edge compression, and positive applied voltage but to increase when the plate is subjected to uniform edge tension and negative applied voltage or the value of  $a/h$  becomes smaller. As expected, a fully clamped plate possesses higher vibration frequencies than its CSCS counterpart because it is capable of providing stiffer boundary supporting conditions.

It is worthy of note that the influence of the applied voltage is much more significant on the lower-order frequencies, especially on the fundamental frequencies and at higher temperatures, and it tends to be much weaker on higher-order vibration frequencies and in the absence of temperature rise. Since the lower-order frequencies are generally of the greatest importance in determining the dynamic response of a plate, this feature indicates the great possibility of suppressing the dynamic deflections of pre-stressed FGM plates by using the piezoelectric materials.

#### *Nonlinear vibration of thermo-electro-mechanically stressed FGM laminated plates*

Unless otherwise specified, it is assumed in this subsection that the square FGM laminated plate ( $a = 0.4$  m,  $a/h = 20$ ,  $h_a = 0.001$  m) is fully clamped (CCCC), movable at  $x_1 = 0, 1$  but immovable at  $x_2 = 0, 1$ , subjected to uniaxial compression ( $\lambda_1 = 2\pi^2$ ,  $\lambda_2 = 0$ ), uniform temperature rise ( $\Delta T = 100$  °C) and a constant applied actuator voltage ( $V_a = -200$  V) before dynamic deformation. To obtain a clear view of the effects of thermo-electro-mechanical preloading on the nonlinear vibration characteristics, it is preferred that the results in the following analyses are presented in terms of the normalized frequency  $\omega_{NL}/\omega_{L0}$ , where  $\omega_{NL}$  is the nonlinear fundamental frequency of the pre-stressed FGM plate and,  $\omega_{L0}$  is the linear fundamental frequency of the plate in the absence of the preload, in other words,  $\omega_{L0}$  is determined from Eq. (11.60) by neglecting [ $G_{d1}(\Delta_b)$ ].

Table 11.13 gives the normalized frequencies  $\omega_{NL}/\omega_{L0}$  for fully movable, CCCC FGM laminated rectangular plates ( $a/b = 1.0, 1.5$ ) that are subjected to biaxial in-plane forces only ( $\lambda_1 = \lambda_2 = 0, \pm 3\pi^2$ ). For such a plate, the vibration frequencies are independent of both uniform temperature change and constant actuator voltage as the plate is free from displacement constraints in its in-plane directions. Because of this and because zirconia and aluminum have the same Poisson ratio, the laminated plates with the isotropic zirconia layer and isotropic aluminum layer, though having different  $\omega_{L0}$ , share the same values of  $\omega_{NL}/\omega_{L0}$ .

Table 11.14 shows the normalized frequencies  $\omega_{NL}/\omega_{L0}$  for fully immovable CCCC FGM laminated square plates with varying side-to-thickness ratios

Table 11.13 Normalized frequencies  $\omega_{NL}/\omega_{L0}$  for movable, clamped FGM rectangular plates under equal biaxial in-plane forces

$\lambda_1 = \lambda_2$	$\bar{W}_c/h$	Isotropic	$a/b = 1.0$			$a/b = 1.5$		
			$n = 0.2$	$n = 2$	$n = 10$	Isotropic	$n = 0.2$	$n = 2$
-3 $\pi^2$	0.0	1.2510	1.2507	1.2509	1.2503	1.2072	1.2083	1.2070
	0.2	1.2571	1.2575	1.2569	1.2572	1.2114	1.2115	1.2113
	0.4	1.2751	1.2773	1.2746	1.2729	1.2242	1.2255	1.2238
	0.6	1.3039	1.3089	1.3029	1.2982	1.2447	1.2481	1.2438
	0.8	1.3420	1.3505	1.3406	1.3339	1.2716	1.2777	1.2702
	1.0	1.3880	1.4003	1.3860	1.3728	1.3039	1.3128	1.2935
	0	0.0000	1.0000	1.0000	1.0000	1.0000	1.0000	1.0000
	0.2	1.0083	1.0089	1.0080	1.0072	1.0056	1.0062	1.0055
	0.4	1.0321	1.0352	1.0316	1.0281	1.0220	1.0244	1.0215
	0.6	1.0699	1.0763	1.0689	1.0616	1.0481	1.0529	1.0471
$\omega_{L0}$	0.8	1.1189	1.1294	1.1174	1.1054	1.0821	1.0900	1.0807
	1.0	1.1767	1.1916	1.1746	1.1575	1.1224	1.1335	1.1204
	3 $\pi^2$	0.0	0.6473	0.6483	0.6473	0.6449	0.7255	0.7268
	0.2	0.6612	0.6634	0.6611	0.6572	0.7337	0.7357	0.7337
	0.4	0.7007	0.7063	0.7003	0.6925	0.7576	0.7616	0.7574
$\omega_{L0}$	0.6	0.7604	0.7705	0.7595	0.7463	0.7948	0.8019	0.7943
	0.8	0.8340	0.8491	0.8326	0.8134	0.8427	0.8532	0.8418
	1.0	0.9163	0.9364	0.9145	0.8892	0.8978	0.9121	0.8966
		3.5141 <sup>Z</sup>	3.2031	2.9181	2.8825	5.8314 <sup>Z</sup>	5.3198	4.8422
		2.5188 <sup>A</sup>				4.1797 <sup>A</sup>		4.6750

<sup>Z</sup> Results for laminated plates with purely zirconia layer.

<sup>A</sup> Results for laminated plates with purely aluminum layer.

Table 11.14 Normalized frequencies  $\omega_{NL}/\omega_{L0}$  for immovable CCCC FGM square plates under uniform temperature change and a constant electric field

$\Delta T$ [°C]	$\bar{W}_c/h$	V <sub>a</sub> = -200 V			V <sub>a</sub> = 200 V		
		ZrO <sub>2</sub>	n = 0.2	n = 10	ZrO <sub>2</sub>	n = 0.2	n = 10
0	0.0	1.0069	1.0039	1.0049	1.0069	0.9968	0.9950
	0.2	1.0150	1.0129	1.0130	1.0113	1.0050	1.0032
	0.4	1.0387	1.0389	1.0364	1.0351	1.0290	1.0314
	0.6	1.0761	1.0799	1.0734	1.0727	1.0668	1.0728
	0.8	1.1248	1.1328	1.1217	1.1216	1.1248	1.1261
	1.0	1.1822	1.1948	1.1787	1.1792	1.1822	1.1741
	0.0	0.8010	0.7225	0.6004	0.5455	0.4015	0.7929
	0.2	0.8118	0.7359	0.6155	0.5605	0.4249	0.8038
	0.4	0.8430	0.7740	0.6579	0.6026	0.4876	0.8353
	0.6	0.8912	0.8320	0.7214	0.6653	0.5746	0.8841
100	0.8	0.9525	0.9040	0.7989	0.7415	0.6739	0.9459
	1.0	1.0229	0.9853	0.8848	0.8257	0.7782	0.9169
	3.5141	3.2031	2.9181	2.8825	2.5188	2.5141	3.2031
	$\omega_{L0}$						
	0	1.0002	1.0001	1.0001	1.0001	1.0001	1.0001
	0.2	1.0099	1.0105	1.0099	1.0091	1.0097	1.0097
	0.4	1.0381	1.0405	1.0381	1.0352	1.0379	1.0403
	0.6	1.0820	1.0869	1.0822	1.0762	1.0819	1.0867
	0.8	1.1379	1.1458	1.1383	1.1289	1.1378	1.1377
	1.0	1.2030	1.2138	1.2036	1.1901	1.2029	1.2028
300	0	0.9828	0.9778	0.9693	0.9646	0.9599	0.9827
	0.2	0.9928	0.9885	0.9796	0.9741	0.9703	0.9927
	0.4	1.0217	1.0195	1.0091	1.0016	1.0002	1.0216
	0.6	1.0666	1.0673	1.0549	1.0445	1.0465	1.0665
	0.8	1.1237	1.1277	1.1131	1.0992	1.1051	1.1236
	1.0	1.1899	1.1973	1.1805	1.1630	1.1729	1.1898
	11.053	10.213	9.1637	8.6528	7.9228	11.053	10.213
	$\omega_{L0}$						
	0						
	$d/h = 5$						

@ Seismicisolation

( $a/h = 5, 20$ ) and under different thermo-electric preloads ( $V_a = \pm 200$  V,  $\Delta T = 0^\circ$  C,  $300^\circ$  C). The plate is electrically loaded only when  $\Delta T = 0^\circ$  C.

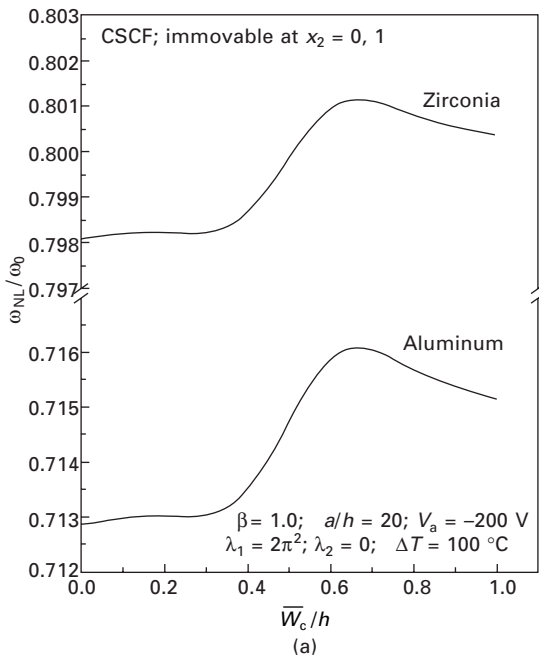
The linear fundamental frequencies  $\omega_{L0}$  for the laminated plates are also provided in Tables 11.13 and 11.14, where the values with superscripts Z and A are for the plates with the purely zirconia layer and with the purely aluminum layer, respectively. Note that the normalized frequency  $\omega_{NL}/\omega_{L0}$  at  $\bar{W}_c/h = 0.0$  is virtually the ratio between the linear frequency of a pre-stressed plate and that of the same plate without initial loading.

It is seen that the effect of geometrical nonlinearity, which is to raise the nonlinear frequencies, is very important at large vibration amplitudes. The fundamental frequency at  $\bar{W}_c/h = 1.0$  is increased by up to 44.4% for a square plate ( $n = 0.2$ ) subjected to  $\lambda_1 = \lambda_2 = 3\pi^2$  and by nearly 110% for an immovable square plate (Al) with  $a/h = 20$  and under thermo-electric loading  $V_a = 200$  V,  $\Delta T = 300^\circ$  C, indicating that nonlinear effect should not be neglected, especially when the plate is in a initial compressive stress state induced by in-plane compression or thermo-electric preload. Note that a square plate has a larger nonlinearity than a rectangular plate.

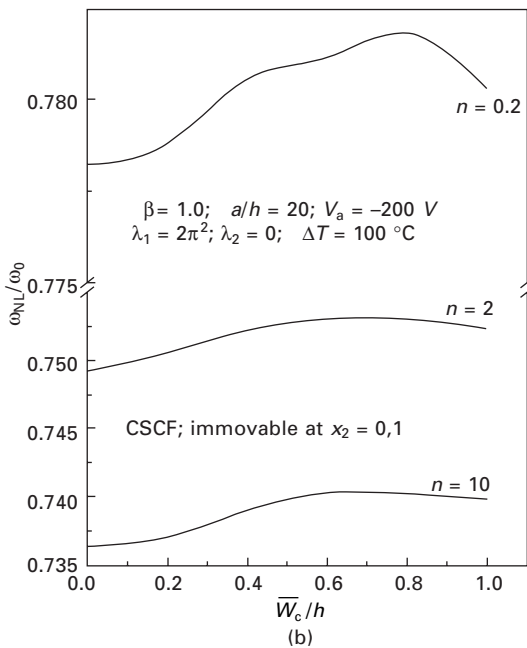
Results show that the normalized frequency of pre-stressed FGM plates increases with the application of tensile in-plane forces, and decreases with the increase of the volume fraction exponent  $n$ , the compressive in-plane forces, the environmental temperature, and the plate aspect ratio  $a/b$ . Both the linear frequency  $\omega_{L0}$  and normalized frequency are the maximum for the plate with full zirconia layer in all preloading cases, whereas they are the minimum for the plate with fully aluminum layer when thermal load is present. The reason is that aluminum has a lower Young's modulus and greater thermal expansion coefficient than zirconia, thus resulting in a more serious thermally induced compressive stress state in the plate. Note that for the plate that is initially compressed due to temperature rise  $\Delta T = 300^\circ$  C or in-plane edge force, the value of  $\omega_{NL}/\omega_{L0}$  at  $\bar{W}_c/h = 0.0$  is smaller than 1.0. Moreover, the normalized frequency is observed to increase as the side-to-thickness ratio  $a/h$  decreases, i.e. as the plate becomes thicker.

Results also show that the negative applied actuator voltage increases the normalized frequencies and the positive applied actuator voltage reduces the normalized frequencies. This effect tends to be more obvious at large vibration amplitudes and when the thermal load is included. As expected, the effects of pre-loads, especially of the applied voltage, are more pronounced for thinner laminated plates than for thicker ones. This is because the stiffness of thinner plates is lower than thicker plates.

A large number of examples have been solved to further examine the large amplitude vibration behavior of FGM plates under different out-of-plane boundary conditions, Figs 11.9–11.11 depict, respectively, the normalized frequency versus vibration amplitude curves for thermo-electro-mechanically stressed CCCC, CSCF, and CFCF square plates that are immovable at



(a)



(b)

11.10 Normalized frequencies versus vibration amplitudes for thermo-electro-mechanically pre-stressed CSCF FGM laminated plates: (a) isotropic; (b) graded.

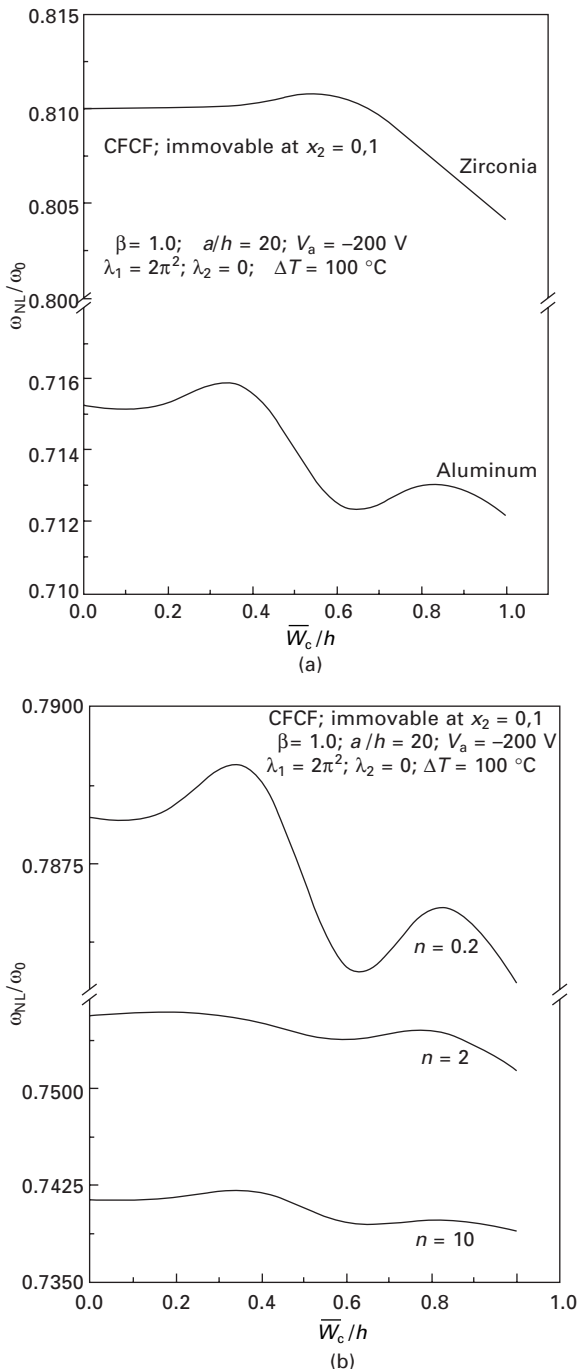
$x_2 = 0, 1$ . The out-of-plane boundary support has a highly significant influence on the nonlinear vibration response. The curves of CCCC plates are quite different from those of CSCF plates and CFCF plates. Of great interest is that the CSCF and CFCF laminated plates even change the well-known inherent ‘hard-spring’ nonlinear vibration character to so-called ‘soft-spring’ behavior at large vibration amplitudes, i.e. when  $\bar{W}_c/h \geq 0.6 \sim 0.8$  for CSCF plates and  $\bar{W}_c/h \geq 0.4 \sim 0.6$  for CFCF plates.

The effects of in-plane forces are studied in Fig. 11.12, where normalized frequency versus in-plane force curves at both small vibration amplitude  $\bar{W}_c/h = 0.4$  and large vibration amplitude  $\bar{W}_c/h = 1.0$  are provided for CCCC FGM square plates that are subjected to uniaxial edge force in the  $x_2$  direction, uniform temperature change  $\Delta T = 100$  °C, and applied voltage  $V_a = -200$  V. The results demonstrate that the normalized frequencies of the laminated plate can be increased up to 23–30% at  $\bar{W}_c/h = 0.4$  and up to 24–26% at  $\bar{W}_c/h = 1.0$  when the plate is subjected to  $\lambda_1 = -5\pi^2$ . Contrarily, the normalized frequencies are reduced by about 45–51% at  $\bar{W}_c/h = 0.4$  and by about 32–35% at  $\bar{W}_c/h = 1.0$  when the plate is compressed by  $\lambda_1 = 5\pi^2$ . This indicates that the in-plane compressive force has greater influence on the nonlinear vibration behavior than the in-plane tensile force.

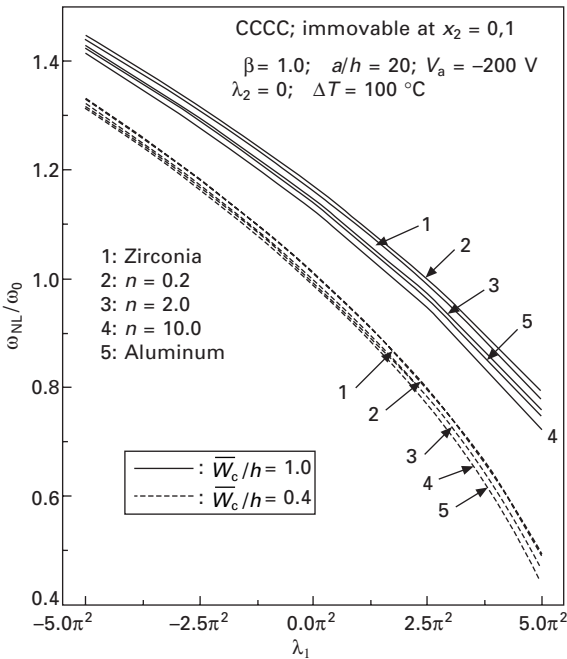
Fig. 11.13 investigates the effect of temperature change on the large amplitude vibration of thermo-electro-mechanically stressed CCCC FGM laminated plates. It is evident from the figure that the normalized frequency decreases considerably as the temperature rises, especially at small vibration amplitudes. Variations of normalized frequency with temperature change follow a quite similar pattern at both small and large vibration amplitudes. Among the plates considered, the one with purely aluminum layer exhibits the greatest reduction in normalized frequency as the temperature is increased.

In Fig. 11.14, the effect of applied actuator voltage is examined. The solid lines and the dashed lines represent the normalized frequency versus vibration amplitude responses for the cases of  $V_a = -300$  V and  $V_a = 300$  V. As discussed in Table 11.14, the negative applied voltage can help increase both the linear fundamental frequency  $\omega_L$  and the normalized frequency  $\omega_{NL}/\omega_{L0}$ , though not so prominently. It also appears that the effect of applied voltage tends to be somewhat weaker at larger vibration amplitudes. Fig. 11.15 presents the large amplitude vibration behavior of FGM laminated plates with different side-to-thickness ratios ( $a/h = 10, 50$ ). It is shown in the figure that the normalized frequencies of thicker ( $a/h = 10$ ) plates are much higher than those of their thinner counterparts ( $a/h = 50$ ).

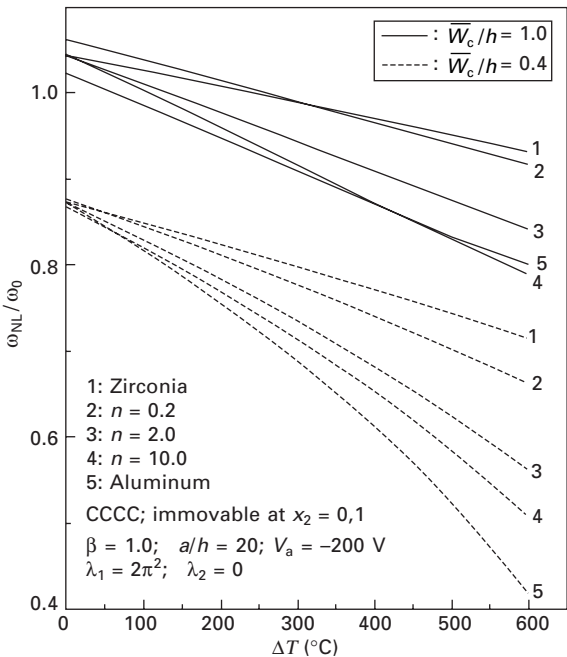
The effects of in-plane displacement constraints are displayed in Fig. 11.16 by comparing the normalized frequency versus vibration amplitude relationships for CCCC FGM laminated plates fully movable or immovable at  $x_2 = 0, 1$  and under thermo-electro-mechanical preloading. The dashed curves are for fully movable plates. As can be seen, the normalized frequencies



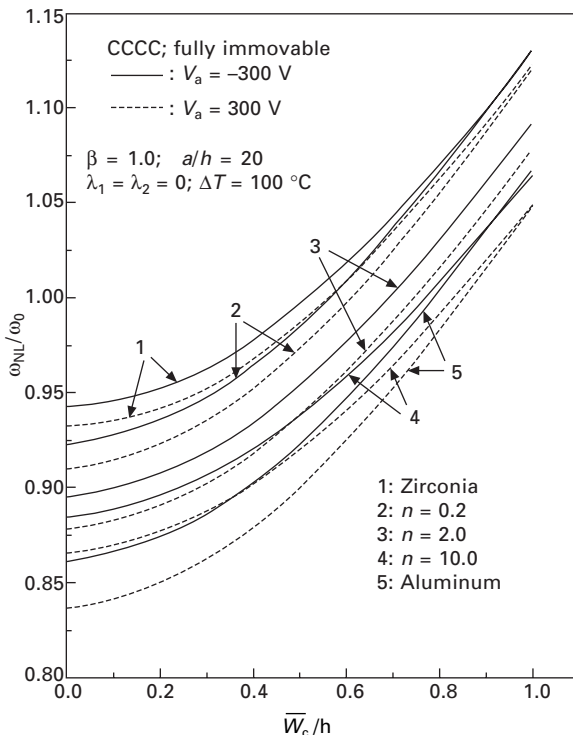
11.11 Normalized frequencies versus vibration amplitudes for thermo-electro-mechanically pre-stressed CFCF FGM laminated plates: (a) isotropic; (b) graded.



11.12 Variations of normalized frequencies with initial in-plane forces for thermo-electro-mechanically pre-stressed CCCC FGM laminated plates.



11.13 Variations of normalized frequencies with temperature change for thermo-electro-mechanically pre-stressed CCCC FGM laminated plates.

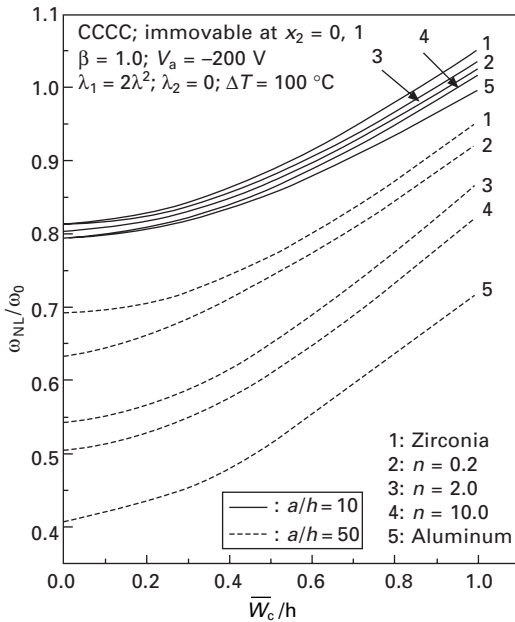


11.14 Normalized frequencies versus vibration amplitudes for thermo-electro-mechanically pre-stressed CCCC FGM laminated plates under varying applied actuator voltages.

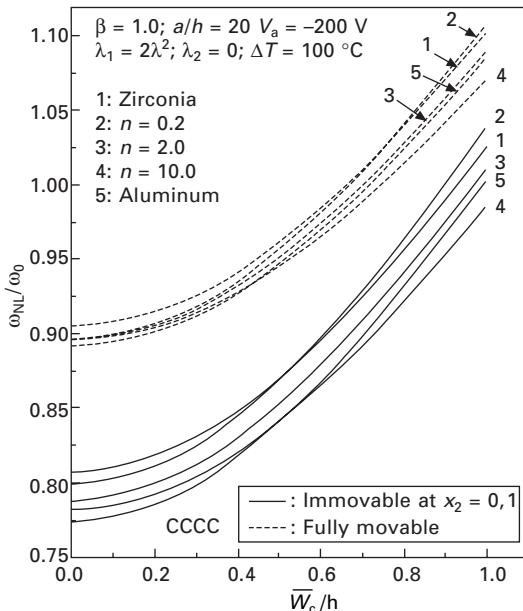
of immovable plates (the solid curves) are much lower than those of movable plates. This is due to the fact that the initial compressive stresses induced by the thermo-electro-mechanical load are much higher in the laminated plates with immovable edges.

## 11.7 Conclusions

In this chapter, the nonlinear vibration of perfect and imperfect, shear deformable FGM laminated rectangular plates with or without the application of thermo-electro-mechanical preload is studied in detail. The theoretical formulations are based on Reddy's higher-order shear deformation plate theory, including the effects of initial geometrical imperfection of general modes. A semi-analytical method that makes use of one-dimensional differential quadrature approximation, the Galerkin technique, and the direct iterative scheme is used to solve the vibration frequencies of FGM laminated plates with general boundary conditions. The numerical results demonstrate that the linear and nonlinear vibration behavior of the pre-stressed laminated plates is greatly influenced by the vibration amplitude, material composition,



11.15 Normalized frequencies versus vibration amplitudes for thermo-electro-mechanically pre-stressed CCCC FGM laminated plates with varying side-to-thickness ratios.



11.16 Normalized frequencies versus vibration amplitudes for thermo-electro-mechanically pre-stressed CCCC FGM laminated plates with different in-plane constraints.

out-of-plane boundary support, temperature change, in-plane compression, and the side-to-thickness ratio, and can be controlled by the applied actuator voltage. Moreover, although most of the thermo-electro-mechanically pre-stressed FGM laminated plates show the inherent ‘hard-spring’ characteristic, the CSCF and CFCF ones exhibit ‘soft-spring’ behavior at large vibration amplitudes. The influence of geometric imperfections, especially the localized type, is found to be highly significant on the vibration behavior of such laminated plate structures. The presence of localized imperfection at the plate center may significantly increase the linear frequencies and nonlinear normalized frequencies. FGM laminated plates with free edges, in the absence of prestresses may also show the transition from ‘hard-spring’ behavior to a ‘soft-spring’ character when the imperfection magnitude reaches a certain level. The results also indicate that the vibration frequencies of thicker plates are much more sensitive to geometric imperfections than those of thinner plates.

## 11.8 Acknowledgment

The work described in this paper was supported by a research grant from the Research Grants Council of the Hong Kong Special Administrative Region, China (Project No. CityU1039/04E). The authors are grateful for this financial support.

## 11.9 References

- Benjeddou A, (2000), ‘Advances in piezoelectric finite element modeling of adaptive structural elements: a survey’, *Comput Struct*, **76**, 347–363.
- Bert CW, Malik M, (1996), ‘Differential quadrature method in computational mechanics: a review’, *Appl Mech Rev ASME*, **49**, 1–28.
- Bhimaraddi A, (1993), ‘Large amplitude vibrations of imperfect antisymmetric angle-ply laminated plates’, *J Sound Vib*, **162**, 457–470.
- Bhimaraddi A, Chandrashekara K, (1993), ‘Nonlinear vibrations of heated antisymmetric angle-ply laminated plates’, *Int J Solids Struct*, **30**, 1255–1268.
- Celep Z, (1976), ‘Free flexural vibration of initially imperfect thin plates with large elastic amplitudes’, *ZAMM*, **56**, 423–428.
- Celep Z, (1980), ‘Shear and rotatory inertia effects on the nonlinear vibration of the initially imperfect plates’, *J Appl Mech ASME*, **47**, 662–666.
- Chen CS, (2005), ‘Nonlinear vibration of a shear deformable functionally graded plate’, *Compos Struct*, **68**, 295–302.
- Chen CS, Cheng WS, Chien RD, Doong JL, (2002), ‘Large amplitude vibration of an initially stressed cross ply laminated plate’, *Appl Acoust*, **63**, 939–956.
- Chen LW, Doong JL, (1983a), ‘Large amplitude vibrations of an initially stressed moderately thick plate’, *J Sound Vib*, **89**, 499–508.
- Chen LW, Doong JL, (1983b), ‘Large amplitude vibrations of an initially stressed thick circular plate’, *AIAA*, **21**, 1317–1324.

- Chen LW, Lin CC, (1992), 'Effects of geometric imperfections and large amplitudes on vibrations of an initially stressed Mindlin plate', *Appl Acoust*, **35**, 265–282.
- Chen LW, Yang JY, (1993), 'Nonlinear vibration of antisymmetric imperfect angle-ply laminated plates', *Compos Struct*, **23**, 39–46.
- Chen WQ, Ding HJ, (2002), 'On free vibration of a functionally graded piezoelectric rectangular plate', *Acta Mechanica*, **153**, 207–216.
- Cheng ZQ, Batra RC, (2000), 'Exact correspondence between eigenvalues of membranes and functionally graded simply supported polygonal plates', *J Sound Vib*, **229**, 879–895.
- Elmajid A, Taya M, Hudnut S, (2001), 'Analysis of out-of-plane displacement and stress field in a piezocomposite plate with functionally graded microstructure', *Int J Solids Struct*, **38**, 3377–3391.
- He XQ, Ng TY, Sivashanker S, Liew KM, (2001), 'Active control of FGM plates with integrated piezoelectric sensors and actuators', *Int J Solids Struct*, **38**, 1641–1655.
- Huang XL, Shen HS, (2004), 'Nonlinear vibration and dynamic response of functionally graded plates in thermal environments', *Int J Solids Struct*, **41**, 2403–2427.
- Hui D, (1983), 'Large amplitude axisymmetric vibrations of geometrically imperfect circular plates', *J Sound Vib*, **91**, 239–246.
- Hui D, (1985), 'Soft-spring nonlinear vibrations of antisymmetrically laminated rectangular plates', *Int J Mech Sci*, **27**, 397–408.
- Hui D, Leissa AW, (1983), 'Effects of geometric imperfections on large amplitude vibrations of biaxially compressed rectangular flat plates', *J Appl Mech ASME*, **50**, 750–756.
- Jonnalagadda KD, Blendford GE, Tauchert TR, (1994), 'Piezothermoelastic composite plate analysis using first-order shear deformation theory', *Comput Struct*, **51**, 79–89.
- Kapania RK, Yang TY, (1987), 'Buckling, postbuckling, and nonlinear vibrations of imperfect plates', *AIAA*, **25**, 1338–1346.
- Liew KM, Han JB, (1997), 'A four-node differential quadrature method for straight-sided quadrilateral Reissner/Mindlin plates', *Commun Numer Methods Eng*, **13**, 62–73.
- Liew KM, Xiang Y, Kitipornchai S, (1993), 'Transverse vibration of thick rectangular plates-Influence of isotropic in-plane pressure', *Comput Struct*, **49**, 69–78.
- Liew KM, He XQ, Ng TY, Sivashanker S, (2001), 'Active control of FGM plates subjected to a temperature gradient: modeling via finite element method based on FSDT', *Int J Numer Methods Eng*, **52**, 1253–1271.
- Liew KM, He XQ, Ng TY, Kitipornchai S, (2002a), 'Active control of FGM shells subjected to a temperature gradient via piezoelectric sensor/actuator patches', *Int J Numer Methods Eng*, **55**, 653–668.
- Liew KM, Lim HK, Tan MJ, He XQ, (2002b), 'Analysis of laminated composite beams and plates with piezoelectric patches using the element-free Galerkin method', *Comput Mech*, **29**, 486–497.
- Liew KM, Kitipornchai S, Zhang XZ, Lim CW, (2003a), 'Analysis of the thermal stress behavior of functionally graded hollow circular cylinders', *Int J Solids Struct*, **40**, 2355–2380.
- Liew KM, Yang J, Kitipornchai S, (2003b), 'The postbuckling of piezoelectric FGM plates subjected to thermo-electro-mechanical loading', *Int J Solids Struct*, **40**, 3869–3892.
- Liew KM, Yang J, Kitipornchai S, (2004), 'Thermal postbuckling of laminated plates comprising FGM with temperature-dependent material properties', *J Appl Mech ASME*, **71**, 839–850.

- Lim CW, He LH, (2001), 'Exact solution of a compositionally graded piezoelectric layer under uniform stretch, bending and twisting', *Int J Mech Sci*, **43**, 2479–2492.
- Lin CC, Chen LW, (1989), 'Large amplitude vibration of an initially imperfect moderately thick plate', *J Sound Vib*, **135**, 213–224.
- Liu FL, Liew KM, (1999a), 'Differential quadrature element method for static analysis of Reissner–Mindlin polar plates', *Int J Solids Struct*, **36**, 5101–5123.
- Liu FL, Liew KM, (1999b), 'Differential quadrature method: a new approach for free vibration analysis of polar Mindlin plates having discontinuities', *Comput Methods Appl Mech Eng*, **179**, 407–423.
- Mei C, (1978), 'Large amplitude vibration of plate with initial stresses', *J Sound Vib*, **60**, 461–464.
- Ng TY, He XQ, Liew KM, (2002), 'Finite element modeling of active control of functionally graded shells in frequency domain via piezoelectric sensors and actuators', *Comput Mech*, **28**, 1–9.
- Noda N, (1999), 'Thermal stresses in functionally graded materials', *J Therm Stresses*, **22**, 477–512.
- Ootao Y, Tanigawa Y, (2000), 'Three-dimensional transient piezothermoelasticity in functionally graded rectangular plate bonded to a piezoelectric plate', *Int J Solids Struct*, **37**, 4377–4401.
- Praveen GN, Reddy JN, (1998), 'Nonlinear transient thermoelastic analysis of functionally graded ceramic-metal plates', *Int J Solids Struct*, **35**, 4457–4476.
- Qian LF, Batra RC, Chen LM, (2004), 'Static and dynamic deformations of thick functionally graded elastic plates by using higher-order shear and normal deformable plate theory and meshless local Petrov–Galerkin method'. *Compos Part B: Eng*, **35**, 685–697.
- Raju KK, Hinton E, (1980), 'Nonlinear vibrations of thick plates using Mindlin plate theory', *Int J Numer Methods Eng*, **15**, 249–257.
- Reddy JN, (1984), 'A refined nonlinear theory of plates with transverse shear deformation', *Int J Solids Struct*, **20**, 881–896.
- Reddy JN, (2000), 'Analysis of functionally graded plates', *Int J Numer Methods Eng*, **47**, 663–684.
- Reddy JN, Cheng ZQ, (2001), 'Three-dimensional solutions of smart functionally graded plates', *J Appl Mech ASME*, **68**, 234–241.
- Reddy JN, Chin CD, (1998), 'Thermomechanical analysis of functionally graded cylinders and plates', *J Therm Stresses*, **21**, 593–626.
- Reddy JN, Wang CM, Kitipornchai S, (1999), 'Axisymmetric bending of functionally graded circular and annular plates', *Eur J Mech A/Solids*, **18**, 185–199.
- Roufaeil OL, Dawe DJ, (1982), 'Rayleigh–Ritz vibration analysis of rectangular Mindlin plates subjected to membrane stresses', *J Sound Vib*, **85**, 263–275.
- Sathyamoorthy M, (1987), 'Nonlinear vibration of plates: A review and survey of current developments', *Appl Mech Rev ASME*, **40**, 1553–1561.
- Sathyamoorthy M, (1997), *Nonlinear Analysis of Structures*, Boca Raton: CRC Press.
- Shen HS, (1995), 'Postbuckling analysis of moderately thick rectangular plates on two-parameter elastic foundations', *Eng Struct*, **17**, 523–529.
- Singh PN, Sundararajan V, Das YC, (1974), 'Large amplitude vibration of some moderately thick structural elements', *J Sound Vib*, **36**, 375–387.
- Teo TM, Liew KM, (1999), 'A differential quadrature procedure for three-dimensional buckling analysis of rectangular plates', *Int J Solids Struct*, **36**, 1149–1168.
- Vel SS, Batra RC, (2002), 'Exact solution for thermoelastic deformations of functionally graded thick rectangular plates', *AIAA*, **40**, 1421–1433.

- Vel SS, Batra RC, (2004), 'Three-dimensional exact solution for the vibration of functionally graded rectangular plates', *J Sound Vib*, **272**, 703–730.
- Wadee MA, (2000), 'Effects of periodic and localized imperfections on struts on nonlinear foundations and compression sandwich panels', *Int J Solids Struct*, **37**, 1191–1209.
- Wu XH, Chen C, Shen YP, Tian XG, (2002), 'A higher order theory for functionally graded piezoelectric shells', *Int J Solids Struct*, **39**, 5325–5344.
- Yamaki N, Otomo K, Chiba M, (1983), 'Nonlinear vibrations of a clamped rectangular plate with initial deflection and initial edge displacement – Part 2: Experiment'. *Thin-walled Struct*, **1**, 101–109.
- Yang J, Shen HS, (2001), 'Dynamic response of initially stressed functionally graded rectangular plates resting on elastic foundations', *Compos Struct*, **54**, 497–508.
- Yang J, Shen HS, (2002), 'Vibration characteristics and transient response of shear deformable functionally graded plates in thermal environment', *J Sound Vib*, **255**, 579–602.
- Yang J, Shen HS, (2003a), 'Nonlinear bending analysis of shear deformable functionally graded plates subjected to thermo-mechanical loads and under various boundary conditions', *Compos Part B: Eng*, **34**, 103–115.
- Yang J, Shen HS, (2003b), 'Nonlinear analysis of functionally graded plates under transverse and in-plane loads', *Int J Non-linear Mech*, **38**, 467–482.
- Yang J, Kitipornchai S, Liew KM, (2004a), 'Nonlinear analysis of thermo-electro-mechanical behavior of shear deformable FGM plates with piezoelectric actuators', *Int J Numer Methods Eng*, **59**, 1605–1632.
- Yang J, Liew KM, Kitipornchai S, (2004b), 'Dynamic stability of laminated FGM plates based on higher-order shear deformation theory', *Comput Mech*, **33**, 305–315.
- Yang TY, Han AD, (1983), 'Buckled plate vibrations and large amplitude vibrations using higher-order triangular elements', *AIAA*, **21**, 758–766.

## Nonlinear vibration and transient analysis of hybrid laminated plates

H-S S H E N and X-L H U A N G, Shanghai Jiao Tong University, People's Republic of China

### 12.1 Introduction

The design of missiles and launch vehicles, nuclear components and shipbuilding structures makes extensive use of composite laminated plates. The reliability of these structures depends directly on their component performance. The dynamic behavior of these structures is of keen interest when designing structural elements in the aerospace, aeronautical and other industries. In most conditions of severe environments, when the plate deflection-to-thickness ratio is greater than 0.4, the nonlinearity is very important and should be given consideration. Therefore, the nonlinear free and forced vibration of laminated plates subjected to different loads has given rise to a number of studies.

A comprehensive survey of nonlinear vibration analysis of plates using approximate analytical and finite element methods is presented by Sathyamoorthy (1987). An excellent review by Chia (1988) deals mostly with nonlinear vibrations of composite laminated thin plates. Owing to low transverse shear moduli relative to the in-plane Young's moduli, transverse shear deformations are even more pronounced in composite laminates. Moreover, the lay-up of loaded laminates may play a much more important role for thick plates than for thin ones. As a result, the analysis of moderately thick laminated plates requires the use of shear deformation plate theory. Among those, Bhimaraddi (1992a, 1993) studied the nonlinear free vibration of perfect and imperfect, shear deformable composite laminated plates using a regular perturbation technique and concluded that the formulation based on von Kármán-type nonlinearity is quite satisfactory. Note that only single-mode solution was formulated in his studies. Chen and Yang (1993) presented nonlinear free vibrations of imperfect, antisymmetric angle-ply laminated plates. In their analysis a multi-mode solution was formulated, and they found that the existence of geometric imperfections may result in a drastic change on the nonlinear vibration behavior.

Incorporating the multi-mode formulation, the large amplitude free vibration analysis of composite plate was carried out by Tenneti and Chandrashekara (1994) and Attia and El-Zafrany (1999) using the finite element method (FEM), and by Ribiro (2005) using FEM and employing a  $p$ -version, hierarchical finite element. Employing a reduced basis technique and a computational procedure, Noor *et al.* (1994) studied nonlinear vibrational response, and evaluating the first-order sensitivity coefficients of composite plates. In the area of nonlinear dynamic analysis of laminated plates, Reddy (1983) carried out the geometrically nonlinear transient analysis of laminated composite plates under going moderately large deformations using the finite element method and the effects of plate thickness, lamination scheme, boundary conditions and loading on the deflections and stresses were investigated. The large amplitude forced vibration of shear deformable composite laminates was presented by Lee and Ng (2001) using the finite element modal reduction method, and by Ganapathi *et al.* (2004) using FEM based on a higher-order shear deformation plate theory (HSDPT). In the above studies the boundary conditions are considered to be simply supported (SSSS) and/or clamped (CCCC). The nonlinear transient analysis for shear deformable laminated plates with combinations of simply supported (S), clamped (C) and free (F) boundary conditions, e.g. CSCS, CCFF and CCCF, was presented by Nath and Shukla (2001) using Chebyshev polynomials. The finite element equation was formulated based on the first-order shear deformation plate theory (FSDPT).

All the aforementioned studies were limited to plates of no initial stress state. Chen and Sun (1985) used FEM to obtain the nonlinear transient response of initially stressed composite plates. Bhimaraddi (1987, 1992b) used single mode approach and Galerkin technique to obtain the large amplitude, flexural vibrations and dynamics of laminated rectangular plates subject to in-plane forces. Liu and Huang (1996) calculated nonlinear free vibration frequencies of laminated composite plates subjected to temperature changes by using FEM based on the first-order shear deformation plate theory. Bhimaraddi and Chandrashekara (1993) investigated the nonlinear vibration and postbuckling response of antisymmetric angle-ply laminated plates subjected to a uniform temperature rise based on a parabolic shear deformation plate theory. Performing the Galerkin procedure and the Runge-Kutta method, the large amplitude vibration of an initially stressed, imperfect, cross-ply laminated plate was presented by Yang and Chen (1993) for uniform initial stress state, and by Chen *et al.* (2002) and Chien and Chen (2005) for non-uniform stress state. Furthermore, Huang and Zheng (2003) presented the nonlinear vibration and dynamic response of simply supported, shear deformable, antisymmetric angle-ply and symmetric cross-ply laminated plates with or without elastic foundations subjected to a transverse dynamic load combined with initial in-plane static loads. The effects of foundation stiffness,

in-plane boundary conditions and initial in-plane loads on the frequency ratios and dynamic responses were studied parametrically.

All the studies mentioned above investigated a plate laminated with only one material. Few studies have yet been undertaken on the nonlinear vibration of hybrid composite. The nonlinear free vibration of laminated hybrid composite thin plates was studied by Lee and Kim (1996). In this work, Lagrangian equations based on classical plate theory (CPT) was used, and the effects of laminate stacking sequences, aspect ratios and number of layers on the nonlinear vibration were investigated. Chen and Fung (2004) studied the large amplitude vibration of an initially stressed hybrid composite plate. An analytical approach using the Galerkin method and based on the first-order shear deformation plate theory was employed. The initial stress was taken to be a combination of pure bending stress and a uniform normal stress in the plane of the plate.

One of the recent advances in material and structural engineering is in the field of smart structures which incorporates adaptive materials. Oh *et al.* (2000) studied the nonlinear vibration and thermal postbuckling of piezolaminated plates with fully covered or partially distributed actuators subjected to thermal and electrical loads. In their analysis, nonlinear finite element equations based on layerwise displacement theory were formulated. Ishihara and Noda (2003a,b) investigated the buckling, nonlinear vibration and static large deflection of a piezothermoelastic laminate subjected to mechanical, thermal and electrical loads using the Galerkin method. In their analysis the formulations were based on the classical plate theory and the first-order shear deformation plate theory, respectively. Huang and Shen (2005) presented the nonlinear vibration and dynamic response of simply supported, shear deformable cross-ply laminated plates with piezoelectric actuators subjected to mechanical, electrical and thermal loads. They concluded that the deflection is increased, but bending moment is decreased with the increase of the plus voltage, whereas the minus control voltage decreases the deflection and increases the bending moment of the plate at the same temperature rise.

Functionally graded materials (FGMs) are microscopically inhomogeneous composites usually made from a mixture of metals and ceramics. Praveen and Reddy (1998) analyzed the nonlinear static and dynamic response of functionally graded ceramic–metal plates in a steady temperature field and subjected to dynamic transverse loads by FEM. Reddy (2000) developed both theoretical and finite element formulations for thick FGM plates according to the higher-order shear deformation plate theory, and studied the nonlinear dynamic response of FGM plates subjected to suddenly applied uniform pressure. Yang *et al.* (2003) presented a large amplitude vibration analysis of an initially stressed FGM plate with surface-bonded piezoelectric layers by using a semi-analytical method based on one-dimensional differential

quadrature and the Galerkin technique. Also, Chen (2005) studied the large amplitude vibration of an initially stressed FGM plate by using the Galerkin method and based on the first-order shear deformation plate theory. In his study, the initial stress was taken to be a combination of pure bending stress and an extensional stress in the plane of the plate. However, in the references cited above (Praveen and Reddy 1998, Reddy 2000, Yang *et al.* 2003, Chen 2005), the material properties were assumed to be independent of temperature. Since FGMs always serve in the high-temperature environments, the material properties of FGM plates must be temperature dependent and position dependent. Recently, Kitipornchai *et al.* (2004) studied nonlinear free vibration of imperfect FGM laminated plates with various boundary conditions and with temperature-dependent material properties. On the other hand, ceramics and the metals used in FGM do store different amounts of heat, and therefore the heat conduction usually occurs. This leads to a nonuniform distribution of temperature through the plate thickness, but it is not accounted for in the above study. Also, Huang and Shen (2004, 2006) provided nonlinear free and forced vibration analysis of shear deformable FGM plates with or without surface-bonded piezoelectric layers in thermal environments. In their studies, heat conduction and temperature-dependent material properties were both taken into account.

This chapter describes the nonlinear free and forced vibration of shear deformable hybrid laminated plates. The material properties are assumed to be temperature-dependent. The formulations, including thermo-piezoelectric effects, are based on Reddy's higher-order shear deformation plate theory (Reddy 1984a,b) and general von Kármán-type equations (Shen 1997). An improved perturbation technique is employed to determine the nonlinear frequencies and dynamic responses of the hybrid laminated plate. Extensive numerical results are presented showing the effects of varying the load and geometric parameters of the plate on the different response characteristics.

## 12.2 Governing equations

Consider a rectangular plate of length  $a$ , width  $b$  and constant thickness  $h$ , consisting of  $N$  plies. Each ply may be made of different materials. The plate is subjected to a transverse dynamic load  $q(X, Y, t)$  combined with initial in-plane static loads  $p_x$  in the  $X$ -direction and  $p_y$  in the  $Y$ -direction, and thermal and/or electrical loads. As usual, the coordinate system has its origin at the corner of the plate on the mid-plane. Let  $\bar{U}$ ,  $\bar{V}$  and  $\bar{W}$  be the plate displacements parallel to a right-hand set of axes  $(X, Y, Z)$ , where  $X$  is longitudinal and  $Z$  is perpendicular to the plate.  $\bar{\Psi}_x$  and  $\bar{\Psi}_y$  are the mid-plane rotations of the normal about the  $Y$  and  $X$  axes, respectively.

Reddy (1984a) developed a simple higher-order shear deformation plate theory, in which the transverse shear strains are assumed to be parabolically

distributed across the plate thickness. The theory is simple in the sense that it contains the same dependent unknowns ( $\bar{U}$ ,  $\bar{V}$ ,  $\bar{W}$ ,  $\bar{\Psi}_x$  and  $\bar{\Psi}_y$ ) as in the first-order shear deformation theory, and no shear correction factors are required. Based on Reddy's higher-order shear deformation theory with a von Kármán-type of kinematic nonlinearity (1984b) and including thermal effects, Shen (1997) derived a set of general von Kármán-type equations which can be expressed in terms of a transverse displacement  $\bar{W}$ , two rotations  $\bar{\Psi}_x$  and  $\bar{\Psi}_y$ , and stress function  $\bar{F}$  defined by  $\bar{N}_x = \bar{F}_{,yy}$ ,  $\bar{N}_y = \bar{F}_{,xx}$  and  $\bar{N}_{xy} = -\bar{F}_{,xy}$ , where a comma denotes partial differentiation with respect to the corresponding coordinates. In the present case, the motion equations of the hybrid laminated plate including thermal effects are

$$\begin{aligned} \tilde{L}_{11}(\bar{W}) - \tilde{L}_{12}(\bar{\Psi}_x) - \tilde{L}_{13}(\bar{\Psi}_y) + \tilde{L}_{14}(\bar{F}) - \tilde{L}_{15}(\bar{N}^T) - \tilde{L}_{16}(\bar{M}^T) \\ = \tilde{L}(\bar{W}, \bar{F}) + \bar{L}_{17}(\ddot{\bar{W}}) + I_8 \left( \frac{\partial \ddot{\bar{\Psi}}_x}{\partial X} + \frac{\partial \ddot{\bar{\Psi}}_y}{\partial Y} \right) + q \end{aligned} \quad 12.1$$

$$\tilde{L}_{21}(\bar{F}) + \tilde{L}_{22}(\bar{\Psi}_x) + \tilde{L}_{23}(\bar{\Psi}_y) - \tilde{L}_{24}(\bar{W}) - \tilde{L}_{25}(\bar{N}^T) = -\frac{1}{2} \tilde{L}(\bar{W}, \bar{W}) \quad 12.2$$

$$\begin{aligned} \tilde{L}_{31}(\bar{W}) + \tilde{L}_{32}(\bar{\Psi}_x) + \tilde{L}_{33}(\bar{\Psi}_y) + \tilde{L}_{34}(\bar{F}) - \tilde{L}_{35}(\bar{N}^T) - \tilde{L}_{36}(\bar{S}^T) \\ = I_9 \frac{\partial \ddot{\bar{\Psi}}}{\partial X} + I_{10} \ddot{\bar{\Psi}}_x \end{aligned} \quad 12.3$$

$$\begin{aligned} \tilde{L}_{41}(\bar{W}) + \tilde{L}_{42}(\bar{\Psi}_x) + \tilde{L}_{43}(\bar{\Psi}_y) + \tilde{L}_{44}(\bar{F}) - \tilde{L}_{45}(\bar{N}^T) - \tilde{L}_{46}(\bar{S}^T) \\ = I_9 \frac{\partial \ddot{\bar{\Psi}}}{\partial Y} + I_{10} \ddot{\bar{\Psi}}_y \end{aligned} \quad 12.4$$

in which

$$\begin{aligned} \tilde{L}_{17}(\cdot) &= \frac{4}{3h^2} \left( I_5 - \frac{I_4 I_2}{I_1} \right) \left( \frac{\partial^2}{\partial X^2} + \frac{\partial^2}{\partial Y^2} \right) - I_1 \\ I_8 &= \frac{I_2 \bar{I}_2}{I_1} - \bar{I}_3 - \frac{4}{3h^2} \bar{I}_5, \quad I_9 = \frac{4}{3h^2} \left( \bar{I}_5 - \frac{\bar{I}_2 I_4}{I_1} \right), \quad I_{10} = \frac{\bar{I}_2 \bar{I}_2}{I_1} - \bar{I}_3 \\ \bar{I}_2 &= I_2 - (4/3h^2) I_4, \quad \bar{I}_5 = I_5 - (4/3h^2) I_7, \\ \bar{I}_3 &= I_3 - (8/3h^2) I_5 + (16/9h^4) I_7 \\ (I_1, I_2, I_3, I_4, I_5, I_7) &= \sum_{k=1}^N \int_{h_{k-1}}^{h_k} \rho_k(1, Z, Z^2, Z^3, Z^4, Z^6) \, dZ \end{aligned} \quad 12.5$$

where  $\rho_k$  is the mass density of the  $k$ th ply, and all other linear operators  $\tilde{L}_{ij}()$  and the nonlinear operator  $\tilde{L}()$  in Eqs. (12.1)–(12.4) are defined as in the appendix of Shen (1997, 2006).

The forces and moments caused by elevated temperature are defined by

$$\begin{bmatrix} \bar{N}_x^T & \bar{M}_x^T & \bar{P}_x^T \\ \bar{N}_y^T & \bar{M}_y^T & \bar{P}_y^T \\ \bar{N}_{xy}^T & \bar{M}_{xy}^T & \bar{P}_{xy}^T \end{bmatrix} = \sum_{k=1}^N \int_{h_{k-1}}^{h_k} \begin{bmatrix} A_x \\ A_y \\ A_{xy} \end{bmatrix} (1, Z, Z^3) \Delta T(X, Y, Z) dZ \quad 12.6a$$

$$\begin{bmatrix} \bar{S}_x^T \\ \bar{S}_y^T \\ \bar{S}_{xy}^T \end{bmatrix} = \begin{bmatrix} \bar{M}_x^T \\ \bar{M}_y^T \\ \bar{M}_{xy}^T \end{bmatrix} - \frac{4}{3h^2} \begin{bmatrix} \bar{P}_x^T \\ \bar{P}_y^T \\ \bar{P}_{xy}^T \end{bmatrix} \quad 12.6b$$

in which  $\Delta T(X, Y, Z)$  is temperature rise, and

$$\begin{bmatrix} A_x \\ A_y \\ A_{xy} \end{bmatrix} = - \begin{bmatrix} \bar{Q}_{11} & \bar{Q}_{12} & \bar{Q}_{16} \\ \bar{Q}_{12} & \bar{Q}_{22} & \bar{Q}_{26} \\ \bar{Q}_{16} & \bar{Q}_{26} & \bar{Q}_{66} \end{bmatrix} \begin{bmatrix} c^2 & s^2 \\ s^2 & c^2 \\ 2cs & -2cs \end{bmatrix} \begin{bmatrix} \alpha_{11} \\ \alpha_{22} \end{bmatrix} \quad 12.7$$

where  $\alpha_{11}$  and  $\alpha_{22}$  are the thermal expansion coefficients measured in the longitudinal and transverse directions, respectively, and  $\bar{Q}_{ij}$  are the transformed elastic constants, defined by

$$\begin{bmatrix} \bar{Q}_{11} \\ \bar{Q}_{12} \\ \bar{Q}_{22} \\ \bar{Q}_{16} \\ \bar{Q}_{26} \\ \bar{Q}_{66} \end{bmatrix} = \begin{bmatrix} c^4 & 2c^2s^2 & s^4 & 4c^2s^2 \\ c^2s^2 & c^4 + s^4 & c^2s^2 & -4c^2s^2 \\ s^4 & 2c^2s^2 & c^4 & 4c^2s^2 \\ c^3s & cs^3 - c^3s & -cs^3 & -2cs(c^2 - s^2) \\ cs^3 & c^3s - cs^3 & -c^3s & 2cs(c^2 - s^2) \\ c^2s^2 & -2c^2s^2 & c^2s^2 & (c^2 - s^2)^2 \end{bmatrix} \begin{bmatrix} Q_{11} \\ Q_{12} \\ Q_{22} \\ Q_{26} \\ Q_{66} \end{bmatrix} \quad 12.8a$$

$$\begin{bmatrix} \bar{Q}_{44} \\ \bar{Q}_{45} \\ \bar{Q}_{55} \end{bmatrix} = \begin{bmatrix} c^2 & s^2 \\ -cs & cs \\ s^2 & c^2 \end{bmatrix} \begin{bmatrix} Q_{44} \\ Q_{45} \\ Q_{55} \end{bmatrix} \quad 12.8b$$

where

$$\begin{aligned} Q_{11} &= \frac{E_{11}}{(1 - \nu_{12}\nu_{21})}, \quad Q_{22} = \frac{E_{22}}{(1 - \nu_{12}\nu_{21})}, \quad Q_{12} = \frac{\nu_{21}E_{11}}{(1 - \nu_{12}\nu_{21})} \\ Q_{44} &= G_{23}, \quad Q_{55} = G_{13}, \quad Q_{66} = G_{12} \end{aligned} \quad 12.8c$$

$E_{11}$ ,  $E_{22}$ ,  $G_{12}$ ,  $G_{13}$ ,  $G_{23}$ ,  $\nu_{12}$  and  $\nu_{21}$  have their usual meanings, and

$$c = \cos \theta, \quad s = \sin \theta \quad 12.8d$$

where  $\theta$  is the lamination angle with respect to the plate  $X$ -axis.

All four edges are assumed to be simply supported. Depending upon the in-plane behavior at the edges, two cases, movable edges (referred to herein as SS1) and immovable edges (referred to herein as SS2), will be considered, which state that

$X = 0, a$ :

$$\bar{W} = \bar{\Psi}_y = 0 \quad 12.9a$$

$$\bar{M}_x = \bar{P}_x = 0 \quad 12.9b$$

$$\int_0^b \bar{N}_x dY + \sigma_x b h = 0 \quad (\text{SS1}) \quad 12.9c$$

$$\bar{U} = 0 \quad (\text{SS2}) \quad 12.9d$$

$Y = 0, b$ :

$$\bar{W} = \bar{\Psi}_x = 0 \quad 12.9e$$

$$\bar{M}_y = \bar{P}_y = 0 \quad 12.9f$$

$$\int_0^a \bar{N}_y dY + \sigma_y a h = 0 \quad (\text{SS1}) \quad 12.9g$$

$$\bar{V} = 0 \quad (\text{SS2}) \quad 12.9h$$

where  $\sigma_x$  and  $\sigma_y$  are the average axial compressive stresses,  $\bar{M}_x$  and  $\bar{M}_y$  are the bending moments per unit width and per unit length of the plate, and  $\bar{P}_x$  and  $\bar{P}_y$  are the higher-order moments as defined in Reddy (1984a,b).

The condition expressing the immovability condition,  $\bar{U} = 0$  (on  $X = 0, a$ ) and  $\bar{V} = 0$  (on  $Y = 0, b$ ), is fulfilled on the average sense as

$$\int_0^b \int_0^a \frac{\partial \bar{U}}{\partial X} dY dY = 0 \quad 12.10a$$

or

$$\int_0^b \int_0^a \left\{ \left[ \left( A_{11}^* \frac{\partial^2 \bar{F}}{\partial Y^2} + A_{12}^* \frac{\partial^2 \bar{F}}{\partial X^2} - A_{16}^* \frac{\partial^2 \bar{F}}{\partial X \partial Y} \right) + \left( B_{11}^* - \frac{4}{3h^2} E_{11}^* \right) \frac{\partial \bar{\Psi}_x}{\partial X} \right. \right. \\ \left. \left. + \left( B_{12}^* - \frac{4}{3h^2} E_{12}^* \right) \frac{\partial \bar{\Psi}_y}{\partial Y} + \left( B_{16}^* - \frac{4}{3h^2} E_{16}^* \right) \left( \frac{\partial \bar{\Psi}_x}{\partial Y} + \frac{\partial \bar{\Psi}_y}{\partial X} \right) \right] - \frac{1}{2} \left( \frac{\partial \bar{W}}{\partial X} \right)^2 \right. \\ \left. - \frac{4}{3h^2} \left( E_{11}^* \frac{\partial^2 \bar{W}}{\partial X^2} + E_{12}^* \frac{\partial^2 \bar{W}}{\partial Y^2} + 2E_{16}^* \frac{\partial^2 \bar{W}}{\partial X \partial Y} \right) \right] - \frac{1}{2} \left( \frac{\partial \bar{W}}{\partial X} \right)^2 \\ \left. - \frac{\partial \bar{W}}{\partial X} \frac{\partial \bar{W}^*}{\partial X} - (A_{11}^* \bar{N}_x^T + A_{12}^* \bar{N}_y^T + A_{16}^* \bar{N}_{xy}^T) \right\} dX dY = 0 \quad 12.10b$$

and

$$\int_0^a \int_0^b \frac{\partial \bar{V}}{\partial Y} dY dX = 0 \quad 12.10c$$

or

$$\int_0^a \int_0^b \left\{ \left[ \left( A_{22}^* \frac{\partial^2 \bar{F}}{\partial X^2} + A_{12}^* \frac{\partial^2 \bar{F}}{\partial Y^2} - A_{26}^* \frac{\partial^2 \bar{F}}{\partial X \partial Y} \right) + \left( B_{21}^* - \frac{4}{3h^2} E_{21}^* \right) \frac{\partial \bar{\Psi}_x}{\partial X} \right. \right. \\ \left. \left. + \left( B_{22}^* - \frac{4}{3h^2} E_{22}^* \right) \frac{\partial \bar{\Psi}_y}{\partial Y} \right] + \left( B_{26}^* - \frac{4}{3h^2} E_{26}^* \right) \left( \frac{\partial \bar{\Psi}_x}{\partial Y} + \frac{\partial \bar{\Psi}_y}{\partial X} \right) \right. \\ \left. - \frac{4}{3h^2} \left( E_{21}^* \frac{\partial^2 \bar{W}}{\partial X^2} + E_{22}^* \frac{\partial^2 \bar{W}}{\partial Y^2} + 2E_{26}^* \frac{\partial^2 \bar{W}}{\partial X \partial Y} \right) \right] - \frac{1}{2} \left( \frac{\partial \bar{W}}{\partial Y} \right)^2 \\ \left. - \frac{\partial \bar{W}}{\partial Y} \frac{\partial \bar{W}^*}{\partial Y} - (A_{12}^* \bar{N}_x^T + A_{22}^* \bar{N}_y^T + A_{26}^* \bar{N}_{xy}^T) \right\} dY dX = 0 \quad 12.10d$$

The initial conditions are assumed as:

$$\bar{W}|_{t=0} = \frac{\partial \bar{W}}{\partial t}|_{t=0} = 0 \quad 12.11a$$

$$\bar{\Psi}_x|_{t=0} = \frac{\partial \bar{\Psi}_x}{\partial t}|_{t=0} = 0 \quad 12.11b$$

$$\bar{\Psi}_y|_{t=0} = \frac{\partial \bar{\Psi}_y}{\partial t}|_{t=0} = 0 \quad 12.11c$$

In the above equations and what follows, the reduced stiffness matrices  $[A_{ij}^*]$ ,  $[B_{ij}^*]$ ,  $[D_{ij}^*]$ ,  $[E_{ij}^*]$ ,  $[F_{ij}^*]$  and  $[H_{ij}^*]$  ( $i, j = 1, 2, 6$ ) are functions of temperature, determined through relationships (Shen 1997)

$$\begin{aligned}\mathbf{A}^* &= \mathbf{A}^{-1}, \mathbf{B}^* = -\mathbf{A}^{-1}\mathbf{B}, \mathbf{D}^* = \mathbf{D} - \mathbf{B}\mathbf{A}^{-1}\mathbf{B}, \mathbf{E}^* = -\mathbf{A}^{-1}\mathbf{E}, \\ \mathbf{F}^* &= \mathbf{F} - \mathbf{E}\mathbf{A}^{-1}\mathbf{B}, \mathbf{H}^* = \mathbf{H} - \mathbf{E}\mathbf{A}^{-1}\mathbf{E}\end{aligned}\quad 12.12$$

where  $A_{ij}$ ,  $B_{ij}$ , etc., are the plate stiffnesses, defined in the standard way, i.e.

$$\begin{aligned}(A_{ij}, B_{ij}, D_{ij}, E_{ij}, F_{ij}, H_{ij}) \\ = \sum_{k=1}^N \int_{h_{k-1}}^{h_k} (\bar{\mathcal{Q}}_{ij})_k(1, Z, Z^2, Z^3, Z^4, Z^6) dZ \quad (i, j = 1, 2, 6)\end{aligned}\quad 12.13a$$

$$(A_{ij}, D_{ij}, F_{ij}) = \sum_{k=1}^N \int_{h_{k-1}}^{h_k} (\bar{\mathcal{Q}}_{ij})_k(1, Z^2, Z^4) dZ \quad (i, j = 4, 5) \quad 12.13b$$

## 12.3 Solution methodology

Perturbation technique is a powerful tool for solving nonlinear problems, e.g. nonlinear bending, postbuckling and nonlinear vibration of shear deformable laminated plates (Shen 2001, 2002, 2004, Huang and Shen 2004, Huang *et al.* 2004). Before proceeding, it is convenient to define the following dimensionless quantities:

$$\begin{aligned}x &= \pi X/a, \quad y = \pi Y/b, \quad \beta = a/b, \\ (W, W^*) &= (\bar{W}, \bar{W}^*)/[D_{11}^* D_{22}^* A_{11}^* A_{22}^*]^{1/4} \\ F &= \bar{F}/[D_{11}^* D_{22}^*]^{1/2}, \quad (\Psi_x, \Psi_y) = (\bar{\Psi}_x, \bar{\Psi}_y) a / \pi [D_{11}^* D_{22}^* A_{11}^* A_{22}^*]^{1/4} \\ \gamma_{14} &= [D_{22}^* / D_{11}^*]^{1/2}, \quad \gamma_{24} = [A_{11}^* / A_{22}^*]^{1/2}, \quad \gamma_5 = -A_{12}^* / A_{22}^* \\ (M_x, M_y, P_x, P_x) &= \frac{(\bar{M}_x, \bar{M}_y, 4\bar{P}_x/3t^2, 4\bar{P}_y/3t^2)a^2}{\pi^2 D_{11}^* [D_{11}^* D_{22}^* A_{11}^* A_{22}^*]^{1/4}} \\ (\gamma_{T1}, \gamma_{T2}) &= \frac{(A_x^T, A_y^T)a^2}{\pi^2 [D_{11}^* D_{22}^*]^{1/2}}, \quad (\lambda_x, \lambda_y) = \frac{(\sigma_x b^2, \sigma_y a^2)h}{\pi^2 [D_{11}^* D_{22}^*]^{1/2}} \\ (\gamma_{T3}, \gamma_{T4}, \gamma_{T6}, \gamma_{T7}) &= \frac{(D_x^T, D_y^T, F_x^T, F_y^T)a^2}{\pi^2 h D_{11}^*} \\ \gamma_{170} &= \frac{-I_1 E_0 a^2}{\pi^2 \rho_0 D_{11}^*}, \quad \gamma_{171} = (4/3h^2) \frac{E_0 (I_5 I_1 - I_4 I_2)}{\rho_0 I_1 D_{11}^*} \\ (\gamma_{80}, \gamma_{90}, \gamma_{10}) &= (I_8, I_9, I_{10})(E_0 / \rho_0 D_{11}^*), \\ \omega_L &= \bar{\omega}_L (a/\pi) \sqrt{\rho_0/E_0} \\ \tau &= (\pi t/a) \sqrt{E_0/\rho_0}, \quad \lambda_q = \frac{qa^4}{\pi^4 D_{11}^* [D_{11}^* D_{22}^* A_{11}^* A_{22}^*]^{1/4}}\end{aligned}\quad 12.14$$

where  $E_0$  and  $\rho_0$  are the reference values of  $E_{11}$  and  $\rho$  in the environmental condition, and let

$$\begin{bmatrix} A_x^T & D_x^T & F_x^T \\ A_y^T & D_y^T & F_y^T \end{bmatrix} = -\sum_{k=1}^N \int_{h_{k-1}}^{h_k} \begin{bmatrix} A_x \\ A_y \end{bmatrix} (1, Z, Z^3) dZ \quad 12.15$$

The nonlinear Eqs. (12.1)–(12.4) may then be written in dimensionless form as

$$\begin{aligned} L_{11}(W) - L_{12}(\Psi_x) - L_{13}(\Psi_y) + \gamma_{14}L_{14}(F) - L_{16}(M^T) \\ = \gamma_{14}\beta^2 L(W, F) + L_{17}(\ddot{W}) + \gamma_{80} \left( \frac{\partial \ddot{\Psi}_x}{\partial x} + \beta \frac{\partial \ddot{\Psi}_y}{\partial y} \right) + \lambda_q \end{aligned} \quad 12.16$$

$$\begin{aligned} L_{21}(F) + \gamma_{24}L_{22}(\Psi_x) + \gamma_{24}L_{23}(\Psi_y) - \gamma_{24}L_{24}(W) \\ = -\frac{1}{2}\gamma_{24}\beta^2 L(W, W) \end{aligned} \quad 12.17$$

$$\begin{aligned} L_{31}(W) + L_{32}(\Psi_x) - L_{33}(\Psi_y) + \gamma_{14}L_{34}(F) - L_{36}(S^T) \\ = \gamma_{90} \frac{\partial \ddot{W}}{\partial x} + \gamma_{10} \ddot{\Psi}_x \end{aligned} \quad 12.18$$

$$\begin{aligned} L_{41}(W) - L_{42}(\Psi_x) + L_{43}(\Psi_y) + \gamma_{14}L_{44}(F) - L_{46}(S^T) \\ = \gamma_{90} \beta \frac{\partial \ddot{W}}{\partial y} + \gamma_{10} \ddot{\Psi}_y \end{aligned} \quad 12.19$$

where

$$\begin{aligned} L_{11}() &= \gamma_{110} \frac{\partial^4}{\partial x^4} + \gamma_{111} \beta \frac{\partial^4}{\partial x^3 \partial y} + 2\gamma_{112} \beta^2 \frac{\partial^4}{\partial x^2 \partial y^2} \\ &\quad + \gamma_{113} \beta^3 \frac{\partial^4}{\partial x \partial y^3} + \gamma_{114} \beta^4 \frac{\partial^4}{\partial y^4} \\ L_{12}() &= \gamma_{120} \frac{\partial^3}{\partial x^3} + \gamma_{121} \beta \frac{\partial^3}{\partial x^2 \partial y} + \gamma_{122} \beta^2 \frac{\partial^3}{\partial x \partial y^2} + \gamma_{123} \beta^3 \frac{\partial^3}{\partial y^3} \\ L_{13}() &= \gamma_{130} \frac{\partial^3}{\partial x^3} + \gamma_{131} \beta \frac{\partial^3}{\partial x^2 \partial y} + \gamma_{132} \beta^2 \frac{\partial^3}{\partial x \partial y^2} + \gamma_{133} \beta^3 \frac{\partial^3}{\partial y^3} \\ L_{14}() &= \gamma_{140} \frac{\partial^4}{\partial x^4} + \gamma_{141} \beta \frac{\partial^4}{\partial x^3 \partial y} + \gamma_{142} \beta^2 \frac{\partial^4}{\partial x^2 \partial y^2} \\ &\quad + \gamma_{143} \beta^3 \frac{\partial^4}{\partial x \partial y^3} + \gamma_{144} \beta^4 \frac{\partial^4}{\partial y^4} \end{aligned}$$

$$L_{16}(M^T) = \frac{\partial^2}{\partial x^2}(M_x^T) + 2\beta \frac{\partial^2}{\partial x \partial y}(M_{xy}^T) + \beta^2 \frac{\partial^2}{\partial y^2}(M_y^T)$$

$$L_{17}(\cdot) = \gamma_{170} + \gamma_{171} \frac{\partial^2}{\partial x^2} + \gamma_{171} \beta^2 \frac{\partial^2}{\partial y^2}$$

$$L_{21}(\cdot) = \frac{\partial^4}{\partial x^4} + \gamma_{211} \beta \frac{\partial^4}{\partial x^3 \partial y} + 2\gamma_{212} \beta^2 \frac{\partial^4}{\partial x^2 \partial y^2}$$

$$+ \gamma_{213} \beta^3 \frac{\partial^4}{\partial x \partial y^3} + \gamma_{214} \beta^4 \frac{\partial^4}{\partial y^4}$$

$$L_{22}(\cdot) = L_{34}(\cdot) = \gamma_{220} \frac{\partial^3}{\partial x^3} + \gamma_{221} \beta \frac{\partial^3}{\partial x^2 \partial y}$$

$$+ \gamma_{222} \beta^2 \frac{\partial^3}{\partial x \partial y^2} + \gamma_{223} \beta^3 \frac{\partial^3}{\partial y^3}$$

$$L_{23}(\cdot) = L_{44}(\cdot) = \gamma_{230} \frac{\partial^3}{\partial x^3} + \gamma_{231} \beta \frac{\partial^3}{\partial x^2 \partial y}$$

$$+ \gamma_{232} \beta^2 \frac{\partial^3}{\partial x \partial y^2} + \gamma_{233} \beta^3 \frac{\partial^3}{\partial y^3}$$

$$L_{24}(\cdot) = \gamma_{240} \frac{\partial^4}{\partial x^4} + \gamma_{241} \beta \frac{\partial^4}{\partial x^3 \partial y} + \gamma_{242} \beta^2 \frac{\partial^4}{\partial x^2 \partial y^2}$$

$$+ \gamma_{243} \beta^3 \frac{\partial^4}{\partial x \partial y^3} + \gamma_{244} \beta^4 \frac{\partial^4}{\partial y^4}$$

$$L_{31}(\cdot) = \gamma_{31} \frac{\partial}{\partial x} + \gamma_{32} \beta \frac{\partial}{\partial y} + \gamma_{310} \frac{\partial^3}{\partial x^3} + \gamma_{311} \beta \frac{\partial^3}{\partial x^2 \partial y}$$

$$+ \gamma_{312} \beta^2 \frac{\partial^3}{\partial x \partial y^2} + \gamma_{313} \beta^3 \frac{\partial^3}{\partial y^3}$$

$$L_{32}(\cdot) = \gamma_{31} - \gamma_{320} \frac{\partial^2}{\partial x^2} - \gamma_{321} \beta \frac{\partial^2}{\partial x \partial y} - \gamma_{323} \beta^2 \frac{\partial^2}{\partial y^2}$$

$$L_{33}(\cdot) = \gamma_{32} - \gamma_{330} \frac{\partial^2}{\partial x^2} - \gamma_{331} \beta \frac{\partial^2}{\partial x \partial y} - \gamma_{332} \beta^2 \frac{\partial^2}{\partial y^2}$$

$$L_{34}(\cdot) = L_{22}(\cdot)$$

$$L_{36}(S^T) = \frac{\partial}{\partial x}(S_x^T) + \beta \frac{\partial}{\partial y}(S_{xy}^T)$$

$$L_{41}(\cdot) = \gamma_{41} \frac{\partial}{\partial x} + \gamma_{42} \beta \frac{\partial}{\partial y} + \gamma_{410} \frac{\partial^3}{\partial x^3} + \gamma_{411} \beta \frac{\partial^3}{\partial x^2 \partial y}$$

$$+ \gamma_{412} \beta^2 \frac{\partial^3}{\partial x \partial y^2} + \gamma_{413} \beta^3 \frac{\partial^3}{\partial y^3}$$

$$L_{42}(\cdot) = L_{33}(\cdot)$$

$$L_{43}(\cdot) = \gamma_{41} - \gamma_{430} \frac{\partial^2}{\partial x^2} - \gamma_{431} \beta \frac{\partial^2}{\partial x \partial y} - \gamma_{432} \beta^2 \frac{\partial^2}{\partial y^2}$$

$$L_{44}(\cdot) = L_{23}(\cdot)$$

$$L_{46}(S^T) = \frac{\partial}{\partial x}(S_{xy}^T) + \beta \frac{\partial}{\partial y}(S_y^T)$$

$$L(\cdot) = \frac{\partial^2}{\partial x^2} \frac{\partial^2}{\partial y^2} - 2 \frac{\partial^2}{\partial x \partial y} \frac{\partial^2}{\partial x \partial y} + \frac{\partial^2}{\partial y^2} \frac{\partial^2}{\partial x^2} \quad 12.20$$

The boundary conditions expressed by Eq. (12.9) become

$x = 0, \pi$ :

$$W = \Psi_y = 0 \quad 12.21a$$

$$M_x = P_x = 0 \quad 12.21b$$

$$\frac{1}{\pi} \int_0^\pi \beta^2 \frac{\partial^2 F}{\partial y^2} dy + \lambda_x \beta^2 = 0 \quad (\text{SS1}) \quad 12.21c$$

$$\delta_x = 0 \quad (\text{SS2}) \quad 12.21d$$

$y = 0, \pi$ :

$$W = \Psi_x = 0 \quad 12.21e$$

$$M_y = P_y = 0 \quad 12.21f$$

$$\frac{1}{\pi} \int_0^\pi \frac{\partial^2 F}{\partial x^2} dx + \lambda_y = 0 \quad (\text{SS1}) \quad 12.21g$$

$$\delta_y = 0 \quad (\text{SS2}) \quad 12.21h$$

in which

$$\begin{aligned} \delta_x = & -\frac{1}{4\pi^2 \beta^2 \gamma_{24}} \int_0^\pi \int_0^\pi \left\{ \left[ \gamma_{24}^2 \beta^2 \frac{\partial^2 F}{\partial y^2} - \gamma_5 \frac{\partial^2 F}{\partial x^2} \right. \right. \\ & + \gamma_{24} \left( \gamma_{511} \frac{\partial \Psi_x}{\partial x} + \gamma_{233} \beta \frac{\partial \Psi_y}{\partial y} \right) + \gamma_{24} \gamma_{223} \left( \beta \frac{\partial \Psi_x}{\partial y} + \frac{\partial \Psi_y}{\partial x} \right) \\ & \left. \left. - \gamma_{24} \left( \gamma_{611} \frac{\partial^2 W}{\partial x^2} + \gamma_{244} \beta^2 \frac{\partial^2 W}{\partial y^2} + 2\gamma_{516} \beta \frac{\partial^2 W}{\partial x \partial y} \right) \right] \right. \\ & \left. - \frac{1}{2} \gamma_{24} \left( \frac{\partial W}{\partial x} \right)^2 - \gamma_{24} \frac{\partial W}{\partial x} \frac{\partial W^*}{\partial x} + (\gamma_{24}^2 \gamma_{T1} - \gamma_5 \gamma_{T2}) \Delta T \right\} dx dy \end{aligned} \quad 12.22a$$

$$\begin{aligned}
\delta_y = & -\frac{1}{4\pi^2\beta^2\gamma_{24}} \int_0^\pi \int_0^\pi \left\{ \left[ \frac{\partial^2 F}{\partial x^2} - \gamma_5 \beta^2 \frac{\partial^2 F}{\partial y^2} \right. \right. \\
& + \gamma_{24} \left( \gamma_{220} \frac{\partial \Psi_x}{\partial x} + \gamma_{522} \beta \frac{\partial \Psi_y}{\partial y} \right) + \gamma_{24} \gamma_{230} \left( \beta \frac{\partial \Psi_x}{\partial y} + \frac{\partial \Psi_y}{\partial x} \right) \\
& \left. \left. - \gamma_{24} \left( \gamma_{240} \frac{\partial^2 W}{\partial x^2} + \gamma_{622} \beta^2 \frac{\partial^2 W}{\partial y^2} + 2\gamma_{526} \beta \frac{\partial^2 W}{\partial x \partial y} \right) \right] \right. \\
& \left. - \frac{1}{2} \gamma_{24} \beta^2 \left( \frac{\partial W}{\partial y} \right)^2 - \gamma_{24} \beta^2 \frac{\partial W}{\partial y} \frac{\partial W^*}{\partial y} + (\gamma_{T2} - \gamma_5 \gamma_{T1}) \Delta T \right\} dy dx
\end{aligned} \tag{12.22b}$$

in Eq. (12.21) and what follows,  $\gamma_{ijk}$  are also defined as in the appendix of Shen (1997, 2006).

The initial conditions of Eqs. (12.11a)–(12.11c) become

$$W|_{\tau=0} = \frac{\partial W}{\partial \tau}|_{\tau=0} = 0 \tag{12.23a}$$

$$\Psi_x|_{\tau=0} = \frac{\partial \Psi_x}{\partial \tau}|_{\tau=0} = 0 \tag{12.23b}$$

$$\bar{\Psi}_y|_{\tau=0} = \frac{\partial \bar{\Psi}_y}{\partial \tau}|_{\tau=0} = 0 \tag{12.23c}$$

Now one is in a position to solve Eqs. (12.16)–(12.19) with boundary conditions (12.21). We assume that the solutions can be expressed as

$$\begin{aligned}
W(x, y, \tau) &= W^*(x, y) + \tilde{W}(x, y, \tau) \\
\Psi_x(x, y, \tau) &= \Psi_x^*(x, y) + \tilde{\Psi}_x(x, y, \tau) \\
\Psi_y(x, y, \tau) &= \Psi_y^*(x, y) + \tilde{\Psi}_y(x, y, \tau) \\
F(x, y, \tau) &= F^*(x, y) + \tilde{F}(x, y, \tau)
\end{aligned} \tag{12.24}$$

where  $W^*(x, y)$  is an initial deflection due to initial thermal bending moment, and  $\tilde{W}(x, y, \tau)$  is an additional deflection.  $\Psi_x^*(x, y)$ ,  $\Psi_y^*(x, y)$  and  $F^*(x, y)$  are the mid-plane rotations and stress function corresponding to  $W^*(x, y)$ .  $\tilde{\Psi}_x(x, y, \tau)$ ,  $\tilde{\Psi}_y(x, y, \tau)$  and  $\tilde{F}(x, y, \tau)$  are defined analogously to  $\Psi_x^*(x, y)$ ,  $\Psi_y^*(x, y)$  and  $F^*(x, y)$ , but is for  $\tilde{W}(x, y, \tau)$ .

Owing to the bending–stretching coupling effect in the unsymmetric laminated plate, the thermal preload will bring about deflections and bending curvatures which have significant influences on the plate vibration characteristics. To account for this effect, the pre-vibration solutions

$W^*(x, y)$ ,  $\Psi_x^*(x, y)$ ,  $\Psi_y^*(x, y)$  and  $F^*(x, y)$  are sought at the first step from the following nonlinear equations

$$\begin{aligned} L_{11}(W^*) - L_{12}(\Psi_x^*) - L_{13}(\Psi_y^*) + \gamma_{14} L_{14}(F^*) - L_{16}(M^T) \\ + \gamma_{14} \beta^2 \left( P_x^T \frac{\partial^2 W^*}{\partial x^2} + P_y^T \frac{\partial^2 W^*}{\partial y^2} \right) = \gamma_{14} \beta^2 L(W^*, F^*) \end{aligned} \quad 12.25$$

$$\begin{aligned} L_{21}(F^*) + \gamma_{24} L_{22}(\Psi_x^*) + \gamma_{24} L_{23}(\Psi_y^*) - \gamma_{24} L_{24}(W^*) \\ = -\frac{1}{2} \gamma_{24} \beta^2 L(W^*, W^*) \end{aligned} \quad 12.26$$

$$\begin{aligned} L_{31}(W^*) + L_{32}(\Psi_x^*) - L_{33}(\Psi_y^*) + \gamma_{14} L_{34}(F^*) - L_{36}(S^T) = 0 \\ 12.27 \end{aligned}$$

$$\begin{aligned} L_{41}(W^*) - L_{42}(\Psi_x^*) + L_{43}(\Psi_y^*) + \gamma_{14} L_{44}(F^*) - L_{46}(S^T) = 0 \\ 12.28 \end{aligned}$$

In Eq. (12.25),  $P_x^T$  and  $P_y^T$  are edge compressive stresses induced by temperature change with edge restraints.

Then  $\tilde{W}(x, y, \tau)$ ,  $\tilde{\Psi}_x(x, y, \tau)$ ,  $\tilde{\Psi}_y(x, y, \tau)$  and  $\tilde{F}(x, y, \tau)$  satisfy the nonlinear dynamic equations

$$\begin{aligned} L_{11}(\tilde{W}) - L_{12}(\tilde{\Psi}_x) - L_{13}(\tilde{\Psi}_y) + \gamma_{14} L_{14}(\tilde{F}) \\ = \gamma_{14} \beta^2 L(\tilde{W} + W^*, \tilde{F}) + L_{17}(\ddot{\tilde{W}}) + \gamma_{80} \left( \frac{\partial \ddot{\tilde{\Psi}}_x}{\partial x} + \beta \frac{\partial \ddot{\tilde{\Psi}}_y}{\partial y} \right) + \lambda_q \end{aligned} \quad 12.29$$

$$\begin{aligned} L_{21}(\tilde{F}) + \gamma_{24} L_{22}(\tilde{\Psi}_x) + \gamma_{24} L_{23}(\tilde{\Psi}_y) - \gamma_{24} L_{24}(\tilde{W}) \\ = -\frac{1}{2} \gamma_{24} \beta^2 L(\tilde{W} + 2W^*, \tilde{W}) \end{aligned} \quad 12.30$$

$$L_{31}(\tilde{W}) + L_{32}(\tilde{\Psi}_x) - L_{33}(\tilde{\Psi}_y) + \gamma_{14} L_{34}(\tilde{F}) = \gamma_{90} \frac{\partial \ddot{\tilde{W}}}{\partial x} + \gamma_{10} \ddot{\tilde{\Psi}}_x \quad 12.31$$

$$L_{41}(\tilde{W}) - L_{42}(\tilde{\Psi}_x) - L_{43}(\tilde{\Psi}_y) + \gamma_{14} L_{44}(\tilde{F}) = \gamma_{90} \beta \frac{\partial \ddot{\tilde{W}}}{\partial y} + \gamma_{10} \ddot{\tilde{\Psi}}_y \quad 12.32$$

A perturbation technique is now used to solve Eqs. (12.29)–(12.32). The essence of this procedure, in the present case, is to assume that

$$\tilde{W}(x, y, \tilde{\tau}, \varepsilon) = \sum_{j=1} \varepsilon^j w_j(x, y, \tilde{\tau})$$

$$\tilde{F}(x, y, \tilde{\tau}, \varepsilon) = \sum_{j=0} \varepsilon^j f_j(x, y, \tilde{\tau})$$

$$\begin{aligned}\tilde{\Psi}_x(x, y, \tilde{\tau}, \varepsilon) &= \sum_{j=1} \varepsilon^j \psi_{xj}(x, y, \tilde{\tau}) \\ \tilde{\Psi}_y(x, y, \tilde{\tau}, \varepsilon) &= \sum_{j=1} \varepsilon^j \psi_{yj}(x, y, \tilde{\tau}) \\ \lambda_q(x, y, \tilde{\tau}, \varepsilon) &= \sum_{j=1} \varepsilon^j \lambda_j(x, y, \tilde{\tau})\end{aligned}\quad 12.33$$

where  $\varepsilon$  is a small perturbation parameter. Here we introduce an important parameter  $\tilde{\tau} = \varepsilon\tau$  to improve perturbation procedure for solving nonlinear dynamic problems.

Substituting Eq. (12.33) into Eqs. (12.29)–(12.32) and collecting the terms of the same order of  $\varepsilon$ , we obtain a set of perturbation equations which can be written, for example, as

$O(\varepsilon^0)$ :

$$L_{14}(f_0) = 0 \quad 12.34a$$

$$L_{21}(f_0) = 0 \quad 12.34b$$

$$L_{34}(f_0) = 0 \quad 12.34c$$

$$L_{44}(f_0) = 0 \quad 12.34d$$

$O(\varepsilon^1)$ :

$$\begin{aligned}L_{11}(w_1) - L_{12}(\psi_{x1}) - L_{13}(\psi_{y1}) + \gamma_{14}L_{14}(f_1) \\ = \gamma_{14}\beta^2 L(w_1 + W^*, f_0) + \lambda_1\end{aligned}\quad 12.35a$$

$$L_{21}(f_1) + \gamma_{24}L_{22}(\psi_{x1}) + \gamma_{24}L_{23}(\psi_{y1}) - \gamma_{24}L_{24}(w_1) = 0 \quad 12.35b$$

$$L_{31}(w_1) + L_{32}(\psi_{x1}) - L_{33}(\psi_{y1}) + \gamma_{14}L_{34}(f_1) = 0 \quad 12.35c$$

$$L_{41}(w_1) - L_{42}(\psi_{x1}) + L_{43}(\psi_{y1}) + \gamma_{14}L_{44}(f_1) = 0 \quad 12.35d$$

$O(\varepsilon^2)$ :

$$\begin{aligned}L_{11}(w_2) - L_{12}(\psi_{x2}) - L_{13}(\psi_{y2}) + \gamma_{14}L_{14}(f_2) \\ = \gamma_{14}\beta^2 [L(w_2, f_0) + L(w_1 + W^*, f_1)] + \lambda_2\end{aligned}\quad 12.36a$$

$$\begin{aligned}L_{21}(f_2) + \gamma_{24}L_{22}(\psi_{x2}) + \gamma_{24}L_{23}(\psi_{y2}) - \gamma_{24}L_{24}(w_2) \\ = -\frac{1}{2}\gamma_{24}\beta^2 L(w_1 + 2W^*, w_1)\end{aligned}\quad 12.36b$$

$$L_{31}(w_2) + L_{32}(\psi_{x2}) - L_{33}(\psi_{y2}) + \gamma_{14}L_{34}(f_2) = 0 \quad 12.36c$$

$$L_{41}(w_2) - L_{42}(\psi_{x2}) + L_{43}(\psi_{y2}) + \gamma_{14}L_{44}(f_2) = 0 \quad 12.36d$$

$O(\varepsilon^3)$ :

$$\begin{aligned}L_{11}(w_3) - L_{12}(\psi_{x3}) - L_{13}(\psi_{y3}) + \gamma_{14}L_{14}(f_3) \\ = \gamma_{14}\beta^2 [L(w_3, f_0) + L(w_2, f_1) + L(w_1 + W^*, f_2)] + \lambda_3\end{aligned}\quad 12.37a$$

$$\begin{aligned} L_{21}(f_3) + \gamma_{24} L_{22}(\psi_{x3}) + \gamma_{24} L_{23}(\psi_{y3}) + \gamma_{14} L_{24}(w_3) \\ = -\frac{1}{2} \gamma_{24} \beta^2 L(w_1 + 2W^*, w_2) \end{aligned} \quad 12.37b$$

$$\begin{aligned} L_{31}(w_3) + L_{32}(\psi_{x3}) - L_{33}(\psi_{y3}) + \gamma_{14} L_{34}(f_3) \\ = \gamma_{90} \frac{\partial \ddot{w}_1}{\partial x} + \gamma_{10} \ddot{\psi}_{x1} \end{aligned} \quad 12.37c$$

$$\begin{aligned} L_{41}(w_3) - L_{42}(\psi_{x3}) + L_{43}(\psi_{y3}) + \gamma_{14} L_{44}(f_3) \\ = \gamma_{90} \beta \frac{\partial \ddot{w}_1}{\partial y} + \gamma_{10} \ddot{\psi}_{y1} \end{aligned} \quad 12.37d$$

To solve these perturbation equations of each order, the amplitudes of the terms  $w_j(x, y)$ ,  $f_j(x, y)$ ,  $\psi_{xj}(x, y)$  and  $\psi_{yj}(x, y)$  can be determined step by step, and the asymptotic solutions can then be obtained, as shown in the next section.

## 12.4 Nonlinear vibration and dynamic response of initially stressed antisymmetric angle-ply laminated plates

First, we consider the nonlinear free and forced vibration of initially stressed, shear deformable, antisymmetric angle-ply laminated plates from which results for symmetric cross-ply laminated plates are obtained as a limiting case. In such a case, the following plate stiffnesses are identically zero, i.e.

$$\begin{aligned} A_{16} = A_{26} = D_{16} = D_{26} = F_{16} = F_{26} = H_{16} = H_{26} = 0 \\ A_{45} = D_{45} = F_{45} = 0 \end{aligned} \quad 12.38a$$

$$\begin{aligned} B_{11} = B_{22} = B_{12} = B_{66} = 0, E_{11} = E_{22} = E_{12} = E_{66} = 0 \\ (\text{for antisymmetric angle-ply laminates}) \end{aligned} \quad 12.38b$$

$$B_{ij} = E_{ij} = 0 \quad (\text{for symmetric cross-ply laminates}) \quad 12.38c$$

Since no thermal loadings are involved in this section, the solutions of Eqs. (12.16)–(12.19) can be expressed as

$$\begin{aligned} W(x, y, \tau) &= \varepsilon [w_1(\tau) + g_1 \ddot{w}_1(\tau)] \sin mx \sin ny \\ &+ \varepsilon^3 w_1^3(\tau) [\alpha g_{311} \sin mx \sin ny + g_{331} \sin 3mx \sin ny \\ &+ g_{313} \sin mx \sin 3ny] + O(\varepsilon^4) \end{aligned} \quad 12.39$$

$$\begin{aligned} \Psi_x(x, y, \tau) &= \varepsilon [g_{11}^{(1,1)} w_1(\tau) + g_2 \ddot{w}_1(\tau)] \cos mx \sin ny \\ &+ \varepsilon^2 w_1^2(\tau) g_{12} \sin 2ny + \varepsilon^3 w_1^3(\tau) [\alpha g_{11}^{(1,1)} g_{311} \cos mx \sin ny \\ &+ g_{11}^{(3,1)} g_{331} \cos 3mx \sin ny \\ &+ g_{11}^{(1,3)} g_{313} \cos mx \sin 3ny] + O(\varepsilon^4) \end{aligned} \quad 12.40$$

$$\begin{aligned}
\Psi_y(x, y, \tau) = & \varepsilon [g_{21}^{(1,1)} w_1(\tau) + g_3 \ddot{w}_1(\tau)] \sin mx \cos ny \\
& + \varepsilon^2 w_1^2(\tau) g_{22} \sin 2mx + \varepsilon^3 w_1^3(\tau) [\alpha g_{21}^{(1,1)} g_{311} \sin mx \cos ny \\
& + g_{21}^{(3,1)} g_{331} \sin 3mx \cos ny + g_{21}^{(1,3)} g_{313} \sin mx \cos 3ny] + O(\varepsilon^4)
\end{aligned} \quad 12.41$$

$$\begin{aligned}
F(x, y, \tau) = & \left[ -B_{00}^{(0)} \frac{y^2}{2} - b_{00}^{(0)} \frac{x^2}{2} \right] + \varepsilon [g_{31}^{(1,1)} w_1(\tau) \\
& + g_4 \ddot{w}_1(\tau)] \cos mx \cos ny + \varepsilon^2 w_1^2(\tau) \\
& \times \left[ -B_{00}^{(0)} \frac{y^2}{2} - b_{00}^{(0)} \frac{x^2}{2} + g_{402} \cos 2ny + g_{420} \cos 2mx \right] \\
& + \varepsilon^3 w_1^3(\tau) [\alpha g_{31}^{(1,1)} g_{311} \cos mx \cos ny + g_{31}^{(3,1)} g_{331} \cos 3mx \cos ny \\
& + g_{31}^{(3,1)} g_{313} \cos mx \cos 3ny] + O(\varepsilon^4)
\end{aligned} \quad 12.42$$

$$\lambda_q(x, y, \tau) = \varepsilon [g_{41} w_1(\tau) + g_{43} \ddot{w}_1(\tau)] \sin mx \sin ny + \varepsilon^3 w_1^3(\tau) [\bar{\alpha} g_{42} \sin mx \sin ny + O(\varepsilon^4)] \quad 12.43$$

In Eqs. (12.39)–(12.43), all coefficients  $g_{11}^{(i,j)}$ ,  $g_{21}^{(i,j)}$ ,  $g_{31}^{(i,j)}$  ( $i, j = 1, 3$ ), etc. are defined as in Huang and Zheng (2003).

Then multiplying Eq. (12.43) by  $(\sin mx \sin ny)$  and performing integration over the plate area yields

$$g_{43}(\varepsilon \ddot{w}_1(\tau)) + \bar{\alpha} g_{42}(\varepsilon w_1)^3 + g_{41}(\varepsilon w_1) = \bar{\lambda}_q(\tau) \quad 12.44$$

Eq. (12.44) is a well-known Duffing-type equation, in which

$$\bar{\lambda}_q(\tau) = \frac{4}{\pi^2} \int_0^\pi \int_0^\pi \lambda_q(x, y, \tau) \sin mx \sin ny \, dx \, dy \quad 12.45$$

### 12.4.1 Free vibration

For the case of free vibration, we take  $\bar{\alpha} = 1$  and  $\lambda_q(\tau) = 0$ , from Eq. (12.44). The nonlinear to linear frequency ratio can be obtained as

$$\frac{\omega_{NL}}{\omega_L} = \left[ 1 + \frac{3}{4} \left( \frac{\alpha_1}{\omega_L} \frac{\bar{W}_{max}}{h} \right)^2 \right]^{1/2} \quad 12.46$$

In Eq. (12.46),  $\alpha_1 = [g_{42}/g_{43}]^{1/2}$  and  $\omega_L = [g_{41}/g_{43}]^{1/2}$  is the linear frequency.

### 12.4.2 Forced vibration

When the forced vibration is under consideration, we take  $\bar{\alpha} = 0$ . In such a case, Eq. (12.44) can be re-written as

$$\varepsilon \ddot{w}_1(\tau) + \omega_L^2 \varepsilon w_1(\tau) + O(\varepsilon^4) = \frac{\bar{\lambda}_q(\tau)}{g_{43}} \quad 12.47$$

Substituting Eqs. (12.39)–(12.42) into initial condition (12.23), yields

$$w_1(\tau) = \dot{w}_1(\tau) = \ddot{w}_1(\tau) = \dddot{w}_1(\tau) = 0 \quad 12.48$$

From Eqs. (12.47) and (12.48), one has

$$\varepsilon w_1(\tau) = \frac{1}{g_{43} \omega_L} \int_0^\tau \sin \omega_L (\tau - \varsigma) \bar{\lambda}_q(\varsigma) d\varsigma \quad 12.49$$

Next, upon substitution of Eq. (12.49) into Eqs. (12.39)–(12.42), both displacements and stress function are determined.

Tables 12.1–12.3 show the comparisons of linear and nonlinear frequencies for anti-symmetric angle-ply and symmetric cross-ply laminated plates without or with initial in-plane static loads. The dimensionless natural frequencies ( $\Omega = \bar{\omega}_L a^2 \sqrt{\rho/E_{22} h^2}$ ) for  $(\pm 45)_T$  and  $(\pm 45)_{4T}$  laminated square plates are calculated and compared in Table 12.1 with the FEM results of Reddy and Phan (1985) and Fourier series solution of Matsunaga (2001), based on different kinds of higher-order shear deformation plate theories. The material properties adopted are:  $E_{11}/E_{22} = 40$ ,  $G_{12}/E_{22} = G_{13}/E_{22} = 0.6$ ,  $G_{23}/E_{22} = 0.5$ , and  $\nu_{12} = 0.25$ . Then the linear to nonlinear frequency ratios ( $\omega_L/\omega_{NL}$ ) for a  $(\pm 45)_T$  laminated square plate with SS2 in-plane boundary conditions are calculated and compared in Table 12.2 with the Fourier series solution of Bhimaraddi (1993) based on the first-order shear deformation plate theory.

Table 12.1 Comparisons of dimensionless natural frequencies  $\Omega$  for  $(\pm 45)_T$  and  $(\pm 45)_{4T}$  laminated square plates

$a/h$	$(\pm 45)_T$			$(\pm 45)_{4T}$		
	Reddy and Phan (1985)	Matsunaga (2001)	Present	Reddy and Phan (1985)	Matsunaga (2001)	Present
10	13.263	12.644	13.296	19.266	19.083	19.231
20	14.246	14.044	14.263	23.239	23.165	23.234
100	14.621	14.612	14.622	25.174	25.171	25.175

Table 12.2 Comparison of linear to nonlinear frequency ratios ( $\omega_L/\omega_{NL}$ ) for a  $(\pm 45)_T$  laminated square plate

$\bar{W}_{max}/h$	0.0	0.2	0.4	0.6	0.8	1.0	1.2	1.4	1.6	1.8	2.0
Bhimaraddi (1993)	1.0	1.032	1.121	1.253	1.417	1.602	1.803	2.013	2.231	2.455	2.683
Present	1.0	1.033	1.130	1.281	1.452	1.657	1.877	2.108	2.347	2.568	2.808

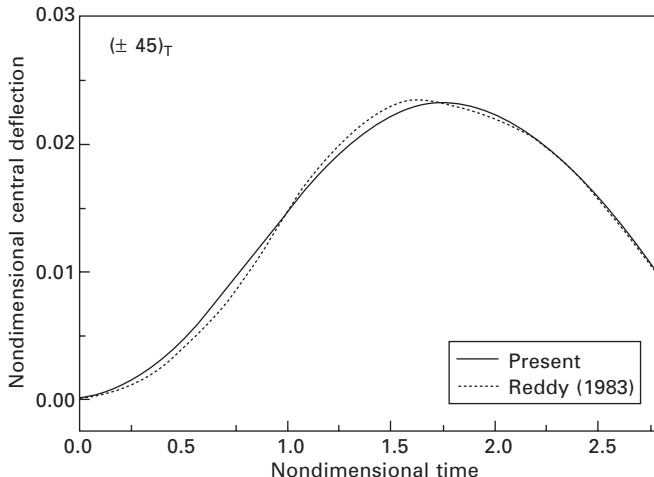
Table 12.3 Comparisons of linear to nonlinear frequency ratios ( $\omega_L/\omega_{NL}$ ) for initially stressed (0/90/0) laminated square plates with different values of  $E_{11}/E_{22}$  ( $G_{12} = G_{13} = G_{23} = 0.5E_{22}$ ,  $v_{12} = 0.25$ ,  $a/h = 10$ ,  $p_x = p_y = -N_c/h$ )

$E_{11}/E_{22}$		$\overline{W}_{\max}/h$				
		$\omega^*$	0.25	0.50	0.75	1.00
5	Bhimaraddi (1987)	0.49962	0.9933	0.9739	0.9442	0.9069
	Present	0.49894	0.9933	0.9870	0.9440	0.9064
10	Bhimaraddi (1987)	0.42891	0.9917	0.9679	0.9320	0.8881
	Present	0.42887	0.9917	0.9679	0.9318	0.8875
15	Bhimaraddi (1987)	0.39590	0.9905	0.9638	0.9238	0.8756
	Present	0.39287	0.9904	0.9698	0.9224	0.8731
25	Bhimaraddi (1987)	0.35737	0.9887	0.9571	0.9108	0.8564
	Present	0.35734	0.9887	0.9570	0.9103	0.8550
40	Bhimaraddi (1987)	0.32195	0.9863	0.9486	0.8947	0.8331
	Present	0.32045	0.9862	0.9480	0.8931	0.8301
60	Bhimaraddi (1987)	0.29056	0.9834	0.9385	0.8760	0.8068
	Present	0.29048	0.9833	0.9381	0.8748	0.8045

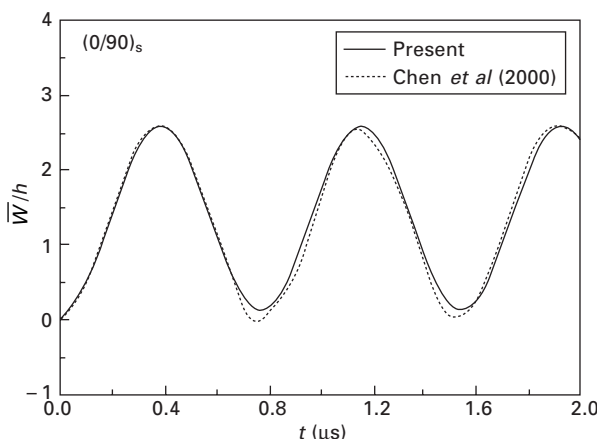
The material properties adopted are:  $E_{11} = 181.0$  GPa,  $E_{22} = 10.3$  GPa,  $G_{12} = G_{13} = 7.17$  GPa,  $G_{23} = 6.21$  GPa and  $v_{12} = 0.28$ . Moreover, the linear to nonlinear frequency ratios ( $\omega_L/\omega_{NL}$ ) for initially stressed (0/90/0) laminated square plates with different values of  $E_{11}/E_{22}$  are calculated and compared in Table 12.3 with the Galerkin solutions of Bhimaraddi (1987), based on a higher-order shear deformation plate theory. In Table 12.3,  $\omega^* = \omega_L/\sqrt{E_{11}/\rho a^2}$  is the dimensionless linear frequency, and  $N_C$  is the buckling load of the plate, defined as in Bhimaraddi (1987). The additional material properties adopted are:  $G_{12}/E_{22} = G_{13}/E_{22} = G_{23}/E_{22} = 0.5$  and  $v_{12} = 0.25$ .

Figures 12.1 and 12.2 show the comparisons of the dynamic response for antisymmetric angle-ply and symmetric cross-ply laminated plates without initial in-plane static loads. The curves of central deflection as functions of time for a  $(\pm 45)_T$  laminated square plate are calculated and compared in Fig. 12.1 with FEM results of Reddy (1983). The computing data adopted are:  $a/h = 5$ ,  $E_{11}/E_{22} = 25$ ,  $G_{12} = G_{13} = 0.5E_{22}$ ,  $G_{23} = 0.2E_{22}$ ,  $v_{12} = 0.25$ ,  $\rho = 1.0$ , and a uniform sudden load with  $q_0 = 0.005$  is applied. Then the curves of central deflection as functions of time for a (0/90)<sub>S</sub> laminated square plate are calculated and compared in Fig. 12.2 with finite strip method (FSM) results of Chen *et al.* (2000). The computing data adopted are:  $a = b = 250$  mm,  $h = 5$  mm,  $E_{11} = 525$  GPa,  $E_{22} = 21$  GPa,  $G_{12} = G_{13} = G_{23} = 10.5$  GPa,  $v_{12} = 0.25$ ,  $\rho = 800$  kg/m<sup>3</sup>, and a uniform step load with  $q_0 = 1$  MPa is applied.

These comparisons show that the results from the present method are in good agreement with the existing results, thus verifying the reliability and accuracy of the present method.



12.1 Comparison of nonlinear transient deflections for a  $(\pm 45)_T$  laminated square plate.



12.2 Comparison of nonlinear transient deflections for a  $(0/90)_s$  laminated square plate.

## 12.5 Nonlinear vibration and dynamic response of an unsymmetric cross-ply laminated plate with piezoelectric layers

We now turn our attention to the nonlinear free and forced vibration of shear deformable laminated plates with piezoelectric actuators subjected to a dynamic transverse load combined with thermal and electrical loads. The plate is assumed to have unsymmetric cross-plies. In such a case, the zero-valued plate stiffnesses are

$$\begin{aligned} A_{16} &= A_{26} = D_{16} = D_{26} = F_{16} = F_{26} = H_{16} = H_{26} = 0 \\ A_{45} &= D_{45} = F_{45} = 0, B_{16} = B_{26} = E_{16} = E_{26} = 0 \end{aligned} \quad 12.50$$

and we need to replace  $\bar{N}^T$ ,  $\bar{M}^T$  and  $\bar{S}^T$  in Eqs. (12.1)–(12.4) and (12.10) with equivalent thermo-piezoelectric loads  $\bar{N}^P$ ,  $\bar{M}^P$  and  $\bar{S}^T$ , which are defined by

$$\begin{bmatrix} \bar{N}^P \\ \bar{M}^P \\ \bar{S}^P \end{bmatrix} = \begin{bmatrix} \bar{N}^T \\ \bar{M}^T \\ \bar{S}^T \end{bmatrix} + \begin{bmatrix} \bar{N}^E \\ \bar{M}^E \\ \bar{S}^E \end{bmatrix} \quad 12.51$$

where  $\bar{N}^T$ ,  $\bar{M}^T$ ,  $\bar{P}^T$  and  $\bar{N}^E$ ,  $\bar{M}^E$ ,  $\bar{P}^E$  are the forces, moments and higher-order moments caused by the elevated temperature and electric field, respectively.

The temperature field considered is assumed to be a uniform distribution over the plate surface and a linear variation through the plate thickness

$$\Delta T = T_0 + T_1 \frac{Z}{h} \quad 12.52$$

For the plate-type piezoelectric material, only the transverse direction electric field component  $E_Z$  is dominant, and  $E_Z$  is defined as  $E_Z = -\Phi_Z$ , where  $\Phi$  is the potential field. If the voltage applied to the actuator is in the thickness only, then

$$E_Z = \frac{V_k}{h_p} \quad 12.53$$

where  $V_k$  is the applied voltage across the  $k$ th ply and  $h_p$  is the thickness of the piezoelectric ply.

The forces, moments and higher-order moments caused by electric field are defined by

$$\begin{bmatrix} \bar{N}_x^E & \bar{M}_x^E & \bar{P}_x^E \\ \bar{N}_y^E & \bar{M}_y^E & \bar{P}_y^E \\ \bar{N}_{xy}^E & \bar{M}_{xy}^E & \bar{P}_{xy}^E \end{bmatrix} = \sum_{k=1}^{t_k} \int_{t_{k-1}}^{t_k} \begin{bmatrix} B_x \\ B_y \\ B_{xy} \end{bmatrix} (1, Z, Z^3) \frac{V_k}{h_p} dZ \quad 12.54a$$

$$\begin{bmatrix} \bar{S}_x^E \\ \bar{S}_y^E \\ \bar{S}_{xy}^E \end{bmatrix} = \begin{bmatrix} \bar{M}_x^E \\ \bar{M}_y^E \\ \bar{M}_{xy}^E \end{bmatrix} - \frac{4}{3h^2} \begin{bmatrix} \bar{P}_x^E \\ \bar{P}_y^E \\ \bar{P}_{xy}^E \end{bmatrix} \quad 12.54b$$

in which

$$\begin{bmatrix} B_x \\ B_y \\ B_{xy} \end{bmatrix} = - \begin{bmatrix} \bar{Q}_{11} & \bar{Q}_{12} & \bar{Q}_{16} \\ \bar{Q}_{12} & \bar{Q}_{22} & \bar{Q}_{26} \\ \bar{Q}_{16} & \bar{Q}_{26} & \bar{Q}_{66} \end{bmatrix} \begin{bmatrix} c^2 & s^2 \\ s^2 & c^2 \\ 2cs & -2cs \end{bmatrix} \begin{bmatrix} d_{31} \\ d_{32} \end{bmatrix} \quad 12.55$$

where  $d_{31}$  and  $d_{32}$  are the piezoelectric strain constants of a single ply, and  $\bar{Q}_{ij}$  are the transformed elastic constants defined as in Eq. (12.8). It is noted that from Eqs. (12.6) and (12.53), in the present case, the thermal and electric forces  $\bar{N}_{xy}^T$  and  $\bar{N}_{xy}^E$  are all zero.

All four edges are assumed to be simply supported, and the in-plane boundary condition is assumed to be immovable (SS2). It is noted that for such a plate the stretching–bending coupling gives rise to bending curvatures under the action of in-plane loading, no matter how small these loads may be. Hence, the boundary conditions of zero bending moment, i.e. Eqs. (12.9b) and (12.9f), cannot be incorporated accurately.

In the present case, the solutions of Eqs. (12.25)–(12.28) can be expressed as

$$\begin{aligned} W^*(x, y) &= \sum_{k=1,3,\dots} \sum_{l=1,3,\dots} w_{kl} \sin kx \sin ly \\ \Psi_x^*(x, y) &= \sum_{k=1,3,\dots} \sum_{l=1,3,\dots} (\Psi_x)_{kl} \cos kx \sin ly \\ \Psi_y^*(x, y) &= \sum_{k=1,3,\dots} \sum_{l=1,3,\dots} (\Psi_y)_{kl} \sin kx \cos ly \\ F^*(x, y) &= \left( -B_{00}^{(0)} \frac{y^2}{2} y^2 - b_{00}^{(0)} \frac{x^2}{2} \right) + \sum_{k=1,3,\dots} \sum_{l=1,3,\dots} f_{kl} \sin kx \sin ly \end{aligned} \quad 12.56$$

We also expand the thermo-piezoelectric forces and bending moments in the double Fourier sine series as

$$\begin{bmatrix} M_x^P & S_x^P \\ M_y^P & S_y^P \end{bmatrix} = - \sum_{k=1,3,\dots} \sum_{l=1,3,\dots} \begin{bmatrix} M_x^{(0)} & S_x^{(0)} \\ M_y^{(0)} & S_y^{(0)} \end{bmatrix} \frac{1}{kl} \sin kx \sin ly \quad 12.57$$

where

$$\begin{aligned} \begin{bmatrix} M_x^{(0)} & S_x^{(0)} \\ M_y^{(0)} & S_y^{(0)} \end{bmatrix} &= \frac{16h}{\pi^2 [D_{11}^* D_{22}^* A_{11}^* A_{22}^*]^{1/4}} \\ &\times \left( \begin{bmatrix} \gamma_{T3} & (\gamma_{T3} - \gamma_{T6}) \\ \gamma_{T4} & (\gamma_{T4} - \gamma_{T7}) \end{bmatrix} \Delta T + \begin{bmatrix} \gamma_{E3} & (\gamma_{E3} - \gamma_{E6}) \\ \gamma_{E4} & (\gamma_{E4} - \gamma_{E7}) \end{bmatrix} \Delta V \right) \end{aligned} \quad 12.58$$

Substituting Eqs. (12.56)–(12.58) into Eqs. (12.25)–(12.28), applying the Galerkin procedure to the Eqs. (12.25) and (12.26),  $W_{kl}$ ,  $(\Psi_x)_{kl}$ ,  $(\Psi_y)_{kl}$  and  $f_{kl}$  can be determined, the detailed expressions can be found in the appendix of Huang and Shen (2006). Then the solutions of Eqs. (12.29)–(12.32) can be expressed as

$$\begin{aligned}\tilde{W}(x, y, \tau) = & \varepsilon[w_1(\tau) + g_1\ddot{w}_1(\tau)]\sin mx \sin ny \\ & + \varepsilon^3 w_1^3(\tau)[\alpha g_{311} \sin mx \sin ny + g_{331} \sin 3mx \sin ny \\ & + g_{313} \sin mx \sin 3ny] + O(\varepsilon^4)\end{aligned}\quad 12.59$$

$$\begin{aligned}\Psi_x(x, y, \tau) = & \varepsilon[g_{11}^{(1,1)}w_1(\tau) + g_2\ddot{w}_1(\tau)]\cos mx \sin ny \\ & + \varepsilon^2 w_1^2(\tau)g_{12} \sin 2mx + \varepsilon^3 w_1^3(\tau)[\alpha g_{11}^{(1,1)}g_{311} \cos mx \sin ny \\ & + g_{11}^{(3,1)}g_{331} \cos 3mx \sin ny + g_{11}^{(3,1)}g_{313} \cos mx \sin 3ny] + O(\varepsilon^4)\end{aligned}\quad 12.60$$

$$\begin{aligned}\Psi_y(x, y, \tau) = & \varepsilon[g_{21}^{(1,1)}w_1(\tau) + g_3\ddot{w}_1(\tau)]\sin mx \cos ny \\ & + \varepsilon^2 w_1^2(\tau)g_{22} \sin 2ny + \varepsilon^3 w_1^3(\tau)[\alpha g_{21}^{(1,1)}g_{311} \sin mx \cos ny \\ & + g_{21}^{(3,1)}g_{331} \sin 3mx \cos ny + g_{21}^{(1,3)}g_{313} \sin mx \cos 3ny] + O(\varepsilon^4)\end{aligned}\quad 12.61$$

$$\begin{aligned}\tilde{F}(x, y, \tau) = & \varepsilon[g_{31}^{(1,1)}w_1(\tau) + g_4\ddot{w}_1(\tau)]\sin mx \sin ny \\ & + \varepsilon^2 w_1^2(\tau)\left[-B_{00}^{(2)}\frac{y^2}{2} - b_{00}^{(2)}\frac{x^2}{2} + g_{402} \cos 2ny + g_{420} \cos 2mx\right] \\ & + \varepsilon^3 w_1^3(\tau)[\alpha g_{31}^{(1,1)}g_{311} \sin mx \sin ny + g_{31}^{(3,1)}g_{331} \sin 3mx \sin ny \\ & + g_{31}^{(1,3)}g_{313} \sin mx \sin 3ny] + O(\varepsilon^4)\end{aligned}\quad 12.62$$

$$\begin{aligned}\lambda_q(x, y, \tau) = & \varepsilon[g_{41}w_1(\tau) + g_{43}\ddot{w}_1(\tau)]\sin mx \sin ny \\ & + \varepsilon^2 w_1^2(\tau)[g_{441} \cos 2mx + g_{442} \cos 2ny] \\ & + \varepsilon^2 w_1^2(\tau)\sum_k \sum_l w_{kl} \gamma_{14} \beta^2 [-B_{00}^{(2)}k^2 - b_{00}^{(2)}l^2 + 4k^2 n^2 g_{402} \cos 2ny \\ & + 4l^2 m^2 g_{420} \cos 2mx] \sin kx \sin ly \\ & + \varepsilon^3 w_1(\tau)^3[\bar{\alpha} g_{42} \sin mx \sin ny] + O(\varepsilon^4)\end{aligned}\quad 12.63$$

Not that all coefficients in Eqs. (12.59)–(12.63) are somewhat different from those in Eqs. (12.39)–(12.43) and defined as in Huang and Shen (2006).

Multiplying Eq. (12.63) by  $(\sin mx \sin ny)$  and performing integration over the plate area, one has

$$g_{43}(\varepsilon\ddot{w}_1(\tau)) + \bar{\alpha}g_{42}(\varepsilon w_1)^3 + g_{44}(\varepsilon w_1)^2 + g_{41}(\varepsilon w_1) + O(\varepsilon^4) = \bar{\lambda}_q(\tau) \quad 12.64$$

where

$$\bar{\lambda}_q(\tau) = \frac{4}{\pi^2} \int_0^\pi \int_0^\pi \lambda_q(x, y, \tau) \sin mx \sin ny dx dy \quad 12.65$$

### 12.5.1 Free vibration

As in Section 12.4.1, we take  $\bar{\alpha} = 1$  and  $\lambda_q(\tau) = 0$  from Eq. (12.64). The nonlinear to linear frequency ratios can be obtained as

$$\frac{\omega_{NL}}{\omega_L} = \left[ 1 + \frac{9g_{42}g_{41} - 10g_{44}^2}{12g_{41}^2} \left( \frac{\bar{W}_{\max}}{h} \right)^2 \right]^{1/2} \quad 12.66$$

### 12.5.2 Forced vibration

As in Section 12.4.2, we take  $\bar{\alpha} = 0$ . In such a case Eq. (12.64) can be rewritten as

$$\varepsilon \ddot{w}_1(\tau) + \omega_L^2 \varepsilon w_1(\tau) + \frac{g_{44}}{g_{43}} (\varepsilon w_1(\tau))^2 + O(\varepsilon^4) = \frac{\bar{\lambda}_q(\tau)}{g_{43}} \quad 12.67$$

which can be solved by the Runge–Kutta iteration scheme.

We first consider the effect of stacking sequence on the frequency parameters of a square laminated plate with eight graphite–epoxy layers. Four different plate configurations are considered. The first has no piezoelectric layers (referred to as ‘a’); the second and third plates have a single PZT-5A piezoelectric layer at the top surface and at the mid-thickness, respectively (referred to as ‘b’ and ‘c’); and the fourth plate has two PZT-5A piezoelectric layers at the top and bottom surfaces (referred to as ‘d’). The layers of the four plates are of equal thickness and the material properties adopted are:  $E_{11} = 181.0$  GPa,  $E_{22} = 10.3$  GPa,  $G_{12} = G_{13} = 7.17$  GPa,  $G_{23} = 2.87$  GPa,  $\nu_{12} = 0.28$ ,  $\rho = 1580$  kg/m<sup>3</sup>,  $\alpha_{11} = 0.02 \times 10^{-6}/^\circ\text{C}$ ,  $\alpha_{22} = 22.5 \times 10^{-6}/^\circ\text{C}$  for the graphite–epoxy; and  $E = 61.0$  GPa,  $\nu = 0.35$ ,  $\rho = 7750$  kg/m<sup>3</sup>,  $\alpha_{11} = \alpha_{22} = 1.5 \times 10^{-6}/^\circ\text{C}$ ,  $d_{31} = d_{32} = -171 \times 10^{-12}$  m/V for the PZT-5A layers. The fundamental frequencies  $\bar{\omega}_L$  for these four plates are calculated and compared in Table 12.4 with three-dimensional solutions of Xu *et al.* (1997) and FSDPT solutions of Benjeddou *et al.* (2002).

We then investigated the effect of initial temperature changes on the fundamental frequencies of the same hybrid plate ‘b’ as in the above example. The initial temperature change is independent of the surface coordinates and varies through the plate thickness, i.e. in Eq. (12.52)  $T_0 = T_0 = (T^t + T^b)/2$  and  $T_1 = T^t - T^b$ , where  $T^t$  and  $T^b$  are the temperature changes at the top and bottom surfaces of the plate, respectively. Four different values of  $\bar{T}_0$ , three different values of  $T_1$  and three different values of  $h/a$  are considered, namely,  $\bar{T}_0 = 0, 1, 2, 3$ ;  $T_1 = 0, 10, 100$ ; and  $h/a = 0.01, 0.1, 0.2$ . The dimensionless temperature rise  $\bar{T}_0$  are defined by  $\bar{T}_0 = c_f T_0$ ,  $c_f = 10^{-3} E_{22} [\rho_f a^2 (\bar{\omega}_L^0)^2]$ , where  $\rho_f$  and  $E_{22}$ , respectively, are the mass density and transverse Young’s modulus of the graphite–epoxy layer. The initially thermally stressed natural

Table 12.4 Comparisons of fundamental frequencies  $\bar{\omega}_L$ (rad/s) for the four unstressed plates

Plate	$a/h = 100$			$a/h = 10$			$a/h = 5$		
	Xu <i>et al.</i> (1997)	Benjeddou <i>et al.</i> (2002)	Present	Xu <i>et al.</i> (1997)	Benjeddou <i>et al.</i> (2002)	Present	Xu <i>et al.</i> (1997)	Benjeddou <i>et al.</i> (2002)	Present
<i>a</i>	333.02	340.86	340.79	2939.2	3098.3	3035.73	4576.8	5055.4	4792.19
<i>b</i>	290.38	300.64	292.80	2554.7	2703.7	2656.37	3964.4	4337.0	4134.23
<i>c</i>	285.26	285.16	284.78	2547.5	2643.0	2613.36	4049.1	4441.2	4218.76
<i>d</i>	268.86	283.93	269.12	2357.7	2516.7	2397.06	3648.0	3953.2	3769.61

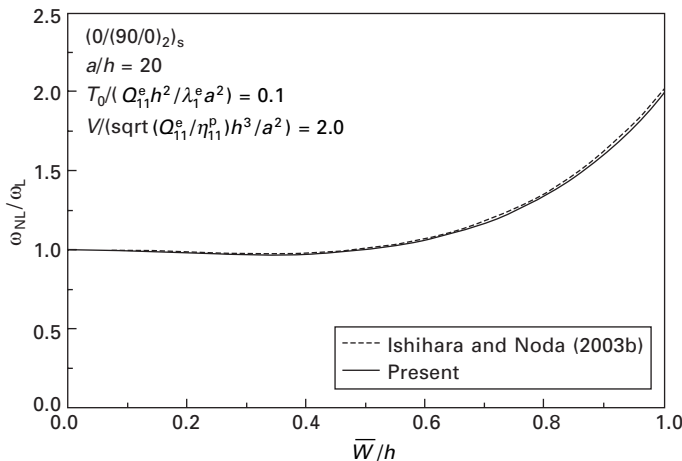
frequency to unstressed natural frequency ratio ( $\bar{\omega}_L/\omega_L^0$ ) are calculated and compared in Table 12.5 with three-dimensional solutions of Xu *et al.* (1997).

Now we examine the nonlinear frequency and large deflection of a (0/(90/0)<sub>2</sub>)<sub>S</sub> square plate which consists of two layers of BaTiO<sub>3</sub> at the top and bottom of the plate and eight layers of graphite–epoxy subjected to thermal and electric loads. The material properties adopted are:  $Q_{11}^e = 182$  GPa,  $Q_{22}^e = 10.3$  GPa,  $Q_{12}^e = 2.90$  GPa,  $Q_{44}^e = 2.87$  GPa,  $Q_{55}^e = Q_{66}^e = 7.17$  GPa,  $\lambda_1^e = 68.8 \times 10^3$  Pa/K,  $\lambda_2^e = 233 \times 10^3$  Pa/K,  $\rho^e = 1580$  kg/m<sup>3</sup> for graphite–epoxy layers; and  $Q_{11}^p = Q_{22}^p = 120$  GPa,  $Q_{12}^p = 36.2$  GPa,  $Q_{44}^p = Q_{55}^p = 44.0$  GPa,  $Q_{66}^p = 42.0$  GPa,  $\lambda_1^p = \lambda_2^p = 1.33 \times 10^6$  Pa/K,  $\rho^p = 5700$  kg/m<sup>3</sup>,  $e_{31} = e_{32} = -12.3$  C/m<sup>2</sup>,  $e_{15} = e_{24} = 11.4$  C/m<sup>2</sup>,  $\eta_{11}^p = \eta_{22}^p = 9.87 \times 10^{-9}$  C<sup>2</sup>/N m<sup>2</sup> and  $\eta_{33}^p = 13.2 \times 10^{-9}$  C<sup>2</sup>/N m<sup>2</sup> for BaTiO<sub>3</sub> layers. The plate width-to-thickness ratio  $a/h = 20$ . The curves of nonlinear to linear frequency ratio as functions of deflection and the curves of central deflection as functions of applied voltage are plotted in Figs 12.3 and 12.4, and compared with the Galerkin solutions of Ishihara and Noda (2003b) based on the first-order shear deformation theory.

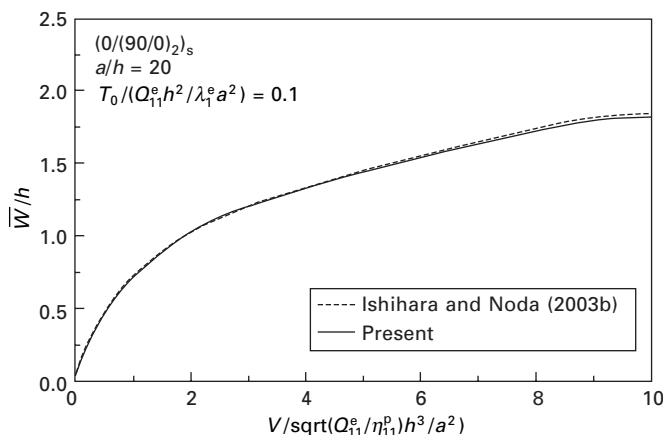
In addition, the curves of the central deflection as functions of time for the (0<sub>B</sub>/90<sub>C</sub>) hybrid laminated square plate made of two kinds of materials of BFRP and CFRP under initial excitation are plotted and compared in Fig. 12.5 with the results obtained by Lee and Kim (1996). The computing data adopted are:  $a = 0.25$  m,  $a/h = 80$ ,  $E_{11} = 181.0$  GPa,  $E_{22} = 10.3$  GPa,  $G_{12} = 7.17$  GPa,  $\rho = 1600$  kg/m<sup>3</sup>,  $v_{12} = 0.28$  for CFRP and  $E_{11} = 204.0$  GPa,  $E_{22} = 18.5$  GPa,  $G_{12} = 5.59$  GPa,  $\rho = 2000$  kg/m<sup>3</sup>,  $v_{12} = 0.23$  for BFRP. Again, good agreement is achieved in each of these comparisons.

*Table 12.5 Comparison of thermally stressed to unstressed natural frequency ratio ( $\bar{\omega}_L/\omega_L^0$ )<sup>2</sup> for configuration 'b'*

$h/a$	$T_1$	Source	$\bar{T}_0$		
			1	2	3
0.01	0	Xu <i>et al.</i> (1997)	0.7965	0.593	0.3894
		Present	0.7998	0.5995	0.3991
	10	Xu <i>et al.</i> (1997)	0.797	0.5935	0.39
		Present	0.8002	0.5966	0.3996
	100	Xu <i>et al.</i> (1997)	0.8016	0.5981	0.3946
		Present	0.8029	0.5998	0.403
0.1	0, 10, 100		0.797	0.594	0.3909
	Present	0.805	0.608	0.4102	
0.2	0, 10, 100		0.7981	0.5959	0.3935
	Present	0.8087	0.6124	0.4218	



12.3 Comparisons of the curves of nonlinear to linear frequency ratio as functions of deflection for a hybrid laminated plate subjected to thermal and electrical loads.



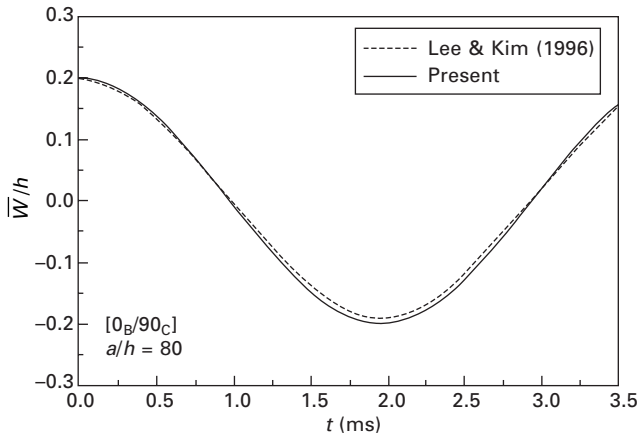
12.4 Comparisons of the curves of central deflection as functions of applied voltage for a hybrid laminated plate subjected to thermal and electrical loads.

In this section graphite–epoxy composite material and PZT-5A are selected for the substrate orthotropic layers and piezoelectric layers, respectively. The elastic constants and thermal expansion coefficients of each ply are assumed to be linear functions of temperature change  $\Delta T$ , but Poisson's ratio depends weakly on temperature change and is assumed to be constant.

$$E_{11}(T) = E_{110}(1 + E_{111}\Delta T), \quad E_{22}(T) = E_{220}(1 + E_{221}\Delta T)$$

$$E_{12}(T) = E_{120}(1 + E_{121}\Delta T), \quad E_{13}(T) = E_{130}(1 + G_{131}\Delta T)$$

$$E_{23}(T) = G_{230}(1 + G_{231}\Delta T)$$



12.5 The curve of central deflection versus time for (0<sub>B</sub>/90<sub>C</sub>) plate subject to initial excitation.

$$\alpha_{11}(T) = \alpha_{110}(1 + \alpha_{111}\Delta T), \quad \alpha_{22}(T) = \alpha_{220}(1 + \alpha_{221}\Delta T) \quad 12.68$$

where  $E_{110}$ ,  $E_{220}$ ,  $G_{120}$ ,  $G_{130}$ ,  $G_{230}$ ,  $\alpha_{110}$ ,  $\alpha_{220}$ ,  $E_{111}$ ,  $E_{221}$ ,  $G_{121}$ ,  $G_{131}$ ,  $G_{231}$ ,  $\alpha_{111}$ ,  $\alpha_{221}$  are constants. Typical values adopted are: for graphite–epoxy orthotropic layers  $E_{110} = 150.0$  GPa,  $E_{220} = 9.0$  GPa,  $G_{120} = G_{130} = 7.1$  GPa,  $G_{230} = 2.5$  GPa,  $\nu_{12} = 0.3$ ,  $\rho = 1580$  kg/m<sup>3</sup>,  $\alpha_{110} = 1.1 \times 10^{-6}/^\circ\text{C}$ ,  $\alpha_{220} = 25.2 \times 10^{-6}/^\circ\text{C}$ , and for PZT-5A piezoelectric layers  $E_{110} = E_{220} = 63.0$  GPa,  $G_{120} = G_{130} = G_{230} = 24.2$  GPa,  $\nu_{12} = 0.3$ ,  $\alpha_{110} = \alpha_{220} = 0.9 \times 10^{-6}/^\circ\text{C}$ ,  $\rho = 7600$  kg/m<sup>3</sup> and  $d_{31} = d_{32} = 2.54 \times 10^{-10}$  m/V; and  $E_{111} = -0.0005$ ,  $E_{221} = G_{121} = G_{131} = G_{231} = -0.0002$ ,  $\alpha_{111} = \alpha_{221} = 0.0005$  for both graphite–epoxy orthotropic layers and piezoelectric layers.

For the sake of brevity, (0/90)<sub>2T</sub> antisymmetric cross-ply and (0/90)<sub>S</sub> symmetric cross-ply laminated plates with a double-thickness piezoelectric layer bonded at the top surface or embedded at the middle surface are referred to as (P/0/90/0/90), (P/0/90/90/0), (0/90/P/0/90) and (0/90/P/90/0), respectively, whereas two piezoelectric layers bonded at the top and bottom surfaces are referred to as (P/0/90/0/90/P) and (P/0/90/90/0/P). The side of the square plate is  $a = b = 24$  mm and the total thickness of the plate is 1.2 mm. All orthotropic layers of the substrate are of equal thickness, whereas the thickness of piezoelectric layers is 0.1 mm.

Table 12.6 shows the dimensionless frequency parameters  $\Omega = \bar{\omega}_L (a^2/h)\sqrt{\rho_0/E_0}$  of the above six hybrid laminated plates under three uniform temperature changes  $\Delta T = 0$  °C, 100 °C and 300 °C, and six different electric loading cases, where  $V_U$ ,  $V_M$  and  $V_L$  represent the control voltages applied on the top, middle and bottom piezoelectric layers, respectively. In Table 12.6, TD represents material properties for both graphite–epoxy orthotropic layers and piezoelectric layers are temperature-dependent. TID represents material

Table 12.6 Dimensionless natural frequency  $\Omega$  for laminated plates with piezoelectric actuators

Stacking sequence	Control voltage	Temperature rise					
		$\Delta T = 0^\circ\text{C}$		$\Delta T = 100^\circ\text{C}$		$\Delta T = 300^\circ\text{C}$	
		TID	TD	TID	TD	TID	TD
(P/0/90/0/90)	$V_U = -100 \text{ V}$	12.370	11.521	11.327	9.621	8.682	
	$V_U = 0 \text{ V}$	12.284	11.428	11.235	9.500	8.557	
	$V_U = +100 \text{ V}$	12.199	11.333	11.142	9.378	8.431	
(P/0/90/90/0)	$V_U = -100 \text{ V}$	12.788	11.967	11.767	10.132	9.181	
	$V_U = 0 \text{ V}$	12.706	11.878	11.679	10.025	9.073	
	$V_U = +100 \text{ V}$	12.623	11.789	11.592	9.916	8.964	
(0/90/P/0/90)	$V_M = -100 \text{ V}$	11.891	10.996	10.813	8.941	7.993	
	$V_M = 0 \text{ V}$	11.809	10.907	10.725	8.832	7.882	
	$V_M = +100 \text{ V}$	11.726	10.818	10.637	8.721	7.770	
(0/90/P/90/0)	$V_M = -100 \text{ V}$	12.389	11.533	11.339	9.594	8.639	
	$V_M = 0 \text{ V}$	12.310	11.448	11.256	9.492	8.537	
	$V_M = +100 \text{ V}$	12.231	11.363	11.172	9.388	8.433	
(P/0/90/0/90/P)	$V_L = V_U = -50 \text{ V}$	12.798	12.159	11.961	10.770	9.915	
	$V_L = V_U = 0 \text{ V}$	12.740	12.099	11.902	10.702	9.848	
	$V_L = V_U = +50 \text{ V}$	12.683	12.038	11.842	10.634	9.780	
(P/0/90/90/0/P)	$V_L = V_U = -50 \text{ V}$	13.068	12.444	12.242	11.091	10.231	
	$V_L = V_U = 0 \text{ V}$	13.012	12.385	12.184	11.025	10.166	
	$V_L = V_U = +50 \text{ V}$	12.956	12.326	12.126	10.958	10.101	

properties for both graphite/epoxy orthotropic layers and piezoelectric layers are temperature-independent, i.e.  $E_{111} = E_{221} = G_{121} = G_{131} = G_{231} = \alpha_{111} = \alpha_{221} = 0$  in Eq. (12.68). Note that now  $\rho_0$  and  $E_0$  are the values of  $\rho$  and  $E_{22}$  of the graphite/epoxy orthotropic layer. Then Tables 12.7 and 12.8 show, respectively, the effects of uniform temperature rise and control voltage on the nonlinear vibration of the same six hybrid laminated plates. It can be seen that temperature rise and plus control voltage decrease the natural frequencies and increase the nonlinear to linear frequency ratios. In contrast, the minus control voltage increases frequencies and decreases nonlinear to linear frequency ratios.

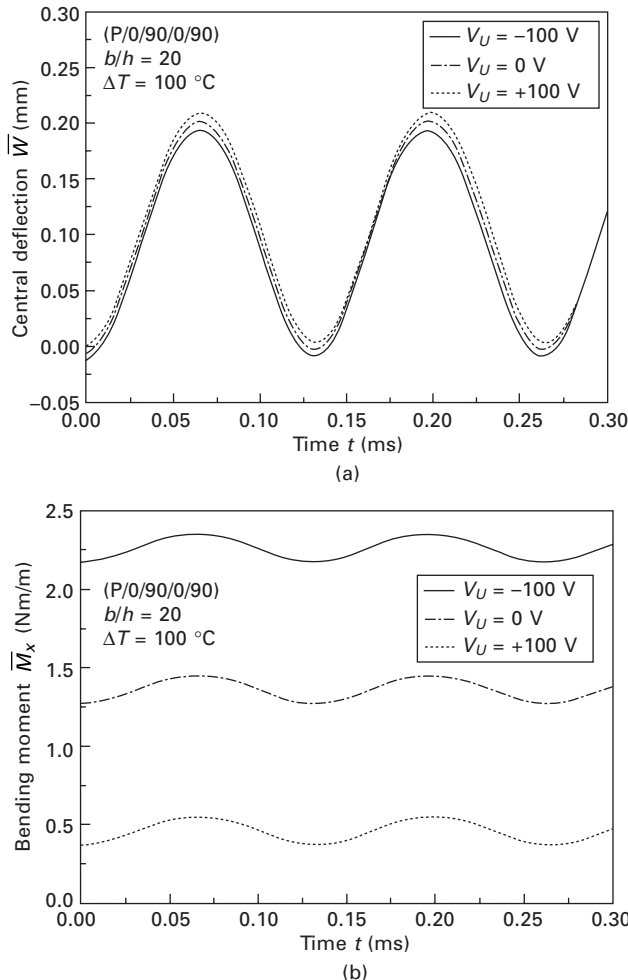
Figure 12.6 shows effect of control voltage  $V_U$  ( $= -100, 0$  and  $+100 \text{ V}$ ) on the dynamic response of a (P/0/90/0/90) square plate subjected to a sudden applied load with  $q_0 = 0.5 \text{ MPa}$ , under thermal loading condition  $\Delta T = 100^\circ\text{C}$ . It can be seen that the deflection is increased, but bending moment is decreased with the increase of the plus voltage. In contrast, the minus control voltage decreases the deflection and increases the bending moment of the plate at the same temperature rise. It also confirms that the temperature-dependent thermoelastic property has a significant effect on both vibration frequencies and dynamic response, but it has a small effect on the nonlinear to linear frequency ratio of the hybrid laminated plate.

Table 12.7 Effects of temperature rise on the nonlinear to linear frequency ratio for laminated plates with piezoelectric actuators

Stacking sequence	Temperature rise (°C)	$\bar{W}_{\max}/h$					
		0.2	0.4	0.6	0.8	1.0	TD
(P/0/90/0/90)	$\Delta T = 0$	1.024	1.024	1.093	1.199	1.333	1.488
	$\Delta T = 100$	1.028	1.028	1.107	1.227	1.378	1.551
	$\Delta T = 300$	1.040	1.044	1.150	1.166	1.314	1.737
(P/0/90/90/0)	$\Delta T = 0$	1.022	1.022	1.087	1.187	1.315	1.462
	$\Delta T = 100$	1.026	1.026	1.099	1.100	1.213	1.519
	$\Delta T = 300$	1.036	1.040	1.136	1.150	1.287	1.680
(0/90/P/0/90)	$\Delta T = 0$	1.026	1.026	1.101	1.215	1.359	1.524
	$\Delta T = 100$	1.030	1.031	1.117	1.248	1.411	1.597
	$\Delta T = 300$	1.046	1.052	1.174	1.196	1.361	1.834
(0/90/P/90/0)	$\Delta T = 0$	1.024	1.024	1.093	1.199	1.334	1.489
	$\Delta T = 100$	1.028	1.028	1.107	1.227	1.379	1.552
	$\Delta T = 300$	1.040	1.045	1.152	1.170	1.318	1.746
(P/0/90/0/90/P)	$\Delta T = 0$	1.018	1.018	1.072	1.156	1.264	1.390
	$\Delta T = 100$	1.020	1.020	1.080	1.171	1.289	1.426
	$\Delta T = 300$	1.026	1.028	1.101	1.108	1.215	1.555
(P/0/90/90/0/P)	$\Delta T = 0$	1.018	1.018	1.069	1.150	1.254	1.376
	$\Delta T = 100$	1.020	1.020	1.076	1.164	1.277	1.410
	$\Delta T = 300$	1.025	1.026	1.095	1.101	1.203	1.498

Table 12.8 Effects of control voltage on the nonlinear to linear frequency ratio for shear deformable laminated plates with piezoelectric actuators ( $\Delta T = 100^\circ\text{C}$ ).

Stacking sequence	Control voltage $V_U (V_m)$	$\bar{W}_{\max}/h$						TD	TID	TD	TID
		0.2 TID	0.4 TID	0.6 TID	0.8 TID	1.0 TID	TD				
(P/0/90/0/90)	-100 V	1.027	1.105	1.224	1.373	1.543	1.545				
	0 V	1.028	1.107	1.227	1.378	1.551	1.553				
	+100 V	1.028	1.109	1.231	1.384	1.559	1.562				
(P/0/90/90/0)	-100 V	1.025	1.098	1.209	1.349	1.510	1.512				
	0 V	1.026	1.099	1.212	1.354	1.517	1.519				
	+100 V	1.026	1.101	1.215	1.359	1.524	1.526				
(0/90/P/0/90)	-100 V	1.030	1.115	1.245	1.406	1.589	1.591				
	0 V	1.030	1.031	1.117	1.248	1.411	1.413				
	+100 V	1.031	1.031	1.119	1.252	1.417	1.419				
(0/90/P/90/0)	-100 V	1.027	1.105	1.224	1.374	1.545	1.547				
	0 V	1.028	1.107	1.227	1.379	1.552	1.554				
	+100 V	1.028	1.108	1.230	1.384	1.558	1.560				
(P/0/90/0/90/P)	-100 V	1.020	1.079	1.170	1.286	1.423	1.424				
	0 V	1.020	1.020	1.080	1.171	1.289	1.426				
	+100 V	1.021	1.021	1.080	1.173	1.292	1.430				
(P/0/90/90/0/P)	-100 V	1.019	1.019	1.076	1.163	1.275	1.406				
	0 V	1.020	1.020	1.076	1.164	1.277	1.410				
	+100 V	1.020	1.077	1.077	1.166	1.280	1.413				



12.6 Effects of control voltage on the dynamic response of (P/0/90/0/90) square plates: (a) central deflection versus time; (b) bending moment versus time.

## 12.6 Nonlinear vibration and dynamic response of FGM hybrid laminated plates

Finally, we consider the nonlinear free and forced vibration of FGM hybrid laminated plates. The plate is assumed to be made of a substrate FGM layer with surface-bonded piezoelectric layers. The substrate FGM layer is made of the combined ceramic and metallic materials with continuously varying mix-ratios comprising ceramic and metal. The length, width and total thickness of the hybrid laminated plate are  $a$ ,  $b$  and  $h$ . The thickness of the FGM layer is  $h_f$ , while the thickness of the piezoelectric layer is  $h_p$ .

In order to accurately model the material properties of functionally graded materials, the properties must be temperature-dependent and position-dependent. This is achieved by using a simple rule of mixture of composite materials. We assume that the material composition varies smoothly from the upper to the lower surface of the FGM layer, such that the upper surface ( $Z = h_2$ ) of the FGM layer is ceramic-rich, and the lower surface ( $Z = h_1$ ) is metal-rich. Hence, the effective material properties  $P_f$ , like Young's modulus  $E_f$  or thermal expansion coefficient  $\alpha_f$ , can be expressed as

$$P_f = P_c V_c + P_m V_m \quad 12.69$$

where  $P_c$  and  $P_m$  denote the temperature-dependent properties of the ceramic and metal, respectively, and  $V_c$  and  $V_m$  are the ceramic and metal volume fractions and are related by

$$V_c + V_m = 1 \quad 12.70$$

It is assumed that the constituent material properties can be expressed as a nonlinear function of temperature (Touloukian 1967)

$$P_j = P_0(P_{-1}T^{-1} + 1 + P_1T + P_2T^2 + P_3T^3) \quad 12.71$$

in which  $T = T_0 + \Delta T$ , and  $T_0 = 300$  K.  $P_0$ ,  $P_{-1}$ ,  $P_1$ ,  $P_2$  and  $P_3$  are the coefficients of temperature  $T$ (K) and are unique to the constituent materials.

In addition, a simple power law exponent of the volume fraction distribution is used to provide a measure of the amount of ceramic and metal in the functionally graded material. In the present case, the volume fraction of ceramic is defined as

$$V_c = \left( \frac{Z - h_1}{h_2 - h_1} \right)^N \quad 12.72$$

where the volume fraction index  $N$  dictates the material variation profile through the FGM layer thickness.

It is assumed that the effective Young's modulus  $E_f$  and thermal expansion coefficient  $\alpha_f$  are temperature dependent, whereas the thermal conductivity  $\kappa_f$  and mass density  $\rho_f$  are independent to the temperature. Poisson's ratio  $\nu_f$  depends weakly on temperature change and is assumed to be a constant. From Eqs. (12.69)–(12.72), one has

$$E_f(Z, T) = [E_c(T) - E_m(T)] \left( \frac{Z - h_1}{h_2 - h_1} \right)^N + E_m(T) \quad 12.73a$$

$$\alpha_f(Z, T) = [\alpha_c(T) - \alpha_m(T)] \left( \frac{Z - h_1}{h_2 - h_1} \right)^N + \alpha_m(T) \quad 12.73b$$

$$\rho_f(Z) = (\rho_c - \rho_m) \left( \frac{Z - h_1}{h_2 - h_1} \right)^N + \rho_m \quad 12.73c$$

$$\kappa_f(Z) = (\kappa_c - \kappa_m) \left( \frac{Z - h_1}{h_2 - h_1} \right)^N + \kappa_m \quad 12.73d$$

It is evident that when  $Z = h_1$ ,  $E_f = E_m(T_m)$  and  $\alpha_f = \alpha_m(T_m)$ , and when  $Z = h_2$ ,  $E_f = E_c(T_c)$  and  $\alpha_f = \alpha_c(T_c)$ . Furthermore,  $E_f$  and  $\alpha_f$  are both temperature and position dependent. Note that for an FGM layer,  $\alpha_{11} = \alpha_{22} = \alpha_f$  is given in detail in Eq. (12.73b), and  $\bar{Q}_{ij} = Q_{ij}$  in which

$$\begin{aligned} Q_{11} = Q_{22} &= \frac{E_f(Z, T)}{1 - v_f^2}, \quad Q_{12} = \frac{v_f E_f(Z, T)}{1 - v_f^2} \\ Q_{16} = Q_{26} &= 0, \quad Q_{44} = Q_{55} = Q_{66} = \frac{E_f(Z, T)}{2(1 + v_f)} \end{aligned} \quad 12.74$$

where  $E_f$  is also given in detail in Eq. (12.73a), and varies in the thickness direction.

We assume that the temperature variation occurs in the thickness direction only and one dimensional temperature field is assumed to be constant in the XY plane of the plate. In such a case, the temperature distribution along the thickness can be obtained by solving a steady-state heat transfer equation

$$-\frac{d}{dZ} \left[ \kappa(Z) \frac{dT}{dZ} \right] = 0 \quad 12.75$$

where

$$\kappa(Z) = \begin{cases} \kappa_p (h_0 < Z < h_1) \\ \kappa_f(Z) (h_1 < Z < h_2) \\ \kappa_p (h_2 < Z < h_3) \end{cases} \quad 12.76a$$

$$T(Z) = \begin{cases} \tilde{T}_p(Z) & (h_0 \leq Z \leq h_1) \\ T_f(Z) & (h_1 \leq Z \leq h_2) \\ T_p(Z) & (h_2 \leq Z \leq h_3) \end{cases} \quad 12.76b$$

where  $\kappa_p$  is the thermal conductivity of the piezoelectric layer. Eq. (12.75) is solved by imposing the boundary conditions  $T = T_U$  at  $Z = h_3$  and  $T = T_L$  at  $Z = h_0$ , and the continuity conditions

$$\tilde{T}_p(h_1) = T_f(h_1) = T_m, \quad T_p(h_2) = T_f(h_2) = T_c \quad 12.77a$$

$$\kappa_p \frac{d\tilde{T}_p(Z)}{dZ} \Big|_{Z=h_1} = \kappa_m \frac{dT_f(Z)}{dZ} \Big|_{Z=h_1},$$

$$\kappa_p \frac{dT_p(Z)}{dZ} \Big|_{Z=h_2} = \kappa_c \frac{dT_f(Z)}{dZ} \Big|_{Z=h_2} \quad 12.77b$$

The solution of Eqs. (12.75)–(12.77), by means of polynomial series, is

$$\tilde{T}_p(Z) = \frac{1}{h_p} [(T_L h_1 - T_m h_0) + (T_m - T_L) Z] \quad 12.78a$$

$$T_f(Z) = T_m + (T_c - T_m) \eta(Z) \quad 12.78b$$

$$T_p(Z) = \frac{1}{h_p} [(T_c h_3 - T_U h_2) + (T_U - T_c) Z] \quad 12.78c$$

in which

$$\begin{aligned} \eta(Z) = & \frac{1}{C} \left[ \left( \frac{Z - h_1}{h_2 - h_1} \right) - \frac{\kappa_{mc}}{(N+1)\kappa_c} \left( \frac{Z - h_1}{h_2 - h_1} \right)^{N+1} \right. \\ & + \frac{\kappa_{mc}^2}{(2N+1)\kappa_c^2} \left( \frac{Z - h_1}{h_2 - h_1} \right)^{2N+1} - \frac{\kappa_{mc}^3}{(3N+1)\kappa_c^3} \left( \frac{Z - h_1}{h_2 - h_1} \right)^{3N+1} \\ & \left. + \frac{\kappa_{mc}^4}{(4N+1)\kappa_c^4} \left( \frac{Z - h_1}{h_2 - h_1} \right)^{4N+1} - \frac{\kappa_{mc}^5}{(5N+1)\kappa_c^5} \left( \frac{Z - h_1}{h_2 - h_1} \right)^{5N+1} \right] \end{aligned} \quad 12.79a$$

$$\begin{aligned} C = & 1 - \frac{\kappa_{mc}}{(N+1)\kappa_c} + \frac{\kappa_{mc}^2}{(2N+1)\kappa_c^2} - \frac{\kappa_{mc}^3}{(3N+1)\kappa_c^3} \\ & + \frac{\kappa_{mc}^4}{(4N+1)\kappa_c^4} - \frac{\kappa_{mc}^5}{(5N+1)\kappa_c^5} \end{aligned} \quad 12.79b$$

$$G = 1 - \frac{\kappa_{mc}}{\kappa_c} + \frac{\kappa_{mc}^2}{\kappa_c^2} - \frac{\kappa_{mc}^3}{\kappa_c^3} + \frac{\kappa_{mc}^4}{\kappa_c^4} - \frac{\kappa_{mc}^5}{\kappa_c^5} \quad 12.79c$$

where  $\kappa_{mc} = \kappa_m - \kappa_c$ , and

$$T_c = \frac{\frac{1}{h_f C} (\kappa_c G T_L + \kappa_m T_U) + \frac{\kappa_p}{h_p} T_U}{\frac{1}{h_f C} (\kappa_c G + \kappa_m) + \frac{1}{h_p} \kappa_p} \quad 12.80a$$

$$T_m = \frac{\frac{1}{h_f C} (\kappa_c G T_L + \kappa_m T_U) + \frac{\kappa_p}{h_p} T_L}{\frac{1}{h_f C} (\kappa_c G + \kappa_m) + \frac{1}{h_p} \kappa_p} \quad 12.80b$$

It has been pointed out by Shen (2002), the governing differential equations for an FGM plate are identical in form to those of unsymmetric cross-ply laminated plates. In such a case, Eq. (12.50) is still valid, and the solutions (12.56)–(12.63) have the similar form.

We first examine the free vibration of an FGM square plate with symmetrically fully covered G-1195N piezoelectric layers. The substrate FGM plate is made of aluminum oxide and Ti-6Al-4V. The material properties adopted are:  $E_c = 320.24$  GPa,  $v_c = 0.26$ ,  $\rho_c = 3750$  kg/m<sup>3</sup> for aluminum oxide;  $E_m = 105.70$  GPa,  $v_m = 0.2981$ ,  $\rho_m = 4429$  kg/m<sup>3</sup> for Ti-6Al-4V;  $E_p = 63.0$  GPa,  $v_p = 0.3$ ,  $\rho_p = 7600$  kg/m<sup>3</sup>,  $d_{31} = d_{32} = 254 \times 10^{-12}$  m/V. The side and thickness of the substrate FGM square plate are 400 mm and 5 mm, and the thickness of each piezoelectric lay is 0.1 mm. The initial ten frequencies of the plate as a function of the volume fraction index  $N$  are listed in Table 12.9 and compared with the FEM results of He *et al.* (2001) based on classical laminated plate theory (CLPT).

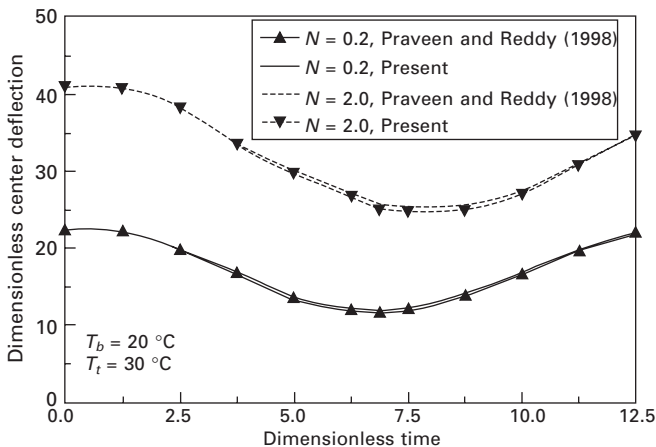
We then examine the dynamic response of an FGM square plate subjected to a uniform sudden load with  $q_0 = 1.0$  MPa in thermal environments. The FGM plate is made of aluminum and alumina. The side and thickness of the square plate are 200 mm and 10 mm, respectively. The top surface is ceramic-rich, whereas the bottom surface is metal-rich. The temperature is varied only in the thickness direction and determined by the steady-state heat conduction equation with the boundary conditions. A stress-free temperature  $T_0 = 0$  °C was taken. The material properties adopted are:  $E_b = 70$  GPa,  $v_b = 0.3$ ,  $\rho_b = 2707$  kg/m<sup>3</sup>,  $\alpha_b = 23.0 \times 10^{-6}/^\circ\text{C}$ ,  $\kappa_b = 204$  W/mK for aluminum; and  $E_t = 380$  GPa,  $v_t = 0.3$ ,  $\rho_t = 3800$  kg/m<sup>3</sup>,  $\alpha_t = 7.4 \times 10^{-6}/^\circ\text{C}$ ,  $\kappa_t = 10.4$  W/mK for alumina. The curves of central deflection as functions of time are plotted and compared in Fig. 12.7 with the FEM results of Praveen and Reddy (1998) based on first-order shear deformation plate theory. In Fig. 12.7, dimensionless central deflection and time are defined by  $W = (\bar{W} E_m h / q_0 a^2)$  and  $\tilde{t} = t [E_m / a^2 \rho_m]^{1/2}$ , respectively.

Good agreement can be seen in these two comparisons. Note that in these two examples the material properties are assumed to be independent of temperature.

In this section, two types of the hybrid FGM plate are considered. The first hybrid FGM plate has fully covered piezoelectric actuators on the top surface (referred to as P/FGM), and the second has two piezoelectric layers symmetrically bonded to the top and bottom surfaces (referred to as P/FGM/P). Silicon nitride ( $\text{Si}_3\text{N}_4$ ) and stainless steel (SUS304) are chosen to be the constituent materials of the substrate FGM layer. The mass density  $\rho_f$ , Poisson's ratio  $v_f$  and thermal conductivity  $\kappa_f$  are 2370 kg/m<sup>3</sup>, 0.24, 9.19 W/mK for  $\text{Si}_3\text{N}_4$ , and 8166 kg/m<sup>3</sup>, 0.33, 12.04 W/mK for SUS304. Young's modulus  $E_f$  and thermal expansion coefficient  $\alpha_f$  for these two constituent materials are listed in Table 12.10 (Reddy and Chin 1998). PZT-5A is selected for the piezoelectric layers. The material properties of which, as linear functions of temperature, are:  $E_{110} = E_{220} = 63$  GPa,  $G_{120} = G_{130} = G_{230} = 24.2$  GPa,  $\alpha_{110} = \alpha_{220} = 0.9 \times 10^{-6}/\text{K}$ ,  $\rho_p = 7600$  kg/m<sup>3</sup>,  $v_p = 0.3$ ,  $\kappa_p = 2.1$  W/mK, and  $d_{31} = d_{32} = 2.54 \times 10^{-10}$  m/V, and  $E_{111} = -0.0005$ ,  $E_{221} = G_{121} = G_{131} = G_{231}$

Table 12.9 Comparison of natural frequency  $\bar{\omega}_L$  (Hz) for FGM plates with piezoelectric actuator bonded on the top and bottom surfaces

Mode	Method	$N = 0$	$N = 0.5$	$N = 1$	$N = 5$	$N = 15$	$N = 100$	$N = 1000$
1	He <i>et al.</i> (2001)	144.25	185.45	198.92	230.46	247.30	259.35	261.73
	Present	143.25	184.73	198.78	229.47	246.86	258.78	260.84
2	He <i>et al.</i> (2001)	359.00	462.65	495.62	573.82	615.58	645.55	651.49
	Present	358.87	461.02	494.65	571.87	613.95	643.92	649.83
3	He <i>et al.</i> (2001)	359.00	462.47	495.62	573.82	615.58	645.55	651.49
	Present	358.87	461.02	494.65	571.87	613.95	643.92	649.83
4	He <i>et al.</i> (2001)	564.10	731.12	778.94	902.04	967.78	1014.94	1024.28
	Present	563.42	727.98	778.61	899.91	964.31	1012.54	1023.72
5	He <i>et al.</i> (2001)	717.80	925.45	993.11	1148.12	1231.00	1290.78	1302.64
	Present	717.65	922.83	992.87	1146.87	1229.44	1288.73	1301.34
6	He <i>et al.</i> (2001)	717.80	925.45	993.11	1148.12	1231.00	1290.78	1302.64
	Present	717.65	922.83	992.87	1146.87	1229.44	1288.73	1301.34
7	He <i>et al.</i> (2001)	908.25	1180.93	1255.98	1453.32	1558.77	1634.65	1649.70
	Present	907.87	1177.34	1223.36	1451.66	1557.12	1632.18	1648.56
8	He <i>et al.</i> (2001)	908.25	1180.93	1255.98	1453.32	1558.77	1634.65	1649.70
	Present	907.87	1177.34	1223.36	1451.66	1557.12	1632.18	1648.56
9	He <i>et al.</i> (2001)	1223.14	1576.91	1697.15	1958.17	2097.91	2199.46	2219.67
	Present	1219.32	1571.65	1695.17	1956.79	2095.67	2197.47	2217.94
10	He <i>et al.</i> (2001)	1223.14	1576.91	1697.15	1958.17	2097.91	2199.46	2219.67
	Present	1219.32	1571.65	1695.17	1956.79	2095.67	2197.47	2217.94



12.7 Comparisons of central deflection versus time curves for an FGM square plate subjected to a sudden load in thermal environments.

Table 12.10 Temperature-dependent coefficients for ceramic and metals, from Reddy and Chin (1998)

Materials	Properties	$P_0$	$P_{-1}$	$P_1$	$P_2$	$P_3$
$\text{Si}_3\text{N}_4$	$E(\text{Pa})$	$348.43 \times 10^9$	0.0	$-3.070 \times 10^{-4}$	$2.160 \times 10^{-7}$	$-8.964 \times 10^{-11}$
	$\alpha(1/\text{K})$	$5.8723 \times 10^{-6}$	0.0	$9.095 \times 10^{-4}$	0.0	0.0
SUS304	$E(\text{Pa})$	$201.04 \times 10^9$	0.0	$3.079 \times 10^{-4}$	$-6.534 \times 10^{-7}$	0.0
	$\alpha(1/\text{K})$	$12.330 \times 10^{-9}$	0.0	$8.086 \times 10^{-4}$	0.0	0.0

$= -0.0002$ ,  $\alpha_{111} = \alpha_{221} = 0.0005$ . The side of the hybrid FGM plate is  $a = b = 24$  mm. The thickness of the substrate FGM layer  $h_f = 1.0$  mm whereas the thickness of each piezoelectric layer  $h_p = 0.1$  mm.

Tables 12.11 and 12.12 present the natural frequency parameter  $\Omega = \bar{\omega}_L(a^2/h_f)[\rho_0/E_0]^{1/2}$  of these two types of the FGM hybrid plate with different values of the volume fraction index  $N$  ( $= 0.0, 0.5, 2.0, 4.0$  and  $\infty$ ) under different sets of thermal and electric loading conditions. Here,  $E_0$  and  $\rho_0$  are the reference values of SUS304 at room temperature ( $T_0 = 300$  K). TD represents material properties for both substrate FGM layer and piezoelectric layers are temperature dependent. TD-F represents material properties of substrate FGM layer are temperature dependent but material properties of piezoelectric layers are temperature independent, i.e.  $E_{111} = E_{221} = G_{121} = G_{131} = G_{231} = \alpha_{111} = \alpha_{221} = 0$  in Eq. (12.68). TID represents material properties for both piezoelectric layers and substrate FGM layer are temperature-independent, i.e. in a fixed temperature  $T_0 = 300$  K for FGM layer, as previously used in Yang and Shen (2001). Six different applied voltages:  $V_U = -200$  V,  $V_U = 0$  V,  $V_U = 200$  V,

Table 12.11 Natural frequency parameter  $\Omega = \bar{\omega}_L (a^2/h_f) [\rho_0/E_0]^{1/2}$  for the hybrid (P/FGM) plates under different sets of thermal and electric loading conditions

	$V_U = V_L$	$Si_3N_4$ ( $N = 0$ )	$N = 0.5$	$N = 2.0$	$N = 4.0$	SUS304 ( $N = \infty$ )
<b>(P/FGM), TID</b>						
$T_U = 300\text{ K}$	-200 V	10.726	7.885	6.334	5.920	5.194
$T_L = 300\text{ K}$	0 V	10.704	7.868	6.320	5.906	5.179
	+200 V	10.682	7.852	6.306	5.892	5.164
$T_U = 400\text{ K}$	-200 V	10.149	7.380	5.852	5.427	4.668
$T_L = 300\text{ K}$	0 V	10.134	7.371	5.846	5.422	4.665
	+200 V	10.119	7.363	5.841	5.418	4.663
$T_U = 600\text{ K}$	-200 V	9.237	6.667	5.277	4.903	4.324
$T_L = 300\text{ K}$	0 V	9.248	6.685	5.299	4.926	4.352
	+200 V	9.260	6.704	5.322	4.950	4.378
<b>(P/FGM), TD-F</b>						
$T_U = 400\text{ K}$	-200 V	10.099	7.346	5.824	5.402	4.649
$T_L = 300\text{ K}$	0 V	10.084	7.336	5.819	5.397	4.646
	+200 V	10.070	7.328	5.814	5.393	4.645
$T_U = 600\text{ K}$	-200 V	9.093	6.592	5.242	4.882	3.432
$T_L = 300\text{ K}$	0 V	9.109	6.614	5.266	4.907	3.277
	-200 V	9.125	6.636	5.291	4.932	3.159
<b>(P/FGM), TD</b>						
$T_U = 400\text{ K}$	-200 V	10.080	7.331	5.812	5.390	4.635
$T_L = 300\text{ K}$	0 V	10.066	7.322	5.807	5.385	4.633
	-200 V	10.052	7.315	5.803	5.382	4.632
$T_U = 600\text{ K}$	-200 V	9.042	6.557	5.216	4.858	3.183
$T_L = 300\text{ K}$	0 V	9.055	6.576	5.238	4.881	3.089
	-200 V	9.070	6.595	5.259	4.902	3.010

and  $V_L = V_U = -200\text{ V}$ ,  $V_L = V_U = 0\text{ V}$ ,  $V_L = V_U = 200\text{ V}$  are used, where subscripts ‘L’ and ‘U’ imply the low and upper piezoelectric layer. It can be seen that the natural frequency of these two plates is decreased by increasing temperature and volume fraction index  $N$ . The plus voltage decreases, but the minus voltage increases the plate natural frequency.

Tables 12.13–12.15 show, respectively, the effect of volume fraction index  $N$ , control voltage and temperature field on the nonlinear to linear frequency ratios  $\omega_{NL}/\omega_L$  of these two types of FGM hybrid plates. It can be seen that the ratios  $\omega_{NL}/\omega_L$  increase as the volume fraction index  $N$  or temperature increases. It is noted that the control voltage only has a small effect on the frequency ratios. It is found that the decrease of natural frequency is about -46% for the P/FGM plate, and about -43% for the P/FGM/P one, from  $N = 0$  to  $N = 4$ , in thermal environmental condition  $T_L = 300\text{ K}$ ,  $T_U = 400\text{ K}$  under TD-F and TD cases. It can also be seen that the natural frequency and the nonlinear to linear frequency ratio under TD-F and TD cases are very close.

Figure 12.8 shows the effect of temperature dependency and volume fraction

Table 12.12 Natural frequency parameter  $\Omega = \bar{\omega}_L(a^2/h_t)[\rho_0/E_0]^{1/2}$  for the hybrid (P/FGM/P) plates under different sets of thermal and electric loading conditions

	$V_U = V_L$	$\text{Si}_3\text{N}_4$ ( $N = 0$ )	$N = 0.5$	$N = 2.0$	$N = 4.0$	SUS304 ( $N = \infty$ )
<b>(P/FGM/P), TID</b>						
$T_U = 300 \text{ K}$	-200 V	9.121	7.032	5.794	5.446	4.810
$T_L = 300 \text{ K}$	0 V	9.085	7.000	5.766	5.418	4.782
	+200 V	9.050	6.969	5.738	5.391	4.755
$T_U = 400 \text{ K}$	-200 V	8.435	6.344	5.102	4.740	4.058
$T_L = 300 \text{ K}$	0 V	8.397	6.310	5.070	4.709	4.026
	+200 V	8.358	6.276	5.038	4.678	3.995
$T_U = 600 \text{ K}$	-200 V	7.124	5.004	3.886	3.622	1.521
$T_L = 300 \text{ K}$	0 V	7.085	4.971	3.860	3.601	1.424
	+200 V	7.046	4.938	3.837	3.581	1.323
<b>(P/FGM/P), TD-F</b>						
$T_U = 400 \text{ K}$	-200 V	8.372	6.295	5.059	4.698	4.022
$T_L = 300 \text{ K}$	0 V	8.333	6.260	5.027	4.668	3.990
	+200 V	8.294	6.226	4.996	4.636	3.959
$T_U = 600 \text{ K}$	-200 V	6.900	4.854	3.816	2.511	1.287
$T_L = 300 \text{ K}$	0 V	6.863	4.825	3.797	2.370	1.172
	-200 V	6.826	4.795	3.778	2.246	1.045
<b>(P/FGM/P), TD</b>						
$T_U = 400 \text{ K}$	-200 V	8.340	6.266	5.033	4.673	3.996
$T_L = 300 \text{ K}$	0 V	8.303	6.233	5.002	4.643	3.966
	-200 V	8.266	6.200	4.972	4.613	3.936
$T_U = 600 \text{ K}$	-200 V	6.806	4.777	3.763	2.190	0.976
$T_L = 300 \text{ K}$	0 V	6.775	4.752	3.747	2.094	0.847
	-200 V	6.744	4.729	3.731	2.003	0.695

index  $N$  ( $= 0.5, 2.0$ ) on the dynamic response of P/FGM plates subjected to a sudden applied load with  $q_0 = 2.0 \text{ MPa}$ , under electric loading condition  $V_U = 200 \text{ V}$  and in the thermal environmental condition  $T_L = 300 \text{ K}$ ,  $T_U = 400 \text{ K}$ . The results show that the dynamic deflections of the P/FGM plate are increased by increasing volume fraction index  $N$ .

This is because the stiffness of the plate becomes weaker when the volume fraction index  $N$  is increased. It can also be seen that the dynamic response becomes greater when the temperature-dependent properties are taken into account.

## 12.7 Conclusions

In order to assess the effects of temperature dependency, temperature field and control voltage on the vibration characteristics of hybrid laminated plates, a fully nonlinear free and forced vibration analysis has been described. The governing equations are based on a higher-order shear deformation plate

Table 12.13 Effect of volume fraction index  $N$  on nonlinear to linear frequency ratio  $\omega_{NL}/\omega_L$  for the hybrid FGM plates in thermal environments ( $T_L = 300$  K,  $T_U = 400$  K)

	$\bar{W}_{max}/h$					
	0.0	0.2	0.4	0.6	0.8	1.0
<b>(P/FGM) (<math>V_U = +200</math> V), TID</b>						
$\text{Si}_3\text{N}_4$	1.000	1.021	1.081	1.175	1.294	1.434
0.5	1.000	1.022	1.084	1.182	1.305	1.449
2.0	1.000	1.022	1.084	1.180	1.303	1.446
4.0	1.000	1.021	1.082	1.178	1.299	1.440
SUS304	1.000	1.022	1.087	1.188	1.315	1.463
<b>(P/FGM) (<math>V_U = +200</math> V), TD-F</b>						
$\text{Si}_3\text{N}_4$	1.000	1.021	1.081	1.175	1.296	1.435
0.5	1.000	1.022	1.085	1.182	1.307	1.451
2.0	1.000	1.022	1.084	1.181	1.305	1.448
4.0	1.000	1.021	1.083	1.179	1.301	1.442
SUS304	1.000	1.023	1.088	1.189	1.317	1.466
<b>(P/FGM) (<math>V_U = +200</math> V), TD</b>						
$\text{Si}_3\text{N}_4$	1.000	1.021	1.082	1.176	1.296	1.436
0.5	1.000	1.022	1.085	1.183	1.307	1.452
2.0	1.000	1.022	1.084	1.182	1.306	1.449
4.0	1.000	1.021	1.083	1.179	1.301	1.444
SUS304	1.000	1.023	1.088	1.190	1.318	1.467
<b>(P/FGM/P) (<math>V_L = V_U = +200</math> V), TID</b>						
$\text{Si}_3\text{N}_4$	1.000	1.021	1.082	1.177	1.298	1.439
0.5	1.000	1.022	1.087	1.186	1.313	1.460
2.0	1.000	1.022	1.088	1.188	1.315	1.463
4.0	1.000	1.022	1.087	1.187	1.314	1.460
SUS304	1.000	1.025	1.096	1.205	1.343	1.502
<b>(P/FGM/P) (<math>V_L = V_U = +200</math> V), TD-F</b>						
$\text{Si}_3\text{N}_4$	1.000	1.021	1.082	1.177	1.299	1.439
0.5	1.000	1.023	1.087	1.187	1.315	1.462
2.0	1.000	1.023	1.088	1.189	1.318	1.467
4.0	1.000	1.023	1.088	1.188	1.316	1.465
SUS304	1.000	1.025	1.096	1.205	1.343	1.502
<b>(P/FGM/P) (<math>V_L = V_U = +200</math> V), TD</b>						
$\text{Si}_3\text{N}_4$	1.000	1.021	1.083	1.178	1.300	1.441
0.5	1.000	1.023	1.088	1.188	1.316	1.464
2.0	1.000	1.023	1.089	1.190	1.320	1.470
4.0	1.000	1.023	1.088	1.190	1.318	1.468
SUS304	1.000	1.025	1.097	1.207	1.346	1.506

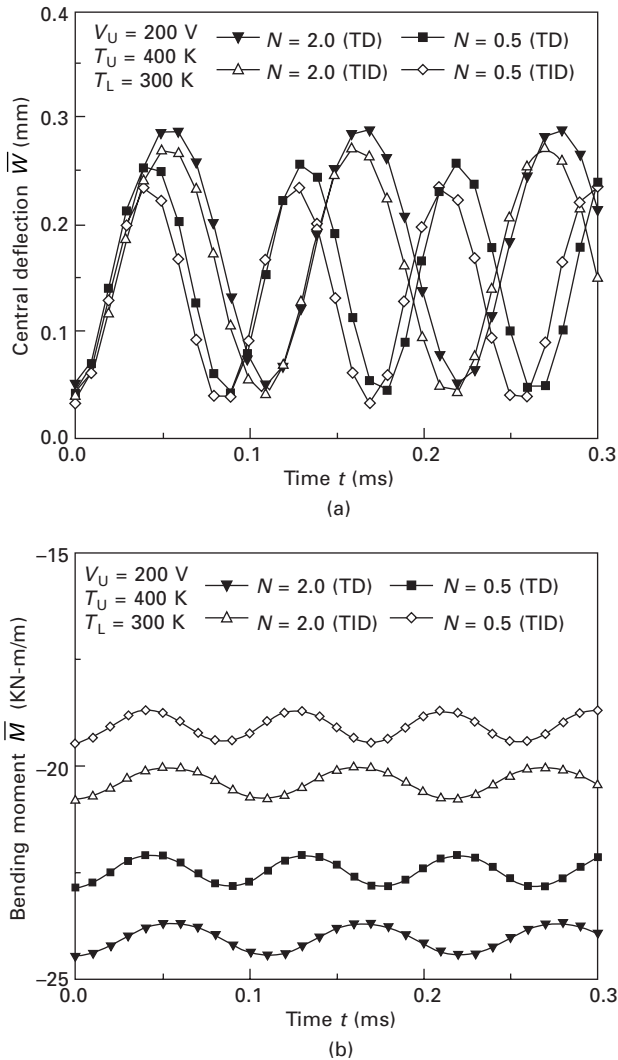
theory that includes thermo-piezoelectric effects. An improved perturbation technique is employed to determine nonlinear frequencies and dynamic responses of hybrid laminated plates. Numerical calculations have been made for (1) fiber-reinforced composite antisymmetric angle-ply and symmetric

Table 12.14 Effect of temperature field on nonlinear to linear frequency ratio  $\omega_{NL}/\omega_L$  for the hybrid FGM plates ( $N = 0.5$ )

	$\bar{W}_{max}/h$					
	0.0	0.2	0.4	0.6	0.8	1.0
<b>(P/FGM) (<math>V_U = +200</math> V), TID</b>						
$T_L = 300$ K, $T_U = 300$ K	1.000	1.019	1.075	1.161	1.272	1.402
$T_L = 300$ K, $T_U = 400$ K	1.000	1.022	1.084	1.182	1.306	1.450
$T_L = 300$ K, $T_U = 600$ K	1.000	1.026	1.099	1.211	1.352	1.515
<b>(P/FGM) (<math>V_U = +200</math> V), TD-F</b>						
$T_L = 300$ K, $T_U = 400$ K	1.000	1.022	1.085	1.182	1.307	1.451
$T_L = 300$ K, $T_U = 600$ K	1.000	1.025	1.096	1.205	1.343	1.502
<b>(P/FGM) (<math>V_U = +200</math> V), TD</b>						
$T_L = 300$ K, $T_U = 400$ K	1.000	1.022	1.085	1.183	1.307	1.452
$T_L = 300$ K, $T_U = 600$ K	1.000	1.025	1.096	1.206	1.345	1.504
<b>(P/FGM//P) (<math>V_U = V_L = +200</math> V), TID</b>						
$T_L = 300$ K, $T_U = 300$ K	1.000	1.018	1.071	1.153	1.259	1.384
$T_L = 300$ K, $T_U = 400$ K	1.000	1.022	1.087	1.186	1.313	1.460
$T_L = 300$ K, $T_U = 600$ K	1.000	1.035	1.134	1.282	1.464	1.670
<b>(P/FGM//P) (<math>V_U = V_L = +200</math> V), TD-F</b>						
$T_L = 300$ K, $T_U = 400$ K	1.000	1.023	1.087	1.187	1.315	1.462
$T_L = 300$ K, $T_U = 600$ K	1.000	1.034	1.128	1.271	1.447	1.645
<b>(P/FGM//P) (<math>V_U = V_L = +200</math> V), TD</b>						
$T_L = 300$ K, $T_U = 400$ K	1.000	1.023	1.088	1.188	1.316	1.464
$T_L = 300$ K, $T_U = 600$ K	1.000	1.033	1.128	1.270	1.445	1.643

Table 12.15 Effect of applied voltage on nonlinear to linear frequency ratio  $\omega_{NL}/\omega_L$  for the hybrid FGM plates in thermal environments ( $T_L = 300$  K,  $T_U = 400$  K,  $N = 2.0$ )

	$\bar{W}_{max}/h$					
	0.0	0.2	0.4	0.6	0.8	1.0
<b>(P/FGM), TID</b>						
$V_U = -200$ V	1.000	1.022	1.084	1.180	1.302	1.445
$V_U = 0$ V	1.000	1.022	1.084	1.180	1.303	1.446
$V_U = +200$ V	1.000	1.022	1.084	1.180	1.304	1.447
<b>(P/FGM), TD-F</b>						
$V_U = -200$ V	1.000	1.022	1.084	1.180	1.304	1.446
$V_U = 0$ V	1.000	1.022	1.084	1.181	1.304	1.447
$V_U = +200$ V	1.000	1.022	1.084	1.181	1.305	1.448
<b>(P/FGM), TD</b>						
$V_U = -200$ V	1.000	1.022	1.084	1.181	1.304	1.448
$V_U = 0$ V	1.000	1.022	1.084	1.181	1.305	1.448
$V_U = +200$ V	1.000	1.022	1.084	1.182	1.306	1.450
<b>(P/FGM/P), TID</b>						
$V_U = V_L = -200$ V	1.000	1.022	1.085	1.183	1.308	1.454
$V_U = V_L = 0$ V	1.000	1.022	1.086	1.186	1.312	1.458
$V_U = V_L = +200$ V	1.000	1.022	1.087	1.188	1.315	1.463
<b>(P/FGM/P), TD-F</b>						
$V_U = V_L = -200$ V	1.000	1.022	1.086	1.185	1.311	1.457
$V_U = V_L = 0$ V	1.000	1.022	1.087	1.187	1.314	1.462
$V_U = V_L = +200$ V	1.000	1.023	1.088	1.189	1.318	1.467
<b>(P/FGM/P), TD</b>						
$V_U = V_L = -200$ V	1.000	1.022	1.087	1.186	1.313	1.460
$V_U = V_L = 0$ V	1.000	1.023	1.088	1.188	1.316	1.465
$V_U = V_L = +200$ V	1.000	1.023	1.089	1.190	1.320	1.470



12.8 Effect of temperature dependency on the dynamic response of P/FGM plate subjected to a sudden load, control voltage and in thermal environments: (a) central deflection versus time; (b) central bending moment versus time.

cross-ply laminated plates; (2) unsymmetric cross-ply laminated plates with surface-bonded or embedded piezoelectric actuators; and (3) FGM plates with fully covered piezoelectric actuators. The results reveal that in these cases the plate has lower vibration frequencies and larger transient deflections when the temperature-dependent properties are taken into account. The results also confirm that the temperature field has a significant effect, but the control voltage only has a small effect on the nonlinear vibration characteristics of the hybrid laminated plate.

## 12.8 Acknowledgment

The support for this work, provided by the National Natural Science Foundation of China under Grant 59975058 and 50375091, is gratefully acknowledged.

## 12.9 References

- Attia O, El-Zafrany A (1999), ‘A nonlinear higher-order shear element for nonlinear vibration analysis of composite layered plates and shell’, *International Journal of Mechanical Sciences*, **41**, 461–486.
- Benjeddou A, Deü JF, Letcombe S (2002), ‘Free vibrations of simply-supported piezoelectric adaptive plates: an exact sandwich formulation’, *Thin-walled Structures*, **40**, 573–593.
- Bhimaraddi A (1987), ‘Nonlinear flexural vibration of rectangular plates subjected to in-plane forces using a new shear deformation theory’, *Thin-walled Structures*, **5**, 309–327.
- Bhimaraddi A (1992a), ‘Nonlinear free vibration of laminated composite plates’, *Journal of Engineering Mechanics ASCE*, **118**, 147–189.
- Bhimaraddi A (1992b), ‘Nonlinear dynamics of in-plane loaded imperfect rectangular plates’, *Journal of Applied Mechanics ASME*, **59**, 893–901.
- Bhimaraddi A (1993), ‘Large amplitude vibrations of imperfect antisymmetric angle-ply laminated plates’, *Journal of Sound and Vibration*, **162**, 457–470.
- Bhimaraddi A, Chandrasekhar K (1993), ‘Nonlinear vibrations of heated antisymmetric angle-ply laminated plates’, *International Journal of Solids and Structures*, **30**, 1255–1268.
- Chen C-S (2005), ‘Nonlinear vibration of a shear deformable functionally graded plate’, *Composite Structures*, **68**, 295–302.
- Chen C-S, Fung C-P (2004), ‘Nonlinear vibration of initially stressed hybrid composite plates’, *Journal of Sound and Vibration*, **274**, 1013–1029.
- Chen C-S, Cheng W-S, Chien R-D, Doong J-L (2002), ‘Large amplitude vibration of an initially stressed cross-ply laminated plates’, *Applied Acoustics*, **63**, 939–956.
- Chen IN, Dawe DJ, Wang S (2000), ‘Nonlinear transient analysis of rectangular composite laminated plates’, *Composite Structures*, **49**, 129–123.
- Chen J-K, Sun C-T (1985), ‘Nonlinear transient response of initially stressed composite plates’, *Computers and Structures*, **21**, 513–520.
- Chen L-W, Yang J-Y (1993), ‘Nonlinear vibration of antisymmetric imperfect angle-ply laminated plates’, *Composite Structures*, **23**, 39–46.
- Chia C-Y (1988), ‘Geometrically nonlinear behavior of composite plates: a review’, *Applied Mechanics Reviews*, **41**, 439–451.
- Chien R-D, Chen, C-S (2005), ‘Nonlinear vibration of laminated plates on a nonlinear elastic foundation’, *Composite Structures*, **70**, 90–99.
- Ganapathi M, Patel BP, Makhecha DP (2004), ‘Nonlinear dynamic analysis of thick composite/sandwich laminates using an accurate higher-order theory’, *Composites: Part B*, **35**, 345–355.
- He XQ, Ng TY, Sivashanker S, Liew KM (2001), ‘Active control of FGM plates with integrated piezoelectric sensors and actuators’, *International Journal of Solids and Structures*, **38**, 1641–1655.

- Huang X-L, Shen H-S (2004), 'Nonlinear vibration and dynamic response of functionally graded plates in thermal environments', *International Journal of Solids and Structures*, **41**, 2403–2427.
- Huang X-L, Shen H-S (2005), 'Nonlinear free and forced vibration of simply supported shear deformable laminated plates with piezoelectric actuators', *International Journal of Mechanical Sciences*, **47**, 187–208.
- Huang X-L, Shen H-S (2006), 'Vibration and dynamic response of functionally graded plates with piezoelectric actuators in thermal environments', *Journal of Sound and Vibration*, **289**, 25–53.
- Huang X-L, Zheng J-J (2003), 'Nonlinear vibration and dynamic response of simply supported shear deformable laminated plates on elastic foundations', *Engineering Structures*, **5**, 1107–1119.
- Huang X-L, Shen H-S, Zheng J-J (2004), 'Nonlinear vibration and dynamic response of shear deformable laminated plates in hygrothermal environments', *Composites Science and Technology*, **64**, 1419–1435.
- Ishihara M, Noda N (2003a), 'Nonlinear dynamic behaviour of a piezothermoelastic laminated plate with anisotropic material properties', *Acta Mechanica*, **166**, 103–118.
- Ishihara M, Noda N (2003b), 'Nonlinear dynamic behaviour of a piezothermoelastic laminate considering the effect of transverse shear', *Journal of Thermal Stresses*, **26**, 1093–1112.
- Kitipornchai S, Yang J, Liew KM (2004), 'Semi-analytical solution for nonlinear vibration of laminated FGM plates with geometric imperfections', *International Journal of Solids and Structures*, **41**, 2235–2257.
- Lee Y-S, Kim Y-W (1996), 'Analysis of nonlinear vibration of hybrid composite plates', *Computers and Structures*, **61**, 573–578.
- Lee YY, Ng CG (2001), 'Nonlinear response of composite of plates using the finite element model reduction method', *Engineering Structures*, **23**, 1104–1114.
- Liu C-F, Huang C-H (1996), 'Free vibration of composite laminated plates subjected to temperature changes', *Computers and Structures*, **60**, 95–101.
- Matsunaga H (2001), 'Vibration and stability of angle-play laminated composite plates subjected to in-plane stresses', *International Journal of Mechanical Sciences*, **43**, 1925–1944.
- Nath Y, Shukla KK (2001), 'Non-linear transient analysis of moderately thick laminated composite plates', *Journal of Sound and Vibration*, **247**, 509–526.
- Noor AK, Hadian MJ, Peters JM (1994), 'Reduced basis technique for evaluating the sensitivity of the nonlinear vibrational response of composite plates', *Computers and Structures*, **52**, 1097–1105.
- Oh IK, Han JH, Lee I (2000), 'Postbuckling and vibration characteristics of piezolaminated composite plate subjected to thermo-piezoelectric loads', *Journal of Sound and Vibration*, **233**, 19–40.
- Praveen GN, Reddy JN (1998), 'Nonlinear transient thermoelastic analysis of functionally graded ceramic-metal plates', *International Journal of Solids and Structures*, **35**, 4457–4476.
- Reddy JN (1983), 'Geometrically nonlinear transient analysis of laminated composite plates', *AIAA Journal*, **21**, 621–629.
- Reddy JN (1984a), 'A simple higher-order theory for laminated composite plates', *Journal of Applied Mechanics ASME*, **51**, 745–752.
- Reddy JN (1984b), 'A refined nonlinear theory of plates with transverse shear deformation', *International Journal of Solids and Structures*, **20**, 881–896.

- Reddy JN (2000), 'Analysis of functionally graded plates', *International Journal for Numerical Methods in Engineering*, **47**, 663–684.
- Reddy JN, Chin CD (1998), 'Thermoelastical analysis of functionally graded cylinders and plates', *Journal of Thermal Stresses*, **21**, 593–626.
- Reddy JN, Phan DN (1985), 'Stability and vibration of isotropic, orthotropic and laminated plates according to a high-order shear deformation plate theory', *Journal of Sound and Vibration*, **98**, 157–170.
- Ribiro P (2005), 'First-order shear deformation,  $p$ -version, finite element for laminated plate nonlinear vibrations', *AIAA Journal*, **43**, 1371–1379.
- Sathyamoorthy M (1987), 'Nonlinear vibration analysis of plates: a review and survey of current developments', *Applied Mechanics Reviews*, **40**, 1553–1561.
- Shen H-S (1997), 'Kármán-type equations for a higher-order shear deformation plate theory and its use in the thermal postbuckling analysis', *Applied Mathematics and Mechanics*, **18**, 1137–1152.
- Shen H-S (2001), 'Postbuckling of shear deformable laminated plates with piezoelectric actuators under complex loading conditions', *International Journal of Solids and Structures*, **38**, 7703–7721.
- Shen H-S (2002), 'Nonlinear bending response of functionally graded plates subjected to transverse loads and in thermal environments', *International Journal of Mechanical Sciences*, **44**, 561–584.
- Shen H-S (2004), 'Nonlinear bending analysis of unsymmetric cross-ply laminated plates with piezoelectric actuators in thermal environments', *Composite Structures*, **63**, 167–177.
- Shen H-S (2006), Thermal buckling and postbuckling of laminated plates. In *Analysis and Design of Plated Structures* (eds. N.E. Shanmugam and C.M. Wang), Vol. 1 Stability, pp. 170–213, Woodhead Publishing Ltd, Cambridge.
- Tenneti R, Chandrashekara RK (1994), 'Large amplitude flexural vibration of laminated plates using a higher order shear deformation theory', *Journal of Sound and Vibration*, **176**, 279–285.
- Touloukian YS (1967), *Thermophysical Properties of High Temperature Solid Materials*, Macmillan, New York.
- Xu KM, Noor AK, Tang YY (1997), 'Three-dimensional solutions for free vibration of initially stressed thermoelectroelastic multilayered plates', *Computer Methods in Applied Mechanics and Engineering*, **141**, 125–139.
- Yang J, Shen H-S (2001), 'Dynamic response of initially stressed functionally graded rectangular thin plates', *Composite Structures*, **54**, 497–508.
- Yang J, Kitipornchai S, Liew KM (2003), 'Large amplitude vibration of thermo-electric-mechanically stressed FGM laminated plates', *Computational Methods in Applied Mechanics and Engineering*, **192**, 3861–3885.
- Yang J-Y, Chen L-W (1993), 'Large amplitude vibration of antisymmetric imperfect cross-ply laminated plates', *Composite Structures*, **24**, 149–159.

## A hybrid strategy for parameter identification of plated structures

---

C G K O H and S L Z H A O National University of Singapore, Singapore

### 13.1 Introduction

System identification is essentially a process of determining parameters of a dynamic system based on input and output (I/O) observations. It is an important tool for structural health monitoring by identifying changes in structural stiffness parameters in a non-destructive way. By comparing the identified parameters with the original ones, information on the health condition of structures can be derived. Structural identification is the application of system identification to engineering structures and has become an important research topic in civil engineering. In recent years, many researchers have been involved in this field, thereby causing a rapid development in structural health monitoring and damage assessment. This is also needed in structural control, which is an efficient tool for adjusting the structure in case of undesirable forces, such as earthquake or severe weather.

Although structural identification has begun to see its application to special structures such as cable bridges, it has not been widely used for other forms of engineering structures. One reason is the high cost of instrumentation for structural identification, but rapid advances in sensor engineering mean the cost is likely to drop to an affordable level in the near future. The other reason is the numerical difficulty associated with structural identification, which is an inverse problem in nature. The lack of robust and efficient structural identification methods has inhibited the use of structural identification in practice.

### 13.2 Genetic algorithms (GA)

#### 13.2.1 General

For complex optimization problems with many unknowns, conventional methods are usually not feasible owing to several limitations, such as requiring a good initial guess, being too sensitive to noise and having the tendency of

converging to local optimal points. In recent years, unconventional methods have been developed which have great potential to deal with complex optimization problems. In particular, the use of genetic algorithms (GA) has many advantages over conventional methods, including population-to-population search, relative insensitivity to noise and relative ease of implementation. As an evolutionary algorithm, GA simulates the biological evolution based on Darwin's principle of 'survival of the fittest' (Holland, 1975). By means of selection, crossover and mutation, a good balance is generally achieved between exploitation and exploration.

Structural identification can be posed as an optimization problem involving minimization of errors between the estimated response and measured response, or maximization of fitness value as defined in the GA. The soft computing approach of GA has already been widely used in many fields, such as electrical, control, industrial and systems engineering, and more recently, on various inverse problems in civil engineering. Tesar and Drzik. (1995) used GA for the resonance tuning of structures in the ultimate dynamic state. Hegazy (1999) solved a time-cost trade-off problem in construction by applying the GA method. Doyle (1994) applied GA to identify the impact location on an aluminum beam. Zhao *et al.* (1997) researched into the damage detection and qualification for a rectangular plate by using GA. Specifically for large structural identification, Koh *et al.* (2000) proposed a 'modal GA' method to identify a fairly large system with 52 unknowns. Sub-structural identification methods employing GA were also developed to deal with large structural systems (Koh *et al.*, 2003).

### 13.2.2 Formulation

In nature, animals and plants that can adapt to the environment will have better chances to survive and prosper. In GA, the fitness function acts like the 'environment' factor. Each chromosome is evaluated by a fitness function, and thus the fitness value assigned controls the destiny of each chromosome. It is important to use a proper fitness function because it affects the identification results to a great extent. For the identification of plated structures as considered in this chapter, the fitness function is defined as the negative of the following mean-square error:

$$\varepsilon = \frac{\sum_{i=1}^M \sum_{j=1}^L |\ddot{u}_m(i, j) - \ddot{u}_e(i, j)|^2}{ML} \quad 13.1$$

where  $\ddot{u}_m$  = measured acceleration,  $\ddot{u}_e$  = estimated acceleration,  $M$  = number of measurement locations, and  $L$  = number of time steps. The lower the mean-square error, the higher is the fitness value. By minimizing the difference between measured accelerations and estimated accelerations, GA searches

unknown parameters towards the global optima. Estimated responses are obtained by forward analysis with trial parameters. The dynamic equation of the structural system can be written in matrix notation as follows:

$$\mathbf{M}\ddot{\mathbf{u}} + \mathbf{C}\dot{\mathbf{u}} + \mathbf{K}\mathbf{u} = \mathbf{P} \quad 13.2$$

where  $\mathbf{M}$  = mass matrix,  $\mathbf{C}$  = damping matrix,  $\mathbf{K}$  = stiffness matrix,  $\mathbf{u}$  = displacement vector, and  $\mathbf{P}$  = force vector. Rayleigh damping is adopted:

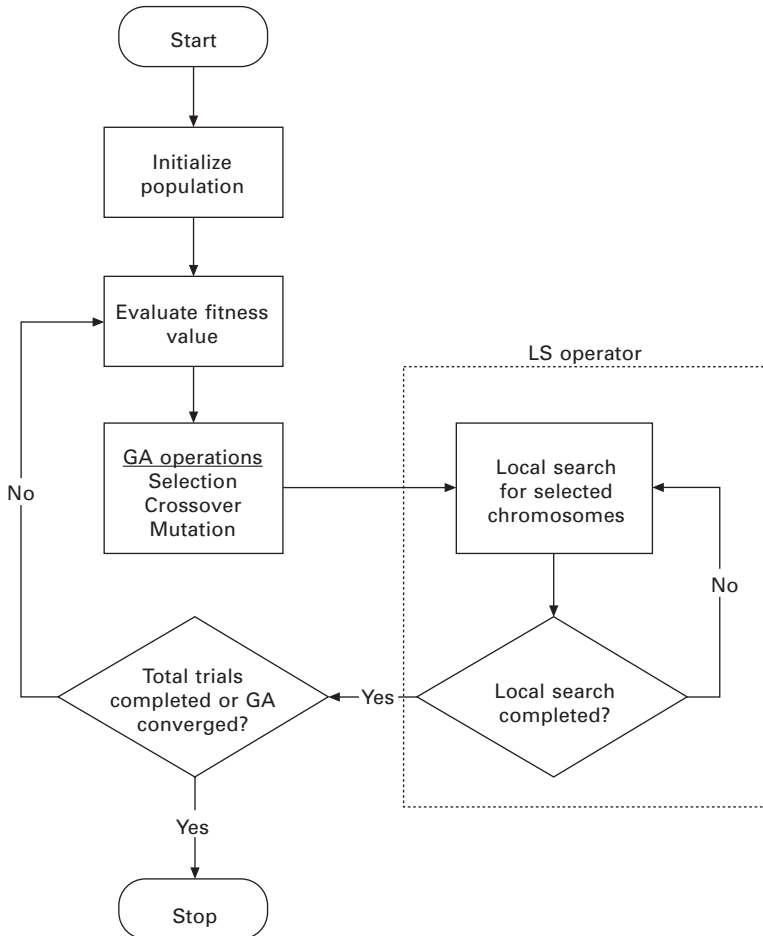
$$\mathbf{C} = \alpha\mathbf{M} + \beta\mathbf{K} \quad 13.3$$

where  $\alpha$  and  $\beta$  are damping coefficients which can be related to the damping ratios of two selected modes.

### 13.3 Hybrid GA-MV method

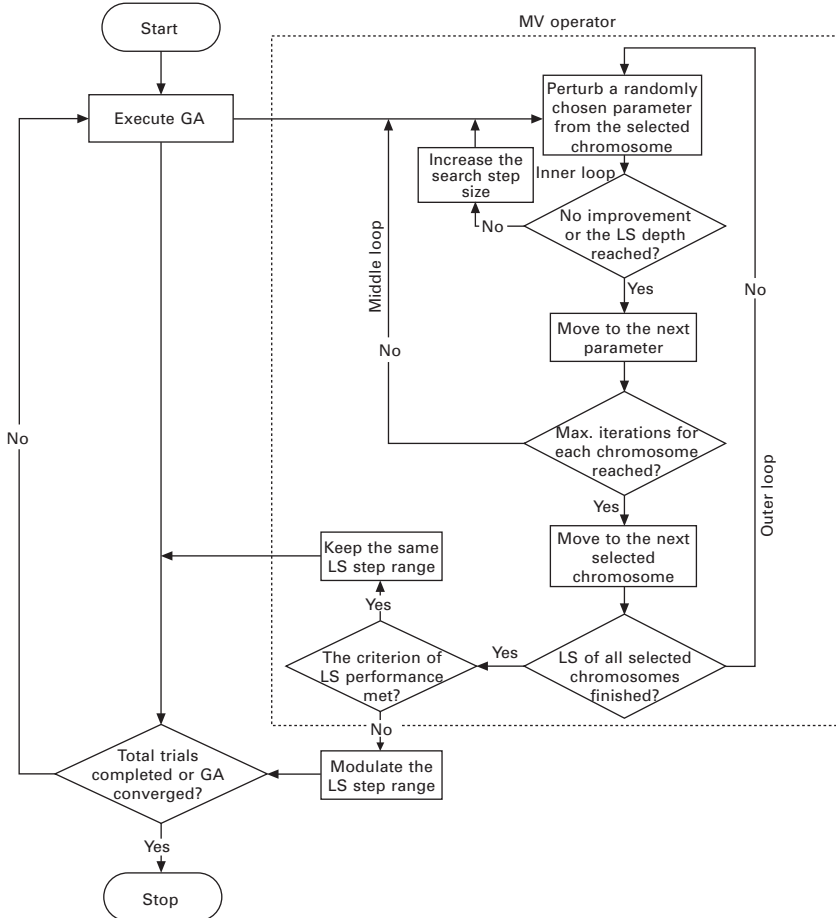
While the GA approach has many undeniable advantages, it is still a relatively new method for structural identification. A drawback is that the approach is not necessarily efficient in the fine-tuning, i.e. when the solution is near the global optimal solution, particularly for large systems. Thus, it is advantageous to incorporate a suitable local search (LS) method so as to improve the numerical efficiency and accuracy. In a broader context on optimization problems, some researchers have proposed various hybrid GA-LS methods. Porsani *et al.* (2000) introduced a hybrid GA-LS to solve the problem of seismic waveform inversion. Castillo *et al.* (2000) optimized multilayer perceptrons in a neural network by combining GA with local search. Magyar *et al.* (2000) used an adaptive hybrid GA for solving the three-matching problem in electrical and electronics engineering. Ye *et al.* (2000) applied a hybrid GA approach to the frame design of a hydroelectric set. To solve a pattern recognition problem, Yin (1999) identified circle and ellipse with a hybrid GA-LS technique.

The hybrid GA-LS approach has the beauties of both GA and local search. GA takes care of the global search while the embedded LS operator aims to fine-tune locally, as illustrated in Fig. 13.1. Koh *et al.* (2002) identified a 10-DOF structural system with 22 unknowns by a hybrid GA-LS approach, i.e. GA-MV (shown in Fig. 13.2). To the author's knowledge, this was the first study of GA-LS on structural identification. The LS operator proposed by Koh *et al.* (2002) is developed from a 'multivariate' (MV) method. It does not change GA's main algorithm and performs independently as a useful plug-in. Furthermore, the LS operator is easily implemented without forming gradients or derivatives in the process of identification. And most important, the fine-tuning work of local search is very adaptive. The step size of local search can be modulated automatically according to the efficiency of the LS operator.



13.1 Solution flowchart of the hybrid GA-LS approach.

Several operational parameters should be defined for the LS operation in advance, including  $[l_0, r_0]$ ,  $C_0$  ( $C_0 < 1$ ),  $I_0$ ,  $D_0$  and  $L_0$ .  $[l_0, r_0]$  is the LS step range,  $C_0$  is the performance criterion,  $I_0$  is the LS intensity (a ratio to the total number of population  $P_0$ ),  $D_0$  is the LS depth and  $L_0$  is the maximum iteration number for each chromosome. Let all the counters used in LS, i.e.  $p$ ,  $l$ ,  $n$ ,  $k$  and  $d$ , be zero initially. For each generation, the chromosomes are ranked from the best to the worst, and the top chromosomes are thereby selected based on LS intensity. Then the LS operator is applied to selected chromosomes one by one. The LS operator contains three loops, i.e. an inner loop, a middle loop and an outer loop, which operate on a gene, a chromosome and a population respectively. The three loops are described below.



13.2 Flowchart for hybrid GA-MV method.

- **Inner loop:** Perturb a parameter  $g$  selected randomly along the positive direction with a step size  $s$ , which lies within the range  $[l_k, r_k]$ . If the fitness value of  $g + s$  is better than  $g$ , replace  $g$  with  $g + s$ . Otherwise, perturb  $g$  along the negative direction. If the fitness value of  $g - s$  is better than  $g$ , replace  $g$  with  $g - s$ . Then let  $l_k$  be  $0.5(l_k + s)$ , and increase  $n$  by 1 and  $d$  by 1. If there is no improvement for the fitness value in both directions or if  $d$  reaches  $D_0$ , let  $d$  be zero and go to the middle loop.
- **Middle loop:** After each inner loop is finished, move to the next parameter and increase  $l$  by 1. Then return to the inner loop. If  $l$  reaches  $L_0$ , let  $l$  be zero and go to the outer loop.
- **Outer loop:** After each middle loop is finished, increase  $p$  by 1. Then move from the current chromosome to the next one, and return to the inner loop. If  $p$  reaches  $I_0 P_0$ , let  $p$  be zero, and stop the LS operation.

After the LS operation for the current generation, if  $n$  is less than the criterion  $C_0 L_0 I_0 P_0$ , the LS operation is viewed not efficient and the LS step range should be modulated from  $[l_0, r_0]$  to  $0.6[l_0, r_0]$ . Otherwise, keep the same LS step range. Then let  $n$  be zero and return to GA's global search for the next generation.

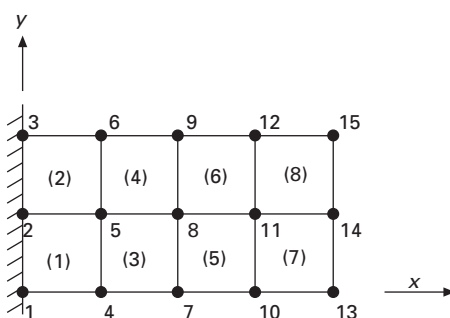
The numerical study here focuses on the comparison between the direct GA (without LS) and a hybrid GA-LS approach (GA-MV). Two cases regarding the identification of a cantilever plate are presented herein.

### 13.3.1 Case A

Consider a cantilever plate modeled by eight 4-node shell elements, as shown in Fig. 13.3. The size of the plate is  $1200 \times 600$  mm with four different thickness values:  $t_1 = 40$  mm for group 1 (elements 1 and 2),  $t_2 = 30$  mm for group 2 (elements 3 and 4),  $t_3 = 20$  mm for group 3 (elements 5 and 6) and  $t_4 = 10$  mm for group 4 (elements 7 and 8). Except for those along the fixed side, each node has three DOFs, viz.  $z$ -translation,  $x$ -rotation and  $y$ -rotation. The total number of DOFs of the plate model is 36. Effects of damping are included, by assuming 5% critical damping for the first two modes. Response measurement is numerically simulated for 0.1 s at time step of 0.0001 s by Wilson-theta algorithm (Bathe *et al.* 1974). The GA parameters are: crossover rate = 0.6, mutation rate = 0.001 and population size = 50. The search range is [0.5, 1.5] of the exact value.

The vertical excitation taken as the Gaussian white noise signal is assumed to apply at the 15th node, which would give, in addition to vertical translation, torsional response due to the asymmetry. Response measurements of accelerations are assumed to be available at the 4th–15th nodes. The number of unknown parameters is seven ( $t_i$  where  $i = 1$  to 4,  $E$  and two damping constants).

For fair comparison of identification accuracy, the time needed for the direct GA and the hybrid GA-LS approach should be about the same. The



13.3 Finite element mesh of an eight-element cantilever plate.

former is used with a total of 30 000 trials while the latter is used with 4500 trials. In the numerical study, an LS intensity of 60% appears to be optimal and is thus adopted. Three I/O noise levels are considered: 0%, 5% and 10%. As shown in Tables 13.1 and 13.2, the identification accuracy improves considerably due to the fine-tuning effort by the local search.

### 13.3.2 Case B

In this case, response measurements are assumed to be available at eight nodes (4th, 6th, 7th, 9th, 10th, 12th, 13th, 15th nodes). In terms of measurement availability, there are only eight DOFs measured out of a total of 36 (i.e. less than one-quarter availability). All other conditions are the same as Case A. As illustrated in Tables 13.3 and 13.4, more accurate identification results are obtained by the GA-MV method than the direct GA. Especially in the presence of 10% I/O noise, the mean and maximum errors decrease from 4.9% and 11.9% to 1.8% and 2.4%, respectively.

*Table 13.1 Identification results using the direct GA in Case A*

Parameter	Exact value	Estimated value					
		0% I/O noise		5% I/O noise		10% I/O noise	
		Value	Absolute error	Value	Absolute error	Value	Absolute error
$E_1$	70	67.22	3.97%	61.67	11.90%	69.44	0.80%
$t_1$	0.04	0.03968	0.80%	0.04413	10.33%	0.03714	7.15%
$t_2$	0.03	0.03167	5.57%	0.03071	2.37%	0.03262	8.73%
$t_3$	0.02	0.02016	0.80%	0.02206	10.30%	0.01984	0.80%
$t_4$	0.01	0.01024	2.40%	0.01056	5.60%	0.01008	0.80%
Mean absolute error		2.71%		8.10%		3.66%	
Max. absolute error		5.57%		11.90%		8.73%	

*Table 13.2 Identification results using the GA-MV method in Case A*

Parameter	Exact value	Estimated value					
		0% I/O noise		5% I/O noise		10% I/O noise	
		Value	Absolute error	Value	Absolute error	Value	Absolute error
$E_1$	70	69.44	0.80%	68.33	2.39%	66.11	5.56%
$t_1$	0.04	0.03968	0.80%	0.04032	0.80%	0.04159	3.98%
$t_2$	0.03	0.03071	2.37%	0.03024	0.80%	0.03024	0.80%
$t_3$	0.02	0.01984	0.80%	0.02048	2.40%	0.02111	5.55%
$t_4$	0.01	0.01008	0.80%	0.01008	0.80%	0.01024	2.40%
Mean absolute error		1.11%		1.44%		3.66%	
Max. absolute error		2.37%		2.40%		5.56%	

Table 13.3 Identification results using the direct GA in Case B

Parameter	Exact value	Estimated value					
		0% I/O noise		5% I/O noise		10% I/O noise	
		Value	Absolute error	Value	Absolute error	Value	Absolute error
$E_1$	70	66.11	5.56%	71.67	2.39%	69.44	0.80%
$t_1$	0.04	0.04286	7.15%	0.03778	5.55%	0.03651	8.73%
$t_2$	0.03	0.02976	0.80%	0.03119	3.97%	0.03357	11.90%
$t_3$	0.02	0.02079	3.95%	0.01952	2.40%	0.01952	2.40%
$t_4$	0.01	0.01024	2.40%	0.00992	0.80%	0.01008	0.80%
Mean absolute error		3.97%		3.02%		4.93%	
Max. absolute error		7.15%		5.55%		11.90%	

Table 13.4 Identification results using the GA-MV method in Case B

Parameter	Exact value	Estimated value					
		0% I/O noise		5% I/O noise		10% I/O noise	
		Value	Absolute error	Value	Absolute error	Value	Absolute error
$E_1$	70	68.33	2.39%	71.67	2.39%	68.33	2.39%
$t_1$	0.04	0.04095	2.38%	0.03841	3.98%	0.03968	0.80%
$t_2$	0.03	0.03024	0.80%	0.03071	2.37%	0.03071	2.37%
$t_3$	0.02	0.02016	0.80%	0.01952	2.40%	0.02048	2.40%
$t_4$	0.01	0.01008	0.80%	0.00992	0.80%	0.01008	0.80%
Mean absolute error		1.43%		2.39%		1.75%	
Max. absolute error		2.39%		3.98%		2.40%	

### 13.4 Two new local search operators

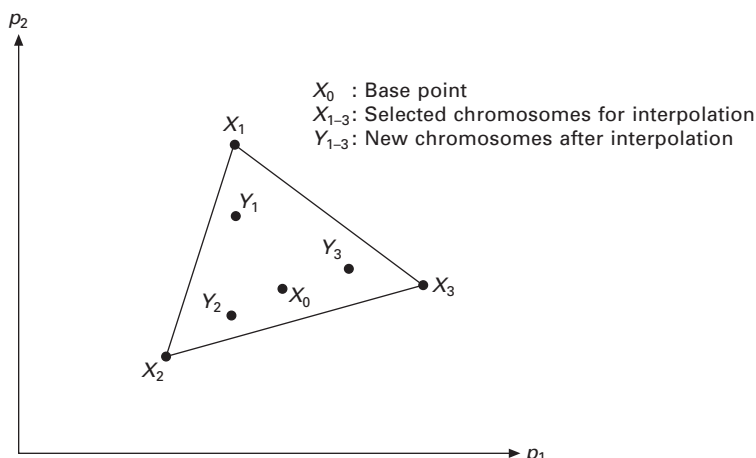
Improvement of LS efficiency is necessary in the interest of practical application. GA deals with structural identification problems by way of fitness evaluation. Once a new chromosome is generated, it will be evaluated by the objective function that aims to compare the exact response history with the estimated one. The finite element analysis is employed to get the estimated response for the plated structure to be identified. For plated structures with many DOFs, many new chromosomes will be evaluated within the search range during the whole identification process. Thus the computational cost on evaluations cannot be ignored and is a key factor of consideration in structural identification.

In this regard, the GA-MV method still has several shortcomings. First, the evaluation number required in the LS phase appears to be relatively high. The GA-MV method perturbs only one selected parameter at a time while other parameters are fixed. In addition, the unidirectional fine-tuning procedure

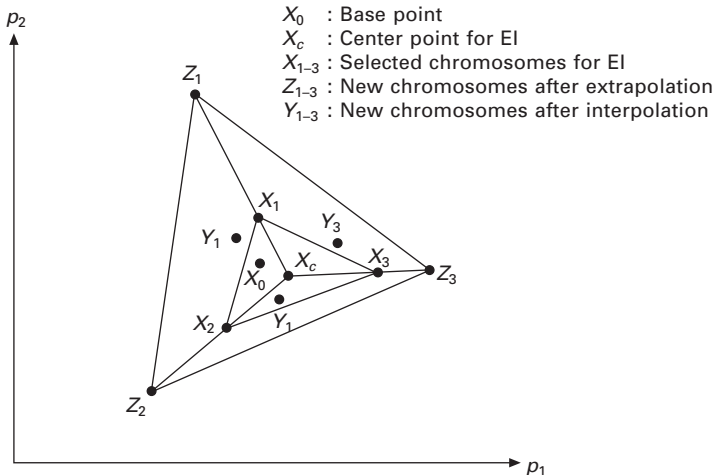
needs to adjust the LS step size for the selected parameter. These factors undoubtedly increase the number of evaluations.

Second, 60% of the chromosomes in a population participate in the fine-tuning for the GA-MV method. From the viewpoint of LS, it is not worth spending time on ordinary chromosomes. The purpose of LS is to seek better local chromosomes in the vicinity of well-performing ones. Although considering a number of ordinary chromosomes can avoid losing neighboring good ones, the cost on computational time is very high. For this reason, it is necessary to reduce the number of chromosomes selected for LS, and thus only well-performing individuals judged by some criteria should be considered.

In order to replace the LS operator in the GA-MV method, interpolation and extrapolation–interpolation (EI) operators are proposed herein. For illustration, the interpolation and EI operators for a two-dimensional identification problem (with two unknown parameters  $p_1$  and  $p_2$ ) are shown in Figs 13.4 and 13.5, respectively. The LS pool consists of only well-performing chromosomes (defined in Step 1 in the interpolation and EI operators as follows). In the interpolation operator,  $X_0$  is a randomly selected chromosome from the LS pool as the base point.  $X_1$ ,  $X_2$  and  $X_3$ , which are also randomly selected from the LS pool, are nearby well-performing chromosomes within a certain distance from  $X_0$ . By a linear three-point interpolation, three new chromosomes of  $Y_1$ ,  $Y_2$  and  $Y_3$  are generated. Among  $X_1$ ,  $X_2$ ,  $X_3$ ,  $Y_1$ ,  $Y_2$  and  $Y_3$ , the best three chromosomes are thereby used to replace  $X_1$ ,  $X_2$  and  $X_3$ . In the EI operator, a three-point extrapolation is conducted first after  $X_1$ ,  $X_2$  and  $X_3$  are selected, thereby forming three chromosomes of  $Z_1$ ,  $Z_2$  and  $Z_3$ . Then by a linear three-point interpolation of  $Z_1$ ,  $Z_2$  and  $Z_3$ , the new chromosomes of  $Y_1$ ,  $Y_2$  and  $Y_3$  are generated. Finally,



13.4 Illustration of local search by interpolation.



13.5 Illustration of local search by extrapolation–interpolation.

$X_1, X_2$  and  $X_3$  are replaced by the best three chromosomes among  $X_1, X_2, X_3, Y_1, Y_2$  and  $Y_3$ .

Both the interpolation and EI operators seek new chromosomes multidirectionally. Every parameter in selected chromosomes takes part in interpolation and/or extrapolation. In addition, only well-performing chromosomes are selected for the LS operation. Thus, the time spent on fine-tuning of ordinary chromosomes is avoided. The main difference between these two operators lies in the LS area. For the interpolation operator, new chromosomes are limited in the area surrounded by the triangle  $X_1X_2X_3$ . Nevertheless, for the EI operator, new chromosomes can be generated within or outside that area. For instance, in Fig. 13.5,  $Y_2$  is within the triangle  $X_1X_2X_3$ , while  $Y_1$  and  $Y_3$  are outside.

It is observed that the interpolation and EI operators adopt the three-point interpolation and/or extrapolation, rather than the two-point interpolation. New chromosomes are confined in a straight line if two-point interpolation and/or extrapolation is used. Nevertheless, the three-point interpolation and/or extrapolation generate new chromosomes in a plane, and thus the diversity of new chromosomes is enriched. The three-point interpolation and/or extrapolation can be extended to the four-point or five-point one, but evaluation time will increase. To keep a good balance between the diversity and the computational efficiency, the three-point interpolation and/or extrapolation are applied in this study.

Several parameters should be defined for the interpolation and EI operators. The factor of distance limit  $\mu$  ensures that three nearby chromosomes for interpolation or extrapolation are selected. The maximum iteration number  $t_0$  indicates the maximum iteration times for the two operators. In addition, the extrapolation limit  $\zeta$  is defined in the EI operator, which determines the

largest range for extrapolation. The procedures of the interpolation and EI operators are presented below in detail, which are also schematically illustrated in Figs 13.6 and 13.7, respectively.

### 13.4.1 Interpolation operator

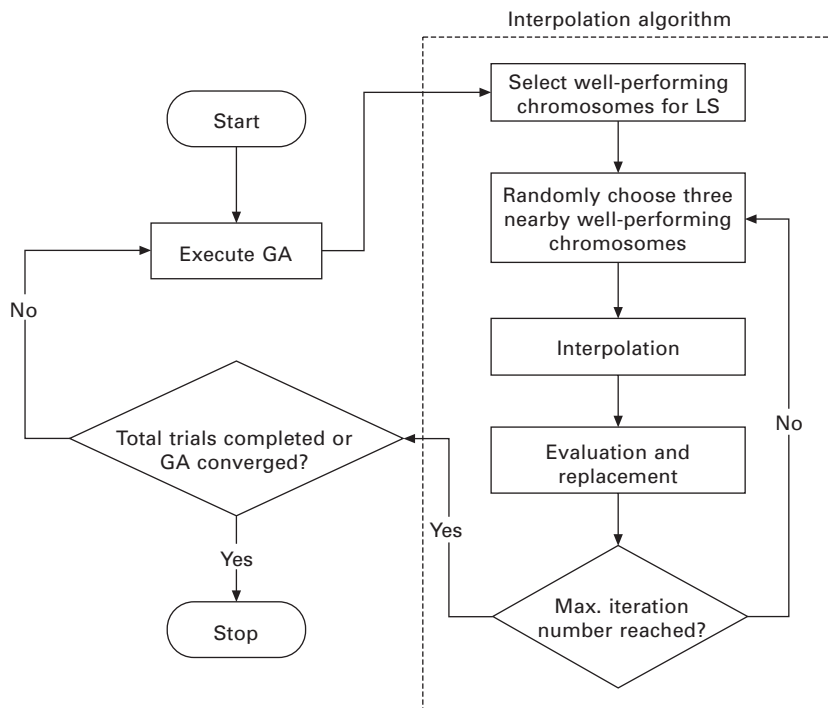
**Step 1:** In the current population, calculate the difference  $D$  of fitness value between the best chromosome and the worst one. Thereafter, compare every chromosome with the best one in terms of fitness value. If the difference is less than  $0.1D$ , the chromosome will be selected as a member of the LS pool.

**Step 2:** Randomly select a chromosome  $X_0(x_0^1, x_0^2, x_0^3, \dots, x_0^{n-1}, x_0^n)$  in the LS pool as the base point. Calculate the distance  $r$  between the base point and any other chromosome  $X_m(x_m^1, x_m^2, x_m^3, \dots, x_m^{n-1}, x_m^n)$  in the LS pool.

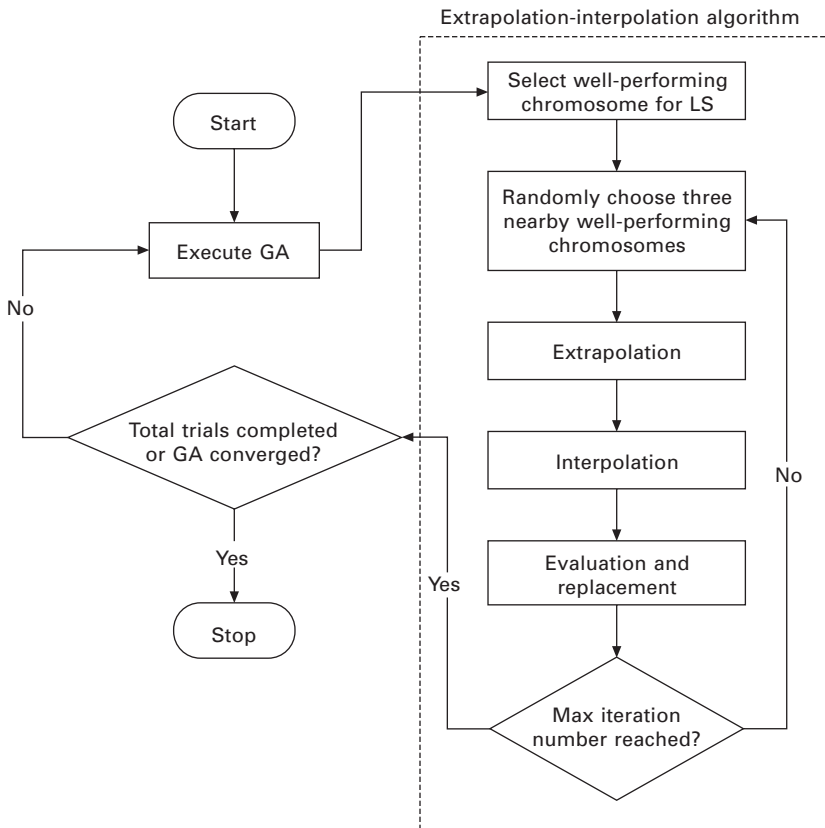
$$r = \sqrt{\sum_{i=1}^n (x_m^i - x_0^i)^2} \quad (i = 1, 2, \dots, n) \quad 13.4$$

The maximum distance  $R$  of the search space is defined as

$$R = \sqrt{\sum_{i=1}^n (M_1^i - M_2^i)^2} \quad (i = 1, 2, \dots, n) \quad 13.5$$



13.6 Flowchart for hybrid GA-interpolation approach.



13.7 Flowchart for hybrid GA-EI approach.

where  $M_1^i$  and  $M_2^i$  are the upper limit and lower limit of the search range for the  $i$ th gene. If  $r$  is less than  $\mu R$ , the chromosome  $X_m$  will enter the candidate pool.

**Step 3:** Randomly select three chromosomes from the candidate pool, viz.

$$X_1(x_1^1, x_1^2, x_1^3, \dots, x_1^{n-1}, x_1^n), X_2(x_2^1, x_2^2, x_2^3, \dots, x_2^{n-1}, x_2^n) \text{ and}$$

$$X_3(x_3^1, x_3^2, x_3^3, \dots, x_3^{n-1}, x_3^n)$$

For  $i = 1, 2, 3, \dots, n$ ,

$$y_1^i = \alpha_1 x_1^i + \alpha_2 x_2^i + \alpha_3 x_3^i \quad 13.6$$

$$y_2^i = \alpha_2 x_1^i + \alpha_3 x_2^i + \alpha_1 x_3^i \quad 13.7$$

$$y_3^i = \alpha_3 x_1^i + \alpha_1 x_2^i + \alpha_2 x_3^i \quad 13.8$$

where

$$\alpha_1 = \text{rand}(0, 1) \quad 13.9$$

$$\alpha_2 = \text{rand}(0, 1 - \alpha_1) \quad 13.10$$

$$\alpha_3 = 1 - \alpha_1 - \alpha_2 \quad 13.11$$

Therefore three new chromosomes are formed, viz.

$$Y_1(y_1^1, y_1^2, y_1^3, \dots, y_1^{n-1}, y_1^n), Y_2(y_2^1, y_2^2, y_2^3, \dots, y_2^{n-1}, y_2^n) \text{ and}$$

$$Y_3(y_3^1, y_3^2, y_3^3, \dots, y_3^{n-1}, y_3^n)$$

**Step 4:** Evaluate the new chromosomes  $Y_1$ ,  $Y_2$  and  $Y_3$ . Compare the fitness values of the six chromosomes  $X_1$ ,  $X_2$ ,  $X_3$ ,  $Y_1$ ,  $Y_2$  and  $Y_3$ . Select the best three chromosomes to replace  $X_1$ ,  $X_2$  and  $X_3$ .

**Step 5:** If the maximum iteration number  $t_0$  is reached, stop the interpolation and let GA generate a new population. Otherwise, return to Step 2.

### 13.4.2 Extrapolation-interpolation operator

**Steps 1 and 2:** Same as Steps 1 and 2 in the above interpolation operator.

**Step 3:** Randomly select three chromosomes from the candidate pool, viz.

$$X_1(x_1^1, x_1^2, x_1^3, \dots, x_1^{n-1}, x_1^n), X_2(x_2^1, x_2^2, x_2^3, \dots, x_2^{n-1}, x_2^n) \text{ and}$$

$$X_3(x_3^1, x_3^2, x_3^3, \dots, x_3^{n-1}, x_3^n)$$

Define the center  $X_c(x_c^1, x_c^2, x_c^3, \dots, x_c^{n-1}, x_c^n)$  of  $X_1$ ,  $X_2$  and  $X_3$  by

$$x_c^i = \frac{x_1^i + x_2^i + x_3^i}{3} \quad (i = 1, 2, \dots, n) \quad 13.12$$

**Step 4:** Use extrapolation to create three outer chromosomes, viz.

$$Z_1(z_1^1, z_1^2, z_1^3, \dots, z_1^{n-1}, z_1^n), Z_2(z_2^1, z_2^2, z_2^3, \dots, z_2^{n-1}, z_2^n) \text{ and}$$

$$Z_3(z_3^1, z_3^2, z_3^3, \dots, z_3^{n-1}, z_3^n)$$

$$z_1^i = x_c^i + \beta_1 \times (x_1^i - x_c^i) \quad 13.13$$

$$z_2^i = x_c^i + \beta_2 \times (x_2^i - x_c^i) \quad 13.14$$

$$z_3^i = x_c^i + \beta_3 \times (x_3^i - x_c^i) \quad (i = 1, 2, \dots, n) \quad 13.15$$

where  $\beta_1$ ,  $\beta_2$  and  $\beta_3$  are random real numbers between 1 and  $\zeta$  (extrapolation limit).

**Step 5:** Based on the outer chromosomes  $Z_1$ ,  $Z_2$  and  $Z_3$ , interpolation is executed to form three new chromosomes, viz.

$$Y_1(y_1^1, y_1^2, y_1^3, \dots, y_1^{n-1}, y_1^n), Y_2(y_2^1, y_2^2, y_2^3, \dots, y_2^{n-1}, y_2^n) \text{ and}$$

$$Y_3(y_3^1, y_3^2, y_3^3, \dots, y_3^{n-1}, y_3^n)$$

$$y_1^i = \alpha_1 \times z_1^i + \alpha_2 \times z_2^i + \alpha_3 \times z_3^i \quad 13.16$$

$$y_2^i = \alpha_2 \times z_1^i + \alpha_3 \times z_2^i + \alpha_1 \times z_3^i \quad 13.17$$

$$y_3^i = \alpha_3 \times z_1^i + \alpha_1 \times z_2^i + \alpha_2 \times z_3^i \quad (i = 1, 2, \dots, n) \quad 13.18$$

$$\alpha_1 = rand(0, 1) \quad 13.19$$

$$\alpha_2 = rand(0, 1 - \alpha_1) \quad 13.20$$

$$\alpha_3 = 1 - \alpha_1 - \alpha_2 \quad 13.21$$

**Steps 6 and 7:** Same as Steps 4 and 5 in the interpolation operator.

## 13.5 Identification of plated structure

### 13.5.1 Modeling of an aircraft wing

The three GA-LS methods are now applied to a plated structure which resembles an airforce aircraft wing model. The main challenge lies in reducing the computational cost, viz. how to identify unknown parameters in a manageable time frame using desktop PC technology. The structure is modeled by quadrilateral shell elements and thus the time needed to carry out the forward analysis (i.e. step-by-step integration of equations of motion) is very long. For practical parameter identification such as estimation of thickness and elastic modulus values of several groups, it may not be necessary or worthwhile to have a very refined FE model (525 elements), as shown in Fig. 13.8. Hence, it is justifiable to reduce the model size without losing its main dynamic characteristics, e.g. the first 20 modes that are of interest to the analysis and design in this case.

Based on this ‘reduced model’ approach, the number of elements is 48, as shown in Fig. 13.9. Four element groups are considered, each group having its own geometric and material properties (their exact values are shown in Table 13.5):

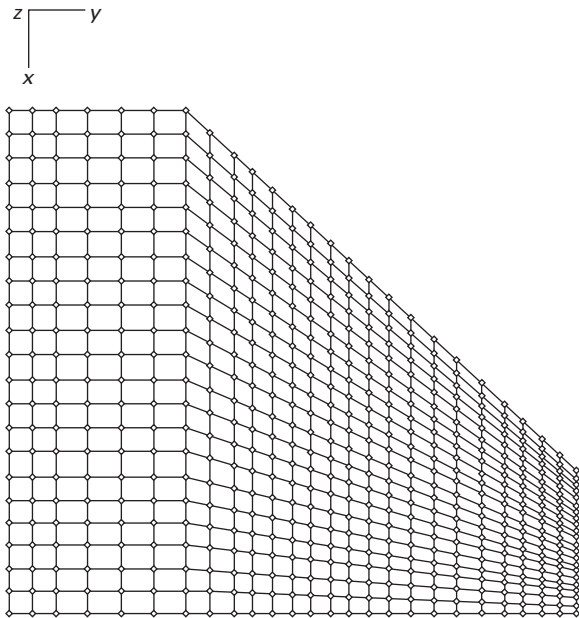
Group 1: Elements 1–12

Group 2: Elements 13–24

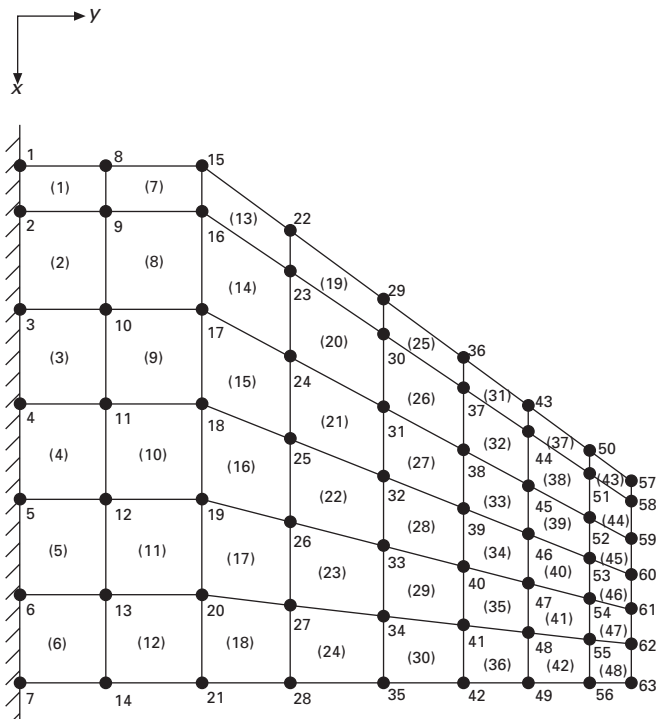
Group 3: Elements 25–36

Group 4: Elements 3–48

Furthermore, in view of the dynamic modes of interest, it is possible to reduce the number of time steps from 1000 to 200 at time step of 0.0001 in the simulations. In this way, there is a significant saving of computational time, with little effect on the natural frequencies of the first 20 modes. The mean error of natural frequencies between the refined FE model (525 elements) and the reduced FE model (48 elements) is found to be only 1.6%, and the maximum error is less than 5%, as shown in Table 13.6.



13.8 Finite element model of a 525-element plate.



13.9 Finite element model of a 48-element plate.

Table 13.5 Comparison of identification results with 0% I/O noise for a typical run

Parameter	Exact value	Estimated value					
		GA-MV		GA-interpolation		GA-EI	
		Value	Absolute error	Value	Absolute error	Value	Absolute error
$E_1$	70	63.12	9.83%	74.33	6.19%	76.59	9.41%
$E_2$	70	73.06	4.37%	72.16	3.09%	65.67	6.19%
$E_3$	70	70.39	0.56%	69.65	0.50%	70.39	0.56%
$E_4$	70	67.06	4.20%	64.40	8.00%	65.22	6.83%
$t_1$	0.012	0.01237	3.08%	0.01167	2.75%	0.01171	2.42%
$t_2$	0.012	0.01191	0.75%	0.01194	0.50%	0.01234	2.83%
$t_3$	0.006	0.00609	1.50%	0.00618	3.00%	0.00613	2.17%
$t_4$	0.0045	0.004488	0.27%	0.004501	0.02%	0.004485	0.33%
Mean absolute error		3.07%		3.01%		3.84%	
Max. absolute error		9.83%		8.00%		9.41%	

Table 13.6 Comparison of natural frequencies between the refined model and the reduced model

Mode no.	Natural frequency (Hz) based on 525 elements	Natural frequency (hz) based on 48 elements	Absolute error
1	84.37	83.24	1.34%
2	226.32	224.41	0.84%
3	300.17	294.75	1.81%
4	464.09	458.68	1.17%
5	672.27	655.24	2.53%
6	721.93	699.64	3.09%
7	982.14	958.11	2.45%
8	1134.93	1132.70	0.20%
9	1194.30	1159.28	2.93%
10	1423.32	1418.23	0.36%
11	1672.71	1609.05	3.81%
12	1768.21	1777.76	0.54%
13	1790.49	1817.55	1.51%
14	1979.88	1965.56	0.72%
15	2110.39	2096.07	0.68%
16	2269.54	2269.54	0.00%
17	2468.49	2415.97	2.13%
18	2723.13	2694.49	1.05%
19	3012.80	2863.19	4.97%
20	3074.87	3082.82	0.26%
Mean absolute error		1.62%	
Max. absolute error		4.97%	

### 13.5.2 Parameter identification of an aircraft wing model

Even with the reduced model, the total number of DOFs is 280. Considering that response measurements (vertical accelerations) are available at 32 nodes,

information availability is less than one-eighth, making the task of parameter identification a difficult one.

There are ten unknown parameters, including four Young's moduli, four thickness values and two damping coefficients. The vertical excitation taken as the Gaussian white noise is assumed to apply at node 63. Two I/O noise levels are considered: 0% (i.e. no noise) and 10%.

The main GA parameter values are all the same for the three GA-LS methods considered. The population size is 50, the search range [0.7, 1.3], the crossover rate 0.6 and the mutation rate 0.001. The parameter values for the LS operator of the three methods are set as follows, which have been tested to be suitable for most cases:

- **MV:** The LS intensity  $I_0$  is 0.6, the LS step range is [2, 4], the maximum iteration number  $L_0$  is 6, and the LS depth  $D_0$  is 2.
- **Interpolation:** The factor of distance limit  $\mu$  is 0.3, and the maximum iteration number is 30.
- **EI:** The factor of distance limit  $\mu$  is 0.3, the extrapolation limit  $\zeta$  is 6, and the maximum iteration number is 30.

In order to reduce the bias caused by the effect of initial populations, five cases are carried out to get an overall performance with different random seeds. For the purpose of fair comparison, the number of evaluations should be the same, and 32000 evaluations are thus used for each of the three GA-LS methods. Identification results for one typical run with the same initial population for all three GA-LS methods are compared in Tables 13.5 and 13.7 for 0% and 10% I/O noise levels, respectively. Table 13.5 shows the mean and maximum errors for three hybrid GA-LS methods are very close in the absence of I/O noise (ideal case). But in the presence of 10% I/O

*Table 13.7 Comparison of identification results with 10% I/O noise for a typical run*

Para-meter	Exact value	Estimated value					
		GA-MV		GA-interpolation		GA-EI	
		Value	Absolute error	Value	Absolute error	Value	Absolute error
$E_1$	70	82.50	17.86%	68.62	1.97%	78.31	11.87%
$E_2$	70	50.15	28.36%	75.85	8.36%	67.52	3.54%
$E_3$	70	69.61	0.56%	68.46	2.20%	68.79	1.73%
$E_4$	70	71.79	2.56%	66.24	5.37%	64.85	7.36%
$t_1$	0.012	0.01183	1.42%	0.01184	1.33%	0.01155	3.75%
$t_2$	0.012	0.01340	11.67%	0.01174	2.17%	0.01210	0.83%
$t_3$	0.006	0.00598	0.33%	0.00617	2.83%	0.00618	3.00%
$t_4$	0.0045	0.004520	0.44%	0.004538	0.84%	0.004538	0.84%
Mean absolute error		7.90%		3.13%		4.12%	
Max. absolute error		28.36%		8.36%		11.87%	

noise, the mean and maximum errors for GA-MV increase to 7.90% and 28.36%, respectively. The corresponding errors for GA-EI and GA-Interpolation are significantly smaller, as shown in Table 13.7. The overall performance of three GA-LS methods is assessed based on the identification results for the five different cases of initial populations. The results are summarized in Tables 13.8 and 13.9 which show that the identification results by using GA-EI are the most accurate. The overall mean and maximum errors obtained by GA-EI are the lowest without and with I/O noise.

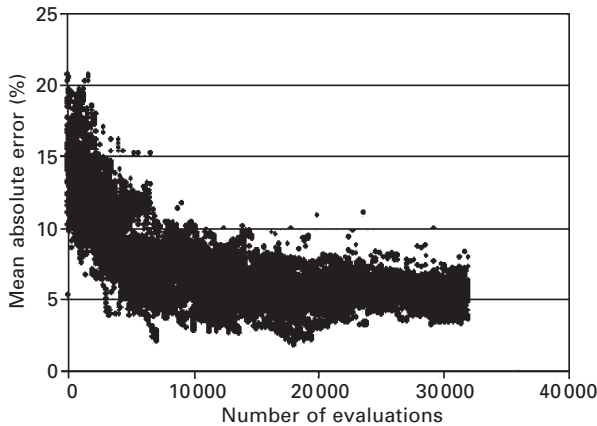
The scatter of mean absolute errors versus evaluations is studied for a typical run with the same initial population for all three GA-LS methods without I/O noise. The diversity of chromosomes is reflected by this scatter which shows the performance of chromosomes. The larger the performance of chromosomes differs, the more the diversity of chromosomes tends to be. It is noted that the diversity of chromosomes for the GA-Interpolation method is much less than for GA-MV and GA-EI, as shown in Figs 13.10–13.12. After a certain number of evaluations, most chromosomes have roughly the same mean error of 3%. For GA-interpolation, deficiency in diversity results from the fact that the interpolation is carried out within the area limited by

*Table 13.8 Overall comparison of three GA-LS methods with 0% I/O noise*

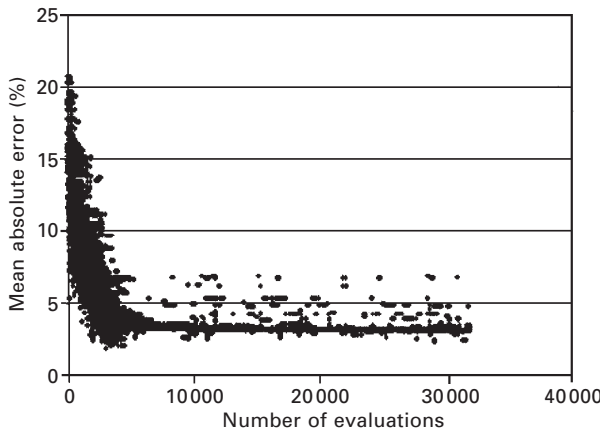
Different initial seeds	Mean absolute error			Max. absolute error		
	GA-MV	GA-interpolation	GA-EI	GA-MV	GA-interpolation	GA-EI
Case 1	3.07%	3.01%	3.84%	9.83%	8.00%	9.41%
Case 2	2.87%	4.64%	3.64%	7.89%	12.46%	7.60%
Case 3	0.92%	5.07%	1.58%	3.26%	10.00%	4.01%
Case 4	3.69%	3.21%	2.37%	11.93%	8.66%	4.84%
Case 5	3.98%	2.02%	1.57%	10.47%	5.84%	2.79%
Overall mean value	2.91%	3.59%	2.60%	8.67%	8.99%	5.73%

*Table 13.9 Overall comparison of three GA-LS methods with 10% I/O noise*

Different initial seeds	Mean absolute error			Max. absolute error		
	GA-MV	GA-interpolation	GA-EI	GA-MV	GA-interpolation	GA-EI
Case 1	7.90%	3.13%	4.12%	28.36%	8.36%	11.87%
Case 2	7.65%	4.33%	3.44%	16.57%	10.17%	9.83%
Case 3	6.25%	8.87%	2.04%	17.10%	14.76%	5.77%
Case 4	3.86%	1.30%	2.54%	13.57%	3.79%	9.41%
Case 5	3.75%	3.42%	3.83%	10.30%	9.36%	7.36%
Overall mean value	5.88%	4.21%	3.19%	17.18%	9.29%	8.85%



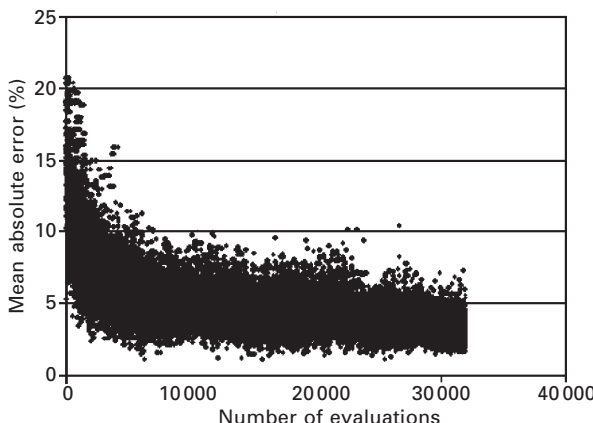
13.10 Scatterness of identification errors by using GA-MV method without I/O noise.



13.11 Scatterness of identification errors by using GA-interpolation method without I/O noise.

the selected three points, thereby losing the exploration of possible better points outside the three points. When the GA-interpolation method continues running for several generations, the chromosomes in one population will concentrate on a gradually smaller area at the expense of exploring outside the area. Thus, while it is possible to get good results by this method, there is also a higher risk of converging to wrong local optimal points.

The above study assumes that the exact values of parameters are known in advance, which is used to evaluate and compare the performance of three hybrid GA-LS methods. Nevertheless, in reality, it is impossible to know the exact values of parameters to be identified. The question is how to select the ‘best’ set of identified values from the five sets of identification results. In this regard, it is proposed that the identified values of each parameter be



13.12 Scatterness of identification errors by using GA-EI method without I/O noise.

averaged in order to reduce biases caused by the stochastic nature of the GA-LS method. Accordingly, the average results are presented in Tables 13.10 and 13.11 for 0% and 10% noise levels, respectively. It can be seen that the GA-EI method gives the lowest mean error of 0.96% and maximum error of 2.95% without I/O noise. In the case of 10% I/O noise, the GA-EI method and the GA-interpolation method performs equally well and better than GA-MV. Overall, it may be concluded that the GA-EI method is the best in terms of convergence rate, accuracy and consistency among the three GA-LS methods. Therefore, the GA-EI method is preferred over the other two methods considered and is strongly recommended for practical application.

## 13.6 Conclusions

The success of structural identification for real problems depends to a great extent on the robustness and efficiency of the methods. It is noted that the soft computing approach of GA offers a powerful tool for tackling challenging problems because of its many attractive advantages. In particular, the GA method enhances the chances of converging to global optimal point by the population-to-population search rather than the point-to-point search. This method can be easily implemented without complex mathematical formulations. It does not need a good initial guess for unknown parameters. All of these make GA more and more popular among researchers in various disciplines requiring optimization.

Despite its many merits, GA lacks fine-tuning efforts when near the global optimal solution. To overcome this shortcoming, local search (LS) operation is necessary to form the hybrid GA-LS method, with global search and local search alternating in the process of identification. An existing hybrid GA-LS

Table 13.10 Average identified values with 0% I/O noise based on five different cases of initial populations

Para- meter	Exact value	Estimated value					
		GA-MV		GA-interpolation		GA-EI	
		Value	Absolute error	Value	Absolute error	Value	Absolute error
$E_1$	70	67.97	2.89%	72.30	3.29%	72.06	2.95%
$E_2$	70	72.83	4.05%	70.53	0.76%	68.94	1.52%
$E_3$	70	70.85	1.22%	66.79	4.58%	70.78	1.12%
$E_4$	70	70.04	0.06%	71.02	1.46%	69.69	0.45%
$t_1$	0.012	0.01207	0.62%	0.01187	1.07%	0.01191	0.75%
$t_2$	0.012	0.01185	1.23%	0.01196	0.32%	0.01206	0.50%
$t_3$	0.006	0.00599	0.17%	0.00602	0.27%	0.00601	0.13%
$t_4$	0.0045	0.004476	0.54%	0.004575	1.66%	0.004488	0.26%
Mean absolute error		1.35%		1.68%		0.96%	
Max. absolute error		4.05%		4.58%		2.95%	

Table 13.11 Average identified values with 10% I/O noise based on five different cases of initial populations

Para- meter	Exact value	Estimated value					
		GA-MV		GA-Interpolation		GA-EI	
		Value	Absolute error	Value	Absolute error	Value	Absolute error
$E_1$	70	74.81	6.87%	69.43	0.81%	69.77	0.33%
$E_2$	70	61.44	12.23%	70.356	0.51%	67.42	3.69%
$E_3$	70	69.52	0.69%	67.92	2.97%	69.48	0.75%
$E_4$	70	73.26	4.65%	67.632	3.38%	73.13	4.48%
$t_1$	0.012	0.011916	0.70%	0.01196	0.37%	0.01204	0.30%
$t_2$	0.012	0.012554	4.62%	0.01207	0.58%	0.01212	0.98%
$t_3$	0.006	0.005952	0.80%	0.00614	2.27%	0.00594	0.93%
$t_4$	0.0045	0.004521	0.47%	0.004560	1.33%	0.004524	0.53%
Mean absolute error		3.88%		1.53%		1.50%	
Max. absolute error		12.23%		3.38%		4.48%	

method, i.e. GA-MV, is compared with the direct GA (without LS) in the numerical study with regards to identification of a cantilever plate. The hybrid GA-MV method performs better than the direct GA, even when response measurements are not complete and I/O information is contaminated with noise (up to 10% considered here).

Nevertheless, there are two factors that may adversely affect the efficiency of the GA-MV method. First, the MV operator searches unidirectionally, perturbing only one selected parameter at a time while other parameters are kept fixed. Second, the MV operator spends unnecessary time on a high

proportion of ordinary chromosomes for fine-tuning in a population. Two new LS operators, interpolation and extrapolation-interpolation (EI), are thus proposed to speed up the convergence rate and to improve the identification accuracy. Unlike the MV operator, interpolation and EI search multidirectionally, generating new local points based on the interpolation and/or extrapolation of all parameters. In addition, interpolation and EI only consider top chromosomes for fine-tuning in a population. Numerical studies are carried out for identification of a plated structure modeling an aircraft wing with a total of 280 DOFs. It is demonstrated that the hybrid GA-EI method gives the best identification results, based on the overall performance for five cases with different initial seeds.

### 13.7 Acknowledgment

The authors are grateful to the DSO National Laboratories (Singapore) for providing the research grant. The financial support by means of research scholarship provided by the National University of Singapore to the second author is also greatly appreciated.

### 13.8 References

- Bathe, K. J., Wilson, E. L. and Peterson, F. E. (1974). *SAP IV: a Structural Analysis Program for Static and Dynamic Response of Linear Systems*, University of California, Berkeley.
- Castillo, P. A., Merelo, J. J., Prieto, A., Rivas, V. and Romero, G. (2000). ‘G-Prop: global optimization of multilayer perceptrons using GAs.’ *Neurocomputing*, **35**, 149–163.
- Doyle, J. F. (1994). ‘A genetic algorithm for determining the location of structural impacts.’ *Exp. Mech.*, **34**, 37–44.
- Hegazy, T. (1999). ‘Optimization of construction time–cost trade-off analysis using genetic algorithms.’ *Canadian Journal of Civil Engineering*, **26**(6), 685–697.
- Holland, J. (1975). *Adaptation in Natural and Artificial Systems*, University of Michigan Press, Ann Arbor.
- Koh, C. G., Chen, Y. F. and Liaw, C. Y. (2002). ‘A hybrid computational strategy for identification of structural parameters.’ *Computers and Structures*, **81**, 107–117.
- Koh, C. G., Hong, B. and Liaw, C. Y. (2000). ‘Parameter identification of large structural systems in time domain.’ *Journal of Structural Engineering*, **126**(8), 957–963.
- Koh, C. G., Hong, B. and Liaw, C. Y. (2003). ‘Substructural and progressive structural identification methods.’ *Engineering Structures*, **25**, 1551–1563.
- Magyar, G., Johnsson, M. and Nevalainen, O. (2000). ‘An adaptive hybrid genetic algorithm for the three-matching problem.’ *IEEE Transactions on Evolutionary Computation*, **4**(2), 135–146.
- Porsani, M. J., Stoffa, P. L., Sen, M. K. and Chunduru, R. K. (2000). ‘Fitness functions, genetic algorithms and hybrid optimization in seismic waveform inversion.’ *Journal of Seismic Exploration*, **9**(2), 143–164.
- Tesar, A. and Drzik, M. (1995). ‘Genetic algorithms for dynamic tuning of structures.’ *Computers & Structures*, **57**(2), 287–295.

- Ye, Z. P., Li, X. L. and Dang, C. Y. (2000). 'Optimization of the main parts of hydroelectric sets using hybrid genetic algorithm.' *Journal of Materials Processing Technology*, **105**, 152–160.
- Yin, P. Y. (1999). 'A new circle/ellipse detector using genetic algorithms.' *Pattern Recognition Letters*, **20**, 731–740.
- Zhao, F., Zeng, X. and Louis, S. (1997). 'Genetic algorithms for inverse problem solutions.' *Computing in Civil Engineering Proceedings of the 4th Congress Held in Conjunction with A/E/C*, 725–732.

## Hydroelastic analysis of floating plated structures

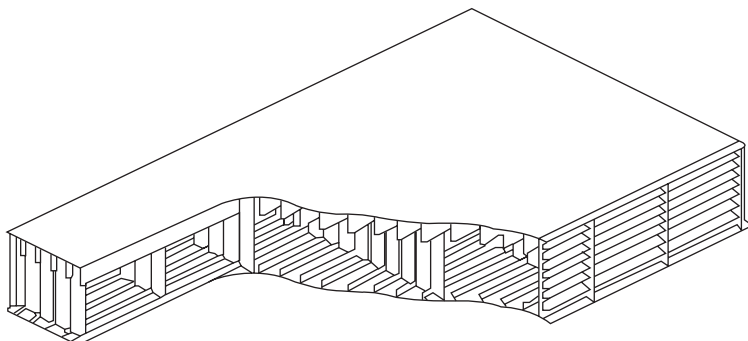
T U T S U N O M I Y A, Kyoto University, Japan

### 14.1 Introduction

The construction of the Mega-Float, a test runway of 1 km long and 60–120 m wide and 3 m deep in 1998 sparked off a considerable interest in very large floating structures (VLFS). Engineers became excited about the numerous applications of VLFS and many research studies have been conducted (see, for example, Kashiwagi, 2000; Watanabe *et al.*, 2004a; Newman, 2005; Ohmatsu, 2005; Suzuki, 2005) to refine this innovative technology, which has considerably advantages over the traditional land reclamation solution for creating land from the sea. Some of these advantages include the economic viability of floating structures when the water depth is deep and the seabed is soft, the minimal effect that it has on the marine environment, current flow and water quality, its shorter construction time and the fact that it is inherently base isolated that makes it ideal for use in seismic regions. VLFS has so far been used as floating oil storage tanks, floating piers and emergency bases (Watanabe *et al.*, 2004b).

Most VLFS that were built in Japan are essentially large steel-plated structures as shown in Fig. 14.1. Owing to their relatively small depth in relation to length dimensions, pontoon-type VLFS are relatively flexible and behave like an elastic plate, unlike ships that behave like rigid bodies. In the design of such a structure, the dynamic response due to waves must be accurately estimated. Apart from a vibrating plate in air, a vibrating plate on water is much influenced by the reaction pressures from the water. The effect is basically represented as added-mass and radiation damping. These terms can be calculated by using the potential theory for the fluid, assuming that the fluid is incompressible and inviscid and the fluid motion to be irrotational. Past studies indicate that these assumptions are basically acceptable for estimating flexural responses of a pontoon-type VLFS.

This chapter is concerned with the hydroelastic analysis of floating plated structures (or VLFS). The hydroelastic analysis may be carried out using the modal expansion approach. In this approach, the fluid part could be solved



14.1 General section for plated mega-float (courtesy of Ship Research Center of Japan).

by the higher-order boundary element method (HOBEM) using eight-noded quadrilateral panels (Utsunomiya *et al.*, 1998). The floating structure is modeled as an elastic thin plate and its dynamic response is assumed to comprise modal functions represented by products of the modal function of freely vibrating beams.

In solving the fluid part, it is very time consuming even with the use of a super-computer because the BEM generates a full matrix with large number of unknowns. The computer resources are of the order  $O(N^2)$  for storage and with either  $O(N^2)$  or  $O(N^3)$  for CPU time depending on the selection of the solver either as an iterative type or an LU-factorization type, where  $N$  represents the number of unknowns for fluid part.

In order to overcome the aforementioned computational difficulties, researchers have proposed the use of the finite element method (FEM) where band storage characteristics of the system matrix are utilized (e.g. Seto *et al.*, 2005), or by the semi-analytical approaches (e.g. Ohmatsu, 2000), or by the BEM utilizing higher-order panels such as B-spline functions (e.g. Kashiwagi, 1998; Newman, 2005). However, semi-analytical approaches can only handle rather simple shapes of floating bodies such as box-shaped pontoons, whereas FEM requires the tedious task of discretizing the fluid domain into meshes. Higher-order BEM using B-spline functions do not converge well when an iterative solver is used. Thus, large problems with a huge number of unknowns cannot be solved by the B-spline functions method.

Utsunomiya and Watanabe (2002) applied the acceleration method known as the fast multipole method (Rokhlin, 1985; Barnes and Hut, 1986; Greengard and Rokhlin, 1987; Greengard, 1988) to perform efficiently the hydroelastic analysis of VLFS with large number of unknowns. The essential theoretical background of the fast multipole method, described in this chapter, is based on Graf's addition theorem of Bessel functions which appear in the free surface Green's function, the use of a hierarchical algorithm to compute the system equations, and the employment of an iterative solver. Although a

similar approach to accelerate BEM for wave diffraction/radiation problems can be found using the pre-corrected FFT algorithm (Korsmeyer *et al.*, 1996, 1999; Kring *et al.*, 2000), it is restricted for now to a low-order panel and a deep-water case.

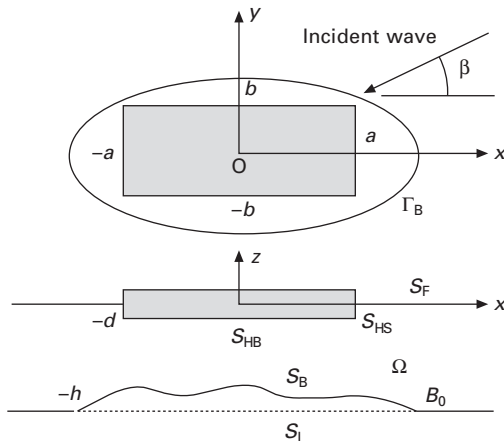
Some details of the accelerated Green's function method and its efficiency are also described in this chapter. Formulations are presented for the hydroelastic analysis of VLFS subject to different conditions such as variable seabed topology and wave periods. The storage requirement of  $O(N)$  and CPU time characteristics of  $O(N \log N)$  are shown by the numerical examples.

## 14.2 The boundary value problem

Consider a box-like VLFS of length  $2a$  ( $= L$ ), width  $2b$  ( $= B$ ), and draft  $d$ , floating in the open sea of variable depth (with constant depth  $h$  at infinity) as shown in Fig. 14.2. The variable depth sea-bottom surface  $S_B$  is defined such that the boundary line  $\Gamma_B$  touches on the flat bottom base-surface of  $z = -h$  and  $S_B$  must be above the base surface  $z = -h$ . The coordinate system is defined such that the  $xy$  plane locates on the undisturbed free surface and the  $z$  axis points upwards. The center of the VLFS is on the  $z$  axis as shown in Fig. 14.2.

Consider the long-crested harmonic wave with small amplitude. The amplitude of the incident wave is defined by  $A$ , the circular frequency by  $\omega$ , and the angle of incidence by  $\beta$  ( $\beta = 0$  corresponds to the head wave from positive  $x$  direction and  $\beta = \pi/2$  to the beam wave from positive  $y$  direction).

By assuming the water to be a perfect fluid with no viscosity and incompressible, and the fluid motion to be irrotational, then the fluid motion can be represented by a velocity potential  $\Phi$ . Also, we consider the steady-



14.2 Configuration of the analytical model.

state harmonic motions of the fluid and the structure, with the circular frequency  $\omega$ . Then, all of the time-dependent quantities can be similarly represented as

$$\Phi(x, y, z; t) = \operatorname{Re}[\phi(x, y, z)e^{i\omega t}] \quad 14.1$$

where  $i$  is the imaginary unit ( $i^2 = -1$ ) and  $t$  is the time. In the following, all time-dependent variables are represented in the frequency domain unless stated explicitly.

Moreover, the fluid and structural motions are assumed to be small so that the linear potential theory can be applied for formulating the fluid-motion problem. With these assumptions, the following boundary value problem may be formulated:

$$\nabla^2 \phi = 0 \quad \text{on } \Omega \quad 14.2$$

$$\frac{\partial \phi}{\partial z} = K\phi \quad \text{on } S_F \quad 14.3$$

$$\frac{\partial \phi}{\partial n} = 0 \quad \text{on } S_B \quad 14.4$$

$$\frac{\partial \phi}{\partial z} = 0 \quad \text{on } B_0 \quad 14.5$$

$$\frac{\partial \phi}{\partial n} = i\omega w(x, y) \quad \text{on } S_{HB} \quad 14.6$$

$$\frac{\partial \phi}{\partial n} = 0 \quad \text{on } S_{HS} \quad 14.7$$

$$\lim_{r \rightarrow \infty} \sqrt{r} \left( \frac{\partial(\phi - \phi_1)}{\partial r} - ik(\phi - \phi_1) \right) = 0 \quad \text{on } S_\infty \quad 14.8$$

$$\phi_1 = i \frac{gA}{\omega} \frac{\cosh kh(z+h)}{\cosh kh} e^{ik(x \cos \beta + y \sin \beta)} \quad 14.9$$

where  $\phi_1$  is the incident wave potential. The symbols  $\Omega$ ,  $S_F$ ,  $S_B$  and  $B_0$  represent the fluid domain, the free surface, the variable depth sea-bottom surface, and the flat-bottom base surface on  $z = -h$ , respectively. The symbols  $S_{HB}$ ,  $S_{HS}$  and  $S_\infty$  denote the bottom surface of the floating body, the wetted side surface of the floating body, and the artificial fluid boundary at infinity, respectively. The symbol  $K$  represents the wave number at infinite depth sea ( $= \omega^2/g$ ;  $g$  is the gravitational acceleration), whereas  $k$  is the wave number at the constant depth  $h$  satisfying the following dispersion relation:

$$k \tanh kh = K \quad 14.10$$

The symbol  $n$  represents a unit normal vector with the positive direction pointing out of the fluid domain. The complex-valued variable  $w(x, y)$  represents

the vertical deflection of the bottom surface of the floating body. The variable  $r$  in Eq. (14.8) represents the horizontal distance between the origin and the referred point.

### 14.3 The boundary integral equation

The fundamental equation for representing the aforementioned boundary value problem is an integral equation given by (Teng and Eatock Taylor, 1995; Utsunomiya *et al.*, 1998):

$$\begin{aligned} & \left( 4\pi + \int_{S_I} \frac{\partial G_2(\vec{x}, \vec{\xi})}{\partial z} dS \right) \phi(\vec{x}) \\ & + \int_{S_{HB} \cup S_{HS} \cup S_B} \left\{ \phi(\vec{\xi}) \frac{\partial G(\vec{x}, \vec{\xi})}{\partial n} - \phi(\vec{x}) \frac{\partial G_2(\vec{x}, \vec{\xi})}{\partial n} \right\} dS \\ & - \int_{S_{HB} \cup S_{HS} \cup S_B} G(\vec{x}, \vec{\xi}) \frac{\partial \phi(\vec{\xi})}{\partial n} dS = 4\pi \phi_1(\vec{x}) \end{aligned} \quad 14.11$$

where  $\vec{x} = (x, y, z)$  and  $\vec{\xi} = (\xi, \eta, \zeta)$ . The symbol  $S_I$  designates the inner plane of  $z = -h$  inside the boundary  $\Gamma_B$ . It is noted that the integral in Eq. (14.11) is performed for  $\vec{\xi} = (\xi, \eta, \zeta)$  and the normal derivative is made on the same surface. Using Eq. (14.11), the evaluations of solid angles and CPV integrals that may be needed in Fredholm-type integral equations can be avoided. The function  $G(\vec{x}, \vec{\xi})$  denotes Green's function, which represents water waves, and satisfies the boundary conditions on the free surface, on the flat sea-bottom ( $z = -h$ ), and the radiation condition at infinity. The series form can be represented as follows (Newman, 1985; Linton, 1999):

$$G(\vec{x}, \vec{\xi}) = \sum_{m=0}^{\infty} \frac{2K_0(k_m R)}{N_m} \cos k_m(z + h) \cos k_m(\zeta + h) \quad 14.12$$

$$N_m = \frac{h}{2} \left( 1 + \frac{\sin 2k_m h}{2k_m h} \right) \quad 14.13$$

$$k_m \tan k_m h = -K \quad 14.14$$

where  $k_m (m \geq 1)$  is a positive real number, and  $k_0 = ik$ . The following relationship is also used:

$$K_0(ikR) = -\frac{1}{2}\pi i H_0^{(2)}(kR) \quad 14.15$$

where  $K_0$  is the modified Bessel function of the second kind, and  $H_0^{(2)}$  the Hankel function. The symbol  $R$  represents the horizontal distance between

$\vec{x}$  and  $\vec{\xi}$ . The function  $G_2(\vec{x}, \vec{\xi})$  is given as (Teng and Eatock Taylor, 1995):

$$G_2(\vec{x}, \vec{\xi}) = \frac{1}{r} + \frac{1}{r_1} + \frac{1}{r_{21}} + \frac{1}{r_{31}} \quad 14.16$$

where  $r = [R^2 + (z - \zeta)^2]^{1/2}$ ,  $r_1 = [R^2 + (z + \zeta)^2]^{1/2}$ ,  $r_{21} = [R^2 + (z - \zeta - 2h)^2]^{1/2}$  and  $r_{31} = [R^2 + (z + \zeta + 2h)^2]^{1/2}$ .

## 14.4 Equation of motion for VLFS deflections

It is now widely accepted that the vertical deflection of VLFS can be well captured by modeling the entire VLFS as an elastic plate. Thus, by adopting the classical thin plate theory, the governing equation of motion for VLFS vertical deflections is given by

$$D\nabla^4 w(x, y) - \omega^2 \gamma w(x, y) + kw(x, y) = p(x, y) \quad 14.17$$

where  $D$  is the plate rigidity,  $\gamma$  is the mass per unit area,  $k = \rho g$  ( $\rho$ : density of fluid) modeling the hydrostatic restoring forces, and  $p(x, y)$  is the dynamic pressure on the bottom surface of the VLFS. The dynamic pressure  $p(x, y)$  relates to the velocity potential on the bottom surface of the VLFS from the linearized Bernoulli equation:

$$p(x, y) = -i\rho\omega\phi(x, y, -d) \quad 14.18$$

The floating body subjected to no constraint in the vertical direction along its edges must satisfy the following static boundary conditions for a free edge:

$$\left[ \frac{\partial w^3(x, y)}{\partial x^3} + (2 - \nu) \frac{\partial w^3(x, y)}{\partial x \partial y^2} \right]_{x=\pm a} = 0 \quad 14.19$$

$$\left[ \frac{\partial w^2(x, y)}{\partial x^2} + \nu \frac{\partial w^2(x, y)}{\partial y^2} \right]_{x=\pm a} = 0 \quad 14.20$$

where  $\nu$  is the Poisson ratio. The boundary conditions along the edges  $y = \pm b$  are given similarly.

The objective is to solve the stationary solution which is governed by Eq. (14.17) and the free boundary conditions by Eqs. (14.19) and (14.20). In the following, we first represent the deflection  $w(x, y)$  by a series of the products of the modal functions  $f_l(x, y)$  and the complex amplitudes  $\zeta_l$ , and then derive the equation of motion for the modal amplitudes using the Ritz-Galerkin method:

$$w(x, y) = \sum_{l=1}^P \zeta_l f_l(x, y) \quad 14.21$$

The Hamilton principle is used to derive the equation of motion, i.e.

$$\delta(U - T + V) = 0 \quad 14.22$$

where  $U$  represents the strain energy,  $T$  the kinetic energy, and  $V$  the potential energy due to external force. They are given, respectively, by

$$U = \frac{1}{2} \int_{S_{HB}} \left[ D \left\{ \left( \frac{\partial^2 w}{\partial x^2} \right)^2 + \left( \frac{\partial^2 w}{\partial y^2} \right)^2 + 2\nu \frac{\partial^2 w}{\partial x^2} \frac{\partial^2 w}{\partial y^2} \right. \right. \\ \left. \left. + 2(1-\nu) \left( \frac{\partial^2 w}{\partial x \partial y} \right)^2 \right\} + kw^2 \right] dS \quad 14.23$$

$$T = \frac{1}{2} \omega^2 \gamma \int_{S_{HB}} w^2 dS \quad 14.24$$

$$V = - \int_{S_{HB}} p(x, y) w dS \quad 14.25$$

By substituting Eq. (14.18), Eqs. (14.23)–(14.25) into Eq. (14.22), and then taking the variation of total energy functional with respect to  $w$  leads to

$$D \int_{S_{HB}} \left[ \frac{\partial^2 w}{\partial x^2} \frac{\partial^2 \delta w}{\partial x^2} + \frac{\partial^2 w}{\partial y^2} \frac{\partial^2 \delta w}{\partial y^2} + \nu \frac{\partial^2 w}{\partial x^2} \frac{\partial^2 \delta w}{\partial y^2} + \nu \frac{\partial^2 w}{\partial y^2} \frac{\partial^2 \delta w}{\partial x^2} \right. \\ \left. + 2(1-\nu) \frac{\partial^2 w}{\partial x \partial y} \frac{\partial^2 \delta w}{\partial x \partial y} \right] dS + k \int_{S_{HB}} w \delta w dS - \omega^2 \gamma \int_{S_{HB}} w \delta w dS \\ = -i\rho\omega \int_{S_{HB}} \phi(x, y, -d) \delta w dS \quad 14.26$$

By substituting Eq. (14.21) and the variation into Eq. (14.26), and considering the arbitrariness of  $\delta \zeta_l$ , one finally obtains the following equation of motion in the modal coordinates:

$$\sum_{l=1}^P \zeta_l (K_{lj} - \omega^2 M_{lj}) = -i\rho\omega \int_{S_{HB}} \phi(x, y, -d) f_j dS \quad 14.27$$

where

$$K_{lj} = D \int_{S_{HB}} \left[ \frac{\partial^2 f_l}{\partial x^2} \frac{\partial^2 f_j}{\partial x^2} + \frac{\partial^2 f_l}{\partial y^2} \frac{\partial^2 f_j}{\partial y^2} + \nu \frac{\partial^2 f_l}{\partial x^2} \frac{\partial^2 f_j}{\partial y^2} \right. \\ \left. + \nu \frac{\partial^2 f_l}{\partial y^2} \frac{\partial^2 f_j}{\partial x^2} + 2(1-\nu) \frac{\partial^2 f_l}{\partial x \partial y} \frac{\partial^2 f_j}{\partial x \partial y} \right] dS + k \int_{S_{HB}} f_l f_j dS \quad 14.28$$

$$M_{lj} = \gamma \int_{S_{HB}} f_l f_j dS \quad 14.29$$

are the generalized stiffness matrix and the generalized mass matrix, respectively. The selection of the modal function has in fact some arbitrariness; e.g. dry-modes of the plate may be used. For this chapter, the modal functions comprising a tensor product of modal functions of a vibrating free-free beam in the  $x$  and  $y$  directions (Utsunomiya *et al.*, 1998) are chosen.

## 14.5 Formulation for hydroelastic analysis

By substituting Eqs. (14.4), (14.6) and (14.7) into Eq. (14.11), one gets

$$\begin{aligned} & \left( 4\pi + \int_{S_I} \frac{\partial G_2(\vec{x}, \vec{\xi})}{\partial z} dS \right) \phi(\vec{x}) \\ & + \int_{S_{HB} \cup S_{HS} \cup S_B} \left\{ \phi(\vec{\xi}) \frac{\partial G(\vec{x}, \vec{\xi})}{\partial n} - \phi(\vec{x}) \frac{\partial G_2(\vec{x}, \vec{\xi})}{\partial n} \right\} dS \\ & - i\omega \int_{S_{HB}} G(\vec{x}, \vec{\xi}) w(\xi, \eta) dS = 4\pi \phi_I(\vec{x}) \end{aligned} \quad 14.30$$

Moreover, the substitution of Eq. (14.21) into Eq. (14.30) yields

$$\begin{aligned} & \left( 4\pi + \int_{S_I} \frac{\partial G_2(\vec{x}, \vec{\xi})}{\partial z} dS \right) \phi(\vec{x}) \\ & + \int_{S_{HB} \cup S_{HS} \cup S_B} \left\{ \phi(\vec{\xi}) \frac{\partial G(\vec{x}, \vec{\xi})}{\partial n} - \phi(\vec{x}) \frac{\partial G_2(\vec{x}, \vec{\xi})}{\partial n} \right\} dS \\ & - i\omega \sum_{l=1}^P \zeta_l \int_{S_{HB}} G(\vec{x}, \vec{\xi}) f_l(\xi, \eta) dS = 4\pi \phi_I(\vec{x}) \end{aligned} \quad 14.31$$

The problem is solved if the unknown modal amplitudes  $\zeta_l$  ( $l = 1, \dots, P$ ) and the unknown nodal potentials  $\phi_i$  ( $i = 1, \dots, N$ ) to be distributed on the surface  $S_{HB}$ ,  $S_{HS}$ , and  $S_B$  are determined. This can be done by solving the simultaneous equations composed of (14.27) and (14.31).

The right-hand side of Eq. (14.27) may be rewritten as

$$\int_{S_{HB}} \phi(x, y, -d) f_j dS = \sum_{e=1}^{NHB} \int_{S_e} [N^1, \dots, N^8] f_j dS \begin{Bmatrix} \phi^1 \\ \vdots \\ \phi^8 \end{Bmatrix}_e$$

$$= \sum_{e=1}^{NHB} [L_j]_e \begin{Bmatrix} \phi^1 \\ \vdots \\ \phi^8 \end{Bmatrix}_e = [L_j]\{\phi\} \quad (j = 1, \dots, P) \quad 14.32$$

In Eq. (14.32), the symbol  $S_e$  represents each element (or panel) on the bottom surface of the floating body  $S_{HB}$ , and the number of elements is represented by  $NHB$ .

That is

$$S_{HB} = \bigcup_{e=1}^{NHB} S_e \quad 14.33$$

The symbols  $N^1, \dots, N^8$  represent shape functions for interpolating the potential  $\phi$  inside each element from the nodal values of  $\phi^1, \dots, \phi^8$  (when an eight-noded panel is used). The complex valued vector  $\{\phi\}$  has elements of the potentials at nodes  $\phi_i$  ( $i = 1, \dots, N$ ), and the row vector  $[L_j]$  (of size  $N$ ) is composed by a superposition of  $[L_j]_e$  at the corresponding nodes. By substituting Eq. (14.32) into Eq. (14.27), and expressing it in the matrix form, one obtains

$$[K - \omega^2 M] \{\zeta\} = -i\rho\omega [L] \{\phi\} \quad 14.34$$

where  $\{\zeta\}$  is the complex valued vector with elements  $\zeta_l$  ( $l = 1, \dots, P$ ),  $[K - \omega^2 M]$  is the real matrix (of size  $P \times P$ ) having elements  $K_{lj} - \omega^2 M_{lj}$  ( $l, j = 1, \dots, P$ ), and  $[L]$  is the real matrix (of size  $P \times N$ ) with a row that is composed by  $[L_j]$  ( $j = 1, \dots, P$ ).

Equation (14.31) may be represented in a matrix form as

$$[A]\{\phi\} - i\omega[B]\{\zeta\} = 4\pi\{\phi_I\} \quad 14.35$$

where  $[A]$  is a complex valued matrix (of size  $N \times N$ ),  $[B]$  is a complex valued matrix (of size  $N \times P$ ), and  $\{\phi_I\}$  is a vector (of size  $N$ ). From Eq. (14.34),

$$\{\zeta\} = -i\rho\omega[K - \omega^2 M]^{-1}[L]\{\phi\} \quad 14.36$$

The substitution of Eq. (14.36) into Eq. (14.35) leads to

$$([A] - \rho\omega^2[B][K - \omega^2 M]^{-1}[L])\{\phi\} = 4\pi\{\phi_I\} \quad 14.37$$

In Eq. (14.37), the only unknowns are  $\phi_i$  ( $i = 1, \dots, N$ ). By solving first Eq. (14.37) for  $\phi_i$  ( $i = 1, \dots, N$ ) and then substituting them into Eq. (14.36),  $\zeta_l$  ( $l = 1, \dots, P$ ) may be obtained. Thus the given problem is solved.

In Eq. (14.37), the LU factorization of  $[K - \omega^2 M]$  has to be solved in advance. However, it is to be noted that for most cases  $P \ll N$  and also  $[K - \omega^2 M]$  is a real banded matrix, thus the LU decomposition would be trivial in the total computation time. When Eq. (14.37) is employed for solving the velocity potential via an iterative solver, the final solution can be obtained with an iterative procedure. This feature is the most important advantage over the conventional modal method when an iterative solver is used. It can be shown that the computational time is reduced by a factor of  $1/(\text{number of modes})$ .

## 14.6 Multipole expansion of Green's function

In the following, we consider the multipole expansion of the free surface Green's function in the series form, i.e. Eq. (14.12). As an alternative expression of Graf's addition theorem for the Bessel function, Eq. (14.38) can be obtained (Utsunomiya *et al.*, 2001):

$$K_0(k_m R) = \sum_{n=-\infty}^{\infty} K_n(k_m r) e^{in\theta} I_n(k_m \rho) e^{-in\Phi} \quad 14.38$$

Here,  $\vec{x} = (r, \theta, z)$  and  $\vec{\xi} = (\rho, \Phi, \zeta)$  are the points measured from the newly defined cylindrical coordinate systems, where the origin  $O$  may be referred to as the multipole expansion point. The multipole expansion point  $O$  can be located arbitrarily on the undisturbed free surface (thus on the  $xy$  plane of the global rectangular coordinate system) under the restriction of  $\rho < r$ . By substituting Eq. (14.38) into Eq. (14.12), one obtains

$$G(\vec{x}, \vec{\xi}) = \sum_{m=0}^{\infty} \sum_{n=-\infty}^{\infty} M_{mn} K_n(k_m r) e^{in\theta} \cos k_m(z + h) \quad 14.39$$

$$M_{mn} = \frac{2}{N_m} I_n(k_m \rho) e^{-in\Phi} \cos k_m(\zeta + h) \quad 14.40$$

Thus, the expression of Green's function may be represented in the form of the multipole expansions. The normal derivative of Green's function can be obtained similarly as

$$\frac{\partial G(\vec{x}, \vec{\xi})}{\partial n} = \sum_{m=0}^{\infty} \sum_{n=-\infty}^{\infty} \frac{\partial M_{mn}}{\partial n} K_n(k_m r) e^{in\theta} \cos k_m(z + h) \quad 14.41$$

$$\frac{\partial M_{mn}}{\partial n} = n_\rho \frac{\partial M_{mn}}{\partial \rho} + n_\Phi \frac{\partial M_{mn}}{\partial \Phi} + n_\zeta \frac{\partial M_{mn}}{\partial \zeta} \quad 14.42$$

Here,  $(n_\rho, n_\Phi, n_\zeta)$  represent the coordinate values in the directions of  $(\rho, \Phi, \zeta)$  of the normal vector  $\vec{n}$  defined at  $\vec{\xi}$ , where  $n_\rho = n_\zeta \cos \Phi + n_\eta \sin \Phi$  and  $n_\Phi = -n_\zeta \sin \Phi + n_\eta \cos \Phi$ .

The multipole expansion point  $O$  can be moved to an arbitrary position in the global  $xy$  plane if the constraint  $\rho < r$  is satisfied. The expansion coefficient  $\tilde{M}_{mn}$  with respect to the newly defined multipole expansion point  $O'$  relates to the original expansion coefficient  $M_{mn}$  as follows (Utsunomiya *et al.*, 2001):

$$\tilde{M}_{mv} = \sum_{n=-\infty}^{\infty} M_{mn} I_{v-n}(k_m \xi) e^{-i(v-n)\psi} \quad 14.43$$

where  $(\xi, \psi)$  represent the polar coordinate values of the original multipole expansion point  $O$  with respect to the newly defined multipole expansion point  $O'$ . Similarly, the following relationship is satisfied:

$$\frac{\partial \tilde{M}_{mv}}{\partial n} = \sum_{n=-\infty}^{\infty} \frac{\partial M_{mn}}{\partial n} I_{v-n}(k_m \xi) e^{-i(v-n)\psi} \quad 14.44$$

## 14.7 Implementation to higher-order boundary element method

In Eq. (14.31), the distribution of the potential within each element (or panel) may be expressed by using the second-order interpolation functions and the potentials at the nodal points of the element as follows:

$$\phi(\xi, \eta, \zeta) = \sum_{k=1}^8 N^k(\bar{\xi}, \bar{\eta}) \phi^k \quad 14.45$$

where  $(\bar{\xi}, \bar{\eta})$  represents the coordinate values in the curved plane coordinate system defined on the surface of each element. The substitution of Eq. (14.45) into Eq. (14.31) yields

$$\begin{aligned} & \left( 4\pi + \sum_{e=1}^{NI} \int \int_{-1}^1 \frac{\partial G_2}{\partial z} |J_e| d\xi d\bar{\eta} \right) \phi(\vec{x}) \\ & + \sum_{e=1}^{NE} \int \int_{-1}^1 \left\{ \frac{\partial G}{\partial n} \sum_{k=1}^8 N^k \phi^k - \frac{\partial G_2}{\partial n} \phi(\vec{x}) \right\} |J_e| d\xi d\bar{\eta} \\ & - i\omega \sum_{l=1}^P \zeta_l \sum_{e=1}^{NHB} \int \int_{-1}^1 G f_l(\bar{\xi}, \bar{\eta}) |J_e| d\xi d\bar{\eta} = 4\pi \phi_1(\vec{x}) \end{aligned} \quad 14.46$$

where  $J_e = J_e(\bar{\xi}, \bar{\eta})$  represents the Jacobian defined for each element  $e$ . The symbols NHB, NHS, NB, and NI represent the number of elements on the surfaces of  $S_{HB}$ ,  $S_{HS}$ ,  $S_B$ , and  $S_I$ , respectively, and

$$NE = NHB + NHS + NB \quad 14.47$$

Equation (14.46) may be rearranged as

$$\begin{aligned}
& \left( 4\pi + \sum_{e=1}^{NI} \int \int_{-1}^1 \frac{\partial G_2}{\partial z} |J_e| d\xi d\bar{\eta} - \sum_{\substack{e=1 \\ (\vec{x} \notin e)}}^{NE} \int \int_{-1}^1 \frac{\partial G_2}{\partial n} |J_e| d\xi d\bar{\eta} \right) \phi(\vec{x}) \\
& + \sum_{\substack{e=1 \\ (\vec{x} \in e)}}^{NE} \int \int_{-1}^1 \left\{ \frac{\partial G}{\partial n} \sum_{k=1}^8 N^k \phi^k - \frac{\partial G_2}{\partial n} \phi(\vec{x}) \right\} |J_e| d\xi d\bar{\eta} \\
& + \sum_{\substack{e=1 \\ (\vec{x} \notin e)}}^{NE} \int \int_{-1}^1 \frac{\partial G}{\partial n} \sum_{k=1}^8 N^k \phi^k |J_e| d\xi d\bar{\eta} \\
& - i\omega \sum_{e=1}^{NHB} \int \int_{-1}^1 G \sum_{l=1}^P \zeta_l f_l(\xi, \bar{\eta}) |J_e| d\xi d\bar{\eta} = 4\pi \phi_I(\vec{x}) \quad 14.48
\end{aligned}$$

where  $\vec{x} \in e$  corresponds to the case when the collocation point  $\vec{x}$  is included in the element  $e$ , and  $\vec{x} \notin e$  to the case when  $\vec{x}$  is outside the element  $e$ . Further substitution of Eqs. (14.39) and (14.41) into (14.48) furnishes

$$\begin{aligned}
& \left( 4\pi + \sum_{e=1}^{NI} \int \int_{-1}^1 \frac{\partial G_2}{\partial z} |J_e| d\xi d\bar{\eta} - \sum_{\substack{e=1 \\ (\vec{x} \notin e)}}^{NE} \int \int_{-1}^1 \frac{\partial G_2}{\partial n} |J_e| d\xi d\bar{\eta} \right) \phi(\vec{x}) \\
& + \sum_{\substack{e=1 \\ (\vec{x} \in e)}}^{NE} \int \int_{-1}^1 \left\{ \frac{\partial G}{\partial n} \sum_{k=1}^8 N^k \phi^k - \frac{\partial G_2}{\partial n} \phi(\vec{x}) \right\} |J_e| d\xi d\bar{\eta} \\
& + \sum_{\substack{e=1 \\ (\vec{x} \notin e) \cap (e: \text{near to } \vec{x})}}^{NE} \int \int_{-1}^1 \frac{\partial G}{\partial n} \sum_{k=1}^8 N^k \phi^k |J_e| d\xi d\bar{\eta} \\
& + \sum_{m=0}^{\infty} \sum_{n=-\infty}^{\infty} \sum_{\substack{e=1 \\ (\vec{x} \notin e) \cap (e: \text{far from } \vec{x})}}^{NE} K_n(k_m r) e^{in\theta} \cos k_m(z + h) \\
& \int \int_{-1}^1 \frac{\partial M_{mn}}{\partial n} \sum_{k=1}^8 N^k \phi^k |J_e| d\xi d\bar{\eta} \\
& - i\omega \sum_{\substack{e=1 \\ (e: \text{near to } \vec{x})}}^{NHB} \int \int_{-1}^1 G \sum_{l=1}^P \zeta_l f_l(\xi, \bar{\eta}) |J_e| d\xi d\bar{\eta} \\
& - i\omega \sum_{m=0}^{\infty} \sum_{n=-\infty}^{\infty} \sum_{\substack{e=1 \\ (e: \text{far from } \vec{x})}}^{NHB} K_n(k_m r) e^{in\theta} \cos k_m(z + h) \\
& \int \int_{-1}^1 M_{mn} \sum_{l=1}^P \zeta_l f_l(\xi, \bar{\eta}) |J_e| d\xi d\bar{\eta} = 4\pi \phi_I(\vec{x}) \quad 14.49
\end{aligned}$$

## 14.8 Application of the fast multipole method

When Eq. (14.49) is solved by an iterative method,  $\{\zeta\}$  is calculated for an assumed  $\{\phi\}$  using Eq. (14.36), and then the left-hand side of Eq. (14.49) is obtained for the assumed  $\{\phi\}$ . The values of  $\{\phi\}$  are then updated in order to minimize the error between the left-hand side and the right-hand side values of Eq. (14.49). In the calculation of the left-hand side values of Eq. (14.49), the diagonal terms of the coefficient matrices are stored in the core memory. On the other hand, the off-diagonal terms are calculated in each step of the iterative process. This enables a significant reduction of the storage requirement to  $O(N)$ . However, of course, the computation associated with the off-diagonal terms of the coefficient matrices has to be accelerated.

The calculation for the off-diagonal terms may be separated into two parts: the first one involves the calculation of elements near  $\vec{x}$  (third and sixth lines in Eq. (14.49)), and the second one involves the calculation of elements far from  $\vec{x}$  (fourth, fifth, seventh and eighth lines in Eq. (14.49)). In the following, we explain the accelerated calculation method of the terms in the fourth and fifth lines in Eq. (14.49) as an example for the second part. Consider the part of Eq. (14.49) given by

$$\hat{b}(\vec{x}) = \sum_{m=0}^{\infty} \sum_{n=-\infty}^{\infty} \sum_{e=1}^{N_E} K_n(k_m r) e^{in\theta} \cos k_m(z + h) \\ \int_{-1}^1 \frac{\partial M_{mn}}{\partial n} \sum_{k=1}^8 N^k \hat{\phi}^k |J_e| d\bar{\xi} d\bar{\eta} \quad 14.50$$

As has already been defined, the values of  $(r, \theta, z)$  in Eq. (14.50) define the collocation point  $\vec{x}$  measured from the multipole expansion point  $O$ . The multipole expansion point  $O$  can be located in an arbitrary horizontal position under the restriction of  $\rho < r$ ; with the multipole expansion point  $O$  being located on the projection of the origin of the local coordinate system  $(\bar{\xi}, \bar{\eta})$  of each element to the  $xy$  plane of the global coordinate system.

As is clear from Eq. (14.42), the integrand in Eq. (14.50) includes only the values in terms of  $(\rho, \Phi, \zeta)$ . This implies that the integral can be evaluated beforehand regardless of the position of  $\vec{x}$ . By storing the values of the calculated integral in the core memory, an efficient algorithm may be obtained. However, it still has an efficiency of only  $O(N^2)$ .

Next, we introduce the concept of ‘cells’ that gather the influences from many far field elements into an influence from one large cell (Rokhlin, 1985). For this purpose, Eq. (14.50) is modified as

$$\hat{b}(\vec{x}) = \sum_{m=0}^{\infty} \sum_{n=-\infty}^{\infty} \sum_{k=1}^{N_{cell}} K_n(k_m r) e^{in\theta} \cos k_m(z + h) \\ (k: \text{far from } \vec{x})$$

$$\sum_{e \in \text{Cell } k} \int_{-1}^1 \frac{\partial M_{mn}}{\partial n} \sum_{l=1}^8 N^l \hat{\phi}^l |J_e| d\bar{\xi} d\bar{\eta} \quad 14.51$$

In Eq. (14.51), the summation for elements is replaced by the summation for cells. In Eq. (14.51), the cell  $k$  should be as large as possible so as to include as many elements as possible for computational efficiency. In Eq. (14.51), the multipole expansion point  $O$  is located on the center of each cell, and  $(r, \theta, z)$ , the coordinates of the collocation point  $\vec{x}$ , is newly defined correspondingly. In general, as the cell size gets larger, the number of cells,  $N_{cell}$ , becomes smaller, thereby translating to a shorter computation time.

The quadrant-tree is employed to define the tree structure of cells and the hierarchical computation algorithm (Greengard and Rokhlin, 1987; Greengard, 1988; Fukui and Katsumoto, 1997). For simplicity, the shape of each cell is chosen to be a square. The hierarchical cell structure is organized on the  $xy$  plane (on the undisturbed free surface). First, the level-0 cell of square shape is defined. The shape must include all the analyzed area ( $S_{HB}$ ,  $S_{HS}$ , and  $S_B$ ). Then, the level-0 square cell is divided into four even square cells which are defined as level-1 cells. Similarly, level-2 cells are defined by dividing each level-1 cell into four even square cells. This process is repeated until the bottom level cells (leaf cells) include some appropriate number of elements. In the division process, the cell that includes no elements is deleted from the definition list of cells.

The method to define ‘far’ cells and ‘near’ cells is based on that made by Greengard and Rokhlin (1987). That is, the cell  $i$  that includes the collocation point  $\vec{x}$  inside and the cells that enclose the cell  $i$  adjacent to it are defined as ‘near’ cells; otherwise the cells are categorized as ‘far’ cells. Note that this categorization into ‘near’ and ‘far’ cells should be made on the same level of the tree structure. In the calculation of Eq. (14.49), the computation for ‘near’ cells is made for each element (corresponding to lines 3 and 6 in Eq. (14.49)).

In the actual computation, the integral of Eq. (14.51) is calculated around the center of each element as the multipole expansion point. Then by using Eq. (14.44), the multipole expansion coefficients are converted to the coefficients for the center of a leaf cell. By gathering the coefficients of all elements included in the leaf cell, the multipole expansion coefficient for the leaf cell can be obtained. The calculation of the multipole expansion coefficients for upper level cells can be made similarly, by using Eq. (14.44) and gathering the coefficients included in the upper level cell. With these procedures, all of the necessary multipole coefficients can be set up, without specifying the collocation point  $\vec{x}$ .

Next, we specify the collocation point  $\vec{x}$  to coincide a nodal point on either of  $S_{HB}$ ,  $S_{HS}$ , or  $S_B$ . At this stage, the calculations are performed from upper level to lower level, by selecting larger cells as far as possible. This

hierarchical algorithm is known to be  $O(N \log N)$  in computation time (Barnes and Hut, 1986).

The truncation of the infinite summations in Eq. (14.51) is made as  $m_{\max} = [6h/R]$  (Newman, 1985),  $n_{\max} = 20$  ( $ka < 5$ ), and  $n_{\max} = [1.2ka + 15]$  ( $ka \geq 5$ ) where  $a$  is the maximum cell size to be used in the actual computation.

## 14.9 Numerical examples

In order to check the accuracy and the computational efficiency, the wave response analysis of a box-like VLFS has been made by using the fast multipole method as described in this chapter and by the program using the direct LU factorization solver (Utsunomiya *et al.*, 1998). The specifications of the VLFS are: length  $L = 1500$  m, width  $B = 150$  m, the draft  $d = 1$  m, the flexural rigidity  $D = 3.88 \times 10^7$  kN m, and the Poisson ratio  $\nu = 0.3$ . The number of modal functions employed is 160 (20 in the longitudinal direction and eight in the transverse direction). The constant water depth is 8 m. The wave period is 18 seconds (with the corresponding incident wavelength of  $\lambda = 156.8$  m), and the angle of wave incidence is  $\beta = \pi/4$ .

Table 14.1 shows the performance of the benchmark calculations, where, in the developed program, GMRES solver is used (Barrett *et al.*, 1994) with the residual tolerance  $\varepsilon = 10^{-4}$ . The CPU time is measured by using a single CPU of a parallel computer (IBM RS/6000 SP; CPU: POWER 3-II, 375 MHz) unless otherwise stated. It can be observed that the fast multipole method (FMM) is efficient both in CPU time and memory allocation compared with the direct method using either LU factorization solver or GMRES solver. Further, the memory consumption is almost  $O(N)$  for the FMM. The CPU time is a little bit slower than the predicted  $O(N \log N)$ , but much faster than  $O(N^2)$ .

Table 14.2 shows the number of iterations and CPU time to converge in GMRES for various incident wavelengths. It can be seen that the number of iterations is sensitive to the incident wavelength, but insensitive to panel divisions as observed in Table 14.1. Although no preconditioning method is applied, convergent results have been obtained even at a high frequency of  $L/\lambda = 62$ . The efficiency of the parallel computation is also noteworthy. The computation time for model D is reduced to 22% with the use of five CPUs. The increase in number of iterations with the wave frequency may be due to ill-conditioning at the short waves. Further studies are needed to confirm this, and to reduce the number of iteration by developing a suitable preconditioner.

Figure 14.3 shows that the deflection amplitudes by FMM are in agreement with those obtained by the direct method within the graphical accuracy of  $\varepsilon = 10^{-3}$ . Although there are some differences in the two graphical lines when  $\varepsilon = 10^{-2}$ , the results by FMM may be regarded as satisfactory.

Table 14.1 Performance of the fast multipole method and the direct method

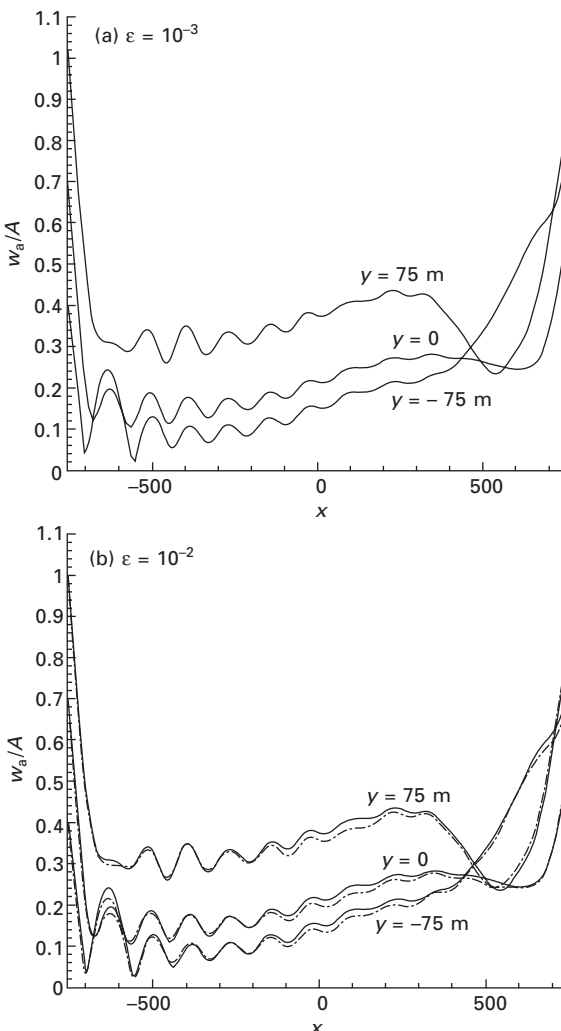
Model	Typical panel size (m)	Number of nodes	Fast multipole method			Direct method		
			Number of iteration	CPU time per iteration (s)	CPU time (min)	CPU time		
						LU factorization	GMRES solver	Memory allocation
A	25.0	1609	31	3	1.8	27 MB	1.55 min	3.28 min
B	12.5	5377	32	15	10.4	89 MB	28.5 min	36.4 min
C	6.25	19393	32	86	77.4	315 MB	(907 min)	(474 min)
D	3.125	73345	32	570	775	1.15 GB	(708 h)	(113 h)
E	1.5625	284929	31	1081*	1689*	1.75 GB*	(1658 days)	(71 days)

\*Parallel computation using six CPUs; number of modal function is 120.

Table 14.2 Number of iterations of GMRES and CPU times for various  $L/\lambda$ 

Model	$L/\lambda$	Wave period (s)	Number of iterations		CPU time (h)	
			$\varepsilon = 10^{-3}$	$\varepsilon = 10^{-4}$	$\varepsilon = 10^{-3}$	$\varepsilon = 10^{-4}$
C	9.57	18	25	32	1.15	1.29
C	17.9	10	112	148	3.46	4.40
C	33.2	6	252	497	8.23	15.7
D	62.0	4	287		63.8	
D	62.0	4	287		14.5*	

\*Parallel computation using five CPUs.



14.3 Deflection amplitudes of VLFS on constant water depth for model B (solid line: FMM, dash-dotted line: direct method).

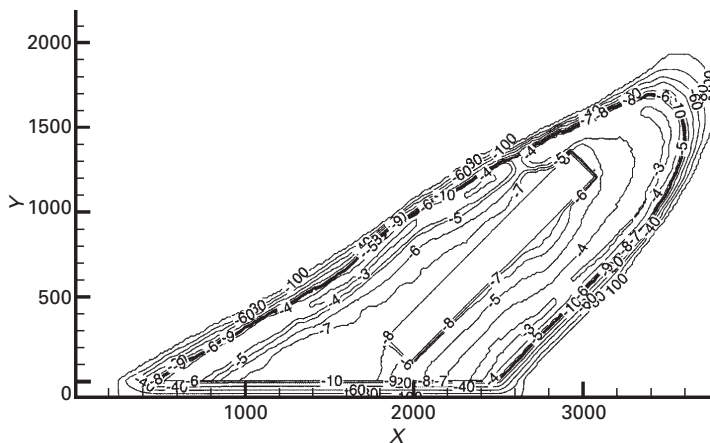
Next, the wave response analysis of the same VLFS model located on the variable water depth is performed. The contour plot of the variable depth configuration is shown in Fig. 14.4, where the water depth at infinity is assumed to be 100 m. This configuration corresponds to the experiment conducted in the Port and Airport Research Institute, Japan (Shiraishi *et al.*, 2001). The variable depth surface ( $S_B$ ) is discretized into 20278 elements of size of  $12.5 \text{ m} \times 12.5 \text{ m}$ , and the number of nodes is 61721. For meshing the VLFS model, the model B (number of nodes is 5377) in Table 14.1 is used; thus the total node number of the analyzed model becomes 67098. The computation time was 38.4 h using five CPUs for the wave period of 18 s the wave direction of  $\beta = \pi/4$ , and the residual tolerance  $\varepsilon = 10^{-2}$ .

In Fig. 14.5, the deflection amplitudes on the variable water depth and on the constant water depth ( $h = 8 \text{ m}$ ) are presented. We observe a considerable difference in the response characteristics when the VLFS is located on the variable water depth from those on the constant water depth. This shows the importance of including the effect of variable depth under the VLFS.

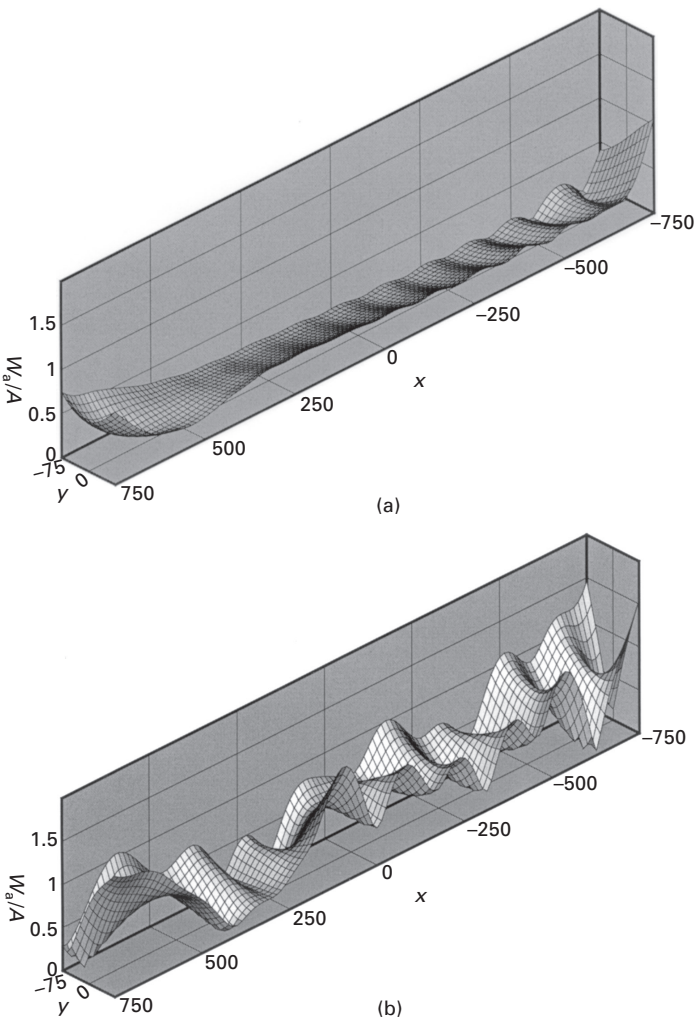
Figure 14.6 shows a snapshot of the surface elevation around the floating body, where the diffraction and the radiation waves are both included. As can be seen in Fig. 14.6, the refraction of waves and the change of wavelength (about  $\lambda = 157 \text{ m}$  inside the reef corresponding to 8 m water depth) by dispersion are clear.

## 14.10 Concluding remarks

In this chapter, the hydroelastic analysis of a VLFS by an accelerated higher-order boundary element method using a fast multipole algorithm is presented. The analysis has been carried out for a VLFS on a variable water depth



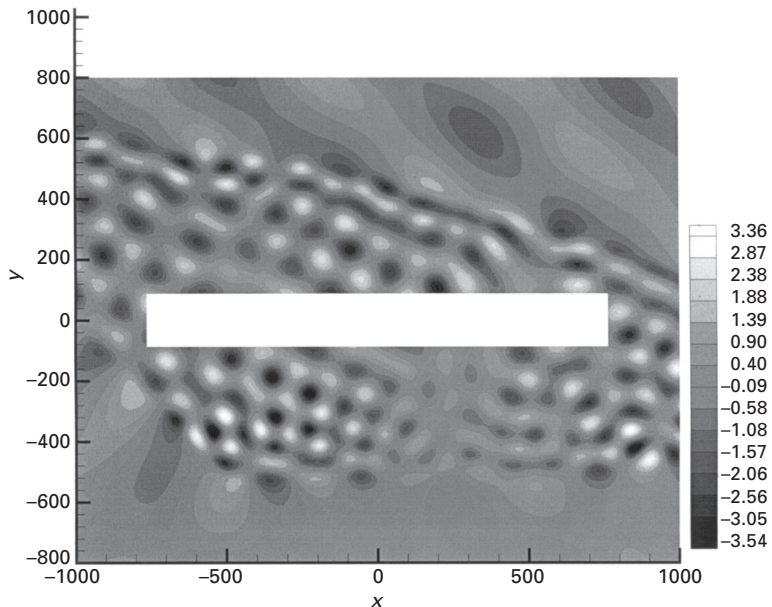
14.4 Contour plot of the variable depth configuration.



14.5 Deflection amplitude at  $T = 18$  s: (a) on constant water depth ( $h = 8$  m); (b) on variable water depth.

environment in order to demonstrate the effectiveness of the method. The theoretical requirements of the memory allocation of  $O(N)$  and the computation time of  $O(N \log N)$  have been demonstrated by the developed program through numerical examples. The large-scale hydroelastic problems with about 300 000 unknowns have been demonstrated to be solvable by the proposed accelerated BEM program within about one day, showing the advantage of the proposed method for large-scale analysis such as VLFS problems.

The presented method has also been applied for the hydroelastic analysis of a hybrid-type VLFS composed of a pontoon part and semi-submersible



14.6 Snapshot of the surface elevation around the floating body on the variable water depth.

part (Utsunomiya and Watanabe, 2003). The number of iterations for converged results has been reduced considerably by combining the OSP-ILUC preconditioner and GMRES-DR solver (Makihata *et al.*, 2005).

## 14.11 References

- Barnes J and Hut P (1986), ‘A hierarchical  $O(N \log N)$  force-calculation algorithm’, *Nature*, **324**, 446–449.
- Barrett R, Berry M, Chan TF, Demmel J, Donato J, Dongarra J, Eijkhout V, Pozo R, Romine C and Vorst H van der (1994), *Templates for the Solution of Linear Systems: Building Blocks for Iterative Methods*, SIAM, Philadelphia, PA.
- Fukui T and Katsumoto J (1997), ‘Fast multipole algorithm for two dimensional Helmholtz equation and its application to boundary element method’, *Proc 14th Japan National Symp on Boundary Element Methods*, Japan Society for Computational Methods in Engineering, 81–86 (in Japanese).
- Greengard L (1988), *The rapid evaluation of potential fields in particle systems*, MIT Press, Cambridge, MA.
- Greengard L and Rokhlin V (1987), ‘A fast algorithm for particle simulations’, *J Comput Phys*, **73**, 325–348.
- Kashiwagi M (1998), ‘A B-spline Galerkin scheme for calculating the hydroelastic response of a very large floating structure in waves’, *J Marine Sci Technol*, **3**, 37–49.
- Kashiwagi M (2000), ‘Research on hydroelastic responses of VLFS: recent progress and future work’, *Int J Offshore Polar Eng*, **10** (2), 81–90.
- Korsmeyer T, Phillips J and White J (1996), ‘A precorrected-FFT algorithm for accelerating

- surface wave problems', *Proc 11th Int Workshop on Water Waves and Floating Bodies*, Hamburg, Germany.
- Korsmeyer T, Klemas T, White J and Phillips J (1999), 'Fast hydrodynamic analysis of large offshore structures', *Proc 9th Int Offshore and Polar Eng Conf*, Brest, France, 27–34.
- Kring D, Korsmeyer T, Singer J and White, J (2000), 'Analyzing mobile offshore bases using accelerated boundary element methods', *Marine Structures*, **13**, 301–313.
- Linton CM (1999), 'Rapidly convergent representations for Green's functions for Laplace's equation', *Proc R Soc Lond A*, **455**, 1767–1797.
- Makihata N, Utsunomiya T and Watanabe E (2005), 'Effectiveness of GMRES-DR and OSP-ILUC for wave diffraction analysis of a very large floating structure (VLFS)', *Engineering Analysis with Boundary Elements*, **30**, 49–58.
- Newman JN (1985), 'Algorithms for the free-surface Green function', *J Eng Maths*, **19**, 57–67.
- Newman JN (2005), 'Efficient hydrodynamic analysis of very large floating structures', *Marine Structures*, **18**, 169–180.
- Ohmatsu S (2000), 'Numerical calculation method for the hydroelastic response of pontoon-type very large floating structure close to a breakwater', *J Marine Sci Technol*, **5**, 147–160.
- Ohmatsu S (2005), 'Overview: research on wave loading and responses of VLFS', *Marine Structures*, **18**, 149–168.
- Rokhlin V (1985), 'Rapid solution of integral equations of classical potential theory', *J Comput Phys*, **60**, 187–207.
- Seto H, Ohta M, Ochi M and Kawakado S (2005), 'Integrated hydrodynamic–structural analysis of very large floating structures (VLFS)', *Marine Structures*, **18**, 181–200.
- Shiraishi S, Harasaki K, Yoneyama H, Iijima K and Hiraishi T (2001), 'Experimental study on elastic response and mooring forces of very large floating structures moored inside reef', *Proc 20th Int Conf on Offshore Mech & Arctic Eng*, Rio de Janeiro, Brazil, OMAE01-5203.
- Suzuki H (2005), 'Overview of Megafloat: concept, design criteria, analysis, and design', *Marine Structures*, **18**, 111–132.
- Teng B and Eatock Taylor R (1995), 'New higher-order boundary element methods for wave diffraction/radiation', *Applied Ocean Research*, **17**, 71–77.
- Utsunomiya T and Watanabe E (2002), 'Accelerated higher order boundary element method for wave diffraction/radiation problems and its applications', *Proc 12th Int Offshore & Polar Eng Conf*, Kitakyushu, Japan, 305–312.
- Utsunomiya T and Watanabe E (2003), 'Wave response analysis of hybrid-type VLFS by accelerated BEM', *Proc. 3rd Int. Conf. Hydroelasticity in Marine Technology*, Oxford, UK, 297–303.
- Utsunomiya T, Watanabe E and Eatock Taylor R (1998), 'Wave response analysis of a box-like VLFS close to a breakwater', *Proc 17th Int Conf on Offshore Mech & Arctic Eng*, OMAE98-4331.
- Utsunomiya T, Watanabe E and Nishimura N (2001), 'Fast multipole algorithm for wave diffraction/radiation problems and its application to VLFS in variable water depth and topography', *Proc 20th Int Conf on Offshore Mech & Arctic Eng*, Rio de Janeiro, Brazil, OMAE01-5202.
- Watanabe E, Utsunomiya T and Wang CM (2004a), 'Hydroelastic analysis of pontoon-type VLFS: a literature survey', *Eng Struct*, **26**, 245–256.
- Watanabe E, Wang CM, Utsunomiya T and Moan T (2004b), 'Very large floating structures: applications, analysis and design', CORE report no 2004–02. Available for download from <[www.eng.nus.edu.sg/core/publications/researchreports.htm](http://www.eng.nus.edu.sg/core/publications/researchreports.htm)>

## Index

---

- ABAQUS 64–6, 70  
abrupt changes in properties 254–74  
    case studies 259–72  
        internal line hinges 264–72  
        multi-span plates 263–4, 265, 266,  
            267, 268  
        stepped thickness variations 260–3  
mathematical modelling 255–9  
    Levy solution procedure and state-  
        space technique 255–9  
    problem definition and governing  
        differential equation 255  
absolute error 428, 429, 435, 437,  
    438–41, 442  
admissible functions 230–1  
aircraft wing model 435–41  
    parameter identification 437–41, 442  
aluminium 357, 365  
aluminium-alumina FGM plates 312–16,  
    317  
aluminium-zirconia FGM plates 312–16,  
    317  
amplitude of vibration  
    imperfect FGM laminated plates 352–6  
    pre-stressed FGM laminated plates  
        365–7, 368  
analytical methods 118, 219, 254  
    tapered beams with both ends  
        supported 8–17  
angle of orientation 80, 81  
annular plates  
    LSFD method 141, 142  
            Pasternak foundations 170–1, 174  
antisymmetric angle-ply laminated plates  
    391–5
- arc-length iteration 182–6, 187, 188, 189  
average identified values 440–1, 442
- backbone curves 182  
skew plate with nonlinear vibration  
    183–6  
trapezoidal plate with nonlinear  
    vibration 186, 187, 188
- barium titanate 401  
beam finite element 53–5  
    tapered thin-walled composite  
        members 100–3  
bending analysis of FGM plates 303–11,  
    312  
bending-membrane material stiffness  
    coefficients 320  
bending moments  
    circular plates 137, 138  
    FGM laminated plates 414–15, 418  
    GBT and I-section beams 56, 66–73  
    Levy solution procedure and state-  
        space technique 258–9  
    modal bending moment  
        clamped square plate 205–6, 207  
        free square plate 210–15, 216, 217  
        unsymmetric cross-ply laminated plate  
            with piezoelectric layers 404, 407
- Bessel functions 1, 5, 10  
boron epoxy 108  
both-ends-supported tapered beams 3–5,  
    6–17  
    analytical formulation 8–17  
    numerical formulation 6–8, 9, 10
- boundary conditions  
    differential quadrature element  
        method 334

- validation studies 339–45
- DTFM**
- multidimensional continua 230–1
  - one-dimensional continua 220, 221, 222–3
  - stepped cylindrical shell 247–8, 249
- extended Kantorovich method 196
- clamped square plates 197–207
  - completely free square plates 207–15, 216, 217
- FGM laminated plates
- imperfect 334, 348–50, 351, 352–6
  - thermo-electro-mechanically pre-stressed 357–70, 371
- GBT 63–6, 67
- hybrid laminated plates 387–8
- Levy solution procedure and state-space technique 258–9
- hinged plates 259, 264–72
  - multi-span plates 259, 263–4, 265, 266, 267, 268
  - stepped thickness variations 258, 260–3
- LSFD method
- governing equation and boundary conditions 126–7
  - numerical implementation 128–34
  - simply supported polygonal plates 282, 285–6
- tapered beams 5
- finite element approach 25
  - linearly tapered cantilever 17–18
  - propced cantilever 20
- see also* clamped ends/edges; free edges
- boundary element method (BEM) 446
- higher-order 446, 455–64
- boundary points 124–6
- boundary value problem 447–9
- boundary integral equation 449–50
- branched open cross-sections 45, 48–50
- branching nodes 45, 48–50, 52
- buckling
- buckling analysis in DTFM 227
  - I-section beams 67–9, 73
  - thin-walled members 77–8
- built-in tapered beams 8, 9, 10
- straight-tapered combination 16, 17
- cantilevers
- hybrid GA-MV method for cantilever plates 427–9
- linearly tapered beams 17–20
- propced cantilevers 20, 21
  - quadrilateral plates 157, 158
- thin-walled composite beams
- analysis compared with FEAST-C 108–9, 110
  - free vibration of nonprismatic beam 111–12, 113
  - semicircular 112, 113–14
- tapered 1
- cells 457–9
- central deflection
- antisymmetric angle-ply and symmetric cross-ply laminated plates 394, 395
- FGM hybrid laminated plates 411, 413, 414–15, 418
- FGM square plates 305–6, 307, 308
- laminated plates 303–5, 306
- unsymmetric cross-ply laminated plate with piezoelectric layers 401, 402, 403, 404, 407
- centroid 79
- ceramic-metal plates *see* functionally graded material (FGM) hybrid laminated plates; functionally graded material (FGM) plates
- chain rule 123–4, 127–8
- chord ratio 186, 188
- circular beam 109–11
- circular plates
- DTFM 238–40
  - LSFD method 135–9
- clamped ends/edges
- abrupt changes in properties 258, 259–72
  - extended Kantorovich method for square plates 197–207
- isotropic thick plates
- linear vibration under equal biaxial forces 340, 342
  - nonlinear vibration 340–3
- LSFD method 126, 129–30
- p*-finite element method
- geometric nonlinear vibration 174–89
  - pentagonal-star plates 159, 163 with point supports 173, 180
  - regular polygonal plates 158–9, 161, 162, 176, 178
- tapered beams 29, 30

- classical thin plate theory (CPT) 118, 123, 193, 255, 275–6, 450  
 equations of free vibration 278–80  
 frequency relationships with shear deformable theories 280–91  
 frequency results 286–8, 289  
 FSDT and CPT 280–3  
 modification for complicating effects 288–91  
 TSDT and CPT 283–6
- CLPROP 103
- composite materials 2
- composite structures 293  
 stiffness matrix for composite lamina 106–7  
 tapered thin-walled composite members *see* tapered thin-walled composite members  
*see also* functionally graded material (FGM) plates
- computation time 446, 458–9, 460, 461
- condition number (CN) 146–9
- constitutive equations  
 differential quadrature element method 328–9  
 functionally graded plates 295–7  
 tapered thin-walled composite members 91–7
- coordinate systems 79, 80, 81
- critical buckling 69, 73
- critical buckling moment 67, 68, 69, 71
- cross-section analysis 40, 44, 45–53  
 illustration 52–3  
 intermediate nodes 50–2
- cross-section constants 22–3
- curvatures of tapered thin-walled composite members 82–6
- curved boundaries, plates with 240–4
- cylindrical shells 244–6  
 stepped and stiffened 246–50
- Darcy's law 207
- deflections  
 central *see* central deflection  
 floating plated structures 450–2, 459, 461  
 variable water depth 462, 463  
 free end deflection of circular beam 109–11  
 tip end of cantilever beam 108, 110
- deformation modes 39, 40–1, 52–3
- I-section beams 67, 68
- lipped channel members 56–9
- modal participation diagrams *see* modal participation diagrams
- degrees of freedom 302
- dependent natural nodes (DN) 48, 49, 50
- derivatives  
 approximation and LSFD method 119–23  
 discretisation of 123–4, 127–8
- differential quadrature element method 322–75
- DQ-Galerkin method 325–6
- imperfection modes 338–9  
 numerical results 345–70  
 FGM laminated plates under thermo-electro-mechanical loading 357–70, 371  
 imperfect FGM laminated plates 345–56
- theoretical formulations 327–38  
 basic equations 327–31  
 nonlinear governing equations 331–4  
 nonlinear vibration analysis 336–8  
 pre-vibration analysis 334–6  
 validation studies 339–45
- dimension reduction 227–8
- direct stiffness method 24–31
- discrete finite element model 300–2
- discretisation of derivatives 123–4, 127–8
- displacement  
 GBT 41, 43  
 membrane displacements 46, 47, 49–50, 175  
 warping displacement 49–50  
 generalised 55, 91  
 Levy solution method and transverse displacement 255–6  
 tapered thin-walled composite members 82–6, 89, 91  
 strain in terms of displacement 103–6
- through-the-thickness distribution  
 FGM square plates 306–9  
 laminated rectangular plates 305, 306
- trapezoidal Mindlin plate elements and transverse displacement 175

- displacement field  
 CPT 193, 275–6  
 differential quadrature element  
 method 327–8  
 FSDT 277  
 GBT 41, 46–7, 48, 51, 55  
 TSDT 277  
 displacement method 46–7  
 distortional vibration 36, 52–3  
*see also* generalised beam theory  
 (GBT)  
 distributed transfer function method  
 (DTFM) 219–53  
 free vibration of plates and shells  
 235–50  
 circular and sectorial plates  
 238–40  
 cylindrical shells 244–6  
 other plate and shell structures 250  
 plates with curved boundaries  
 240–4  
 rectangular plates 236–8  
 stepped and stiffened cylindrical  
 shells 246–50  
 for multidimensional continua 227–35  
 comparison of methods 234–5  
 finite difference DTFM 233,  
 234–5, 236, 237  
 Fourier series-based DTFM  
 229–30, 234–5, 244–50  
 general concepts 227–8  
 Ritz-based DTFM 230–2, 234–5  
 strip DTFM 232–3, 234–5, 236–7,  
 238, 239–40  
 for one-dimensional continua 220–7  
 dynamic response via distributed  
 transfer functions 224–5  
 eigenvalue solutions 223  
 nonuniformly distributed systems  
 227  
 spatial state formulation 220–3  
 synthesis of multi-body systems  
 225–7  
 domain decomposition method 254–74  
 Donnell-Mushtari cylindrical shells  
 245–6, 247–50  
 dynamic stiffness matrix of tapered  
 member 24
- eigenfunction expansion 219  
 eigenvalue problems 53
- eigenvalue solutions for DTFM 223  
 electrical loading  
 applied actuator voltage and pre-  
 stressed FGM laminated plates  
 367, 370  
 FGM hybrid laminated plates 413–15,  
 416, 417, 418  
 thermo-electro-mechanical preload *see*  
 thermo-electro-mechanical  
 preload  
 unsymmetric cross-ply laminated  
 plates 404, 406, 407  
*see also* piezoelectrics  
 element stiffness matrix 24, 26–7, 55  
 elementary flexural functions 51  
 elementary warping functions 46, 47, 48,  
 49, 50  
 elliptical plates 135–7  
 end shear 17  
 energy function  
 tapered beams 7, 24  
 vibrations of rectangular plates 193–6  
 equations of motion  
 classical thin plate theory 255  
 differential quadrature element  
 method 327–31  
 nonlinear governing equations  
 331–4  
 extended Kantorovich method 194–7  
 free vibration of plates 123  
 and boundary conditions 126–7  
 discretisation by LSFD method  
 127–8, 133–4  
 hybrid laminated plates 379–84  
 plate theories 277–80  
 tapered beams 4–5, 7  
 linearly tapered cantilever 17–18  
 straight-tapered beam combination  
 14–15  
 VLFS deflections 450–2  
 equilateral triangular plates 156  
 equilibrium equations  
 GBT 44  
 thin-walled composite members  
 97–100  
 dynamic equations of equilibrium  
 99–100  
 incremental equilibrium equation 99  
 total equilibrium equation 97–8  
 exact element method 196–7  
 extended Kantorovich method 192–218

- numerical examples 197–215  
 clamped plate 197–207  
 completely free plate 207–15, 216,  
 217  
 vibrations of rectangular plates 193–7  
   basic equations 193–4  
   derivation of equations of motion  
   194–6  
 Kantorovich procedure 194  
   solution procedure 196–7  
 external forces, work due to 3–4, 297–9,  
 451  
 extrapolation-interpolation operator  
 429–32, 434–5  
 hybrid GA-EI approach 433, 434–5,  
 443  
 identification of plated structure  
 435–41, 442
- ‘far’ cells 458  
 fast multipole method 446–7, 454–64  
   application 457–9  
   implementation to higher-order  
     boundary element method  
   455–6  
   numerical examples 459–62, 463, 464  
 FEAST-C 108, 110, 113  
 fibre-reinforced plastic (FRP) 77  
 finite difference DTFM (FD-DTFM) 233,  
 234–5  
   rectangular plate 236, 237  
 finite difference method (FDM) 118  
 finite element method (FEM) 77, 145,  
 219, 254, 446  
   aircraft wing model 435–7  
   circular and sectorial plates 239–40  
   comparison with DTFM 234, 235  
   FGM plates 299–302  
     discrete finite element model  
       300–2  
     variational formulation 299–300  
   GBT vibration analysis and 53–5  
   h-version 145  
   L-shaped plates 238  
   p-version *see p*-finite element method  
   plates with curved boundaries 242, 243  
   rectangular plates 236–7  
   ring-stiffened cylindrical shell 249–50  
   tapered beams 2, 20–31  
   tapered thin-walled composite  
     members
- beam model 100–3  
 plate/shell formulation 103–8  
 thin-walled members 37–8  
 finite strip method 219, 254  
   thin-walled members 38–9  
 first-order branches 48, 49  
 first-order shear deformation theory  
 (FSDT) 276–7, 324  
 equations of free vibration 278–80  
 FGM plates 301–2  
   bending analysis 303–11  
   free vibration analysis 312–16  
 frequency relationship with CPT  
 280–3  
 frequency results 286–8, 289  
 modification of frequency  
   relationship for complicating  
   effects 288–91  
 fitness function 423  
 flexural-torsional vibration (global  
   vibration) 36–40, 52–3  
   *see also* generalised beam theory  
 (GBT)  
 floating plated structures 445–65  
   application of fast multipole method  
   457–9  
   boundary integral equation 449–50  
   boundary value problem 447–9  
   equation of motion for deflections  
   450–2  
   formulation for hydroelastic analysis  
   452–4  
   implementation to higher-order  
     boundary element method  
   455–6  
   multipole expansion of Green’s  
     function 454–5  
   numerical examples 459–62, 463, 464  
 forced vibration  
   FGM hybrid laminated plate 411–15,  
   416, 417, 418  
   initially stressed antisymmetric angle-  
     ply laminated plate 392–5  
   p-finite element method for clamped  
     plates 182–6, 187, 188, 189  
   unsymmetric cross-ply laminated  
     plate with piezoelectric layers  
     399–407  
 Fourier p-elements 145–6, 150  
   ill-conditioning problem 146–9  
   *see also* p-finite element method

- Fourier series 182, 219  
 Fourier series-based DTFM (FS–DTFM) 229–30, 234–5  
 cylindrical shells 244–6  
 stepped and stiffened cylindrical shells 246–50  
 free edges  
   abrupt changes in properties 258, 259–72  
   extended Kantorovich method for completely free square plates 207–15, 216, 217  
 imperfect FGM laminated plates 354, 356  
 LSFD method and thin plates 126–7, 131–4  
 $p$ -finite element method for polygonal plates 177, 179  
 free vibration  
   analysis for FGM plates 311–16, 317  
   DTFM and free vibration analysis 226–7  
     plates and shells 235–50  
   equations for CPT, FSDT and TSDT 277–80  
   FGM hybrid laminated plates 411, 412  
   initially stressed antisymmetric angle-ply laminated plate 392  
 $p$ -finite element method for clamped plates 182–6, 187, 188, 189  
 unsymmetric cross-ply laminated plate with piezoelectric layers 399  
 frequency parameters  
   abrupt changes in properties  
     hinged plates 264–8, 269, 270–2  
     multi-span plates 264, 265, 267, 268  
     stepped thickness variations 260, 261, 263  
   differential quadrature element method 340, 341, 342  
 FGM laminated plates  
   imperfect 346–50, 351  
   pre-stressed 357–62  
 free vibration of thin plates 126  
 linearly tapered cantilever 18–20  
   proped cantilever 20, 21  
 LSFD method  
   annular plates 141, 142  
   circular and elliptical plates 135–7  
   symmetric trapezoidal plates 139–41  
 $p$ -finite element method 173–4  
 annular plate on Pasternak foundations 170–1, 174  
 cantilever quadrilateral plates 157  
 equilateral triangular plates 156  
 fully clamped regular polygonal plates 158, 162  
 hexagonal plates on Pasternak foundations 176–7  
 nonlinear vibration of symmetric trapezoidal plates 183, 184  
 octagonal plates on Pasternak foundations 178–9  
 pentagonal plate with cut-out 158, 160  
 pentagonal-star plates 163  
 quadrilateral plate 157  
 simply supported square plates 154, 155, 159–61, 165  
 skew plate 166  
 skew plate on Pasternak foundations 168  
 square plates on Pasternak foundations 167  
 trapezoidal plates on Pasternak foundations 169, 171  
 triangular plates on Pasternak foundations 170, 173  
 tapered beams  
   finite element method 30, 31  
   straight-tapered combination 16, 17  
   supported at both ends 8, 9, 10, 13, 14  
 frequency relationships 275–92  
   equations of free vibration 277–80  
   frequency results 286–8, 289  
   modification for complicating effects 288–91  
 plate theories 275–7  
 relationship between frequencies of FSDT and CPT 280–3  
 relationship between frequencies of TSDT and CPT 283–6  
 frequency response of a continuum 224  
 frequency response function curves  
   skew plate and nonlinear vibration 186, 187  
   trapezoidal plate and nonlinear vibration 186, 189  
 functionally graded material (FGM)  
   hybrid laminated plates 407–15

- forced vibration 411–15, 416, 417, 418  
 free vibration 411, 412  
 functionally graded material (FGM)  
   plates 293–321  
   finite element model 299–302  
     discrete finite element model  
       300–2  
     variational formulation 299–300  
 numerical results 302–16  
   bending analysis 303–11, 312  
   free vibration analysis 311–16, 317  
 theoretical formulation 294–9  
   constitutive equations 295–7  
   Hamilton's principle and stress  
     resultants 297–9  
   kinematics of TSDT 294–5  
 functionally graded materials (FGMs)  
   323–5, 378–9  
 nonlinear vibrations of FGM  
   laminated plates *see* differential  
     quadrature element method  
   *see also* functionally graded material  
     (FGM) hybrid laminated plates;  
     functionally graded material  
     (FGM) material plates  
 fundamental frequencies  
   abrupt changes in properties  
     hinged plates 268–70  
     multi-span plates 263–4, 266  
     stepped thickness variations 262–3  
   FGM plates 312–16, 317  
   laminated plates 311–12, 313, 314  
   pre-stressed FGM laminated plates  
     363, 364, 365  
   ring-stiffened cylindrical shell 249–50  
   tapered beams 8, 10, 29, 30  
   unsymmetric cross-ply laminated plate  
     399–401  
   *see also* natural frequencies  
 fundamental vibration mode  
   I-section beams 70, 71, 72  
   lipped channel members 59–61, 64, 66  
     shape 66, 67  
   shape and LSFD for circular plate  
     137–8, 139  
 FUNGEN 103  
 Galerkin method 53–4, 219  
   DQ-Galerkin method 325–6  
 generalised beam theory (GBT) 36–76  
   background 39–40  
   illustrative examples 56–73  
     I-section beams 66–73  
     lipped channel members 56–66, 67  
   vibration analysis 40–55  
     cross-section analysis 40, 44,  
       45–53  
     formulation 40–4  
     member analysis 40, 44, 53–5  
 generalised differential quadrature (GDQ)  
   method 118  
 generalised displacement 55, 91  
 generalised forces 94–6  
 generalised strain 91  
 generalised stress resultants 96–7  
 generalised torsion stiffness components  
   42–3  
 generalised warping stiffness components  
   42  
 genetic algorithms (GA) 422–4, 427–8,  
   429, 441  
   formulation 423–4  
   hybrid GA-EI approach 433, 434–5,  
     443  
     identification of plated structure  
       435–41, 442  
   hybrid GA-interpolation approach  
     432–4, 443  
     identification of plated structure  
       435–41, 442  
   hybrid GA-MV method 424–9, 441–3  
     identification of plated structure  
       435–41, 442  
     limitations 429–30  
 geometric imperfection sensitivity 350, 352  
 geometric stiffness 102  
 global strain vector 105  
 global-type imperfections 338–9  
   vibrational behaviour of imperfect  
     FGM laminated plates 348–50,  
       351, 353  
 global vibration phenomena 36–40, 52–3  
   *see also* generalised beam theory  
     (GBT)  
 GMRES solver 459, 460, 461  
 governing equations *see* equations of  
   motion  
 graphite-epoxy 399, 401, 402–3  
 Green Lagrange strain tensor 86  
 Green's function 446–7, 449–50  
   multipole expansion of 454–5

- time-domain formula 224–5  
grid lines 233
- h*-version of FEM 145  
Hamilton's principle 25, 99, 231, 297–9,  
451  
'hard-spring' vibration behaviour 352,  
372  
helicoidal elements 100–2  
hexagonal plates 171–3, 175, 176–7  
hierarchical *p*-elements 145–6  
    ill-conditioning problem 146–9  
        *see also p*-finite element method  
high-order derivatives 123–4  
higher-order boundary element method  
(HOBEM) 446, 455–64  
higher-order branches 48–9  
higher-order shear deformation plate  
theory (HSDPT) 324, 327,  
379–80  
    *see also* third-order shear deformation  
theory (TSDT)  
hinged rectangular plates 259, 264–72  
hybrid GA-EI method 433, 434–5, 443  
    identification of plated structure  
    435–41, 442  
hybrid GA-interpolation method 432–4,  
443  
    identification of plated structure  
    435–41, 442  
hybrid GA-MV method 424–9, 441–3  
    identification of plated structure  
    435–41, 442  
    limitations 429–30  
hybrid laminated plates 376–421  
    FGM hybrid laminated plates 407–15  
        forced vibration 411–15, 416, 417,  
        418  
        free vibration 411, 412  
    governing equations 379–84  
    initially stressed antisymmetric angle-  
        ply laminated plates 391–5  
        forced vibration 392–5  
        free vibration 392  
    solution methodology 384–91  
    unsymmetric cross-ply laminated plate  
        with piezoelectric layers  
        395–407  
        forced vibration 399–407  
        free vibration 399  
hybrid-type VLFS 463–4
- hydroelastic analysis *see* floating plated structures  
HYDYN 103
- I-section beams 56, 66–73  
identification, structural *see* structural identification  
ill-conditioning problem 146–9  
imperfect plates 322–3  
    FGM laminated plates 327–31,  
    345–56, 372  
        linear vibration 346–52  
        nonlinear vibration 352–6  
    imperfection modes 338–9  
    nonlinear vibration of simply supported isotropic plates 343,  
    345  
    nonlinear vibration of simply supported laminated plates 343–4  
in-plane cross-section displacements 43  
in-plane displacement constraints 367–70,  
371  
in-plane stresses  
    FGM square plates 305–9, 310, 311  
    laminated plates 303–4  
    vibration behaviour of pre-stressed  
        FGM laminated plates 367, 369  
independent natural nodes (IN) 48–9, 50  
intermediate line supports 259, 263–4,  
265, 266, 267, 268  
intermediate nodes 50–2  
internal line hinges 259, 264–72  
internal strain energy *see* potential  
(strain) energy  
interpolation functions 2, 21–4  
    compared with direct stiffness  
        approach 29–30  
interpolation operator 429–34  
    hybrid GA-I model 432–4, 443  
        identification of plated structure  
        435–41, 442  
isoparametric strip distributed transfer  
function method (ISDTFM)  
241–4
- Jacobi iteration method 103  
Jacobian matrix 104, 149
- Kantorovich method 192, 194  
    extended *see* extended Kantorovich  
method

- kinetic energy 297–8  
 GBT 43  
 tapered beams 4, 6–7, 25  
 tapered thin-walled composite members 107–8  
 VLFS 451
- Kirchhoff hypothesis 276  
 Kronecker delta 147–8
- L-shaped plate 237–8  
 Lagrange interpolation functions 301–2  
 lamina, composite 106–7  
 laminated composite structures 293, 376–8  
 laminated plates  
   cross-ply laminated plates  
 bending analysis 303–5, 306  
 free vibration analysis 311–12, 313, 314  
   hybrid laminated plates *see* hybrid laminated plates  
 least squares-based finite difference method (LSFD) 118–44  
   chain rule for discretisation of derivatives 123–4, 127–8  
   computation of stress resultants 134–5  
   discretisation of the governing equation 127–8  
 formulations for derivative approximation 119–23  
 formulations in local coordinates at boundary 124–6  
 governing equation and boundary conditions for thin plates 126–7  
 numerical examples 135–41  
   annular plate 141, 142  
   circular and elliptical plates 135–9  
   symmetric trapezoidal plate 139–41  
 numerical implementation of boundary conditions 128–34  
   clamped edge 129–30  
   free edge 131–4  
   simply supported edge 128–9  
 Legendre  $p$ -elements 145–6, 150  
   ill-conditioning problem 146–9  
   *see also*  $p$ -finite element method  
 Levy approach 254–9  
   in association with domain decomposition method and state-space technique 254–74
- Lévy-type solution 230  
 line supports, plates with 259, 263–4, 265, 266, 267, 268  
 linear behaviour theory 102  
 linear finite elements (LFE) 183, 184  
 linear vibration  
   imperfect FGM laminated plates 346–52  
   pre-stressed FGM laminated plates 357–62  
 lipped channel members 56–66, 67  
 local coordinates 105  
   LSFD formulation in local coordinates at boundary 124–6  
 local-plate deformation 36, 50–3  
   *see also* generalised beam theory (GBT)  
 local scaling 120–1  
 local search (LS) operators  
   extrapolation-interpolation operator 429–32, 434–5  
   interpolation operator 429–34  
   *see also* hybrid GA-EI method; hybrid GA-interpolation method; hybrid GA-MV method  
 local-type imperfections 338–9  
   vibrational behaviour of FGM laminated plates 348, 349, 351, 353, 354  
 local vibration phenomena 36–40  
   *see also* generalised beam theory (GBT)  
 LU factorisation 454, 459, 460
- mass matrices  
 GBT 55  
 ill-conditioning problem 147–8  
 $p$ -finite element method  
   nonlinear vibration 180–1  
   plates on Pasternak foundations 164–7  
   trapezoidal Mindlin plate elements 151–4  
   tapered beams 24, 27–9  
   tapered thin-walled composite members 100, 107–8  
 maximum absolute error 435, 437, 438–9, 441, 442  
 mean absolute error 435, 437, 438–41, 442  
 mean-square error 423  
 mega-float 445, 446  
   *see also* floating plated structures

- member analysis 40, 44, 53–5  
 beam finite element 54–5  
 membrane displacements 46, 47, 49–50, 175  
 membrane stress 306–11  
 memory allocation 446, 457, 459, 460  
 minimum energy, principle of 195  
 modal expansion approach 445–6  
 modal participation diagrams  
   I-section beams 68, 69, 70, 72  
   lipped channel members 59–60, 61–3,  
     65, 66  
 mode shapes  
   cantilever semicircular beam 113, 114  
 DTFM  
   plates with curved boundaries 243  
   stepped cylindrical shells 248, 249  
 extended Kantorovich method  
   clamped square plate 198–205  
   completely free square plate 207,  
     208–14  
 LSFD method 137–8, 139  
 quadrilateral plate 158  
 thin-walled composite cantilever beam  
   113  
 trapezoidal plate on Pasternak  
   foundations 169–70, 172  
 modification factors 288–91  
 modified warping constant 88  
 multi-body systems 225–7, 235, 237–8  
   assembly of components 225–6  
   static and dynamic analysis 226–7  
   transfer function representation of  
     components 225  
 multidimensional continua, DTFM and  
   227–35  
 multipole expansion point 454–5, 457, 458  
   *see also* fast multipole method  
 multi-span rectangular plates 259, 263–4,  
   265, 266, 267, 268  
 multivariate (MV) method 424  
   hybrid GA-MV method 424–9, 441–3  
     identification of plated structure  
       435–41, 442  
     limitations 429–30  
 natural frequencies  
   aircraft wing model 435, 437  
   antisymmetric angle-ply laminated  
     plates 393  
 DTFM  
   L-shaped plate 238  
 plates with curved boundaries 242,  
   243  
 rectangular plates 236–7  
 semicircular plate 239–40  
 stepped cylindrical shells 247–8  
 extended Kantorovich method 197  
   clamped square plate 197–8  
   completely free square plate 207, 208  
 FGM hybrid laminated plates 411,  
   412, 413–14, 415  
 GBT analysis  
   I-section beams 69–73  
   lipped channel members 59–63,  
     64–6  
 ill-conditioning problem 148–9  
 nonprismatic thin-walled composite  
   beam 112  
 plates with point supports 173, 180  
 simply supported wide flange thin-  
   walled composite beam 111  
 unsymmetric cross-ply laminated  
   plates with piezoelectric layers  
     403–4  
   *see also* fundamental frequencies  
 natural nodes 45, 46, 48–9, 50, 51, 52, 53  
 ‘near’ cells 458  
 nodal displacements 105–6, 225–6, 227  
 nodal lines 232  
 nodal patterns 275  
 nodal rotations 46–7  
 nodes 225, 226  
 nonlinear to linear frequency ratio  
   clamped isotropic thick plates 340–3  
   FGM hybrid laminated plates 414–15,  
     416, 417  
 FGM laminated plates  
   imperfect 351, 352–6  
   pre-stressed 362–70, 371  
 initially stressed laminated plates 392,  
   393–4  
 unsymmetric cross-ply laminated plate  
   with piezoelectric layers 399,  
     401, 402, 404, 405, 406  
 nonlinear vibration  
   clamped plates 174–89  
     arc-length iteration for free and  
       forced vibration 182–6, 187,  
       188, 189  
   differential quadrature element  
     method *see* differential  
       quadrature element method

- FGM laminated plates  
 imperfect 352–6  
 pre-stressed 362–70, 371
- hybrid laminated plates *see* hybrid laminated plates
- nonuniformly distributed systems 227
- normal stress resultant 44
- number of iterations 459, 461
- numerical approaches to tapered beams 5, 6–8, 9, 10
- numerical integration  
 errors and *p*-version elements 159–61  
 properties of a tapered thin-walled composite member 102–3
- octagonal plates 171–3, 175, 178–9
- one-dimensional continua, DTFM for 220–7
- orthotropic approximation 249–50
- out-of-plane cross-section displacements 43
- p*-finite element method 145–91  
 condition number 146–9  
 geometric nonlinear vibration of clamped plates 174–86  
 arc-length iteration for free and forced vibration 182–6, 187, 188, 189  
 transverse vibration of plates on Pasternak foundations 164–74, 175, 176, 177, 178, 179, 180
- trapezoidal Mindlin plate elements 149–64  
 effect of numerical integration 159–61  
 equilateral triangular plates 156
- fully clamped pentagonal-star plates 159, 163
- fully clamped polygonal plates 158–9, 161, 162
- pentagonal plate with cut-out 157–8, 159, 160
- quadrilateral plate 157, 158
- square plates 154–5
- parameter identification *see* structural identification
- Pasternak foundations  
 FSDT-CPT relationship 290  
 transverse vibration of plates on 164–74, 175, 176, 177, 178, 179, 180
- pb-2 Ritz method 154, 157, 159, 163
- pentagonal plate with central cut-out 157–8, 159, 160
- pentagonal-star plate 159, 163
- perturbation technique 384, 389–91
- Picard method 335–6
- piezoelectrics 324–5, 328–9, 378
- FGM hybrid laminated plates 407–15, 416, 417, 418
- nonlinear vibrations of FGM laminated plates *see* differential quadrature element method
- thermo-electro-mechanical preload *see* thermo-electro-mechanical preload
- unsymmetric cross-ply laminated plate with piezoelectric layers 395–407
- plate/steel element approach for tapered thin-walled composite members 103–8
- point supports 173, 180
- polygonal plates 145  
 frequency relationships for simply supported 286–8, 289  
 CPT and FSDT 282–3  
 CPT and TSDT 285–6  
 modifications of FSDT-CPT relationship 288–91
- p*-element analysis  
 fully clamped 158–9, 161, 162  
 on Pasternak foundations 171–3, 175, 176–9
- potential (strain) energy  
 composite lamina 106  
 GBT 42  
 tapered beams 3–4, 6–7, 25  
 VLFS 451
- power series 7
- pre-stressed laminated plates 322, 377–8  
 antisymmetric angle-ply laminated plates 391–5  
 forced vibration 392–5  
 free vibration 392
- FGM laminated plates  
 nonlinear governing equations 331–4  
 nonlinear vibration analysis 336–8  
 pre-vibration analysis 334–6  
 vibrational behaviour 346, 357–72
- prismatic-linearly tapered beam 14–17

- propced cantilever 20, 21  
 pyramid beam 30  
 PZT-5A 399, 402–3  
 PZT G-1195N 357
- quadrant-tree 458  
 quadrilateral cantilever plate 157, 158
- Rayleigh-Ritz method 53–4  
 rectangular plates  
   abrupt changes in properties 255–9  
     hinged plates 259, 264–72  
     multi-span plates 259, 263–4, 265,  
       266, 267, 268  
     stepped thickness variations 258,  
       260–3  
   bending analysis of laminated plates  
     303–5, 306  
 DTFM 228–35  
   free vibration 236–8  
 extended Kantorovich method *see*  
   extended Kantorovich method  
 frequency parameters for simply  
   supported plates 286, 287  
 reduced FE model 435–7  
 refined FE model 435–7  
 ring-stiffened cylindrical shells 246, 247,  
   248–50  
 Ritz-based DTFM (R-DTFM) 230–2,  
   234–5  
 Ritz method 219, 254  
   pb-2 Ritz method 154, 157, 159, 163  
 Rodrigues formula 147  
 rotation  
   tapered thin-walled composite  
     members 82–6  
   trapezoidal Mindlin plate elements 175  
 rotational restraint stiffnesses 13, 14
- sandwich plate 290–1  
 sectorial plates 238–40  
 semi-analytical approaches 219, 446  
   DTFM *see* distributed transfer  
     function method  
 semi-analytical finite strip analysis 38  
 semicircular cantilever beam 112, 113, 114  
 semicircular plate 239–40  
 sensitivity indicator 350, 352  
 series solution methods 219, 240–1  
   comparison with DTFM 234, 235  
   tapered beams 7–8
- seventh-order interpolation polynomial  
   21–4  
 shear centre 79  
 shear correction factor 158–9  
 shear deformable plate theories 118, 275,  
   276–7  
 equations of free vibration 278–80  
 frequency relationships between CPT  
   and 280–91  
 frequency results 286–8, 289  
 modification for complicating  
   effects 288–91  
*see also* first-order shear deformation  
   theory (FSDT); higher-order  
   deformation plate theory  
   (HSDPT); third-order shear  
   deformation theory (TSDT)
- shear force 137, 139  
 effective shear forces for plates with  
   abrupt changes in properties  
   258–9  
 modal effective shear force  
   clamped square plate 205–6, 207  
   free square plate 210–15, 216, 217
- shear locking 154  
 shear material stiffness coefficients 321  
 shear strain 87–8  
 shear stress resultant 44  
 shell/plate element approach for tapered  
   thin-walled composite members  
   103–8
- side-thickness ratio 304, 313, 317  
 vibration behaviour of FGM  
   laminated plates  
   imperfect 348  
   pre-stressed 367, 371
- silicon nitride 345, 411, 413
- simple supports  
   abrupt changes in properties 258,  
     259–72  
   free vibration analysis for wide flange  
     beam 111  
   imperfect FGM laminated plates  
     346–8, 353, 354, 355, 356  
   linear vibration of FGM thin plates  
     340, 341  
   nonlinear vibration of imperfect  
     isotropic square plates 343, 344  
   nonlinear vibration of imperfect  
     laminated plates 343–4  
   polygonal plates and frequency

- relationships 282–3, 285–8, 289  
 tapered beams 8, 9, 10  
     straight-tapered combination 16  
 thin plates and LSFD method 126,  
     128–9  
 sine-type imperfections 338–9  
     vibrational behaviour of imperfect  
         FGM laminated plates 346–8,  
         351  
 skew angle 168, 171, 183–6, 188  
 skew plates  
     frequency relationships for simply  
         supported 289  
 $p$ -finite element method 161, 164, 165  
     nonlinear vibration 183–6, 187  
     Pasternak foundations 168, 169  
 ‘soft-spring’ vibration behaviour 356,  
     367, 372  
 space of test functions (space of  
     admissible variations) 299–300  
 spatial state formulation 220–3  
 spline finite strip method 38  
 square plates  
     bending analysis  
         FGM plates 305–11  
         laminated plates 303–4  
     extended Kantorovich method  
         197–215  
         clamped plate 197–207  
         completely free plate 207–15, 216,  
         217  
     free vibration analysis  
         FGM plates 312–16, 317  
         laminated plates 311–12, 313, 314  
     frequency parameters for simply  
         supported 286, 287  
     linear vibration of simply supported  
         FGM thin plates 340, 341  
     nonlinear vibration of simply  
         supported imperfect isotropic  
         plates 343, 344  
 $p$ -finite element method  
     numerical integration errors and  
         simply supported plates  
         159–61, 165  
     Pasternak foundations 167  
     trapezoidal Mindlin plate elements  
         154–5  
 stacking sequence 399, 400  
 stainless steel 345, 411, 413  
 state-space technique 255–9  
     in association with Levy approach and  
         domain decomposition method  
         254–74  
 static response of a continuum 224  
 stepped cylindrical shells 246, 247–8,  
     249  
 stepped thickness variations 258, 260–3  
 stiffened cylindrical shells 246, 247,  
     248–50  
 stiffness coefficients 299, 320–1  
 stiffness matrices  
     composite lamina 106–7  
     DTFM 226–7  
     element stiffness matrix 24, 26–7, 55  
     extended Kantorovich method 197  
     finite element beam model 100, 102  
     GBT 42–3, 55  
     hybrid laminated plates 383–4  
 $p$ -finite element method  
     nonlinear vibration 180–1  
     plates on Pasternak foundations  
         164–7  
     trapezoidal Mindlin plate elements  
         151–4  
 tapered beams 24  
 direct stiffness method 24–31  
 straight-tapered beam combination  
     13–17  
 strain  
     finite strains in tapered thin-walled  
         composite members 86–91  
     in terms of displacement for tapered  
         thin-walled composite member  
         103–6  
 stress distributions 306–11, 312  
 stress resultants  
     clamped square plate and extended  
         Kantorovich method 206–7  
     CPT, FSĐT and TSĐT 279–80  
     differential quadrature element  
         method 330–1  
     FGM plates 297–9  
     GBT 44  
     generalised 96–7  
     LSFD method 134–5, 143  
         circular plates 137–9  
 strip DTFM (SDTFM) 232–3, 234–5  
     circular and sectorial plates 239–40  
     L-shaped plate 238  
     rectangular plate 236–7  
     structural identification 422–44

- extrapolation-interpolation operator 429–32, 434–5  
 hybrid GA-EI method 433, 434–41, 442, 443  
 genetic algorithms (GA) 422–4, 427–8, 429, 441  
 formulation 423–4  
 hybrid GA-MV method 424–9, 435–43  
 limitations 429–30  
 identification of plated structures 435–41  
 modelling of an aircraft wing 435–7  
 parameter identification of aircraft wing model 437–41, 442  
 interpolation operator 429–34  
 hybrid GA-I method 432–4, 435–41, 442, 443  
 surface elevation 462, 464  
 symmetric cross-ply laminated plates 393–5  
 system identification 422
- tapered beams 1–35  
 background to dynamic response 3–5  
 both ends supported and linear tapering 6–17  
 analytical formulation 8–17  
 numerical formulation 6–8, 9, 10  
 finite element approach 2, 20–31  
 linearly tapered cantilever 17–20, 21  
 straight-tapered beam combination 13–17
- tapered thin-walled composite members 77–117  
 approach 79–80  
 assumptions 81–2  
 constitutive equations 91–7  
 equations of equilibrium 97–100  
   dynamic equations of equilibrium 99–100  
   incremental equilibrium equation 99  
   total equilibrium equation 97–8  
 finite element beam model 100–3  
   numerical integration for finding properties and stress resultants at a cross-section 102–3  
 formulation using plate elements 103–8  
 mass matrix 107–8
- stiffness matrix for composite lamina 106–7  
 strain in terms of displacement 103–6  
 geometric description of undeformed beam 80–1  
 kinematics 82–91  
   displacements, rotations, curvatures and twist 82–6  
   finite strains 86–91  
 numerical examples 108–12, 113, 114
- Taylor series expansion 119–20, 122
- temperature  
 change and vibration behaviour of pre-stressed FGM laminated plates 367, 369  
 FGM hybrid laminated plates 409–10, 413–15, 416, 417, 418  
 temperature dependency 414–15, 418  
 temperature field 414, 417, 418  
 hybrid laminated plates 381–2  
 unsymmetric cross-ply laminated plate with piezoelectric layers 399–401, 404, 405
- thermo-electro-mechanical preload  
 nonlinear governing equations 331–4  
 nonlinear vibration analysis 336–8  
 pre-vibration analysis 334–6  
 vibrational behaviour of FGM  
   laminated plates 346, 355, 357–72  
   linear vibration 357–62  
   nonlinear vibration 362–70, 371
- thickness variations, stepped 258, 260–3
- thin-walled members 36–40  
 composite members of generic section  
   *see* tapered thin-walled composite members  
 finite element analysis 37–8  
 finite strip analysis 38–9  
 GBT *see* generalised beam theory
- third-order shear deformation theory (TSDT) 276, 277
- equations of free vibration 278–80
- FGM plates 301–2  
 bending analysis 303–11  
 free vibration analysis 312–16  
 kinematics 294–5
- frequency relationship with CPT 283–6  
 frequency results 286–8, 289
- torsional strains 89

- transfer matrix method 39  
 transformation matrix 47, 85  
   finite element beam model 100–2  
   transient response of a continuum 224–5  
   translational restraint stiffnesses 13, 14  
 transverse displacement  
   Levy solution method 255–6  
   trapezoidal Mindlin plate elements 175  
   transverse shear stress 306–11, 312  
 trapezoidal Mindlin plate elements 149–64  
   effect of numerical integration 159–61  
   equilateral triangular plates 156  
   fully clamped pentagonal-star plates  
     159, 163  
   fully clamped polygonal plates 158–9,  
     161, 162  
   nonlinear vibration of clamped plates  
     174–82  
   pentagonal plate with cut-out 157–8,  
     159, 160  
   quadrilateral plate 157, 158  
   square plates 154–5  
 trapezoidal *p*-elements 145  
 trapezoidal plates  
   frequency relationships for simply  
     supported 289  
   nonlinear vibration 183, 184, 186,  
     187, 188, 189  
   Pasternak foundations 168–70, 171,  
     172  
   symmetric and LSFD method 139–41  
 triangular *p*-elements 145  
 triangular plates  
   frequency parameters for simply  
     supported 288  
   *p*-finite element method  
     equilateral triangular plates 156  
     plates on Pasternak foundations  
       170, 172, 173  
 twist 82–6  
 twisting moment 137, 138  
 unbranched open cross-sections 45–8  
 unbranched sub-section 45–6, 48  
 uniform initial stress 288–90  
 unsymmetric cross-ply laminated plate with  
   piezoelectric layers 395–407  
   forced vibration 399–407  
   free vibration 399  
 variable water depth 442, 462, 463, 464  
 velocity potential 447–8  
 very large floating structures (VLFS)  
   445, 446  
   *see also* floating plated structures  
 vibration frequency relationships *see*  
   frequency relationships  
 virtual kinetic energy 297–8  
 virtual work  
   due to internal and external forces  
     297–9  
   tapered beams 3–5  
   tapered thin-walled composite  
     members 97–100  
 voltage *see* electrical loading  
 volume fraction 296  
   FGM hybrid laminated plates 408,  
     414, 416  
   FGM laminated plates  
     imperfect 345, 355, 356  
     pre-stressed 357–62  
   free vibration analysis 312, 313, 315,  
     316  
   square plates 306, 307, 308  
 wall transverse bending stiffness  
   components 42–3  
 warping displacement 49–50  
 wave response analysis *see* floating  
   plated structures  
 wedge beam 31  
 weighting functions 121–2  
 zirconia 357, 365  
   aluminium-zirconia FGM plates  
     312–16, 317